

Lecture Notes in Mechanical Engineering

Vitalii Ivanov · Ivan Pavlenko ·  
Oleksandr Liaposhchenko ·  
José Machado · Milan Edl *Editors*


# Advances in Design, Simulation and Manufacturing V

Proceedings of the 5th International  
Conference on Design, Simulation,  
Manufacturing: The Innovation  
Exchange, DSMIE-2022,  
June 7–10, 2022, Poznan, Poland –  
Volume 2: Mechanical and  
Chemical Engineering

 Springer

# Lecture Notes in Mechanical Engineering

## Editorial Board Member

Francisco Cavas-Martínez , Departamento de Estructuras, Construcción y Expresión Gráfica Universidad Politécnica de Cartagena, Cartagena, Murcia, Spain


## Series Editor

Fakher Chaari, National School of Engineers, University of Sfax, Sfax, Tunisia

## Editorial Board Member

Francesca di Mare, Institute of Energy Technology, Ruhr-Universität Bochum, Bochum, Nordrhein-Westfalen, Germany

## Series Editor

Francesco Gherardini , Dipartimento di Ingegneria “Enzo Ferrari”, Università di Modena e Reggio Emilia, Modena, Italy

## Editorial Board Member

Mohamed Haddar, National School of Engineers of Sfax (ENIS), Sfax, Tunisia

## Series Editor

Vitalii Ivanov, Department of Manufacturing Engineering, Machines and Tools, Sumy State University, Sumy, Ukraine

## Editorial Board Members

Young W. Kwon, Department of Manufacturing Engineering and Aerospace Engineering, Graduate School of Engineering and Applied Science, Monterey, CA, USA

Justyna Trojanowska, Poznan University of Technology, Poznan, Poland

**Lecture Notes in Mechanical Engineering (LNME)** publishes the latest developments in Mechanical Engineering—quickly, informally and with high quality. Original research reported in proceedings and post-proceedings represents the core of LNME. Volumes published in LNME embrace all aspects, subfields and new challenges of mechanical engineering. Topics in the series include:

- Engineering Design
- Machinery and Machine Elements
- Mechanical Structures and Stress Analysis
- Automotive Engineering
- Engine Technology
- Aerospace Technology and Astronautics
- Nanotechnology and Microengineering
- Control, Robotics, Mechatronics
- MEMS
- Theoretical and Applied Mechanics
- Dynamical Systems, Control
- Fluid Mechanics
- Engineering Thermodynamics, Heat and Mass Transfer
- Manufacturing
- Precision Engineering, Instrumentation, Measurement
- Materials Engineering
- Tribology and Surface Technology

To submit a proposal or request further information, please contact the Springer Editor of your location:

**China:** Ms. Ella Zhang at [ella.zhang@springer.com](mailto:ella.zhang@springer.com)

**India:** Priya Vyas at [priya.vyas@springer.com](mailto:priya.vyas@springer.com)

**Rest of Asia, Australia, New Zealand:** Swati Meherishi at [swati.meherishi@springer.com](mailto:swati.meherishi@springer.com)

**All other countries:** Dr. Leontina Di Cecco at [Leontina.dicecco@springer.com](mailto:Leontina.dicecco@springer.com)

To submit a proposal for a monograph, please check our Springer Tracts in Mechanical Engineering at <https://link.springer.com/bookseries/11693> or contact [Leontina.dicecco@springer.com](mailto:Leontina.dicecco@springer.com)

**Indexed by SCOPUS. All books published in the series are submitted for consideration in Web of Science.**

More information about this series at <https://link.springer.com/bookseries/11236>

Vitalii Ivanov · Ivan Pavlenko ·  
Oleksandr Liaposhchenko ·  
José Machado · Milan Edl  
Editors

# Advances in Design, Simulation and Manufacturing V

Proceedings of the 5th International  
Conference on Design, Simulation,  
Manufacturing: The Innovation Exchange,  
DSMIE-2022, June 7–10, 2022, Poznan,  
Poland – Volume 2: Mechanical and Chemical  
Engineering

 Springer

*Editors*

Vitalii Ivanov  
Sumy State University  
Sumy, Ukraine

Ivan Pavlenko  
Sumy State University  
Sumy, Ukraine

Oleksandr Liaposhchenko  
Sumy State University  
Sumy, Ukraine

José Machado  
University of Minho  
Guimarães, Portugal

Milan Edl  
University of West Bohemia  
Pilsen, Czech Republic

ISSN 2195-4356

ISSN 2195-4364 (electronic)

Lecture Notes in Mechanical Engineering

ISBN 978-3-031-06043-4

ISBN 978-3-031-06044-1 (eBook)

<https://doi.org/10.1007/978-3-031-06044-1>

© The Editor(s) (if applicable) and The Author(s), under exclusive license to Springer Nature Switzerland AG 2022, corrected publication 2022

This work is subject to copyright. All rights are solely and exclusively licensed by the Publisher, whether the whole or part of the material is concerned, specifically the rights of translation, reprinting, reuse of illustrations, recitation, broadcasting, reproduction on microfilms or in any other physical way, and transmission or information storage and retrieval, electronic adaptation, computer software, or by similar or dissimilar methodology now known or hereafter developed.

The use of general descriptive names, registered names, trademarks, service marks, etc. in this publication does not imply, even in the absence of a specific statement, that such names are exempt from the relevant protective laws and regulations and therefore free for general use.

The publisher, the authors and the editors are safe to assume that the advice and information in this book are believed to be true and accurate at the date of publication. Neither the publisher nor the authors or the editors give a warranty, expressed or implied, with respect to the material contained herein or for any errors or omissions that may have been made. The publisher remains neutral with regard to jurisdictional claims in published maps and institutional affiliations.

This Springer imprint is published by the registered company Springer Nature Switzerland AG  
The registered company address is: Gewerbestrasse 11, 6330 Cham, Switzerland

# Preface

This volume of Lecture Notes in Mechanical Engineering contains selected papers presented at the 5th International Conference on Design, Simulation, Manufacturing: The Innovation Exchange (DSMIE-2022), held in Poznan, Poland, on June 7–10, 2022. The conference was organized by the Sumy State University, Poznan University of Technology, and International Association for Technological Development and Innovations, in partnership with Technical University of Kosice (Slovak Republic), Kielce University of Technology (Poland), University of West Bohemia (Czech Republic), Association for Promoting Innovative Technologies—Innovative FET (Croatia), and Society for Robotics of Bosnia and Herzegovina (Bosnia and Herzegovina).

DSMIE Conference Series is the international forum for fundamental and applied research and industrial applications in engineering. The conference focuses on a broad range of research challenges in the fields of manufacturing, materials, mechanical, and chemical engineering, addressing current and future trends in design approaches, simulation techniques, computer-aided systems, innovative production approaches, Industry 4.0 strategy implementation for engineering tasks solving, and engineering education. DSMIE-2022 brings together researchers from academic institutions, leading industrial companies, and government laboratories worldwide to promote and popularize the scientific fundamentals of engineering.

DSMIE-2022 received 159 contributions from 20 countries around the world. After a thorough peer-reviewed process, the Program Committee accepted 84 papers written by 337 authors from 16 countries. Thank you very much to the authors for their contribution. These papers are published in the present book, achieving an acceptance rate of about 53%. Extended versions of selected best papers will be published in scientific journals: Management and Production Engineering Review (Poland), Journal of Engineering Sciences (Ukraine), Advances in Thermal Processes and Energy Transformation (Slovak Republic), Assembly Techniques and Technology (Poland), Machines (Switzerland), and a special issue of Sustainability (Switzerland) “Industry 4.0 Technologies for Sustainable Asset Life Cycle Management.”

We would like to thank members of the Program Committee and invited external reviewers for their efforts and expertise in contributing to reviewing, without which it would be impossible to maintain the high standards of peer-reviewed papers. One hundred five Program Committee members and 23 invited external reviewers devoted their time and energy to peer-reviewing manuscripts. Our reviewers come from all over the world, represent 19 countries, and are affiliated with more than 80 institutions.

Thank you very much to keynote speakers: Prof. George-Christopher Vosniakos (National Technical University of Athens, Greece), Prof. Dariusz Mazurkiewicz (Lublin University of Technology, Poland), Prof. Szymon Wojciechowski (Poznan University of Technology, Poland), Prof. Sahin Yildirim (Erciyes University, Turkey), Dr. Valdimir Dolgikh (Seco Tools AB, Sweden), and Mr. Krystian Kogut and Przemyslaw Pasich (InterMarium, Poland).

The book “Advances in Design, Simulation and Manufacturing V” was organized in two volumes according to the main conference topics: Volume 1—Manufacturing and Materials Engineering and Volume 2—Mechanical and Chemical Engineering. Each volume is devoted to research in design, simulation, and manufacturing in the main conference areas.

The second volume consists of four parts. The first part aims at ensuring vibration reliability of turbines, studying the behavior of a rod under external loads and the stress–strain state of structures. Recent advancements in rotor dynamics and stability of centrifugal pumps for nuclear power plants are also presented in this part. Moreover, this part included research works on the influence of inertial loads on the operation of overhead crane girders and the dynamics of a particle by a curvilinear surface under rotation. Finally, supersonic flows in blade channels are also studied in this part.

The second part includes a model of the pneumatic unit and a new method for optimization synthesis of vibro-impact systems. Also, it presents studies in designing hydraulic motors, modeling lifting particles of technological material by a vertical auger, and reducing working fluid pulsations in hydraulic machines. Finally, the effect of manufacturing tolerances on the hydrodynamic characteristics of plain bearings is also presented in the second part.

The third part is devoted to designing and modernizing fuel oil heating and tar cooling systems, oilfield wastewater systems, and heat exchange equipment. It demonstrates studies in comparative evaluation of the contact elements efficiency for barium sulfide solution carbonization and the application of low-frequency mechanical vibrations to develop highly efficient continuous extraction equipment. This part includes modeling hydraulic resistance and spray transfer in stabilized multiphase systems, designing reactors with mechanical mixers in biodiesel production, and justification of vibroventric external load during mechanical pressing of glycerin-containing products. Research on reducing granular material losses in a vortex chamber and designing wheat fiber with pumpkin pectin plant additive for use in the meat industry is also presented in this part.

The fourth part is based on recent developments in gas-dynamic cooling systems, designing marine diesel engines, and combined air cooling systems. Exhaust heat recovery in an integrated energy plant, jet-reactive turbine circular efficiency, and innovative hybrid power plant design are also included. Finally, this part is devoted to ensuring the efficiency of cooling air at the inlet of a marine engine with exhaust gas recirculation by ejector and absorption refrigeration.

We appreciate the partnership with Springer Nature, iThenticate, EasyChair, and our sponsors for their essential support during the preparation of DSMIE-2022.

Thank you very much to DSMIE team. Their involvement and hard work were crucial to the success of the conference.

DSMIE's motto is "*Together we can do more for science, technology, engineering, and education.*"

June 2022

Vitalii Ivanov  
Ivan Pavlenko  
Oleksandr Liaposhchenko  
José Machado  
Milan Edl





Robert Cep	VSB-Technical University of Ostrava, Czech Republic
Yelizaveta Chernysh	Sumy State University, Ukraine
Olivian Chiver	Technical University of Cluj-Napoca, Romania
Vasile George Cioata	Polytechnic University of Timisoara, Romania
Olaf Ciszak	Poznan University of Technology, Poland
Oguz Colak	Eskisehir Technical University, Turkey
Radu Cotetiu	Technical University of Cluj-Napoca, Romania
Nadezda Cubonova	University of Zilina, Slovak Republic
Ivan Cvitic	University of Zagreb, Croatia
Predrag Dasic	University Union "Nikola Tesla," Serbia
Yuliia Denysenko	Sumy State University, Ukraine
Oleksandr Derevianchenko	Odessa Polytechnic National University, Ukraine
Sergey Dobrotvorskiy	National Technical University "Kharkiv Polytechnic Institute," Ukraine
Milan Edl	University of West Bohemia, Czech Republic
Sulaymon Eshkabilov	North Dakota State University, USA
Mathieu Gautier	University Lyon, France
Renata Gnatowska	Czestochowa University of Technology, Poland
Mihaly Gorbe	John von Neumann University, Germany
Marta Grabowska	Poznan University of Technology, Poland
Jakub Grabski	Poznan University of Technology, Poland
Marek Gucwa	Czestochowa University of Technology, Poland
Domenico Guida	University of Salerno, Italy
Oleksandr Gusak	Sumy State University, Ukraine
Michal Hatala	Technical University of Kosice, Slovak Republic
Ihor Hrytsay	Lviv Polytechnic National University, Ukraine
Ihor Hurey	Lviv Polytechnic National University, Ukraine
Jozef Husar	Technical University of Kosice, Slovak Republic
Vitalii Ivanov	Sumy State University, Ukraine
Maryna Ivanova	National Technical University "Kharkiv Polytechnic Institute," Ukraine
Reza Jazar	Royal Melbourne Institute of Technology, Australia
Lydmila Kalafatova	Donetsk National Technical University, Ukraine
Isak Karabegovic	University of Bihac, Bosnia and Herzegovina
Gennadii Khavin	National Technical University "Kharkiv Polytechnic Institute," Ukraine
Lucia Knapcikova	Technical University of Kosice, Slovak Republic
Kateryna Kostyk	National Technical University "Kharkiv Polytechnic Institute," Ukraine
Jan Krmela	Alexander Dubcek University of Trencin, Slovak Republic
Ivan Kuric	University of Zilina, Slovak Republic
Yaroslav Kusy	Lviv Polytechnic National University, Ukraine

Maria Lazar	University of Petrosani, Romania
Vladimir Lebedev	Odessa Polytechnic National University, Ukraine
Oleksandr Liaposhchenko	Sumy State University, Ukraine
Slawomir Luszcynski	Kielce University of Technology, Poland
Jose Mendes Machado	University of Minho, Portugal
Ole Madsen	Aalborg University, Denmark
Angelos Markopoulos	National Technical University of Athens, Greece
Dariusz Mazurkiewicz	Lublin University of Technology, Poland
Mykola Melnychuk	Lutsk National Technical University, Ukraine
Ronald Mersky	Widener University, USA
Viktor Molnar	University of Miskolc, Hungary
Ronald Iosif Moraru	University of Petrosani, Romania
Dmitriy Muzylyov	Kharkiv Petro Vasylenko National Technical University of Agriculture, Ukraine
Arun Nagarajah	University of Duisburg-Essen, Germany
Marek Ochowiak	Poznan University of Technology, Poland
Daniela Onofrejova	Technical University of Kosice, Slovak Republic
Oleh Onysko	Ivano-Frankivsk National Technical University of Oil and Gas, Ukraine
Vitalii Pasichnyk	National Technical University of Ukraine “Igor Sikorsky Kyiv Polytechnic Institute,” Ukraine
Ivan Pavlenko	Sumy State University, Ukraine
Dragan Perakovic	University of Zagreb, Croatia
Marco Perisa	University of Zagreb, Croatia
Oleksandr Permiakov	National Technical University “Kharkiv Polytechnic Institute,” Ukraine
Jan Pitel	Technical University of Kosice, Slovak Republic
Grigore Marian Pop	Technical University of Cluj-Napoca, Romania
Oleksandr Povstyanoy	Lutsk National Technical University, Ukraine
Erwin Rauch	Free University of Bolzano, Italy
Michal Rogalewicz	Poznan University of Technology, Poland
Andrii Rogovyi	Kharkiv National Automobile and Highway University, Ukraine
Yiming Rong	Southern University of Science and Technology, China
Joanna Rosak-Szyrocka	Czestochowa University of Technology, Poland
Alessandro Ruggiero	University of Salerno, Italy
Vira Shendryk	Sumy State University, Ukraine
Lesya Shkitsa	Ivano-Frankivsk National Technical University of Oil and Gas, Ukraine
Robert Sika	Poznan University of Technology, Poland
Dusan Simsik	Technical University of Kosice, Slovak Republic
Volodymyr Sokolov	V. Dahl East Ukrainian National University, Ukraine
Marcin Sosnowski	Jan Długosz University of Częstochowa, Poland

Vadym Stupnytskyy	Lviv Polytechnic National University, Ukraine
Antoni Swic	Lublin University of Technology, Poland
Anastasiia Symonova	Kremenchuk Mykhailo Ostrohradskyi National University, Ukraine
Marek Szostak	Poznan University of Technology, Poland
Yuliia Tarasevych	AGH University of Science and Technology, Poland
Volodymyr Tonkonogyi	Odessa Polytechnic National University, Ukraine
Justyna Trojanowska	Poznan University of Technology, Poland
Michael Tseitlin	National Technical University “Kharkiv Polytechnic Institute,” Ukraine
Nicolae Ungureanu	Technical University of Cluj-Napoca, Romania
Alper Uysal	Yildiz Technical University, Turkey
Leonilde Rocha Varela	University of Minho, Portugal
George-Christopher Vosniakos	National Technical University of Athens, Greece
Jerzy Winczek	Czestochowa University of Technology, Poland
Szymon Wojcechowski	Poznan University of Technology, Poland
Oleg Zabolotnyi	Lutsk National Technical University, Ukraine
Jozef Zajac	Technical University of Kosice, Slovak Republic
Volodymyr Zavalov	National University of Food Technologies, Ukraine
Przemyslaw Zawadzki	Poznan University of Technology, Poland
Jan Zdebor	University of West Bohemia, Czech Republic
Lianyu Zheng	Beihang University, China
Predrag Zivkovic	University of Nis, Serbia
Justyna Zywiolok	Czestochowa University of Technology, Poland

### **Invited External Reviewers (in alphabetical order)**

Iryna Ablieieva	Sumy State University, Ukraine
Tygran Dzhuguryan	Maritime University of Szczecin, Poland
Oksana Gaponova	Sumy State University, Ukraine
Kateryna Ivanova	Sumy State University, Ukraine
Nikolaos Karkalos	National Technical University of Athens, Greece
Nadiia Kharchenko	Sumy State University, Ukraine
Vitalii Kolesnyk	Sumy State University, Ukraine
Sergii Kotliar	National Technical University of Ukraine “Igor Sikorsky Kyiv Polytechnic Institute,” Ukraine
Oleksandr Kupriyanov	Ukrainian Engineering Pedagogics Academy, Ukraine
Iurii Merzliakov	Sumy State University, Ukraine
Panagiotis Karmiris	National Technical University of Athens, Greece
Obratanski	

Emmanouil Papazoglou	National Technical University of Athens, Greece
Vita Pavlenko	Sumy State University, Ukraine
Emanuala Pop	Technical University of Cluj-Napoca, Romania
Serhii Sharapov	Sumy State University, Ukraine
Dimitrios Skondras-Giousios	National Technical University of Athens, Greece
Olexii Solovar	National Technical University of Ukraine “Igor Sikorsky Kyiv Polytechnic Institute,” Ukraine
Sebastian Sonntag	University of Duisburg-Essen, Germany
Valentin Tikhenko	Odessa Polytechnic National University, Ukraine
Anatolii Tkachuk	Lutsk National Technical University, Ukraine
Iryna Vaskina	Sumy State University, Ukraine
Tatiana Volina	National University of Life and Environmental Sciences of Ukraine, Ukraine
Dmytro Zhyhylii	Sumy State University, Ukraine

### **DSMIE Team (in alphabetical order)**

Kristina Berladir	Sumy State University, Ukraine
Olaf Ciszak	Poznan University of Technology, Poland
Yuliia Denysenko	Sumy State University, Ukraine
Oleksandr Gusak	Sumy State University, Ukraine
Vitalii Ivanov	Sumy State University, Ukraine
Oleksandr Liaposhchenko	Sumy State University, Ukraine
Slawomir Luscinski	Kielce University of Technology, Poland
Ivan Pavlenko	Sumy State University, Ukraine
Justyna Trojanowska	Poznan University of Technology, Poland

# Contents

## Fluid, Solid and Structural Mechanics

<b>Vibration Reliability of the Turbine Unit’s Housing Considering Random Imperfections</b> .....	3
Sergey Krasnikov, Andrii Rogovyi, Igor Mishchenko, Andrii Avershyn, and Valerii Solodov	
<b>The Behaviour of a Rod (Beam) Under the Influence of an External Power Load</b> .....	13
Viktoriya Pasternak, Oleg Zabolotnyi, Nataliia Ilchuk, José Machado, and Kostiantyn Svirzhevskiy	
<b>Stress-Strain State of the Floating Bollard’s Structure for a Shipping Gateway</b> .....	23
Ihor Sydorenko, Vladimir Tonkonogyi, Vladimir Semenyuk, Valeriy Lingur, and Yunxuan Zhang	
<b>Rotor Dynamics and Stability of the Centrifugal Pump CPN 600-35 for Nuclear Power Plants</b> .....	33
Ivan Pavlenko, Vitalii Simonovskiy, Anton Verbovyi, Oleksandr Ivchenko, and Vitalii Ivanov	
<b>Influence of Horizontal Inertial Loads on the Operation of Overhead Crane Girders</b> .....	47
Anatoliy Tkachev, Aleksey Tkachev, Oleksandr Fomin, Oleksandr Bondar, and Elena Naidenko	
<b>Organization of Transportation of a Particle by an Inclined Cylinder Rotating Around the Axis</b> .....	55
Tatiana Volina, Serhii Pylypaka, Yaroslav Kremets, Olena Kozlova, and Alla Rebrii	

<b>Supersonic Flow in the Blade Channel of the Nozzle with a Rotary Diaphragm at Small Degrees of Opening . . . . .</b>	<b>66</b>
Oleksandr Zhyrkov, Oleksandr Usatyi, Olena Avdieieva, and Yuri Torba	
<b>Numerical Simulations of Coupled Systems</b>	
<b>Model of the Pneumatic Positional Unit with a Discrete Method for Control Dynamic Characteristics . . . . .</b>	<b>81</b>
Mikhaylo Cherkashenko, Oleksandr Gusak, Aleksandr Fatyeyev, Nadezhda Fatieieva, and Alexander Gasiyk	
<b>A New Method of Optimization Synthesis of Vibro-Impact Systems . . .</b>	<b>91</b>
Volodymyr Gursky, Vitaliy Korendiy, Igor Kuzio, and Oleksandr Kachur	
<b>Influence of the Design Features of Orbital Hydraulic Motors on the Change in the Dynamic Characteristics of Hydraulic Drives . . . . .</b>	<b>101</b>
Anatolii Panchenko, Angela Voloshina, Shahriyor S. Sadullozoda, Oleg Boltyansky, and Valeriia Panina	
<b>Mathematical Model of Lifting Particles of Technological Material by Vertical Auger . . . . .</b>	<b>112</b>
Serhii Pylypaka, Tatiana Volina, Iryna Hryshchenko, Serhii Dieniezhnikov, and Iryna Rybenko	
<b>The Effect of Manufacturing Tolerances on the Hydrodynamic Characteristics of Plain Bearings . . . . .</b>	<b>123</b>
Yuliia Tarasevych and Ievgen Savchenko	
<b>Reducing Working Fluid Pulsations in Planetary Hydraulic Machines by Rational Design of the Distribution Systems . . . . .</b>	<b>133</b>
Oksana Yeremenko, Mamadamon A. Abdullo, Nataliia Boltianska, Stepan Mikhalchenko, and Valentyna Verkholantseva	
<b>Chemical Process Technology and Heat and Mass Transfer</b>	
<b>Design and Modernization of Circuit for Fuel Oil Heating and Tar Cooling . . . . .</b>	<b>147</b>
Tatiana Babak, Alexey Demirskyy, Gennadii Khavin, and Irina Riabova	
<b>Protection of Condensing Heat Exchange Surfaces of Boilers from Sulfuric Acid Corrosion . . . . .</b>	<b>157</b>
Victoria Kornienko, Roman Radchenko, Dmytro Konovalov, Viktor Gorbov, and Ivan Kalinichenko	
<b>Purification of Oilfield Wastewater by Inertial Methods . . . . .</b>	<b>167</b>
Oleksandr Liaposhchenko, Viktor Moiseev, Eugenia Manoilo, and Houssein Seif	

<b>Comparative Evaluation of the Contact Elements Efficiency for Barium Sulfide Solution Carbonization</b> . . . . .	177
Yurij Masikevych, Musii Tseitlin, Valentyna Raiko, Oleksii Shestopalov, and Vladimir Panasenko	
<b>Hydraulic Resistance and Spray Transfer in a Stabilized Three-Phase Foam Layer</b> . . . . .	187
Viktor Moiseev, Eugenia Manoilo, Kalif Repko, Natalia Ponomarova, and Denis Davydov	
<b>Design of Reactors with Mechanical Mixers in Biodiesel Production</b> . . .	197
Mikhailo Mushtruk, Larysa Bal-Prylypko, Natalia Slobodyanyuk, Yuriy Boyko, and Mykola Nikolaienko	
<b>Justification of Vibroventrentic External Load During Mechanical Pressing of Glycerin-Containing Products</b> . . . . .	208
Igor Palamarchuk, Mikhailo Mushtruk, Igor Lypovy, Ievgenii Petrychenko, and Ivan Vlasenko	
<b>Reduction of Granular Material Losses in a Vortex Chamber Supercharger Drainage Channel</b> . . . . .	218
Andrii Rogovyi, Volodymyr Korohodskyi, Artem Neskorozhenyi, Iryna Hrechka, and Serhii Khovanskyi	
<b>Application of Low-Frequency Mechanical Vibrations for Development of Highly Efficient Continuous Extraction Equipment</b> . . .	227
Volodymyr Zavialov, Taras Mysiura, Nataliia Popova, Yuliia Zaporozhets, and Valentyn Chornyi	
<b>Research of Wheat Fiber with Pumpkin Pectin Plant Additive</b> . . . . .	237
Marija Zheplinska, Volodymyr Vasylyv, Olena Deviatko, Sergii Ulianko, and Nataliia Kanivets	
<b>Energy Efficient Technologies</b>	
<b>Development of the Gas-Dynamic Cooling System for Gas Turbine Over-Expansion Circuit</b> . . . . .	249
Dmytro Konovalov, Halina Kobalava, Mykola Radchenko, Viktor Gorbov, and Ivan Kalinichenko	
<b>Marine Diesel Engine Inlet Air Cooling by Ejector Chiller on the Vessel Route Line</b> . . . . .	259
Maxim Pyrysunko, Andrii Radchenko, Veniamin Tkachenko, Anatoliy Zubarev, and Artem Andreev	
<b>Exhaust Heat Recovery in Integrated Energy Plant</b> . . . . .	269
Andrii Radchenko, Serhiy Forduy, Viktor Khaldobin, Oleksii Zielikov, and Oleksandr Rizun	



**Turbine Intake Air Combined Cooling Systems** . . . . . 278  
Mykola Radchenko, Volodymyr Korobko, Serhiy Kantor,  
Anatoliy Zubarev, and Olena Girzheva

**Jet-Reactive Turbine Circular Efficiency** . . . . . 288  
Tetiana Rodymchenko, Serhii Vanieiev, Stanislav Meleychuk,  
Michal Hatala, and Olha Miroshnychenko

**Innovative Hybrid Power Plant Design** . . . . . 299  
Lyudmila Rozhkova, Marina Savchenko-Pererva, Oleg Radchuk,  
Sergey Sabadash, and Eduard Kuznetsov






**Correction to: Mathematical Model of Lifting Particles  
of Technological Material by Vertical Auger** . . . . . C1  
Serhii Pylypaka, Tatiana Volina, Iryna Hryshchenko,  
Serhii Dieniezhnikov, and Iryna Rybenko

**Author Index**. . . . . 309

# **Fluid, Solid and Structural Mechanics**



# Vibration Reliability of the Turbine Unit's Housing Considering Random Imperfections

Sergey Krasnikov<sup>1</sup> , Andrii Rogovyi<sup>2</sup> , Igor Mishchenko<sup>1</sup> ,  
Andrii Avershyn<sup>1</sup> , and Valerii Solodov<sup>1</sup> 

<sup>1</sup> Kharkiv National Automobile and Highway University, 25, Yaroslava Mudrogo Street, Kharkiv 61002, Ukraine

<sup>2</sup> National Technical University “Kharkiv Polytechnic Institute”,  
2, Kyrpychova Street, Kharkiv 61000, Ukraine  
asrogovoy@ukr.net

**Abstract.** The solution to the problem of the power turbines vibration reliability at failures arising as a result of resonant frequency hit in the operating range of a rotor considering the randomness of the support rigidity change on the foundation is considered. The study finds a complex machine-building object - the steam turbine housing on the foundation. The subject of the study is the failure as a result of vibration resonance in the operating frequency range. The reason for failures can be various design and technological imperfections. They can be divided into two groups: imperfections resulting from design and creation, and on the other hand - deviations from the design parameters as a result of the long-time operation. A special factor in the occurrence of various imperfections (deviations) is the time over which the probability of trouble-free operation decreases. To solve the problem, the methods of oscillation theory, reliability, and the widely used finite element method are used. Based on experimental data on the accumulation of rigidity imperfections on the foundation, the series of calculations of natural frequencies and forms, which are once again compared with experimental data, is carried out. The obtained results determined the probability of failures in the operating frequency range from the most dangerous resonances.

**Keywords:** Industrial growth · Steam turbine · Stiffness · Fatigue failures · Eigenvalue · Reliability · Energy efficiency

## 1 Introduction

The actual power unit of the power plant is a complex system of turbines and a generator connected by a standard rotor and foundation [1, 2]. In addition to these elements, there are other essential systems and units, but they are not connected by a single foundation and are partially or entirely located in other workshops [3]. Typically, a single steam turbine system includes high (HP) and medium (MP) pressure cylinders, several low-pressure cylinders (LP), the generator, and the generator exciter [4]. The most pliable are the outriggers of the low-pressure rotor bearing, structurally made in one piece with the LP housing, which rests on the foundation through the plate balcony [5, 6]. Therefore, all

the LP housing structural elements are involved in reinforcing the bearings of the rotor bearings. This fundamentally distinguishes the fastening system of the rotor LP from the rotors HP, MP, and generator, whose bearing supports rest directly on the foundation. This approach is not generally accepted but is implemented in hundreds of actually created energy blocks [3, 7]. Many of these units are still in operation.

## 2 Literature Review

The authors have previously conducted numerical studies of various models of dynamic characteristics of the turbine-generator-foundation system elements and similar systems in general [8, 9]. Multiple approaches to modeling the turbine-generator-foundation system and comparing the efficiency of their application are described in [8]. The features of assessing the reliability of complex systems are described in [9]. The results of field tests [10, 11] allowed us to propose the following model of the turbine unit: LP, which is a complex system of shells, plates, and rods; foundation in the form of the system of plates and rods; other equipment [12, 13] is modeled in the form of concentrated masses.

When designing the foundation for turbines, from the very beginning, there is possible random scatter in the modulus of elasticity of concrete, associated with the manufacturing technology [14–16], which was higher at thermal power plants and nuclear power plants in the last century in the missing coalition [3, 10]. Recently, due to the depletion of the resources of most power plants in Europe, the task of modernizing existing power plants and using renewable energy [17, 18] has become urgent [18, 19]. It is economically advantageous to carry out a partial replacement of equipment, for example, leaving the old foundation to install a new turbine and generator. Therefore, considering the statistical variance of the characteristics of the stiffness of the resistance is an important problem since during the service life, there are temporary changes in the structure of concrete [3, 20]. This requires consideration of the rigidity of the LP body support as a random variable.

## 3 Research Methodology

We will use the solution to the reliability problem according to the following method: (1) creation of the mathematical model; (2) construction of geometric and computational models; (3) conducting a series of calculations of natural frequencies and forms of the system; (4) verification of the obtained intermediate results reliability; (5) obtaining reliability characteristics; (6) analysis of the obtained results.

We will use well-known approaches to the theory of oscillations, reliability, and the finite element method for mathematical modeling.

### 3.1 Mathematical Model for the Analysis of Natural Frequencies and Forms

The simple-element problem statement of the system natural frequencies has the form [8, 21]:

$$\left(\mathbf{K} - p_i^2 \mathbf{M}\right) \mathbf{V}_i = 0, i = 1 \div n, \quad (1)$$

where  $\mathbf{K}$ ,  $\mathbf{M}$  are the matrices of stiffness and mass, respectively,  $p_i^2$  is the natural frequency for  $\mathbf{V}_i$  natural form.

The method of iterations in subspace was used to determine the natural frequencies and forms.

### 3.2 Mathematical Model for Reliability Analysis

When solving the reliability problem, it is assumed that the rigidity of the body support on the foundation  $\mathbf{C}$  is a random variable whose probability density  $f(\mathbf{C})$  obeys the normal law with known parameters:  $m_C$  is the average (nominal) value;  $\delta_C^2$  is the variance. The maximum limit value  $\mathbf{C}$  corresponds to a rigid support. Since the stiffness parameters of the system under study are random [22, 23], the natural frequency spectrum  $\omega_i$  ( $i = 1, \dots, n$ ) will also be random. It is assumed [9] that in the small neighborhood of the nominal values of the natural frequencies  $P_i(m_C)$ , as a function of the stiffness  $\mathbf{C}$ , can be approximated by the Taylor series while preserving only the linear terms:

$$\omega_i(\mathbf{C}) = \omega_i(m_c) + (\mathbf{C} - m_c) \left. \frac{d\omega_i}{d\mathbf{C}} \right|_{\mathbf{C}=m_c}, \quad (i = 1, \dots, n). \quad (2)$$

In this case, the relationship between  $\omega_i$  and  $\mathbf{C}$  will be linear and the probability densities of the natural frequencies  $f_i(\omega_i)$  will obey the normal law with mathematical expectation  $m_{\omega_i}$  and variance  $\delta_{\omega_i}^2$ , which according to the Eq. (2) are determined from the relations:

$$m_{\omega_i} = \omega_i(m_C); \quad \delta_{\omega_i}^2 = \left[ \left. \frac{dP_i}{d\mathbf{C}} \right|_{\mathbf{C}=m_c} \right]^2 \delta_C^2 \quad (3)$$

The derivative  $dP_i/d\mathbf{C}$  is determined using finite-difference equations, the central differences were used in this paper.

The vibration reliability of the system [24–26] when considering failures that occur as a result of the natural frequencies in the operating range  $[\omega_n, \omega_k]$ , can be estimated by the failure probability  $Q_i$  ( $Q = \Sigma Q_i$ ), which represents the probability of the natural frequency  $\omega_i$  ( $i = 1, \dots, n$ ) in set operating range:

$$Q_i = P(\omega_H \leq \omega_i \leq \omega_B) = \int_{\omega_H}^{\omega_B} f(\omega_i) d\omega_i \quad (4)$$

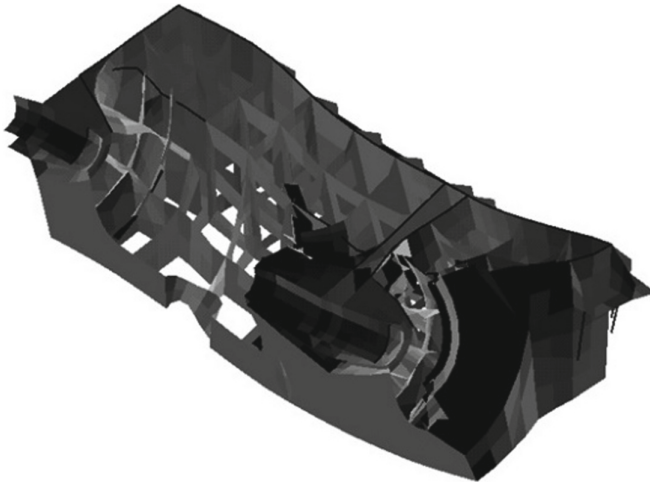
The final reliability value will be assessed by its integrated indicator - the availability factor  $K_g$ .

$$K_g = \frac{t}{t + t} \quad (5)$$

The availability factor  $K_g$  (the probability of an operable state of the system at an arbitrary moment in time) is the ratio of the time of good operation  $t_{CP}$  (without failures) to the sum of the times of good operation and forced downtime of the object ( $t_{CP} + t_B$ ) or their mathematical expectations.

### 3.3 Construction of Geometric and Computational Models

Based on the drawings of an actual steam turbine, the basis of the geometric model was created. Then, using the finite element method, a computational model of the system was created. Figure 1 shows the symmetrical part of the lower half of the steam turbine K-325-25,3 housing for 1, 2, and 3 streams.



**Fig. 1.** Calculation model. Forms of natural oscillations 8.

Accounting for the stiffness of only the lower half of the LP housing simplifies the calculation scheme. The system of masses considers the upper part. The plane of symmetry passes through the rotor axis. The lower parts of the LP of all streams are made in a single body, so they have a standard support balcony and are installed in one cell of the frame foundation. In addition, a feature of this design is a single rotor MP and LP 1st flow, which requires modeling of the LP housing as a shell and articulation with the LP housing into a single model. This version of the design of the LP is used for all turbines of the K-320-240 type, which were installed at many power plants in Eastern Europe and Asia in the 60-80s of the last century [27, 28]. Almost half of them have already exhausted their project resources. The latest modification of this series is the turbine K-325-25,3. It has the same dimensions but more power and efficiency.

The computational model (Fig. 1) has 3325 finite elements, 3186 nodes, and 19062 degrees of freedom. Quasi-shell finite elements in the form of a linear combination of plates for bending and flat stress were used for modeling. The LP building lies freely on the foundation. The support on the foundation was modeled by a system of stiffnesses attached to each particular unit of the supporting balcony. The reliability of the frequency analysis results is based on a comparison with another model, which has 24458 degrees of freedom. The average error in the values of natural frequencies is 6%.

## 4 Results

### 4.1 Calculations of Natural Frequencies and Forms of the System

Numerical calculations of natural frequencies and forms of oscillations are performed when varying the value of the stiffness of the foundation in the range from one rigid fastening to  $C = 1 \cdot 10^7$  N/m<sup>2</sup>. It is known from experimental data that the stiffness of foundation individual elements can vary significantly [29, 30]. This intensified, especially with the transition from monolithic foundations to prefabricated ones. Analysis of experimental data showed a scatter of stiffness up to 50% for one foundation structure and several times for foundation structures of monolithic and prefabricated types. A wide range is chosen to vary the foundation stiffness based on this. The calculation results are shown in Table 1.

From Table 1, it is seen that the whole spectrum of frequencies, depending on the stiffness of the support, can be divided into two parts: sensitive frequencies and insensitive. The values of the latter do not depend on the support rigidity. Some deviations of these frequencies are possible (P11, P4), but they are minor and related to their proximity at a given stiffness of moving frequencies. Analysis of the oscillation's forms showed that these frequencies belong to the "local", i.e., their forms are determined by the oscillations of individual structural elements: the housing walls, guide flows, etc. These frequencies cannot be the cause of failure when changing the stiffness characteristics of the foundation, and, therefore can be excluded from the spectrum in the reliability analysis. Analysis of the oscillations forms of sensitive frequencies showed that they belong to the "global", i.e., their forms are determined by the oscillations of most structures. It is seen in Figs. 1 and 2 shows the type of eigenforms for 8 and 13 eigenfrequencies.

Comparison of the obtained natural frequency values with the experimental values (Table 1) shows a good correlation, indicating the obtained results' reliability. The limited experimental data is associated with the experiment method, where the measurements were performed discretely and in the range of 30–52 Hz. This is due to the high cost of experiments and the inadmissibility of measurements near the resonance.

Figure 3 shows a graph of the dependence of the values of "global" natural frequencies on the stiffness of the support, which shows that the frequency P8 takes values in the operating range (48–52 Hz), and the frequency P13 can get into it. Therefore, these factors will have the most substantial impact on the structure reliability in the studied model of failure.

### 4.2 Calculations of Reliability Indicators

Table 2 shows the values of the failure probability  $Q_i$ , mathematical expectations  $m_{\omega_i}$ , variance  $\delta_{\omega_i}$  and the frequency gradient  $\frac{d\omega_i}{dC}$  for the "global" natural frequencies of the LP when varying the values of the stiffness of the support in the range  $1 \cdot 10^7..4 \cdot 10^8$  N/m<sup>2</sup>. The operating frequency range was taken equal to 48–52 Hz.

There is a high failure probability of the frequency P8 in the operating range (Table 2). The natural form of this frequency (Fig. 2) is characterized by the joint deformation of

**Table 1.** The natural frequencies (Hz) of the LP when varying the stiffness of the support.

№	The value of the stiffness of the support ( $10^7$ N/m <sup>2</sup> )											
	Experimental	Rigid	1000	100	70	40	20	10	7	5	3	1
1	–	28	27.9	26.8	26.2	24.8	22.1	18.5	16.5	14.6	11.9	7.2
2	31	32.0	31.5	29.1	28.7	28.3	28.0	28.7	29	27.9	27.8	27.7
3	42	41.3	40.9	38.9	38.3	36.8	33.7	27.4	24.7	21.6	17.3	10.4
4		45.3	45.4	45.4	45.4	45.3	45.4	45.3	45.3	45.3	45.3	45.3
5		45.4	45.4	45.4	45.4	45.4	45.4	45.3	45.4	45.4	45.4	45.4
6		45.6	45.6	45.6	45.6	45.6	45.6	45.6	45.6	45.6	45.6	45.6
7		55.2	55.2	55.2	55.2	55.3	55.2	55.2	55.3	55.3	55.3	55.2
8	–	56.5	56.5	56.1	55.8	54.6	50.3	45.7	44.0	43.0	42.0	41
9	–	60.5	60.4	59.5	59.1	58.2	57.4	57.2	57.2	57.1	57	56.7
10		61.7	61.7	61.7	61.6	61.6	62	61.5	61.5	61.5	61.5	61.5
11		62.6	62.5	62.2	62.1	62.1	61.6	61.9	61.7	62.2	62	62
12		66.7	66.7	66.7	66.8	66.7	66.6	66.7	66.6	66.6	66.6	66.5
13	–	68.5	68.5	67.7	66.5	63.2	58.7	55.6	54.2	53.3	52.2	51.0

**Fig. 2.** Forms of natural oscillations 13.



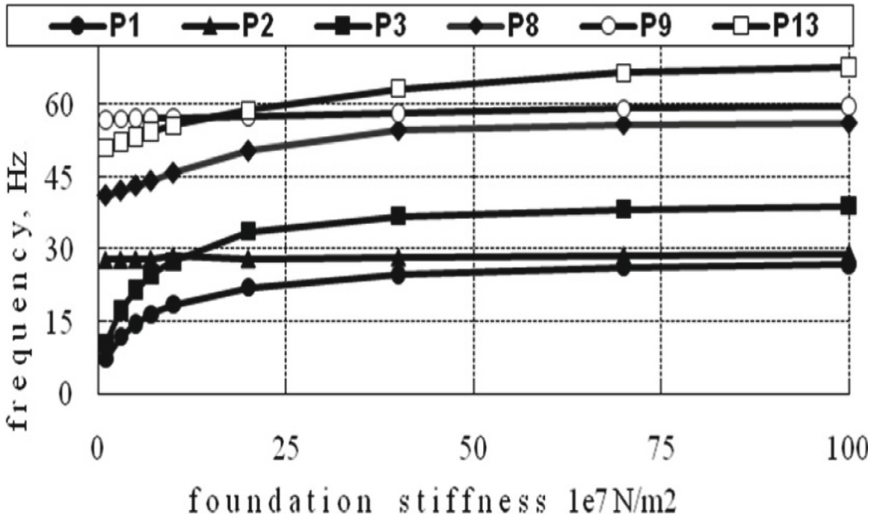


Fig. 3. Effect of natural frequencies on the uniform stiffness of the foundation.

Table 2. Characteristics of LP vibration reliability.

Eigenvalues	$Q_i$	$m_{\omega_i}$	$\delta_{\omega_i}$	$\frac{d\omega_i}{dC}$
P1	3.52E-19	22.06	2.9230	4.497E-8
P2	0.00	28.00	0.0950	1.461E-9
P3	5.574E-4	33.67	4.4066	6.779E-8
P8	0.6128	50.29	2.2683	3.490E-8
P9	0.00	57.44	0.2550	3.920E-9
P13	4.651E-4	58.71	2.0266	3.118E-8

bending and torsion of the structure as a whole, so to change the value of this frequency requires completion of the entire structure.

Summing up the probabilities of failures at different frequencies, we get the final value  $Q = 0.6138$ . Given that the park resource of steam turbines is 270 thousand hours, and the repair time is 1248–1560 h, we get the time of failure-free operation 104 274 h and availability factor (formula 5)  $Kg = 0.987$ .

## 5 Conclusions

Mathematical models for solving the problems of natural oscillations and the reliability of the turbine unit are formulated considering random imperfections. Geometric and computational models building are completed. A series of natural frequencies calculations and forms of the system, comparisons with experimental data are performed. The natural frequencies in the spectrum with high sensitivity to the rigidity of the foundation,

the forms of which are characterized by the global deformation of the whole system, are determined. Reliability characteristics are determined, which show a high probability of getting individual natural frequencies in the operating range. This can lead to accidents in the system under study. The uptime and availability factors have been calculated. The time of failure-free operation given in the study is slightly longer than the time recommended by factories of 70–100 thousand hours before repair. However, this time is determined by the wear of the flow path (blades, diaphragms), which is also affected by the vibration level. Therefore, the study results correlate well with long-term experimental studies of factories to manufacture steam turbines. Additional research is needed to determine effective measures to prevent system failure.

## References

1. Avramov, K., Nikonov, O., Uspensky, B.: Nonlinear modes of piecewise linear systems forced vibrations close to superharmonic resonances. *Proc. Inst. Mech. Eng.* **233**(23–24), 7489–7497 (2019)
2. Garmash, N., Glyadya, A., Gontarovskiy, P., Shulzhenko, N.: Estimating the vibrations of turbounit-foundation-base system exposed to seismic loads. *Bull. NTU “KhPI”* **10**(1232), 25–29 (2017)
3. Herz, F., Nordmann, R.: *Vibrations of Power Plant Machines*. Springer, Cham (2020). <https://doi.org/10.1007/978-3-030-37344-3>
4. Xie, D., Zhang, H., Zheng, H., Huang, X., Guo, Y., Ziyue, M.: Numerical study on deformation of gland seal housing at LP ends on a nuclear steam turbine. In: *ASME Turbo Expo 2018: Turbomachinery Technical Conference and Exposition*, pp. 1–10 (2019)
5. Garmash, N.G., Grishin, N.N., Gontarovskii, P.P., Shul’zhenko, N.G.: Torsional vibrations and damageability of turboset shaftings under extraordinary generator loading. *Strength Mater.* **47**(2), 227–234 (2015)
6. Avramov, K., Martynenko, G., Martynenko, V., Rusanov, A.: Detection of accident causes on turbine-generator sets by means of numerical simulations. In: *IEEE 3rd International Conference on Intelligent Energy and Power Systems (IEPS)*, pp. 51–54 (2018)
7. Khadersab, A., Shivakumar, S.: Vibration analysis techniques for rotating machinery and its effect on bearing faults. *Procedia Manuf.* **20**, 247–252 (2018)
8. Krasnikov, S.V.: Features of modeling the system of turbine unit with a variable contact zone of its stator parts. *SN Appl. Sci.* **3**(10), 1–15 (2021). <https://doi.org/10.1007/s42452-021-04773-4>
9. Zhovdak, V.A., Iglin, S.P., Mishchenko, I.V.: The reliability prediction of structures with random parameters subjected to stationary stochastic input. *Technische Mechanik* **17**(1), 51–65 (1997)
10. Abrosimov, N., Chikhachev, I.: Studies of the dynamic pliability of the system “turbine unit-foundation-base” of the head unit with a capacity of 1200 MW before laying the shaft line. *Izv. VNIIG Vedeneeva* **173**, 12–20 (1984)
11. Kank, H., Kobayashi, M., Tanaka, M., Matsushita, O., Keogh, P.: *Vibrations of Rotating Machinery*, vol. 2. *Advanced Rotordynamics: Applications of Analysis, Troubleshooting and Diagnosis*. Springer, Tokyo (2019). <https://doi.org/10.1007/978-4-431-55453-0>
12. Marchenko, A., Grabovskiy, A., Tkachuk, M., Shut, O., Tkachuk, M.: Detuning of a supercharger rotor from critical rotational velocities. In: Ivanov, V., Pavlenko, I., Liaposhchenko, O., Machado, J., Edl, M. (eds.) *DSMIE 2021. LNME*, pp. 137–145. Springer, Cham (2021). [https://doi.org/10.1007/978-3-030-77823-1\\_14](https://doi.org/10.1007/978-3-030-77823-1_14)

13. Panchenko, A., Voloshina, A., Luzan, P., Panchenko, I., Volkov, S.: Kinematics of motion of rotors of an orbital hydraulic machine. In: IOP Conference Series: Materials Science and Engineering, vol. 1021, no. 1, p. 012045. IOP Publishing (2021)
14. Panchenko, A., Voloshina, A., Titova, O., Panchenko, I., Caldare, A.: Design of hydraulic mechatronic systems with specified output characteristics. In: Ivanov, V., Pavlenko, I., Lia-poshchenko, O., Machado, J., Edl, M. (eds.) DSMIE 2020. LNME, pp. 42–51. Springer, Cham (2020). [https://doi.org/10.1007/978-3-030-50491-5\\_5](https://doi.org/10.1007/978-3-030-50491-5_5)
15. Ivanov, V., Pavlenko, I., Trojanowska, J., Zuban, Y., Samokhvalov, D., Bun, P.: Using the augmented reality for training engineering students. In: 4th International Conference of the Virtual and Augmented Reality in Education, VARE 2018, pp. 57–64 (2018)
16. Buñ, P., Trojanowska, J., Ivanov, V., Pavlenko, I.: The use of virtual reality training application to increase the effectiveness of workshops in the field of lean manufacturing. In: 4th International Conference of the Virtual and Augmented Reality in Education, VARE 2018, pp. 65–71 (2018)
17. Zaitsev, R.V., Khrypunov, G.S., Veselova, N.V., Kirichenko, M.V., Kharchenko, M.M., Zaitseva, L.V.: The cadmium telluride thin films for flexible solar cell received by magnetron dispersion method. *J. Nano Electron. Phys.* **9**(3), 03015 (2017)
18. Minakova, K.A., Zaitsev, R.V.: Improving the solar collector base model for PVT system. *J. Nano Electron. Phys.* **12**(4), 04028 (2020)
19. Fazal, M., Mehdi, S.N., Kumar, B.P.: Performance optimization of 500 MW steam turbine by condition monitoring technique using vibration analysis method. *Int. J. Adv. Res. Eng. Technol.* **10**(5), 1–8 (2019)
20. Huang, B., Mo, J.L., Ouyang, H., Wang, R.L., Wang, X.C.: Friction-induced stick-slip vibration and its experimental validation. *Mech. Syst. Signal Process.* **142**, 106705 (2020)
21. Chelabi, M.A., Basova, Y., Hamidou, M.K., Dobrotvorskiy, S.: Analysis of the three-dimensional accelerating flow in a mixed turbine rotor. *J. Eng. Sci.* **8**(2), D1–D7 (2021). [https://doi.org/10.21272/jes.2021.8\(2\).d2](https://doi.org/10.21272/jes.2021.8(2).d2)
22. Krol, O., Sokolov, V.: Research of modified gear drive for multioperational machine with increased load capacity. *Diagnostyka* **21**(3), 87–93 (2020)
23. Panchenko, A., Voloshina, A., Panchenko, I., Pashchenko, V., Zasiadko, A.: Influence of the shape of windows on the throughput of the planetary hydraulic motor's distribution system. In: Ivanov, V., Pavlenko, I., Lia-poshchenko, O., Machado, J., Edl, M. (eds.) DSMIE 2021. LNME, pp. 146–155. Springer, Cham (2021). [https://doi.org/10.1007/978-3-030-77823-1\\_15](https://doi.org/10.1007/978-3-030-77823-1_15)
24. Bogajevskiy, A., Arhun, S., Hnatov, A., Dvadenko, V., Kunicina, N., Patlins, A.: Selection of methods for modernizing the regulator of the rotation frequency of locomotive diesels. In: 2019 IEEE 60th International Scientific Conference on Power and Electrical Engineering of Riga Technical University (RTUCON), pp. 1–6. IEEE (2019)
25. Pavlenko, I., Trojanowska, J., Gusak, O., Ivanov, V., Pitel, J., Pavlenko, V.: Estimation of the reliability of automatic axial-balancing devices for multistage centrifugal pumps. *Period. Polytech. Mech. Eng.* **63**(1), 52–56 (2019). <https://doi.org/10.3311/PPme.12801>
26. Krol, O., Porkuian, O., Sokolov, V., Tsankov, P.: Vibration stability of spindle nodes in the zone of tool equipment optimal parameters. *Comptes rendus de l'Acadé'mie bulgare des Sciences* **72**(11), 1546–1556 (2019)
27. Shicheng, H., Ying, L., Dalei, Q.: Research and apply on zero output operation of low pressure cylinder of 350 MW steam turbine. *Shandong Electric Power* **45**, 63–67 (2018)
28. Jianguo, C., Huairan, F., Zhengxian, X.: Zero output technology of the low-pressure cylinder of 300 MW unit turbine. *Therm. Power Gener.* **47**, 106–110 (2018)

29. Monkova, K., et al.: Condition monitoring of Kaplan turbine bearings using vibro-diagnostics. *Int. J. Mech. Eng. Robot. Res.* **9**(8), 1182–1188 (2020)
30. Arhun, S., Migal, V., Hnatov, A., Ponikarovska, S., Hnatova, A., Novichonok, S.: Determining the quality of electric motors by vibro-diagnostic characteristics. *EAI Endorsed Trans. Energy Web* **7**(29) (2020)



# The Behaviour of a Rod (Beam) Under the Influence of an External Power Load

Viktoriya Pasternak<sup>1</sup> , Oleg Zabolotnyi<sup>1</sup> , Nataliia Ilchuk<sup>1</sup> ,  
José Machado<sup>2</sup> , and Kostiantyn Svirzhevskiy<sup>1</sup> 

<sup>1</sup> Lutsk National Technical University, 75, Lvivska Street, Lutsk 43018, Ukraine  
volynasi@gmail.com

<sup>2</sup> Department of Mechanical Engineering, METRICs Research Centre, University of Minho,  
4804-533 Guimarães, Portugal

**Abstract.** This paper justifies the primary conditions for the strength, rigidity, and stability of the part's structural elements (a mechanism). They presented the theoretical and practical part of the conditions for checking the strength of a beam (Rod). Graphically presented the stress  $\sigma_n$ ,  $\tau_n$  in height. We investigated the behavior of the rod (beam) model when calculating the tensile-compressive strength. Based on the results obtained, plots of longitudinal forces were constructed. It was found that at each point of the cross-section, internal bonds (forces-N) arise, which are evenly distributed. It should be noted that the constructed plots of tensile forces were carried out based on improved equilibrium equations. In this case, the axial force formed on the first section was determined by the algebraic sum of all forces located only on one side of the section. We investigated the strength conditions that did not exceed the limits of permissible limit norms. We also investigated the main parameters and limits of permissible norms of reference reactions, confirming a reliable test for all three main strength conditions. It should also be noted that the SolidWorks software product performed computer modeling based on strength analysis, which made it possible to design the main structural elements of this part. Also, to study the behavior of the calculated beam model under various influences in terms of static, part stability, natural frequency fluctuations, and external load application.

**Keywords:** Detail · Deformation · Reference reactions · Strength conditions · Cross-section · Statistical equations · Plots · Numerical analysis · Manufacturing innovation

## 1 Introduction

The study of real bodies is currently an urgent task since parts' behavior and model can deform (strain is a physical quantity, the result of a deforming load), changing their shape, position, and dimensions. Therefore, it is essential to consider the definition of all possible sizes of elements of any structure, in which the size of the part and their shape will not exceed the specified values, which are mainly determined by the

operating conditions. It is also important to remember the stability of the structure itself and maintain the shape of the balance and size.

It should be noted that the deformation of bodies occurs due to the application of external force loads to them. When the body and its critical (dangerous) points, lines, or cross-sections are deformed, they move to another plane or space relative to their original (initial) position. Thus, one of the essential tasks of applied mechanics is to assess the strength and rigidity of any structure to ensure reliable and actual dimensions of the cross-section of the part.

## 2 Literature Review

After considering the scientific work presented in [1], it can be stated that the authors experimented with a general estimate of the flexural strength of the most significant productivity of the working areas of beams. At the same time, the research teams used such starting materials that contained small elements of fiber and alloy, which in turn caused destruction and cracks in the samples. In [2], the results of the reliability of the circular moment of a beam (rod) based on stress concentration coefficients and using the Monte Carlo modeling method are analyzed and justified. The authors of [3] focused their attention on the behavior of models of curved composite beams under constant load. At the same time, the limits of the maximum load, the maximum deviation, and the spread of a deep crack that occurred at the bends of the most dangerous points were not considered. In scientific studies presented in [4], standard conditions for the strength and shear of a part (beam) were considered.

It should be noted that the authors used outdated RC system designs. The scientific results covered in [5] are unusual. The authors pay special attention to the study of cross-sections and inclusions, which can improve the stress coefficient due to thermal expansion and the pyroelectric effect. Works [6] aim to experimental and analytical calculations of bending modernization of T-shaped beams using CFRP sheets. It is important to note that these structural materials do not fully provide the primary operating conditions. In [7], numerical intervention is based on strengthening steel beam profiles. Cold-formed steels that were used to make part profiles were subjected to various manufacturing scenarios and could bend. In this experiment, only a monotonous load was used. Research teams [8] investigated a fiber-based aggregate beam's width and crack propagation. The main goal was to reduce the spread of these cracks, as this is essential for protecting any reinforcement from various types of corrosion.

The authors of [9] investigated the technology and software tools for controlling samples made of structurally inhomogeneous materials. It should be noted that the proposed algorithm for recognizing problems of destruction (deformation) of samples is effective since it allows analyzing the surface and internal connections of materials, which makes it possible to improve the strength and stability of parts for any purpose. The efficiency of the DIC system for measuring beam reinforcement is highlighted in [10]. The authors investigated the strength-to-weight ratio of the part, its durability, and its low price. Linear differential results (LVDT) measurements were tested using a DIC system. Papers [11–13] performed numerical studies of the dynamic responses of various mechanical systems. Also, based on the obtained results, a model was developed

to simulate the study of the structural reaction of a T-shaped beam (rod) [14]. This simulation model functions only under shock load conditions. Works in [15] are based on the bending behavior of beams considered for stretching. It was found that high stress reduces the plasticity of the beam and violates the primary tensile condition [16]. In addition, samples made from hardened rebar have been shown to exhibit better limiting moments and ductility than samples made from hardened steel [17]. The main problems of vibration of beams (rod) are justified in the works [14]. The authors propose solving equations using linear variables and Coriolis force [18]. The article [19] is devoted to studying an S-shaped beam with uniform bending.

The extensive use of the ANSYS program with artificial neural networks is applied in [20, 21] for nonlinear analysis of the finite element beam method. In [22–24], new methods for strengthening are proposed. Polymer (CFRP) ropes were studied based on a T-shaped test cross-section that causes transverse displacement. Critical moments were recorded with the intervention of a monotonous load mode. The authors of this study claim that fatigue cracks strongly influence the manufacture of such structures and mechanisms. They propose to solve this problem using the methods of mathematical equations of Johnson and Cafoll. However, the literature review does not allow us to thoroughly study the behavior and model of parts under the influence of external force load. Thus, it is proposed to pay more attention to the cross-sectional dimensions of the rod (beam) based on improving the primary strength conditions.

### 3 Research Methodology

#### 3.1 Primary Conditions for the Strength, Rigidity, and Stability of the Part

The article's primary purpose is to study reliable dimensions of the cross-section of a part (rod) using the SolidWorks software product, which is affected by external power loads.

It is necessary to perform calculations for the strength and rigidity of the beam to ensure the necessary stability of the elements of any structure or mechanism. To meet the strength conditions, the dimensions of the cross-section of the part (beam) must be determined from the conditions that the possibility of destruction is excluded under any action of an external force load. In turn, the destruction of the sample occurs due to the highest values of tangential stresses or normal stresses or the overlap of a simultaneous combination of them. Therefore, these values are limited to certain permissible values and are set by the following main parameters:  $\sigma$  is the normal stress;  $\tau$  is the tangential stress.

It should also be noted that the following main elements of the study should be taken into account when calculating strength:

1. Design calculation (external loads acting on the material are known in advance, as a result of which it is necessary to find the dimensions of the cross-section of the part (rod)).
2. Verification calculation (structurally inhomogeneous material and part dimensions are known in advance. A mandatory condition for this calculation is to check the

conditions of the external power load and whether this structure or mechanism will withstand the external power load acting on it).

3. Correlation of the designed and tested calculations (previously known inhomogeneous material, part dimensions and its load scheme. The primary purpose of this calculation is to find out certain permissible values of normal and tangential stresses and what maximum external load the beam (rod) can withstand).

All the main elements (calculations) are based on certain strength conditions, which should not exceed the limit values:  $100 \text{ mm}^2$ – $148 \text{ mm}^2$ . Under which the effective value of the external force stress should not exceed the permissible values. That is, we get:  $\sigma_{max} \leq \sigma$  and  $\tau \leq \tau$ .

It should be noted that the stiffness conditions were calculated based on the maximum values of linear and angular deformations. We obtain:

$$\Delta l \leq [\Delta l], \quad \theta \leq [\theta] \quad (1)$$

where  $\Delta l$  – changing the part size;  $[\Delta l]$  – acceptable values for this change;  $\theta$ ,  $[\theta]$  – angular deformation, the angle of twisting of the structure (mechanism) and permissible values of this value.

### 3.2 Theoretical Part of Checking the Strength of a Beam (Rod)

Three main strength conditions must be met to implement and test the strength of a beam part:

1. the primary condition must correspond to the following ratio:

$$\sigma_{max} = \frac{M_{max}}{W_z} \leq \sigma \quad (2)$$

It should be noted that the check must be performed in the section where:  $M(x) = M_{max}$ .

2.  $\tau = \frac{Q_{max} \cdot S_z}{d \cdot I_z} \leq \tau$ . The condition must be met in the section where:  $Q(x) = Q_{max}$ .
3.  $\sigma_r = \sqrt{\sigma_n^2 + 4\tau_n^2} \leq \sigma$ . This check should be performed in the cross-section of the most problematic area of the part (beam), where:  $M(x) = Q(x)$  acts simultaneously. In this section of the most problematic zone, it is necessary to select a dangerous point of application of force  $F$ , which is simultaneously affected by normal and tangential stresses reaching large values  $\sigma_n$ ,  $\tau_n$ . In this case, the dangerous and problematic point of the part (beam) is the point “n”, which is responsible for the transition from one element of the part to another. We get:

$$\sigma_n = \frac{M(x) \cdot y_n}{I_z} = \frac{M(x) \cdot \left(\frac{h}{2} - t\right)}{I_z}, \quad \tau_n = \frac{Q(x) \cdot S^p}{d \cdot I_z} = \frac{Q(x) \cdot b \cdot t \cdot \left(\frac{h}{2} - \frac{t}{2}\right)}{d \cdot I_z}, \quad (3)$$

where:  $I_z$  – the moment of inertia relative to the axis  $z$ ;  $S_z^p$  – the static moment of the axis area  $z$ .



Figure 1 shows plots of external stresses  $\sigma$  and  $\tau$ , which are affected by large values of stresses  $\sigma_n, \tau_n$  at the dangerous point «n» of the section.

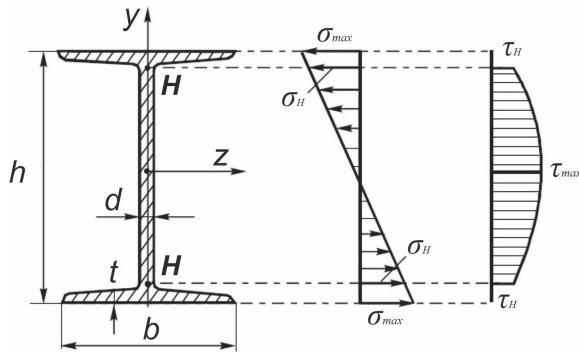


Fig. 1. Stress distribution  $\sigma_n, \tau_n$  by height.

From this Fig. 1, it can be seen that the cross-section method determines the normal forces that occur in cross-sections. In this case, each section divides the beam (rod) into two parts. In this case, the actual direction of the normal force applied in relation to the cross-section is established when considering the equilibrium of one part of the part to another. To do this, it is necessary to consider the elementary equilibrium equation. If its weight is not considered when the part is stretched or compressed, then the normal forces must be determined using the specified external forces  $F_i$ . It was found that at each point of the cross-section, the internal bonds (forces) are evenly distributed. Thus, the internal forces per unit cross-sectional area are further determined by the normal stress  $\sigma$ .

## 4 Results

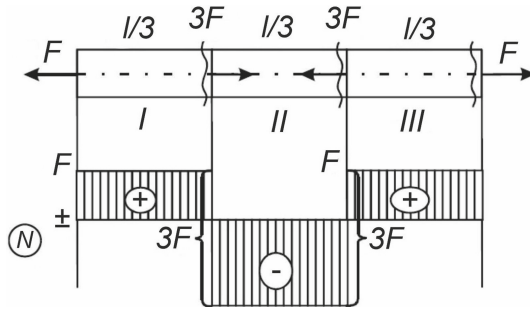
### 4.1 Model of Behaviour of the Rod (Beam) in the Calculation of Tension-Compression

It should be noted that any tensile-compressive calculation is based on the basic strength conditions that must comply with certain normative mathematical norms, we obtain:

$$\sigma_{max} \leq [\sigma], \quad \sigma_{max} = \frac{N_{max}}{A}, \quad \frac{N_{max}}{A} \leq [\sigma] \quad (4)$$

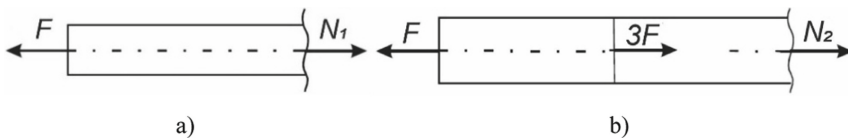
where  $N$  – longitudinal force;  $A$  – the cross-sectional area of the part (beam), measured in  $\pi d^2/4$ .

In this way, you can plot the longitudinal forces  $N$  in order to get the maximum value of  $N_{max}$ . Figure 2 shows the cross-sectional area in individual places where an external power load is applied. Where:  $l = 600-700$  mm,  $F = 11750$  [H], the material of the beam (rod) is steel,  $[\sigma] = 158$  [H/mm<sup>2</sup>].



**Fig. 2.** The cross-sectional area of external power load application.

In Fig. 2, the formation of certain areas of cross-sections and end sections at the places where external forces are applied is visible. There is a selection of 3 sections I, II, III in this case. In turn, in the section in which a tensile or compressive external force is applied on plot  $N$ , we observe specific changes in fixed jumps by the amount of external force. So, in Fig. 3a) we present and consider plot I. And in Fig. 3b) section II is presented:



**Fig. 3.** Plot area, where: a) plot area I; b) plot area II.

From the presented Fig. 3a) it can be seen that the equilibrium is equal to the following relation, we get:  $\sum F_i = 0$ . In this case, for the condition  $F - N_1 = 0$ , we use the following rule: the axial force formed on section I is determined by the algebraic sum of all forces located only on one side of the section. We found out that force  $F$  is tensile. Hence we got,  $N_1 = F$ . Thus, we obtained the following value of the force  $N_1 = F$ , which will be constant for the entire section (region) I.

After that, we considered the characteristic cross-section that occurs at the border of sections I and II (Fig. 3b)). It is worth noting that a compressive force of  $3F$  acts in this section. According to the above rule, we conclude that the jump must be made to the negative zone by an amount of  $3F$ . That is, we get the following relation:  $F - 3F = -2F$ . After that, we consider the cross-section at the end of the selected area of Section II. we obtain the following equilibrium conditions:

$$\sum F_i = 0, F - 3F - N_2 = 0 \tag{5}$$

This leads to the following relation we get:  $N_2 = F - 3F = -2F$ . It should be noted that this is a constant value that acts on section II. It was found that the tensile force  $3F$  acts in the cross-section of sections II and III. We get the following mathematical relation:  $-2F + 3F = F$ .

Considering the last section that occurs at the end of the region of section III, we can write the equilibrium equation on different sides of the section:

To the left  $\rightarrow F - 3P + 3P - N_3 = 0$ ; It follows that  $N_3 = F$ .

To the right  $\rightarrow F - N_3 = 0$ ; From here, we get:  $N_3 = F$ .

Accordingly, the strength conditions will take the following form:

$$\frac{2F}{A} \leq [\sigma] \tag{6}$$

From here, we get:  $A = \frac{\pi d^2}{4} = \frac{2 \cdot 11750}{158} \geq 148,7 \text{ mm}^2$ . It follows that  $d \geq 1,13\sqrt{A} \geq 13,7 \text{ mm}$ . Therefore, the more considerable value in the direction of the common value will be  $d = 14 \text{ mm}$ .

### 4.2 Ensuring Beam Strength Based on Static Equations

To check the support reactions in certain sections  $Q(x)$  and  $M(x)$  of the beam (Fig. 4), it is necessary to perform a full-strength check of the part (point 3.2), as well as select the I-beam section.

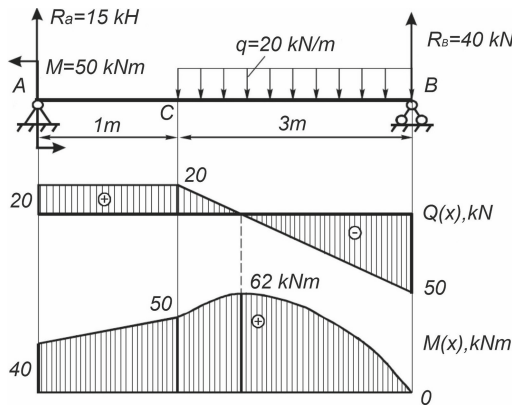


Fig. 4. General view of the beam (rod) diagram.

It should be noted that the normal and tangential stresses, in this case, are  $\sigma = 170 \text{ MPa}$ ,  $\tau = 70 \text{ MPa}$ . In Fig. 4. the load diagram and transverse force plots are presented, as well as the bending moment of the beam is recorded. This study of the support reactions on certain sections of the beam (rod) showed that the plots  $Q(x)$  and  $M(x)$  are equal to the following parameters:  $M_{max} = 62 \text{ kNm}$ ,  $Q_{max} = 40 \text{ kN}$ . We found that the most dangerous cross-section is the section in zone C, where  $M(x) = 50 \text{ kNm}$  and  $Q(x) = 20 \text{ kN}$ . The main parameters and limits of permissible norms of reference reactions, which were obtained based on the study (Fig. 4), are presented in Table 1.

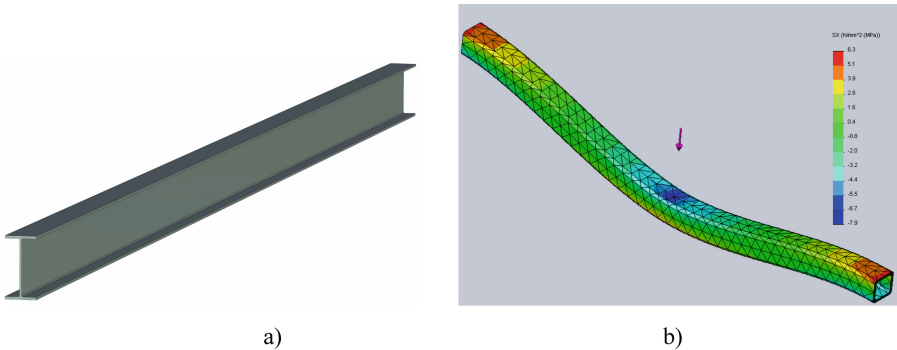
**Table 1.** Basic parameters and limits of permissible norms of reference reactions.

Basic parameters	Limits of acceptable standards
$R_A$ , kN	15
$R_B$ , kN	40
$W_Z$ , $\text{cm}^3$	406
$I_Z$ , $\text{cm}^4$	5500
$S_Z$ , $\text{cm}^3$	230
h, mm	260
b, mm	140
d, mm	7,0
t, mm	10,1

Therefore, we can conclude that a full test for all three main strength conditions is performed. Thus, this means that the strength of the selected part (beam) is fully ensured.

### 4.3 The Behavior of a Part (Beam) Using Computer Modelling

Computer simulations were performed in SolidWorks software. Since it was this functional modeling complex that allowed us to model a solid-state object by the finite element method. In Fig. 5, the model of the part–beam (rod) behavior is presented.



**Fig. 5.** Part model using the SolidWorks software system, where: a) part model-beam (rod); b) generation of a finite element grid of the part-beam (rod).

As a result of the simulation performed by the SolidWorks system, we calculated the strength and rigidity of the part. Because of modeling, the following basic properties were set: thermal conductivity, density, Poisson’s coefficient, yield strength; modulus of elasticity; coefficient of thermal expansion; tensile-compressive strength.

## 5 Conclusions

It was found that the maximum stress is ranged from 70 MPa to 170 MPa. It occurs at certain points in the cross-section, acts on the part, and distributed evenly. At the same time, all three main strength conditions are met, which lie within acceptable standards, which allows us to assert the reliability of the calculation results. Based on the calculations made, the following main factors were predicted: (1) load and voltage distribution; (2) occurrence of deformation in the part structure; (3) part stability margin coefficient, natural frequency fluctuations, and their shape; (4) preliminary temperature distribution in the part structure-beam (Rod); (5) this model's mass and moment of inertia relative to the x, y, and z coordinate system.






## References

1. Chi-Young, J., Jong-Han, L.: Crack closure and flexural tensile capacity with SMA fibers randomly embedded on tensile side of mortar beams. *Nanotechnol. Rev.* **1**(9), 354–366 (2020)
2. Mayda, M.: Monte carlo simülasyon yöntemi ile dairesel delikli ankastre kirişin gerilme-yiğilme faktörüne bağlı güvenilirlik analizi. *GU J. Sci.* **6**(1), 241–249 (2018)
3. Abdulkhaliq, A., Saba, K.: Behavior of curved steel-concrete composite beams under monotonic load. *Int. J. Math. Eng. Manag. Sci.* **5**(6), 1210–1233 (2020)
4. Lavorato, D., Nuti, C., Santini, S.: Experimental investigation of the shear strength of RC beams extracted from an old structure and strengthened by carbon FRP U-Strips. *Appl. Sci.* **8**(1182), 1–29 (2018)
5. Pasternak, Ia., Pasternak, R., Pasternak, V., Sulym, H.: Boundary element analysis of 3D cracks in anisotropic thermomagnetoelastoelectroelastic solids. *Eng. Anal. Bound. Elem.* **74**, 70–78 (2017)
6. Yannian, Z., Moncef, N.: Experimental and analytical investigation on flexural retrofitting of RC T-Section beams using CFRP sheets. *Appl. Sci.* **10**(1233), 1–14 (2020)
7. Taheri, Eh., Firouzianhaji, Ah., Mehrabi, P., Hosseini, B., Samali, B.: Experimental and numerical investigation of a method for strengthening cold-formed steel profiles in bending. *Appl. Sci.* **10**(3855), 1–31 (2020)
8. Ghalehnovi, M., Karimipour, A., Brito, J., Reza Chaboki, H.: Crack width and propagation in recycled coarse aggregate concrete beams reinforced with steel fibres. *Appl. Sci.* **10**(7587), 1–27 (2020)
9. Zabolotnyi, O., Pasternak, V., Ilchuk, N., Hulieva, N., Cagáňová, D.: Powder technology and software tools for microstructure control of AlCu2 samples. In: Ivanov, V., Trojanowska, J., Pavlenko, I., Zajac, J., Peraković, D. (eds.) *DSMIE 2021. LNME*, pp. 585–593. Springer, Cham (2021). [https://doi.org/10.1007/978-3-030-77719-7\\_58](https://doi.org/10.1007/978-3-030-77719-7_58)
10. Funari, M., Verre, S.: The effectiveness of the DIC as a measurement system in SRG shear strengthened reinforced concrete beams. *Curr. Comput. Aided Drug Des.* **11**(265), 1–11 (2021)
11. Ivanov, V., Pavlenko, I., Kuric, I., Kosov, M.: Mathematical modeling and numerical simulation of fixtures for fork-type parts manufacturing. In: Knapčíková, L., Balog, M. (eds.) *Industry 4.0: Trends in Management of Intelligent Manufacturing Systems. EICC*, pp. 133–142. Springer, Cham (2019). [https://doi.org/10.1007/978-3-030-14011-3\\_12](https://doi.org/10.1007/978-3-030-14011-3_12)
12. Ivanov, V., Dehtiarov, I., Pavlenko, I., Kosov, M., Hatala, M.: Technological assurance and features of fork-type parts machining. In: Ivanov, V., et al. (eds.) *DSMIE 2019. LNME*, pp. 114–125. Springer, Cham (2020). [https://doi.org/10.1007/978-3-030-22365-6\\_12](https://doi.org/10.1007/978-3-030-22365-6_12)

13. Huiling, Z., Xiangqing, K., Ying, F., Yihan, G., Xuezhi, W.: Numerical investigation on dynamic response of RC T-Beams strengthened with CFRP under impact loading. *Curr. Comput. Aided Drug Des.* **10**(890), 1–16 (2020)
14. Szewczak, I., Rozylo, P., Rzeszut, K.: Influence of mechanical properties of steel and CFRP tapes on the effectiveness of strengthening thin-walled beams. *Materials* **14**(2388), 1–14 (2021)
15. Elamary, Ah., Alharthi, Y., Abdalla, O., Alqurashi, M., Sharaky, I.A.: Failure mechanism of hybrid steel beams with trapezoidal corrugated-web non-welded inclined folds. *Materials* **14**(1424), 1–18 (2021)
16. Barichello, C., Landesmann, Al., Camotim, D.: Distortional failure and DSM design of cold-formed steel S-shaped beams under uniform bending. *Latin Am. J. Solids Struct.* **14**(1), 2123–2140 (2017)
17. Chalioris, C., Kosmidou, P., Papadopoulos, N.: Investigation of a new strengthening technique for RC deep beams using carbon FRP ropes as transverse reinforcements. *Fibers* **6**(52), 1–18 (2018)
18. Wu, F., Tang, W., Xue, C., Sun, G., Feng, Y., Zhang, H.: Experimental investigation on the static performance of stud connectors in steel-HSFRC composite beams. *Materials* **14**(2744), 1–19 (2021)
19. Gencturk, B., Aryan, H., Hanifehzadeh, M., Chambreuil, C., Wei, J.: A computational study of the shear behavior of reinforced concrete beams affected from alkali–silica reactivity damage. *Materials* **14**(3346), 1–23 (2021)
20. Pavlenko, I., Simonovskiy, V., Ivanov, V., Zajac, J., Pitel, J.: Application of artificial neural network for identification of bearing stiffness characteristics in rotor dynamics analysis. In: Ivanov, V., et al. (eds.) *DSMIE 2018. LNME*, pp. 325–335. Springer, Cham (2019). [https://doi.org/10.1007/978-3-319-93587-4\\_34](https://doi.org/10.1007/978-3-319-93587-4_34)
21. Basil, I., Moussa, L., Salah, A., Samer, B.: Shear strength of externally U-bonded carbon fiber-reinforced polymer high-strength reinforced concrete. *Materials* **14**(3659), 1–26 (2021)
22. Hurey, I., Gurey, V., Bartoszuk, M., Hurey, T.: Formation of residual stresses during discontinuous friction treatment. *J. Eng. Sci.* **8**(1), C38–C44 (2021). [https://doi.org/10.21272/jes.2021.8\(1\).c5](https://doi.org/10.21272/jes.2021.8(1).c5)
23. Altoubat, S., Karzad, A., Maalej, M., Barakat, S., Junaid, T.: Experimental study of the steel/CFRP interaction in shearstrengthened RC beams incorporating macro-synthetic fibers. *Structures* **25**, 88–98 (2020)
24. Hovorun, T., et al.: Improvement of the physical and mechanical properties of the cutting tool by applying wear-resistant coatings based on Ti, Al, Si, and N. *J. Eng. Sci.* **8**(2), C13–C23 (2021). [https://doi.org/10.21272/jes.2021.8\(2\).c3](https://doi.org/10.21272/jes.2021.8(2).c3)



# Stress-Strain State of the Floating Bollard's Structure for a Shipping Gateway

Ihor Sydorenko<sup>(✉)</sup> , Vladimir Tonkonogyi , Vladimir Semenyuk ,  
Valeriy Lingur , and Yunxuan Zhang 

Odessa Polytechnic National University, 1, Shevchenko Avenue, Odessa 65044, Ukraine  
[igs.ods@gmail.com](mailto:igs.ods@gmail.com)

**Abstract.** The floating ballard is one of the main elements of the mooring equipment included in the lock. The reliability of this element largely determines the performance of this complex hydraulic unit and reduces the costs associated with the accident rate of both the lock itself and the ships passing through it. The close relationship between the reliability of the bollard and the magnitude of external forces (acting on its structure) requires a deep analysis of the stress-strain state of both the bollard elements and their connection places. The article deals with studying an actual composite welded structure of a ship's lock floating bollard under short-term action of loads exceeding the nominal load due to the dynamics of mooring operations and weather conditions. The studies were carried out on the developed 3D model of the device, and the analysis of the stress-strain state of its elements and the places of their conjugation. Some simplifications were applied, and the finite element method was used. A graphical representation of the results of the study made it possible to establish a general picture of the stress-strain state of the bollard elements, as well as to establish the local places of probable damage. Based on the results obtained, appropriate conclusions are drawn that determine possible solutions to the identified problems.

**Keywords:** Ship lock · Mooring equipment · Floating bollard · Stress-strain state · Finite element method · Industrial growth

## 1 Introduction

To date, the mooring of a vessel in a lock chamber is one of the most essential operations that determine the performance and efficiency of a ship lock. That is why the mooring equipment used in this operation is subject to increased requirements in terms of its reliability. The key element of the lock's mooring equipment is the floating bollard.

The specifics of the operation of this device (in addition to the fact that it is floating) is in the nature of its loading. Many external factors determine the nature of the loading of a floating bollard. First of all, it should be noted that the mooring of ships in the lock is carried out using relatively rigid and heavy ropes. However, the ropes are elastic elements, and as a result, their stretching under load and subsequent sagging lead to significant ship movements both along and across the lock chamber. The movement

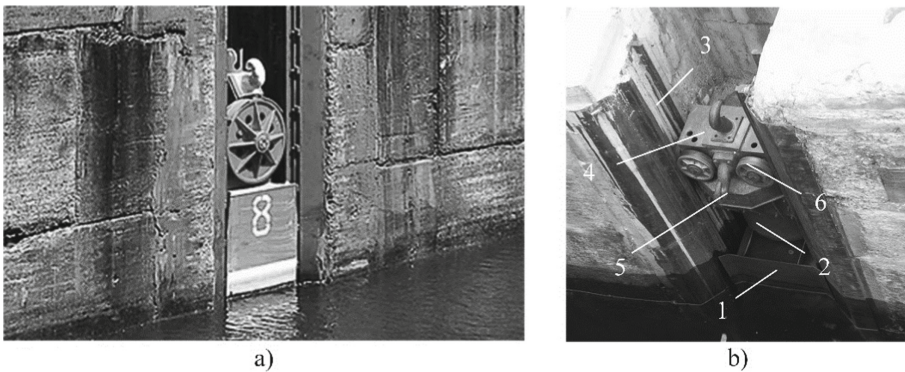
of ships is one of the leading causes of inertial jerks with a variable direction, which are perceived by the design of a floating bollard. Selective, due to the complexity of the design, the use of devices for damping inertial jerks in mooring systems does not fundamentally change the situation, and the kinetic energy of jerks remains quite large. This leads to the destruction (breakage) of the mooring ropes and the global destruction in the form of the structures of floating bollards.

It should be noted that during the locking of ships, especially heavy ones, another additional and difficult to take into account when designing a bollard loading occurs, which affects the elastically deformed state of its elements. The occurrence of this loading is often associated with two factors. The first factor in the occurrence of additional bollard exposure is the excess of the normative hydrodynamic force when filling or emptying the sluice chamber. Secondly, and no less important factor, is the unpredictable change in the mass of the moored vessel due to its freezing in the winter.

The analysis of the stress-strain state of the bollard elements under the action of the indicated loads, both at the stage of designing new devices and those in operation, is quite relevant.

## 2 Literature Review

The floating bollard is the main element included in almost any ship lock (Fig. 1a). The designs of such devices are quite diverse. However, despite the design differences, these devices have similar design elements that determine their functional purpose, making it possible to classify these designs as typical.



**Fig. 1.** Mooring equipment of the ship's lock: floating bollard (a); floating bollard elements (b)

In a typical floating bollard structure, there is always float 1, which ensures its buoyancy. Attached to the float is a metal structure 2, made of shaped profiles or sheet metal, in most cases using welding (Fig. 1b). There are designs in which the metal structure itself forms the float cavity.

In the event of a change in water level, the vertical movement of the bollard is ensured by its placement in a special shaft of the mooring pier 3. The metal structure of



the bollard, which is not part of the float, usually consists of structurally identical upper carriage 4, which is in the surface position, and the lower carriage, which is below the water level. On the upper carriage 4, for attaching the mooring piping, an eye 5 is fixedly fixed, sometimes made in the form of a hook. One or more support rollers 6, located on the upper and lower carriages, are designed to orient and hold the bollard in the pier shaft [1].

The operational experience of floating bollards indicates two main types of destruction (emergencies) that determine its complete or partial failure [2–5]. Simultaneously, the available data also indicate a precise localization of one or another type of damage in the pedestal structure. Most accidents with various technological equipment are associated with the deformation of loaded parts [6–10]. The picture of destruction, in this case, is a critical plastic deformation of the guide rollers of the bollard in the shaft, which causes the bollard to skew, and as a result, it jams. In this case, the destruction of the concrete structure of the mine is sometimes observed at the points of fastening of the guides [7]. It has been established that the presented type of bollard failure is a direct consequence of more severe damage but related directly to the bollard structure itself. 80% of accidents occur, at which the critical plastic deformation of the metal structure of the bollard (sometimes complete destruction) was recorded at the points of attachment of the eye and guide rollers on it [11, 12]. The results of the presented studies, particularly in the infrastructure development [13–16], allow us to state that the main element that determines the performance of the ship lock mooring equipment system is the bollard metal structure [17]. Based on the presented conclusions, it should be recognized that the study of the metal structure of bollards, both at the design stage and during operation, is one of the priority scientific and applied tasks.

Studies in mathematical modeling of the stress-strain state of the bollard metal structure at the design stage can significantly reduce the risk of emergencies by creating a rational bollard metal structure, and research in the process of operation makes it possible to upgrade existing equipment and thereby increase its reliability. As noted earlier, the bollard metal structure is a structure that can be classified as a combined one. The combination, in this case, contains rod, plate, or shell elements [18]. Rarely enough are metal structures assembled using only threaded or welded joints. As a rule, when assembling the metal structure of a bollard, these two types of connections are used. The bulk of the connections are welded, and the fastening of individual elements can be performed using a threaded connection [19, 20].

To analyze the stress-strain state of the considered metal structure, it is possible to use several methods known from structural mechanics. Among them, one can single out the finite difference method, the weighted residual method, variational methods, as well as the finite element method [21]. At present, the finite element method is the most common method for solving problems in the mechanics of a deformable elastic body. This method is based on the approximation of a continuous medium, which is the object of study, some simple elements interconnected at nodal points. At these points, some fictitious interaction forces are applied that characterize the action of distributed internal stresses applied along the joining boundaries of adjacent elements [21, 22].

The development of design technologies makes it possible to model the research object in a 3D model using CAD systems. Since there is a close relationship between

CAD and CAE systems, where the finite element method (FEM) has already been implemented, it is quite apparent that this method is used to conduct studies whose subject is the stress-strain state.

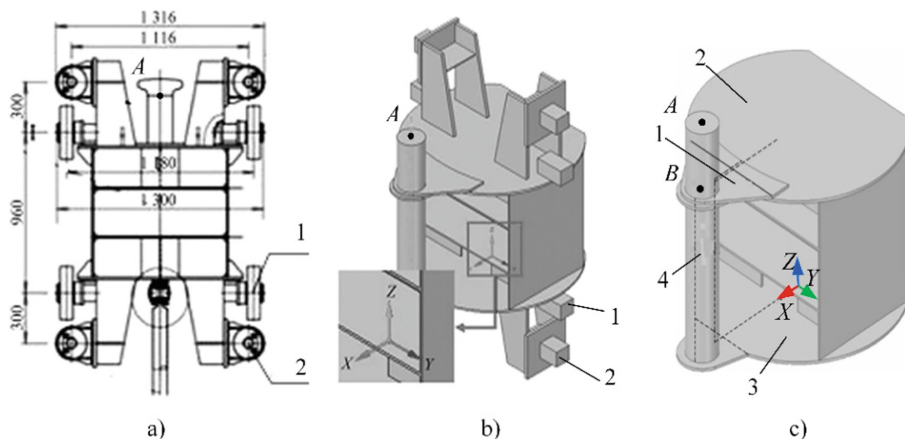
### 3 Research Methodology

The research object in this article is the existing bollard design (the most loaded upper part with an eye), which is in actual operation. The subject of the study is the stress-strain state of structural elements when external loads change in a particular range.

The range of external loads of the bollard is adopted, considering the following factors. The load on the eye of the bollard (taken during the design of the bollard), considering the stretching of the ropes and the action of the nominal hydrodynamic force on the moored vessel of the maximum allowable tonnage when opening the gates of the lock chamber  $F_1 = 150$  kN, is set as the initial one. The experience of operating a lock in the spring shows that an increase in the water level in the upper cascade of the lock due to snowmelt can cause a significant increase in the nominal hydrodynamic force. When modeling such a situation, the load on the eye of the bollard is assumed to be  $F_2 = 200$  kN. The operation of the lock in winter determines one more factor, which is taken into account in the simulation. Vessel icing is considered as such a factor, in which its mass increases by 20... 25% on average. This, in turn, leads to an increase in the load on the bollard eye to the value  $F_3 = 300$  kN. Considering the last factor and determining the relationship between it and the stress-strain state of the bollard elements is the most important since the most significant number of damages to the considered bollard was recorded in the winter period. Other force factors, namely the gravity force of the bollard metal structure, were not considered since this device has positive buoyancy, and the gravity forces of the structure are compensated by the expulsion force of the aquatic environment acting on the float.

The CAD system Autodesk Inventor was used to creating a corresponding 3D model based on the object of study. The basis for the creation was a set of working drawings of the operated bollard (Fig. 2a), specification of the product materials and technological maps for its manufacture. In the 3D modeling of the research object, some simplifications were adopted: the lateral guide rollers 1 and 2 of the real design (Fig. 2a) in the 3D model are represented by the protrusions in the form of prisms 1 and 2, about 8 units totally (Fig. 2b). This simplification is based on the fact that damage to the guide rollers is not fixed in real situations. At this stage, the XYZ coordinate system is introduced into the model, located by the XY plane at the lower end of the structure. The Z-axis of the introduced coordinate system passes along the axis of symmetry of the structure.

Considering the structural design of the simulated metal structure and information about the fixed damages in the developed 3D model, four main elements were identified for the analysis of their stress-strain state under changing external loading (Fig. 2c). These include the upper plate 1 for fixing the eye (as the most often deformable one), which is a “kerchief” element made of rolled stainless steel sheet 1.4541 EN 10088-1:2019 with a thickness of 30 mm; top 2 and bottom 3 round covers with two segments removed, made of rolled C45 ISO 6929:1987 structural steel sheet 25 mm thick; eye 4, made of a rolled round profile of low-carbon steel E 235-C (Fe 360-C) ISO 630:1995



**Fig. 2.** Modeling of the bollard structure under study: general overall dimensions of the structure (a); 3D model with accepted simplifications and coordinate system (b); structural elements under study and binding of reference points (s)

with a diameter of 100 mm. When conducting studies of the stress-strain state of the selected elements, it was considered that external loading in the form of a mooring force is applied at the first reference point A on the eye, located at a distance of  $\frac{3}{4}$  of the height of the eye from the top cover 2. The loading action is along the X-axis of the adopted system coordinates.

Analysis of the stress-strain state of the selected elements was carried out using the ANSYS Workbench CAE system after exporting the developed model from the CAD system to it. To reduce the error of geometric discretization when constructing a computational finite element mesh with one cell in the form of a cube with a side of 15 mm, adaptive mesh refinement by cells in the form of a cube with a side of 5 mm is implemented, which is used in some places of the model (the total volume of cells is increased by 18%). Adaptive mesh refinement is performed in the Solid186 block of the used CAE system. The nodes of each finite element of the computational grid of finite elements are subject to restrictions on 6 degrees of freedom, which determine their zero displacements and rotation angles.

The verification of the adequacy of the developed model and the corresponding computational finite element mesh was carried out by comparing the results of the test calculation of the bending stresses of element 4 (eye) both using the FEM and in the case of its simplified modeling by a beam with a uniform cross-section at a place determined by the second reference point B (see Fig. 2c). Simultaneously, the upper and lower elements of the “kerchief” of the bollard metal structure were considered as hinged supports of this beam, limiting its movement along the OX axis of the adopted coordinate system and making it statically determinate.

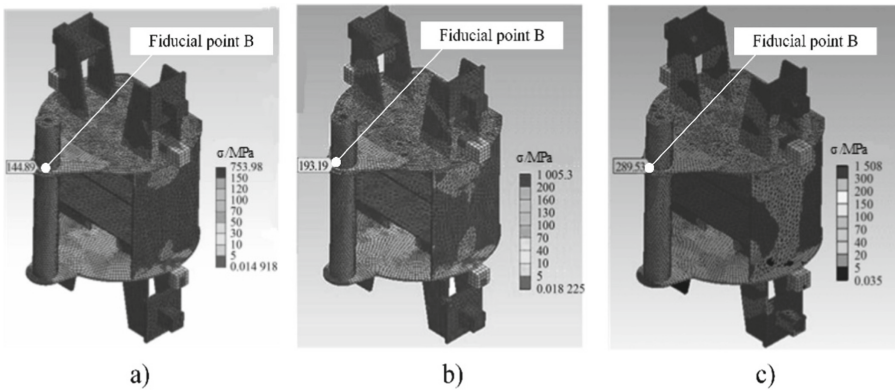
The calculated bending stresses, in this case, are obtained by the ratio of the obtained bending moments along the axis of the beam correlated to the area of its cross-section, which determines the expression

$$\sigma = M_{nz}/(W_{nz}) \quad (1)$$

where  $M_{nz}$  is the value of the bending moment in a particular section  $n$ , perpendicular to the longitudinal axis  $Z$  of the considered beam;  $W_{nz}$  is the area of the beam in some section  $n$ , perpendicular to the longitudinal axis  $Z$  of the considered beam.

The following was obtained when comparing the results of test calculations performed under the action of a load on the reference point of eye A with the value  $F_1 = 150$  kN. The stresses at the reference point B are 144.9 MPa and 141.3 MPa, respectively, for the FEM and the simplified calculation version. Thus, a relative error of about 2.5% was established, which allows us to assert that the developed model of the metal structure of a floating bollard of an actual design is fully adequate and that further research is possible.

In carrying out further studies, which consisted of a series of calculations of the considered structure in the accepted range of external loads, it was possible to obtain specific results in the form of appropriate stress diagrams associated with the geometric parameters of the elements selected for the study (Fig. 3).

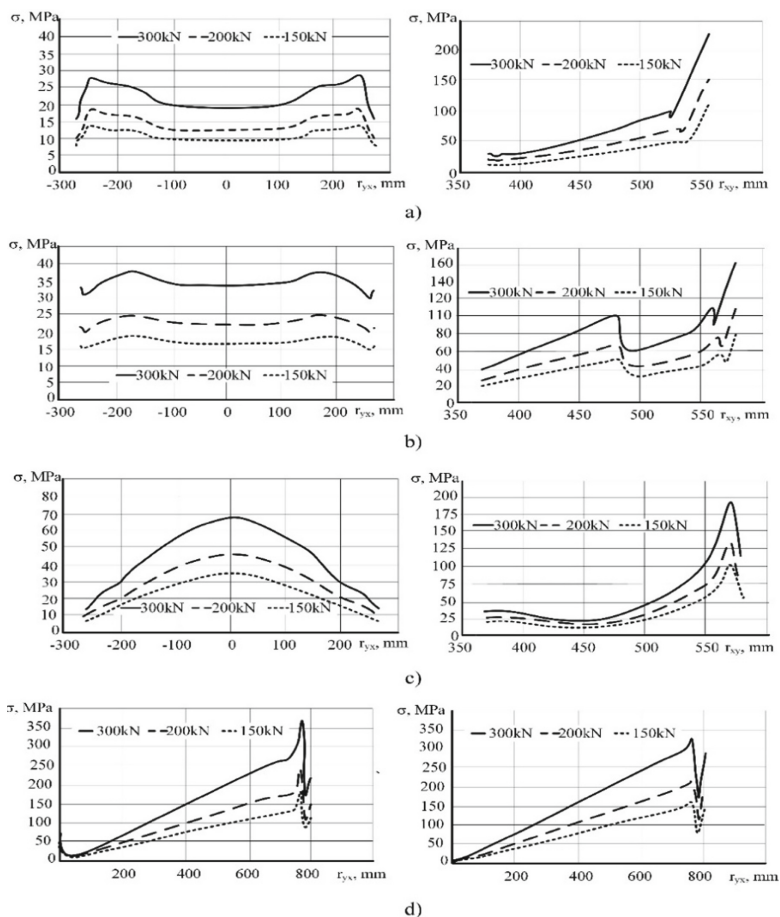


**Fig. 3.** Stress diagrams when modeling a bollard by the finite element method: under the action of a load  $F_1$  on the eye (a); under the action of load  $F_2$  on the eye (b); under the action of the load  $F_3$  on the eye (c)

## 4 Results

In the course of the studies carried out, it was found that in the case of variation in the load applied at the reference point A by the values  $F_1 = 150$  kN,  $F_2 = 200$  kN,  $F_3 = 300$  kN at the second reference point B, the position of which, in the accepted coordinate system, is determined by the values  $X = 715$  mm,  $Y = 0$  mm,  $Z = 800$  mm, corresponding stresses arise  $\sigma_1 = 144.9$  MPa,  $\sigma_2 = 193.2$  MPa,  $\sigma_3 = 289.5$  MPa. This determines the relationship between the load change and the stresses and shows the consistency of the simulation with the actual situation.

Graphical interpretation of the calculated stress distribution diagram on element 1 “kerchief” in a plane parallel to the XY plane of the adopted coordinate system shows the following (Fig. 4a).



**Fig. 4.** Distribution of stresses in a structural elements bollard: eltmt 1 (a); element 2 (b); element 3 (c); element 4 (d) ( $r_{yx}$  - distance between Y direction and axis X;  $r_{xy}$  - distance between X direction and axis Y)

With different loading options, the stress distribution in this element has an apparent symmetry. When the Y coordinate has a value of  $-250$  mm or  $250$  mm (which determines the width of the “kerchief”), the presence of the most significant stresses is recorded. In the case of an increase in the X coordinate (which determines the height of the “gusset”), as it approaches element 4, the stress level gradually increases, and in the area close to element 4 ( $X \approx 550$  mm), the calculated stresses are maximum.

Graphical interpretation of the calculated stress distribution on element 2 (top cover) shows the following (Fig. 4b). The pattern of stress distribution on this element is also symmetrical. As for the selected element 1, the maximum stresses are fixed in the case when the Y coordinate reaches the value of  $-250$  mm or  $250$  mm. As the X coordinate increases, the stresses on element 2 first increase, then decrease, then gradually increase,

and finally increase sharply. At the value of the coordinate  $X = 370$  mm, which determines the overlap of elements 1 and 2, the stresses decrease. This is due to a sharp change in the total cross-section of these two elements due to their permanent connection by welding. When the coordinate  $X \approx 550$  mm, thus defining a place close to element 4, a significant increase in the voltage on element 2 was recorded.

Graphical interpretation of the calculated stress distribution on element 3 (bottom cover) shows the following (Fig. 4c). The stress distribution on this element is also symmetrical. But in contrast to the distribution of stresses on elements 1 and 2, the value of the Y coordinate  $-250$  mm or  $250$  mm for element 3 determines the presence of the lowest stresses. As the X-coordinate increases, the stresses on element 3 first increase and then decrease. At  $X = 550$  mm, the maximum stress values were recorded for the element under consideration.

Graphical interpretation of the calculated stress distribution on element 4 shows the following (Fig. 4d). At different loading values, the stress on the inner and outer surfaces of element 4 gradually increases with the increase in the Z coordinate, which determines the place of application of the external load. When the coordinate takes the value  $Z \approx 750$  mm, determining the place of connection between elements 1, 2 and 4, the stress values are maximum. Moreover, the stresses on the inner surface of the element of element 4 are 25% greater than on its outer surface.

Thus, based on the study, it follows that the stress peak point is located at the junction of elements 1, 2, and 4.

## 5 Conclusions

Based on the research carried out, the following conclusions were obtained:

1. Comparative analysis of the results of the calculation of the stress-strain state at the selected reference point, obtained in the case of using the created finite element model of the device under consideration and its simplified calculation model, indicate their identity with a relative error of 2.5%, which confirms the adequacy the developed model and the reliability of the results of the conducted numerical simulation.
2. The stress peak point established during the study, located at the junction of elements 1, 2, and 4, allows a number of works to optimize the shaping of the connected elements and technological requirements when creating the connection itself. Given that the connection is welded, it is possible to recommend using additional strength elements at the junction or an increase in the height of the “kerchief”, which will increase the overlap between the elements and increase the area of the welds.
3. The obtained data provide a theoretical basis for installing warning sensors about the force state of the ship’s floating bollard at the place of the stress peak or in its immediate vicinity.
4. The use of the proposed system of control sensors will allow organizing service for the preliminary cleaning of ships from snow and ice in winter before locking.

## References

1. Felski, A., Zwolak, K.: The ocean-going ships-challenges and threats. *J. Mar. Sci. Eng.* **8**, 41–50 (2020)
2. Ivanov, V., Pavlenko, I., Kuric, I., Kosov, M.: Mathematical modeling and numerical simulation of fixtures for fork-type parts manufacturing. In: Knapčíková, L., Balog, M. (eds.) *Industry 4.0: Trends in Management of Intelligent Manufacturing Systems*. EICC, pp. 133–142. Springer, Cham (2019). [https://doi.org/10.1007/978-3-030-14011-3\\_12](https://doi.org/10.1007/978-3-030-14011-3_12)
3. Yudin, Yu.: Variable components of the effect of regular waves on the ship's hull. *Vestnik MGTU: works of Murman. state tech. un-that* **12**(3), 471–476 (2011)
4. Yang, S., Ringsberg, J.: Towards the assessment of impact of unmanned vessels on maritime transportation safety. *Realiab. Eng. Syst. Saf.* **165**, 155–169 (2017)
5. Bergdahl, L., Palm, J., Eskilsson, C., Lindahl, J.: Dynamically scaled model experiment of a mooring cable. *J. Mar. Sci. Eng* **4**, 5–12 (2016)
6. Johanning, L., Smith, G., Wolfram, J.: Measurements of static and dynamic mooring line damping and their importance for floating WEC devices. *Ocean Eng.* **34**, 1918–1934 (2007)
7. Martinelli, L., Ruol, P., Cortellazzo, G.: On mooring design of wave energy converters: the seabreath application. *Coast. Eng. Proc.* **1**, 3–18 (2012)
8. Pavlenko, I.: Static and dynamic analysis of the closing rotor balancing device of the multistage centrifugal pump. *Appl. Mech. Mater.* **630**, 248–254 (2014). <https://doi.org/10.4028/www.scientific.net/AMM.630.248>
9. Ivanov, V., Dehtiarov, I., Pavlenko, I., Kosov, I., Kosov, M.: Technology for complex parts machining in multiproduct manufacturing. *Manag. Prod. Eng. Rev.* **10**(2), 25–36 (2019). <https://doi.org/10.24425/mper.2019.129566>
10. Ivanov, V., Dehtiarov, I., Pavlenko, I., Kosov, M., Hatala, M.: Technological assurance and features of fork-type parts machining. In: Ivanov, V., et al. (eds.) *DSMIE 2019. LNME*, pp. 114–125. Springer, Cham (2020). [https://doi.org/10.1007/978-3-030-22365-6\\_12](https://doi.org/10.1007/978-3-030-22365-6_12)
11. Tsukrov, I., Eroshkin, O., Paul, W.: Celikkol B. Numerical modeling of nonlinear elastic components of mooring systems. *IEEE J. Ocean. Eng.* **30**, 37–46 (2005)
12. Xu, Z., Huang, S.: Numerical investigation of mooring line damping and the drag coefficients of studless chain links. *J. Mar. Sci. Appl.* **13**(1), 76–84 (2014). <https://doi.org/10.1007/s11804-014-1235-0>
13. Trojanowski, P., Trojanowska, J.: Reliability of road transport means as a factor affecting the risk of failure – the transport problem case study. In: Ivanov, V., Trojanowska, J., Pavlenko, I., Zajac, J., Peraković, D. (eds.) *DSMIE 2021. LNME*, pp. 253–261. Springer, Cham (2021). [https://doi.org/10.1007/978-3-030-77719-7\\_26](https://doi.org/10.1007/978-3-030-77719-7_26)
14. Trojanowski, P., Filina-Dawidowicz, L.: Diagnostic and repair centers locating methodology for vehicles carrying sensitive cargo. *Transp. Res. Procedia* **55**, 410–417 (2021). <https://doi.org/10.1016/j.trpro.2021.07.004>
15. Lasinska, N.: Hybrid management methodology for transport projects related to rolling stock. *J. Eng. Sci.* **8**(2), B7–B11 (2021). [https://doi.org/10.21272/jes.2021.8\(2\).b2](https://doi.org/10.21272/jes.2021.8(2).b2)
16. Trojanowski, P.: Comparative analysis of the impact of road infrastructure development on road safety – a case study. *Sci. J. Maritime Univ. Szczecin* 23–28 (2020). <https://doi.org/10.17402/436>
17. Spanos, P., Arena, F., Richichi, A., Malara, G.: Efficient dynamic analysis of a nonlinear wave energy harvester model. *J. Offshore Mech. Arctic Eng.* **138**, 40–49 (2016)
18. Chai, Y., Varyani, K., Barltrop, N.: Semi-analytical quasi-static formulation for three-dimensional partially grounded mooring system problems. *Ocean Eng.* **29**, 627–649 (2002)
19. Pascoal, R., Huang, S., Barltrop, N., Soares, C.: Equivalent force model for the effect of mooring systems on the horizontal motions. *Appl. Ocean Res.* **27**, 165–172 (2005)

20. Bate, K.: Finite Element Methods. Fizmatlit, Moscow (2010)
21. Pavlenko, I.V., Simonovskiy, V.I., Demianenko, M.M.: Dynamic analysis of centrifugal machines rotors supported on ball bearings by combined application of 3D and beam finite element models. IOP Conf. Ser. Mater. Sci. Eng. **233**(1), 012053 (2017). <https://doi.org/10.1088/1757-899X/233/1/012053>
22. Ivanov, V., et al.: Numerical simulation of the system “fixture–workpiece” for lever machining. Int. J. Adv. Manuf. Technol. **91**(1–4), 79–90 (2016). <https://doi.org/10.1007/s00170-016-9701-2>





# Rotor Dynamics and Stability of the Centrifugal Pump CPN 600-35 for Nuclear Power Plants

Ivan Pavlenko<sup>(✉)</sup> , Vitalii Simonovskiy, Anton Verbovyi , Oleksandr Ivchenko ,  
and Vitalii Ivanov 

Sumy State University, 2, Rymskogo-Korsakova Street, Sumy 40007, Ukraine  
i.pavlenko@omdm.sumdu.edu.ua

**Abstract.** The paper ensures the vibration reliability of the centrifugal pump CPN 600-35 for the water supply of an industrial circuit at nuclear power plants by improving its technical designs. The main aim of the research is to develop an approach for parameter identification of rotor dynamics and analyze the dynamic stability of the rotor movement. For this purpose, the modified design of the centrifugal pump CPN 600-35 was developed. Also, the main parameters of the rotor dynamics model (e.g., equivalent stiffness and discrete mass) were evaluated based on the parametric identification approach. Moreover, the eigenfrequencies and the corresponding mode shapes of free oscillations were obtained based on the finite element method. Finally, the dynamic stability of the rotor movement was studied based on the developed mathematical model of its oscillations considering the circulating and internal friction forces. Finally, based on the Routh-Hurwitz criterion, the stability region of rotor movement in terms of the dimensionless frequency and friction coefficient was analytically obtained.

**Keywords:** Energy efficiency · Oscillations · Critical frequency · Discrete-mass model · Parameter identification · Circulating force · Internal Friction · Routh-Hurwitz criterion · Industrial growth

## 1 Introduction

Ensuring centrifugal machines' energy efficiency and vibration reliability is one of the primary tasks in their design and operation [1]. This problem is to provide rotation stability and a sufficiently low vibration level. It is aggravated by the presence in power machines not only centrifugal forces caused by imbalances, with a frequency equal to the rotational speed but also by high-frequency forces (e.g., blade component) with the frequencies many times higher than the rotor speed [2].

Notably, in the case of stability loss, which can be estimated based on a linear model of rotor oscillations, the total amplitudes may not exceed the permissible. Nevertheless, unacceptable self-oscillations occur, which are typical for nonlinear dynamic systems. Their presence can be determined based on spectral analysis [3]. In this case, an inappropriate state of rotor dynamics can be detected using special equipment, which is not always ensured during the operation of power machines.

According to the mentioned above, the rotor dynamics and stability of centrifugal pumps for nuclear power plants is an urgent problem, particularly considering the internal friction [4]. Its solving is supplemented by up-to-date computational means in their comprehensive combination with the analytical methods.

Therefore, the main aim is to develop a general approach for ensuring the vibration reliability of centrifugal pumps for nuclear power plants.

The scientific novelty of this study is in considering a single-mass model of rotor dynamics. In this model, equivalent mass and stiffness are determined by the parameter identification approach based on the finite element analysis of rotor dynamics [5]. In this case, stability conditions are determined by an analytical dependence. Moreover, it should analyze the impact of the main design parameters and operating modes on the dynamic stability of the rotor movement.

## 2 Literature Review

Recent advancements in rotor dynamics and stability are presented in a number of scientific publications worldwide.

Zhou et al. [6] carried out a multiple-frequency synchronization experiment with a dual-rotor actuation vibration system. As a result, the stability criterion between eccentric rotors was developed based on the Poincare–Lyapunov principle. Kumar and Affijulla [7] studied rotor dynamics for power systems. As a result, a rotor stability monitoring system was proposed. Li et al. [8] investigated leakage and dynamic characteristics for different annular gas seals operating in supercritical turbomachinery. As a result, it was shown that the inlet swirl brake significantly reduces the preswirl velocity, lowering the crossover frequency to maximize the operational frequency range. Chao et al. [9] proposed the hierarchical power flow control methodology in smart grids. As a result, rotor stability with demand-side flexibility was enhanced. Chelabi et al. [10] highlighted advancements in analyzing the spatial accelerating flow in a mixed turbine's rotor. Sokolov et al. [11] proposed the methodology for designing automatic rotary motion electrohydraulic drive to ensure technological equipment's vibration reliability.

Also, Li et al. [12] proposed the methodology of dynamic balancing for magnetic bearings supporting rigid rotors based on extended state observers. Filsoof et al. [13] studied critical aeroelastic modes of a tri-rotor wind turbine. As a result, it was shown that the dynamics of the lower rotors change significantly both in eigenfrequencies and damping ratios. Chen et al. [14] investigated dynamics of the vibration system driven by three homodromy eccentric rotors using control synchronization. As a result, the fundamentals for designing vibration machines using control synchronization were provided. Yashchenko et al. [15] studied the impact of bearing housings on centrifugal pump rotor dynamics.

Additionally, Shrestha and Gonzalez-Longatt [16] carried out a parametric sensitivity analysis of rotor angle stability indicators. As a result, the methodology was proposed to estimate critical fault clearing time, eigenvalue points, damping ratio, frequency deviation, voltage deviation, and generator's speed deviation. Li et al. [17] studied the dynamics and stability of a rotor-bearing system with the bolted-disk joint. Krol et al. [18] investigated the vibration stability of spindle nodes to ensure optimal parameters

of the technological equipment. Jiang [19] proposed a comprehensive approach based on finite element analysis and multi-objective optimization to study the dynamics of flexible rotor-bearing systems.

Additionally, Li and Tang [20] simulated a numerically high-speed rolling bearing-dual rotor spindle system through discrete modeling dynamics. Zhang et al. [21] studied dynamic characteristics of a novel pocket damper seal with self-regulated injection. Liu et al. [22] proposed a passivity-based control system for quad-tilt rotor unmanned aerial vehicles. Zhao et al. [23] studied vibration characteristics of the helical gear rotor system considering a mixed modification. Also, Osadchiy et al. [24] developed an integrated technology for manufacturing gear systems. Moreover, Volina et al. [25, 26] and Pylypaka et al. [27] studied the movement of blades in centrifugal machines. Finally, Saeed et al. [28] investigated nonlinear dynamics and motion bifurcations of the rotor active magnetic bearings system with a novel control scheme.

Moreover, a number of scientific results were obtained in enhancing the tribological characteristics of functional materials [29]. Particularly, Tarelnyk et al. [30] developed an up-to-date method for surfacing steel shafts. Also, Martsynkovskyy et al. [31] proposed protecting shafts and couplings. Moreover, Svirzhevskiy et al. [32] analyzed methods for evaluating the wear resistance of the contact surfaces for rolling bearings. Finally, Kotliar et al. [33] proposed an approach for ensuring rotor systems' reliability and performance criteria.

### 3 Research Methodology

#### 3.1 The Design of the Centrifugal Pump

The multistage centrifugal pump CPN 600-35 ensures the water supply for an industrial circuit at nuclear power plants. Its nominal parameters are feed  $600 \text{ m}^3/\text{h}$ , head 35 m, and operating frequency 1500 rpm.

The pump design must correspond to the following national standards concerning rules and regulations in the nuclear power industry according to the requirements of SE "NNEGC "Energoatom": SOU NAEK 158:2020 "Ensuring technical safety. Technical requirements for the design and safe operation of equipment and pipelines of nuclear power plants with the WWER", 159:2020 "Ensuring technical safety. Welding and surfacing of equipment and pipelines of nuclear power plants with the WWER", 160:2020 "Ensuring technical safety. Quality control of the base metal welded joints and surfacing of equipment and pipelines of nuclear power plants with the WWER"; PNAE G-7-002-86 "Rules of strength calculation for equipment and pipelines of nuclear power plants".

According to the requirements presented above, the following design of the centrifugal pump CPN 600-35 for nuclear power plants (Fig. 1) has been developed within the research project "Fulfillment of tasks of the perspective plan of development of a scientific direction "Technical sciences" Sumy State University" ordered by the Ministry of Education and Science of Ukraine (State Reg. No. 0121U112684).



### 3.2 Parameter Identification of a Single-Mass Model

The problem of rotor dynamics is mainly studied using the finite element method. However, it does not allow us to evaluate the dynamic stability of rotor systems analytically. Therefore, the parameter identification approach is applied comprehensively with the finite element analysis and analytical approaches.

The procedure of parameter identification of a single-mass mathematical model of rotor dynamics is based on the hypothesis that the compliance of the rotor and its first eigenfrequency can be the same as for the finite-element model. In this regard, the following equations should be satisfied:

$$c_e = \frac{F_{unit}}{x_{res}}; m_e = \frac{c_e}{\omega_1^2}, \quad (1)$$

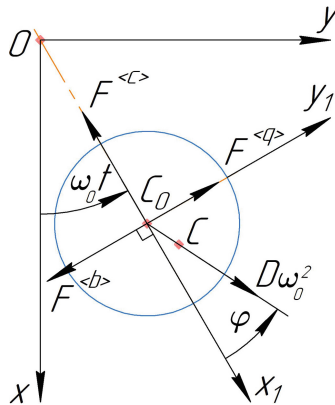
where  $c_e$  – equivalent stiffness, N/m;  $m_e$  – equivalent mass, kg;  $F_{unit}$  – unit force applied at the impeller's mass center at a near-zero value of operating frequency, N;  $x_{res}$  – resulting displacement of the impeller's mass center, m;  $\omega_1$  – the 1st eigenfrequency.

### 3.3 The Mathematical Model of the Single-Mass Rotor Dynamics

The proposed model of rotor dynamics in a complex form is as follows (Fig. 3):

$$m_e \ddot{z} + c_e z = D \omega_0^2 e^{i(\omega_0 t + \varphi)} + F_c + F_b + F_q + F_\zeta, \quad (2)$$

where  $z = x + i \cdot y$  – complex displacement of the mass center;  $x, y$  – components of the mass center's displacement in the plane perpendicular to the rotation axis, m;  $D$  – permissible residual imbalance, kg·m;  $\omega_0$  – operating speed, rad/s;  $t$  – time, s;  $\varphi$  – phase shift, rad;  $i$  – imaginary unit.



**Fig. 3.** The design scheme of rotor oscillations:  $x, y$  – global coordinates;  $x_1, y_1$  – local coordinates;  $C_0$  – the geometric center of the cross-section;  $C$  – the mass center of the rotor.

This model also includes the hydrodynamic forces acting to the impeller, particularly hydrodynamic stiffness force  $F_c$  proportional to the displacement, damping force  $F_b$  proportional to the velocity, and circulating force  $F_q$  proportional to the cross-displacements [34]:

$$F_c = -c_0 z; F_b = -b_0 \dot{z}; F_q = iq_0 z, \quad (3)$$

where  $c_0$  – coefficient of the hydrodynamic stiffness, N/m;  $b_0$  – damping factor, N·s/m;  $q_0$  – coefficient of the circulating force, N/m.

The hydrodynamic coefficients are determined by the following dependencies [35]:

$$c_0 = \frac{\pi d_0 l_0}{4h_0} \Delta p_0; b_0 = \frac{\pi \mu d_0 l_0^3}{24h_0^3}; q_0 = \frac{1}{2} b_0 \omega_0, \quad (4)$$

where  $d_0$ ,  $l_0$ , and  $h_0$  – diameter, length, and radial gap of the throttle, m;  $\mu$  – dynamic viscosity of the operating fluid, Pa·s/m;  $\Delta p_0$  – pressure difference on the gap, Pa.

Additionally, the internal viscous friction force proportional to the relative velocity is considered. Its value in the moving and fixed coordinate systems are as follows [36]:

$$F_{1\zeta} = -\zeta \dot{z}_1; F_\zeta = -\zeta (\dot{z} - i\omega_0 z), \quad (5)$$

where  $\zeta$  – internal friction coefficient, N·s/m.

Overall, the initial differential equation of rotor dynamics (2) takes the form:

$$m_e \ddot{z} + (b_0 + \zeta) \dot{z} + [c_e + c_0 - i(q_0 + \zeta \omega_0)] z = D \omega_0^2 e^{i(\omega_0 t + \varphi)}, \quad (6)$$

or in projections on the coordinates  $x$  and  $y$ , and considering formula (4):

$$\begin{cases} m_e \ddot{x} + (b_0 + \zeta) \dot{x} + (c_e + c_0)x + \frac{1}{2}(b_0 + 2\zeta)\omega_0 y = D \omega_0^2 \cos(\omega_0 t + \varphi); \\ m_e \ddot{y} + (b_0 + \zeta) \dot{y} + (c_e + c_0)y - \frac{1}{2}(b_0 + 2\zeta)\omega_0 x = D \omega_0^2 \sin(\omega_0 t + \varphi). \end{cases} \quad (7)$$

### 3.4 Dynamic Stability of the Rotor Movement

It is known that internal friction does not affect the amplitude-frequency response. However, the impact of this force on rotor stability was not considered entirely.

The dynamic stability of the rotor's motion can be studied according to the Routh-Hurwitz criterion [37]. In this case, components in the right parts of Eqs. (3) are zero, and the differential operator  $p$  is introduced. Consequently, the system of linear algebraic equations can be obtained:

$$\begin{cases} [m_e p^2 + (b_0 + \zeta)p + c_e + c_0]x + \frac{1}{2}(b_0 + 2\zeta)\omega_0 y = 0; \\ -\frac{1}{2}(b_0 + 2\zeta)\omega_0 x + [m_e p^2 + (b_0 + \zeta)p + c_e + c_0]y = 0. \end{cases} \quad (8)$$

Therefore, the internal friction increases the terms concerning damping and the circulating forces.

The corresponding characteristic equation is as follows:

$$\left| \begin{bmatrix} m_e p^2 + b_0 p + c_e + c_0 & \frac{1}{2}(b_0 + 2\zeta)\omega_0 \\ -\frac{1}{2}(b_0 + 2\zeta)\omega_0 & m_e p^2 + (b_0 + \zeta)p + c_e + c_0 \end{bmatrix} \right| = \sum_{j=0}^4 a_j p^{4-j} = 0, \quad (9)$$

where the following coefficients have been introduced:

$$\begin{aligned} a_0 &= m_e^2; a_1 = 2(b_0 + \zeta)m_e; a_2 = (b_0 + \zeta)^2 + 2(c_e + c_0)m_e; \\ a_3 &= 2(b_0 + \zeta)(c_e + c_0); a_4 = c^2 + (b_0 + \zeta)\zeta\omega_0^2 + \frac{1}{4}b_0^2\omega_0^2. \end{aligned} \quad (10)$$

The negative parts of solutions  $p_j$  determine the stability region of rotor movement. According to the Routh-Hurwitz criterion, this requirement is completely satisfied for the following inequalities:

$$\begin{cases} a_j > 0; \\ \Delta_2 = a_1a_2 - a_0a_3 = 2m_e(b_0 + \zeta)[(c_e + c_0)m_e + (b_0 + \zeta)^2] > 0; \\ \Delta_2a_3 - a_1^2a_4 = m_e(b_0 + \zeta)[(c_e + c_0)(b_0 + \zeta)^2 - m_e(b_0 + 2\zeta)^2\omega_0^2] > 0. \end{cases} \quad (11)$$

The first two of these inequalities are automatically satisfied. However, the last one leads to the following stability condition (Fig. 4):

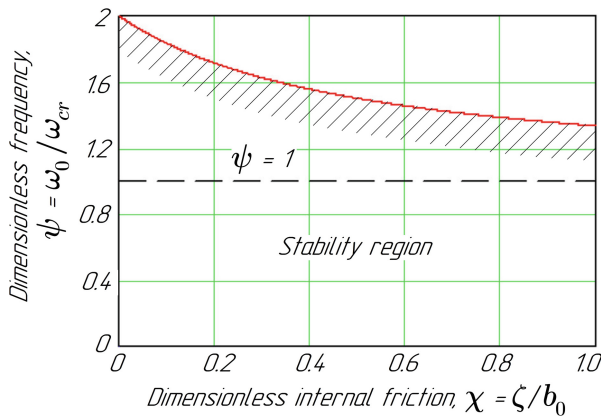
$$\psi(\chi) < \frac{2(1 + \chi)}{1 + 2\chi}, \quad (12)$$

where the following dimensionless frequency  $\psi$  and friction ratio  $\chi$  have been introduced:

$$\psi = \frac{\omega_0}{\omega_{cr}}; \chi = \frac{\zeta}{b_0}, \quad (13)$$

where  $\omega_{cr}$  – critical frequency,

$$\omega_{cr} = \sqrt{\frac{c_e + c_0}{m_e}} = \omega_1 \sqrt{1 + \frac{c_0}{c_e}}. \quad (14)$$



**Fig. 4.** The stability region of rotor movement.

Therefore, despite the internal friction not affecting the amplitude-frequency response, it impacts the rotor stability. Moreover, according to the stability criterion, the maximum operating frequency should be less than the maximum value  $\psi\omega_{cr}$ , where the dimensionless coefficient varies in a range of  $1 \leq \psi < 2$  depending on the value of the internal friction coefficient  $\zeta$ . Remarkably, if the dimensionless frequency  $\psi < 1$ , the rotor motion is stable for a whole range of change in the internal friction coefficient.

## 4 Results

The initial data for dynamic analysis and stability of the designed centrifugal pump CPN 600-35 based on the finite-element model is summarized in Table 1. The calculations are realized using the authors' operating file "Critical frequencies of the rotor" of the computer algebra system MathCAD.

**Table 1.** The initial data of the dynamic analysis.

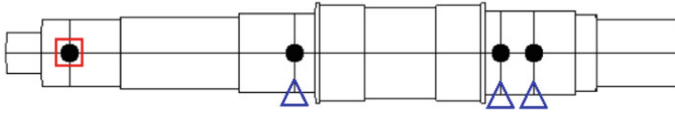
Section no.	Length, m	Diameter, m	Local mass, kg	Moment of inertia, kg·m <sup>2</sup>	Stiffness, N/m
1	0.045	0.036	–	–	–
2	0.036	0.060	–	–	–
3	0.064	0.060	24.37	0.391	–
4	0.149	0.065	–	–	–
5	0.07	0.070	–	–	–
6	0.026	0.070	4.35	–	$1 \cdot 10^{12}$
7	0.005	0.090	–	–	–
8	0.057	0.086	–	–	–
9	0.090	0.082	–	–	–
10	0.057	0.086	–	–	–
11	0.005	0.090	–	–	–
12	0.019	0.075	–	–	–
13	0.042	0.075	3.47	–	$1 \cdot 10^{12}$
14	0.053	0.075	3.47	–	$1 \cdot 10^{12}$
15	0.026	0.068	–	–	–
16	0.105	0.060	–	–	–

The traditional design scheme corresponding to Fig. 2 and Table 1 is presented in Fig. 5.

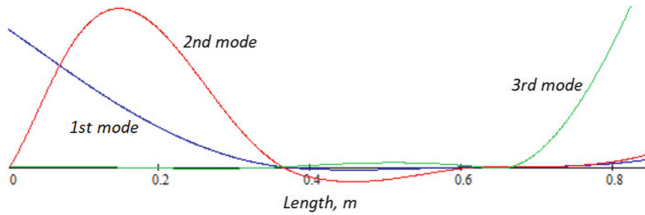
The first three resulting mode shapes of free oscillations are presented in Fig. 6.

The corresponding critical frequencies were obtained using the finite element method using the authors' operating file "Critical frequencies of the rotor" of the computer





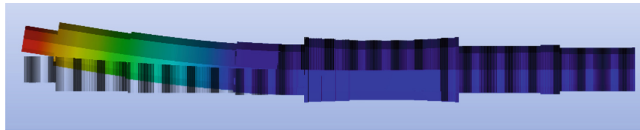
**Fig. 5.** The traditional design scheme of the rotor:  $\triangle$ – bearing support;  $\bullet$ – local mass;  $\square$ – moment of inertia.



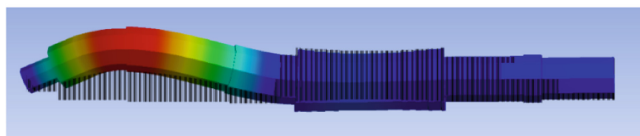
**Fig. 6.** The mode shapes of free oscillations, obtained using the program “Critical frequencies of the rotor”.

algebra system MathCAD. The corresponding values are:  $\omega_{cr1} = 702$  rad/s,  $\omega_{cr2} = 2525$  rad/s, and  $\omega_{cr3} = 9995$  rad/s.

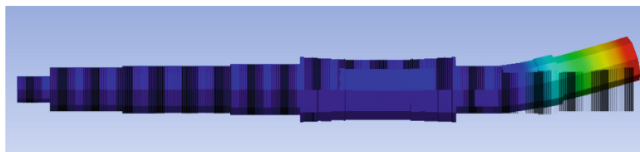
The reliability of this model is proved by the similar results obtained using the ANSYS software (Fig. 7).



a



b



c

**Fig. 7.** The 1st (a), 2nd (b), and 3rd (c) mode shapes of free oscillations, obtained using the ANSYS software.

The comparison of the results obtained using the MathCAD and ANSYS software is presented in Table 2.

**Table 2.** Comparison of the results.

Software	Eigenfrequency, rad/s		
	1st	2nd	3rd
MathCAD	702	2525	9995
ANSYS	687	2432	8723
Relative error, %	2.2	3.8	14.6

The relative error for evaluating the 1st eigenfrequency  $\omega_1$  does not exceed 2.2%. Therefore, the authors' methodology, realized within the operating file "Critical frequencies of the rotor", is reliable for the designed centrifugal pump CPN 600-35 for nuclear power plants.

Notably, since the 1st critical frequency  $\omega_{cr1} = 732$  rad/s is 4.47 times higher than the operating speed  $\omega_0 = 157$  rad/s, detuning from the resonance is equal to 347%. Therefore, mechanical vibrations can be considered according to the international standard ISO 1940-1:2003 "Mechanical vibration – Balance quality requirements for rotors in a constant (rigid) state – Part 1: Specification and verification of balance tolerances (IDT)".

According to formula (1), the equivalent stiffness can be determined using the finite element method using the authors' operating file "Forced oscillations of the rotor" of the computer algebra system MathCAD. After calculations, the corresponding value is equal to  $c_e = 2.02 \cdot 10^7$  N/m. Also, the equivalent mass (1) is equal to  $m_e = 41.0$  kg. Also, for the particular case study, the following physical and geometrical parameters of the throttling gaps have been considered: pressure difference  $\Delta p_0 = 3.43 \cdot 10^5$  Pa; dynamic viscosity of the operating fluid at normal conditions  $\mu = 1.0 \cdot 10^{-3}$  Pa·s. According to the pump design (Fig. 1), the following geometrical parameters of the radial throttle have been considered: diameter  $d_0 = 0.2245$  m; length  $l_0 = 0.045$  m; gap  $h_0 = (0.25 \dots 0.30) \cdot 10^{-3}$  m.

According to formulas (4) and (13), the following parameters have been evaluated: damping factor  $b_0 = 99.1 \dots 171.4$  N·s/m.

Due to the results presented by Roy and Tiwari [38], for a similar rotor, and under the common assumption that the variation coefficient is equal to 0.2, the friction coefficient in a three-sigma range is equal to  $\zeta = 8 \dots 32$  N·s/m. According to formula (14), the dimensionless friction ratio  $\chi = 0.047 \dots 0.323$ , and the dimensionless frequency  $\psi = 0.180 \dots 0.186$ .

Finally, the maximum dimensionless frequency (12) is equal to  $\psi_{max} = 1.608$ . Therefore, since this value is 8.64 times higher than the value  $\psi = 0.186$ , the rotor motion is stable with a margin of 764%.

## 5 Conclusions

Thus, in the paper, the centrifugal pump CPN 600-35 for the water supply of an industrial circuit at nuclear power plants has been modernized. This design corresponds to national standards concerning rules and regulations in the nuclear power industry according to SE “NNEGC “Energoatom” requirements, i.e., SOU NAEK 158:2020, 59:2020, 160:2020, and PNAE G-7-002-86.

For ensuring vibration reliability of the designed pump, the parameter identification approach has been applied jointly with the finite element analysis and analytical modeling. As a result, the equivalent mass and stiffness of the rotor system have been evaluated. The mathematical model of rotor dynamics has been developed considering inertia, stiffness, damping, circulating, and internal friction forces.

Since the operating speed of 157 rad/s is significantly less than the first critical frequency of 702 rad/s, detuning from the resonance equals 347%. Therefore, dynamic balancing of the rotor should be carried out according to the international standard ISO 1940-1:2003.

Moreover, the first three eigenfrequencies have been calculated numerically using the ANSYS software and the developed operating file “Critical frequency of the rotor” of the computer algebra system MathCAD. Each program is based on the finite element method. The relative difference between the first two eigenfrequencies does not exceed 4%.

Finally, based on the Routh-Hurwitz criteria, the dynamic stability of the rotor movement has been assessed in terms of operating frequency and friction coefficient, and the corresponding stability region has been built. Notably, for the designed rotor, its motion is dynamically stable with a margin of 764%.

Notably, the presented research corresponds to the objective “Increasing the pressure of the stages of pumping units and ensuring the vibration reliability of the functional elements of the complex hydrodynamic system based on improving the design of pumping equipment of nuclear power plants (NPPs) by developing technical designs for water supply pumps and auxiliary systems” according to the Agreement No. BF/26-2021 between Sumy State University and Ministry of Education and Science of Ukraine.

**Acknowledgment.** The scientific results have been obtained within the research project “Fulfillment of tasks of the perspective plan of development of a scientific direction “Technical sciences” Sumy State University” ordered by the Ministry of Education and Science of Ukraine (State Reg. No. 0121U112684). The research was partially supported by the Research and Educational Center for Industrial Engineering (Sumy State University) and International Association for Technological Development and Innovations.

## References

1. Hadroug, N., Hafaifa, A., Alili, B., Iratni, A., Chen, X.: Fuzzy diagnostic strategy implementation for gas turbine vibrations faults detection: towards a characterization of symptom–fault correlations. *J. Vib. Eng. Technol.* (2021). <https://doi.org/10.1007/s42417-021-00373-z>

2. Qin, J., Gao, X., Yan, Q., Huang, W.-C., Yao, G.: High frequency modal test and dynamic performance evaluation of turbine rotor blades. In: 31st Congress of the International Council of the Aeronautical Sciences, ICAS 2018, p. 143115 (2018)
3. Yanez-Borjas, J.J., Camarena-Martinez, D., Vasquez-Barrera, M.A., Romero-Troncoso, R.J., Morinigo-Sotelo, D.: Experimental validation of the broken rotor bar fault evolution in lined induction motors. In: 2018 IEEE International Autumn Meeting on Power, Electronics and Computing. ROPEC 2018, pp. 1–7 (2019). <https://doi.org/10.1109/ROPEC.2018.8661426>
4. Dimentberg, M.F.: Vibration of a rotating shaft with randomly varying internal damping. *J. Sound Vib.* **285**, 759–765 (2005). <https://doi.org/10.1016/j.jsv.2004.11.025>
5. Simonovskiy, V., Pavlenko, I., Pitel, J., Stremoukhov, D., Ivanov, V.: Methods and algorithms for calculating nonlinear oscillations of rotor systems. In: Ivanov, V., Pavlenko, I., Liaposhchenko, O., Machado, J., Edl, M. (eds.) DSMIE 2021. LNME, pp. 63–74. Springer, Cham (2021). [https://doi.org/10.1007/978-3-030-77823-1\\_7](https://doi.org/10.1007/978-3-030-77823-1_7)
6. Zou, M., Fang, P., Hou, Y., Peng, H.: Investigation on multiple-frequency synchronization experiment of vibration system with dual-rotor actuation. *Mech. Syst. Signal Process.* **164**, 108261 (2022). <https://doi.org/10.1016/j.ymsp.2021.108261>
7. Kumar, M., Affijulla, S.: On-line estimation of alternators rotor angle dynamics in the modern power system. *Int. J. Electr. Power Energy Syst.* **134**, 107314 (2022). <https://doi.org/10.1016/j.ijepes.2021.107314>
8. Li, Z., Li, Z., Li, J., Feng, Z.: Leakage and rotordynamic characteristics for three types of annular gas seals operating in supercritical CO<sub>2</sub> turbomachinery. *J. Eng. Gas Turbines Power* **143**(10), 101002 (2021). <https://doi.org/10.1115/1.4051104>
9. Chao, D., Chakraborty, P., Nishikawa, T., Motter, A.E.: Hierarchical power flow control in smart grids: enhancing rotor angle and frequency stability with demand-side flexibility. *IEEE Trans. Control Netw. Syst.* **8**(3), 1046–1058 (2021). <https://doi.org/10.1109/TCNS.2021.3070665>
10. Chelabi, M.A., Basova, Y., Hamidou, M.K., Dobrotvorskiy, S.: Analysis of the three-dimensional accelerating flow in a mixed turbine rotor. *J. Eng. Sci.* **8**(2), D1–D7 (2021). [https://doi.org/10.21272/jes.2021.8\(2\).d2](https://doi.org/10.21272/jes.2021.8(2).d2)
11. Sokolov, V., Porkuian, O., Krol, O., Stepanova, O.: Design calculation of automatic rotary motion electrohydraulic drive for technological equipment. In: Ivanov, V., Trojanowska, J., Pavlenko, I., Zajac, J., Peraković, D. (eds.) DSMIE 2021. LNME, pp. 133–142. Springer, Cham (2021). [https://doi.org/10.1007/978-3-030-77719-7\\_14](https://doi.org/10.1007/978-3-030-77719-7_14)
12. Li, K., Peng, C., Deng, Z., Huang, W., Zhang, Z.: Field dynamic balancing for active magnetic bearings supporting rigid rotor shaft based on extended state observer. *Mech. Syst. Signal Process.* **158**, 107801 (2021). <https://doi.org/10.1016/j.ymsp.2021.107801>
13. Filsoof, O.T., Yde, A., Bøttcher, P., Zhang, X.: On critical aeroelastic modes of a tri-rotor wind turbine. *Int. J. Mech. Sci.* **204**, 106525 (2021). <https://doi.org/10.1016/j.ijmecsci.2021.106525>
14. Chen, X., Liu, J., Li, L.: Dynamics of the vibration system driven by three homodromy eccentric rotors using control synchronization. *Appl. Sci.* **11**(16), 7691 (2021). <https://doi.org/10.3390/app11167691>
15. Yashchenko, A.S., Rudenko, A.A., Simonovskiy, V.I., Kozlov, O.M.: Effect of bearing housings on centrifugal pump rotor dynamics. *IOP Conf. Ser. Mater. Sci. Eng.* **233**(1), 012054 (2017). <https://doi.org/10.1088/1757-899X/233/1/012054>
16. Shrestha, A., Gonzalez-Longatt, F.: Parametric sensitivity analysis of rotor angle stability indicators. *Energies* **14**(16), 5023 (2021). <https://doi.org/10.3390/en14165023>
17. Li, Y., Luo, Z., Liu, J., Ma, H., Yang, D.: Dynamic modeling and stability analysis of a rotor-bearing system with bolted-disk joint. *Mech. Syst. Signal Process.* **158**, 107778 (2021). <https://doi.org/10.1016/j.ymsp.2021.107778>

18. Krol, O., Porkuian, O., Sokolov, V., Tsankov, P.: Vibration stability of spindle nodes in the zone of tool equipment optimal parameters. *Comptes Rendus de l'Académie Bulgare des Sciences* **72**(11), 1546–1556 (2019). <https://doi.org/10.7546/CRABS.2019.11.12>
19. Jiang, L.: Finite element analysis and multi-objective optimization of flexible rotor-bearing system. *Atomic Energy Sci. Technol.* **55**, 327–334 (2021). <https://doi.org/10.7538/yzk.2021.zhuankan.0144>
20. Li, Y., Tang, Z.: High-speed rolling bearing-dual rotor spindle system numerical simulation analysis of discrete modeling dynamics. *J. Mech. Strength* **43**(4), 798–807 (2021). <https://doi.org/10.16579/j.issn.1001.9669.2021.04.006>
21. Zhang, W., Qin, P., Zhang, X., Ma, K., Yin, L., Li, C.: Rotordynamic characteristics of a novel pocket damper seal with self-regulated injection. *J. Mech. Sci. Technol.* **35**(8), 3421–3434 (2021). <https://doi.org/10.1007/s12206-021-0715-9>
22. Liu, Z., He, Y.-Q., Gu, F., Yang, L.-Y., Han, J.-D.: Passivity-based control and flight experiment of quad-tilt rotor unmanned aerial vehicle. *Control Theory Appl.* **38**(8), 1287–1298 (2021). <https://doi.org/10.7641/CTA.2021.00346>
23. Zhao, B.-S., Li, N., Ma, H., Han, H.-Z., Zhao, Z.-F.: Vibration characteristics of the helical gear rotor system considering mixed modification. *J. Vib. Eng.* **34**(4), 704–711 (2021). <https://doi.org/10.16385/j.cnki.issn.1004-4523.2021.04.006>
24. Osadchiy, I., Kryvoruchko, D., Kolesnyk, V., Hatala, M., Duplak, J., Mital, D.: Development of integrated technology of FRP gear manufacturing. *Manufact. Technol.* **16**(3), 574–578 (2016)
25. Volina, T., Pylypaka, S., Rebrii, A., Pavlenko, O., Kremets, Y.: Particle movement on concave coupler of the centrifugal distributor with radially installed vertical blades. In: Tonkonogyi, V., et al. (eds.) *InterPartner 2020. LNME*, pp. 237–246. Springer, Cham (2021). [https://doi.org/10.1007/978-3-030-68014-5\\_24](https://doi.org/10.1007/978-3-030-68014-5_24)
26. Volina, T., Pylypaka, S., Nesvidomin, V., Pavlov, A., Dranovska, S.: The possibility to apply the Frenet trihedron and formulas for the complex movement of a point on a plane with the predefined plane displacement. *Eastern-Eur. J. Enterp. Technol.* **3**(7(111)), 45–50 (2021). <https://doi.org/10.15587/1729-4061.2021.232446>
27. Pylypaka, S., Volina, T., Nesvidomin, A., Zakharova, I., Rebrii, A.: Particle movement in a centrifugal device with vertical blades. In: Ivanov, V., Pavlenko, I., Liaposhchenko, O., Machado, J., Edl, M. (eds.) *DSMIE 2021. LNME*, pp. 156–165. Springer, Cham (2021). [https://doi.org/10.1007/978-3-030-77823-1\\_16](https://doi.org/10.1007/978-3-030-77823-1_16)
28. Saeed, N.A.-F., Mahrous, E., Nasr, E.A., Awrejcewicz, J.: Nonlinear dynamics and motion bifurcations of the rotor active magnetic bearings system with a new control scheme and rub-impact force. *Symmetry* **13**(8), 1502 (2021). <https://doi.org/10.3390/sym13081502>
29. Berladir, K.V., Hovorun, T.P., Bilous, O.A., Baranova, S.V.: The modeling of the composition and properties of functional materials based on polytetrafluoroethylene. *Funct. Mater.* **25**(2), 342–347 (2018). <https://doi.org/10.15407/fm25.02.342>
30. Tarelnyk, V., et al.: New sulphiding method for steel and cast iron parts. *IOP Conf. Ser. Mater. Sci. Eng.* **233**(1), 012049 (2017). <https://doi.org/10.1088/1757-899X/233/1/012049>
31. Martsynkovskyy, V., Tarelnyk, V., Konoplianchenko, I., Gaponova, O., Dumanchuk, M.: Technology support for protecting contacting surfaces of half-coupling—shaft press joints against fretting wear. In: Ivanov, V., et al. (eds.) *DSMIE 2019. LNME*, pp. 216–225. Springer, Cham (2020). [https://doi.org/10.1007/978-3-030-22365-6\\_22](https://doi.org/10.1007/978-3-030-22365-6_22)
32. Svirzhevskiy, K., Zabolotnyi, O., Tkachuk, A., Zablotskiy, V., Cagaňová, D.: Methods of evaluating the wear resistance of the contact surfaces of rolling bearings. In: Tonkonogyi, V., et al. (eds.) *InterPartner 2020. LNME*, pp. 453–463. Springer, Cham (2021). [https://doi.org/10.1007/978-3-030-68014-5\\_45](https://doi.org/10.1007/978-3-030-68014-5_45)

33. Kotliar, A., Gasanov, M., Basova, Y., Panamariova, O., Gubskiy, S.: Ensuring the reliability and performance criterias of crankshafts. *Diagnostyka* **20**(1), 23–32 (2019). <https://doi.org/10.29354/diag/99605>
34. Simonovskiy, V.I.: *Dynamics of Rotors of Centrifugal Machines*. Sumy State University, Sumy, Ukraine (2006)
35. Martsynkovskyy, V.A., Pozovnyi, O.O.: The impact of the multi-gap seals on rotor dynamics. *J. Eng. Sci.* **4**(1), C7–C12 (2017). [https://doi.org/10.21272/jes.2017.4\(1\).c2](https://doi.org/10.21272/jes.2017.4(1).c2)
36. Simonovskiy, V.: *Dynamics of Rotor Machines*. Sumy State University, Sumy, Ukraine (2011)
37. Gadyaka, V., Leikykh, D., Simonovskiy, V.: Phenomena of stability loss of rotor rotation at tilting pad bearings. *Procedia Eng.* **39**, 244–253 (2012). <https://doi.org/10.1016/j.proeng.2012.07.031>
38. Roy, D.K., Tiwari, R.: Estimation of the internal and external damping from the forward and backward spectrum of a rotor with a fatigue crack. *Propuls. Power Res.* **9**(1), 62–74 (2020). <https://doi.org/10.1016/j.jprr.2020.01.001>



# Influence of Horizontal Inertial Loads on the Operation of Overhead Crane Girders

Anatoliy Tkachev , Aleksey Tkachev , Oleksandr Fomin , Oleksandr Bondar ,  
and Elena Naidenko 

Odessa Polytechnic National University, 1, Shevchenko Avenue, Odessa 65044, Ukraine  
a.lena2808@ukr.net

**Abstract.** Crane spans with prestressed girders operate under the same conditions, modes, and load capacities as conventional cranes. The load-carrying capacity of their spans must be provided with high strength and stiffness in two planes - in the main vertical plane and the horizontal plane. However, studies of the stress-strain state of a crane with a prestressed bridge operating in the horizontal plane have not been conducted. A mathematical model of the pre-stressed main beam has been developed in the paper. An analysis of its deformed state from the plane of cargo suspension and under the simultaneous influence of vertical and horizontal forces has been carried out, which allowed establishing. The obtained results can be further used to design bridge-type cranes with prestressed span beams to increase their lifting capacity and extend their service life without disassembly. As well as improving the existing structures and engineering methods of calculation, both at the design stages and under real operating conditions.

**Keywords:** Industrial growth · Bridge crane · Stress-strain state · Prestressed beams · Beam deflections

## 1 Introduction

The paper deals with the issues related to bridge-type cranes with prestressed spans. Such cranes are used to a limited extent in the industry [1]. It should be noted that cranes with prestressed span girders have considerably less weight, owing to less moment of inertia of beam section that positively influences on many other parameters improving operating conditions of the machine and is a significant advantage [2]. At the same time, such span beams are more deformable, which can lead to structural failure or malfunction [3].

This is because the metal structures of such cranes are more deformable than conventional cranes [4], which may be one of the causes of performance failure and unnecessary energy consumption to overcome the track gradient [5]. These factors are among those that limit the use of these cranes.

At the same time, cranes with prestressed span girders have significantly less weight and smaller dimensions than conventional cranes and a lower cost of the crane's metal structure, which can be 75–80% of the cost of the crane.

Note that the operation of cranes with pre-stressed beams occurs under the same conditions, operating modes, and the same lifting capacities as usual, for which the calculation in the design of the crane bridge is carried out following the established design combinations of loads - “a” (IIa, Ia) and “B” (II<sub>B</sub>, I<sub>B</sub>) [6]. The combination of loads “a” corresponds to the mode of lifting the load or its braking when lowering (with the other mechanisms turned off). In this case, the crane bridge is loaded in the plane of the suspension of the load with vertical loads [7]. Prevention of the destruction of the crane bridge and the occurrence of permanent deformations with a given probability is guaranteed if the conditions are met [8].

$$\sigma_a = \frac{(-EJ_1)y''}{W_1} \leq Rm, \quad y \leq [y] \quad (1)$$

The combination of load “B” corresponds to the mechanism of the crane’s movement when the load is suspended. Thus, the crane bridge experiences an oblique bend, as it is loaded in two planes: in the plane of the suspension of the load ( $xoy$ ) by vertical loads, and from the plane of the suspension ( $xoz$ ) - by the horizontal inertial load  $Fu$ . Then the condition for preventing its destruction will have the form

$$\sigma_{II_B(I_B)} = \frac{(-EJ_1)y''_1}{W_1} + \frac{(-EJ_2)z''}{W_2} \leq Rm, \quad (y + z) \leq [y], \quad (2)$$

where  $EJ_1$ ,  $EJ_2$  - is the rigidity of the crane bridge when bending in the plane of the suspension and from the plane of the suspension of the load, respectively;  $W_1$ ,  $W_2$  - moments of inertia of the section in the same planes, respectively;  $R$  - design steel resistance;  $m$  - coefficient of working conditions;  $y$ ,  $z$  [ $y$ ] - the deflections of the span beam, in the planes  $xoy$ ,  $xoz$  and the allowable deflection, respectively.

Thus, during the operation of a pre-stressed crane bridge in conditions of oblique bending, the bridge must be provided with high strength and rigidity in two planes - in the main vertical plane  $xoy$  and the horizontal -  $xoz$ . This condition must be considered in matters related to the calculation and design of cranes with prestressed bridges. It requires additional research in relation to the real operating conditions of the crane. In this connection, the issues related to the calculation and design of such structures require special attention and study and are very relevant.

## 2 Literature Review

The analysis of the publications shows that the mathematical models of span beams were subjected to separate studies [9], numerical modeling of prestressed beams was carried out [10]. But at the same time, studies related to oblique bending of beams were carried out only for conventional crane bridges [11] exposed to transverse [12] and horizontal inertial loads [13, 14]. Such mathematical models cannot be used in our case. Since the beams are also exposed to longitudinal compressive forces, which in turn requires the development and consideration of a different mathematical model.

In addition, studies were carried out for prestressed beams on the issues of their static stiffness [15]. However, the work of the bridge superstructure was considered only in the vertical plane [16, 17].



It should be noted the works where the preformation of the bridge was determined as the difference between the deflections from the action of transverse forces and the deflection of the beam from the action of the longitudinal forces of the preliminary stress and self-tension in the tightening [18, 19]. This also cannot be considered by us, since prestressed beams refer to systems that do not obey the principle of superposition. And this approach will not always be correct and gives only approximate results.

It follows from all that there have been no publications related to the operation of a prestressed beam for load combinations “B”.

This, in turn, requires the development and consideration of a new mathematical model, where the maximum approximation of the design scheme to the real operating conditions of the crane is put forward in the first place.

The purpose of this study. Thus, the purpose of this work is to study further the stress-strain state of a pre-stressed main beam operating simultaneously in two planes. The issues considered in it are those in which the nature of the action of loads on the beam is put forward in the first place with the maximum approximation of the design scheme to the real constructive form.

To achieve this goal, it is necessary to solve the following tasks to develop a mathematical model of a pre-stressed crane bridge, taking into account the work of the main beams in the horizontal and vertical planes; investigate to analyze the results obtained.

### 3 Research Methodology

When developing the mathematical model, following the requirements put forward for the crane bridge operation, we notice that it is necessary to consider two types of bridge design diagrams: the first for the load combination “a” and the second for the load combination “B”. When compiling design diagrams, we assume that all elements of the crane are solid, the beam operates in the elastic stage, and rests on ideal hinges.

Let us introduce the notation

$$U = \cos k_1 x + \sin k_1 x \operatorname{tg}(0,5 k_1 l) - 1, \quad (3)$$

$$k_1^2 = \frac{S}{EJ_1} \quad (4)$$

Then the expression of the curve of the crane bridge deflections and bending moments in the  $xoy$  plane will be (Fig. 1)

$$y = -hU + \frac{F}{S} \left( \frac{\sin k_1 a \sin k_1 x}{k_1 \sin k_1 l} - \frac{ax}{l} \right), \quad (5)$$

$$M = -hS(U - 1) + \frac{F \sin k_1 a \sin k_1 x}{k_1 \sin k_1 l}, \text{ if } 0 \leq x \leq (l - a) \quad (6)$$

$$y = -hU + \frac{F}{S} \left( \frac{\sin k_1(l - a) \sin k_1(l - x)}{k_1 \sin k_1 l} - \frac{(l - a)(l - x)}{l} \right), \quad (7)$$

$$M = -hS(U - 1) + \frac{F \sin k(l - a) \sin k(l - x)}{k \sin kl}, \text{ if } l \geq x \geq (l - a) \quad (8)$$

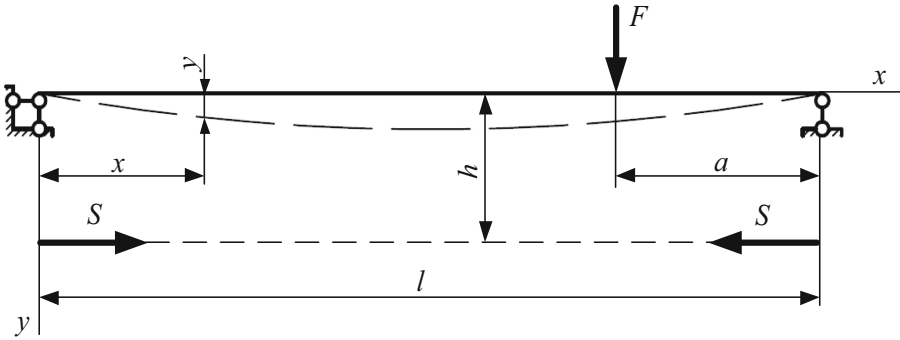


Fig. 1. Calculation scheme of the bridge for the load combination “a”.

### 4 Results

With the combination of loads “B” on the prestressed crane bridge acts (in the plane  $xoz$ ) horizontal inertial load  $F_u$  determined by the masses of the bridge  $m_m$ , cart  $m_t$ , cargo  $m$ , and acceleration  $\gamma$

$$F_u = (m_m + m_t + m) \cdot \gamma \tag{9}$$

The design diagram of the span beam, when it works in the horizontal plane, is shown in Fig. 2.

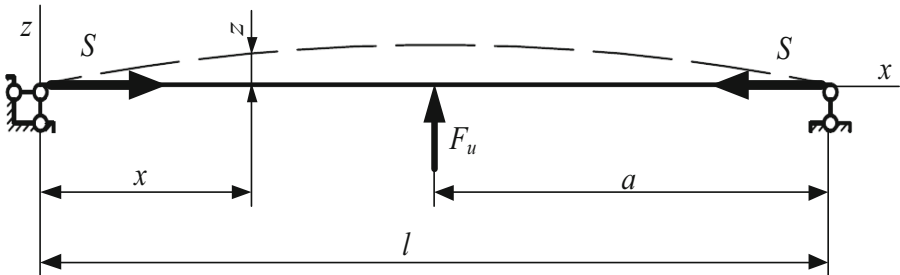


Fig. 2. Calculation scheme of the bridge for the load combination “B”.

Let's point

$$z^2 = \frac{S}{EJ_2} \tag{10}$$

Then, the differential equations of the deflection arrows for the left and right parts of the prestressed crane bridge, at  $a = 0,5l$ , will be, respectively

$$\frac{d^2z}{dx^2} + k^2z = -\frac{0,5 F_u x}{EJ_2}, \text{ if } 0 \leq x \leq (l - a) \tag{11}$$

$$\frac{d^2z}{dx^2} + k^2z = -\frac{0,5 F_u(l-x)}{EJ_2}, \text{ if } x \geq (l-a) \quad (12)$$

The total integral of this equation is

$$\begin{aligned} z &= C_1 \cos kx + C_2 \sin kx - \frac{0,5F_Hx}{S} \\ z &= C_1 \cos kx + C_2 \sin kx - \frac{0,5F_u x}{S} \\ z &= C_3 \cos kx + C_4 \sin kx - \frac{0,5F_u(l-x)}{S}, \end{aligned} \quad (13)$$

The integration constants  $C_1, C_3$  are determined from the conditions at the ends of the beam, where the deflections are zero, and  $C_2, C_4$  - at the point of force  $F_u$ , where both sections of the beam deformation curve have the same deflection and common tangent

$$C_1 = 0, \quad (14)$$

$$C_2 = \frac{F_u \sin 0,5kl}{Nk \sin kl}, \quad (15)$$

$$C_3 = \frac{F_u \sin 0,5kl}{Nk}, \quad (16)$$

$$C_4 = -\frac{F_u \sin 0,5kl}{Nk \operatorname{tg} kl} \quad (17)$$

In our case, the force  $F_u$  is applied in the middle of the beam, so the deformation curve is symmetrical. Thus, we can consider one of the two sections of the beam. After simple transformations, we obtain the corresponding expression for the beam deflection arrow

$$z = \frac{F_u}{S} \left( \frac{\sin 0,5kl \sin kx}{k \sin kl} - 0,5x \right) \quad (18)$$

We get the bending moment by differentiating the last expression twice

$$M = -EJ_2 \left( \frac{d^2z}{dx^2} \right) = \frac{F_u}{S} \left( \frac{\sin 0,5kl \sin kx}{k \sin kl} - 0,5x \right) \quad (19)$$

According to the obtained expressions, for combinations of loads “a” and “B”, mathematical research of the deformed state of the beam with the span of  $l = 10$ . Deformations of the bridge are presented in the form of beam deflections.

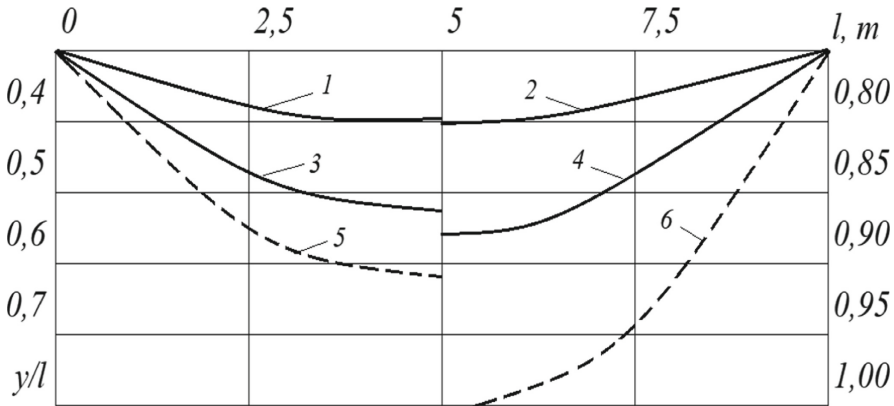
$$\frac{y/l}{[y/l]}; \quad \frac{z/l}{[y/l]}; \quad \frac{(z+y)/l}{[y/l]} \quad (20)$$

The analysis of the results obtained with the combination of loads “a” has researched that, with the ratio of forces acting on the beam  $F/1, 5$ , the use of prestressing gives a possibility to minimize the deflection of the span.

**Table 1.** Conditional deflections of the main beam.

$\frac{F_i}{S_i}$	Sectional location	Load capacity, $F_i, m$								
		$F_1 = 0,5$			$F_2 = 0,63$			$F_3 = 1,0$		
		$\frac{F_a}{S_i}$	$\frac{F_b}{S_i}$	$\frac{F_c}{S_i}$	$\frac{F_a}{S_i}$	$\frac{F_b}{S_i}$	$\frac{F_c}{S_i}$	$\frac{F_a}{S_i}$	$\frac{F_b}{S_i}$	$\frac{F_c}{S_i}$
$\frac{F_i}{0,75}$	$0,5 l$	0,49	0,5	0,69	0,64	0,66	0,92	0,97	0,81	1,26
	$l$	-0,08		-0,51	-0,08		-0,66	-0,08		-0,81
$\frac{F_i}{1,0}$	$0,5 l$	0,42	0,6	0,73	0,6	0,73	0,94	0,94	0,86	1,62
	$l$	-0,11		-0,61	-0,11		-0,74	-0,11		-0,86
$\frac{F_i}{1,25}$	$0,5 l$	0,37	0,65	0,75	0,56	0,8	0,97	0,9	0,9	1,3
	$l$	-0,16		-0,67	-0,16		-0,69	-0,16		-0,91
$\frac{F_i}{1,5}$	$0,5 l$	0,35	0,68	0,76	0,54	0,84	0,99	0,89	0,94	1,67
	$l$	-0,18		-0,7	-0,18		-0,86	-0,18		-0,95
$\frac{F_i}{1,75}$	$0,5 l$	0,29	0,74	0,79	0,46	0,92	1,03	0,8	1,0	1,3
	$l$	-0,25		-0,78	-0,25		-0,95	-0,25		-1,03
$\frac{F_i}{2,0}$	$0,5 l$	0,27	0,82	0,86	0,40	1,0	1,1	0,75	1,2	1,4
	$l$	-0,3		-0,87	-0,3		-1,04	-0,3		-1,3

The Conditional deflections of the main beam, are shown in Table 1. Deformations of the bridge in the plane  $xoy$ , is shown in Fig. 3; deformations of the bridge in the planes  $xoy, xoz$ , is shown in Fig. 4.

**Fig. 3.** Deformations of the bridge in the plane  $xoy$ .

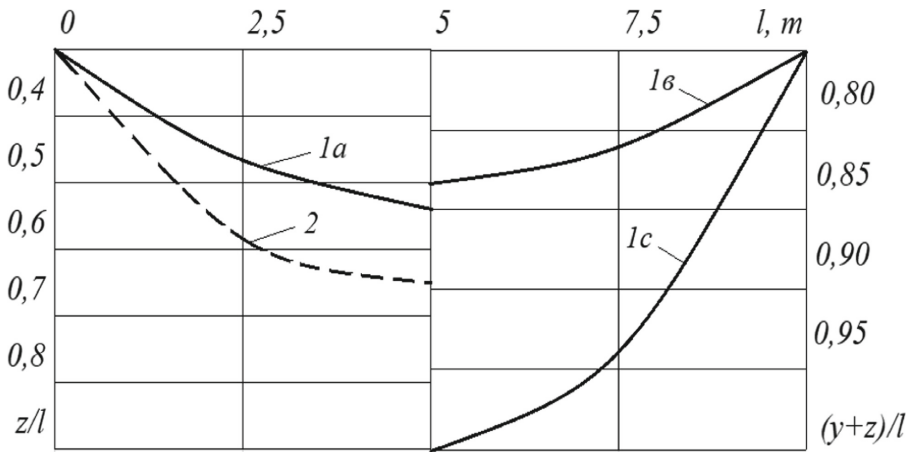


Fig. 4. Deformations of the bridge in the planes  $xoy, xoz$ .

## 5 Conclusions

Thus, Table 1 and Fig. 3 show that when the eccentric compressive force  $S$  is applied, the beam's deflections can be reduced by 50–70%, which has a positive effect on the deformed state of the span bridge.

Besides, Table 1 and Fig. 4 show that for the combination of “B” loads, an increase in the magnitude of compressive forces leads to a significant increase in deformations in the horizontal plane. The ratio of forces  $F/1.5$  (Fig. 4) can be acceptable for the crane bridge. At the same time, note that the beam deformations at oblique bending (curves  $1b$  and  $1c$ ) exceed the limits of deflections from temporary load  $F$  of the usual bridge without unloading devices. It requires special attention when designing prestressed crane bridges.

The results obtained in this work can also be used in the future for modernization to increase their carrying capacity, increase the service life without dismantling, and improve existing structures and engineering calculation methods during design and in real operation conditions.

## References

1. Bonopera, M., Chang, K., Lee, Zheng-Kuan.: State-of-the-Art Review on Determining Prestress Losses in Prestressed Concrete Girders. *Appl. Sci.* 10, 72–57 (2020).
2. Chebrovsky, A., Savva, Y.: Review of the state of prestressed metal beams and the study results of operating crane beams when operating on a moving load. *PNU Bull. Khabarovsk* 4(31), 383–402 (2013)
3. Tkachev, A., Tkachev, A., Predrag, D., Prokopovych, I., Kostina, M.: Static stiffness of the crane bridges under moving load distribution. In: Tonkonogyi, V., Ivanov, V., Trojanowska, J., Oborskyi, G., Pavlenko, I. (eds.) *Advanced Manufacturing Processes III. LNME*, pp. 43–52. Springer, Cham (2022). [https://doi.org/10.1007/978-3-030-91327-4\\_5](https://doi.org/10.1007/978-3-030-91327-4_5)

4. Yifei, T., Lijin, L., Guomin, S., Dongbo, L., Xiangdong, L.: Overhead crane camber deformation assessment and energy analysis. *Proc. Inst. Mech. Eng. Part B* **6**, 55–52 (2014)
5. Qu, X., Xu, G., Fan, X., Bi, X.: Intelligent optimization methods for the design of an overhead traveling crane. *Chinese J. Mech. Eng.* **28**(1), 187–196 (2015)
6. Zhegulsky, V., Mironov, I., Lukashuk, O.: *Design and Calculation of Crane Metal Structures*. Ural Publishing House University, Russia (2019)
7. Menzel, U.: Krane – Einsatzerfahrungen und Entwicklungstendenzen. *Kranfachtagung* **14**, 77–86 (2006)
8. Oguamanam, D., Hansen, J.: Dynamics of a three-dimensional overhead crane system. *J. Sound Vib.* **242**(3), 411–426 (2012)
9. Lou, T.J., Lopes, S.M.R., Lopes, A.V.: Numerical modeling of externally prestressed steel 436-concrete composite beams. *J. Constr. Steel Res.* **121**, 229–236 (2016)
10. Zou, J., Huang, Y., Feng, W., Chen, Y., Huang, Y.: Experimental study on flexural behavior of concrete T-beams strengthened with externally prestressed tendons. *Math. Biosci. Eng.* **16**(6), 6962–6974 (2019)
11. Cho, K., Kim, S.T., Cho, J.R., Park, Y.H.: Estimation of tendon force distribution in prestressed concrete girders using smart strand. *Appl. Sci.* **7**, 1319 (2017). <https://doi.org/10.3390/app7121319>
12. Kim, J., Kim, J.W., Park, S.: Investigation of applicability of an embedded EM sensor to measure the tension of a PSC girder. *J. Sens.* **2019**, 2469647 (2019). <https://doi.org/10.1155/2019/2469647>
13. Jianqun, W., Shenghua, T., Zheng, H., Zhou, C., Zhu, M.: Flexural behavior of a 30-meter full-scale simply supported prestressed concrete box girder. *Appl. Sci.* **10**(9), 30–76 (2020)
14. Yao, D.L., Jia, J.Q., Yu, F.: Analysis on shear ductility of prestressed ultra-high reinforced concrete beams. *J. Harbin Eng. Univ.* **34**(5), 593–598 (2013)
15. Iodchik, A.: Deflections of a steel beam, pre-stressed by bending of the I-beam. *Bull. VSSTU* **5**(44), 45–52 (2013)
16. Iodchik, A., Kravchuk, V.: Engineering calculation of steel prestressed beam. *TOGU Gazette* **2**(29), 64–72 (2013)
17. Zhang, K.X., Sun, Q.S.: Experimental study of reinforced concrete T-beams strengthened with a composite of prestressed steel wire ropes embedded in polyurethane cement (PSWR-PUC). *Int. J. Civil Eng.* **16**(9), 1109–1123 (2018)
18. Park, H., Jeong, S., Lee, S.C., Cho, J.Y.: Flexural behavior of post-tensioned prestressed concrete girders with high-strength strands. *Eng. Struct.* **112**, 90–99 (2016). <https://doi.org/10.1016/j.engstruct.2016.01.004>
19. Garcia, J.M., Bonett, R.L., Schultz, A.E., Carrillo, J., Ledezma, C.: Flexural behavior of ungrouted post-tensioned concrete masonry beams with unbonded bars. *Constr. Build. Mater.* **203**, 210–221 (2019). <https://doi.org/10.1016/j.conbuildmat.2018.12.101>
20. Tkachov, A., Tkachov, O., Sydorenko, I.: Improvement of the deformed state of flight beams of bridge cranes. In: Bovnegra, L. (eds) *Modern Technologies and Design Art: Series of Monographs Faculty of Architecture, Civil Engineering and Applied Arts: Monograph*, vol. 37, pp. 118–125. Katowice School of Technology, Katowice (2020)



# Organization of Transportation of a Particle by an Inclined Cylinder Rotating Around the Axis

Tatiana Volina<sup>1,3</sup>  , Serhii Pylypaka<sup>1</sup> , Yaroslav Kremets<sup>1</sup> , Olena Kozlova<sup>2</sup> , and Alla Rebrii<sup>3</sup> 

<sup>1</sup> National University of Life and Environmental Sciences of Ukraine, 15, Heroyiv Oborony Street, Kyiv 03041, Ukraine

t.n.zaharova@ukr.net

<sup>2</sup> Sumy State Pedagogical University named after AS Makarenko, 87, Romenskaya Street, Sumy 40002, Ukraine

<sup>3</sup> Sumy National Agrarian University, 160, Kondratieva Street, Sumy 40021, Ukraine

**Abstract.** The movement of a material particle on the inner surface of an inclined cylinder rotating around its axis with a constant angular velocity is investigated in the article. When a particle hits the surface of a horizontal cylinder, it begins to oscillate in the cross-sectional plane of the cylinder with a certain amplitude in the angular dimension. Its value depends on the incidence point, friction coefficient, and initial absolute velocity. Differential equations of movement in projections on the axis of a fixed coordinate system are compiled. They are solved numerically. Under the appropriate initial conditions, which are determined analytically, the particle in absolute movement can be stationary, being at a point on the cylinder at a certain distance from the lower point in the angular dimension in the direction of the rotation of the cylinder. Some movement cases are described when the angle of inclination of the cylinder's axis to the horizontal plane is greater, equal, or less than the friction angle on the cylinder's surface. An analytical solution for the last case that describes the particle's movement after stabilization is found. Visualization of the obtained results is made.

**Keywords:** Angular velocity · Horizontal cylinder · Differential equations · Axial direction · Friction force · Industrial growth

## 1 Introduction

Cylindrical surfaces are an integral part of agricultural machinery. In hoisting and transport machines, such surfaces are casing, inside which the active working body rotates. An inclined cylinder that rotates around its axis is used in drum grain dryers [1] and inertial separators [2, 3]. The interaction of particles of material with the surface of the cylinder, which rotates around its axis, leads to their sliding, the character of which depends on the angle of the cylinder inclination.

## 2 Literature Review

Many research works are conducted on increasing the reliability and durability of machines in general and their components. It is proposed to solve this problem in various ways. For example, in [4], a new technique to sulfide the surfaces of details with electrical discharge machining are proposed. The authors of [5] a way to strengthen the surfaces of steel components, including cementation and nitriding processes, is presented. In [6], applying a multilayer coating using electrical discharge machining is devised. But it is not a secret that such recommendations are insufficient [7]. In similar works, the surfaces are proposed to be improved by developing new ways to strengthen surfaces, which is expensive. Instead, this question can be solved easier by methods of geometric modeling.

Engineering practice often deals with the problems of geometric designing of objects, which are proposed to solve in different ways. For example, within a multidimensional space by approximating a solution to differential equations [8]; by the method of multidimensional parabolic interpolation [9]; by means of interpolation of geometric space [10] and so on. It is even easier to take the final terms as the initial conditions. In such a case, the geometric designing of technological objects comes down to finding the analytical dependencies of their interaction. Such interaction in mechanical engineering is the interaction between the working body and material. It takes place during separation of mixtures [11, 12], aspiration separation [13], soil fertilizing [14] and prilling [15], etc. The movement of a single particle cannot be identified with a movement of material, which consists of individual particles, but it allows identifying laws of the movement, which can be transferred to the material. In [16], the results of studies of particle movement on rough surfaces and in [17] – in the rotary disasters were presented. Also, dynamic analysis of a particle in accelerating flow is presented in [18].

However, in some cases, the study of body motion can also be reduced to a particle [19]. This applies to the case when the inertia forces from the body's rotation can be neglected due to the small angular velocities of their rotation [20]. Therefore, the range of applied problems that require an analytical description of the movement of a particle on a plane is multifaceted. Based on the foregoing, the research aims to find the movement patterns for a material particle on the inner surface of a cylinder rotating around an axis, set at an angle to the horizon.

## 3 Research Methodology

The parametrical equations of a cylinder with a horizontal axis directed along the  $OX$  axis can be written:

$$X = u; Y = R\sin\alpha; Z = -R\cos\alpha, \quad (1)$$

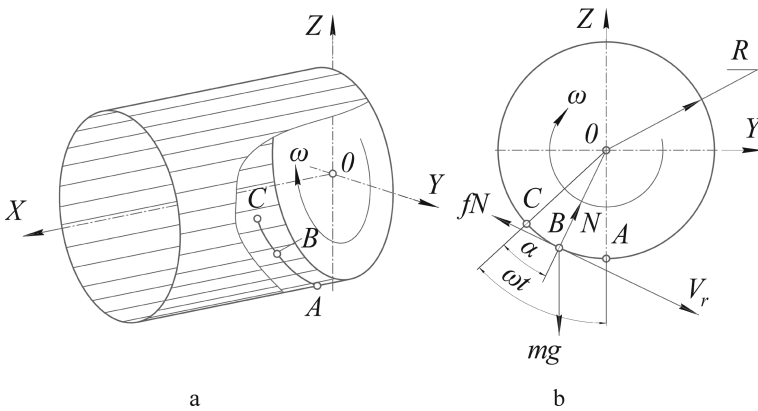
where  $R$  is the radius of the cylinder (a constant value);

$\alpha$  and  $u$  are independent variables of the surface. Moreover,  $\alpha$  is the angular coordinate,  $u$  is the linear coordinate (length of the generatrix of the cylinder). The sign “-” in the last Eq. (1) is taken to ensure that the value  $\alpha = 0$  corresponds to the lowest generatrix, where is the particle's initial position.



At the beginning, the particle is at point  $A$  on the lower generatrix (Fig. 1a). Let us rotate the cylinder around the axis with a constant angular velocity  $\omega$ . During time  $t$ , it rotates at an angle  $\omega t$ , and its lower generatrix moves to point  $C$ . The particle also moves but does not reach point  $C$  because it slides on it (Fig. 1b). Suppose it has reached point  $B$ , which corresponds to the angle of sliding  $\alpha$ . Since the axis of rotation is horizontal, the trajectory is the arc. If the cylinder is inclined, a component of the force of gravity arises and causes the particle to slide in the  $OX$  direction.

Firstly, let us consider the movement of a particle on the surface of a horizontal cylinder. If a specific dependence connects the variables  $\alpha$  and  $u$  of the surface, for example, of time  $t$ , Eq. (1) will be transformed into the equation of one variable, describing a line on the cylinder. This line is considered a sliding trajectory, and the dependencies  $\alpha = \alpha(t)$  and  $u = u(t)$  are unknown and should be found. To find them, it is necessary to compose a system of differential equations of motion of the particle in the projections on the axes of the coordinate system  $OXYZ$ .



**Fig. 1.** Illustrations for drawing up equations of movement of a particle: a) axonometric image of the cylinder; b) projection of the cylinder when the axis  $OX$  is directed at the observer and applied to the particle at the point  $B$  forces.

The equation of the movement of a particle is  $m\bar{w} = \bar{F}$ , where  $\bar{w}$  is the vector of absolute acceleration,  $\bar{F}$  is the resulting vector of forces applied to the particle. Such forces are the force of gravity  $mg$  ( $m$  is the mass of the particle,  $g$  is the acceleration of gravity), the reaction of the surface  $N$ , and friction force  $f \cdot N$  ( $f$  is the coefficient of friction). Let us find the directing cosines (the unit directing vectors of action of forces). The force of gravity is directed downwards, so the projections of the directing vector:

$$mg : \{0; 0; -1\}. \tag{2}$$

The friction force  $f \cdot N$  is opposite to the velocity vector of relative movement  $V_r$  (of the sliding). To find the velocity  $V_r$  of the relative movement, it is essential to differentiate Eq. (1) by time  $t$ . Wherein  $\alpha = \alpha(t)$  and  $u = u(t)$ , i.e., Eq. (1), are the equations of the line on the cylinder (the relative trajectory). To distinguish the equations of line and surface,

in the equations of the relative trajectory, the lowercase letters with the index “r” are used instead of the uppercase letters:

$$\dot{x}_r = \dot{u}; \quad \dot{y}_r = R\dot{\alpha}\cos\alpha; \quad \dot{z}_r = R\dot{\alpha}\sin\alpha. \quad (3)$$

The geometric sum of the components (3) gives the value of the sliding velocity of the particle on the cylinder in relative movement:

$$V_r = \sqrt{\dot{x}_r^2 + \dot{y}_r^2 + \dot{z}_r^2} = \sqrt{\dot{u}^2 + R^2\dot{\alpha}^2}. \quad (4)$$

The unit vector of the tangent to the trajectory of relative movement in the projections on the axis of the  $OXYZ$  system is obtained by dividing (3) by (4). The friction force  $f \cdot N$  is opposite to the vector  $V_r$  of relative velocity. Let us write a unit directing vector of action of the friction force with the opposite sign:

$$f \cdot N : \left\{ \begin{array}{l} -u/\sqrt{\dot{u}^2 + R^2\dot{\alpha}^2}; \\ -R\dot{\alpha}\cos\alpha/\sqrt{\dot{u}^2 + R^2\dot{\alpha}^2}; \\ -R\dot{\alpha}\sin\alpha/\sqrt{\dot{u}^2 + R^2\dot{\alpha}^2} \end{array} \right\}. \quad (5)$$

The reaction of the surface  $N$  is directed from a point on the cylinder to the rotation axis (Fig. 1b). If the radius vector of a point is determined by the 2<sup>nd</sup> and 3<sup>rd</sup> expressions (1), the surface’s reaction can be analogous with the opposite sign. The projections of the unit reaction vector  $N$  take a form:

$$N : \{0; -\sin\alpha; \cos\alpha\}. \quad (6)$$

The cylinder rotates clockwise at an angle  $\theta = -\omega \cdot t$ . At point A, the generatrix will occupy point C (Fig. 1b). Let us rotate the cylinder (1) around the axis  $OX$  at an angle  $\theta = -\omega \cdot t$ . After simplifications, equations take the form:

$$X = u; \quad Y = -R\sin(\omega t - \alpha); \quad Z = -R\cos(\omega t - \alpha). \quad (7)$$

Equations (7) with  $\alpha = \alpha(t)$  and  $u = u(t)$  are the equations of the absolute trajectory of the particle. The cylinder was rotated at an angle  $\theta = -\omega \cdot t$  and the particle was sliding on it in the opposite direction, was rotated at an angle  $\alpha = \alpha(t)$  and took a position at point B (Fig. 1b). The absolute particle velocity can be found by differentiating Eq. (7) with the indications through the lowercase letters with the index “a”:  $\dot{x}_a = \dot{u}$ ;  $\dot{y}_a = -R(\omega - \dot{\alpha})\cos(\omega t - \alpha)$ ;  $\dot{z}_a = R(\omega - \dot{\alpha})\sin(\omega t - \alpha)$ . By differentiating Eq. (7) the projections of the vector of absolute acceleration:

$$\begin{aligned} \ddot{x}_a &= \ddot{u}; \quad \ddot{y}_a = R(\omega - \dot{\alpha})^2\sin(\omega t - \alpha) + R\ddot{\alpha}\cos(\omega t - \alpha); \\ \ddot{z}_a &= R(\omega - \dot{\alpha})^2\cos(\omega t - \alpha) - R\ddot{\alpha}\sin(\omega t - \alpha). \end{aligned} \quad (8)$$

Since the surface rotates at an angle  $\theta = -\omega \cdot t$ , vectors (5) and (6) must also be rotated at this angle in the same way as the surface (7), so:

– unit directing vector of action of friction force  $f \cdot N$ :

$$f \cdot N : \left\{ -\frac{\dot{u}}{\sqrt{\dot{u}^2 + R^2\dot{\alpha}^2}}; -\frac{R\dot{\alpha}\cos(\omega t - \alpha)}{\sqrt{\dot{u}^2 + R^2\dot{\alpha}^2}}; \frac{R\dot{\alpha}\sin(\omega t - \alpha)}{\sqrt{\dot{u}^2 + R^2\dot{\alpha}^2}} \right\}; \quad (9)$$

– unit directing vector of action of the reaction force  $N$ :

$$N : \{0; \sin(\omega t - \alpha); \cos(\omega t - \alpha)\}. \quad (10)$$

A vector equation  $m\bar{w} = \bar{F}$  should be compiled in the projections on the axis of the fixed coordinate system  $OXYZ$  for a horizontal cylinder because (8), (2), (9), (10) are known:

$$\begin{aligned} m\ddot{x}_a &= -fN\dot{u}/\sqrt{\dot{u}^2 + R^2\dot{\alpha}^2}; \\ m\ddot{y}_a &= -fNR\dot{\alpha}\cos(\omega t - \alpha)/\sqrt{\dot{u}^2 + R^2\dot{\alpha}^2} + N\sin(\omega t - \alpha); \\ m\ddot{z}_a &= -mg + fNR\dot{\alpha}\sin(\omega t - \alpha)/\sqrt{\dot{u}^2 + R^2\dot{\alpha}^2} + N\cos(\omega t - \alpha). \end{aligned} \quad (11)$$

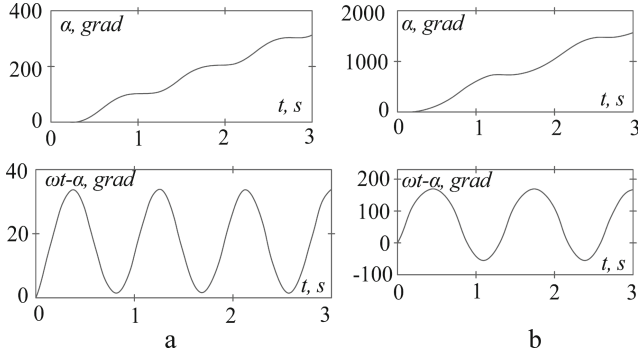
By substituting (8) in (11), one can obtain a system of three equations with three unknown dependencies:  $\alpha = \alpha(t)$ ,  $u = u(t)$  and  $N = N(t)$ . It should be used in the case when the initial velocity  $\dot{u}$  of the particle is set in the direction of the  $OX$  axis. When  $\ddot{u} = \dot{u} = 0$  (i.e., when a particle slides on the circle), the first Eq. (11) becomes the identity  $0 = 0$ . The solution of the system in respect to  $\ddot{\alpha} = \ddot{\alpha}(t)$  and  $N = N(t)$  gives:

$$\begin{aligned} \ddot{\alpha} &= g[\sin(\omega t - \alpha) - f\cos(\omega t - \alpha)]/R - f(\omega - \dot{\alpha})^2; \\ N &= m[R(\omega - \dot{\alpha})^2 + g\cos(\omega t - \alpha)]. \end{aligned} \quad (12)$$

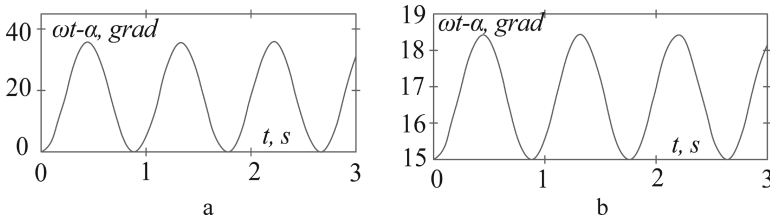
The first Eq. (12) is differential and can be solved independently. It can be assumed that when a horizontal cylinder is rotating, the particle which is located on it (Fig. 1b, point  $A$ ) rotates with the cylinder without sliding to point  $C$ , and then it slides down to a certain point below, and this process will be repeated. Numerical integration of first Eq. (12) showed that such an assumption is valid only for small angular velocities. An important role in numerical integration has the initial conditions, which depend on the nature of the particle's movement. The initial conditions assumed that the particle is initially located on the lower generatrix and the angular sliding velocity is absent, i.e.,  $\alpha = \dot{\alpha} = 0$ . In Fig. 2, the graphs of changes of the kinematic characteristics of the particle's movement during 3 s at  $R = 0.2$  m,  $f = 0.3$ , and different angular velocities are presented. The horizontal part of the graph  $\alpha = \alpha(t)$  indicates that at this time, there is no sliding, the particle "sticks" and rotates with the cylinder. "Sticking" (rising) periodically alternates with sliding (falling). The graph of the change of the difference of angles  $\omega \cdot t - \alpha$  shows the amplitude of oscillations.

The graphs show that the amplitude of particle oscillations increases as the angular velocity of the rotation increases. If at  $\omega = 2$  s<sup>-1</sup> the particle during rising upwards rotated at approximately 35° and fell almost to the lower generatrix, then these angles are respectively 165° and -40° at  $\omega = 10$  s<sup>-1</sup>, i.e., the particle oscillates in a circle, covering more than half of its arc. With a further increase in the angular velocity  $\omega$  of the cylinder rotation, the particle practically "sticks" and rotates with it.

If at the initial moment the particle has an angular sliding velocity  $\dot{\alpha} = \omega$ , i.e., at the beginning of its movement, its absolute velocity of rotation is equal to zero, then the further movement of the particle will differ from the considered cases. For example, let us take  $\omega = 10$  s<sup>-1</sup> (Fig. 2b at the bottom for the initial conditions  $\alpha = \dot{\alpha} = 0$ ). Let us change only one initial condition:  $\alpha = 0$ ,  $\dot{\alpha} = \omega$ . This replacement significantly changed the character of the oscillations – their amplitude decreased (Fig. 3a).



**Fig. 2.** Graphs of changes of the sliding angle  $\alpha$  (at the top) and the angle of deviation of the particle  $\omega \cdot t - \alpha$  (at the bottom) from zero value in absolute movement: a)  $\omega = 2 \text{ s}^{-1}$ ; b)  $\omega = 10 \text{ s}^{-1}$ .



**Fig. 3.** Graphs of change of the deviation angle  $\omega t - \alpha$  from zero value in the absolute movement at  $\omega = 10 \text{ s}^{-1}$  and different initial conditions: a)  $\dot{\alpha} = \omega, \alpha = 0$ ; b)  $\dot{\alpha} = \omega, \alpha = -15^\circ$ .

Research results have shown that when the angular velocity of rotation increases, the particle does not “stick”, but oscillates with the same amplitude (within  $0^\circ \dots 35^\circ$ ), i.e. the angular velocity does not affect the amplitude of oscillations, unlike the second initial condition, supplemented by the first. In Fig. 3a, a graph is constructed for  $\alpha = -15^\circ$ , i.e., at the initial moment, the particle is not located at the lower point of the cylinder but slightly higher in the rotation direction. The amplitude of oscillations has decreased ( $15^\circ \dots 18.5^\circ$ ), and it is evident that in both cases (Fig. 3), oscillations occur relative to the midpoint (approximately  $17^\circ$ ). If the initial condition is  $\alpha = -17^\circ$ , the amplitude of oscillations practically disappears, and the particle remains stationary. This is confirmed by a solution of the first Eq. (12).

Let the solution of first Eq. (12) be the dependence  $\alpha = \omega \cdot t + \alpha_0$ . Then  $\dot{\alpha} = \omega, \ddot{\alpha} = 0$ . Substitution of these expressions into the first differential Eq. (12) satisfies the last one. As a result:  $-\sin\alpha_0 - f \cos\alpha_0 = 0$ , wherence  $\alpha_0 = -\text{Arctg}f$ . Thus, the angle  $\alpha_0$  is equal to the angle of friction. For the accepted value of  $f = 0.3$  angle is  $\alpha_0 = -16.7^\circ$ . Under these initial conditions, the particle will slide on the surface, remaining stationary in the absolute movement at a certain height from the lower generatrix.

To compile differential equations of movement of a particle, it is necessary to rotate the cylinder and align all vectors of forces and absolute acceleration according to its position. The rotation will be done clockwise around the axis  $OY$  at an angle  $\beta$ . So, the

particle sliding direction down along the generatrices coincides with the direction of the axis  $OX$ . The vector of the weight force is directed downwards, i.e., does not change its direction. The vectors of the remaining forces and the absolute acceleration are rigidly bound to the cylinder surface or the lines (trajectories) on it, so they must be rotated in the same way as the cylinder.

After rotation at the angle  $\beta$ , the following expressions can be obtained:

- parametrical equations of the cylinder:

$$X = u\cos\beta - R\sin\beta\cos\alpha; \quad Y = R\sin\alpha; \quad Z = u\sin\beta - R\cos\beta\cos\alpha;$$

- projections of the absolute trajectory:

$$x_a = u\cos\beta - R\sin\beta\cos(\omega t - \alpha); \quad y_a = R\sin(\omega t - \alpha); \quad z_a = u\sin\beta - R\cos\beta\cos(\omega t - \alpha);$$

- projections of the absolute acceleration:

$$\begin{aligned} \ddot{x}_{a\beta} &= R\sin\beta(\omega - \dot{\alpha})^2\cos(\omega t - \alpha) + \ddot{u}\cos\beta - R\ddot{\alpha}\sin\beta\sin(\omega t - \alpha); \\ \ddot{y}_{a\beta} &= R(\omega - \dot{\alpha})^2\sin(\omega t - \alpha) + R\ddot{\alpha}\cos(\omega t - \alpha); \\ \ddot{z}_{a\beta} &= R\cos\beta(\omega - \dot{\alpha})^2\cos(\omega t - \alpha) - \ddot{u}\sin\beta - R\ddot{\alpha}\cos\beta\sin(\omega t - \alpha); \end{aligned} \quad (13)$$

- projections of the unit directing vector of action of friction force  $f \cdot N$ :

$$f \cdot N : \left\{ \begin{array}{l} (R\dot{\alpha}\sin\beta\sin(\omega t - \alpha) - \dot{u}\cos\beta)/\sqrt{\dot{u}^2 + R^2\dot{\alpha}^2}; \\ -(R\dot{\alpha}\cos(\omega t - \alpha))/\sqrt{\dot{u}^2 + R^2\dot{\alpha}^2}; \\ (R\dot{\alpha}\cos\beta\sin(\omega t - \alpha) + \dot{u}\sin\beta)/\sqrt{\dot{u}^2 + R^2\dot{\alpha}^2} \end{array} \right\}; \quad (14)$$

- projections of the unit directing vector of action of the reaction force  $N$ :

$$N : \{\sin\beta\cos(\omega t - \alpha); \sin(\omega t - \alpha); \cos\beta\cos(\omega t - \alpha)\}. \quad (15)$$

Similarly, as for the horizontal cylinder, a system of differential equations considering the rotated vectors (13–15) is made:

$$\begin{aligned} m\ddot{x}_{a\beta} &= fN(R\dot{\alpha}\sin\beta\sin(\omega t - \alpha) - \dot{u}\cos\beta)/\sqrt{\dot{u}^2 + R^2\dot{\alpha}^2} + N\sin\beta\cos(\omega t - \alpha); \\ m\ddot{y}_{a\beta} &= -fN(R\dot{\alpha}\cos(\omega t - \alpha))/\sqrt{\dot{u}^2 + R^2\dot{\alpha}^2} + N\sin(\omega t - \alpha); \\ m\ddot{z}_{a\beta} &= -mg + \frac{fN(R\dot{\alpha}\cos\beta\sin(\omega t - \alpha) + \dot{u}\sin\beta)}{\sqrt{\dot{u}^2 + R^2\dot{\alpha}^2}} + N\cos\beta\cos(\omega t - \alpha). \end{aligned} \quad (16)$$

Let us substitute (13) in (16) and solve it in respect to  $\ddot{\alpha} = \ddot{\alpha}(t)$ ,  $\ddot{u} = \ddot{u}(t)$  and  $N = N(t)$ :

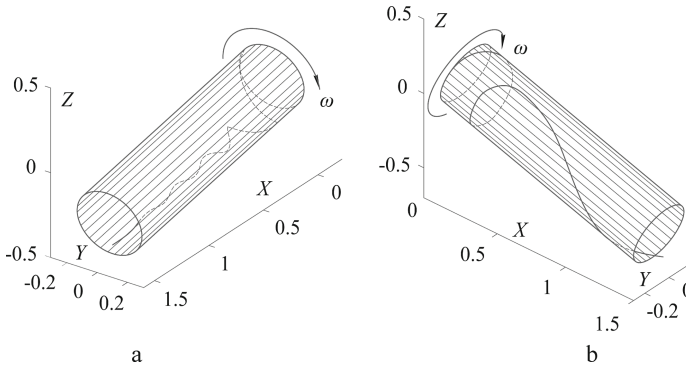
$$\begin{aligned} \ddot{\alpha} &= \frac{g}{R}\cos\beta\sin(\omega t - \alpha) - f\dot{\alpha}[g\cos\beta\cos(\omega t - \alpha) + R(\omega - \dot{\alpha})^2]/\sqrt{\dot{u}^2 + R^2\dot{\alpha}^2}; \\ \ddot{u} &= g\sin\beta - f\dot{u}[g\cos\beta\cos(\omega t - \alpha) + R(\omega - \dot{\alpha})^2]/\sqrt{\dot{u}^2 + R^2\dot{\alpha}^2}; \\ N &= m[g\cos\beta\cos(\omega t - \alpha) + R(\omega - \dot{\alpha})^2]. \end{aligned} \quad (17)$$

## 4 Results

By numerical integration, the kinematic characteristics of the particle movement inside the cylinder were obtained, and they significantly depend on two parameters: the angle of inclination  $\beta$  of the cylinder and the angular velocity  $\omega$  of its rotation. Figure 4 shows the absolute trajectories of the particle for a cylinder of radius  $R = 0.2$  m, which is inclined by an angle  $\beta = 15^\circ$  (less than the angle of friction, which is  $16.7^\circ$  for  $f = 0.3$ ).

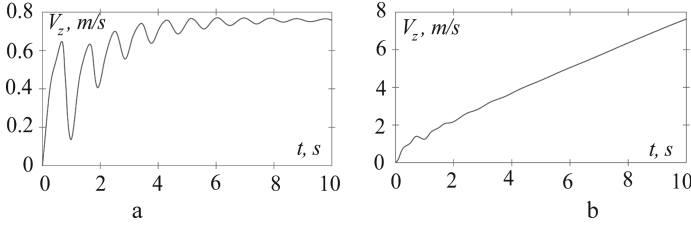
Figure 5 shows the velocity change  $\dot{u} = V_Z$  in the  $OX$  direction. In one case (Fig. 5a), the inclination angle is less than the friction angle and more significant in the other (Fig. 5b).

It can be concluded that the particle's movement is stabilized, its velocity in the axial direction is close to a constant value, and the trajectory – to a straight line (Figs. 4a, and 5a). Such stabilization is possible up to a particular value of the angular velocity of the rotation. In Fig. 4b, an absolute trajectory at  $\omega = 10 \text{ s}^{-1}$  is constructed (the oscillations of the particle increase). With a further increase in the angular velocity  $\omega$ , the particle “sticks” and rotates with the cylinder. At low angular velocities of rotation (i.e., to “sticking” of the particle), velocity stabilization is possible only for the angles of inclination of the cylinder, which are less than the angle of friction. The graph of the particle sliding velocity in the axial direction at an angle  $\beta$ , more significant than the friction angle, shows that the sliding velocity increases linearly (Fig. 5b).



**Fig. 4.** Absolute trajectories of the movement of the particle on the inner surface of the cylinder at different angular velocities of its rotation: a)  $\omega = 2 \text{ s}^{-1}$ ; b)  $\omega = 10 \text{ s}^{-1}$ .

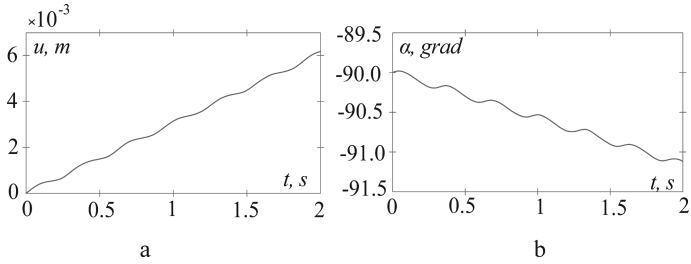
The “sticking” of the particle occurs when reaching the appropriate angular velocity at any angle of its inclination. Graphs of changes of the sliding angle  $\alpha$  and the distance  $u$  of the particle movement in the axial direction at  $\omega = 20 \text{ s}^{-1}$  and the angle of inclination  $\beta = 45^\circ$  are constructed in Fig. 6. The graphs show that during time 2 s the particle moves at 6 mm and rotates at  $1^\circ$ . A further increase in the angular velocity will lead to complete “sticking” of the particle. For angles of inclination of the cylinder, which are less than the friction angle, stabilization is possible when the particle slides at a constant velocity straightforwardly. Let us find the solution for this case and the horizontal cylinder. It should be found in the form  $\alpha = \omega t + \alpha_0$ , supplementing it with a constant velocity in



**Fig. 5.** Graphs of the change of velocity  $\dot{u} = V_z$  in the direction of the axis of the cylinder at  $\omega = 5 \text{ s}^{-1}$  for different angles  $\beta$  of its inclination: a)  $\beta = 10^\circ$ ; b)  $\beta = 20^\circ$ .

the axial direction  $\dot{u} = V_z = \text{const}$ . Therefore,  $\dot{\alpha} = \omega$ ,  $\ddot{\alpha} = 0$ ,  $\ddot{u} = 0$ . Using substituting these data into the first two Eqs. (18), a system of two equations is obtained:

$$\begin{aligned} 0 &= \frac{g \cos \beta \sin(-\alpha_0)}{R} - (f \omega g \cos \beta \cos(-\alpha_0)) / \sqrt{V_z^2 + R^2 \omega^2}; \\ 0 &= g \sin \beta - (f V_z g \cos \beta \cos(-\alpha_0)) / \sqrt{V_z^2 + R^2 \omega^2}. \end{aligned} \quad (18)$$



**Fig. 6.** Graphs of changes in the kinematic characteristics of the particle movement at  $\omega = 20 \text{ s}^{-1}$  and the inclination angle of  $\beta = 45^\circ$ : a) the graph of the dependence  $u = u(t)$ ; b) the graph of the dependence  $\alpha = \alpha(t)$ .

After solving system (18) regarding  $\alpha_0$  and  $V_z$ , one can obtain:

$$\alpha_0 = -\arctg \sqrt{f^2 \cos^2 \beta - \sin \beta}; \quad V_z = R \omega \sqrt{(1 + f^2) / (f^2 \text{ctg}^2 \beta - 1)}. \quad (19)$$

The result (19) should be understood as follows. Suppose the particle hits the cylinder at  $\alpha_0$  with a relative angular velocity, equal to the angular rotation velocity of and opposite the direction of its rotation and relative translational velocity along the axis  $V_z$ . In that case, it continues to move at this velocity without oscillation.

## 5 Conclusions

When a particle hits the inner surface of a horizontal cylinder that rotates with an angular velocity  $\omega$  around its axis, it begins to oscillate in the cross-sectional plane of the cylinder

with a certain amplitude in the angular dimension. The amplitude value depends on the particle's incidence point, the coefficient of friction, and the initial absolute velocity. Under the appropriate initial conditions, which are determined analytically, the particle in absolute movement can be stationary, being at a point on the cylinder at a certain distance from the lower point in the angular dimension in the direction of the rotation. When an angle  $\beta$  inclines the cylinder to the horizon, the particle begins to move in the axial direction, while the amplitude of oscillations decreases. The angle of inclination of the cylinder is essential: at an angle  $\beta$ , which is less than the angle of friction, there is a stabilization of movement, oscillations stop, and the particle moves straightforwardly in the axial direction with a constant velocity; at an angle  $\beta$ , which is greater or equal to the angle of friction, the stabilization of movement does not occur, the particle moves accelerated in the axial direction. The value of the angular velocity of rotation has great importance. When a particular value is reached, the particle practically "sticks" regardless of the angle of the cylinder.

## References

1. Marchevsky, V.M., Novokhat, O.A., Vozniuk, V.T., Danchyshen, I.A.: Intensification of paper drying on drying cylinders. *J. Eng. Sci.* **7**(1), F45-E49 (2020). [https://doi.org/10.21272/jes.2020.7\(1\).f5](https://doi.org/10.21272/jes.2020.7(1).f5)
2. Sklabinskiy, V., Liaposhchenko, O., Pavlenko, I., Lytvynenko, O., Demianenko, M.: Modelling of liquid's distribution and migration in the fibrous filter layer in the process of inertial-filtering separation. In: Ivanov, V., et al. (eds.) *DSMIE 2018. LNME*, pp. 489–497. Springer, Cham (2019). [https://doi.org/10.1007/978-3-319-93587-4\\_51](https://doi.org/10.1007/978-3-319-93587-4_51)
3. Liaposhchenko, O., Pavlenko, I., Monkova, K., Demianenko, M., Starynskiy, O.: Numerical simulation of aeroelastic interaction between gas-liquid flow and deformable elements in modular separation devices. In: Ivanov, V., et al. (eds.) *DSMIE 2019. LNME*, pp. 765–774. Springer, Cham (2020). [https://doi.org/10.1007/978-3-030-22365-6\\_76](https://doi.org/10.1007/978-3-030-22365-6_76)
4. Tarelnyk, V., et al.: New sulphiding method for steel and cast iron parts. *IOP Conf. Ser. Mater. Sci. Eng.* **233**, 012049 (2017). <https://doi.org/10.1088/1757-899x/233/1/012049>
5. Tarelnyk, V., et al.: New method for strengthening surfaces of heat treated steel parts. *IOP Conf. Ser. Mater. Sci. Eng.* **233**, 012048 (2017). <https://doi.org/10.1088/1757-899x/233/1/012048>
6. Tarel'nik, V.B., Martsinkovskii, V.S., Zhukov, A.N.: Increase in the reliability and durability of metal impulse end seals. Part 1. *Chem. Pet. Eng.* **53**(1–2), 114–120 (2017). <https://doi.org/10.1007/s10556-017-0305-y>
7. Martsinkovsky, V., Yurko, V., Tarelnik, V., Filonenko, Y.: Designing thrust sliding bearings of high bearing capacity. *Proc. Eng.* **39**, 148–156 (2012). <https://doi.org/10.1016/j.proeng.2012.07.019>
8. Konopatskiy, E., Voronova, O., Bezditnyi, A., Shevchuk, O.: About one method of numeral decision of differential equalizations in partials using geometric interpolants. In: *CPT2020 The 8th International Scientific Conference on Computing in Physics and Technology Proceedings* (2020). [https://doi.org/10.30987/conferencearticle\\_5fce27708eb353.92843700](https://doi.org/10.30987/conferencearticle_5fce27708eb353.92843700)
9. Konopatskiy, E.V., Bezditnyi, A.A.: Geometric modeling of multifactor processes and phenomena by the multidimensional parabolic interpolation method. *J. Phys: Conf. Ser.* **1441**(1), 012063 (2020). <https://doi.org/10.1088/1742-6596/1441/1/012063>



10. Konopatskiy, E., Bezdityni, A., Shevchuk, O.: Modeling geometric varieties with given differential characteristics and its application. In: Proceedings of the 30th International Conference on Computer Graphics and Machine Vision (GraphiCon 2020), Part 2, pp. short31-1-short31-8 (2020). <https://doi.org/10.51130/graphicon-2020-2-4-31>
11. Liaposhchenko, O., Pavlenko, I., Ivanov, V., Demianenko, M., Starynskiy, O., Kuric, I., Khukhryanskiy, O.: Improvement of parameters for the multi-functional oil-gas separator of 'heater-treater' type. In: 2019 IEEE 6th International Conference on Industrial Engineering and Applications (ICIEA), Tokyo, Japan, 2019, pp. 66–71 (2019). <https://doi.org/10.1109/IEA.2019.8715203>
12. Abbou-ou-Cherif, E.M., Piron, E., Chateaneuf, A., Miclet, D., Lenain, R., Koko, J.: On-the-field simulation of fertilizer spreading Part 1 – modeling. *Comput. Electron. Agric.* **142**(A), 235–247 (2017). <https://doi.org/10.1016/j.compag.2017.09.006>
13. Bulgakov, V., et al.: Theory of motion of grain mixture particle in the process of aspiration separation. *Agron. Res.* **18**(2), 1177–1188 (2020). <https://doi.org/10.15159/AR.20.069>
14. Kobets, A.S., Ponomarenko, N.O., Kharytonov, M.M.: Construction of centrifugal working device for mineral fertilizer spreading. *INMATEH Agric. Eng.* **51**(1), 5–14 (2017)
15. Pavlenko, I., et al.: Effect of superimposed vibrations on droplet oscillation modes in prilling process. *Processes* **8**(5), 566 (2020). <https://doi.org/10.3390/pr8050566>
16. Golub, G.A., Szalay, K., Kukharets, S.M., Marus, O.A.: Energy efficiency of rotary digesters. *Prog. Agric. Eng. Sci.* **13**(1), 35–49 (2017). <https://doi.org/10.1556/446.13.2017.3>
17. Kurzthaler, C., Zhu, L., Pahlavan, A., Stone, H.: Particle motion nearby rough surfaces. *Phys. Rev. Fluids* **5**, 082101(R) (2020). <https://doi.org/10.1103/PhysRevFluids.5.082101>
18. Chelabi, M.A., Basova, Y., Hamidou, M.K., Dobrotvorskiy, S.: Analysis of the three-dimensional accelerating flow in a mixed turbine rotor. *J. Eng. Sci.* **8**(2), D1–D7 (2021). [https://doi.org/10.21272/jes.2021.8\(2\).d2](https://doi.org/10.21272/jes.2021.8(2).d2)
19. Pylypaka, S., Klendiy, M., Zaharova, T.: Movement of the particle on the external surface of the cylinder, which makes the translational oscillations in Horizontal Planes. In: Ivanov, V., et al. (eds.) DSMIE 2018. LNME, pp. 336–345. Springer, Cham (2019). [https://doi.org/10.1007/978-3-319-93587-4\\_35](https://doi.org/10.1007/978-3-319-93587-4_35)
20. Loveikin, V.S., Romesevych, Y.: Dynamic optimization of a mine winder acceleration mode. *Naukovi Visnyk Natsionalnoho Hirnychoho Universytetu* **4**, 55–61 (2017)



# Supersonic Flow in the Blade Channel of the Nozzle with a Rotary Diaphragm at Small Degrees of Opening

Oleksandr Zhyrkov<sup>1</sup> , Oleksandr Usatyi<sup>2</sup> , Olena Avdieieva<sup>2</sup>(✉) ,  
and Yuri Torba<sup>1</sup> 

<sup>1</sup> SE Ivchenko-Progress, 2 Ivanova Street, Zaporozhye 69068, Ukraine

<sup>2</sup> National Technical University “Kharkiv Polytechnic Institute”,

2 Kyrpychova Street, Kharkiv 61002, Ukraine

[o.avdieieva@gmail.com](mailto:o.avdieieva@gmail.com)

**Abstract.** The article presents a study of the flow of supersonic flow in the interscapular duct of a nozzle with a rotating aperture at low degrees of opening. Modeling and calculation of the working fluid flow were carried out using the Fluent software package. The construction of computational domains, limited by one interscapular channel, for different degrees of opening of the nozzle diaphragm has been carried out. Grids for computational domains have been built. A numerical study of the flow in the interscapular channel of the C-9013R airfoil lattice at  $\pi = 0.3$   $\delta = 0.3$  was carried out using the Reynolds Stress turbulence model. A numerical study of the spatial flow in the interscapular channel has been carried out. As a result of the calculations performed, the flow patterns in the interscapular channel and behind it were obtained. The distribution of the kinetic energy loss coefficients along the grating front at various degrees of opening of the diaphragm at the inlet to the nozzle apparatus. The results obtained in this work will develop a method for multi-parameter optimization of cogeneration steam turbines with controlled steam extraction.

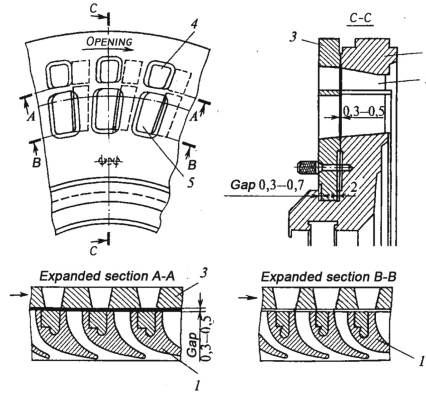
**Keywords:** Supersonic flow · Rotary diaphragm · Blade channel · Energy efficiency

## 1 Introduction

Continuous development and improvement of the design and operating modes of cogeneration turbines have led to the use of steam with supercritical parameters. At this point in time, one of the promising trends in developing thermal power turbines is their operation at supercritical pressure drops [1]. An increase in the steam parameters entails an increase in the flow rates in the inter-blade channels of the nozzle and working channels. In this case, it is necessary to reprofile the flow path to obtain the optimal geometry with the lowest kinetic energy loss coefficients. The development of optimization methods for the flow path of heating turbines is an urgent task.

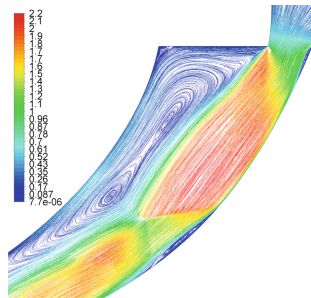
## 2 Literature Review

A large number of works are devoted to investigations of transonic and supersonic flows in channels (reflux channels [2, 3] and other channels [4–7]). But a feature of cogeneration turbines with adjustable steam extraction is the use of nozzle grids with rotary diaphragms [4]. The change in the steam flow rate through the turbine under variable modes is achieved by overlapping, at the inlet, the nozzle apparatus channels (Fig. 1). The part of the nozzle that blocks the inlet channel is called the rotary diaphragm.



**Fig. 1.** Regulating turbine diaphragm: 1 - diaphragm; 2 - nozzles; 3 - rotary ring; 4 and 5 – windows.

The flow structure in the nozzle array channel is greatly influenced by the degree of opening of the diaphragm  $\delta$  [8]. Here  $\delta = \frac{a}{a_0}$  – the degree of opening of the rotary diaphragm is the ratio of the area of the closed rotary diaphragm to the area of the fully open diaphragm (Fig. 2).



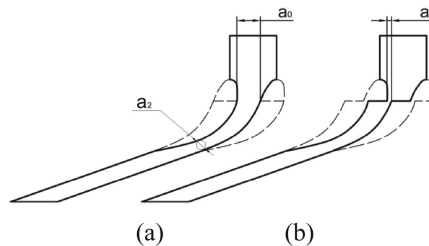
**Fig. 2.** Flow in the computational domain. Isolines of Mach numbers at  $\pi = 0.3$ ,  $\delta = 0.3$ .

In the process of developing a method for the numerical study of a plane flow around a nozzle array with a rotary diaphragm, calculations were performed at various degrees of opening of the rotary diaphragm  $\delta$  and pressure drops  $\pi$  across the array. As a result of calculations, for small degrees of opening of the rotary diaphragm, complex flow patterns were obtained in the blade channel of the nozzle, with the division of the flow core into supersonic regions, shown in Fig. 2. An additional numerical analysis was carried out for a more detailed study of these phenomena. The paper presents some results of a numerical study of supersonic flow in the channel of the nozzle apparatus at the degree of opening of the rotary diaphragm  $\delta = (0,15 \div 0,3)$ .

Numerical studies were carried out using the ANSYS Fluent software package.

### 3 Research Methodology

The computational area is one blade channel formed by the back and the trough of the C-9013R profile developed by MEI (Fig. 3). The main requirement for the computational grid is a high-quality resolution of physical phenomena occurring in the computational domain [9, 10]. On the one hand, the grid must ensure the resolution of phenomena in the boundary layer of the near-wall region and phenomena in the flowing part of the lattice, and beyond it, arising at transonic and supersonic flow rates (shock waves, flow separations, wakes), which requires densification of the mesh in the indicated areas. On the other hand, the size of the grid cells should be limited in terms of the time spent on performing the calculations.



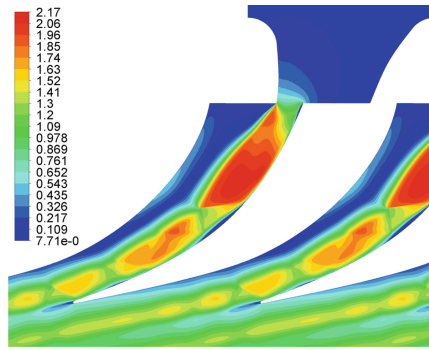
**Fig. 3.** Computational area for the S-9013R profile at  $\delta = 1$  (a) and  $\delta = 0,15$  (b).

The computational domain can be divided into two parts: movable, limited by the rotary diaphragm, and fixed, limited by the interscapular channel behind the rotary diaphragm. In this connection, it is possible to construct separate meshes for these areas once and then, using a non-conformal interface, move them relative to each other, simulating different degrees of diaphragm opening  $\delta$ . In practice, due to the need to compact the mesh at the walls to meet the requirements for the value of  $y^+ \approx 1$ , a poorly matching and curved interface is obtained. Test calculations showed the presence of “discontinuities” and “jumps” on the isolines of the parameters, which forced to abandon the use of the non-conformal interface.

Further, its own grid was built for the computational domain for each of the selected degrees of opening of the rotary diaphragm. Considering all of the above, the following approach was applied when constructing the mesh in the computational domain. Since the position of the shock waves and flow separations in and behind the channel is unknown, the grid was built to ensure the condition  $y^+ \approx 1$  in the near-wall region.

The thickness of the boundary layer was divided into 25 sublayers, with an element magnification factor of 1.2. The rest of the mesh was set equal to the cell size in the last sublayer. As a result, the number of mesh elements ranged from  $1,8 \cdot 10^5$  to  $2,4 \cdot 10^5$ , depending on the degree of opening  $\delta$ .

The preliminary results obtained (Fig. 4) required more detailed studies of the flow in the channels of the gratings with rotary diaphragms:



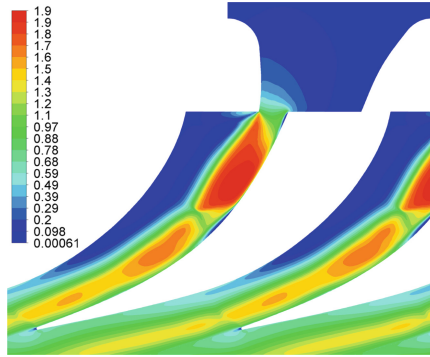
**Fig. 4.** Flow in the computational domain. Isolines of Mach numbers at  $\pi = 0.3$ ,  $\delta = 0.3$ ,  $k-\omega$  SST turbulence model.

1. A numerical study of the flow in the blade channel of the C-9013R profile lattice at  $\pi = 0.3$   $\delta = 0.3$  was carried out using the Reynolds Stress turbulence model. The model is used to simulate turbulence and makes it possible to obtain a good agreement between the results of the calculation of supersonic jet flows with the experiment's results [11]. Since the model uses near-wall functions to resolve the phenomena in the boundary layer, a separate computational domain was built with a mesh satisfying the condition  $y^+ \leq 30$  with the number of elements  $\approx 63000$  pcs.

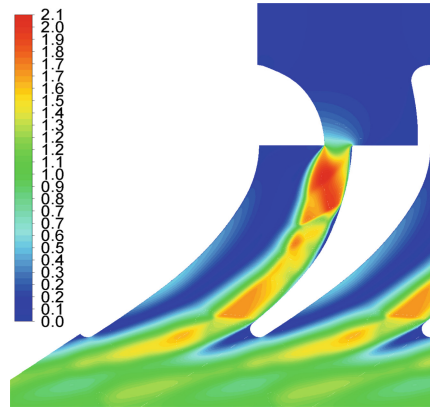
In Fig. 5 shows the flow pattern obtained in the calculation using the Reynolds Stress turbulence model. As can be seen from the figure, the flow pattern in the blade channel obtained by analysis using the Reynolds Stress turbulence model is similar to the previously obtained flow pattern calculated using the  $k-\omega$  SST turbulence model (Fig. 4).

2. Additionally, to assess the possible influence of the profile shape on the flow pattern in the interscapular channel formed from profiles No. 99 developed by TsAGI. The profile was chosen because of the similarity to the C-9013R profile in terms of geometric characteristics.  $t/b = 2$ . For profile No. 99, a computational domain was constructed, corresponding to the degree of opening of the rotary diaphragm  $\delta = 0.3$ . The calculation was performed using the  $k-\omega$  SST turbulence model with the same

settings of the Fluent CFD solver as for the C-9013P profile. The flow pattern in the blade channel of the lattice of profiles No. 99 is shown in Fig. 6. As can be seen, in the blade channel, there are regions similar to the regions obtained when calculating the flow for the C-9013R profile lattice.

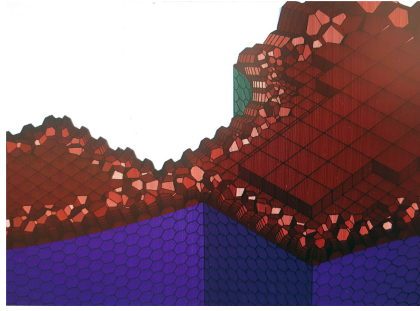


**Fig. 5.** Flow in the computational domain. Isolines of Mach numbers at  $\pi = 0.3$ ,  $\delta = 0.3$ , Reynolds Stress turbulence model.



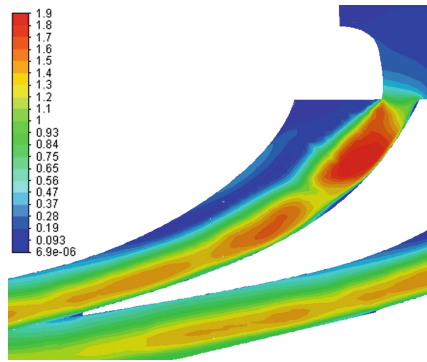
**Fig. 6.** The flow in the computational region of the blade channel of the lattice of profiles No. 99. Isolines of Mach numbers at  $\pi = 0.3$ ,  $\delta = 0.3$ , turbulence model  $k-\omega$  SST.

3. A numerical study of the spatial flow in the blade channel has been carried out. For this, the blade channel of the nozzles was simulated with a diaphragm opening of  $\delta = 0.3$  to calculate the spatial flow. The channel height was 80 mm ( $l/b = 1.3$ ). In the computational domain, a mesh of Poly-Hexcore elements was built (Mosaic<sup>TM</sup> technology, which allows you to construct a mesh consisting of hexagonal prisms in the wall area and to carry out a direct transition from a polyhedral mesh to a hexahedral mesh bypassing tetra-cells) (Fig. 7).



**Fig. 7.** Poly-Hexcore mesh in the computational domain for the C-9013P profile at  $\delta = 0,3$ .

Since the main task was to confirm the previously obtained flow pattern in the blade channel, without calculating the kinetic energy loss coefficients, the computational domain was divided into a relatively small number of elements - a little more than 8 million. All solver settings are the same as for plane flow simulations, using the  $k-\omega$  SST turbulence model. The flow pattern in the plane at the height of 40 mm is shown in Fig. 8.



**Fig. 8.** Flow in the computational domain. Isolines of Mach numbers at  $\pi = 0,3$ ,  $\delta = 0,3$ .

In all three cases of the verification calculation, a flow pattern was obtained in the blade channel with the division of the flow core into supersonic regions. Based on this, a conclusion was made about the presence of similar phenomena in a real nozzles, and a decision was made to conduct an additional study of the flow in the blade channel of a nozzles with a rotary diaphragm at low degrees of opening.

For the numerical study of the plane flow, we used the model of a two-dimensional viscous gas flow of the CFD solver Fluent using a second-order difference method. The working fluid is a viscous compressible gas - air. To calculate the turbulence phenomena, the  $k-\omega$  SST turbulence model (Menter's model) [12] was used. The following were used as boundary conditions at the entrance to the computational domain: air pressure and temperature, for some part of calculations, airflow and temperature; airflow direction; the intensity of turbulence; hydraulic diameter.

Air pressure was set as the boundary condition at the exit from the computational domain. All calculations were performed in two stages. A “rough” flow calculation was performed using the FMG utility. The FMG utility uses the ANSYS FLUENT FAS Multigrid technology to perform calculations on a set of sequentially nested grids. The calculation starts on the coarsest grid, and the results are interpolated to the next finer grid as it settles. As a rule, all “rough” calculations, to achieve residual values  $10^{-6}$ , required no more than  $1000 \div 2000$  iterations. According to the “rough” calculation results, the mesh was adapted in places of large gradients of the calculated parameters and to ensure the condition  $y^+ \leq 1$ . The adaptation resulted in a mesh with suspended nodes. For “finishing” calculations, depending on the values of  $M$  and  $\delta$ , the amount of iterations was  $20,000 \div 33,000$  pieces. The convergence of the calculation was assessed by establishing the equality of the flow rates at the inlet and outlet from the computational domain and by establishing the residuals of the kinetic energy loss coefficient.

## 4 Results

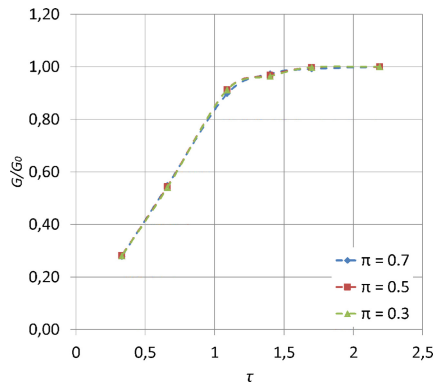
To apply one of the theories describing the phenomena in supersonic flow, it is necessary to solve the problem of the type of flow in the blade channel. On the one hand, this is undoubtedly a supersonic flow in the turning channel; on the other hand, due to the sudden expansion after the turning diaphragm, part of the flow can be considered as the outflow of a supersonic jet into a cavity with pressure almost equal to the pressure in the jet.

It is also possible to distinguish two flow regimes in the computational domain. In the first case, the minimum area is in the throat  $a_2$  of the blade channel (Fig. 2) - confusor flow in the channel. In the second case, at low degrees of opening  $\delta$ , when the ratio  $\tau$  of the channel width at the inlet  $a$  to the throat of the grating  $a_2$  becomes less than unity - the diffuser flow in the channel. In Fig. 10 shows the dependence of the flow rate ratio on the ratio  $\tau$  of the channel width at the inlet  $a$  to the throat of the grating  $a_2$ . As can be seen from the graph (Fig. 9), throttling of the flow begins to occur at values of  $\tau > 1$ .

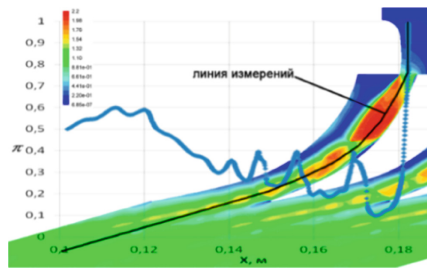
Thus, at  $\tau = 1.7$ , the ratio of the flow rates through the nozzle apparatus is  $G/G_0 = 0.99$ ; at  $\tau = 1.4$ , the ratio  $G/G_0 = 0.97$ , etc. In this case, the ratio of the flow rates through the nozzle  $G/G_0$  does not depend on the pressure difference  $\pi$  on the cascade for the same values of  $\tau$  ( $\delta$ ).

In Fig. 10 shows the calculated area for the degree of opening  $\delta = 0.3$  with the indication of the dashed line, which is the equidistant profile of the trough of the blade with straight sections at the inlet and outlet, along which  $\pi$  is measured as the ratio of the static pressure to the total pressure. Since the condition of equality of the flow rates at the inlet and outlet from the grating must be observed, in the case of a diffuser flow, a local increase in the velocity in the flow core occurs in the channel to compensate for the decrease in the flow area due to the overlap of the rotary diaphragm. As can be seen from the graph in Fig. 10, the pressure ratio immediately after the rotary diaphragm is significantly less than the critical value (0.525).





**Fig. 9.** Dependence of the ratio of airflow rates through the nozzle device  $G/G_0$  on  $\tau$ .

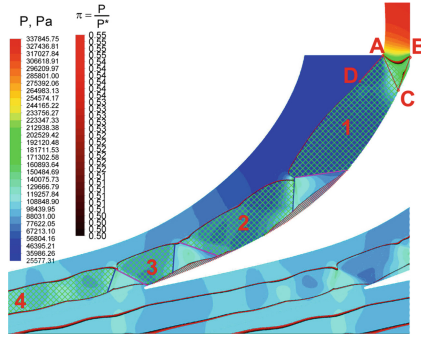


**Fig. 10.** Distribution of the static pressure ratio to total pressure along the channel at  $\pi = 0,3$  and  $\delta = 0,3$ .

Further, the pressure ratio gradually increases as the flow moves towards the outlet from the grid. In this case, the flow rate decreases. That is, the flow moves against a positive pressure gradient. In this case, the interscapular channel is divided into two regions: at the trough of the blade, there is a region of supersonic flow. There is a region of the vortex at the back of the blade, subsonic flow. This is confirmed by the distribution of Mach numbers (Fig. 4) and the position of the regions with a critical drop along the interscapular channel (Fig. 11).

To simplify the description of the phenomena in the channel, we denote the flow regions (Fig. 11). After the flow passes through the rotary diaphragm, the flow in the ABC triangle occurs similarly to the flow in the oblique cut of the nozzle apparatus. Since the pressure in front of the rotary diaphragm is greater than behind it (Fig. 11), the expansion of the gas occurs in the oblique cut ABC, which thus plays the role of the expanding part of the nozzle.

Since the pressure in front of the rotary diaphragm is greater than behind it (Fig. 11), the expansion of the gas occurs in the oblique cut ABC, which thus plays the role of the expanding part of the nozzle. The process of gas expansion in a diagonal cut is as follows. Since the pressure gradually drops from  $P_{cr}$  in section AB to  $P_{in}$  section AC, the isobars corresponding to intermediate pressures are located approximately in the form of rays emanating from point A. Thus, in section BC, the pressure decreases gradually,



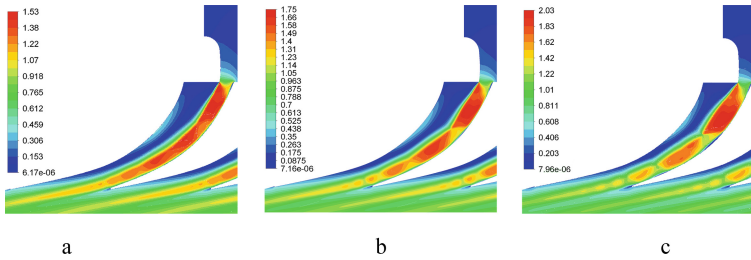
**Fig. 11.** Distribution of static pressure and critical pressure ratio in the interscapular channel at  $\pi = 0,3$  and  $\delta = 0,3$ .

while at point A the pressure drops instantly from  $P_{cr}$  to  $P$ , and, consequently, along with the line AD, which is the boundary of the jet, the pressure will be equal to  $P$ . Under the influence of this pressure difference, a resulting force appears at the boundary of the jet, directed perpendicular to the axis of the channel, which turns the flow by a certain angle. As a result of this rotation, the width of the jet increases, and an expanding nozzle is obtained, which can trigger a supercritical pressure drop [13]. This is what happens in region 1.

Further, since the flow moves against a positive pressure gradient, that is, the pressure in the flow should gradually become equal to the pressure behind the nozzle apparatus, a shock front appears (shown by a pink line) representing a compression wave, pressure, and the gas density in it increases. The shock front begins on the wall, obliquely to it, and is accompanied by the jet’s separation from the blade’s trough (the red shading shows the separations). Having reached the jet boundary, the shock front is reflected from it, and a reflected front appears (shown by the blue line). In this case, the reflected shock front is a rarefaction wave, and the jet boundary diverges again. Then the whole process is repeated - regions 2 and 3. By the action of viscosity at the boundary of the jet, this periodic pattern is finally erased - region 4 [14, 15].

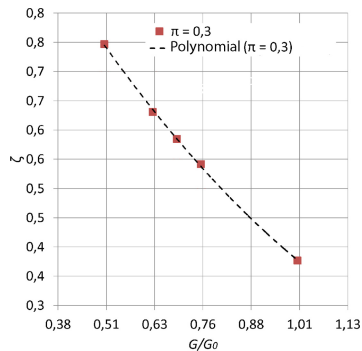
To determine the value of the relative pressure drop across the nozzle apparatus, at which the flow core is divided by shock fronts into separate regions, shown in Fig. 11, additional calculations were performed at relative pressure drops across the nozzle array  $\pi = 0.5; 0.45; 0.4; 0.35; 0.3$  (Fig. 12).

As a result of the performed calculations, it was found that for the degree of opening  $\delta = 0.3$  ( $\tau = 0.66$ ), the division of the flow core of the region by shock fronts into regions begins at a relative difference of  $\pi = 0.4$ . Real nozzle devices with rotary diaphragms operate with steam extraction in the cavity in front of the nozzle device. A significant influence on the nature of the processes in the flow path of the turbine, the efficiency of the nozzle grids of adjustable rotary diaphragms and their stages, as well as on the integral quality indicators of the entire turbine, the pressure levels in the chambers of controlled extraction and the values of the mass flow rates of the extracted steam was confirmed [16]. In this connection, a numerical study of the influence of the amount of air intake on the nature of the flow and the loss of kinetic energy in the lattice was



**Fig. 12.** Flow in the computational domain. Isolines of Mach numbers at a)  $\pi = 0,45$  and  $\delta = 0,3$ ; b)  $\pi = 0,4$  and  $\delta = 0,3$ ; c)  $\pi = 0,35$  and  $\delta = 0,3$ .

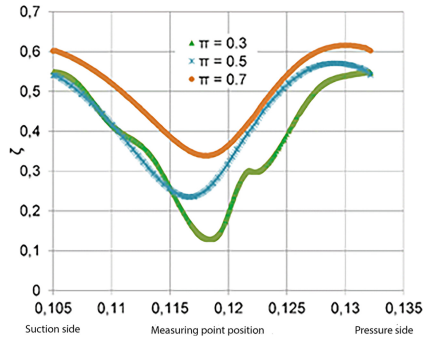
carried out. Calculations were carried out for the values of withdrawals  $G/G_0 = 1; 0,75; 0,6875; 0,625; 0,5$  at degrees of opening of the rotary diaphragm  $\delta = 0,3$ ; at  $\pi = 0,3$ . In Fig. 10 shows the dependence of the coefficient of kinetic energy losses in the nozzle array on the amount of air intake. As shown from Fig. 13, losses increase with increasing air intake in front of the nozzle apparatus.



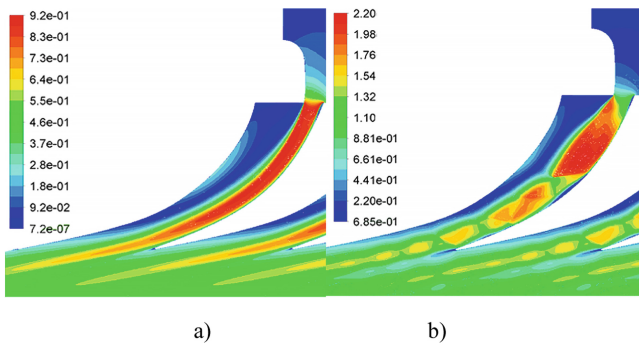
**Fig. 13.** Dependence of the coefficient of kinetic energy losses on the amount of withdrawals  $G/G_0$ .

With a decrease in the airflow value ahead of the nozzle apparatus, the flow pattern changes in the same way as with a decrease in the relative pressure difference  $\pi$ . The division of the flow core by shock fronts into separate regions begins at the ratio  $G/G_0 = 0,6875$ . In Fig. 14 shows the distribution of the kinetic energy loss coefficients along the front of the grating at the degree of opening of the rotary diaphragm  $\delta = 0,3$  at different relative pressure drops across the grating.

Analysis of the graph indicates that the loss of kinetic energy decreases with increasing flow rate, with smaller relative differences in  $\pi$ . In relative terms, the lattice's kinetic energy loss coefficient is 22.5% higher at  $\pi = 0,7$  than at  $\pi = 0,3$ . In Fig. 15 shows the isolines of the Mach numbers in the interscapular channel at  $\pi = 0,7; 0,3$  and  $\delta = 0,3$ .

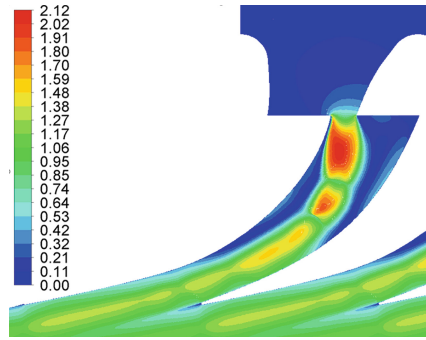


**Fig. 14.** Distribution of kinetic energy loss coefficients along the lattice front at  $\pi = 0,3; 0,5; 0,7$  and  $\delta = 0,3$ .



**Fig. 15.** Isolines of Mach numbers in the interscapular channel at  $\pi = 0,7$  (a) and  $\pi = 0,3$  (b).

The figures show that with a decrease in the relative pressure drop across the lattice, the vortex flow region decreases, and, accordingly, the flow core increases. Considering the above, to Fig. 14 it can be concluded that a decrease in the vortex zone and an increase in the flow core lead to a decrease in the kinetic energy losses in the lattice. In [17], it is indicated that to reduce the length of the zone of separated flows with partial openings of the diaphragms, the rotary ring should be moved to the closing position (in contrast to the method traditionally used in turbines) in the direction from the concave (trough) to the convex surface (back) of the nozzle channel, and in the open position - in the opposite direction. A numerical study was carried out to determine the coefficient of kinetic energy losses, with the opening degree  $\delta = 0.3$  and the position of the movable part of the rotary diaphragms, as indicated above. The flow pattern in the interscapular channel of the nozzle apparatus at  $\pi = 0.3$  in Fig. 16.



**Fig. 16.** Isolines of Mach numbers in the interscapular channel at  $\pi = 0,7$  (a) and  $\pi = 0,3$  (b).

## 5 Conclusions

Based on the results of the work carried out, the following conclusions can be drawn: throttling of the flow passing through the rotary diaphragm of the nozzle apparatus begins to occur when the values of the ratio of the channel width at the entrance to the throat of the grating are greater than unity; the structure of the flow in the interscapular channel of the nozzle apparatus at low degrees of opening is divided into two parts: the supersonic core at the blade trough and the subsonic vortex zone at the blade back; the supersonic core of the flow at specific values of the relative pressure difference across the cascade (or the value of the air flow through the cascade) is divided by shock fronts into several regions; the coefficients of energy losses, for small degrees of opening, decrease with a decrease in the relative pressure drops (with an increase in the flow rate of the flow from the nozzle array); the greatest contribution to the amount of kinetic energy losses is made by the vortex zone in the interscapular channel, and not by wave phenomena in the flow core. Optimization of the flow path of the nozzle apparatus must be carried out to reduce the areas with vortex flow. The results obtained in this work will be used to develop a method for multi-parameter optimization of cogeneration steam turbines with controlled steam extraction.

## References







1. Kondrat'ev, A., et al.: Development of steam turbines for supercritical and supersupercritical gas parameters. *Bull. Bryansk State Tech. Univ.* **1**(54) (2017)
2. Wang, Y., Yu, Y., Hu, D.: Experimental investigation and numerical analysis of separation performance for supersonic separator with novel drainage structure and reflux channel. *Appl. Therm. Eng.* **176**, 115111 (2020). <https://doi.org/10.1016/j.applthermaleng.2020.115111>
3. Ma, C., Wang, Y., Yu, Y., Ren, W., Hu, D.: Structure improvements and performance study of Supersonic Separation device with reflux channel. *Chem. Eng. Process. Process Intensif.* **138**, 73–85 (2019). <https://doi.org/10.1016/J.CEP.2019.03.009>
4. Yang, X., Fu, P., Chen, N., Liu, J., Wei, J.: Mechanisms of pressure pulse for condensing supersonic steam jet in a rectangular channel. *Exp. Therm. Fluid Sci.* **105**, 223–233 (2019). <https://doi.org/10.1016/J.EXPTHERMFLUSCI.2019.04.003>

5. Li, Q., Lyu, Y., Pan, T., Li, D., Lu, H., Gong, Y.: Development of a coupled supersonic inlet-fan Navier-stokes simulation method. *Chinese J. Aeronaut.* **31**, 237–246 (2018). <https://doi.org/10.1016/J.CJA.2017.11.011>
6. Penzin, V.: *Deceleration of the Supersonic Flow in the Channels*. Central Aero-Hydrodynamic Institute, Moscow (2012)
7. Merzliakov, I., Pavlenko, I., Chekh, O., Sharapov, S., Ivanov, V.: Mathematical modeling of operating process and technological features for designing the vortex type liquid-vapor jet apparatus. In: Ivanov, V., et al. (eds.) *DSMIE 2019. LNME*, pp. 613–622. Springer, Cham (2020). [https://doi.org/10.1007/978-3-030-22365-6\\_61](https://doi.org/10.1007/978-3-030-22365-6_61)
8. Slabchenko, O., Kirsanov, D.: Results of calculating the flow in the channels of the regulating rotary diaphragm of the heating turbine NTU “KhPI”. *Bull. Ser. Power Heat Eng. Process. Equip.* **6**, 73–75 (2008)
9. Ershov, S., Yakovlev, V.: Influence of the grid resolution on the results of calculating three-dimensional flows in the flow paths of turbomachines using RANS models. *Probl. Mech. Eng.* **18**(4/1), 18–24 (2015)
10. Hu, W.J., Tan, K., Markovych, S., Liu, X.L.: Study of a cold spray nozzle throat on acceleration characteristics via CFD. *J. Eng. Sci.* **8**(1), F19–F24 (2021). [https://doi.org/10.21272/jes.2021.8\(1\).f3](https://doi.org/10.21272/jes.2021.8(1).f3)
11. Glushko, G., Ivanov, I., Kryukov, I.: Simulation of turbulence in supersonic jet streams. *Physicochem. Kinet. Gas Dyn.* **9**, 1–8 (2010)
12. Avdieieva, O., Usatyi, O., Mykhailova, I.: Optimization of the flowing part of the turbine K-310-240 based on the object-oriented approach. In: Machado, J., Soares, F., Trojanowska, J., Ottaviano, E. (eds.) *icieng 2021. LNME*, pp. 201–213. Springer, Cham (2022). [https://doi.org/10.1007/978-3-030-79165-0\\_20](https://doi.org/10.1007/978-3-030-79165-0_20)
13. Boiko, A., Govorushchenko, Y.: *Optimization of the Axial Turbines Flow Paths*. Science Publishing Group, New York (2016)
14. Razaaly, N., Persico, G., Congedo, P.M.: Impact of geometric, operational, and model uncertainties on the non-ideal flow through a supersonic ORC turbine cascade. *Energy* **169**, 213–227 (2019). <https://doi.org/10.1016/J.ENERGY.2018.11.100>
15. Kelin, A., Larin, O., Naryzhna, R., Trubayev, O., Vodka, O., Shapovalova, M.: Estimation of residual life-time of pumping units of electric power stations. In: *2019 IEEE 14th International Conference on Computer Sciences and Information Technologies (CSIT)*, pp. 153–159. Lviv, Ukraine (2019). DOI: <https://doi.org/10.1109/STC-CSIT.2019.8929748>
16. Boyko, A.V.: Complex mathematical model of processes in a turbine with controlled steam extraction *Bulletin of NTU “KhPI”. Ser. Energy Heat Eng. Process. Install.* **8**(1180), 28–36 (2016)
17. Drokonov, A., Drokonov, A.: Improvement of regulating diaphragms of steam turbines. *Bull. Bryansk State Techn. Univ.* **2**(46), 26–31 (2015)

# **Numerical Simulations of Coupled Systems**



# Model of the Pneumatic Positional Unit with a Discrete Method for Control Dynamic Characteristics

Mikhailo Cherkashenko<sup>1</sup> , Oleksandr Gusak<sup>2</sup>  , Aleksandr Fatyeyev<sup>1</sup> ,  
Nadezhda Fatieieva<sup>1</sup> , and Alexander Gasiyk<sup>1</sup> 

<sup>1</sup> National Technical University “Kharkiv Polytechnic Institute”,  
2, Kyrpychova Street, Kharkiv 61002, Ukraine

<sup>2</sup> Sumy State University, 2, Rymaskogo-Korsakova Street, Sumy 40007, Ukraine  
o.gusak@pgm.sumdu.edu.ua

**Abstract.** At present, it appears that systems of pneumatic units with discrete and analog control, in which the required analog law of motion of the output member is provided with the help of discrete switchgear, offer a promising potential. When developing the schemes of positional hydraulic-pneumatic units, the parameters of the movement of the hydraulic-pneumatic unit are studied, namely: the value of displacement, speed, and acceleration of its output member. To carry out the simulation, a design based on discrete switchgear was taken as the basis for the pneumatic positional unit. Solving the inverse problem, i.e., with the law of motion of the output member of the pneumatic unit (specifying the positioning function) known, we determine the mandatory law of change in the effective areas of the control line and represent each equation of the dynamic model as block diagrams. A mathematical model of the system of pneumatic positional units with program control was developed. It considers the features of the system of pneumatic units and consists of mathematical models of the actuator, a real-time control line model, and a real-time control system. The proposed algorithm for analysis of dynamic characteristics using the MATLAB simulation environment confirms the adequacy of the mathematical models describing the operation of a positional pneumatic unit implemented on discrete pneumatic equipment. The developed algorithm is advisable to analyze the operation of the existing one and for designing new technological equipment.

**Keywords:** Dynamic model · Discrete switchgear · Positioning function · Block diagram · Process innovation

## 1 Introduction

The basic requirements for hydropneumatic positional units are known. They ensure the specified technical characteristics determined by the technological process, ease of manufacture and cost-effectiveness; high reliability and trouble-free operation; the ability to reprogram the control system quickly.



When developing pneumatic positional units, designers are faced with the problem of a limited choice in the range of manufacturers of pneumatic valves with proportional electric control. Therefore, at present, the most promising are systems of pneumatic units with discrete and analog control, i.e., those in which the required analog law of motion of the output member is provided using discrete switchgear. Due to the discreteness of choice in the controlled parameters, the interconnection with digital control devices is facilitated. These systems focused on regulating the working environment in the cavities of the hydraulic and pneumatic motor, allowing to expand of the functionality of hydraulic units. The apparent advantage of such systems is that they can be relatively easy to implement [1–3]. The effectiveness of these control methods is determined by the constant improvement of the control system, which is currently based on microprocessor-based computer technology, allowing applying complex control algorithms [4–6].

## 2 Literature Review

Recently, digital hydraulic and pneumatic units have been widely used in the industry [7, 8]. These systems are logically integrable in the spirit of the Industry 4.0 strategy, according to which these systems can be combined into one network [9], communicate with each other in real-time, self-adjust, and learn new behavior models [10, 11].

The active implementation of digital pneumatic units into the industry is facilitated by the relative simplicity of design and operation, long service life, reliable operation in a low-temperature range in high humidity, dustiness, radiation of the environment, and fire and explosion safety. Digital hydraulic units allow us to increase the positioning accuracy of actuators and increase the system's energy efficiency [12, 13].

When developing the schemes of positional hydraulic-pneumatic units, the parameters of the movement of the hydraulic-pneumatic unit are studied, namely: the value of displacement, speed, and acceleration of its output member. Studies [14–16] show that the main tasks of developers of systems of controlled hydraulic-pneumatic units are associated with the fulfillment of the requirements for the movement of the output member, which led to a variety of methods for controlling the motion parameters of the systems of positional parts [17–19].

The purpose of this work is to develop an algorithm for analyzing the positioning function, which allows you to provide the specified technical characteristics of the pneumatic positional unit by describing the necessary law of change in the effective areas of the control line of the pneumatic positioning unit, implemented on discrete/digital switchgear.

## 3 Research Methodology

A design based on discrete switchgear was taken as the basis for the positional pneumatic unit [20, 21]. The diagram of the pneumatic unit is shown in Fig. 1.

The pneumatic unit consists of the following elements (Fig. 1): 1 - position sensor; 2, 3 - pneumatic valves; 4 - pneumatic throttle valve; 5 - pneumatic cylinder.

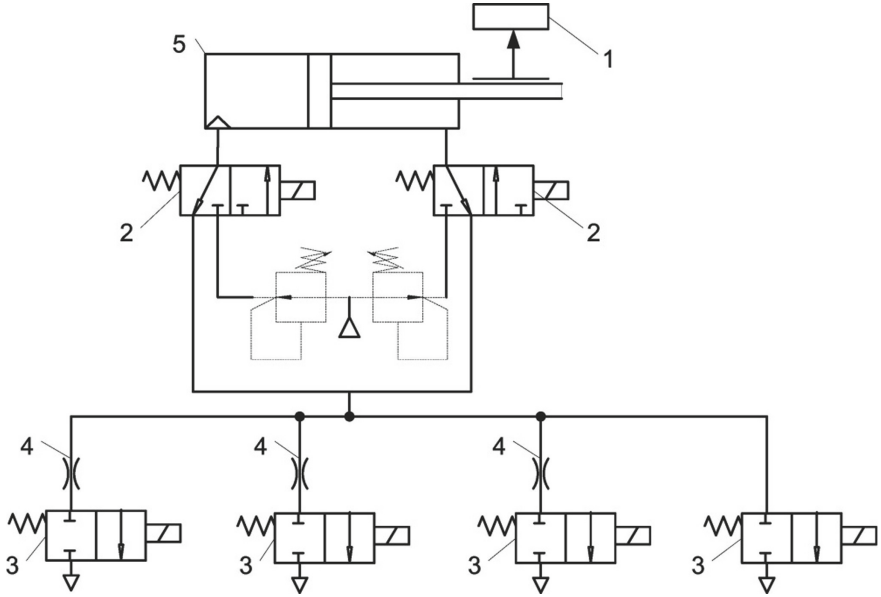


Fig. 1. Diagram of positioning pneumatic unit.

Based on differential equations describing the dynamic characteristics of the pneumatic unit during operation and calculation [22], a dynamic model of the pneumatic unit was created. The designations of the variables used in the dynamic model are shown in Table 1.

System of differential equations describing a dynamic model:

$$\left. \begin{aligned} \dot{p}_1 &= \frac{k}{F_1 x + V_{10}} (f_1^e K_G^1 - p_1 F_1 \dot{x}) \\ \dot{p}_2 &= \frac{k}{F_2 (S-x) + V_{20}} (f_2^e K_G^2 - p_2 F_2 \dot{x}) \\ m \ddot{x} &= p_1 F_1 - p_2 F_2 - p_a (F_1 - F_2) - F_c \end{aligned} \right\}, \quad (1)$$

where at  $p_1 = p_m$  and  $p_2 = p_a$  values of  $K_G^1$  and  $K_G^2$  become:

$$K_G^1 = \mu_1 p_m \sqrt{2RT} \phi \left( \frac{p_1}{p_m} \right); \quad K_G^2 = -\mu_2 p_2 \sqrt{2RT} \phi \left( \frac{p_a}{p_2} \right).$$

Solving the inverse problem, i.e., the law of motion of the output member of the pneumatic unit (specifying the positioning function) known, we determine the required law of change in the effective areas of the control line. In the case of the extension of the actuator, the effective area in the pressure line  $f_1^e$  is set and constant. Then there is the need to determine the change law in the effective area of the discharge line. Thus,

**Table 1.** Designations of variables used in the dynamic model.

No.	Description	Designation	Metric units
1	Mass of inertial load	m	kg
2	Piston area in bottom end of pneumatic cylinder	$F_1$	$m^2$
3	Piston area in rod side of pneumatic cylinder	$F_2$	$m^2$
4	Resistance force	$F_c$	N
5	Effective areas of lumped resistances	$f_1^e, f_2^e$	$m^2$
6	Piston stroke	S	m
7	Piston movement	x	m
8	Piston movement speed	$\dot{x}$	m/s
9	Piston acceleration	$\ddot{x}$	$m/s^2$
10	Pressure in bottom end	$p_1$	Pa
11	Pressure in rod side	$p_2$	Pa
12	Atmospheric pressure	$p_a$	Pa
13	Line pressure	$p_m$	Pa
14	Initial volume of bottom end	$V_{10}$	$m^3$
15	Initial volume of rod side	$V_{20}$	$m^3$
16	Discharge coefficient	$\mu_1, \mu_2$	–
17	Gas constant	R	J/(kg·K)
18	Air temperature in line	T	K
19	Ratio of specific heats	k	–
20	Discharge function	$K_G^1, K_G^2$	–

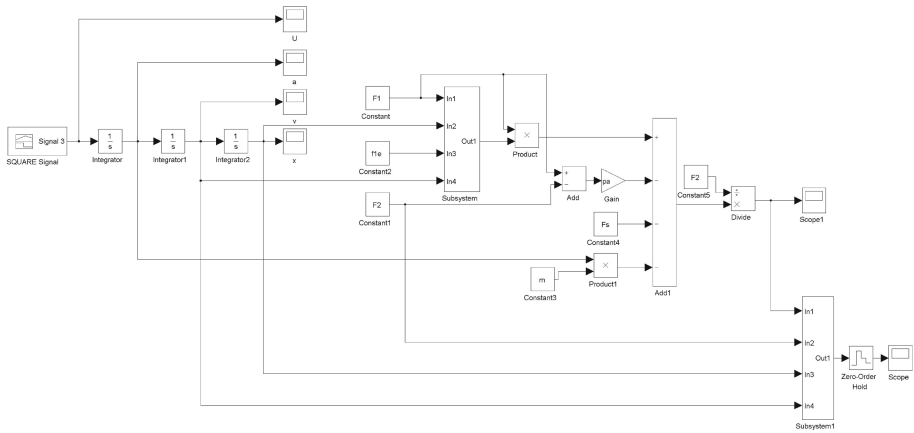
the system of differential equations becomes:

$$\left. \begin{aligned} \dot{p}_1 &= \frac{k}{F_1 x + V_{10}} (f_1^e K_G^1 - p_1 F_1 \dot{x}) \\ f_2^e &= \frac{\dot{p}_2 (F_2 (S-x) + V_{20})}{k \cdot K_G^2} - \frac{p_2 F_2 \dot{x}}{K_G^2} \\ p_2 &= \frac{m \ddot{x} + p_1 F_1 - p_a (F_1 - F_2) - F_c}{F_2} \end{aligned} \right\}. \quad (2)$$

## 4 Results

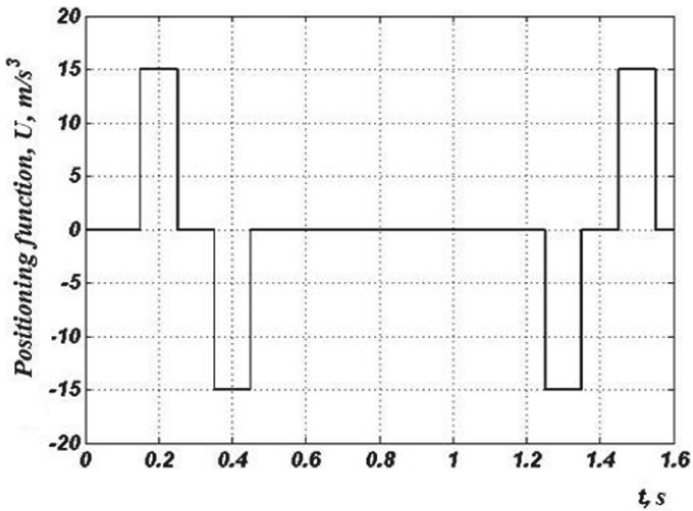
We represent each equation of the dynamic model as block diagrams [23]:

1. A block diagram for solving the inverse problem of the dynamics of the positional pneumatic unit (system of differential Eqs. (2)) is shown in Fig. 2.



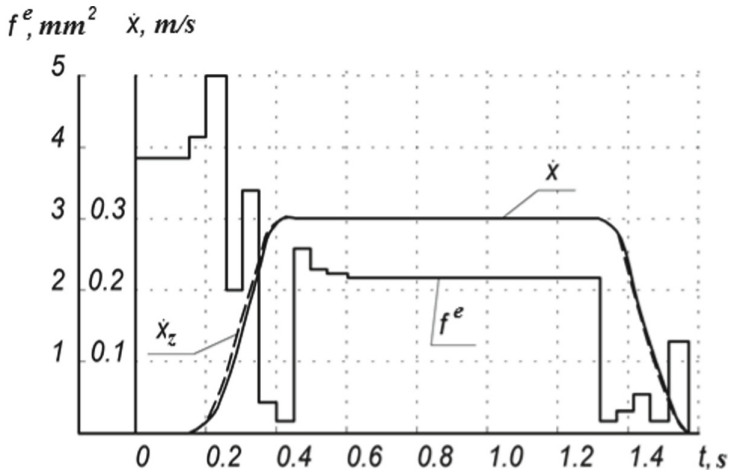
**Fig. 2.** Block diagram for solving the inverse problem of the dynamics of a pneumatic positional unit.

Positioning function  $U$  is shown in (Fig. 3).



**Fig. 3.** Positioning function  $U$ .

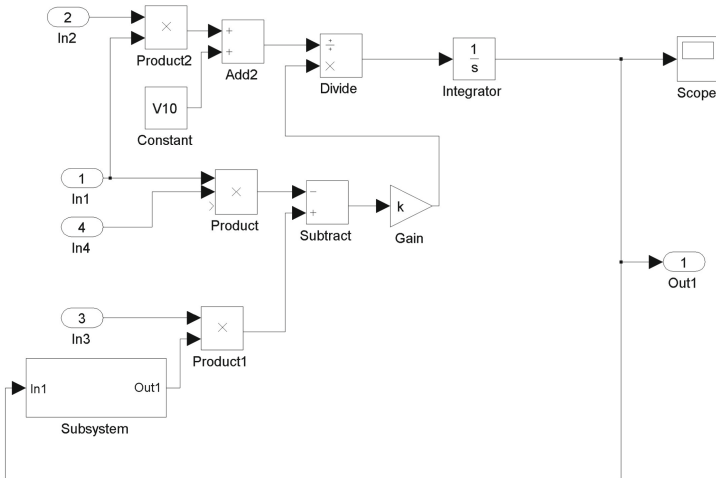
Acceleration  $a$ , speed  $V$  and movement  $x$  of the output member are shown in (Fig. 4).



**Fig. 4.** Values of the effective area in the control line at the outlet  $f_2^e$  to obtain the required law of motion of the output member;  $\dot{x}_z$  - specified speed of movement;  $\dot{x}$  - an obtained speed of movement.

The results show high accuracy of coincidence of the specified and actual speeds.

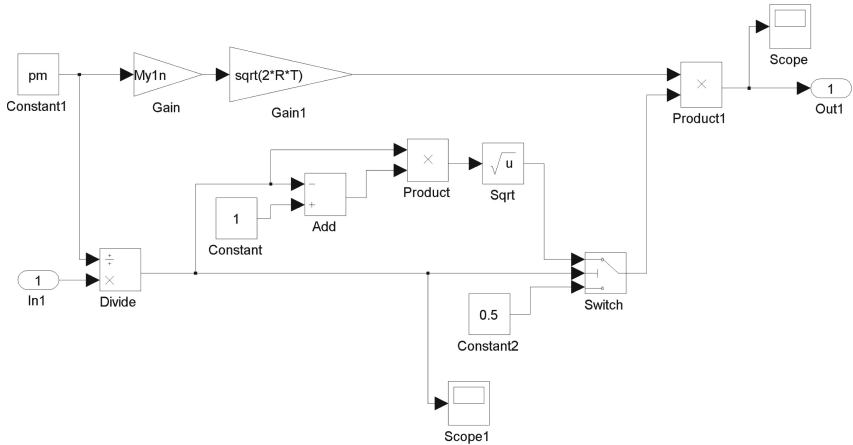
2. The block diagram for calculating the pressure  $p_1$  from the dependence  $\dot{p}_1 = \frac{k}{F_1 \dot{x} + V_{10}} (f_1^e K_G^1 - p_1 F_1 \dot{x})$  is shown in Fig. 5.



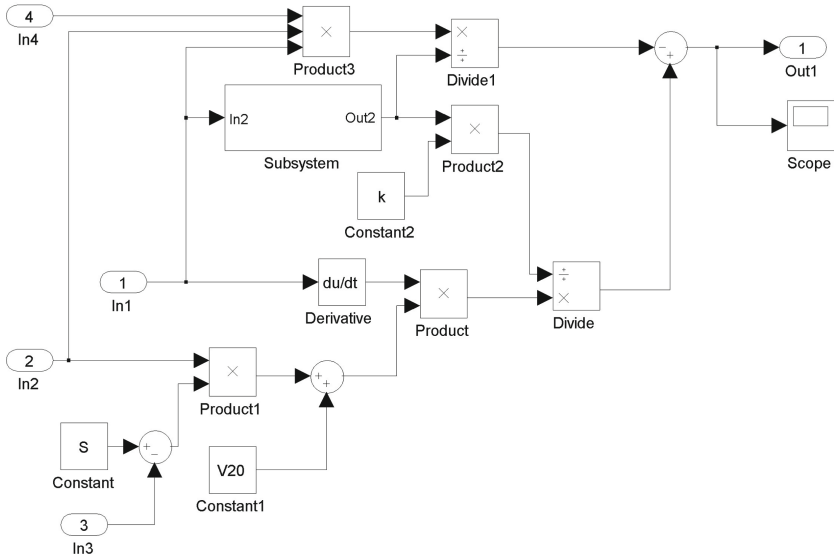
**Fig. 5.** Block diagram for calculating the pressure  $p_1$ .

3. The block diagram for calculating the coefficient  $K_G^1$  from dependence  $K_G^1 = \mu_1 p_m \sqrt{2RT} \phi\left(\frac{p_1}{p_m}\right)$ , taking into account the connection diagram of the pneumatic cylinder is shown in Fig. 6.

4. The block diagram for finding the effective area in the control line at the outlet  $f_2^e$  from dependence  $f_2^e = \frac{\dot{p}_2(F_2(S-x) + V_{20})}{k \cdot K_G^2} - \frac{p_2 F_2 \dot{x}}{K_G^2}$  is shown in Fig. 7.



**Fig. 6.** Block diagram for calculating the coefficient  $K_G^1$ .



**Fig. 7.** Block diagram for calculating the effective area in the control line at the output  $f_2^e$ .

5. The block diagram for calculating the coefficient  $K_G^2$  from dependence  $K_G^2 = -\mu_2 p_2 \sqrt{2RT} \phi \left( \frac{p_a}{p_2} \right)$  considering the connection diagram of the pneumatic cylinder is shown in Fig. 8.

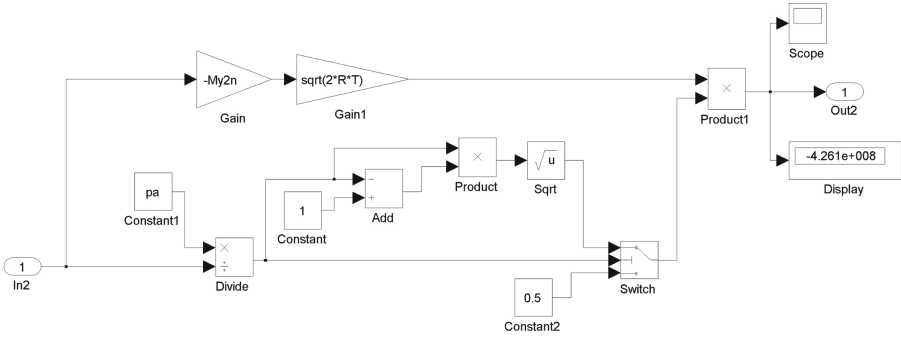


Fig. 8. Block diagram for calculating the coefficient  $K_G^2$ .

### 5 Conclusions

The developed mathematical model of the positional pneumatic unit system with program control allows considering the characteristics of the pneumatic unit system. It includes calculation models of the simulator, real-time control line mode, and real-time control mode system.

The proposed algorithm of analysis of dynamic characteristics using the MATLAB simulation environment confirms the adequacy of the mathematical models describing the operation of the positional pneumatic unit implemented on discrete pneumatic equipment. The developed algorithm is advisable to analyze the operation of the existing and new technological equipment design.

The laws of motion of the positional pneumatic unit output member are obtained. They are based on the developed algorithm of analysis of the positioning function and implemented in the MATLAB environment. Research results can provide the specified technical characteristics for a smooth acceleration of the pneumatic unit output member. Besides, formulated laws of motion allow movement at a steady speed and smooth braking with a stop at the positioning point.

**Acknowledgment.** The scientific results have been obtained within the research project “Fulfillment of tasks of the perspective plan of development of a scientific direction “Technical sciences” Sumy State University” ordered by the Ministry of Education and Science of Ukraine (State Reg. No. 0121U112684). The research was partially supported by the Research and Educational Center for Industrial Engineering (Sumy State University) and International Association for Technological Development and Innovations.

### References

1. Sokol, Y., Cherkashenko, M.: Synthesis of control schemes of drives system. NTU “KhPI” Publ., Kharkiv (2018)
2. Zhou, Y., Li, Y.: PLC control system of pneumatic manipulator automatic assembly line based on cloud computing platform. J. Phys. Conf. Ser. **1744**, 022011 (2021)

3. Chelabi, M.A., Basova, Y., Hamidou, M.K., Dobrotvorskiy, S.: Analysis of the three-dimensional accelerating flow in a mixed turbine rotor. *J. Eng. Sci.* **8**(2), D1–D7 (2021). [https://doi.org/10.21272/jes.2021.8\(2\).d2](https://doi.org/10.21272/jes.2021.8(2).d2)
4. Filatov, D., Minav, T., Heikkine, J.: Adaptive control for direct-driven hydraulic drive. In: 11th International Fluid Power Conference, vol. 1, pp. 110–119. RWTH Aachen University, Aachen (2018)
5. Heikkilä, M., Linjama, M.: Fault-tolerant control of a multi-outlet digital hydraulic pump-motor. In: 11th International Fluid Power Conference, vol. 1, pp. 144–157. RWTH Aachen University, Aachen (2018)
6. Kanagasabai, L.: Real power loss reduction by enhanced RBS algorithm. *J. Eng. Sci.* **8**(2), E1–E9 (2021). [https://doi.org/10.21272/jes.2021.8\(2\).e1](https://doi.org/10.21272/jes.2021.8(2).e1)
7. Zhao, S., Li, D., Zhou, J., Sha, E.: Numerical and experimental study of a flexible trailing edge driving by pneumatic muscle actuators. *J. Actuators* **10**(7), 142 (2021)
8. Cantoni, C., Gobbi, M., Mastinu, G., Meschini, A.: Brake and pneumatic wheel performance assessment – a new test rig. *Measurement* **150**(6), 107042 (2019)
9. Hufnagl, H., Čebular, A., Stemler, M.: Trends in pneumatics – digitalization. In: International Conference “Fluid Power 2021”: Conference Proceedings, pp. 15–28. University Press, Maribor (2021)
10. Zhang, Q., Kong, X., Yu, B., Ba, K., Jin, Z., Kang, Y.: Review and development trend of digital hydraulic technology. *J. Appl. Sci.* **10**(2), 579 (2020)
11. Rager, D., Neumann, R., Post, P., Murrenhoff, H.: Pneumatische antriebe für industrie 4.0 – pneumatic drives for industry 4.0. In: *Mechatronik* (2017)
12. Rager, D., Doll, M., Neumann, R., Berner, M.: New programmable valve terminal enables flexible and energy-efficient pneumatics for Industry 4.0. In: 11th International Fluid Power Conference, vol. 1, pp. 208–221. RWTH Aachen University, Aachen (2018)
13. Siivonen, L., Paloniitty, M., Linjama, M., Sairiala, H., Esque, S.: Digital valve system for ITER remote handling – design and prototype testing. *J. Fusion Eng. Des.* **146**, 1637–1641 (2019)
14. Pavlenko, I., et al.: Effect of superimposed vibrations on droplet oscillation modes in prilling process. *Processes* **8**(5), 566 (2020). <https://doi.org/10.3390/pr8050566>
15. Lu, S., Chen, D., Hao, R., Luo, S., Wang, M.: Design, fabrication and characterization of soft sensors through EGaIn for soft pneumatic actuators. *Measurement* **164**(11), 107996 (2020)
16. Belforte, G., Mauro, S., Mattiazzo, G.: A method for increasing the dynamic performance of pneumatic servosystems with digital valves. *Mechatronics* **14**, 1105–1120 (2004)
17. Pavlenko, I., Ivanov, V., Gusak, O., Liaposhchenko, O., Sklabinskyi, V.: Parameter identification of technological equipment for ensuring the reliability of the vibration separation process. In: Knapcikova, L., Balog, M., Perakovic, D., Perisa, M. (eds.) 4th EAI International Conference on Management of Manufacturing Systems. EICC, pp. 261–272. Springer, Cham (2020). [https://doi.org/10.1007/978-3-030-34272-2\\_24](https://doi.org/10.1007/978-3-030-34272-2_24)
18. Gao, Q., Linjama, M., Paloniitty, M., Zhu, Y.: Investigation on positioning control strategy and switching optimization of an equal coded digital valve system. *Proc. Inst. Mech. Eng. Part I J. Syst. Control Eng.* **234**(8), 959–972 (2019)
19. Ivanov, V., Pavlenko, I., Kuric, I., Kosov, M.: Mathematical modeling and numerical simulation of fixtures for fork-type parts manufacturing. In: Knapčíková, L., Balog, M. (eds.) *Industry 4.0: Trends in Management of Intelligent Manufacturing Systems*. EICC, pp. 133–142. Springer, Cham (2019). [https://doi.org/10.1007/978-3-030-14011-3\\_12](https://doi.org/10.1007/978-3-030-14011-3_12)
20. Šitum, Ž., Beničić, J., Pejić, K., Bača, M., Radić, I., Semren, D.: Design and control of mechatronic systems with pneumatic and hydraulic drive. In: International Conference “Fluid Power 2021”: Conference Proceedings, pp. 179–194. University Press, Maribor (2021)



21. Šitum, Ž., Benić, J., Grbić, Š., Vlahović, F., Jelenić, D., Kosor, T.: Mechatronic systems with pneumatic drive. In: International Conference “Fluid Power 2017”: Conference Proceedings, pp. 281–293. University Press, Maribor (2017)
22. Colombo, F., Mazza, L., Pepe, G., Raparelli, T., Trivella, A.: Inverted pendulum on a cart pneumatically actuated by means of digital valves. In: Aspragathos, N.A., Koustoumpardis, P.N., Moulianitis, V.C. (eds.) RAAD 2018. MMS, vol. 67, pp. 436–444. Springer, Cham (2018). [https://doi.org/10.1007/978-3-030-00232-9\\_46](https://doi.org/10.1007/978-3-030-00232-9_46)
23. Elsaed, E., Abdelaziz, M., Mahmoud, N.: Investigation of a digital valve system efficiency for metering-in speed control using MATLAB/Simulink. In: International Conference on Hydraulics and Pneumatics HERVEX, 23rd edn., pp. 120–129 (2017)



# A New Method of Optimization Synthesis of Vibro-Impact Systems

Volodymyr Gursky , Vitaliy Korendiy<sup>(✉)</sup> , Igor Kuzio , and Oleksandr Kachur 

Lviv Polytechnic National University, 12, S. Bandera Street, Lviv 79013, Ukraine  
vitalii.m.korendii@lpnu.ua

**Abstract.** The paper presents comprehensive research synthesizing inertial and stiffness parameters of two-mass vibratory systems of increased operational efficiency with nonlinear stiffness characteristics. A generalized optimization criterion is proposed considering a wide range of technological and dynamical requirements for implementing energy-efficient vibratory equipment for different technological purposes (screens, crushers, grinders, breakers, mills, vibrating tables, etc.). To simplify the process of synthesizing the optimal piecewise linear stiffness characteristics, two independent coefficients were introduced into the formulas for determining the corresponding stiffness factors. The synthesis was performed based on simultaneous numerical solving of the optimization problem and the simplified system of nonlinear differential equations that did not consider the dynamics of the drive. In the next stage, the generalized system of differential equations of the synthesized vibro-impact system was considered considering the equations describing the operation of the drive. The dynamic analysis of the system was carried out to provide the corresponding characteristics specified during the synthesis process. The study of dynamic stability of the considered system described by the system of nonlinear differential equations of the second order was performed by reducing to the Hill and Mathieu differential equations. The improved design of the vibro-impact machine was implemented in practice and experimentally tested for vibration deposition of metal layers onto the surfaces of various machine parts.

**Keywords:** Resonance · Dynamic analysis · Stability · Operational efficiency · Stiffness characteristic · Optimization criterion · Energy efficiency · Industrial growth

## 1 Introduction

Vibration treatment is one of the most commonly used technological processes ensuring high quality of surfaces using coating and modification of surface layers. While implementing such a treatment for materials with complex physical and mechanical structures, the single-frequency (harmonic) vibratory machines and technological systems are characterized by low efficiency. Therefore, numerous investigations are dedicated to substantiating the possibilities of implementing the systems providing multifrequency oscillations, particularly those based on nonlinear vibro-impact systems. Considering

a wide range of possible operation modes of nonlinear systems, those operating under resonance conditions are of specific interest.

The use of electromagnetic drive for implementation of resonance systems is expedient for relatively small machines with harmonic operation modes, whereas for vibro-impact machines, it is almost never used. This is due to the low efficiency of vibro-impact systems, as they require much higher values of excitation forces. The main reason for the mentioned drawbacks consists in the imperfection (non-idealness) of the applied techniques of their analysis and calculation. The latter should be aimed at establishing and identifying the opportunities to improve the efficiency of vibro-impact systems with electromagnetic drives and extend the obtained results while implementing other types of drives. Therefore, improving existing calculation techniques of vibro-impact systems is an urgent scientific and engineering problem that must be solved to expand the fields of application of vibratory machines, especially with an electromagnetic drive.

## 2 Literature Review

Numerous scientific publications are dedicated to the problems of investigating the dynamic behavior of vibratory systems and synthesizing their structures, ensuring specific operational characteristics. Much attention is paid to the possibilities of implementing vibro-impact working regimes in various vibratory equipment operating under different excitation and loading conditions. The paper [1] considers the dynamics of different technological machines using vibro-impact operating principles. In [2], two different simulation methods are presented of the impact processes taking place during the operation of a two-degree-of-freedom vibro-impact system. In the paper [3], the authors considered the oscillations of nonlinear vibro-impact systems equipped by spring with cubic stiffness and studied the influence of higher harmonics and subharmonics on the system dynamic behavior. New principles of increasing the efficiency of vibratory technological machines by implementing multimode operational regimes are substantiated in [4].

In the paper [5], the authors analyzed forced oscillations of the vibro-impact system excited harmonically and substantiated the system's parameters ensuring the steady-state vibrations under the prescribed operational conditions. The paper [6] is focused on studying the influence of soft impacts on the dynamic behavior of two-degree-of-freedom vibratory system used for compacting and molding concrete products. The technological process of vibro-impact drilling is considered in [7], where the authors investigated the drilling efficiency and energy consumption at different forced frequencies and different values of excitation forces. The modeling and analysis of the vibro-impact system operation excited by the crank-slider mechanism were carried out in [8]. The paper [9] is dedicated to registering the non-linearity of the vibro-impact process by implementing the special measuring device in the system's damping element. In [10], the authors proposed new approaches of analyzing the models describing nonlinear dynamics of two-degree-of-freedom vibro-impact systems subjected to harmonic excitation. The influence of the excitation parameters and the shape of the vibro-impact capsule system on its progression is studied in [11]. The paper [12] presents the results of the investigation of the vibro-impact rig being constrained by two contacting surfaces under

the influence of the external excitation of the rectangular waveform. The vibro-impact system operation being subjected to the impact of multiple excitations is thoroughly studied in [13].

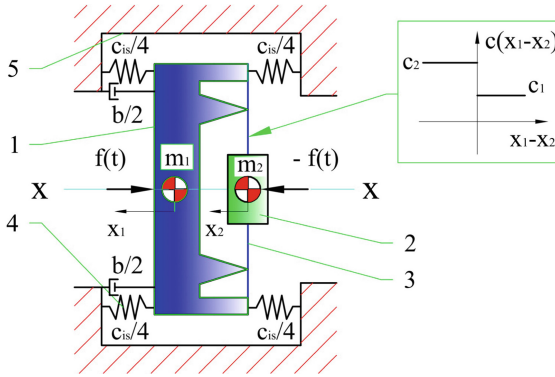
The new design of the vibro-impact mole-draining device has been theoretically and experimentally studied in [14]. The authors initiated the tasks of further optimization of the machine design, development of the adaptive control systems, etc. The paper [15] focuses on the possibilities of implementing electromagnetically driven vibro-impact machines in various industries. It presents the improved designs of such machines characterized by better operational efficiency. In [16], the authors investigated the dynamic behavior of the vibro-impact oscillator subjected to the action of dry friction; in this case, the influence of viscous friction was eliminated. The two-degree-of-freedom system of the vibro-impact energy sink subjected to harmonical excitation was considered in [17]; the authors studied the influence of different design criteria of the multiple sinks acting simultaneously on their operational efficiency in a wide range of forced frequencies. In [18], a new method is proposed to study the nonlinear dynamics of vibro-impact systems with asymmetric clearances.

One way to increase the operational efficiency of vibratory machines is to reduce the energy consumption of their drives by means of simultaneous implementation of near-resonance and vibro-impact operation modes [19]. The possibilities of providing such modes depend on the relations between the system's parameters and the characteristics and conditions of excitation. Herewith, significant attention is to be paid to the parametric synthesis of piecewise linear stiffness characteristics corresponding to the given system of technological and operational requirements. As a result of the implementation of vibro-impact systems with new parameters, it is necessary to carry out an additional analysis of parametric stability. These problems are partially analyzed in the papers [20] and [21]. Due to the intensive development of the applied software for mathematical analysis of different dynamic systems, there is a possibility of solving more complicated problems related to optimization synthesis at the stages of designing and modeling of such systems. Therefore, this paper's major novelty consists of developing a new engineering method allowing to solve complex tasks of dynamic analysis and optimization synthesis of vibro-impact systems and aiming at improving their operational efficiency.

### 3 Research Methodology

#### 3.1 Dynamic Diagram of the Vibro-Impact System

To develop the improved design of the vibro-impact machine, let us consider the dynamic model of the oscillatory system consisting of two movable masses 1 and 2 (Fig. 1). The masses 1 and 2 are connected by the flat spring 3 in such a way that the reduced stiffness coefficient of the flat spring during its bending changes from the value of  $c_1$  to the value of  $c_2$  following the diagram shown in Fig. 1. The vibro-impact system is supported on the stationary frame 5 by vibration isolators 4 characterized by the total stiffness coefficient  $c_{is}$  and damping coefficient  $b$ . The excitation force is of the pulsed type, changes in accordance with the  $f(t)$  law, and is applied between the oscillating masses 1 and 2. In such a case, the vibratory machine's drive can be equipped by the alternating-current electromagnetic vibration exciter.



**Fig. 1.** Dynamic diagram of the vibro-impact system being studied.

The stiffness coefficients  $c_1$  and  $c_2$  are considered as unknowns which are to be determined using a new calculation technique. The latter consists of the following stages: statement of the optimization problem; solving the problem by a certain numerical method; analyzing the parametric stability of the implemented vibro-impact system.

### 3.2 Synthesis of Stiffness Coefficients

To perform the optimization synthesis of the stiffness coefficients characterized by asymmetric piecewise linear characteristics, there were adopted two coefficients  $\Theta$  and  $\Lambda$  included in the equations of frequencies of free-oscillations  $\omega_{01} = \Theta\omega/z$  and  $\omega_{02} = \Lambda\omega_{01}$  [19]. As a result of this, the stiffness coefficients to be determined are the functions of the adopted coefficients  $\Theta$  and  $\Lambda$ :

$$c_1(\Theta) = M(\Theta\omega/z)^2, \quad c_2(\Theta, \Lambda) = M(\Theta\Lambda\omega/z)^2, \tag{1}$$

where  $M = \frac{(m_1 \cdot m_2)}{(m_1 + m_2)}$  is the system's reduced mass;  $\omega$  is the forced frequency;  $z$  is the resonance setting up coefficient.

The reduced frequency of free-oscillations of the quasilinear system is [19]:

$$\omega_0(\Theta, \Lambda) = \frac{2\omega_{01}\omega_{02}}{\omega_{01} + \omega_{02}} = \frac{2\omega\Theta\Lambda}{z(\Lambda + 1)}. \tag{2}$$

Unlike the optimization synthesis carried out directly based on the stiffness coefficients, which change in a wide range and are quite large compared to other parameters, this approach significantly simplifies the calculation process and makes the solving procedure faster. The proposed formulas make it possible to independently synthesize the two mentioned parameters. The existent methods are based on the synthesis taking into account only one parameter  $\Lambda$ , while  $\Theta$  is considered as  $\Theta = 1$ . In any case,  $c_2/c_1 = \Lambda^2$ .

Let us formulate the optimization problem for synthesizing resonant vibro-impact systems, considering the necessity of providing maximal operational efficiency. For this, let us use:

- the target function:

$$\zeta_P(\Theta, \Lambda) \rightarrow \max, \quad (3)$$

where  $\zeta_P$  is the energy criterion of operational efficiency of the vibro-impact system;

- restrictions and limitations:

1. technological and kinematic restrictions are to be chosen in accordance with the machine's technological purpose, operation modes, and treatment conditions;
2. dynamic limitations are specified by the range  $\omega_{0max0min}$  representing frequency characteristics of vibro-impact systems with respect to the value of their free-oscillations frequency  $\omega_0$ . In this case, the possible operation modes are to be specified: main resonance or additional use of the subharmonic of the order  $\omega_0/2$  during pulsed excitation. The corresponding conditions providing the mentioned operation modes are as follows: the main resonance –  $\omega_0 \geq \omega$ , the simultaneous use of the main resonance and the subharmonic –  $\omega_0 \geq 2\omega$ .

Let us explain the new method of optimization synthesis of inertial, stiffness, and excitation parameters of vibro-impact systems. The analytical part of the method is defined by using formulas taking into account the coefficients  $\Theta$  and  $\Lambda$ . At the same time, the while of nonlinear differential equations is presented in the functional form following the synthesized parameters. The optimization problem is formed based on the target energy criterion, considering the set of restrictions and limitations given as functional dependencies. Solving the system of nonlinear differential equations, which are rigid because of the presence of pulsed conditions in the equations of the electromagnetic and mechanical parts, is carried out with the help of corresponding numerical methods. It is expedient to solve the optimization problem in two stages. During the first stage, it is necessary to choose the rational values of the initial estimates by means of the discrete numerical exhaustion. During the second stage, the direct solving of the optimization problem is to be performed with the help of a numerical method (e.g., the method of conjugate gradients).

As a result of solving the optimization problems with corresponding kinematic and dynamic restrictions, the conditions of implementing the vibro-impact systems of improved operational efficiency were detected. For the systems operating in the main resonance mode, the synthesized coefficients are as follows:  $\Theta = 0.7 \dots 0.85$ ,  $\Lambda = 2 \dots 4.5$ . In this case, when the additional subharmonic is used, the following coefficients have been calculated:  $\Theta = 1.25 \dots 1.55$ ,  $\Lambda = 2 \dots 3$ .

## 4 Results

### 4.1 Analysis of the System Parametric Stability

To analyze the dynamic stability of the synthesized vibro-impact systems, they are to be described by the Hill and Mathieu differential equations. The reduced Hill equation can be presented in the following form [21]:

$$\ddot{x}(t) + 2\bar{n} \cdot \dot{x}(t) + [\delta + \varepsilon\psi(t)] \cdot x(t) = \bar{f}(t), \quad (4)$$

where  $x(t) = x_1(t) - x_2(t)$  is the relative generalized coordinate describing the motion of the considered double-mass vibro-impact system;  $2\bar{n} = \frac{b}{M}$ ,  $\delta = \omega_{02}^2 + \frac{t_1}{T}(\omega_{01}^2 - \omega_{02}^2) = \omega_{01}\omega_{02}$ ,  $\varepsilon = 2(\omega_{02}^2 - \omega_{01}^2)/\pi$  are constant coefficients;  $t_1 = \frac{2\pi}{\omega} \frac{\omega_{02}}{\omega_{01} + \omega_{02}}$  is the moment of time, when the change of stiffness characteristic takes place;  $\bar{f}(t) = f(t)/M$ ;  $\psi(t)$  is the excitation function that can be presented in the following form  $\psi(t) = \sum_{k=1}^m \Psi_k \sin(k\omega t + \gamma_k)$ ,

$$\Psi_k = \sqrt{\sin(k\omega t_1/2)^2/k} = \sin(k\omega t_1/2) \cdot c \operatorname{sgn}(\sin(k\omega t_1/2))/k,$$

$$\psi(t) = \psi(t + T),$$

$$\int_0^T \psi(t) dt = 0, \quad c \operatorname{sgn}(z) = \begin{cases} 0, & z = 0, \\ 1, & \operatorname{Re}(z) > 0 \text{ or } (\operatorname{Re}(z) = 0 \text{ and } \operatorname{Im}(z) > 0), \\ -1 & \text{otherwise.} \end{cases}$$

To reduce the Eq. (4) to the Mathieu differential equation, let us adopt the number of harmonics  $m = 1$ . In this case, the excitation function is of the following form:

$$\psi(t) = \Psi_1 \sin(\omega t + \gamma_1) = \sin(\omega t_1/2) \sin(\omega t + \gamma_1),$$

where  $\gamma_1 = \pi + a \tan[\sin(\omega t_1)/2\sin(\omega t_1/2)^2]$ .

Therefore, Eq. (4) can be presented as follows:

$$\ddot{x}(t) + 2\bar{n} \cdot \dot{x}(t) + [\delta + \nu \cdot \sin(\omega t + \gamma_1)] \cdot x(t) = \bar{f}(t), \tag{5}$$

where  $\nu = \varepsilon \cdot \sin(\omega t_1/2) = \frac{2(\omega_{02}^2 - \omega_{01}^2)}{\pi} \cdot \sin(\omega t_1/2)$ .

Let us equalize the right part of the Eq. (5) to zero. In this case, we obtain:

$$\ddot{x}(t) + 2\bar{n} \cdot \dot{x}(t) + \left[ \delta + \nu \cdot \cos\left(\frac{\pi}{2} - \omega t - \gamma_1\right) \right] \cdot x(t) = 0,$$

which can be presented in the classical form:

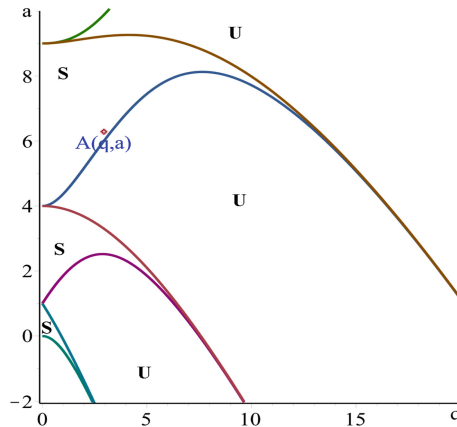
$$\frac{d^2}{d\tau^2} z(\tau) + [a - 2q \cos(2\tau)] \cdot z(\tau) = 0, \tag{6}$$

where  $\tau = \omega t$ ,  $a = \frac{4}{\omega^2} (\omega_{01}\omega_{02} - \bar{n}^2)$ ,  $q = \frac{4(\omega_{01}^2 - \omega_{02}^2)}{\pi\omega^2} \sin(\omega t_1/2)$ .

In accordance with the Eq. (1), let us derive the functional dependencies for the coefficients of the Mathieu equation with respect to the adopted coefficients of synthesis  $\Theta$  and  $\Lambda$ :

$$a(\Theta, \Lambda) = 4 \left( \frac{\Theta^2 \Lambda}{z^2} - \frac{\bar{n}^2}{\omega^2} \right),$$

$$q(\Theta, \Lambda) = \frac{4\Theta^2 (\Lambda^2 - 1)}{\pi z^2} \sin\left(\frac{\pi \Lambda}{\Lambda + 1}\right).$$



**Fig. 2.** Stability diagram for the linear Mathieu equation: S – stable zone, U – unstable zone.

The Eq. (6) can be used to analyze the system's parametric stability according to the diagram (Fig. 2) constructed based on the Mathieu functions with the help of Maple software. To perform the analysis, let us adopt the following parameters based on the implemented design of the vibratory device (Fig. 3):  $M = 41.44$  kg;  $\omega = 314.15$  rad/s;  $z = 0.94$ ;  $b = 2M\omega\zeta$ ;  $\zeta = 0.2$ .

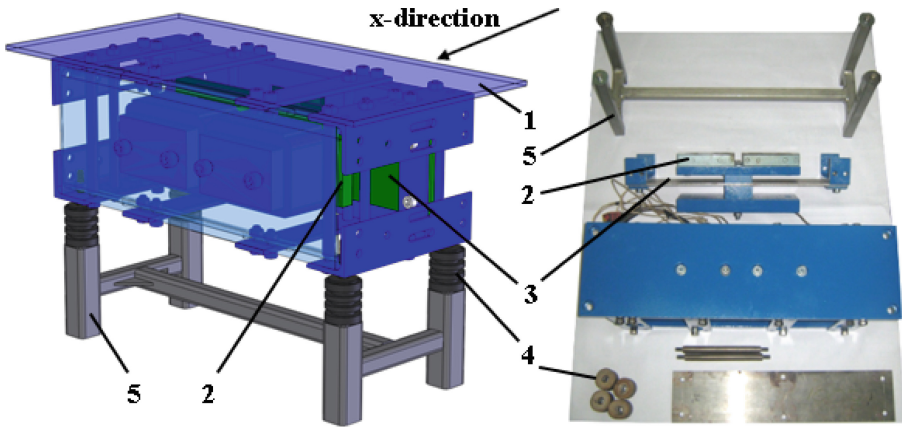
To analyze the stability of the synthesized vibro-impact system, let us use the dependency of the coefficients  $a$  and  $q$  of the Mathieu equation on the parameters  $\Theta$  and  $\Lambda$ . The plot of the parametric function  $a = f(q)$  can be approximately presented as a straight line (see dotted line in Fig. 2). The specific values of the parameters  $\Theta$  and  $\Lambda$  determine the coordinates  $a$  and  $q$  of the point  $A(q; a)$ , and define its location in the corresponding zone of the stability diagram. If the values of the optimized synthesis parameters are following  $\Theta = 0.8$ ,  $\Lambda = 2.2$ , the coordinates of the point A are equal to  $q = 2.945$ ,  $a = 6.214$ . This means that the point  $A(2.945; 6.214)$  is located in a stable zone of the stability diagram (Fig. 2).

## 4.2 General Design and Experimental Prototype of the Vibro-Impact Machine

Based on the synthesized parameters of the dynamic model of the considered vibro-impact system, the corresponding design of the vibratory machine has been developed and implemented in practice (Fig. 3). The working element 1 and the reactive body 2 connected with one another by the flat spring 3 are subjected to harmonic excitation generated by the electromagnets operating off the alternating current supply line. The stiffness coefficients  $c_1(\Theta)$  and  $c_2(\Theta, \Lambda)$  of the spring 3 is to be determined by the formula (1) substituting the synthesized parameters  $\Theta = 0.8$ ,  $\Lambda = 2.2$ . The rubber vibration isolators 4 have several grooves reducing their stiffness in the horizontal direction. The stationary frame 5 consists of seven section pipes welded together. The vibrations of the working element 1 are directed along the  $x$ -axis shown in Fig. 1. The energy-efficient operation is provided at the forced frequency of 50 Hz.

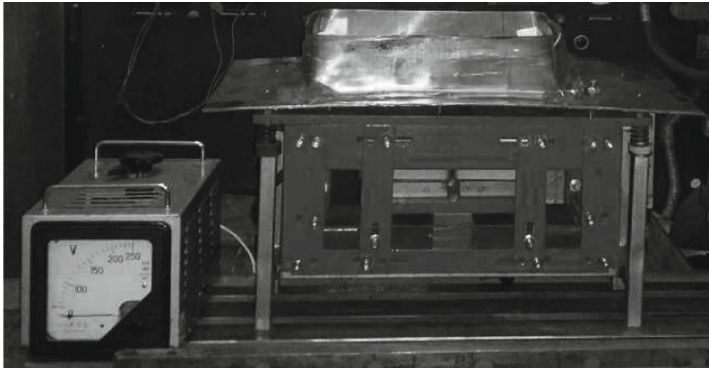
The experimental prototype of the vibro-impact machine has been successfully tested while implementing new technologies of deposition of the reducing wear-resistant metal





**Fig. 3.** General design and experimental prototype of the vibro-impact machine.

layers onto the worn-out surfaces of various machine parts [22] and new submerged arc-welding technologies (Fig. 4). It has been established that the parts being treated or welded under vibration-driven conditions acquire sufficiently better mechanical properties (wear resistance, hardness, impact strength, etc.).



**Fig. 4.** Experimental testing of the developed vibro-impact device.

## 5 Conclusions

The new method of optimization synthesis has allowed substantiating the possibilities of implementing energy-efficient operation modes of vibro-impact systems due to the determination of the rational values of the stiffness coefficients described by piecewise linear characteristics. The corresponding generalized algorithm that ensures the possibility of solving the optimization problem is proposed. The algorithm considers the requirements imposed on the kinematic and dynamic peculiarities of the synthesized vibro-impact system and its parametric stability. Based on the theoretical investigations, the input

parameters for further designing and implementing the vibro-impact machine are determined. The machine has been experimentally tested during the process of deposition of the metal layers onto the surfaces of various machine parts.






## References

1. Stevanović-Hedrih, K., Jović, S.: Models of technological processes on the basis of vibro-impact dynamics. *Sci. Techn. Rev.* **2**, 51–72 (2009)
2. Bazhenov, V.A., Pogorelova, O.S., Postnikova, T.G.: Comparison of two impact simulation methods used for nonlinear vibro-impact systems with rigid and soft impacts. *J. Nonlinear Dyn.* **2**(5), 1–12 (2013). <https://doi.org/10.1155/2013/485676>
3. Peter, S., Reuss, P., Gaul, L.: Identification of sub- and higher harmonic vibrations in vibro-impact systems. In: Kerschen, G. (ed.) *Nonlinear Dynamics, Volume 2*. CPSEMS, pp. 131–140. Springer, Cham (2014). [https://doi.org/10.1007/978-3-319-04522-1\\_12](https://doi.org/10.1007/978-3-319-04522-1_12)
4. Nazarenko, I., Gaidaichuk, V., Dedov, O., Diachenko, O.: Investigation of vibration machine movement with a multimode oscillation spectrum. *Eastern-Eur. J. Enterpr. Technol.* **6**(1–90), 28–36 (2017). <https://doi.org/10.15587/1729-4061.2017.118731>
5. Ragulskis, K., Ragulskis, L.: Forced vibrations of vibro impact system with zero tightening with harmonic resonant excitation. *Math. Models Eng.* **7**, 10–21 (2021). <https://doi.org/10.21595/mme.2021.21922>
6. Bazhenov, V., Pogorelova, O., Postnikova, T.: Crisis-induced intermittency and other nonlinear dynamics phenomena in vibro-impact system with soft impact. In: Altenbach, H., Amabili, M., Mikhlin, Y.V. (eds.) *Nonlinear Mechanics of Complex Structures*. ASM, vol. 157, pp. 185–203. Springer, Cham (2021). [https://doi.org/10.1007/978-3-030-75890-5\\_11](https://doi.org/10.1007/978-3-030-75890-5_11)
7. Cao, Q., Shi, H., Xu, W., Xiong, C., Yang, Z., Ji, R.: Theoretical and experimental studies of impact energy and rock-drilling efficiency in vibro-impact drilling. *J. Energy Res. Technol.* **144**(2), 023201 (2022). <https://doi.org/10.1115/1.4050881>
8. Zukovic, M., Hajradinovic, D., Kovacic, I.: On the dynamics of vibro-impact systems with ideal and non-ideal excitation. *Meccanica* **56**(2), 439–460 (2021). <https://doi.org/10.1007/s11012-020-01280-5>
9. Guo, B., Ringwood, J.: Parametric study of a vibro-impact wave energy converter. *IFAC-PapersOnLine* **53**(2), 12283–12288 (2020). <https://doi.org/10.1016/j.ifacol.2020.12.1166>
10. Herisanu, N., Marinca, V.: A Solution procedure combining analytical and numerical approaches to investigate a two-degree-of-freedom vibro-impact oscillator. *Mathematics* **9**(12), 1374 (2021). <https://doi.org/10.3390/math9121374>
11. Liu, Y., Islam, S., Pavlovskaja, E., Wiercigroch, M.: Optimization of the vibro-impact capsule system. *Strojnicki vestnik J. Mech. Eng.* **62**(7–8), 430–438 (2016). <https://doi.org/10.5545/sv-jme.2016.3754>
12. Liu, Y., PáezChávez, J., Guo, B., Birler, R.: Bifurcation analysis of a vibro-impact experimental rig with two-sided constraint. *Meccanica* **55**(12), 2505–2521 (2020). <https://doi.org/10.1007/s11012-020-01168-4>
13. Wang, J., Leng, X., Liu, X.: The determination of the activation energy for a vibro-impact system under multiple excitations. *Nonlinear Dyn.* **106**(1), 67–80 (2021). <https://doi.org/10.1007/s11071-021-06702-x>
14. Du, V., Nguyen, H.-C., Khoa, N., La, N.-T.: A New Design of Horizontal Electro-Vibro-Impact Devices. *J. Comput. Nonlinear Dyn.* **12**(6), 061002 (2017). <https://doi.org/10.1115/1.4035933>
15. Neyman, L., Neyman, V.: Complex analysis of electromagnetic machines for vibro-impact technologies. *IOP Conf. Ser. Earth Environ. Sci.* **87**(3), 032026 (2017). <https://doi.org/10.1088/1755-1315/87/3/032026>

16. Gendelman, O., Kravets, P., Rachinskii, D.: Mixed global dynamics of forced vibro-impact oscillator with Coulomb friction. *Chaos Interdiscip. J. Nonlinear Sci.* **29**(11), 113116 (2019). <https://doi.org/10.1063/1.5095627>
17. Qiu, D., Seguy, S., Paredes, M.: Design criteria for optimally tuned vibro-impact nonlinear energy sink. *J. Sound Vib.* **442**, 497–513 (2018). <https://doi.org/10.1016/j.jsv.2018.11.021>
18. Li, G., Sun, J., Ding, W.: Dynamics of a vibro-impact system by the global analysis method in parameter-state space. *Nonlinear Dyn.* **97**(1), 541–557 (2019). <https://doi.org/10.1007/s11071-019-04996-6>
19. Gursky, V., Kuzio, I., Korendiy, V.: Optimal synthesis and implementation of resonant vibratory systems. *Univ. J. Mech. Eng.* **6**(2), 38–46 (2018)
20. Awrejcewicz, J., Tomczak, K.: Stability improvement of the vibro-impact discrete systems. In: Babitsky, V.I. (ed.) *Dynamics of Vibro-Impact Systems*, pp. 109–118. Springer, Heidelberg (1999). [https://doi.org/10.1007/978-3-642-60114-9\\_12](https://doi.org/10.1007/978-3-642-60114-9_12)
21. Cattani, C., Grebenikov, E.A., Prokopenya, A.N.: On stability of the Hill equation with damping. *Nonlinear Oscill.* **7**(2), 168–178 (2004). <https://doi.org/10.1007/s11072-005-0003-0>
22. Voitovych, A.A., Pokhmurs'ka, H.V., Student, M.M., Student, O.Z.: Microstructure and abrasive-wear resistance of the vibration-deposited metal of core wires of the basic Fe–Cr–B system. *Mater. Sci.* **52**(3), 365–370 (2016). <https://doi.org/10.1007/s11003-016-9965-6>



# Influence of the Design Features of Orbital Hydraulic Motors on the Change in the Dynamic Characteristics of Hydraulic Drives

Anatolii Panchenko<sup>1</sup> (✉) , Angela Voloshina<sup>1</sup> , Shahriyor S. Sadullozoda<sup>2</sup> ,  
Oleg Boltyansky<sup>1</sup> , and Valeriia Panina<sup>1</sup> 

<sup>1</sup> Dmytro Motorny Tavria State Agrotechnological University, 18, B. Khmelnytsky Avenue, Melitopol 72310, Ukraine

<sup>2</sup> Tajik Technical University named after academician M. Osimi, 10, Academicians Rajabov's Avenue, Dushanbe 734042, Tajikistan

**Abstract.** The operation of power hydraulic drives of self-propelled vehicles is accompanied by oscillatory processes associated with the technical imperfection of the actuating elements of the hydraulic drive. In this regard, the issue of stabilizing the dynamic characteristics of hydraulic drives is an urgent problem. As a result of the research, the initial data and conditions have been substantiated, making it possible to simulate the transient processes occurring in the hydraulic drives of self-propelled vehicles. A structural-functional diagram and a mathematical apparatus have been developed to reveal the dynamics of changes in the characteristics of a hydraulic drive of self-propelled equipment, considering the conditions of its operation. Changes in the stability of the dynamic characteristics of hydraulic drives of self-propelled vehicles, under the influence of the design features of orbital hydraulic motors, have been determined. The acceleration time of the hydraulic motor No. 2 is 12% less than that of the hydraulic motor No. 1, while the pressure and torque fluctuations during steady motion are less by 34% and 17%, respectively. Such changes are due to a decrease in the gap between the teeth of the rotors of the hydraulic motor No. 2 and the elimination of fluctuations in the flow area of its distribution system.

**Keywords:** Energy efficiency · Transient processes · Acceleration · Dynamic characteristics · Output parameters · Structural and functional diagram · Industrial growth

## 1 Introduction

The hydraulic drive is widely used in municipal, road, agricultural, construction, forestry, and other self-propelled machines. Recently, the hydraulic drive has been used as a drive for working equipment and mechanisms for the movement of self-propelled equipment. Such operation of hydraulic drives is accompanied by shock loads and oscillatory processes in hydraulic systems associated with both the occurrence of significant fluctuations

in the pressure and flow of the working fluid [1–4] and as a result of technical imperfection of the actuating elements of the hydraulic drive. Oscillatory processes occurring in the hydraulic drive during acceleration and deceleration have a negative effect on the resource of the hydraulic drive, reduce the utilization factor of the drive's installed power and productivity, and reduce the reliability of the drive and the machine as a whole. Therefore, in designing hydraulic drives for self-propelled machines, one of the important tasks is to study the influence of structural elements of hydraulic machines on changing the characteristics of the entire hydraulic drive during transient processes.

One of the main elements causing the uneven change in the output characteristics of hydraulic drives is hydraulic motors. At present, orbital (gerotor) [5–8] hydraulic motors are widely used in hydraulic power drives of working equipment and mechanisms of movement of self-propelled machines. One of the disadvantages of the considered hydraulic machines is the unevenness of their output characteristics, which occurs during transient processes. The non-uniformity of the characteristics of this type of hydraulic motor is due to the error in the manufacture of the toothed surface of their rotors (fluctuation of the gap  $G_r$  between the teeth of the rotors) [8–10] and the pulsation of the working fluid flow in the distribution systems of these hydraulic machines [12–14].

In this regard, studying the influence of the design features of orbital hydraulic motors on the change in the dynamic characteristics of hydraulic drives to stabilize them is an urgent problem requiring an essential solution.

## 2 Literature Review

A semi-analytical method for analyzing the contact interaction of elements has been proposed [15], methods and models have been developed for studying the stress-strain state considering the contact interaction [16], and the fundamental laws of the stress-strain state of elements have been obtained [17]. A method is proposed for determining the magnitude of the interaction force between bodies and the distribution of contact pressure without limiting the shape of the initial gap between the bodies [18]. The proposed RANS approach using the corrected SST turbulence model allows one to determine the main characteristics [19] and optimal geometric parameters [20] of vortex-chamber pumps, as well as improve the output characteristics [21]. The characteristics of rational regulation of the composition of the fuel-air mixture were determined [22], the effect of the viscosity of Bingham fluids on the energy characteristics of vortex-chamber pumps [23] was investigated, a computational model of losses in the hydraulic circuit with an emphasis on losses caused by the compressibility of the liquid [24] was carried out, experimental studies were carried out showing the presence of pressure fluctuations [25], not provided by the model [24]. The flow of working fluid through the channels of hydraulic machines [26, 27] was considered, an approach to modeling a gerotor pump operating under cavitation conditions [28] was developed, and the occurrence of cavitation in the distribution zone was substantiated [29–32]. Modeling of the processes occurring in the distribution systems of orbital hydraulic machines has not been carried out.

The conditions of static equilibrium of a mobile ground-based robotic complex were established based on the analytical relationship in the form of the sum of the moments of

gravitational processes [33]. A four-mass dynamic model has been constructed, consisting of equations of kinematic constraints and equations of dynamics [34]. Mathematical models have been compiled allow investigating the dynamics and oscillatory processes of multi-element aggregates [35, 36], a measuring system for the dynamics and energy of self-propelled machines has been proposed [37], a parametric model of the dynamics of a cantilever rotor [38], the characteristics of aero- and hydrostatic load-bearing elements are determined [39, 40], the possibility of carrying out hydrodynamic calculations using CFD software packages [41, 42] is considered. The dynamic processes occurring in the hydraulic drives of self-propelled vehicles were not considered.

A universal model of a mechatronic system with a hydraulic drive is considered, the initial conditions of modeling are substantiated [43], proposed mathematical and physical models [44–46], allowing to simulate the processes occurring in planetary hydraulic motors and their elements, hydrodynamic models are considered that will allow one to study the influence of the geometric parameters of the flow paths of a gerotor pump on its output characteristics [47, 48], the dynamics of change in the output characteristics of a mechatronic system with serial and modernized hydraulic motors is investigated, considering the influence of the error in the form of manufacturing elements of the rotor system [5, 49] and the flow area of the distribution system [9, 12]. The dynamics of changes in the output characteristics of hydraulic drives of self-propelled vehicles, considering the design features of orbital hydraulic machines in the conditions of their operation, have not been studied.

Analysis of literature sources related to the solution of the problem posed - stabilization of the output parameters of hydraulic drives, shows that the issues related to the influence of the design features of orbital hydraulic motors on the change in the dynamic characteristics of hydraulic drives have not been given due attention. Therefore, this work is devoted to solving issues related to studying the influence of structural elements of orbital hydraulic motors on the change in the dynamic characteristics of hydraulic drives during their operation on transient processes.

### 3 Research Methodology

Studies of the influence of the design features of orbital hydraulic motors on the change in the dynamic characteristics of hydraulic drives to stabilize their output parameters are carried out by modeling the transient processes arising during the operation of hydraulic drives of self-propelled equipment. To simulate changes in functional parameters and output characteristics of hydraulic drives of self-propelled vehicles in operating conditions, it is necessary:

- to substantiate the initial data allowing to simulate transient processes occurring in hydraulic drives of self-propelled equipment;
- to develop a structural and functional diagram and mathematical apparatus of a dynamic model of a hydraulic drive of self-propelled equipment, taking into account the conditions of its operation;
- to study the influence of the design features of the rotor system and the distribution system of the orbital hydraulic motor on the dynamics of changes in the functional

parameters and output characteristics of the hydraulic drive during the operation of self-propelled equipment.

The developed mathematical model and the results of the performed parametric studies [43] make it possible to study the change in the functional parameters and output characteristics of hydraulic drives of self-propelled vehicles during transient processes, depending on the difference in the geometric parameters of orbital hydraulic motors.

To simulate the change in the functional parameters and output characteristics of the hydraulic drive depending on the difference in the geometric parameters of the orbital hydraulic motors, when describing the pumping station of the hydraulic system (pump, safety valve, working fluid), the initial data outlined in [43] were taken.

The studies were carried out with two orbital hydraulic motors (No. 1 and No. 2) with a working volume of 160 cm<sup>3</sup>. The design differences were as follows: the gap  $G_r$  between the teeth of the rotors (considering the error in the profile shape [5]) is 0.02...0.21 mm – for hydraulic motor No. 1, and 0.02...0.065 mm for hydraulic motor No. 2. The area cross-section of the distribution system of the hydraulic motor No. 1 fluctuates in the range of 200...226 mm<sup>2</sup>, while for the hydraulic motor No. 2, it is constant and amounts to 226 mm<sup>2</sup>. For both hydraulic motors, the moment of resistance is constant and is 365 N·m, the moment of inertia of the rotating masses is 3.6 N·m, the volumetric efficiency is 0.95, and the hydro-mechanical efficiency is 0.9 [9].

The unevenness of the pump flow  $Q_p(t)$  and the change in the load on the working element (expressed by the moment of resistance  $M_r(t)$ ) can be represented [43]:

$$\begin{cases} Q_p(t) = Q_\omega \cdot \sin \omega(t) + Q_\omega \cdot \sin \omega(t - \tau), \\ M_r(t) = M_r(t) \cdot \left(1 - e^{-\frac{t}{T}}\right) + M_\omega \cdot \sin \omega(t). \end{cases} \quad (1)$$

Modeling of changes in functional parameters (pressure  $p(t)$ , flow rate  $Q_{h.m}(t)$  through the hydraulic motor and flow rate  $Q_{vol}(t)$  through the safety valve) under operating conditions during acceleration of the hydraulic drive of self-propelled vehicles was carried out according to the dependencies

$$\begin{cases} p(t) = f(M_r(t)), \\ Q_{h.m}(t) = \mu \cdot \sum_{i=1}^Z \left[ \left( \frac{\pi}{z_2} - \Delta \right) - |\beta_i - \alpha_i(t)| \right] \cdot \frac{(R_2^2 - R_1^2)}{2} \cdot \sqrt{\frac{2p(t)}{\rho}}, \\ Q_{vol}(t) = \mu \cdot \pi \cdot d_{pl} \cdot x(t) \cdot \sqrt{\frac{2p(t)}{\rho}}, \end{cases} \quad (2)$$

where  $\mu$  and  $\rho$  are the flow rate and density of the working fluid;  $z_2$ ,  $\alpha_i$ ,  $\beta_i$ ,  $\Delta$  and  $R_1$ ,  $R_2$  – kinematic, angular and dimensional parameters [9, 12] of the movable and fixed distributors;  $p_{pl}$  and  $x(t)$  are geometrical parameters of the valve.

Modeling of changes in output characteristics (torque  $M_t(t)$  and speed  $n(t)$  on the shaft of the hydraulic motor) under operating conditions during acceleration of the hydraulic drive of self-propelled vehicles was carried out according to the dependencies

$$\begin{cases} M_t(t) = 2 \left( e \pm \frac{G_t}{2} \right) \cdot p(t) \cdot b \cdot (z_1 + 1) \cdot h_i, \\ n(t) = f(Q_{h.m}(t)), \end{cases} \quad (3)$$

where  $e$ ,  $b$ ,  $z_1$  and  $h_i$  are the kinematic parameters of the hydraulic motor rotors [5].

## 4 Results

The study of the dynamics of change in the output parameters of a hydraulic drive with an orbital hydraulic motor was carried out using the VisSim dynamic modeling system. The developed structural and functional diagram of the dynamic model of the hydraulic drive of self-propelled vehicles (Fig. 1) allows simulating the transient processes occurring in hydraulic drives under operating conditions, depending on the design features of the rotor system and the distribution system of the orbital hydraulic motor.

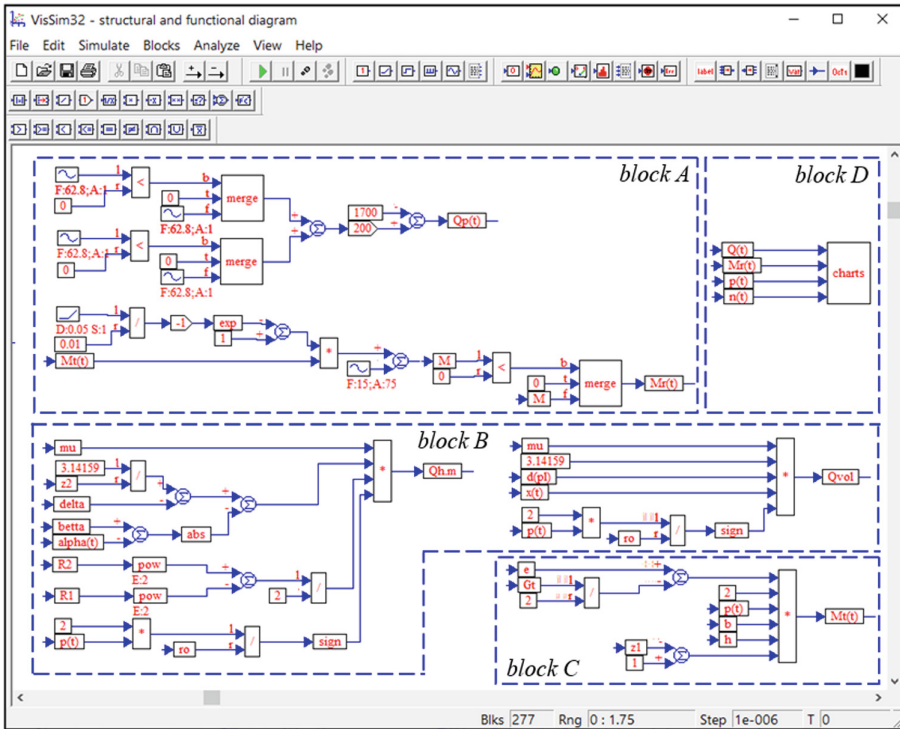
The simulation of the unevenness of the pump flow  $Q_p(t)$  and the change in the load on the working element, described by expressions (1), was carried out by block A (Fig. 1). Expressions (2), implemented in block B, allow simulating the change in the flow rate of the working fluid through the hydraulic motor and the safety valve, taking into account the design features of the distribution system of the hydraulic motor. The change in torque depending on the gap  $G_t$  between the teeth of the rotors, determined by expression (3), is implemented by block C. Block D provides a graphical visualization of the simulation process at each moment of the time.

As a result of the research carried out, dependencies were obtained that characterize the changes in pressure and flow in the hydraulic system (Fig. 2) and changes in the torque and speed on the shaft of the hydraulic motor (Fig. 3). The analysis of the presented dependences shows that the investigated moment of acceleration of the hydraulic drive can be divided into three stages: starting of the hydraulic motor shaft, direct acceleration, and steady motion.

The duration of the first stage, the movement of the hydraulic motor shaft for both hydraulic motors is 0...0.02 s (Fig. 2 – curves 1). The period of the second stage - direct acceleration is 0.02...0.85 s – for hydraulic motor No. 1 and 0.02...0.75 s – for hydraulic motor No. 2. Accordingly, the third stage – steady motion for the hydraulic motor starts from 0.85 s, and for the hydraulic motor 2 – from 0.75 s, which is 12% less.

Analysis of the dependence of the pressure change in the hydraulic system shows that at the first stage, there is a significant pressure jump of 90 MPa and 85 MPa for hydraulic motors No. 1 and No. 2, respectively (Fig. 2a, Fig. 2b – curve 1). Pressure surges are more than 5 times their nominal value. At the second stage, the pressure in the hydraulic system sharply decreases and stabilizes at a value from 29 MPa to 27 MPa, 1.8 times exceeding its nominal value. At the same time, the pressure in the hydraulic motor No. 1 has insignificant pulsations with an amplitude of 3...4 MPa, caused by fluctuations in the flow area of its distribution system and pump flow pulsations (Fig. 2a – curve 1).



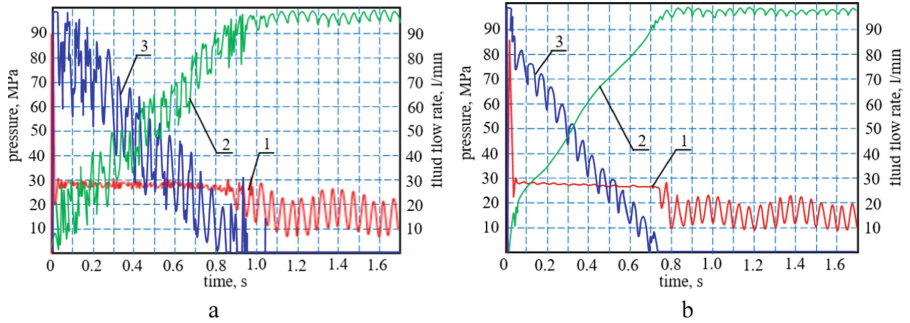


**Fig. 1.** Structural and functional diagram of a dynamic model of a hydraulic drive of self-propelled vehicles under operating conditions.

There are practically no pressure pulsations in hydraulic motor No. 2 (Fig. 2b – curve 1). Analysis of the pressure change dependence at the third stage shows that the pressure in the hydraulic system decreases, reaching its nominal value. However, in the area under consideration, there are significant pressure fluctuations caused by the pump flow pulsation and fluctuations in the moment of resistance with an amplitude of 15 MPa – for hydraulic motor No. 1 and 10 MPa – for hydraulic motor No. 2, which is 34% less.

An analysis of the dependences of the change in the flow rate of the working fluid through the hydraulic motor, considering the design features of its distribution system, shows that at the first and second stages, the flow rate increases uniformly for both hydraulic motors (Fig. 2 – curves 2). It should be noted that for hydraulic motor No. 1, during this period, there are significant flow rate pulsations caused by the imperfect design of its distribution system and pump flow pulsation, the amplitudes of which are 20...30 l/min (Fig. 2a – curve 2). There is no flow pulsation for hydraulic motor No. 2 at the first and second stages (Fig. 2b – curve 2). For both hydraulic motors, the third stage is characterized by insignificant flow rate pulsations of up to 3 l/min for hydraulic motor No. 1 and up to 2 l/min for hydraulic motor No. 2, caused by pump flow pulsations.

Analysis of the dependences of the change in the flow through the safety valve (Fig. 2 – curves 3) shows that for both hydraulic motors at the first stage, the flow has its maximum value of 98 l/min [43] since the safety valve is fully open. The second



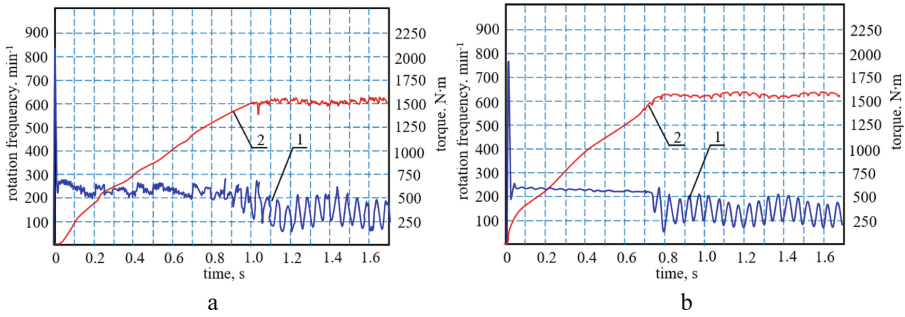
**Fig. 2.** Changes in the functional parameters of the hydraulic drive in operating conditions during acceleration: a – hydraulic motor No.1; b – hydraulic motor No. 2; 1 – hydraulic pressure; 2 – flow across hydraulic motor; 3 – flow across through safety valve.

stage for both hydraulic motors is characterized by a uniform decrease in flow to zero, which means that the safety valve is completely closed. This period is characterized by significant flow rate pulsations caused by pump flow pulsations - for hydraulic motor No. 1, the amplitude of which is up to 30 l/min, and for hydraulic motor No. 2 – up to 10 l/min, which is 3 times less. In the third stage, there is no flow through the safety valve.

Analysis of the results of studies of the change in torque depending on the gap  $G_t$  between the teeth of the rotors shows that for both hydraulic motors at the first stage, there is a rather large jump up to 2100 N·m – for hydraulic motor No. 1 and 1900 N·m – for hydraulic motor No. 2 (Fig. 3 – curves 1). This jump is more than 5 times the rated torque. At the second stage, for both hydraulic motors, there is a sharp decrease in the torque value to 640...620 N·m, 1.8 times exceeding its nominal value. In this section, the torque of the hydraulic motor No. 1 has significant pulsations with an amplitude of 140...150 N·m, caused by the presence of an excessive gap  $G_t$  between the teeth of the rotors (Fig. 3a – curve 1). Fluctuations of the torque on the shaft of the hydraulic motor No. 2 in this section are practically absent (Fig. 3b – curve 1). The third stage is characterized by significant fluctuations in torque caused by fluctuations in the moment of resistance  $M_r$  with an amplitude of 300 N·m for hydraulic motor No. 1 and 250 N·m for hydraulic motor No. 2, which is 17% less.

The analysis of changes in the speed of the hydraulic motor shaft, taking into account the design features of its distribution system, shows that for both hydraulic motors at the first and second stages, the speed values increase, which is due to the gradual closing of the safety valve (Fig. 3 – curves 2). At the third stage, the speed values having reached their nominal value of  $600 \text{ min}^{-1}$  [43] are stabilized. However, there are slight pulsations caused by the pump flow pulsation  $Q_p$  and sinusoidal disturbances caused by fluctuations in the moment of resistance  $M_r$ .

The performed studies have shown that the design features of orbital hydraulic motors significantly impact the change in the dynamic characteristics of hydraulic drives of self-propelled equipment, ensuring their stabilization. Such changes are due to a decrease in the gap  $G_t$  between the teeth of the rotors of the hydraulic motor No. 2 and the elimination of fluctuations in the flow area of its distribution system.



**Fig. 3.** Changes in the output characteristics of the hydraulic drive under operating conditions during acceleration: a – hydraulic motor No. 1; b – hydraulic motor No. 2; 1 – torque on the shaft of the hydraulic motor; 2 – speed of rotation of a shaft of a hydraulic motor.

## 5 Conclusions

As a result of the research, the initial data and conditions were substantiated, making it possible to simulate transient processes occurring in the hydraulic drives of self-propelled vehicles.

A structural-functional diagram and a mathematical apparatus have been developed, making it possible to study changes in the dynamic characteristics of a hydraulic drive of self-propelled equipment, taking into account the conditions of its operation.

Changes in the stability of the dynamic characteristics of hydraulic drives of self-propelled vehicles, under the influence of the design features of orbital hydraulic motors, have been determined. It was found that the acceleration time of the hydraulic motor No. 2 is 12% less than that of hydraulic motor No. 1. In comparison, the pressure and torque fluctuations are less at steady-state motion by 34% and 17%, respectively. Such changes are due to a decrease in the gap  $G_f$  between the teeth of the rotors of the hydraulic motor No. 2 and the elimination of fluctuations in the flow area of its distribution system.

## References

1. Kim, S.-Y., Nam, Y.-J., Park, M.-K.: Design of port plate in gerotor pump for reduction of pressure pulsation. *J. Mech. Sci. Technol.* **20**(10), 1626–1637 (2006). <https://doi.org/10.1007/BF02916266>
2. Sung, H.-J., Min, H.-K., Nam, Y.-J., Park, M.-K.: Design and experimental verification of a port plate in a gerotor pump to reduce pressure pulsation. *J. Mech. Sci. Technol.* **32**(2), 671–678 (2018). <https://doi.org/10.1007/s12206-018-0114-4>
3. Hsieh, C.F.: Flow characteristics of gerotor pumps with novel variable clearance designs. *J. Fluids Eng.* **137**(4), 041107 (2015). <https://doi.org/10.1115/1.4029274>
4. Sokolov, V., Porkuian, O., Krol, O., Stepanova, O.: Design calculation of automatic rotary motion electrohydraulic drive for technological equipment. In: Ivanov, V., Trojanowska, J., Pavlenko, I., Zajac, J., Peraković, D. (eds.) *DSMIE 2021. LNME*, pp. 133–142. Springer, Cham (2021). [https://doi.org/10.1007/978-3-030-77719-7\\_14](https://doi.org/10.1007/978-3-030-77719-7_14)
5. Panchenko, A., Voloshina, A., Titova, O., Panchenko, I., Zasiadko, A.: The study of dynamic processes of mechatronic systems with planetary hydraulic motors. In: Tonkonogyi, V., et al.







- (eds.) InterPartner 2020. LNME, pp. 704–713. Springer, Cham (2021). [https://doi.org/10.1007/978-3-030-68014-5\\_68](https://doi.org/10.1007/978-3-030-68014-5_68)
6. Hsieh, C.F., Hwang, Y.W.: Geometric design for a gerotor pump with high area efficiency. *J. Mech. Des.* **129**(12), 1269–1277 (2007). <https://doi.org/10.1115/1.2779887>
  7. Hsieh, C.F.: Fluid and dynamics analyses of a gerotor pump using various span angle designs. *J. Mech. Des.* **134**(12), 121003 (2012). <https://doi.org/10.1115/1.4007703>
  8. Liu, H., Lee, J.-C., Yoon, A., Kim, S.-T.: Profile design and numerical calculation of instantaneous flow rate of a gerotor pump. *J. Appl. Math. Phys.* **3**(1), 92–97 (2015). <https://doi.org/10.4236/jamp.2015.31013>
  9. Voloshina, A., Panchenko, A., Titova, O., Panchenko, I.: Changes in the dynamics of the output characteristics of mechatronic systems with planetary hydraulic motors. *J. Phys: Conf. Ser.* **1741**, 012045 (2021). <https://doi.org/10.1088/1742-6596/1741/1/012045>
  10. Vecchiato, D., Demenego, A., Argyris, J., Litvin, F.L.: Geometry of a cycloidal pump. *Comput. Methods Appl. Mech. Eng.* **190**, 2309–2330 (2001). [https://doi.org/10.1016/S0045-7825\(00\)00236-X](https://doi.org/10.1016/S0045-7825(00)00236-X)
  11. Demenego, A., Vecchiato, D., Litvin, F.L., Nervegna, N., Mancó, S.: Design and simulation of meshing of a cycloidal pump. *Mech. Mach. Theory* **37**(3), 311–332 (2002). [https://doi.org/10.1016/S0094-114X\(01\)00074-X](https://doi.org/10.1016/S0094-114X(01)00074-X)
  12. Panchenko, A., Voloshina, A., Panchenko, I., Pashchenko, V., Zasiadko, A.: Influence of the shape of windows on the throughput of the planetary hydraulic motor's distribution system. In: Ivanov, V., Pavlenko, I., Liaposhchenko, O., Machado, J., Edl, M. (eds.) DSMIE 2021. LNME, pp. 146–155. Springer, Cham (2021). [https://doi.org/10.1007/978-3-030-77823-1\\_15](https://doi.org/10.1007/978-3-030-77823-1_15)
  13. Choi, T.H., Kim, M.S., Lee, G.S., and others: design of rotor for internal gear pump using cycloid and circular-arc curves. *J. Mech. Des.* **134**(1), 011005 (2012). <https://doi.org/10.1115/1.4004423>
  14. O'Shea, C.: Hydraulic Flow Ripple Cancellation Using the Primary Flow Source. Symposium on Fluid Power and Motion Control FPMC2016-1783 (2016). <https://doi.org/10.1115/FPMC2016-1783>
  15. Tkachuk, M.M., Grabovskiy, A., Tkachuk, M.A., Saverska, M., Hrechka, I.: A semi-analytical method for analysis of contact interaction between structural elements along aligned surfaces. *Eastern-Euro. J. Enterp. Technol.* **1/7**(103), 16–25 (2020). <https://doi.org/10.15587/1729-4061.2020.193985>
  16. Tkachuk, M.M., Grabovskiy, A., Tkachuk, M.A., Hrechka, I., Ishchenko, O., Domina, N.: Investigation of multiple contact interaction of elements of shearing dies. *Eastern-Europ. J. Enterp. Technol.* **4/7**(100), 6–15 (2019). <http://journals.uran.ua/eejet/article/view/174086/175737>
  17. Atroshenko, O., Tkachuk, M., Ustinenko, O., Bondarenko, O., Diomina, N.: A numerical analysis of non-linear contact tasks for the system of plates with a bolted connection and a clearance in the fixture. *Eastern-Europ. J. Enterp. Technol.* **1/7**(79), 24–29 (2016). <http://journals.uran.ua/eejet/article/view/60087>
  18. Tkachuk M.: A numerical method for axisymmetric adhesive contact based on Kalker's variational principle. *Eastern-Europ. J. Enterp. Technol.* **3/7**(93), 34–41 (2018). <https://doi.org/10.15587/1729-4061.2018.132076>
  19. Rogovyi, A., Khovanskyi, S., Hrechka, I., Gaydamaka, A.: Studies of the swirling submerged flow through a confuser. In: Ivanov, V., Pavlenko, I., Liaposhchenko, O., Machado, J., Edl, M. (eds.) DSMIE 2020. LNME, pp. 85–94. Springer, Cham (2020). [https://doi.org/10.1007/978-3-030-50491-5\\_9](https://doi.org/10.1007/978-3-030-50491-5_9)
  20. Rogovyi, A., Korohodskiy, V., Khovanskyi, S., Hrechka, I., Medvediev, Y.: Optimal design of vortex chamber pump. *J. Phys. Conf. Ser.* **1741**(1), 012018 (2021). <https://doi.org/10.1088/1742-6596/1741/1/012018>

21. Andrenko, P., Rogovyi, A., Hrechka, I., Khovanskyi, S., Svyarenko, M.: Characteristics improvement of labyrinth screw pump using design modification in screw. *J. Phys. Conf. Ser.* **1741**(1), 012024 (2021). <https://doi.org/10.1088/1742-6596/1741/1/012024>
22. Korohodskyi, V., Kryshtopa, S., Migal, V., Rogovyi, A., et al.: Determining the characteristics for the rational adjusting of an fuelair mixture composition in a two-stroke engine with internal carburation. *Eastern-Europ. J. Enterp. Technol.* **2**(5), 39–52 (2020). <http://journals.urau.ua/eejet/article/view/200766>
23. Rogovyi, A., Korohodskyi, V., Medvediev, Y.: Influence of Bingham fluid viscosity on energy performances of a vortex chamber pump. *Energy* **218**, 119432 (2021). <https://doi.org/10.1016/j.energy.2020.119432>
24. Van de Ven, J. On fluid compressibility in switch-mode hydraulic circuits. part i: modeling and analysis. *J. Dyn. Syst. Measure. Control* **135**(2), 021013-021013-13 (2012). <https://doi.org/10.1115/1.4023062>
25. Van de Ven J.: On fluid compressibility in switch-mode hydraulic circuits. part II: experimental results. *J. Dyn. Syst. Measure. Control* **135**(2), 021014-021014-7 (2012). <https://doi.org/10.1115/1.4023063>
26. Velev, E.: Study cavitation gerotor motors. Using computer simulation. In: XV International Scientific Conference: Renewable Energies and Innovative Technologies, pp. 64–66 (2016)
27. Marcu, I., Pop, I.: Interconnection possibilities for the working volumes of the alternating hydraulic motors. *Scientific Bulletin of the Politehnica University of Timisoara, Special issue: Transactions on Mechanics*, pp. 365–370 (2004)
28. Buono, D., Schiano di Cola, F.D., Senatore, A., Frosina, E., Buccilli, G., Harrison, J.: Modelling approach on a Gerotor pump working in cavitation conditions. *Energy Procedia* **101**, 701–709 (2016). <https://doi.org/10.1016/j.egypro.2016.11.089>
29. Shah, Y. G., Vacca, A., Dabiri, S. A fast lumped parameter approach for the prediction of both aeration and cavitation in Gerotor pumps. *Meccanica* **53**, 175–191 (2018). <https://doi.org/10.1007/s11012-017-0725-y>
30. Strutynsky, V., Hurzhi, A., Kozlov, L.: Determination of static equilibrium conditions of mobile terrestrial complex with lever-type manipulator. *Naukovyi Visnyk NHU* **5**, 79–86 (2019). <https://doi.org/10.29202/nvngu/2019-5/7>
31. Strutynsky, V., Demyanenko, A.: The development of mechatronic active control system of tool spatial position of parallel kinematics machine tool. *J. Theor. Appl. Mech.* **54**(3), 757–768 (2016). <https://doi.org/10.15632/jtam-pl.54.3.757>
32. Strutynskiy, S.: Defining the dynamic accuracy of positioning of spatial drive systems through consistent analysis of processes of different range of performance. *Naukovyi Visnyk NHU* **3**, 64–73 (2018). <https://doi.org/10.29202/nvngu/2018-3/13>
33. Strutynskiy, S., Nochnichenko, I.: Design of parallel link mobile robot manipulator mechanisms based on function-oriented element base. *Eastern-Europ. J. Enterp. Technol.* **4**(7)(100), 54–64 (2019). <https://doi.org/10.15587/1729-4061.2019.174613>
34. Bulgakov, V., Ivanovs, S., Adamchuk, V., Antoshchenkov, R.: Investigations of the dynamics of a four-element machine-and-tractor aggregate. *Acta Technol. Agric.* **22**(4), 146–151 (2019). <https://doi.org/10.2478/ata-2019-0026>
35. Galych, I., Antoshchenkov, R., Antoshchenkov, V., Lukjanov, I., Diundik, S., Kis, O.: Estimating the dynamics of a machine-tractor assembly considering the effect of the supporting surface profile. *Eastern-Europ. J. Enterp. Technol.* **1**(7)(109), 51–62 (2021). <https://doi.org/10.15587/1729-4061.2021.225117>
36. Pylypaka, S., Klendiy, M., Zaharova, T.: Movement of the particle on the external surface of the cylinder, which makes the translational oscillations in horizontal planes. In: Ivanov, V., et al. (eds.) *DSMIE 2018. LNME*, pp. 336–345. Springer, Cham (2019). [https://doi.org/10.1007/978-3-319-93587-4\\_35](https://doi.org/10.1007/978-3-319-93587-4_35)

37. Dzyuba, O., Dzyuba, A., Polyakov, A., Volokh, V., Antoshchenkov, R., Mykhailov, A.: Studying the influence of structural-mode parameters on energy efficiency of the plough PLN-3–35. *Eastern-Europ. J. Enterp. Technol.* **3**(1)(99), 55–65 (2019). <https://doi.org/10.15587/1729-4061.2019.169903>
38. Tkachuk, M.M., Grabovskiy, A., Tkachuk, M.A., Zarubina, A., Lipeyko, A.: Analysis of elastic supports and rotor flexibility for dynamics of a cantilever impeller. *J. Phys. Conf. Ser.* **1741**(1), 012043 (2021). <https://doi.org/10.1088/1742-6596/1741/1/012043>
39. Heisel, U., Strytinsky, S., Sidorco, V., Filatov, Y., Storchac, M.: Development of controllable spherical fluid friction hinges for exact spatial mechanisms. *German Acad. Soc. Prod. Eng.* **1**, 62–71 (2011). <https://doi.org/10.1007/s11740-010-0291-9>
40. Pavlenko, I., Simonovskiy, V., Ivanov, V., Zajac, J., Pitel, J.: Application of artificial neural network for identification of bearing stiffness characteristics in rotor dynamics analysis. In: Ivanov, V., et al. (eds.) *DSMIE 2018. LNME*, pp. 325–335. Springer, Cham (2019). [https://doi.org/10.1007/978-3-319-93587-4\\_34](https://doi.org/10.1007/978-3-319-93587-4_34)
41. Rezvaya, K., Krupa, E., Shudryk, A., Drankovskiy, V., Makarov, V.: Solving the hydrodynamical tasks using CFD programs. In: *3rd International Conference on Intelligent Energy and Power Systems*, vol. 1, p. 8308004 (2018). <https://doi.org/10.1109/IEPS.2018.8559548>
42. Gentner, C., Sallaberger, M., Widmer, C., Braun, O., Staubli, T.: Numerical and experimental analysis of instability phenomena in pump turbines. *IOP Conf. Ser. Earth Environ. Sci.* **15**(3), 0320422 (2012). <https://doi.org/10.1088/1755-1315/15/3/032042>
43. Panchenko, A., Voloshina, A., Kiurchev, S., and others: Development of the universal model of mechatronic system with a hydraulic drive. *Eastern-Europ. J. Enterp. Technol.* **4**(7)(94), 51–60 (2018). <https://doi.org/10.15587/1729-4061.2018.139577>
44. Kiurchev, S., Luzan, P., Zasiadko, A., Radionov, H., Boltianska, N.: Influence of the flow area of distribution systems on changing the operating parameters of planetary hydraulic motors. *IOP Conf. Ser. Mater. Sci. Eng.* **1021**, 012037 (2021). <https://doi.org/10.1088/1757-899X/1021/1/012037>
45. Pavlenko, I., Trojanowska, J., Ivanov, V., Liaposhchenko, O.: Scientific and methodological approach for the identification of mathematical models of mechanical systems by using artificial neural networks. In: Machado, J., Soares, F., Veiga, G. (eds.) *HELIX 2018. LNEE*, vol. 505, pp. 299–306. Springer, Cham (2019). [https://doi.org/10.1007/978-3-319-91334-6\\_41](https://doi.org/10.1007/978-3-319-91334-6_41)
46. Kalinichenko, P., Gusak, O., Khovanskyy, S., Krutas, Y.: Substantiation and development of the procedure for calculating a hydraulic balancing device under condition of minimal energy losses. *Eastern-Europ. J. Enterp. Technol.* **2**(7–86), 36–41 (2017). <https://doi.org/10.15587/1729-4061.2017.97162>
47. Sokolov, V., Porkuian, O., Krol, O., Baturin, Y.: Design calculation of electrohydraulic servo drive for technological equipment. In: Ivanov, V., Trojanowska, J., Pavlenko, I., Zajac, J., Peraković, D. (eds.) *DSMIE 2020. LNME*, pp. 75–84. Springer, Cham (2020). [https://doi.org/10.1007/978-3-030-50794-7\\_8](https://doi.org/10.1007/978-3-030-50794-7_8)
48. Altare, G., Rundo, M.: Computational fluid dynamics analysis of gerotor lubricating pumps at high-speed: geometric features influencing the filling capability. *J. Fluids Eng.* **138**(11), FE-15–1757 (2016). <https://doi.org/10.1115/1.4033675>
49. Onysko, O., Karabegović, I., Dašić, P., Penderetskiy, M., Melnyk, O.: The stress state of compact mechatronic satellites of a cycloidal reducer. *J. Eng. Sci.* **8**(2), D12–D17 (2021). [https://doi.org/10.21272/jes.2021.8\(2\).d3](https://doi.org/10.21272/jes.2021.8(2).d3)



# Mathematical Model of Lifting Particles of Technological Material by Vertical Auger

Serhii Pylypaka<sup>1</sup> , Tatiana Volina<sup>1,2</sup>  , Iryna Hryshchenko<sup>1</sup> ,  
Serhii Dieniezhnikov<sup>2</sup> , and Iryna Rybenko<sup>3</sup> 

<sup>1</sup> National University of Life and Environmental Sciences of Ukraine, 15, Heroyiv Oborony Street, Kyiv 03041, Ukraine

t.n.zaharova@ukr.net

<sup>2</sup> Sumy State Pedagogical University named after A.S. Makarenko, 87, Romenskaya Street, Sumy 40002, Ukraine

<sup>3</sup> Sumy National Agrarian University, 160, Kondratieva Street, Sumy 40021, Ukraine

**Abstract.** This research aims to investigate the transportation of a material particle by a vertically placed auger limited by a cylindrical casing. The surfaces are coaxial. When the auger rotates, the particle moves to the periphery and interacts with the cylindrical casing. The particle simultaneously slides on both surfaces and rises in absolute movement. Its relative motion is sliding along the periphery of the auger. Differential equations of particle movement in projections on a moving coordinate system that rotates with an auger were compiled. Numerical methods have solved the equations, and graphs of kinematic characteristics were built. The limit value of the rising angle for the helical line was found as the periphery of the auger. At such a position, the rise of the particle stops at a given angular velocity of the auger. It was found that the velocity of particle rising is influenced by constructive and technological parameters. In particular, for a given radius of the cylindrical casing, friction coefficients, and the edge angle of the auger, there is a minimum value of the angular velocity of its rotation. Then the particle “sticks” and rotates together with the auger, describing in absolute motion a circle on the inner surface of the cylindrical casing.

**Keywords:** Material particle · Frene trihedron · Cylindrical casing · Sliding trajectory · Transportation · Industrial growth

## 1 Introduction

Firstly, engineering practice often deals with designing geometric objects, which scientists propose to solve in quite diverse ways. For example, in [1], the authors present a vision of constructing geometric objects within a multidimensional space by approximating a solution to differential equations [2]. In [3], geometric modeling of multifactorial processes and phenomena is proposed to be carried out by the method of multidimensional parabolic interpolation. In [4], geometric characteristics of the object are taken as a basis. Geometric modeling of torse surfaces is shown in [5]. So, the methods for geometric design of objects are quite diverse.

---

The original version of the chapter the affiliation of the author has been revised. A correction to this chapter can be found at [https://doi.org/10.1007/978-3-031-06044-1\\_30](https://doi.org/10.1007/978-3-031-06044-1_30)

Secondly, the operation of machines involves the interaction of particles of technological material with their working bodies. Particles are forced to choose the trajectory of sliding on the surface. The surface can be movable. For example, it can perform a rotational movement. In this case, the particle's movement will consist of two components: the particle relative motion (particle sliding on the surface) and the transient (rotational) motion of the surface itself. The particle relative motion is considered relatively to a moving system of coordinates. The superposition of motions gives the absolute trajectory of the particle movement in a fixed coordinate system.

During the investigation of the dynamics of a point, the equations of equilibrium of applied forces in projections on the axis of the stationary or mobile spatial coordinate system are usually compiled. A moving coordinate system, which in differential geometry is called the accompanying Frenet trihedron of the guide curve, can be applied. It allows solving the problem easier.

## 2 Literature Review

Different approaches are used for the analytical description of the transportation of technological material, which consists of individual particles. This is due to the complexity of the processes that occur when particles interact. Therefore, it is quite common to consider the transportation of a single particle, the motion of which can be described analytically. The obtained patterns, in some way, can be transferred to the technological material. Technological material can be mineral fertilizers [6] various mixtures for separation and purification [7, 8]. The motion of particles on helical and similar surfaces is considered in different articles, for example, in [9], the motion of grain on moving surfaces of sowing machines – in [10], the movement of dispersed particles in curvilinear separation channels – in [11–14]. There may be cases of equating bodies to a material particle if the forces of inertia from their rotation can be neglected due to low angular velocities [15]. Earlier the movable Frenet trihedron was applied to solving some tasks, for instance, to describe the complex motion of a material point [16]. It can also be used for solving different tasks, for example, for increasing the reliability and durability of details using geometrical methods in general [17, 18], which nowadays are proposed to be solved using new methods of details manufacturing [19] or surfaces improvement [20]. Results of the research can be applied in different industries, for example, in buildings [21–23]. Based on the previous, our research aimed to apply movable trihedron and Frenet formulas to analytically describe the complex motion of a material point on the periphery of a vertical auger that rotates inside a coaxial cylindrical casing.

## 3 Research Methodology

In the general case, the guide curve of the accompanying trihedron is spatial. Let consider the case for the flat guide curve  $C_e$  (see Fig. 1). Mutually perpendicular unit orths form the trihedron  $\bar{\tau}, \bar{n}, \bar{b}$ . The orths of the tangent form the tangent plane of the trihedron  $\bar{\tau}$  and main normal  $\bar{n}$ . It coincides with the plane  $\mu$ , where the curve  $C_e$  is located. Point  $B$  in the trihedron system is given by the coordinates  $\rho_\tau, \rho_n$ , and  $\rho_b$ .



Let the accompanying trihedron moves with a velocity  $V_e$  along the curve  $C_e$ . In this case, it rotates at an angle  $\alpha$  with speed depending on the speed of rotation of the tangent  $\bar{\tau}$ . At an interval of the arc length of the curve  $\Delta s$ , the average rotation speed is  $\Delta\alpha/\Delta s$ . The boundary of this ratio during approaches  $\Delta s$  to zero is the curvature  $k$  of the curve. On the other hand, the boundary  $\Delta\alpha/\Delta t$  ( $\Delta t$  is time) is the angular velocity  $\omega$  of rotation of the orth of the tangent  $\bar{\tau}$ . There is a dependence between  $k$  and  $\omega$ :

$$\omega = \frac{d\alpha}{dt} = \frac{d\alpha}{ds} \cdot \frac{ds}{dt} = kV_e. \tag{1}$$

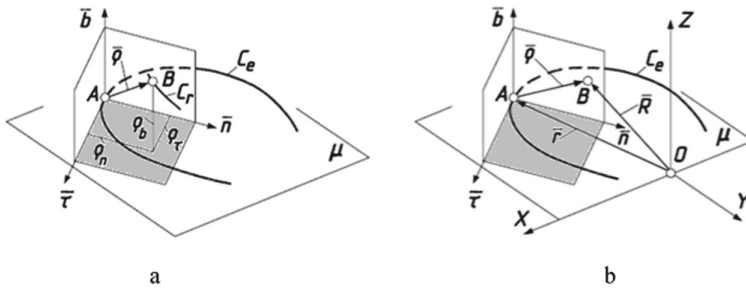
Vector equation of the position of the point  $B$  according to Fig. 1b is:

$$\bar{R} = \bar{r} + \bar{\rho}, \tag{2}$$

where the radius-vector  $\bar{R}$  is the location of the material particle in the stationary system  $OXYZ$ ,

the radius-vector  $\bar{r}$  of the vertex  $A$  of the trihedron location on  $C_e$ ,

the radius-vector  $\bar{\rho}$  indicates the particle position in the trihedron system.



**Fig. 1.** To the complex motion of the particle in Frenet trihedron of the guide curve  $C_e$  system: a) an accompanying trihedron  $\bar{\tau}, \bar{n}, \bar{b}$  with point  $B$  in its system; b) fixed  $OXYZ$  and movable  $\bar{\tau}, \bar{n}, \bar{b}$  coordinate systems with the radius-vector of point  $B$  in them.

The coordinates  $\rho_\tau, \rho_n, \rho_b$  in the system of a trihedron can be variable and depend on its position on the curve  $C_e$ , i.e., depending on the length of the arc  $s$  of the guide curve. Therefore, while the trihedron moves along a curve, point  $B$  moves in its system and describes the relative trajectory  $C_r$  (Fig. 1a). The sum of the transient motion of a trihedron and the relative motion of a point in its system gives the absolute trajectory of point  $B$ . Let decompose the vector  $\bar{\rho}$  into trihedron orths and rewrite the vector Eq. (2):

$$\bar{R} = \bar{r} + \bar{\tau}\rho_\tau + \bar{n}\rho_n + \bar{b}\rho_b. \tag{3}$$

By differentiating (3) by time, the vector of absolute acceleration can be obtained. It can be done conveniently using the Frenet trihedron and formulas. It allows you to find simply the orths  $\bar{\tau}, \bar{n}, \bar{b}$  derivatives in projections on themselves. In this instance,  $s$  (the arc length which is passed by the trihedron vertex on  $C_e$ ) should be the variable. It is

essential to determine the relationship between the absolute velocity  $V_a$  and the vector  $\bar{R}$  derivative by  $s$ :

$$\bar{V}_a = \frac{d\bar{R}}{dt} = \frac{d\bar{R}}{ds} \frac{ds}{dt} = V_e \frac{d\bar{R}}{ds}. \quad (4)$$

In order to obtain the absolute velocity  $V_a$ , it is necessary to multiply the velocity  $V_e$  of the transient motion of the trihedron along the curve  $C_e$  by the derivative of (3). So, (3) should be differentiated by  $s$ , bearing in mind that  $\rho_\tau = \rho_\tau(s)$ ,  $\rho_n = \rho_n(s)$  and  $\rho_b = \rho_b(s)$ :

$$\frac{d\bar{R}}{ds} = \frac{d\bar{r}}{ds} + \left( \frac{d\bar{r}}{ds} \rho_\tau + \bar{\tau} \frac{d\rho_\tau}{ds} \right) + \left( \frac{d\bar{n}}{ds} \rho_n + \bar{n} \frac{d\rho_n}{ds} \right) + \left( \frac{d\bar{b}}{ds} \rho_b + \bar{b} \frac{d\rho_b}{ds} \right). \quad (5)$$

Derivatives  $\frac{d\bar{r}}{ds}$ ,  $\frac{d\bar{\tau}}{ds}$ ,  $\frac{d\bar{n}}{ds}$ ,  $\frac{d\bar{b}}{ds}$  according to Frenet formulas are specified in projections on the orths of the trihedron through the torsion  $\sigma$  and the curvature  $k$  of the guide curve  $C_e$ , which is a flat curve, so  $\sigma = 0$ . For this case Frenet formulas take the following form:

$$\bar{r} = \bar{\tau}; \quad \bar{\tau} = k\bar{n}\bar{n} = -k\bar{\tau}, \quad \bar{b} = 0. \quad (6)$$

After substitution of derivatives (6) in (5) and grouping of projections on orths  $\bar{\tau}$ ,  $\bar{n}$ ,  $\bar{b}$ :

$$\bar{R} = \bar{\tau} + \bar{n}k\rho_\tau + \bar{\tau}\dot{\rho}_\tau - \bar{\tau}k\rho_n + \bar{n}\dot{\rho}_n = \bar{\tau}(1 + \dot{\rho}_\tau - k\rho_n) + \bar{n}(\dot{\rho}_n + k\rho_\tau) + \bar{b}\dot{\rho}_b. \quad (7)$$

Therefore, considering (4) the projections of the absolute velocity on the orths of the trihedron can be written: on ort  $\bar{\tau}$ :  $V_{a\tau} = V_e(1 + \dot{\rho}_\tau - k\rho_n)$ ; on ort  $\bar{n}$ :  $V_{an} = V_e(\dot{\rho}_n + k\rho_\tau)$ ; on ort  $\bar{b}$ :  $V_{ab} = V_e\dot{\rho}_b$ . After differentiation of (4) by time  $t$ , provided that  $V_e = \text{const}$ , the expression of the absolute acceleration  $w$  can be received:

$$\bar{w} = \frac{d\bar{V}_a}{dt} = \frac{d\bar{V}_a}{ds} \frac{ds}{dt} = \frac{d\bar{V}_a}{ds} V_e = V_e^2 \frac{d^2\bar{R}}{ds^2}. \quad (8)$$

The second derivative  $\bar{R}$  is included in (8) and can be identified through differentiating (7) ( $s$  is the variable) applying (6), bearing in mind that the curvature  $k = k(s)$  is a variable. The obtained expressions should be grouped by the orths of the trihedron and multiplied by  $V_e^2$  according to (8). Then absolute acceleration of  $B$ :

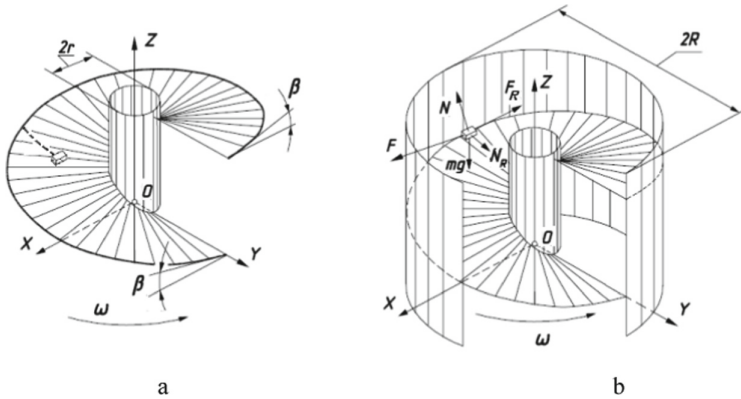
$$\begin{aligned} w_\tau &= V_e^2 [\ddot{\rho}_\tau - \dot{k}\rho_n - k(k\rho_\tau + 2\dot{\rho}_n)]; \\ w_n &= V_e^2 [\ddot{\rho}_n - \dot{k}\rho_\tau + k(1 - k\rho_n + 2\dot{\rho}_\tau)]; \\ w_b &= V_e^2 \ddot{\rho}_b. \end{aligned} \quad (9)$$

Expressions of absolute acceleration  $\bar{w}$  must be used to compile the vector equation:  $m\bar{w} = \bar{F}$ , where  $m$  – the particle mass, and  $\bar{F}$  – the resulted vector of applied forces.

Thus, it can be applied to the analytical description of transporting the particle by a vertical auger, which rotates around its axis inside the cylindrical casing.

### 4 Results

Let us start with the fact, that when the particle hits the auger, it begins to slide on it, moving away from the axis because of the centrifugal force (see A dashed line shows Fig. 2a, the sliding trajectory).



**Fig. 2.** Graphic illustrations of a particle motion: a) one turn of the auger surface with the sliding trajectory of the particle on it; b) the scheme of forces.

At the moment of contact with the cylindrical casing, the particle interacts with both surfaces. At the same time, it is forced to slide along the helical line – the edge of the auger with a constant angle of rising  $\beta$ . If the auger rotates at an angular velocity  $\omega$  counterclockwise, the particle will slide in a helical line in the opposite direction and at the same time should rise upwards. Therefore, the sliding of the particle regarding the auger is clockwise, and the rise is provided by the appropriate direction of winding of the auger (see Fig. 2). The following forces act on the particle: the force of gravity  $mg$ , where  $g = 9,81 \text{ M/c}^2$  is the acceleration of free fall, reaction force of the auger surface  $N$ , reaction force of the cylindrical casing surface  $N_R$ , friction force  $F$  caused by particle sliding along the auger surface and friction force  $F_R$ , caused by the sliding of the particle on the surface of the cylindrical casing (see Fig. 2b).

When the auger rotates, the helical line (its edge) rotates too and a particle slides along it. In the general case, the parametrical equations of the helical line in the system of the trihedron are:

$$\rho_\tau = R \cos \alpha; \rho_n = R \sin \alpha; \rho_b = R \alpha \tan \beta, \tag{10}$$

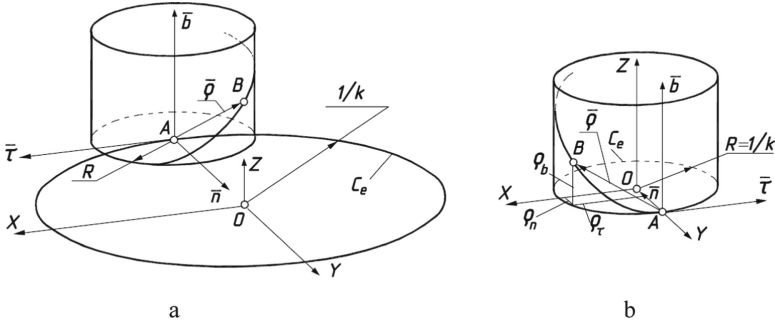
where  $R$  is the radius;

$\beta$  is the helical line rising angle;

$\alpha$  is an independent variable.

Let the guide curve for a trihedron be another circle with a constant curvature  $k$ , i.e., radius  $1/k$  (see Fig. 3a). When the trihedron is moving along the guide circle, point  $B$  must simultaneously slide along the helical line. For combining these movements, it is

necessary to set the dependence  $\alpha = \alpha(s)$ , where  $s$  is the length of the arc of the guide circle. The shape of the absolute trajectory of point  $B$  depends on the dependence  $\alpha = \alpha(s)$ . It will have a spatial shape and will not satisfy the requirements of the auger functioning, in which absolute trajectory does not leave the surface of the cylinder of the radius  $R$  (see Fig. 2b). According to the requirement of the auger functioning, both circles must be equal, i.e.,  $R = 1/k$ , during lifting along the helical line, the particle must rotate clockwise, and the top of the trihedron must move in a circle (see Fig. 3b).



**Fig. 3.** Variants of the formation of the absolute trajectory of point  $B$ , which in the system of a trihedron moves along a helical line: a) the guide circle  $C_e$  and the circle of the base of the cylinder has different radiuses; b) the circles coincide.

These requirements are satisfied by the following parametrical equations of the helical line in the trihedron system:

$$\rho_\tau = -R\sin\alpha; \rho_n = R - R\cos\alpha; \rho_b = R\alpha\text{tg}\beta. \tag{11}$$

To find the absolute acceleration by formulas (10), we need to have the first and second derivatives of Eqs. (11). One can find them, bearing in mind that  $\alpha = \alpha(s)$ :

$$\begin{aligned} \dot{\rho}_\tau &= -R\dot{\alpha}\cos\alpha; \ddot{\rho}_\tau = R\dot{\alpha}^2\sin\alpha - R\ddot{\alpha}\cos\alpha; \\ \dot{\rho}_n &= R\dot{\alpha}\sin\alpha; \ddot{\rho}_n = R\dot{\alpha}^2\cos\alpha + R\ddot{\alpha}\sin\alpha; \\ \dot{\rho}_b &= R\dot{\alpha}\text{tg}\beta; \ddot{\rho}_b = R\ddot{\alpha}\text{tg}\beta. \end{aligned} \tag{12}$$

After substitution of derivatives (12) in (10), bearing in mind that  $k = 1/R$  and  $\dot{k} = 0$  and after simplifications next equations have been derived:

$$\begin{aligned} w_\tau &= V_e^2[(R\dot{\alpha} - 1)^2\sin\alpha - R^2\ddot{\alpha}\cos\alpha]/R; \\ w_n &= V_e^2[(R\dot{\alpha} - 1)^2\cos\alpha + R^2\ddot{\alpha}\sin\alpha]/R; \\ w_b &= V_e^2R\ddot{\alpha}\text{tg}\beta. \end{aligned} \tag{13}$$

For compiling the particle motion equations, it is essential to determine the direction of all forces. The force  $mg$  is directed in the opposite direction to the binormal direction. The projections of the unit vector on the orths of the trihedron are:

$$mg\{0; 0 - 1\}. \tag{14}$$

The direction of reaction of the auger surface  $N$  (see Fig. 2b) can be found using differential geometry. It can be found easier because it is simultaneously perpendicular to two lines: the helical line and the rectilinear generatrix of the surface of the auger, i.e., it is located in the plane tangent to the cylinder. When a particle moves along a helical line, the angle of inclination of the unit vector  $N$  to the horizontal plane is constant. Its component on the horizontal plane is equal to  $\sin\beta$  and on the orth  $\bar{b}$  of the binormal –  $\cos\beta$ . The horizontal component  $\sin\beta$  should be decomposed to orths  $\bar{\tau}$  and  $\bar{n}$  because its rotation at an angle  $\alpha$  occurs clockwise. Thus, the projections of the unit vector of the normal  $N$  on the orths of the trihedron are:

$$N\{\sin\beta\cos\alpha; -\sin\beta\sin\alpha; \cos\beta\}. \quad (15)$$

The reaction  $N_R$  of the cylinder surface is directed perpendicularly to its tangent plane toward the axis (see Fig. 2b). Then the unit vector in the projections on the orths of the trihedron is:

$$N_R\{\sin\alpha; \cos\alpha; 0\}. \quad (16)$$

The friction force is the product of the surface reaction to the coefficient of friction. Let us denote  $f$  as the friction coefficient of the particle on the auger and as  $f_R$  – on the cylindrical casing. So, the friction forces indicated in Fig. 2b, are  $F = fN$ , and  $F_R = f_R N_R$ . Then it is essential to determine the direction of these forces. The force  $F$  is directed opposite to the vector of the particle sliding velocity. The particle slides along the helical line (auger edge), so the direction of sliding is given by the first derivatives of (11), and these derivatives are given in (12). Their geometric sum, multiplied by the velocity  $V_e$ , gives the relative motion velocity  $V_r$ :

$$V_r = V_e \sqrt{\dot{\rho}_\tau^2 + \dot{\rho}_n^2 + \dot{\rho}_b^2} = V_e R \dot{\alpha} / \cos\beta. \quad (17)$$

The direction of the unit vector of relative velocity  $V_r$  can be obtained by dividing its components by the value (17):

$$V_r\{-\cos\beta\cos\alpha; \cos\beta\sin\alpha; \sin\beta\}. \quad (18)$$

The force  $F_R$  is directed opposite to the vector of the particle sliding speed on the surface of the stationary cylindrical casing. The value of the absolute velocity  $V_a$  and the projection of a unit vector is determined similarly:

$$V_a = V_e \sqrt{V_{a\tau}^2 + V_{an}^2 + V_{ab}^2} = V_e \sqrt{(1 - 2R\dot{\alpha})\cos^2\beta + R^2\dot{\alpha}^2} / \cos\beta. \quad (19)$$

$$V_a \left\{ \begin{array}{l} (1 - 2R\dot{\alpha})\cos\beta\cos\alpha / \sqrt{(1 - 2R\dot{\alpha})\cos^2\beta + R^2\dot{\alpha}^2}; \\ (1 - 2R\dot{\alpha})\cos\beta\sin\alpha / \sqrt{(1 - 2R\dot{\alpha})\cos^2\beta + R^2\dot{\alpha}^2}; \\ R\dot{\alpha}\sin\beta / \sqrt{(1 - 2R\dot{\alpha})\cos^2\beta + R^2\dot{\alpha}^2} \end{array} \right\}. \quad (20)$$

Let us decompose the vector equation  $m\bar{a} = \bar{F}$  on the orths  $\bar{\tau}$ ,  $\bar{n}$ ,  $\bar{b}$  because of the directions (14)–(16), (18), and (20) of the acting of corresponding forces  $mg$ ,  $N$ ,  $N_R$ ,  $F = fN$ ,  $F_R = f_R N_R$ :

$$m w_{\bar{\tau}} = N \sin\beta \cos\alpha + N_R \sin\alpha + f N \cos\beta \cos\alpha - f_R N_R \frac{(1 - 2R\dot{\alpha})\cos\beta\cos\alpha}{\sqrt{(1 - 2R\dot{\alpha})\cos^2\beta + R^2\dot{\alpha}^2}};$$

$$\begin{aligned}
 mw_n &= -N \sin \beta \sin \alpha + N_R \cos \alpha - f N \cos \beta \sin \alpha \\
 &\quad - f_R N_R (1 - 2R\dot{\alpha}) \cos \beta \sin \alpha / \sqrt{(1 - 2R\dot{\alpha}) \cos^2 \beta + R^2 \dot{\alpha}^2}; \\
 mw_b &= -mg + N \cos \beta - f N \sin \beta - f_R N_R \frac{R \dot{\alpha} \sin \beta}{\sqrt{(1 - 2R\dot{\alpha}) \cos^2 \beta + R^2 \dot{\alpha}^2}}. \quad (21)
 \end{aligned}$$

After substitution of absolute acceleration from (13) to (21), a system of  $\alpha = \alpha(s)$ ,  $N = N(s)$ , and  $N_R = N_R(s)$  can be received. It should be solved regarding  $\ddot{\alpha}$ ,  $N$ ,  $N_R$ :

$$\ddot{\alpha} = \frac{\cos \beta [f_R (R\dot{\alpha} - 1)^2 (1 - 2R\dot{\alpha} + \cos 2\beta - f \sin 2\beta)]}{2R^2 \sqrt{(1 - 2R\dot{\alpha}) \cos^2 \beta + R^2 \dot{\alpha}^2}} - \frac{g \cos \beta}{RV_e^2} (\sin \beta + f \cos \beta). \quad (22)$$

$$N = m \cos \beta \left[ g + V_e^2 f_R \sin \beta (R\dot{\alpha} - 1)^2 / R \sqrt{(1 - 2R\dot{\alpha}) \cos^2 \beta + R^2 \dot{\alpha}^2} \right]. \quad (23)$$

$$N_R = m V_e^2 (R\dot{\alpha} - 1)^2 / R. \quad (24)$$

(22) can be solved independently, because it does not depend on (23) and (24). This requires the use of numerical methods. The reactions of surfaces (23) and (24) can be found after Eq. (22) is solved.

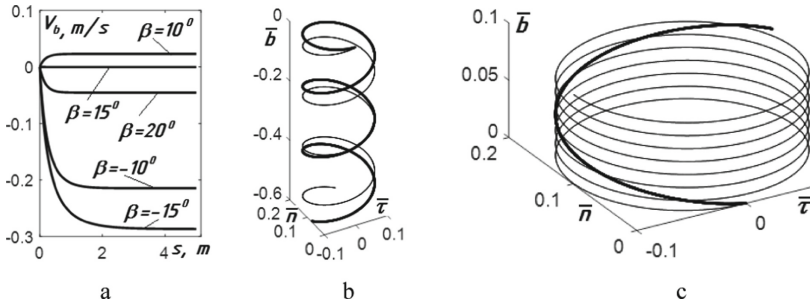
Let us consider an example. Let the angle of rising of the edge of the auger is  $\beta = 15^\circ$ , the radius of the cylindrical casing is  $R = 0,1 \text{ m}$ , the coefficients of friction are  $f = f_R = 0,3$ .

An important indicator is the velocity  $V_b$  of particles rising upward. It is an equal component of both absolute and relative velocities in the vertical direction, i.e. parallel to the orth  $\vec{b}$ . Based on these conditions, it can be written:

$$V_b = V_e \dot{\rho}_b = V_e R \dot{\alpha} \operatorname{tg} \beta. \quad (25)$$

For a given angle  $\beta$  the critical value of the velocity  $\omega = V_e/R$  of the auger rotation can be determined. It takes place at  $\dot{\alpha} = 0$ , so according to (26) there is no vertical particle movement, i.e. the particle “sticks” on the auger. For example, for  $\beta = 15^\circ$   $V_e = 1.42 \text{ m/s}$  or  $\omega = 14.2 \text{ s}^{-1}$ . It can be seen from the graph  $V_b = V_b(s)$ , which was constructed by numerical method (see Fig. 4a).

It shows that at  $\beta = 15^\circ$  the velocity in the vertical direction is  $V_b = 0$ . However, at an angle  $\beta = -15^\circ$ , the velocity  $V_b$  increases become constant over time. But the particle does not move up, but down. This means that the winding direction of the auger has changed to the opposite. And the particle slides in the opposite side to the direction of its rotation and moves down. When the angle  $\beta$  increases to  $20^\circ$ , the particle moves down regardless of its sign. In Fig. 4a, the graph for  $\beta = 20^\circ$  is shown, for  $\beta = -20^\circ$  the graph is not constructed because its velocity of downwards movement increases significantly. Thus, at angles more significant than the limit value  $\beta = 15^\circ$ , the particle cannot move upwards at a constant angular velocity of rotation of the auger. The particle moves up at a smaller value (for example, at  $\beta = 10^\circ$ ). At a change in the sign of the angle  $\beta$ , it moves down. The graphs show that in all cases, the particle’s velocity becomes constant over time.



**Fig. 4.** Graphic illustrations to the motion of the particle at  $R = 0,1\text{ m}$ ,  $f_R = f = 0,3$ ,  $V_e = 1,42\text{ m/s}$ : a) graphs of the velocity of the particle movement in the vertical direction depending on the angle  $\beta$ ; b) particle trajectories at  $\beta = -10^\circ$  (downward motion); c) particle trajectories at  $\beta = 10^\circ$  (upward movement).

In Figs. 4b,c, relative trajectories were built by (11) at different values of the angle  $\beta$  (represented by thin lines). Thickened lines show absolute trajectories. They are constructed by Eqs. (11) when substituting in them instead of the angle  $\alpha = \alpha(s)$  the difference of the angles, at which the auger rotates around its axis ( $s/R$ ) and the particle during sliding on the auger ( $\alpha = \alpha(s)$ ), i.e.  $s/R - \alpha$ .

## 5 Conclusions

Frenet formulas were used in compiling the analytical dependencies of particle motion. As a result of the numerical solution of the equations, it was found that the velocity of particle rising is influenced by constructive and technological parameters. In particular, for a given radius  $R$  of the cylindrical casing, friction coefficients  $f$  and  $f_R$  and the angle  $\beta$  of rising of the helical line – the edge of the auger – there is a minimum value of the angular velocity  $\omega$  of its rotation. The particle, in this case, “sticks” and rotates together with the auger, describing in absolute motion a circle on the inner surface of the cylindrical casing. The obtained results allow the construction of a geometrical form of working bodies of machines according to the final necessary conditions.

## References

1. Konopatskiy, E., Voronova, O., Bezdityni, A., Shevchuk, O.: About one method of numeral decision of differential equalizations in partials using geometric interpolants. In: CPT2020 The 8th International Scientific Conference on Computing in Physics and Technology Proceedings (2020). [https://doi.org/10.30987/conferencearticle\\_5fce27708eb353.92843700](https://doi.org/10.30987/conferencearticle_5fce27708eb353.92843700)
2. Konopatskiy, E.: Solving differential equations by geometric modelling methods. In: GraphiCon 2018. 28th International Conference on Computer Graphics and Vision, pp. 358–361. TUSUR, Tomsk, Russian Federation (2018)
3. Konopatskiy, E.V., Bezdityni, A.A.: Geometric modeling of multifactor processes and phenomena by the multidimensional parabolic interpolation method. J. Phys. Conf. Ser. **1441**(1), 012063 (2020). <https://doi.org/10.1088/1742-6596/1441/1/012063>

4. Konopatskiy, E., Bezdityni, A., Shevchuk, O.: Modeling geometric varieties with given differential characteristics and its application. In: Proceedings of the 30th International Conference on Computer Graphics and Machine Vision (GraphiCon 2020), part 2, short31-1–short31-8 (2020). <https://doi.org/10.51130/graphicon-2020-2-4-31>
5. Konopatskiy, E., Bezdityni, A., Litvinov, A.: Geometric modeling of torse surfaces in BN-calculus. *J. Phys.: Conf. Ser.* **1791**, 012050 (2021). <https://doi.org/10.1088/1742-6596/1791/1/012050>
6. Kobets, A., Ponomarenko, N., Kobets, O., Tesliuk, H., Kharytonov, M., Yaropud, V.: Study of fertilizer spreader centrifugal type under field conditions. *INMATEH Agric. Eng.* **57**(1), 253–260 (2019)
7. Bulgakov, V., et al.: Theory of motion of grain mixture particle in the process of aspiration separation. *Agron. Res.* **18**(2), 1177–1188 (2020). <https://doi.org/10.15159/AR.20.069>
8. Bulgakov, V., et al.: Theory of grain mixture particle motion during aspiration separation. *Agron. Res.* **18**(1), 18–37 (2020). <https://doi.org/10.15159/ar.20.057>
9. Pylypaka, S., Klendii, M., Nesvidomin, V., Trokhaniak, V.: Particle motion over the edge of an inclined plane that performs axial movement in a vertical limiting cylinder. *Acta Polytechnica* **59**(1), 67–76 (2019). <https://doi.org/10.14311/AP.2019.59.0067>
10. Shrestha, K., Parajuli, P., Baral, B., Shrestha, B.: Mathematical modeling, simulation and analysis of rice grain movement for design and fabrication of low-cost winnowing machine. *J. Mech. Eng. Res.* **9**(1), 1–14 (2017). <https://doi.org/10.5897/JMER2016.0403>
11. Pavlenko, I., Ivanov, V., Gusak, O., Liaposhchenko, O., Sklabinskyi, V.: Parameter identification of technological equipment for ensuring the reliability of the vibration separation process. In: Knapcikova, L., Balog, M., Perakovic, D., Perisa, M. (eds.) 4th EAI International Conference on Management of Manufacturing Systems. EICC, pp. 261–272. Springer, Cham (2020). [https://doi.org/10.1007/978-3-030-34272-2\\_24](https://doi.org/10.1007/978-3-030-34272-2_24)
12. Liaposhchenko, O., Pavlenko, I., Monkova, K., Demianenko, M., Starynskyi, O.: Numerical simulation of aeroelastic interaction between gas-liquid flow and deformable elements in modular separation devices. In: Ivanov, V., et al. (eds.) DSMIE 2019. LNME, pp. 765–774. Springer, Cham (2020). [https://doi.org/10.1007/978-3-030-22365-6\\_76](https://doi.org/10.1007/978-3-030-22365-6_76)
13. Kozii, I.S., Plyatsuk, L.D., Hurets, L.L., Volnenko, A.A.: Capturing aerosol particles in a device with a regular pulsating nozzle. *J. Eng. Sci.* **8**(2), F1–F5 (2021). [https://doi.org/10.21272/jes.2021.8\(2\).f1](https://doi.org/10.21272/jes.2021.8(2).f1)
14. Pavlenko, I., Liaposhchenko, A., Ochowiak, M., Demyanenko, M.: Solving the stationary hydroaeroelasticity problem for dynamic deflection elements of separation devices. *Vib. Phys. Syst.* **29**, 2018026 (2018)
15. Loveikin, V., Romasevich, Y., Loveikin, O., Spodoba, A., Pochka, K.: Mathematical model of the dynamics change departure of the jib system manipulator with the simultaneous movement of its links. *Strength Mater. Theory Struct.* **104**, 175–190 (2020)
16. Pylypaka, S., Volina, T., Nesvidomin, V., Pavlov, A., Dranovska, S.: The possibility to apply the frenet trihedron and formulas for the complex movement of a point on a plane with the predefined plane displacement. *East.-Eur. J. Enterp. Technol.* **3**(7(111)), 45–50 (2021)
17. Tarelnyk, V., et al.: New sulphiding method for steel and cast iron parts. *IOP Conf. Ser. Mater. Sci. Eng.* **233**, 012049 (2017). <https://doi.org/10.1088/1757-899x/233/1/012049>
18. Tarelnyk, V., et al.: New method for strengthening surfaces of heat treated steel parts. *IOP Conf. Ser. Mater. Sci. Eng.* **233**, 012048 (2017). <https://doi.org/10.1088/1757-899x/233/1/012048>
19. Tarel'nik, V.B., Martsinkovskii, V.S., Zhukov, A.N.: Increase in the reliability and durability of metal impulse seals. *Chem. Pet. Eng.* **53**(5–6), 385–389 (2017). <https://doi.org/10.1007/s10556-017-0351-5>



20. Tarel'nik, V.B., Martsinkovskii, V.S., Zhukov, A.N.: Increase in the reliability and durability of metal impulse end seals. *Chem. Pet. Eng.* **53**(1–2), 114–120 (2017). <https://doi.org/10.1007/s10556-017-0305-y>
21. Konopatskiy, E., Mashtaler, S., Bezdityni, A.: Study of high-strength steel fiber concrete strength characteristics under the influence of elevated temperatures using mathematical modeling methods. *IOP Conf. Ser. Mater. Sci. Eng.* **687**, 022040 (2019). <https://doi.org/10.1088/1757-899X/687/2/022040>
22. Konopatskiy, E., Bezdityni, A.: Application of mixed geometric interpolants for modeling the strength characteristics of steel fiber concrete. *J. Phys. Conf. Ser.* **1546**, 012037 (2020). <https://doi.org/10.1088/1742-6596/1546/1/012037>
23. Konopatskiy, E., Bumaga, A., Bezdityni, A.: Geometric approach to finding the best possible solutions based on composition optimization of the mixed aggregate of fine-grained concrete. *Mater. Sci. Eng. Conf. Ser.* **962**, 032031 (2020). <https://doi.org/10.1088/1757-899X/962/3/032031>



# The Effect of Manufacturing Tolerances on the Hydrodynamic Characteristics of Plain Bearings

Yuliia Tarasevych<sup>1</sup>   and Ievgen Savchenko<sup>2</sup> 

<sup>1</sup> AGH University of Science and Technology, 30, al. Mickiewicza, 30-059 Krakow, Poland  
jtaras@agh.edu.pl

<sup>2</sup> Sumy State University, 2, Rymaskogo-Korsakova Street, Sumy 40007, Ukraine

**Abstract.** Plain bearing systems are widely used in rotor systems due to their efficiency, simplicity, long life, silent operation, low friction and wear, and in many cases, good heat dissipation. Despite the fact that a significant number of research have been published in the field of calculation and design of plain bearings, the proposed mathematical models and methods for calculating the characteristics do not consider the random changes of some geometric and operating parameters of these complex systems. The thickness of the lubricating film, which is one of the main operational parameters, is determined by the corresponding tolerances for the manufacturing of parts and assembly of the machine and a random variable. This work considers the effect of random changes in middle clearance and eccentricity values on pressure distribution based on the Reynolds equation. It is shown that the possible value of hydrodynamic force in such bearing can substantially differ from calculated under the deterministic models.

**Keywords:** Plain bearing · Random parameters · Mean value · Film thickness · Hydrodynamic pressure · Industrial growth · Process innovation

## 1 Introduction

The operational characteristics of rotary machines are largely determined by the hydrodynamic characteristics of the support and sealing units. The main requirement for seals is higher hermetic ability. Supporting units must meet a number of specific requirements, namely: sufficient bearing capacity under small dimensions, high vibration resistance in a wide range of operation of a rotary machine, minimal friction and wear of working surfaces, low consumption of cooling lubricant, the ability to use as a lubricant working environment, manufacturability and ease to use.

Modern rotor bearings of pumps and compressors are complex tribomechanical systems. Depending on the physical process of creating the required bearing capacity, these systems can be divided into rolling bearings, magnetic bearings, plain and thrust bearings. The use of rolling bearings as supports for high-speed rotors is limited by their extreme speed and durability. Therefore, in most rotary machines, plain bearings are

used to ensure the reliable operation of a rotary machine in a wide range of speeds and loads [1], or magnetic-fluid bearings.

In the process of operation, plain bearings are operated under different modes. When the shaft is stationary, the oil is squeezed out from the bottom part by the weight of the shaft with the parts mounted on it. Only a thin film on the surfaces of the sleeve and the shaft is while start-up and at the initial stage of operation (at low rotation speeds). This film is not able to completely separate the surfaces. During this period, the bearing operates in boundary lubrication mode. Under shaft rotation the liquid lubricant is involved into the cone gap formed between the sleeve and the shaft surfaces. It forms a lubricant layer and causes the shaft to float in this film. As the speed of rotation increases, the thickness of the lubricating layer increases. A hydrodynamic lubrication regime occurs where a lubricant completely separates the surfaces.

During the manufacturing process of parts, deviations from the nominal size are inevitable. Following the requirements of [2], the accuracy classes of the bearing are established. Bearing tolerances refer to three aspects of accuracy: dimensional accuracy, machining accuracy, and running accuracy. For dimensional accuracy, standard prescribe tolerances of external dimensions necessary when installing bearings on shafts or in housings. The dimensional deviation is the difference between an actual bearing dimension and the nominal (target) value. Machining accuracy reflects the precision of the manufacturing process and is a crucial aspect when recommending tolerances for shafts and housings. Running accuracy is defined as the allowable limits for the degree of eccentricity of the bearing (for radial runout). Tolerances and allowable error limits are established for each tolerance class.

The variety of used plain bearing designs has one feature in common: they are all non-standard machine elements under design and calculation. Additional experimental and theoretical studies are required in each specific case. One of the main advantages of water-lubricated plain bearings of shafts is their design simplicity and resulting relatively lower cost compared to expensive oil-lubricated bearings and some complex bearing units. But due to the low viscosity of the water, the thickness of the generated film rarely exceeds 10–12 mkm. So, the characteristics of such bearings are very sensitive to any changes in geometry. Moreover, possible misalignments of the working surfaces and their changes during operation are also random. Therefore, studying the probabilistic characteristics of the operational characteristics of sliding bearing is an urgent scientific and important practical task.

## 2 Literature Review

Despite the fact that a significant number of works have been published in the field of calculation and design of plain bearings, most of the developed mathematical models and the proposed methods are based on a deterministic approach without considering the fact that most of the geometric and operating parameters of these complex units are random. In the study [3], the simplified numerical approach to analyze the influence of macro geometric variations on the operation of a plain bearing is presented, and design experiments methodology is proposed to simulate the shape variation by the Monte-Carlo method. The authors studied the performances of the bearings as a function of

tolerance. Research works [4–6] present theoretical approaches, which allow predicting better system stiffness and damping characteristics of bearing supports. In the research [7], a theoretical analysis of the effects of the manufacturing tolerances on the system's stability is provided. The effects of the dynamic viscosity variation caused by the temperature change, the manufacturing tolerances of the bearing length, and the diameters of both the bearing and the journal are investigated using the Taguchi method. Bearing characteristics are calculated considering dimensional tolerance using optimum design combined with the statistical method in which the dimensional tolerance is assumed to distribute according to the Gaussian distribution [8]. The results of this robust optimum design compared with ones of optimum design neglecting tolerance and the validity of this technique were clarified. An analytical method to calculate the effects of surface roughness of bearing inner surface is presented in [9]. The bearing surface roughness was simulated by linear superposition of waviness using Fourier Transforms. Surfaces with a sinusoidal wave and a single Gaussian dent were analyzed and compared, and a good agreement was obtained. It is well-known that several research focuses on the effect of random surface texturing and wear. A numerical simulation of cylindrical texture shape effect on a hydrodynamic journal bearing characteristics is given in [10]. Lee et al. [11] analyzed the influence of the waviness errors of a hydrostatic journal bearing and revealed that the load-carrying capacity varied according to the amplitude and phase angle of the waviness functions. The significant influence of the directional orientation of the surface roughness on the Rayleigh step-bearing operation is shown in [12]. Theoretical and experimental investigations of plain bearing in both laminar and turbulent regimes using the semianalytical finite element method for different wear depth parameters are developed [13]. The effect of change in geometrical parameters of bearing due to wear on pressure distribution is shown. The effect of manufacturing errors on the overall minimum oil film thickness under various rotational speeds of tilting-pad bearings is investigated [14]. Some interesting experimental data are given in [15, 16]. It is shown that the deviation in the data created by manufacturing tolerances in assessing the instability of the lubrication film can reach  $\pm 20\%$ , depending on the stable operating position. Analysis of the impact of the random change of gap value and eccentricity on bearing load capacity is carried out on the simplified theoretical model in [17]. The presented model does not consider the precession motion and possible oscillations of the shaft axis. However, most works devoted to the influence of random parameters on the plain bearing operation have used complex models, the application of which in practice is quite difficult and requires the use of specific methods or programs. The purpose of the presented work is to develop an easy-use in engineering practice method for predicting the effect of manufacturing tolerances on pressure distribution and hydrodynamic force value of plain bearings.

### 3 Research Methodology

Considered calculation model of a plain bearing is shown on Fig. 1. The inner surface (shaft journal) rotates with angular speed  $\omega$  and its center  $O_1$ , due to dynamic loads, also describes translational motions within the bearing clearance  $h$  with frequency  $\Omega$ . The axis of the shaft journal describes circular centered orbits with an amplitude or

radius  $e$ . The other surface or housing is stationary in most applications. So, the radial and circumferential velocity components on the housing surface are equal to zero. Boundary conditions for velocities with considering a small displacement of the shaft journal relative to the equilibrium position in the housing and possible radial oscillations can be written in the form

$$\begin{aligned}
 u(0) = v(0) = w(0) = 0, w(h) = 0, \\
 u(h) = \omega r + (\Omega e \cos\varphi - \dot{e} \sin\varphi), \\
 v(h) = (\Omega - \omega) e \sin\varphi - \dot{e} \cos\varphi,
 \end{aligned}
 \tag{1}$$

where  $H = R - r \cos\gamma - e \cos(\pi - \varphi)$ . From Fig. 1.  $\cos\gamma_{max} = 1$ , so  $h = R - r + e \cos\varphi$ .

The following assumptions were accepted to solve the problem in the first approximation. The lubricating fluid is incompressible, i.e., “ $\rho = \text{const}$ ,”  $\partial p/\partial t = 0$ , and the flow is steady and isothermal.

The hydrodynamic pressures  $p(x,z)$  in the bearing clearance can be obtained by integrating the generalized Reynolds equation taking into account the boundary conditions for velocities (1), which has the form:

$$\frac{\partial}{\partial x} \left( h^3 \frac{\partial p}{\partial x} \right) + \frac{\partial}{\partial z} \left( h^3 \frac{\partial p}{\partial z} \right) = 6\mu \left( u(h) \frac{\partial h}{\partial x} + h \frac{\partial u(h)}{\partial x} \right) - 12\mu v(h).
 \tag{2}$$

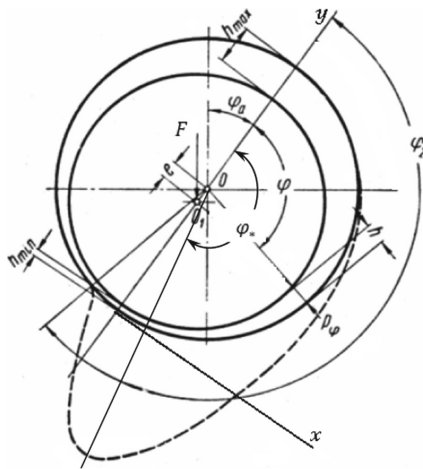


Fig. 1. Calculation model of a plain bearing.

This equation expresses the equilibrium of a viscous fluid located between two surfaces with a small clearance  $h$  ( $\varphi$ ) between them. From Eq. (2), it can be seen that for the appearance of the bearing capacity of the lubricating layer, the presence of a sliding

speed and a narrowing of the lubricating layer is necessary, i.e.,  $dh/dx$  must be less than zero for the arising the proper pressure.

Since the changes in the fluid flow characteristics in the axial direction (along the Oz axis) are much less than their changes in the circumferential direction, the second term in Eq. (1) can also be neglected. Taking into account the accepted assumptions.

The further solution of the problem will be carried out in a moving coordinate system, one of the axes of which passes through the line of centers  $OO_1$  (Fig. 1).

$$\frac{\partial}{\partial x} \left( h^3 \frac{\partial p}{\partial x} \right) = A(\mu, \omega, \Omega, e) + B(\mu, \omega, \dot{e}) + D(\mu, \Omega, e, \dot{e}), \tag{3}$$

where

$$A(\mu, \omega, \Omega, e) = 12\mu \left( \frac{\omega}{2} - \Omega \left( 1 + \frac{H}{2r} \right) \right) e \sin\varphi, \quad B(\mu, \dot{e}) = -12\mu \left( 1 + \frac{H}{2r} \right) \dot{e} \cos\varphi,$$

$$D(\mu, \Omega, e, \dot{e}) = -6\mu \frac{\Omega e^2}{r} \sin 2\varphi - 6\mu \frac{e \dot{e}}{r}.$$

Component  $D(\mu, \Omega, e, \dot{e})$  describes the effect of non-linear components on pressure distribution in the film of a plain bearing. To ensure a hydrodynamic lubrication regime, keeping the minimum amount of lubrication between the sliding surfaces is necessary. Bearing capacity (hydrodynamic force) in a plain bearing occurs only in the area of some clearance values and at certain speeds of rotation and precession of the shaft relative to the stationary axis of the housing. According to (3), if the axis of the shaft journal rotates along circular orbits with a fixed radius  $e$  ( $\dot{e} = 0$ ) than under the frequency of whirl equals 50% of the rotational speed  $\Omega = 0.5\omega$  the right side of Eq. (3) is null, and hence there is no generation of hydrodynamic pressure. Thus, it can result in a sudden loss of bearing support capability.

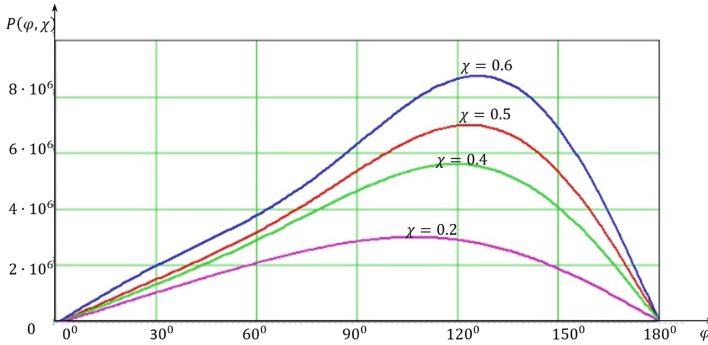
Passing to the cylindrical coordinate  $x = r\varphi$  and after integration

$$p(r, \varphi) = \int \frac{1}{h^3} \left( \int A(\mu, \omega, \Omega, e) + B(\mu, \omega, \dot{e}) + D(\mu, \Omega, e, \dot{e}) r d\varphi + C_1 \right) r d\varphi + C_2.$$

where  $C_1, C_2$  – unknown constants, it can be obtained

$$p(r, \varphi) = -12\mu \frac{r^2}{H^3} \left( \frac{\omega}{2} - \Omega \left( 1 + \frac{H}{2r} \right) \right) e \sin\varphi - 12\mu \frac{r^2}{H^3} \left( 1 + \frac{H}{2r} \right) \dot{e} \cos\varphi + \frac{C_1 r}{H^3} \left( \varphi - 3 \frac{e}{H} \sin\varphi \right) + C_2 + O(\mu, \omega, \Omega, e, \dot{e}). \tag{4}$$

$O(\mu, \omega, \Omega, e, \dot{e})$  describes the effect of non-linear components on pressure distribution in film of a plain bearing. The constants  $C_1, C_2$  can be determined from the condition: for  $p|_{\varphi=0} = p|_{\varphi=2\pi} = p_a$  and accordingly  $\left. \frac{\partial p}{\partial x} \right|_{h_*} = 0$ . In Fig. 2, the pressure distribution is shown for different values of the relative eccentricity  $\chi = e/H$ . The bearing capacity increases with increasing eccentricity  $e$ , and the line of the maximum pressure value is shifted towards the minimum clearance.



**Fig. 2.** Pressure distribution in the angular direction in a plain bearing.

The position of the journal inside the housing and the hydrodynamic pressure distribution is characterized by the following angles (Fig. 1):  $\varphi_a$  is the angle of rotation of the centerline  $OO_1$ , which characterizes the position of the shaft axis relative to the housing (stationary) axis ( $\varphi_{amin} = 0, \varphi_{amax} = \frac{\pi}{2}$ );  $\varphi_1$  is the angle where the bearing zone (hydrodynamic wedge) starts,  $\varphi_2$  is the angle where the bearing zone of the lubricating film ends and  $\varphi_*$  is the angle characterizing the position of the maximum hydrodynamic pressure. As a first approximation for  $\varphi_a$ , some of the authors suggest taking:

$$\varphi_a = \arccos(\chi). \tag{5}$$

In this case, the position of the beginning of the carrier zone:  $\varphi_1 = \frac{\pi}{2} - \arccos(\frac{e}{H})$ .

According to another research, the angel  $\varphi_a$  can be determined by the formula:

$$\varphi_a = \arctg\left(\frac{\pi\sqrt{(1-\chi^2)}}{4\chi}\right). \tag{6}$$

Approaches (5) and (6) generally correspond well for  $0 < \chi < 0.55$ , but for higher values of  $\chi$  the approach (6) is preferred.

Several hypotheses have recently been used to determine the position of the end of the bearing zone in fluid plain bearings [7, 9]. In many works, it is assumed that the lubricating layer ends (breaks off) in the section of the minimum clearance. According to another hypothesis, the hydrodynamic wedge breaks off beyond the section of the minimum gap. In this section  $p = 0$  and  $p|_{h=h_{min}} \approx \frac{1}{2}p_{max}$ , and the cross-section itself is located symmetrically to the maximum pressure relative to the line of centers (Fig. 1). When calculating the dependencies in Fig. 2, the first hypothesis is accepted. But according to the obtained results, the calculation based on the second hypothesis is needed to compare the correctness of both with experimental data.

In practice,  $H$  is a random variable, the measurement limits of which depend on the accepted tolerances. The normal distribution law is usually used for dimensions with two-sided tolerances, so  $H$  can be assumed to obey the normal distribution law. As a mean value of this parameter can be taken, it's calculated (designed) value. The mean clearance's actual (real) value deviates from its design value due to the landing chosen

for the bearing and can be commensurable with the clearance value itself. For instance, for a shaft diameter of 140 mm and for one of the recommended landings of H7/c8, its tolerance is 0.103 mm. The radial clearance is caused by the deviations in the dimensions of the shaft and housing (sleeve) can vary from 0.1 to 0.15 mm.

The random variables  $H, e$  are independent. Therefore, the joint probability density can be written in the form  $f_3(H, e) = f_2(H)f_1(e)$ . For eccentricity, all directions are equally possible, and due to physical properties, this random variable can take only positive values, so for its description, the truncated Rayleigh law can be used:  $f_1(e) = \frac{Ce}{\sigma_e} \exp\left[-\frac{e^2}{2\sigma_e^2}\right]$ , where the constant C is determined from the normalization condition for the probability density:  $C = \left(1 - \exp\left[-\frac{H^2}{2\sigma_e^2}\right]\right)^{-1}$ . Since the probability that the eccentricity takes values close to zero and close to H is equally small, it can be assumed:  $\sigma_e = 0,36H$ ,  $\sigma_e$  - is the standard deviation of the eccentricity. So,  $f_1(e) = \frac{7,88e}{H^2} \exp\left[-\frac{3,858e^2}{H^2}\right]$ .

Based on the foregoing, the values of the bearing zone's initial and final position angles are random values. Probability density  $\varphi_a$  for (5):

$$f_{4.1}(\varphi_a) = \int_{H_{min}}^{H_{max}} \frac{1}{\sqrt{2\pi}\sigma_H} \exp\left[-\frac{(H - H)^2}{2\sigma_H^2}\right] \frac{7,886}{2H} \sin(2\varphi_a) \exp\left[-3,858\cos^2(\varphi_a)dH\right].$$

Probability density  $\varphi_a$  for (6):

$$f_{4.2}(\varphi_a) = \int_{H_{min}}^{H_{max}} \frac{1}{\sqrt{2\pi}\sigma_H} \exp\left[-\frac{(H - H)^2}{2\sigma_H^2}\right] \frac{7,886}{H^2} \frac{32\pi^4 \operatorname{tg}(\varphi) (\operatorname{tg}^2(\varphi) + 1)}{(\operatorname{tg}^2(\varphi) - \pi^2)^3} \exp\left[-3,858\cos^2(\varphi_a)dH\right].$$

where  $\langle H \rangle$  - is the mean value of mean clearance  $\sigma_H$ , - is the standard deviation of mean clearance, respectively.

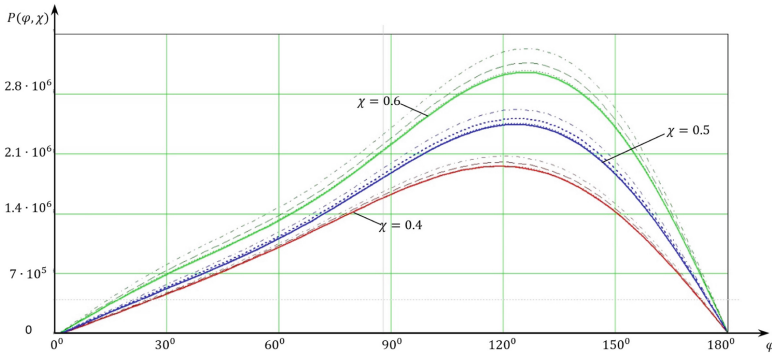
For a half bearing in the eccentricity range  $\chi < 0.5$ , the section in which the hydrodynamic pressure ends:  $\varphi_2 = \pi + \varphi_1$ . Therefore, for such bearings and small eccentricity values, the probabilistic characteristics of the initial angle of hydrodynamic pressure arising determine the probabilistic characteristics of the final angle with a shift  $\pi$ .

## 4 Results

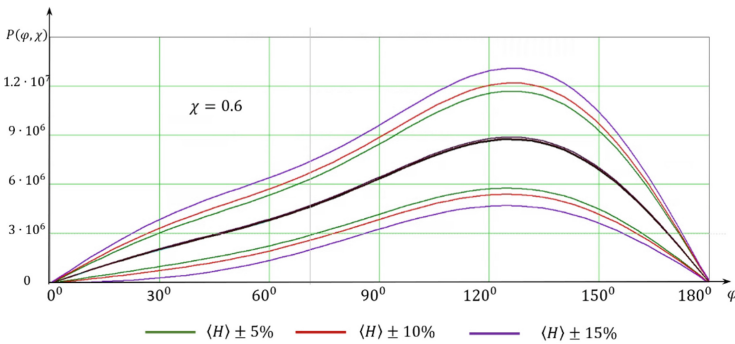
In Fig. 3, the effect of the random changes of middle clearance value on circumferential pressure distribution is presented. Continuous lines describe the deterministic value of hydrodynamic pressure in plain bearing for different values of eccentricity  $\chi$ . Dotted lines present the mean value of the pressure under the normal distribution of the median clearance value in a range  $\langle H \rangle \pm 10\%$ . Dashed lines present the mean value of the pressure under the normal distribution of the median clearance value in the range  $\langle H \rangle \pm 20\%$ , and dash-dotted - in range  $\langle H \rangle \pm 30\%$ .

According to the accepted model, pressure values are the normally distributed values too. The deviations of maximum pressure values from the deterministic ones are up to 33.4% under  $\langle H \rangle \pm 5\%$ , up to 38% under  $\langle H \rangle \pm 10\%$  and up to 49% under  $\langle H \rangle \pm 5\%$ . Under such conditions, the maximum pressure position varies within 3–5°.





**Fig. 3.** Mean value of pressure along the circumference in a plain bearing ( $H$  is a normally distributed value).



**Fig. 4.** Possible variations of pressure values along the circumference in a plain bearing ( $H$  is a normally distributed value).

The main characteristics of the bearing operation are volume flow of the lubricant, the power loss due to friction, bearing capacity.

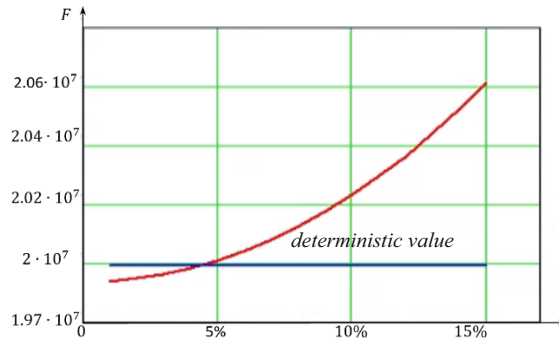
Once the pressure field is obtained, fluid film forces acting on the journal surface can be calculated by integrating the pressure field  $p(r, \varphi)$  (3). An equal opposing force acts on the bearing as well. The bearing reaction forces are expressed in the moving coordinate system as

$$F_r = \int_0^L \int_0^{\varphi_2} p(r, \varphi) \cos \varphi r d\varphi dz, F_t = \int_0^L \int_0^{\varphi} p(r, \varphi) \sin \varphi r d\varphi dz$$

The components of fluid film forces in a fixed coordinate system can be obtained by

$$\begin{bmatrix} F_X \\ F_Y \end{bmatrix} = \begin{bmatrix} \cos \varphi_a & -\sin \varphi_a \\ \sin \varphi_a & \cos \varphi_a \end{bmatrix} \begin{bmatrix} F_r \\ F_t \end{bmatrix}$$

Figure 5 shows the change in the mean value of the hydrodynamic force in a long-length plain bearing depending on the change in the standard deviation of the mean



**Fig. 5.** Mean value of hydrodynamic force in a plain bearing.

clearance value  $H$ . As follows from the studies conducted, the interval of possible radial force values increases as the range of permissible values of  $H$  increases.

## 5 Conclusions

Pressure distribution in circumferential direction and position of the fluid whirl zone with considering manufacturing tolerances for median clearance value and random changes in the eccentricity value is studied by means of solving the Reynolds equation. The main conclusions can be summarized as follows:

- the tolerances of plain bearing diameters have a significant effect on the pressure distribution as well as hydrodynamic restore force and the position of the beginning and the end of the lubrication whirl;
- as the value of the standard deviation of the mean clearance in a plain bearing increases, the actual value of the radial force can differ significantly from the calculated one. For example, with a standard deviation value of 15% of the mean value, the possible deviation of the radial force can differ by up to 49%;
- under further research, it should be considered that hydrodynamic characteristics of a plain bearing are very sensitive to errors in surfaces shape and shaft alignment.


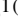




## References

1. Chalabi, M.A., Basova, Y., Hamidou, M.K., Dobrotvorskiy, S.: Analysis of the three-dimensional accelerating flow in a mixed turbine rotor. *J. Eng. Sci.* **8**(2), D1–D7 (2021). [https://doi.org/10.21272/jes.2021.8\(2\).d2](https://doi.org/10.21272/jes.2021.8(2).d2)
2. ISO 12129-1:2019. Plain bearings - Tolerances - Part 1: Fits (2019)
3. Di Gironimo, G., Lanzotti, A., Patalano, S., Russo, R.: Tolerance design of the journal-bearing kinematic joint. Numerical analysis of the effect of the shape variations on the performances. In: Marjanovic, D. (ed.) *DS 30: Proceedings of DESIGN 2002, the 7th International Design Conference*, pp. 1145–1152. Dubrovnik (2002)

4. Xu, W.B., Ogrodnik, P.J., Goodwin, M.J., Bancroft, G.: Effect of manufacturing tolerances on stiffness and damping of hydrodynamic journal bearings. *Adv. Mater. Res.* **139–141**, 2662–2667 (2010). <https://doi.org/10.4028/www.scientific.net/amr.139-141.2662>
5. Pavlenko, I., Simonovskiy, V., Ivanov, V., Zajac, J., Pitel, J.: Application of artificial neural network for identification of bearing stiffness characteristics in rotor dynamics analysis. In: Ivanov, V., et al. (eds.) *DSMIE 2018. LNME*, pp. 325–335. Springer, Cham (2019). [https://doi.org/10.1007/978-3-319-93587-4\\_34](https://doi.org/10.1007/978-3-319-93587-4_34)
6. Pavlenko, I., Trojanowska, J., Ivanov, V., Liaposhchenko, O.: Scientific and methodological approach for the identification of mathematical models of mechanical systems by using artificial neural networks. In: Machado, J., Soares, F., Veiga, G. (eds.) *HELIX 2018. LNEE*, vol. 505, pp. 299–306. Springer, Cham (2019). [https://doi.org/10.1007/978-3-319-91334-6\\_41](https://doi.org/10.1007/978-3-319-91334-6_41)
7. Wang, B., Zhou, J., Xu, M.: Effects of journal roundness phase and amplitude on lubrication of engine bearings with consideration of straightness. *SAE Int. J. Passenger Cars Mech. Syst.* **10**(2), 465–473 (2017)
8. Hashimoto, H., Ochiai, M., Sunami, Y.: Robust optimum design of fluid dynamic bearing for hard disk drive spindle motors. *ASME. J. Tribol.* **134**(4) (2012). <https://doi.org/10.1115/1.4007246>
9. Quinonez, F.A., Morales-Espejel, G.E.: Surface roughness effects in hydrodynamic bearings. *Tribol. Int.* **98**, 212–219 (2016)
10. Tala-Ighil, N., Fillon, M., Maspeyrot, P.: Effect of textured area on the performances of a hydrodynamic journal bearing. *Tribol. Int.* **44**, 211–219 (2011)
11. Lee, S.M., Lee, D.W., Ha, Y.H., Lee, S.J., Hwang, J.H., Choi, Y.H.: A study on the influence of waviness error to a hydrostatic bearing for a crankshaft pin turner. *Tribol. Trans.* **56**, 1077–1086 (2013)
12. Kumar, R., Azam, M.S., Ghosh, S.K.: Influence of stochastic roughness on performance of a Rayleigh step bearing operating under thermo-elastohydrodynamic lubrication considering shear flow factor. *Tribol. Int.* **134**, 264–280 (2019)
13. Hashimoto, H., Wada, S., Nojima, K.: Performance characteristics of worn journal bearings in both laminar and turbulent regimes Part I: steady-state characteristics. *ASLE Trans.* **29**, 565–571 (1986)
14. Dang, P.V., Chatterton, S., Pennacchi, P., Vania, A.: Numerical investigation of the effect of manufacturing errors in pads on the behaviour of tilting-pad journal bearings. *J. Eng. Tribol.* **232**(4), 480–500 (2018). <https://doi.org/10.1177/1350650117721118>
15. Hassan, E., Rasheed, E.: Effect of surface waviness on the hydrodynamic lubrication of a plain cylindrical sliding element Bering. *Wear* **223**, 1–6 (1998)
16. Ogrodnik, P.J., Xu, W., Goodwin, M.J., Bancroft, G.A.: The effects of dimensional manufacturing tolerances on stability of a symmetric hydrodynamic journal bearing rotor system – an experimental investigation. *Proc. Inst. Mech. Eng. Part I J. Eng. Tribol.* **225**(12), 1152–1158 (2011). <https://doi.org/10.1177/1350650111414627>
17. Tarasevych, Y., Savchenko, I., Sovenko, N.: Influence of technological deviations on the basic operational characteristics of hydrodynamic bearings. *IOP Conf. Ser. Mater. Sci. Eng.* **233**, 1–5 (2017)



# Reducing Working Fluid Pulsations in Planetary Hydraulic Machines by Rational Design of the Distribution Systems

Oksana Yeremenko<sup>1</sup>  , Mamadamon A. Abdullo<sup>2</sup> , Nataliia Boltianska<sup>1</sup> ,  
Stepan Mikhalchenko<sup>3</sup> , and Valentyna Verkhohantseva<sup>1</sup> 

<sup>1</sup> Dmytro Motorny Tavria State Agrotechnological University, 18, B. Khmelnytsky Avenue, Melitopol 72310, Ukraine

tia\_tgatu@ukr.net

<sup>2</sup> Tajik Technical University named after academician M. Osimi, 10, Academicians Rajabov's Avenue, Dushanbe 734042, Tajikistan

<sup>3</sup> State Biotechnological University, 44, Alchevskih Street, Kharkiv 61002, Ukraine

**Abstract.** The work studied the influence of changing the throughput of distribution systems on the output characteristics of planetary hydraulic machines to ensure their stabilization at the design stages. A design scheme a mathematical apparatus have been developed, and the initial data have been substantiated, which make it possible to study the effect of changing the geometric parameters of the distribution system on the pulsation of its flow area. The pulsation coefficients of the distribution system throughput and the rotational speed of the hydraulic motor shaft, the pressure of the working fluid, and the torque on the hydraulic motor shaft have been investigated. The starting conditions for the design of distribution systems are substantiated, which exclude pulsations of the working fluid in planetary hydraulic machines for kinematic schemes 5/4, 7/6, 9/8, 11/10, and 13/12. The angular gap between the distribution windows was taken as 0°, 0°25'30'', and 0°51''. The number of additional unloading windows in the distribution system was taken as 0, 2, 3, and 4.

**Keywords:** Energy efficiency · Ripple coefficient · Output characteristics · Flow area · Stabilization · Output parameters · Industrial growth

## 1 Introduction

The hydraulic drive is widely used on construction, road, municipal, agricultural, forestry, and other self-propelled machines. In the hydraulic drives of the working bodies and the running systems of these machines, planetary (orbital) hydraulic motors are increasingly used [1], which make it possible to provide a gearless connection of these hydraulic motors directly to the actuators [2].

Planetary hydraulic motors, despite their numerous advantages, have some disadvantages, one of which is the imperfection of their distribution system [3], as a result of

which the hydraulic motor becomes a source of pulsation of the working fluid [4], causing unsatisfactory operation of the entire hydraulic drive [5]. The emergence of these disadvantages is associated with the lack of comprehensive studies describing the effect of changing the throughput of distribution systems on the output characteristics of planetary hydraulic machines. Carrying out such studies will make it possible to develop the necessary recommendations for calculating the geometric parameters of the distribution systems of planetary hydraulic machines to ensure their stabilization even at the design stages.

In this regard, the issue of increasing the reliability of construction, agricultural and communal machines by stabilizing the output characteristics of planetary hydraulic motors used in hydraulic drives of active working bodies and running systems of self-propelled equipment is an urgent problem. Therefore, this paper sets out the solution of issues related to the study of changing the throughput of distribution systems on the output characteristics of planetary hydraulic machines to ensure their stabilization at the design stages.

## 2 Literature Review

The main parameters were determined [6], numerical and experimental studies of the pump-turbine operation were carried out [7], the dynamic response of pumping turbines [8] was investigated, and the flow rate of centrifugal [9] and gear [10] hydraulic machines were analyzed. The geometrical parameters of the flow path of vortex-chamber pumps have been optimized [11], the operating ranges of the vortex-chamber blower have been determined when pumping Bingham liquids [12], and the characteristics of rational regulation of the composition of the fuel-air mixture have been determined [13]. The flow of a swirling jet through a confuser [14] and an internal flow in bidirectional channels of a cubic type of an axial flow system were investigated by the method of numerical simulation and experiment [15]. The output characteristics of the labyrinth screw pump are improved by improving its flow path [16–18], a numerical calculation and experiment on pressure fluctuations in an axial flow pump [19] are presented. A review of technologies in hydraulic machines showed [1] that, at present, there is not enough literature on the design and manufacture of gerotor pumps and orbital engines.

A universal model of a mechatronic system with an orbital-type hydraulic motor is considered [5], and hydrodynamic analysis of gerotor pumps [20]. The dynamics of change in the output characteristics of a planetary hydraulic motor are investigated considering the design features of the rotor system [21] and the distribution system [22]. Experimental studies of changes in the output characteristics of a planetary hydraulic motor depending on the design features of the rotor system were carried out. [23] and the distribution system [24], regression equations were obtained that adequately describe the change in the output characteristics of a planetary hydraulic motor [25]. A technique for designing mechatronic systems with specified output characteristics based on planetary hydraulic motors has been developed [26]. The design of the elements of the rotor system and the distribution systems of the planetary hydraulic machines was not considered.

An approach was proposed for predicting aeration and cavitation in gerotor pumps [27], cavitation was assessed for the effective flow rate of axial piston hydraulic machines

[28], and the reasons for the occurrence of cavitation phenomena in the distribution zone were substantiated [29]. A kinematic diagram of the movement of rotors of an orbital hydraulic motor [30] has been developed, an optimal tooth profile for cycloidal gears [31], and methods for increasing load capacity [32, 33] have been proposed. Research of wear of working surfaces of rotors of orbital hydromotors is carried out [34]. Methods for determining the vibration reliability by simulating changes in the technical state of rotors were implemented in [35, 36], which particularly were carried out by simulating oscillations of the diametral gap. Issues related to the distribution of the working fluid have not been investigated.

Mathematical and physical models have been developed [37], allowing to simulate the processes occurring in distribution systems, kinematic schemes have been substantiated [4]. The influence of the shape of the distribution windows, in the form of a segment [3], a groove [38], and a circle [39] on the output characteristics of a planetary hydraulic motor, has been studied, a comparison of the windows [40], the angular arrangement of the distribution windows [41] has been substantiated. Also, ways for increasing load capacity have been proposed in [42, 43].

However, the influence of the gap between the distribution windows on the throughput of the planetary hydraulic motor has not been investigated.

A review of manufacturing technologies for gerotor hydraulic machines revealed [1] a lack of literature on the design, calculation, manufacture, and operation of hydraulic machines of this type. It should be noted that if some information can still be found about gerotor pumps, then there is practically no research concerning orbital and planetary hydraulic motors. It should also be noted that the issue of reducing the pulsation of the working fluid in planetary hydraulic machines to increase the reliability of hydraulic drives of self-propelled equipment as a whole remains unresolved. Therefore, theoretical studies of the effect of changing the kinematic, geometric, and functional parameters on reducing the pulsation of the working fluid and stabilizing the output characteristics of planetary hydraulic machines at the design stages is an urgent task.

### 3 Research Methodology

To address issues related to the study of the effect of changing the throughput of distribution systems on the stabilization of the output characteristics of planetary hydraulic machines at the stages of their design, it is necessary:

- to develop a calculation scheme, a mathematical apparatus and substantiate the initial data, allowing to study the effect of changing the geometric parameters of the distribution system from the pulsation of its flow area, depending on the kinematic scheme, the angular gap between the distribution windows and the number of additional windows;
- to investigate the influence of the kinematic diagram of the distribution system, the angular gap between the distribution windows, and the number of additional windows on the changes in the pulsation coefficients of the working fluid flow by simulating the working processes occurring in the working fluid distribution systems;
- to substantiate the starting conditions for the design of distribution systems, allowing to exclude pulsations of the working fluid in planetary hydraulic machines.

Oscillatory processes, which include fluctuations in the flow of the working fluid in the channels of the distribution system, arising during the operation of positive displacement hydraulic machines, are one of the negative factors [4]. Therefore, the distribution system of a planetary hydraulic motor can be considered as a possible source (generator) of fluctuations in the flow of the working fluid, affecting the stability of the output characteristics of the hydraulic drive as a whole.

The developed scheme of the volumetric arrangement of the distribution windows (Fig. 1a) made it possible to visually trace the possible overlapping of the distributor windows during the operation of the planetary hydraulic motor and develop a design scheme (Fig. 1b) to determine the current value of the area  $A_i(t)$  of the flow area. The pulsation of the working fluid flow in the hydraulic motor is caused by fluctuations in the area  $A_i(t)$  of the flow area, expressed by the difference between  $A_{\max}(t)$  and  $A_{\min}(t)$  described in work [3]. Depending on the kinematic diagram [4], overall dimensions and angular clearance  $\Delta$  between the distribution windows, the flow area  $A_i(t)$  of the distribution system at any time is determined by the expression:

$$A_i(t) = \sum_{i=1}^{Z_2} \left( \frac{\pi}{Z_2} - \Delta - |\beta_i - \alpha_i(t)| \right) \cdot \frac{(R_2^2 - R_1^2)}{2}, \quad (1)$$

where  $\alpha_i(t)$  and  $\beta_i$  are the angular position of the windows of the movable and fixed distributors, respectively;  $Z_2$  - number of fixed distributor windows;  $R_1$  and  $R_2$  are the inner and outer radii of the distribution windows, respectively.

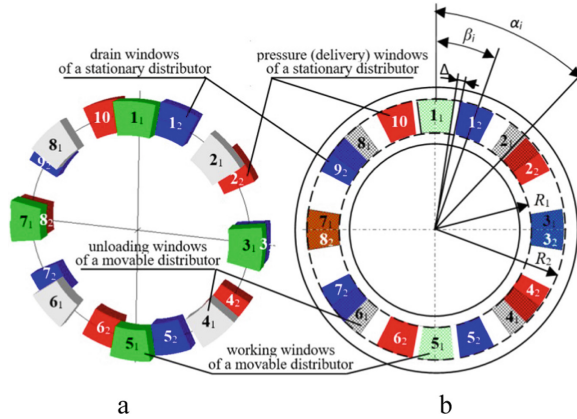
Analysis of Eq. (1) shows that, depending on the listed parameters, the flow area  $A_i(t)$  of the distribution system of the planetary hydraulic motor can vary over a wide range. When studying the effect of changing the throughput of distribution systems on changing the output characteristics of a planetary hydraulic motor to ensure their stabilization, the parameter describing the relative changes in the area fluctuation  $A_i(t)$  is substantiated - the pulsation coefficient.

Based on the research data [4], the pulsation coefficients of the throughput  $R_A(t)$  of the distribution system and the rotational speed  $R_n(t)$  of the hydraulic motor shaft (2), the pressure  $R_p(t)$  of the working fluid and the torque  $R_M(t)$  on the hydraulic motor shaft are substantiated and described (3):

$$R_A(t) = R_n(t) = \frac{2 \cdot (A_{\max}(t) - A_{\min}(t))}{A_{\max}(t) + A_{\min}(t)} 100\%; \quad (2)$$

$$R_p(t) = R_M(t) = \frac{2 \cdot \left( \frac{1}{A_{\min}^2(t)} - \frac{1}{A_{\max}^2(t)} \right)}{\left( \frac{1}{A_{\max}^2(t)} - \frac{1}{A_{\min}^2(t)} \right)} 100\%. \quad (3)$$

Analysis of expressions (2), (3) shows that the main influence on the value of the pulsation of the flow of the working fluid, generated by the distribution system of the planetary hydraulic motor, is exerted by fluctuations in the area of its flow section. Analysis of expression (1) shows that the change (fluctuation) in the flow area of the distribution system depends on its kinematic scheme, determined by the number of windows  $Z_2$  of the fixed distributor.



**Fig. 1.** Overlapping (alignment) of the windows of the movable and fixed distributors during the operation of the planetary hydraulic motor: a – the scheme of the volumetric arrangement of the distributing windows; b – design scheme.

The angular gap  $\Delta$  between the distribution windows of the movable and fixed distributors has a significant effect on the change (fluctuation) of the flow area. The overall dimensions of the distribution system, due to the inner  $R_1$  and outer  $R_2$  radii, limiting the location of the distribution windows, do not cause fluctuations in the flow area but only change its absolute value.

## 4 Results

Studies of the influence of the kinematic diagram, angular clearance, and the number of additional windows on changes in the pulsation coefficients of the working fluid flow were carried out by simulating the working processes occurring in the distribution systems of planetary hydraulic machines using the VisSim application package. Considering the research [24], the following initial conditions were adopted and justified:

- the geometric (angular) parameters of the opening of the distribution windows of the movable and fixed distributors are equal;
- the inner  $R_1$  and outer  $R_2$  radii of the distribution windows are equal to  $R_1 = 29$  mm,  $R_2 = 43$  mm and did not change during the research;
- the maximum angular gap  $\Delta$  between the windows of the movable and stationary distributors, taking into account the studies [24], is equal to  $\Delta = 0^\circ 51'$ , the minimum is  $\Delta = 0^\circ$ , the intermediate value of the angular gap is  $\Delta = 0^\circ 25' 30''$ , the negative value of the angular gap (window overlap) was not considered in the studies because this is due to the overflow of the working fluid (volumetric losses);
- in the study, taking into account the data [41], five frequently used kinematic schemes of distribution systems of planetary hydraulic motors were considered: 5/4; 7/6; 9/8; 11/10, and 13/12;
- the number of used additional unloading windows of the movable distributor, from design considerations and considering the data [41], it was taken: 0, 2, 3, and 4.



The research results are presented by dependencies (Fig. 2) changes in the pulsation coefficients of the throughput, the speed of the hydraulic motor shaft (curves 1), the pressure of the working fluid, and the torque (curves 2). The analysis of the results obtained showed that incorrect design of the distribution system of the planetary hydraulic motor turns it into a source (generator) of pulsations of the working fluid. The change in the pulsation coefficients is caused by three parameters of the distribution system: the kinematic diagram, the angular gap between the distribution windows, and the number of used additional unloading windows of the movable distributor. It was found that the correct variation of these parameters makes it possible to eliminate the pulsation of the working fluid or bring its value closer to zero.

Based on the results (Fig. 2) of the studies carried out, recommendations have been developed for designers of distribution systems of planetary hydraulic machines, which allow designing a hydraulic motor with a given kinematic diagram. The design of distribution systems, using the developed recommendations, will eliminate (or bring to zero) the pulsation of the working fluid.

Consequently, such a design ensures the stabilization of the output characteristics of the planetary hydraulic motor and the hydraulic drive as a whole. The design of the hydraulic motor distribution system begins with the selection (justification) of the kinematic scheme. Therefore, recommendations were made for each scheme.

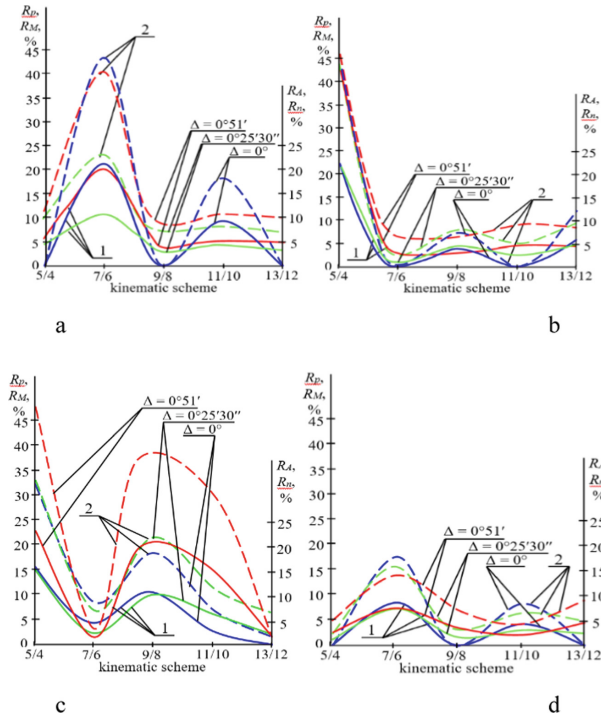
Analysis (Fig. 2a) shows that for kinematic schemes 5/4, 9/8, and 13/12, zero pulsation (pulsation coefficient) of the working fluid is ensured with the number of used additional discharge ports equal to zero and the angular gap between the distribution ports equal to zero ( $\Delta = 0^\circ$ ).

When using kinematic schemes 7/6 and 11/10 (Fig. 2b), zero pulsation of the working fluid can be ensured using two additional discharge windows and an angular clearance equal to zero ( $\Delta = 0^\circ$ ). Sufficiently good results were obtained for the 7/6 scheme when using two unloading windows and an angular gap equal to  $\Delta = 0^\circ 25' 30''$ . The use of such a gap allows increasing the volumetric efficiency of the hydraulic motor, with a relatively low pulsation coefficient of up to 2.5%.

If it is structurally necessary to use three additional windows (Fig. 2c), using an angular gap equal to  $\Delta = 0^\circ 51'$ , it is possible to ensure the maximum value of the volumetric efficiency of the distribution system for kinematic Schemes 7/6 and 13/12 when the ripple coefficient changes to 2.5%.

It was found that when using four additional windows (Fig. 2d), changes in the pulsation coefficients of the throughput, the rotation frequency of the hydraulic motor shaft, the pressure of the working fluid and the torque correspond in nature to the results with the number of used additional windows equal to zero (Fig. 2a). The value of the pulsation coefficients, with such indicators of the distribution system, has almost halved. The recommendations include kinematic schemes 5/4, 9/8 and 13/12 with a zero value of the ripple coefficient at an angular gap equal to  $\Delta = 0^\circ$  between the windows and schemes 5/4 and 11/10, providing an angular gap equal to  $\Delta = 0^\circ 51'$ , with values of the ripple coefficient up to 5%, which is quite acceptable.

The use of discharge windows of the movable distributor as additional allows not only to ensure the kinematic correspondence of the distribution system to the number of teeth of the planetary hydraulic motor rotors but also to significantly increase the



**Fig. 2.** Dependences of the change in the pulsation coefficients of the throughput and the rotational speed of the hydraulic motor shaft (curves 1), the pressure of the working fluid, and the torque (curves 2): a – without unloading windows; b – with two unloading windows; c – with three unloading windows; d – with four unloading windows.

absolute value of the flow area. In turn, an increase in the flow area of the distribution system allows an increase in the nominal value of the output power of the hydraulic motor.

Scientific novelty, in this work, is presented by the developed design kinematic diagram of the distribution system, the mathematical apparatus, and the results of theoretical studies of the influence of kinematic, geometric, and functional parameters on changes in the pulsation coefficients of the working fluid flow.

## 5 Conclusions

As a result of the research, a design scheme and a mathematical apparatus were developed. The initial data were substantiated, allowing to study the influence of changes in the geometric parameters of the distribution system on the pulsation of its flow area depending on the kinematic scheme, the angular gap between the distribution windows, and the number of additional windows. The initial conditions were substantiated and accepted, and the pulsation coefficients of the distribution system throughput and the rotation frequency of the hydraulic motor shaft, the pressure of the working fluid, and

the torque on the hydraulic motor shaft were investigated, which make it possible to simulate the operation of the distribution system of a planetary hydraulic motor.

The influence of the kinematic diagram of the distribution system, the angular gap between the distribution windows, and the number of additional windows on the changes in the pulsation coefficients of the working fluid flow has been investigated, which makes it possible to formulate the starting conditions for the design of distribution systems.

The starting conditions for the distribution systems design are substantiated, which exclude pulsations of the flow of the working fluid in planetary hydraulic machines for kinematic schemes 5/4, 7/6, 9/8, 11/10, and 13/12. The angular gap between the distribution windows was taken as  $0^\circ$ ,  $0^\circ 25' 30''$ , and  $0^\circ 51''$ . The number of additional unloading windows in the distribution system was taken as 0, 2, 3, and 4.

## References

1. Gamez-Montero, P., Codina, E., Castilla, R.: A review of Gerotor technology in hydraulic machines. *Energies* **12**, 2423 (2019). <https://doi.org/10.3390/en12122423>
2. Panchenko, A., Voloshina, A., Milaeva, I., Luzan, P.: Operating conditions' influence on the change of functional characteristics for mechatronic systems with orbital hydraulic motors. In: Nadykto, V. (ed.) *Modern Development Paths of Agricultural Production*, pp. 169–176. Springer, Cham (2019). [https://doi.org/10.1007/978-3-030-14918-5\\_18](https://doi.org/10.1007/978-3-030-14918-5_18)
3. Panchenko, A., Voloshina, A., Boltyskiy, O., et al.: Designing the flow-through parts of distribution systems for the PRG series planetary hydraulic motors. *East. Eur. J. Enterpr. Technol.* **3**(193), 67–77 (2018). <https://doi.org/10.15587/1729-4061.2018.132504>
4. Voloshina, A., Panchenko, A., Boltyskiy, O., Panchenko, I., Titova, O.: Justification of the kinematic diagrams for the distribution system of a planetary hydraulic motor. *Int. J. Eng. Technol.* **7**(4.3), 6–11 (2018). <https://doi.org/10.14419/ijet.v7i4.3.19544>
5. Panchenko, A., Voloshina, A., Kiurchev, S., et al.: Development of the universal model of mechatronic system with a hydraulic drive. *East. Eur. J. Enterpr. Technol.* **4**(794), 51–60 (2018). <https://doi.org/10.15587/1729-4061.2018.139577>
6. Makarov, V., Rezvaya, K., Drankovskiy, V., Mikhaylo, C.: Determination of the main parameters of the pump-turbine using the block-hierarchical approach. *Week Adv. Technol.* 536–540 (2020). <https://doi.org/10.1109/KhPIWeek51551.2020.9250164>
7. Barrio, R., Fernández, J., Blanco, E., Parrondo, J., Marcos, A.: Performance characteristics and internal flow patterns in a reverse-running pump-turbine. *J. Mech. Eng. Sci.* **226**(3), 695–708 (2012). <https://doi.org/10.1177/0954406211416304>
8. Egusquiza, E., Valero, C., Presas, A., et al.: Analysis of the dynamic response of pump-turbine impellers. Influence of the rotor. *Mech. Syst. Sig. Process.* **68**(69), 330–341 (2016). <https://doi.org/10.1016/j.ymsp.2015.05.034>
9. González, J., Oro, J., Argüelles-Díaz, K.: Flow analysis for a double suction centrifugal machine in the pump and turbine operation modes. *Int. J. Numer. Meth. Fluids* **16**(2), 220–236 (2009). <https://doi.org/10.1002/flid.1951>
10. Rundo, M.: Models for flow rate simulation in gear pumps: a review. *Energies* **9**(10), 1261 (2017). <https://doi.org/10.3390/en10091261>
11. Rogovyi, A., Korohodskiy, V., Khovanskyi, S., Hrechka, I., Medvediev, Y.: Optimal design of vortex chamber pump. *J. Phys: Conf. Ser.* **1741**(1), 012018 (2021). <https://doi.org/10.1088/1742-6596/1741/1/012018>
12. Rogovyi, A., Korohodskiy, V., Medvediev, Y.: Influence of Bingham fluid viscosity on energy performances of a vortex chamber pump. *Energy* **218**, 119432 (2021). <https://doi.org/10.1016/j.energy.2020.119432>

13. Korohodskiy, V., Kryshchtopa, S., Migal, V., Rogovyi, A., Polivyanchuk, et al.: Determining the characteristics for the rational adjusting of an fuelair mixture composition in a two-stroke engine with internal carburation. *East. Eur. J. Enterpr. Technol.* **2**(5), 39–52 (2020)
14. Rogovyi, A., Khovanskyi, S., Hrechka, I., Gaydamaka, A.: Studies of the swirling submerged flow through a confuser. In: Ivanov, V., Pavlenko, I., Liaposhchenko, O., Machado, J., Edl, M. (eds.) *DSMIE 2020. LNME*, pp. 85–94. Springer, Cham (2020). [https://doi.org/10.1007/978-3-030-50491-5\\_9](https://doi.org/10.1007/978-3-030-50491-5_9)
15. Liu, C., Jin, Y., Zhou, J., Tang, F., Hao, C., Han, J.: Study of internal flow in cube-type bidirection passages of axial-flow pump system by numerical simulation and experiment. *J. Hydroel. Eng.* **30**(5), 192–198 (2011)
16. Andrenko, P., Rogovyi, A., Hrechka, I., Khovanskyi, S., Svyntarenko, M.: Characteristics improvement of labyrinth screw pump using design modification in screw. *J. Phys: Conf. Ser.* **1741**(1), 012024 (2021). <https://doi.org/10.1088/1742-6596/1741/1/012024>
17. Pavlenko, I., Simonovskiy, V., Ivanov, V., Zajac, J., Pitel, J.: Application of artificial neural network for identification of bearing stiffness characteristics in rotor dynamics analysis. In: Ivanov, V., et al. (eds.) *DSMIE 2018. LNME*, pp. 325–335. Springer, Cham (2019). [https://doi.org/10.1007/978-3-319-93587-4\\_34](https://doi.org/10.1007/978-3-319-93587-4_34)
18. Pylypaka, S., Volina, T., Mukvich, M., Efremova, G., Kozlova, O.: Gravitational relief with spiral gutters, formed by the screw movement of the sinusoid. In: Ivanov, V., Pavlenko, I., Liaposhchenko, O., Machado, J., Edl, M. (eds.) *DSMIE 2020. LNME*, pp. 63–73. Springer, Cham (2020). [https://doi.org/10.1007/978-3-030-50491-5\\_7](https://doi.org/10.1007/978-3-030-50491-5_7)
19. Yao, J., Shi, W., Wu, S., et al.: Numerical calculation and experiment on pressure fluctuation in axial flow pump. *Trans. Chin. Soc. Agri. Mach.* **44**(1), 119–124 (2013). <https://doi.org/10.6041/j.issn.1000-1298.2013.S1.022>
20. Altare, G., Rundo, M.: Computational fluid dynamics analysis of gerotor lubricating pumps at high-speed: geometric features influencing the filling capability. *J. Fluids Eng.* **138**(11), FE-15–1757 (2016). <https://doi.org/10.1115/1.4033675>
21. Panchenko, A., Voloshina, A., Titova, O., Panchenko, I., Zasiadko, A.: The study of dynamic processes of mechatronic systems with planetary hydraulic motors. In: Tonkonogyi, V., et al. (eds.) *InterPartner 2020. LNME*, pp. 704–713. Springer, Cham (2021). [https://doi.org/10.1007/978-3-030-68014-5\\_68](https://doi.org/10.1007/978-3-030-68014-5_68)
22. Voloshina, A., Panchenko, A., Titova, O., Panchenko, I.: Changes in the dynamics of the output characteristics of mechatronic systems with planetary hydraulic motors. *J. Phys: Conf. Ser.* **1741**, 012045 (2021). <https://doi.org/10.1088/1742-6596/1741/1/012045>
23. Panchenko, A., Voloshina, A., Titova, O., Panchenko, I.: The influence of the design parameters of the rotors of the planetary hydraulic motor on the change in the output characteristics of the mechatronic system. *J. Phys: Conf. Ser.* **1741**, 012027 (2021). <https://doi.org/10.1088/1742-6596/1741/1/012027>
24. Voloshina, A., Panchenko, A., Titova, O., Pashchenko, V., Zasiadko, A.: Experimental studies of a throughput of the distribution systems of planetary hydraulic motors. *IOP Conf. Ser. Mater. Sci. Eng.* **1021**(1), 012054 (2021). <https://doi.org/10.1088/1757-899X/1021/1/012054>
25. Voloshina, A., Panchenko, A., Titova, O., Milaeva, I., Pastushenko, A.: Prediction of changes in the output characteristics of the planetary hydraulic motor. In: Tonkonogyi, V., et al. (eds.) *InterPartner 2020. LNME*, pp. 744–754. Springer, Cham (2021). [https://doi.org/10.1007/978-3-030-68014-5\\_72](https://doi.org/10.1007/978-3-030-68014-5_72)
26. Panchenko, A., Voloshina, A., Titova, O., Panchenko, I., Caldare, A.: Design of hydraulic mechatronic systems with specified output characteristics. In: Ivanov, V., Pavlenko, I., Liaposhchenko, O., Machado, J., Edl, M. (eds.) *DSMIE 2020. LNME*, pp. 42–51. Springer, Cham (2020). [https://doi.org/10.1007/978-3-030-50491-5\\_5](https://doi.org/10.1007/978-3-030-50491-5_5)

27. Shah, Y.G., Vacca, A., Dabiri, S., Frosina, E.: A fast lumped parameter approach for the prediction of both aeration and cavitation in Gerotor pumps. *Meccanica* **53**(1–2), 175–191 (2017). <https://doi.org/10.1007/s11012-017-0725-y>
28. Vacca, A., Klop, R., Ivantysynova, M.: A numerical approach for the evaluation of the effects of air release and vapour cavitation on effective flow rate of axial piston machines. *Int. J. Fluid Power* **11**(1), 33–45 (2010). <https://doi.org/10.1080/14399776.2010.10780996>
29. Velev, E.: Study cavitation Gerotor motors, using computer simulation. *Renewable energies and innovative technologies*. Smolyan 64–66 (2016)
30. Panchenko, A., Voloshina, A., Luzan, P., Panchenko, I., Volkov, S.: Kinematics of motion of rotors of an orbital hydraulic machine. *IOP Conf. Ser. Mater. Sci. Eng.* **1021**(1), 012045 (2021). <https://doi.org/10.1088/1757-899X/1021/1/012045>
31. Biernacki, K.: Selection of the optimum tooth profile for plastic cycloidal gears. *J. Mech. Eng. Sci.* **228**(18), 3395–3404 (2014)
32. Biernacki, K.: Methods of Increasing loadability for the plastic cycloidal gears. *Fundament. Mach. Des.* **490**, 156–165 (2012)
33. Tarelnyk, V., et al.: New method for strengthening surfaces of heat treated steel parts. *IOP Conf. Ser. Mater. Sci. Eng.* **233**(1), 012048 (2017). <https://doi.org/10.1088/1757-899X/233/1/012048>
34. Choi, T., Kim, M., Lee, G., et al.: Design of rotor for internal gear pump using cycloid and circular-arc curves. *J. Mech. Des.* **134**(1), 011005-12 (2012). <https://doi.org/10.1115/1.4004423>
35. Panchenko, A., Voloshina, A., Panchenko, I., Titova, O., Pastushenko, A.: Reliability design of rotors for orbital hydraulic motors. *IOP Conf. Ser. Mater. Sci. Eng.* **708**(1), 012017 (2019). <https://doi.org/10.1088/1757-899X/708/1/012017>
36. Monkova, K., et al.: Condition monitoring of Kaplan turbine bearings using vibro-diagnostics. *Int. J. Mech. Eng. Robot. Res.* **9**(8), 1182–1188 (2020). <https://doi.org/10.18178/ijmerr.9.8.1182-1188>
37. Kiurchev, S., Luzan, P., Zasiadko, A., Radionov, H., Boltianska, N.: Influence of the flow area of distribution systems on changing the operating parameters of planetary hydraulic motors. *IOP Conf. Ser. Mater. Sci. Eng.* **1021**, 012037 (2021). <https://doi.org/10.1088/1757-899X/1021/1/012037>
38. Voloshina, A., Panchenko, A., Panchenko, I., Zasiadko, A.: Geometrical parameters for distribution systems of hydraulic machines. In: Nadykto, V. (ed.) *Modern Development Paths of Agricultural Production*, pp. 323–336. Springer, Cham (2019). [https://doi.org/10.1007/978-3-030-14918-5\\_34](https://doi.org/10.1007/978-3-030-14918-5_34)
39. Voloshina, A., Panchenko, A., Boltyansky, O., Titova, O.: Improvement of manufacture workability for distribution systems of planetary hydraulic machines. In: Ivanov, V., et al. (eds.) *DSMIE 2019. LNME*, pp. 732–741. Springer, Cham (2020). [https://doi.org/10.1007/978-3-030-22365-6\\_73](https://doi.org/10.1007/978-3-030-22365-6_73)
40. Panchenko, A., Voloshina, A., Panchenko, I., Pashchenko, V., Zasiadko, A.: Influence of the shape of windows on the throughput of the planetary hydraulic motor's distribution system. In: Ivanov, V., Pavlenko, I., Liaposhchenko, O., Machado, J., Edl, M. (eds.) *DSMIE 2021. LNME*, pp. 146–155. Springer, Cham (2021). [https://doi.org/10.1007/978-3-030-77823-1\\_15](https://doi.org/10.1007/978-3-030-77823-1_15)
41. Voloshina, A., Panchenko, A., Panchenko, I., Titova, O., Zasiadko, A.: Improving the output characteristics of planetary hydraulic machines. *IOP Conf. Ser. Mater. Sci. Eng.* **708**(1), 012038 (2019). <https://doi.org/10.1088/1757-899X/708/1/012038>

42. Onysko, O., Karabegović, I., Dašić, P., Penderetskyi, M., Melnyk, O.: The stress state of compact mechatronic satellites of a cycloidal reducer. *J. Eng. Sci.* **8**(2), D12–D17 (2021). [https://doi.org/10.21272/jes.2021.8\(2\).d3](https://doi.org/10.21272/jes.2021.8(2).d3)
43. Martsinkovsky, V., Yurko, V., Tarelnik, V., Filonenko, Y.: Designing radial sliding bearing equipped with hydrostatically suspended pads. *Procedia Eng.* **39**, 157–167 (2012). <https://doi.org/10.1016/j.proeng.2012.07.020>

# **Chemical Process Technology and Heat and Mass Transfer**



# Design and Modernization of Circuit for Fuel Oil Heating and Tar Cooling

Tatiana Babak , Alexey Demirskyy , Gennadii Khavin<sup>(✉)</sup> , and Irina Riabova 

National Technical University «Kharkiv Polytechnic Institute»,  
2, Kyrpychova Street, Kharkiv 61002, Ukraine  
gennadii.khavin@gmail.com

**Abstract.** The solution to the scientific and practical problem of the modernization of the fuel oil heating department was proposed. The modernization provides two main tasks solutions: maximum heat recovery and existing equipment in the new technological scheme. The limitation of the hardware implementation is the clause of two cross-flow heat exchangers of the Compabloc type presence and two spiral heat exchangers with given surfaces of heat transfer areas. The study's primary goal is to achieve the assigned task of heating fuel oil by using the existing heat exchange equipment and redistributing the flows. In this case, the flow rates, temperatures, and pressure losses indicated in the formulation of the problem are rigidly fixed, but the possibility of installing additional heat exchange equipment is allowed. The original requirement for recuperative heating with the available apparatuses was not feasible. A new scheme of the heating department with an additional spiral heat exchanger installation was proposed to accomplish this task.

**Keywords:** Energy efficiency · Heat recovery · Cross-flow heat exchangers · Spiral heat exchangers · Fuel oil heating

## 1 Introduction

The oil and gas preparation and refining process includes several stages that use heat exchangers. Equipment designed for this industry must meet special requirements: operate at extreme pressures and temperatures, be resistant to aggressive media, have compact dimensions, and work with two-phase media. Oil and gas refineries use shell-and-tube and compact plate heat exchange equipment [1]. It is worth noting that the first type of heat exchanger is much more common than the last [2]. However, the area of compact plate heat exchangers application is gradually expanding. In this regard, the issue of choosing the type of heat exchanger, its calculation, and forecasting of performance is a matter of topical interest that has practical value in the processes of the oil and gas industry. The development of practical recommendations for installing compact heat exchangers is the most important financial task since more suitable equipment contributes to increased efficiency and reduced costs for technological maintenance and repair.



The use of equipment of certain types is associated with the apparatus characteristics and the process features for which they are used. In terms of dimensions, plate and spiral heat exchangers are more compact, which allows them to be installed in a limited space. However, one of the critical parameters is the ease of cleaning. Heat exchangers work with various heat carriers containing many impurities fouling the apparatus in various processes in the oil and gas processing industry. One of the main advantages of compact heating devices in the considered production area is the simplicity and convenience of their mechanical, hydrodynamic cleaning, and chemical washing.

## 2 Literature Review

Currently, the use of compact heat exchangers in the preparation and processing of petroleum products is limited mainly to small industries. These are installations for continuous vacuum distillation of fuel oil [3], with a capacity of 100–300 tons per day for raw materials. The use of compact devices at these installations is explained by the insufficient capacity of the single equipment and the high rates of fouling during operation. However, the advantages over the existing equipment for vacuum distillation of fuel oil such as the simplicity of the device; low cost; the ability to easily integrate into existing small refineries; saving fuel for heating fuel oil; simplification of the distillation process [4], makes their use economically feasible and effective. This is especially important in connection with the rise in world prices for oil and products of its processing.

In this regard, it becomes relevant to obtain deeper oil and fuel oil processing products at small installations to obtain a reasonably high-cost product. In these circumstances, the use of compact heat exchange equipment is indispensable [5].

The widespread use of shell-and-tube devices has shown their high performance and efficiency, proven in the conditions of mass operation [6]. For more profound and more economically less costly processing of raw materials, new, more efficient heat exchange equipment is required: plate cross-flow heat exchangers and spiral heat exchangers [7].

One of the main problems in the operation of all heat exchange equipment, and not only plate units, is the high intensity of the heat transfer surface fouling. Problems arise with increasing energy consumption and greenhouse gas emissions. Various mathematical models have been developed to describe these processes. This can predict the dynamic behavior of a heat exchanger exposed to contamination [8]. Numerous studies on the deterioration of the preheating department operation [9] refer mainly to shell-and-tube equipment, while it is known that spiral heat exchangers have the structural property of self-cleaning. In this case, the high efficiency of calcium deposits chemical cleaning, described in [10], will contribute to the more efficient operation of spiral apparatus and heat exchangers of the Compobloc type. In [11], an attempt is presented to investigate the influence of various forces such as gravity, lift, drag, and thermophoresis on crude oil of heat exchangers fouling using computational fluid dynamics (CFD) simulations. From the simulations, it can be seen that higher particle size and concentration result in higher particle settling.

The settling rate increases for larger particles and decreases for small to medium-sized particles. Higher flow rates and surface roughness increase wall shear and reduce fouling. Smaller temperature gradients on the surface of the heat exchanger reduce the

deposition rate due to the high thermophoretic forces. All these quality achievements must be considered when designing spiral apparatus and heat exchangers of the Compobloc type. On the other hand, the existing achievements in cleaning and flushing the heating networks of oil refineries [12], which significantly increase the performance of heat exchangers, should be revised and adapted for networks of plate units.

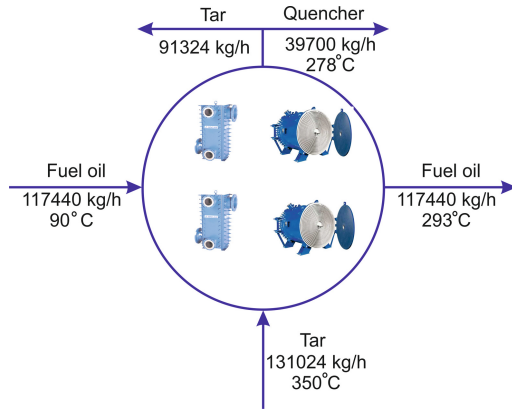
Another way to create an effective plate and spiral heaters system is to optimize their general installation scheme to obtain maximum energy recovery by analogy with the existing studies in this direction of shell-and-tube apparatus networks [13]. The available experience in the design of heat exchange networks [14] makes it possible to predict a significant contribution to cost savings when using spiral and welded plate apparatus, especially in factories of low productivity. In this sense, optimizing heat exchange networks with the application to the distillation of crude oil in an oil refinery has a significant perspective and the developed engineering methods of analysis and modernization [15]. In principle, these developments can be adapted to networks of spiral apparatus and heat exchangers of the Compobloc type. For devices of this class, fouling models are installed and must be introduced into the structure for operational optimization of contamination reduction or cleaning schedules, as suggested in [16]. These flushing measures should be further optimized to minimize overall operating costs. New specific pollution models are needed to implement spiral and welded plate heat exchangers.

### 3 Research Methodology

The general formulation of the problem is as follows. It is necessary to heat 117440 kg/h of fuel oil from a temperature of 90 °C to a temperature of 293 °C and at the same time obtain two cooled streams: a quencher with a flow rate of 39700 kg/h and a temperature of 278 °C and tar with a flow rate of 91324 kg/h, the temperature of which at the outlet not fixed, Fig. 1.

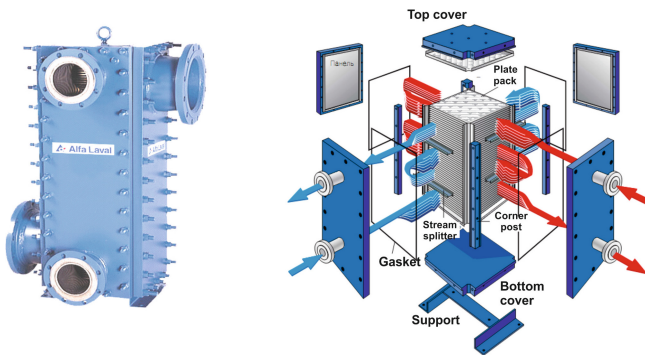
A tar flow with a flow rate of 13024 kg/h and an inlet temperature of 350 °C is used as a heating medium. There are 2 spiral heat exchangers of the 1H – L – 1T brand: S1 and S2 with a working heat exchange area of 90.2 and 86.5 m<sup>2</sup>, respectively, as equipment for fuel oil heating, Fig. 1. Two Compabloc (C1 and C2) type CPK50 – V – 200 heat exchangers (200 working plates) can be used for preheating. The pressure drop in the entire technological scheme should not exceed the following values: on the heating side – 140 kPa (50 kPa for Compabloc and 90 kPa for spiral heat exchangers, on the heated side – 140 kPa (80 kPa for Compabloc heat exchangers and 60 kPa for spiral heat exchangers).

The study's primary goal is to achieve the assigned task of heating fuel oil and quencher using the existing heat exchange equipment and redistributing the flows. At the same time, the flow rates, temperatures, and pressure drops indicated in the formulation of the problem are rigidly fixed; it is possible to install additional heat exchange equipment.



**Fig. 1.** Scheme general problem statement.

The available heat exchangers have the following physical parameters and thermal characteristics. Compabloc is a welded cross-flow apparatus with a collapsible body structure, Fig. 2. The design of Compabloc CPK 50 is based on a package of laser-welded corrugated metal plates in pairs, Fig. 2, which form channels. Each model has its own standard set of inserts to meet the most varied technological requirements. Compabloc frame consists of four corner posts, top and bottom plates, and four side plates with spigots. The entire structure is bolted together and quickly disassembled for inspection or cleaning.



**Fig. 2.** General view and design of the multi-way Compabloc.

Panels and spigots can be coated or even made entirely of the same material as the plates. The size of the nozzles is determined by: frame width (plate size), frame height (number of plates), and number of plates per stroke (for multi-pass heat exchanger). Differences in nozzle sizes and the flexibility of the multi-port layout make the Compabloc suitable for fluid-to-liquid systems with different characteristics. When used as a condenser, the steam inlet must be larger in diameter than the outlet.

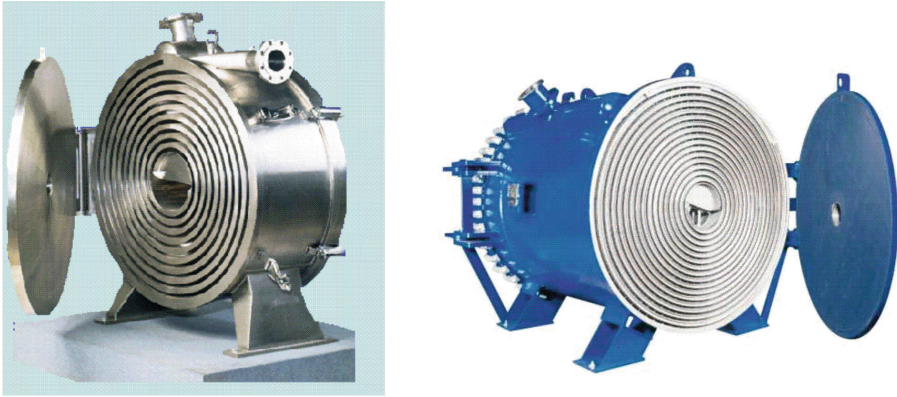
The design characteristics of the available CPK50 – V – 200 Compablocs (200 working plates) are presented in Table 1. The Compabloc, depending on the model, can operate in a pressure range from full vacuum to 35 bar and temperatures from – 29 °C to 350 °C (ASME).

**Table 1.** Design characteristics of available CPK50 Compabloc.

Parameter	Value
Design	Vertical
Number passes/plates	2/202
Grouping	1 * 50 + 1 * 50M/1 * 50 + 1 * 51M
Plate material/thickness, mm	AISI 316 L/1
Working/total area, m <sup>2</sup>	55.8/56.36

There is a whole class of spiral heat exchangers for media with increased contamination by primary treatment products and media with high adhesion to the wall material or heat carriers with a high content of various suspensions (heterogeneous in composition) Fig. 3. Structurally, they have a clock-spring-type cross-sectional configuration of two metal sheets twisted around the open center to form two concentric spiral channels. The ends of one channel are bent and welded, forming a wholly closed channel; the open ends of the other channel are closed with sealed covers. The result is a very developed heat transfer surface with small dimensions. There is only one channel for each of the heat carriers. Almost any material that can be cold formed and welded can be used for the spiral channels: stainless and carbon steel, nickel-based alloys, titanium, etc. Heat exchangers of this type are indispensable for working with media that tend to form deposits on heat transfer surfaces. The design of the spiral heat exchanger provides the effect of “self-cleaning” of the heat transfer channels. At the same time, there is still the possibility of traditional mechanical cleaning and flushing. The main parameters of the unit are pressure 1.5 MPa, temperature up to 400 °C, mass flow rate up to 100 kg/s. Heat transfer surface area up to 300 m<sup>2</sup>, heat transfer coefficient close to 2000–3000 W/(m<sup>2</sup>·K). Spiral heat exchangers are used as condensers, reboilers, and coolers (heaters) for media: liquid-liquid, gas-liquid, (gas + steam) – liquid, gas-gas.

The most common spiral heat exchangers are of two types, which have design features. During vapor-liquid heat exchange, the structure is characterized by a protruding upper cover, which communicates with the open ends of the channel for the heating carrier, and condensate drainage on the lower cover, Fig. 3. In the case of liquid-liquid heat exchange, the connecting pipes are located axially on the cylindrical surface of the apparatus wall.



**Fig. 3.** General view of the spiral heat exchanger.

The increased pressure and high turbulence provide the spiral heat exchanger with a self-cleaning effect, minimizing mechanical cleaning with disassembly or cleaning with chemicals. In addition, the compactness of this type of apparatus requires minimum space for maintenance. In fact, only space is needed for removing the covers. Design characteristics of the available spiral heat exchangers are given in Table 2. Distinctive features of spiral heat exchangers are also the absence of medium overflows and very low heat losses to the surrounding space.

**Table 2.** Design characteristics of the available spiral heat exchangers of grade 1H – L – 1T.

Parameter	Value
Direction of movement	Counterflow
Cylindrical width, mm	2000
Outside diameter, mm	1190
Distance between the coils, mm on the heating/heated side	10/25
Plate material	AISI 316 L
Coil material thickness, mm	3
Working/total area, m <sup>2</sup> :	
– heat exchanger S1	90.3/98.5
– heat exchanger S2	86.5/94.5

The preliminary studies and calculations of the scheme heat balance with four heat exchangers showed that they could not fully ensure the recuperation (heating of fuel oil and cooling of tar) within the framework of the assigned task. Therefore, installing an additional heat exchanger was decided to ensure complete recuperation.

## 4 Results

As a result of the design and study of the heat exchangers operation system as a whole, a basic thermal scheme for solving the problem was proposed, shown in Fig. 4. Table 3 shows the proposed heat exchangers installation design parameters in the scheme in Fig. 4. For calculations, the heat carries properties at the given temperatures were taken according to the available tabular data from the guidelines. The thermophysical properties were calculated using quadratic interpolation or extrapolation for temperatures outside the specified intervals.

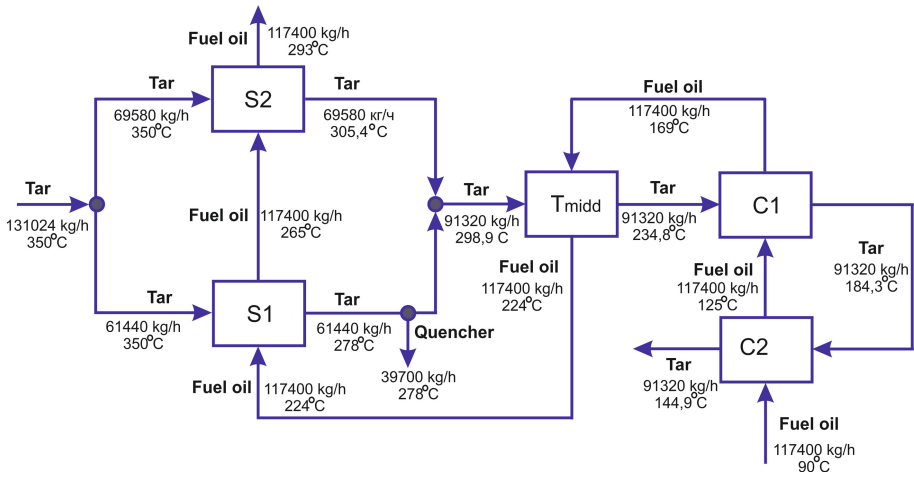


Fig. 4. Schematic diagram of heating fuel oil with an additional heat exchanger.

The mixing temperature of the heating tar stream before feeding to the additional heat exchanger is

$$t_{mix} = \frac{(64440 - 39700) \cdot 278 + 69580 \cdot 305.4}{64440 - 39700 + 69580} = 298.9 \text{ } ^\circ\text{C}$$

A spiral heat exchanger of the same brand 1H – L – 1T was chosen as an additional heat exchanger, and his parameters are given in Table 4. The working surface of the heating device is 128.6 m<sup>2</sup>. The total surface is 138.9 m<sup>2</sup>. The reserve of the working surface for the expected contamination is 10%.

The total pressure loss in the proposed scheme of heating fuel oil and cooling tar is 111.1 kPa on the side of the heating carrier and 57.9 kPa on the side of the heated fuel oil, which fits into the pressure loss limits formulated in the formulation of the problem.

**Table 3.** Design parameters of heat exchangers proposed for installation in the diagram in Fig. 4.

Position	Heat load, kW				
C1	2479	Heating media – tar			
		Flow rate, kg/h	Temperature, °C		Pressure drop, kPa
			Inlet	Outlet	
		131024	184.3	144.9	3.6
		Heated media – fuel oil			
		Flow rate, kg/h	Temperature, °C		Pressure drop, kPa
Inlet	Outlet				
117400	90	125	7.6		
C2	3374	Heating media – tar			
		Flow rate, kg/h	Temperature, °C		Pressure drop, kPa
			Inlet	Outlet	
		91320	234.8	183.4	3.6
		Heated media – fuel oil			
		Flow rate, kg/h	Temperature, °C		Pressure drop, kPa
Inlet	Outlet				
117400	125	169	6.2		
S1	3657	Heating media – tar			
		Flow rate, kg/h	Temperature, °C		Pressure drop, kPa
			Inlet	Outlet	
		61440	350	278	33.2
		Heated media – fuel oil			
		Flow rate, kg/h	Temperature, °C		Pressure drop, kPa
Inlet	Outlet				
117400	224	265	12.6		
S2	2604	Heating media – tar			
		Flow rate, kg/h	Temperature, °C		Pressure drop, kPa
			Inlet	Outlet	
		69580	350	305.4	40.7
		Heated media – fuel oil			
		Flow rate, kg/h	Temperature, °C		Pressure drop, kPa
Inlet	Outlet				
117400	265	293	12.6		

**Table 4.** Design parameters of an additional heat exchanger, intended to be installed in the circuit in Fig. 4.

Position	Heat load, kW				
T <sub>mid</sub>	4585	Heating media – tar			
		Flow rate, kg/h	Temperature, °C		Pressure drop, kPa
			Inlet	Outlet	
		91320	298.9	234.8	30.0
		Heated media – fuel oil			
		Flow rate, kg/h	Temperature, °C		Pressure drop, kPa
Inlet	Outlet				
117400	169	224	18.9		

## 5 Conclusions

The problem of designing a thermal scheme and installing heat-exchange equipment for the fuel oil heating department due to recuperative tar cooling with quencher extraction has been solved. For the existing heat exchange equipment of the Compabloc type (two units) and spiral heat exchangers (two units), various thermal schemes for the recovery of tar heat were designed. However, installing four heat exchangers was not enough to heat the fuel oil. To solve this problem, a new thermal separation scheme was designed with installing an additional spiral heat exchanger. The equipment calculations were carried out, confirming the reliability of the decision made.

## References




1. Mironova, Y., Tsvyak, A., Naumov, S.: Heat exchanger use in oil producing and oil-refining industries review article. *Tech. Sci.* **07**(97), 132–139 (2020). <https://doi.org/10.23670/IRJ.2020.97.7.015>
2. Heat exchangers for the oil and gas industry: TEPLPROFI. <https://www.teploprofi.com/teploobmenniki-neftyanoi-promyshlennosti>. Accessed 11 Nov 2021
3. Mamudu, A.O., Okonkwo, E., Okocha, S.I., et al.: The design of an integrated crude oil distillation column with submerged combustion technology. *Open Chem. Eng. J.* **13**, 7–22 (2019). <https://doi.org/10.2174/1874123101912010007>
4. Compact maintainability for the oil and gas industry. <https://www.tranter.com/app/uploads/2018/02/oil-gas-brochure.pdf>. Accessed 11 Dec 2021
5. Anderson, E.: Minimize refinery costs using SHEs (Alfa Laval). *Special features: thermal technology. Sep. Petrol. Technol. Q.* **13**(2), 75–80 (2008)
6. Kundnaney, N., Kushwaha, D.K.: A critical review on heat exchangers used in oil refinery. In: *Afro-Asian International Conference on Science, Engineering & Technology*, pp. 1–6. Akshar Publication (2015)
7. Anderson, E.: Improving refinery RAM with compact plate heat exchangers. *Hydrocarbon Asia* (2009)



8. Coletti, F., Macchietto, S.: A heat exchanger model to increase energy efficiency in refinery pre heat trains. *Compu. Aid. Chem. Eng.* **26**, 1245–1250 (2009). [https://doi.org/10.1016/S1570-7946\(09\)70207-X](https://doi.org/10.1016/S1570-7946(09)70207-X)
9. Yeap, B.L., Wilson, D.I., Polley, G.T., Pugh, S.J.: Mitigation of crude oil refinery heat exchanger fouling through retrofits based on thermo-hydraulic fouling models. *Chem. Eng. Res. Des.* **82**(1), 53–71 (2004). <https://doi.org/10.1205/026387604772803070>
10. Singh, D.K., Villamayor, A., Lacheheb, L.: Shell and tube heat exchanger progression fouling and its mitigation using chemical cleaning process. *AIP Conf. Proc.* **2317**, 030003 (2021). <https://doi.org/10.1063/5.0036112>
11. Emani, S., Ramasamy, M., Ku, Z., Ku, S.: Crude oil fouling in heat exchangers: a study on effects of influencing forces. In: *International Conference on Process Engineering and Advanced Materials 2020 (ICPEAM2020)*, vol. 287 (2021). <https://doi.org/10.1051/e3sconf/202128703003>
12. Huda, H., Totok, R., Biyanto, R., Wu, W., et al.: Oil refinery heat exchanger network cleaning scheduling strategy with unit cleanability consideration. *Asain J. Chem. Eng.* **20**(1), 31–48 (2020). <https://doi.org/10.22146/ajche.51880>
13. Mohammad, R., Sharifi, F., Sharifi, D., et al.: Optimization of heat exchanger network in olefin unit of oil refinery. *J. Adv. Res. Fluid Mech. Thermal Sci.* **13**(1), 1–16 (2015)
14. Kamel, D.A., Gadalla, M.A., Ashour, F.H.: Analysis and revamping of heat exchanger networks for crude oil refineries using temperature driving force graphical technique. *Clean. Technol. Environ. Policy* **20**(2), 243–258 (2017). <https://doi.org/10.1007/s10098-017-1403-4>
15. Al-Gwaiz, M.M., Murty, K.G.: Optimizing the design of heat exchanger networks in crude oil refineries. In: Murty, K.G. (ed.) *Case Studies in Operations Research*. ISORMS, vol. 212, pp. 217–296. Springer, New York (2015). [https://doi.org/10.1007/978-1-4939-1007-6\\_11](https://doi.org/10.1007/978-1-4939-1007-6_11)
16. Loyola-Fuentes, J., Jobson, J.M., Smith, R.: Fouling modelling and mitigation for crude oil heat exchanger networks using reconciled operating data. *Chem. Eng. Trans.* **70**, 193–198 (2018). <https://doi.org/10.3303/CET1870033>



# Protection of Condensing Heat Exchange Surfaces of Boilers from Sulfuric Acid Corrosion

Victoria Kornienko<sup>1</sup> (✉) , Roman Radchenko<sup>2</sup> , Dmytro Konovalov<sup>1</sup> ,  
Viktor Gorbov<sup>2</sup> , and Ivan Kalinichenko<sup>1</sup> 

<sup>1</sup> Kherson Branch of Admiral Makarov National University of Shipbuilding,  
44, Ushakova Avenue, Kherson 73022, Ukraine  
kornienkovika1987@gmail.com

<sup>2</sup> Admiral Makarov National University of Shipbuilding, 9, Heroes of Ukraine Avenue,  
Mykolaiv 54025, Ukraine

**Abstract.** The method of metal protection of boiler condensing heat exchange surfaces can be successfully used in stationary and ship boilers, which burn fuel oils containing sulfur. The proposed method includes the operation of coating with a protective film against sulfur corrosion of the boiler heat exchange surface at a wall temperature below the dew point temperature of H<sub>2</sub>SO<sub>4</sub> vapor. A passive layer of iron oxides is used as a protective film. It is obtained by passing physicochemical processes of passivation over the entire condensing surface from the beginning of sulfuric acid vapor condensation by pretreatment of exhaust gas flow with ionizing electron beams with a capacity of about 1 Mrad, ozone water-fuel emulsion combustion with a water content of about 30%. The metal surface is under the protection of a very thin passive film, which has a reliable connection with the metal at the level of the crystal structure and eliminates direct contact of the metal with the aggressive environment. The protective film constantly occurs naturally under the condition of creating an equimolar ratio of nitrogen oxides NO<sub>2</sub>:NO (50:50)% in front of the condensing surface in the gas flow. The protection provides a significant increase in the boiler's efficiency (by 4 to 6%) when sulfur fuels combustion in their furnaces and deeper exhaust gases heat utilization in internal combustion engines and gas turbines (to 70%).

**Keywords:** Energy efficiency · Industrial innovation · Water-fuel emulsion · Exhaust gases · Boiler · Condensing heat exchange surface · Passivation

## 1 Introduction

The exhaust gas temperature largely determines the economic performance of auxiliary [1, 2] and exhaust gas boilers (EGB) [3, 4]. Its value is determined not only by the course of heat exchange processes in the elements of boilers, the requirements for their weight and size indicators, which is important for ship boilers but also by the intensity of thermochemical processes, which take place in the exhaust gas flow and on the heat exchange surfaces (HES) [5, 6] with a temperature below the dew point temperature (DPT) of H<sub>2</sub>SO<sub>4</sub> vapor. The minimum value of HES temperature  $t_s$  determines the

minimum exhaust gas temperature and, consequently, the economic indicators of their work. It is more difficult to reduce of exhaust gas temperature, since its value (about 160 °C) is determined by the rate of low-temperature corrosion (LTC) [7, 8], which sharply increases at  $t_s = 130$  °C and reaches the level of the “corrosion peak” ( $K = 1.2$  mm/year) at  $t_s = 110$  °C, reduces the work reliability of HES. Consequently, the thermochemical processes in the gas ducts of boilers and the LTC intensity significantly limit the possibilities of increasing the efficiency of the boiler and the depth of exhaust gases heat utilization of gas turbine (GT) [9, 10], gas engines (GE) [11, 12] and internal combustion engine (ICE) [13, 14].

Therefore, any measures to reduce the level of the “corrosion peak” to an acceptable level (about 0.2 mm/year) will provide reliable work of condensing HES to increase the boiler efficiency and fuel-saving [15, 16]. It is currently impossible to assess the influence of numerous factors on LTC intensity analytically. It is necessary to carry out experimental research of corrosion processes on condensing HES of boilers at  $t_s$  in the range of 60–150 °C and thermochemical processes which take place in exhaust gas flow before these surfaces [17].

## 2 Literature Review

Practically in all works devoted to studies of the  $H_2SO_4$  formation in boilers, the mass flow of acid on the condensing HES, only the contact mechanism of the  $H_2SO_4$  formation is considered. However, the possibility of the  $NO_x$  influence on this process is also indicated. In [18], the author cites data that confirm the hypothesis of the possibility of interaction between  $SO_3$  and  $NO$  with the formation of nitrose. However, work [19] does not provide quantitative estimates of the proposed reactions either from thermodynamic or experimental positions. The weighty circumstance can indicate that with a decrease of the gas temperature, the part of  $SO_3$  is bound by nitrogen oxides, which seems to be confirmed by practice [19], which indicates a slight decrease of  $SO_3$  concentration in exhaust gases.

In addition to the main process of  $H_2SO_4$  formation by the contact mechanism in sulfuric acid production, the process of  $H_2SO_4$  obtained by the nitrous mechanism is also used. The appropriate conditions are created: adsorbed sulfur dioxide  $SO_2$  with nitrogen dioxide  $NO_2$  in the presence of water is oxidized to sulfuric acid with the formation of nitrosylsulfuric and nitric acids and the release water. In this case, sulfuric acid's best absorption of nitrogen oxides occurs at an equimolar ratio of  $NO$  and  $NO_2$  in exhaust gases [20]. Well-cooled ( $\sim 100$  °C) sulfuric acid, which contained 78%  $H_2SO_4$ , is used to obtain nitrose [21]. The same acid concentration is obtained during  $H_2SO_4$  vapors condensation on boilers condensing HES, indicating the possibility of a nitrous mechanism for  $H_2SO_4$  formation in the  $H_2SO_4$  condensate on the condensing HESs.

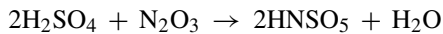
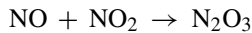
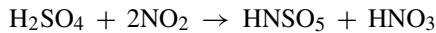
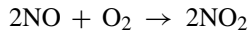
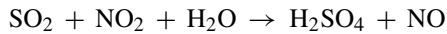
The intensity of the acid and metal interaction is determined by the wall temperature and the acid concentration, the intensity of  $H_2SO_4$  vapors mass flow to the surface, the protective properties of corrosion products, and the passive state of the metal, which can significantly limit the corrosion rate, despite the amount and concentration of acid [22, 23]. It should be noted that according to [24], the absorption of nitrogen oxides by a sulfuric acid solution improves the service conditions of steel equipment due to the

passivation of the steel surface at a temperature of 70 °C. The passivation process lasts 12–20 h.

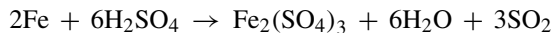
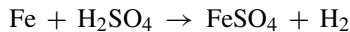
Exhaust gases of power boilers consist of 5% of NO<sub>2</sub> in NO<sub>x</sub> [25], of auxiliary boilers - 12% [26, 27]. With an increase of SO<sub>2</sub> concentration in exhaust gases, the absorption rate of SO<sub>2</sub> by nitrose increases. It also increases with an increase of O<sub>2</sub> concentration in the gases since the rate of O<sub>2</sub> absorption by nitrose increases, enhancing NO to NO<sub>2</sub> in the liquid phase [28, 29].

During radiolysis of a gas flow with an increase in the water vapor content in exhaust gases content at the same radiolysis energy, a faster increase of NO<sub>2</sub> content occurs. For obtaining an equimolar mixture is required not very high radiation energy (about 1 Mrad) [30]. It can be assumed that similar ionic reactions can occur in exhaust gases under the influence of acoustic waves energy arising under the influence of “microexplosions” of the water-fuel emulsion (WFE). Adsorption processes occurring in the pollution layer must necessarily affect the chemical processes in the layer and the concentration of toxic ingredients in exhaust gases at the exit from the boiler.

The presence of nitrogen oxides in a sulfuric acid solution should lead to the appearance of the passivation process of the metal surface. In the theory of passivation, an important role is played by adsorption O<sub>2</sub> and oxide layers formation, which form a passivating protective layer. The O<sub>2</sub> source involved in the formation of passivating layers may be HNO<sub>3</sub>.



Anions that form insoluble salts with metal or oxides can facilitate passivation. The appearance of a salt layer on the surface of iron may be preceded by the oxide passivation of iron in acidic solutions. In particular, this applies to H<sub>2</sub>SO<sub>4</sub> solutions, where FeSO<sub>4</sub> and Fe<sub>2</sub>(SO<sub>4</sub>)<sub>3</sub> layers are formed, i.e., in the presence of Fe<sup>3+</sup> in solution, reducing the critical passivation current.

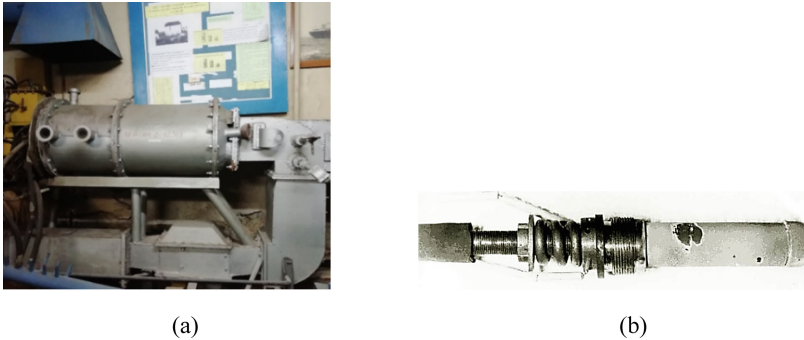


To confirm a significant reduction of LTC intensity in connection with creating a passive protective layer, special studies of this corrosion rate and the processes that confirm this phenomenon of passivation were conducted.

The research aims to confirm the passivation of metal on boiler condensing HES when WFE combustion.

### 3 Research Methodology

Studies of LTC intensity were carried out when fuel oils and WFE with a water content of 10, 15, 20, 30% were burnt. The research was carried out at a special experimental setup [29], where it is possible to ensure the stability of all parameters. This increases the reliability of the obtained results. The general view of the experimental setup and tube sample are presented in Fig. 1.



**Fig. 1.** General view of the experimental setup (a) and tube sample (b).

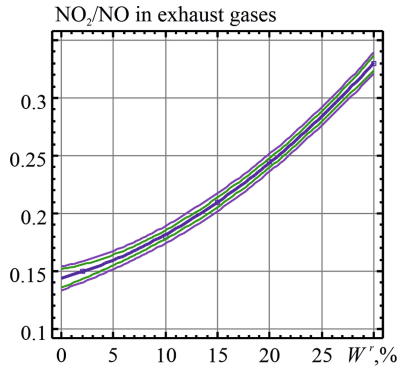
In addition to determining the corrosion rate, analyzes of deposits composition were performed to determine the content of nitrogen oxides (in terms of  $\text{HNO}_3$ ) and ions  $\text{Fe}^{3+}$ . Their content is largely defining the passivation possibility of the metal surface.

The nitrous mechanism for producing sulfuric acid is based on the absorption of  $\text{SO}_2$  and  $\text{NO}_x$ . Therefore, it is possible to confirm the presence of this process in pollution on condensing HES when WFE combustion. For this, it is necessary to determine the change in the content of the  $\text{SO}_x$  and  $\text{NO}_x$  in exhaust gases before and after these HES with an increase of water content in WFE.

Taking into account the data of direct measurements of nitrogen oxides content and the relative content of  $\text{Fe}^{3+}$  in pollutions, experimental data on the intensity of LTC when WFE combustion [29], it can be argued that in this case, there is an additional passage of the nitrous mechanism of sulfuric acid formation in pollutions at the condensing HES at temperatures below the DPT of  $\text{H}_2\text{SO}_4$  vapor. In addition, direct measurements of the content of  $\text{SO}_2$ ,  $\text{NO}$ , and  $\text{NO}_2$  in exhaust gases when WFE combustion and the obtained ratio  $\text{NO}_2:\text{NO}$  will give reasons to assert the possibility of a nitrous process in condensate on these HES.

### 4 Results

The dependences of the exhaust gas composition before the condensing HES, the corrosion rate, and the processes confirming the creation of the passivity of the metal surface were obtained.



**Fig. 2.** Dependence of nitrogen oxides  $\text{NO}_2:\text{NO}$  ratio in exhaust gases before HES on water content  $W^r$  in the emulsion.

An analysis of exhaust gas composition showed (Fig. 2) that when the water content of emulsion  $W^r$  is increased, the  $\text{NO}_2:\text{NO}$  ratio approaches the equimolar mixture.

The polynomial equation of nitrogen oxides  $\text{NO}_2:\text{NO}$  ratio in exhaust gases before condensing HES on water content  $W^r$  in the emulsion was determined ( $R^2 = 0.9998$ ):

$$\text{NO}_2/\text{NO} = 0.1438 + 0.0026W^r + 0.00012(W^r)^2 \quad (1)$$

Figure 2 shows the calculated values for  $\text{NO}_2/\text{NO}$  with the prediction (violet line) and confidence intervals (green line).

To confirm the passivation of metal on boiler condensing surfaces, the dependence of content of absorbed  $\text{NO}_x$  (as calculated on  $\text{HNO}_3$ ) in acid condensation on condensing HES from the metal surface temperature  $t_s$  was obtained (Fig. 3).

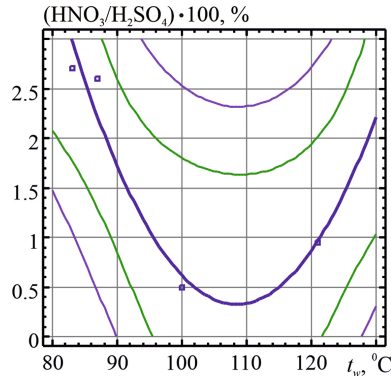
The level of content of  $\text{NO}_x$  in condensate on condensing HES corresponds to sulfuric acid production with a nitrose mechanism. In the technological scheme of this production, to reduce the corrosion of sulfuric acid coolers, the phenomenon of passivation of carbon steel metal surface is provided at the expense of absorbed nitrogen oxides. In the course of the research, the dependences of corrosion rate (Fig. 4a) and the  $\text{Fe}^{3+}$  content (Fig. 4b) from the temperature of metal HES  $t_s$  are obtained.

The polynomial equation of absorbed nitrogen oxides content in sulfuric acid condensate  $\text{HNO}_3/\text{H}_2\text{SO}_4$  on HES temperature  $t_s$  (Fig. 3) was obtained ( $R^2 = 0.9474$ ):

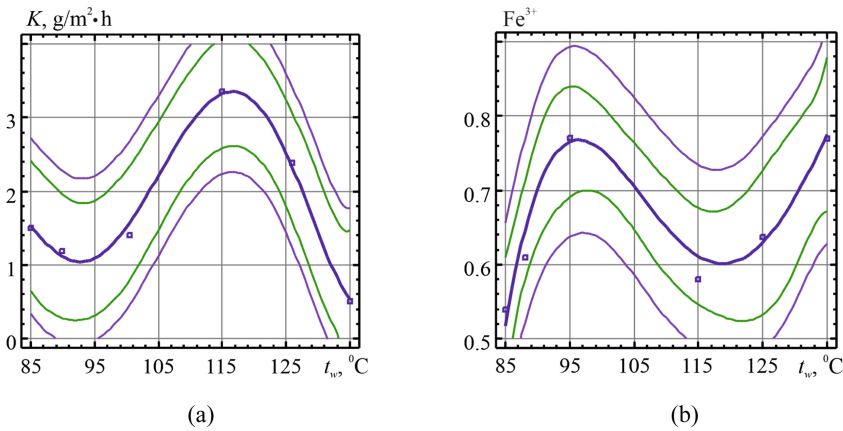
$$\text{HNO}_3/\text{H}_2\text{SO}_4 = 48.4257 - 0,8868t_s + 0,0041(t_s)^2 \quad (2)$$

The polynomial equation of corrosion rate  $K$  on HES temperature  $t_s$  (Fig. 4a), was determined ( $R^2 = 0.9568$ ):

$$K = -2866.51 + 143.504t_s - 2.8298(t_s)^2 + 2.75 \cdot 10^{-2}(t_s)^3 - 1.3141 \cdot 10^{-4}(t_s)^4 + 2.476 \cdot 10^{-7}(t_s)^5 \quad (3)$$



**Fig. 3.** Dependences of the content of absorbed  $\text{NO}_x$  in sulfuric acid condensate on HES temperature  $t_s$ .



**Fig. 4.** Dependences of corrosion rate  $K$  (a) and  $\text{Fe}^{3+}$  content in sulfuric acid condensate (b) on HES temperature  $t_s$ .

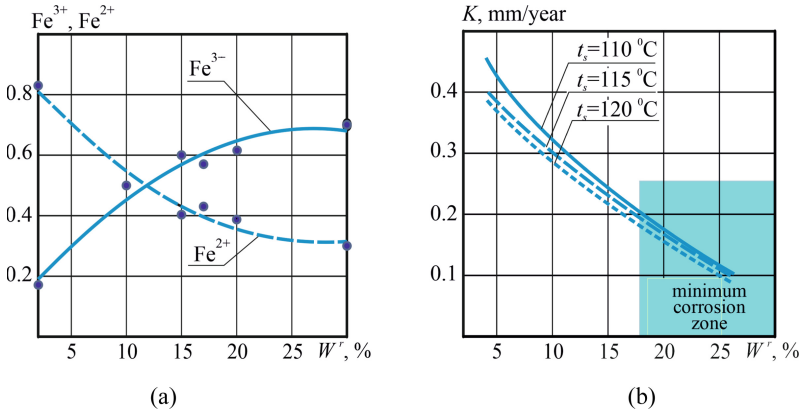
The polynomial equation of  $\text{Fe}^{3+}$  content in sulfuric acid condensate on HES temperature  $t_s$  (Fig. 4b), was selected ( $R^2 = 0.9113$ ):

$$\text{Fe}^{3+} = -106.059 + 3.6901t_s - 4.7121 \cdot 10^{-2}(t_s)^2 + 2.6336 \cdot 10^{-4}(t_s)^3 - 5.4346 \cdot 10^{-7}(t_s)^4 \quad (4)$$

This equations are obtained for the following characteristics of nitrogen oxides  $\text{NO}_2:\text{NO}$  ratio, corrosion rate  $K$  and  $\text{Fe}^{3+}$  content:  $t_s = 85\text{--}135$  °C and  $W^r = 10\%$ . Figure 3, 4a,b shows the calculated values with the prediction (violet line) and confidence intervals (green line).

There is a minimum amount of  $\text{Fe}^{3+}$  at  $t_s = 110$  °C (“peak” of LTC) and at  $t_s = 60$  °C (second maximum). On the contrary, the maximum values of  $\text{Fe}^{3+}$  content are found at  $t_s = 80$  °C and  $130$  °C, where there is a minimum corrosion rate. This is a sign of the growth of the passivation phenomenon of the metal surface. The obtained correlation of  $\text{Fe}^{3+}$  content in sulfuric acid condensate on condensing HES on  $W^r$  in the emulsion

also confirms the significant increase of metal passivation (Fig. 5a). Comparing the dependences of  $Fe^{3+}$  amount (Fig. 5a) and corrosion rate (Fig. 5b) from  $W^r$  in emulsion at metal surface temperatures 110, 115, 120 °C is confirmed the indicated position.



**Fig. 5.** Dependences of  $Fe^{3+}$ ,  $Fe^{2+}$  content in sulfuric acid condensate (a) and corrosion rate  $K$  (b) on water content  $W^r$  in the emulsion.

The comparison of the dependence of corrosion rate on the water content  $W^r$  in WFE (Fig. 5b) and the dependence of  $Fe^{3+}$  content in the corrosion products on  $W^r$  (Fig. 5a) indicates that with increasing of water content in the emulsion  $W^r$  the corrosion rate decreases and reaches a minimum value at  $W^r = 30\%$ . The content of  $Fe^{3+}$ , which is a sign of passivation of metal surface, increases accordingly and reaches a maximum value at the same value  $W^r = 30\%$ . This means that the most passive state of the metal surface is achieved ( $Fe^{3+}$  – maximum,  $Fe^{2+}$  – minimum) when  $W^r = 30\%$ .

An integrated indicator of a sharp decrease of LTC intensity due to surface passivation is indirect measurements and obtained dependences of LTC on wall temperature (Fig. 6). The research results (Fig. 6) show when WFE is burnt with excess air factor  $\alpha = 1.45$  the LTC intensity is at the level of 0.25 mm/year in the range of wall temperatures 70–130 °C in the absence of “corrosion peak”.

Therefore, the main factor contributing to a significant reduction of LTC when WFE is burnt with a water content of WFE more than 20% (and especially at 30% water) is the occurrence of metal passivation.

The minimum corrosion rate values at a level of 0.25 mm/year is provided at the wall temperature up to 70 °C. Comparison of the results in Fig. 6 with data [18] at  $\alpha = 1-1.05$  and water content of WFE  $W^r$  showed a reduction in the corrosion intensity with a decrease in  $\alpha$  and increase of  $W^r$  and coincidence with curves with an accuracy of 10%.



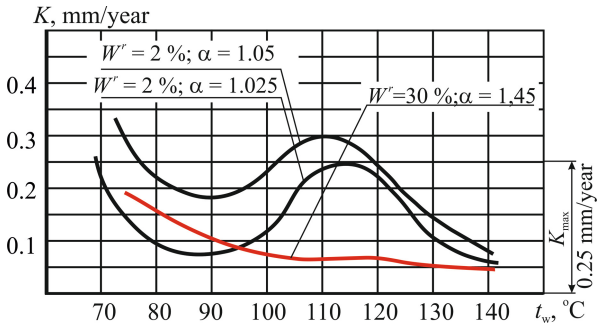


Fig. 6. Dependences of corrosion rate  $K$  on wall temperature.

## 5 Conclusions

This method of protecting metal from LTC provides resistance to thermal and dynamic deformations on the metal surface due to a very thin passive film with a thickness of about 50 Å. This film has a reliable connection with the metal at the crystal structure and eliminates direct metal contact with an aggressive environment.

Improving the boiler efficiency in the protection of metal of condensing HES in this direction is achieved by increasing the stability and operation duration of the metal due to the constant automatic (natural) creation of a passive layer due to the occurrence of physicochemical processes in contact with the exhaust gas flow at metal surface temperatures below DPT of  $H_2SO_4$  vapor (130 °C) and to 70 °C.

The wall temperature range of condensing HES safe operation is determined, revealing the opportunities for deep utilization. It makes it possible to reduce the temperature of the exhaust gases to 80 °C, thus significantly increasing the efficiency of boilers.

## References

1. Hochenaucr, C., Brandstetter, G.: CFD simulation of a low NOx oil fired boiler. In: Proceedings of the ASME Turbo Expo 2, GT2005–68060, pp. 1–10 (2005)
2. Gutiérrez Ortiz, F.J.: Modeling of fire-tube boilers. *Appl. Therm. Eng.* **31**(16), 3463–3478 (2011)
3. Konur, O., Saatcioglu, O.Y., Korkmaz, S.A., Erdogan, A., Colpan, C.O.: Heat exchanger network design of an organic Rankine cycle integrated waste heat recovery system of a marine vessel using pinch point analysis. *Int. J. Energy Res.* **44**(15), 12312–12328 (2020)
4. Kornienko, V., Radchenko, R., Bohdal, Ł., Kukielfka, L., Legutko, S.: Investigation of condensing heating surfaces with reduced corrosion of boilers with water-fuel emulsion combustion. In: Nechyporuk, M., Pavlikov, V., Kritskiy, D. (eds.) ICTM 2020. LNNS, vol. 188, pp. 300–309. Springer, Cham (2021). [https://doi.org/10.1007/978-3-030-66717-7\\_25](https://doi.org/10.1007/978-3-030-66717-7_25)
5. Gruber, T., Schulze, K., Scharler, R., Obernberger, I.: Investigation of the corrosion behavior of 13CrMo4-5 for biomass fired boilers with coupled online corrosion and deposit probe measurements. *Fuel* **144**, 15–24 (2015)
6. Trushliakov, E., Radchenko, M., Radchenko, A., Kantor, S., Zongming, Y.: Statistical approach to improve the efficiency of air conditioning system performance in changeable climatic conditions. In: 5th International Conference on Systems and Informatics, ICSAI 2018, Jiangsu, Nanjing, China, pp. 256–260 (2019)

7. Bohdal, Ł., Kukielka, L., Radchenko, A.M., Patyk, R., Kułakowski, M., Chodór, J.: Modelling of guillotining process of grain oriented silicon steel using FEM. *AIP Conf. Proc.* **2078**, 020080 (2019)
8. Wang, Z., Feng, Z., Zhang, L., Lu, M.-X.: Current application and development trend in electrochemical measurement methods for the corrosion study of stainless steels. *Gongcheng Kexue Xuebao/Chin. J. Eng.* **42**(5), 549–556 (2020)
9. Radchenko, A., Stachel, A., Forduy, S., Portnoi, B., Rizun, O.: Analysis of the efficiency of engine inlet air chilling unit with cooling towers. In: Ivanov, V., Pavlenko, I., Liaposhchenko, O., Machado, J., Edl, M. (eds.) *DSMIE 2020. LNME*, pp. 322–331. Springer, Cham (2020). [https://doi.org/10.1007/978-3-030-50491-5\\_31](https://doi.org/10.1007/978-3-030-50491-5_31)
10. Radchenko, A., Trushliakov, E., Kosowski, K., Mikielwicz, D., Radchenko, M.: Innovative turbine intake air cooling systems and their rational designing. *Energies* **13**(23), 6201 (2020). <https://doi.org/10.3390/en13236201>
11. Radchenko, A., Mikielwicz, D., Forduy, S., Radchenko, M., Zubarev, A.: Monitoring the fuel efficiency of gas engine in integrated energy system. In: Nechyporuk, M., Pavlikov, V., Kritskiy, D. (eds.) *Integrated Computer Technologies in Mechanical Engineering. AISC*, vol. 1113, pp. 361–370. Springer, Cham (2020). [https://doi.org/10.1007/978-3-030-37618-5\\_31](https://doi.org/10.1007/978-3-030-37618-5_31)
12. Radchenko, M., Mikielwicz, D., Andreev, A., Vanyeyev, S., Savenkov, O.: Efficient ship engine cyclic air cooling by turboexpander chiller for tropical climatic conditions. In: Nechyporuk, M., Pavlikov, V., Kritskiy, D. (eds.) *Integrated Computer Technologies in Mechanical Engineering - 2020. ICTM 2020. LNNS*, vol. 188, pp. 498–507. Springer, Cham (2021). [https://doi.org/10.1007/978-3-030-66717-7\\_42](https://doi.org/10.1007/978-3-030-66717-7_42)
13. Radchenko, M., Radchenko, A., Radchenko, R., Kantor, S., Konovalov, D., Kornienko, V.: Rational loads of turbine inlet air absorption-ejector cooling systems. In: *Proceedings of the Institution of Mechanical Engineers, Part A: Journal of Power and Energy* (2021). <https://doi.org/10.1177/09576509211045455>
14. Radchenko, M., Mikielwicz, D., Tkachenko, V., Klugmann, M., Andreev, A.: Enhancement of the operation efficiency of the transport air conditioning system. In: Ivanov, V., Pavlenko, I., Liaposhchenko, O., Machado, J., Edl, M. (eds.) *DSMIE 2020. LNME*, pp. 332–342. Springer, Cham (2020). [https://doi.org/10.1007/978-3-030-50491-5\\_32](https://doi.org/10.1007/978-3-030-50491-5_32)
15. Huang, S., Li, C., Tan, T., Fu, P., Xu, G., Yang, Y.: An improved system for utilizing low-temperature waste heat of flue gas from coal-fired power plants. *Entropy* **19**(423) (2017)
16. Radchenko, A., Trushliakov, E., Tkachenko, V., Portnoi, B., Prjadko, O.: Improvement of the refrigeration capacity utilizing for the ambient air conditioning system. In: Tonkonogiy, V., et al. (eds.) *Advanced Manufacturing Processes II. InterPartner 2020. LNME*, pp. 714–723. Springer, Cham (2021)
17. Chen, H., Pan, P., Wang, Y., Zhao, Q.: Field study on the corrosion and ash deposition of low-temperature heating surface in a large-scale coal-fired power plant. *Fuel* **208**, 149–159 (2017)
18. Tenditnyi, Y.: Impact of the combustion modes of liquid sulfur fuel on the rate of low-temperature corrosion. *Collection of Scientific Publications NUOS* (2017)
19. Kotler, V.P., Enyakin, Yu.P.: Implementation and efficiency of technological methods to suppress nitrogen oxides at thermal electric power plants. *Teploenergetika* **6**, 2–9 (1994)
20. Cui, X., Ning, Z.: Sulfur corrosion and prevention in petroleum processing. *Pet. Refin. Eng.* **29**(8), 61–67 (1999)
21. Radchenko, A., Radchenko, M., Trushliakov, E., Kantor, S., Tkachenko, V.: Statistical method to define rational heat loads on railway air conditioning system for changeable climatic conditions. In: *5th International Conference on Systems and Informatics, ICSAI 2018, Jiangsu, Nanjing, China*, pp. 1294–1298 (2019)

22. Wang, Z., Feng, Z., Fan, X.-H., Zhang, L.: Pseudo-passivation mechanism of CoCrFeNiMo0.01 high-entropy alloy in H<sub>2</sub>S-containing acid solutions. *Corros.Sci.* **179**, 109146 (2021)
23. Bohdal, L., Kukielka, L., Legutko, S., Patyk, R., Radchenko, A.M.: Modeling and experimental analysis of shear-slitting of AA6111-T4 aluminum alloy sheet. *Materials* **13**(14), 3175 (2020)
24. Sosin, D.V., Shtegman, A.V., Kotler, V.R., Tokarev, R.S., Shkrobtak, A.S.: Low cost methods of reducing nox emissions from coal-fired boilers. *Power Technol. Eng.* **45**(5), 361–364 (2012)
25. Deng, J., Wang, X., Wei, Z., Wang, L., Wang, C., Chen, Z.: A review of NO<sub>x</sub> and SO<sub>x</sub> emission reduction technologies for marine diesel engines and the potential evaluation of liquefied natural gas fuelled vessels. *Sci. Total Environ.* **766**, 144319 (2021)
26. Valluri, S., Kawatra, S.K.: Simultaneous removal of CO<sub>2</sub>, NO<sub>x</sub> and SO<sub>x</sub> using single stage absorption column. *J. Environ. Sci. (China)* **103**, 279–287 (2021)
27. Esarte, C., Delgado, J.: Influence of heating oil formulation on the combustion and emissions of domestic condensing boilers using fossil fuel and renewable fuel mixtures. *Energy Fuels* **32**(10), 10106–10113 (2018)
28. Olenius, T., Heitto, A., Roldin, P., Yli-Juuti, T., Duwig, C.: Modeling of exhaust gas cleaning by acid pollutant conversion to aerosol particles. *Fuel* **290**, 120044 (2021)
29. Konovalov, D., Kobalava, H., Radchenko, M., Sviridov, V., Scurtu, I.C.: Optimal sizing of the evaporation chamber in the low-flow aerothermopressor for a combustion engine. In: Tonkonogyi, V. et al. (eds.) *Advanced Manufacturing Processes II. InterPartner 2020. LNME*, pp. 654–663. Springer, Cham (2021). [https://doi.org/10.1007/978-3-030-68014-5\\_63](https://doi.org/10.1007/978-3-030-68014-5_63)
30. Radchenko, R., Pyrysunko, M., Kornienko, V., Scurtu, I.C., Patyk, R.: Improving the ecological and energy efficiency of internal combustion engines by ejector chiller using recirculation gas heat. In: Nechyporuk, M., Pavlikov, V., Kritskiy, D. (eds.) *ICTM 2020. LNNS*, vol. 188, pp. 531–541. Springer, Cham (2021). [https://doi.org/10.1007/978-3-030-66717-7\\_45](https://doi.org/10.1007/978-3-030-66717-7_45)



# Purification of Oilfield Wastewater by Inertial Methods

Oleksandr Liaposhchenko<sup>1</sup> , Viktor Moiseev<sup>2</sup> , Eugenia Manoilo<sup>2</sup> ,  
and Houssein Seif<sup>1,3</sup> 

<sup>1</sup> Sumy State University, 2, Rymyskogo-Korsakova Street, Sumy 40007, Ukraine  
o.liaposhchenko@ohnp.sumdu.edu.ua

<sup>2</sup> National Technical University «Kharkiv Polytechnic Institute»,  
2, Kyrpychova Street, Kharkiv 61002, Ukraine

<sup>3</sup> Al Khorayef Company for Sale, Maintenance and Repair of Oil Production Equipment LLC,  
P.O. Box 46813, 64019 Fahaheel, Kuwait

**Abstract.** Today, industrial ways of oil field development need new apparatus and machines with a significant cleaning result and a single ability, impenetrability, and ease of engineering produce and installation. The article represents an explanation of a hydrocyclone unit for handling wastewater from oilfields based on the application of inertial swirling flows. A new type of installation for wastewater treatment from oilfields has been developed. Due to the radial action in the hydrocyclone and the turbulent flows of the water stream, the oil droplets are damaged, they are increased, and the monodispersity of the liquid phase is growing. In systems with similar types of pollution, it is advisable to use multi-product multihydrocyclones and separators-coalescer with plates having holes and curves both for the removal of petroleum products and for the removal of suspended solids with a density higher than the density of water. Local treatment equipment, consisting of an average of four product hydrocyclones and separators with coalescent plates, will organize water purification systems at wells and use purified wastewater for formation pressure maintenance systems.

**Keywords:** Energy efficiency · Industrial growth · Oil wastewater · Purification · Separation · Process innovation · Multihydrocyclone · Hydrocyclone-separator unit · Coalescing plate

## 1 Introduction

The creation and development of technology and installations to treat oilfield wastewater (OFW) for disposal in oil reservoir flooding systems is an actual problem. Wastewater contaminated with emulsified petroleum products and solid suspended solids are often formed during the production process. About 90% of oil is currently extracted from fields using oil reservoir flooding methods to maintain formation pressure.

Oilfield wastewater (OFW) has a suspension-emulsion character belonging to mineralized polydisperse microheterogenic systems [1, 2]. The properties of OFW, especially

the state of the armor shells on the droplets of the dispersed phase of oil, determine the methods of destruction purification of OFW for a particular time [3].

The purification of OFW for flooding of productive horizons consists of removing oil and mechanical impurities from them to the specified industrial standards. The utilization of purified OFW in oil formation flooding systems is economically and environmentally beneficial to eliminate them in the oil fields.

During the development of oil fields, there is a change in the parameters and properties of the extracted fluids, the properties of reservoir waters, productive formations, residual oil reserves, and the technical and technological condition of oilfield equipment, including apparatuses in general, wastewater treatment plants. These factors determine the need for modernization, improvement, reconstruction of flooding systems, including OFW purification systems.

## 2 Literature Review

The quality of the OFW purification process assumes a reasonably complete and rapid decrease in the kinetic and aggregative stability of OFW by destroying the adsorption armor shell on oil droplets. This OFW movement mode ensures the enlargement of these droplets. These processes are qualitatively carried out with the help of a certain preliminary degree of turbulence of the OFW flow in the cavities of different hydrodynamic droplet generators with the following sedimentation. A high and steady cleansing impact can be reached by preliminary hydrodynamic treatment of the mixture in a swirling stream [4, 5].

The modernized technology of purification of OFW provides for the preliminary destruction of the armor shells on oil droplets' enlargement and reduction of the polydispersity of oil droplets [6, 7] by preliminary hydrodynamic treatment of the initial OFW using centrifugal swirling flows. An installation has been developed for the separation of OFW that operates according to the multihydrocyclone block – separator tank (hydrodynamic purification unit) [8].

The multihydrocyclone block - separator tank for the treatment of oily wastewater, equipped with coalescing nozzles included in the sump design for thin-layer separation. At the same time, in pressure hydrocyclones, not only the destroying of the armor shells on oil droplets and partial delamination of oil-in-water emulsions is carried out, but also coalescence of oil droplets occurs, an increase in the monodispersity of oil emulsions, which significantly intensifies the subsequent process of purification of oily wastewater by settling in sedimentation tanks - separators [9, 10].

OFW also includes effluents generated during car washing, which are contaminated with petroleum products and suspended solids [10]. The cleaned drains from the car wash enter the recycling water supply system of car washes.

OFW may contain dissolved gases: nitrogen, hydrogen sulfide, carbon dioxide, oxygen, methane, ethane, propane, etc., in the amount of 15–180 l/m<sup>3</sup> of water. During the discharge and purification of oily wastewater, 6–25 l of gases are released from 1 m<sup>3</sup> of water; and in available treatment facilities, 6–100 l from 1 m<sup>3</sup> of water for a period of several hours to two days. The OFW of settling tanks operating at a pressure of 0,2–0,6 MPa contains 3–4 times more gas than in the OFW of non-pressurized oil

tanks. Dissolved gases worsen the sanitary condition of the environment, are explosive, increase the aggressiveness of water to metal and concrete [10, 11].

In this study, the scale of linear and angular dimensions of the hydrocyclone for the model is adopted as follows: diameter  $D = 150$  mm, taper angle  $\alpha = 5^\circ$ ; diameter: inlet pipe  $d = 50$  mm, upper drain  $d = 40$  mm, lower drain  $d = 50$  mm, immersion depth of the upper drain pipe  $h = 100$  mm. The mode of fluid movement in a hydrocyclone is characterized by the Reynolds number along the radius in the range of 30000–40000. The pressure at the entrance to the hydrocyclone is usually  $P = 0,2$  MPa [12, 13].

### 3 Research Methodology

Separation processes are an integral part of production in the chemical, petrochemical, and oil refining industries. The problem of developing a theoretical approach to calculating a hydrocyclone separation apparatus for dispersed media of oily wastewater was solved. Research methods include analytical modeling. The calculation equations establishing the relationship between the parameters under consideration were obtained by methods based on the classical provisions of the theory of turbulent migration and mathematical modeling.

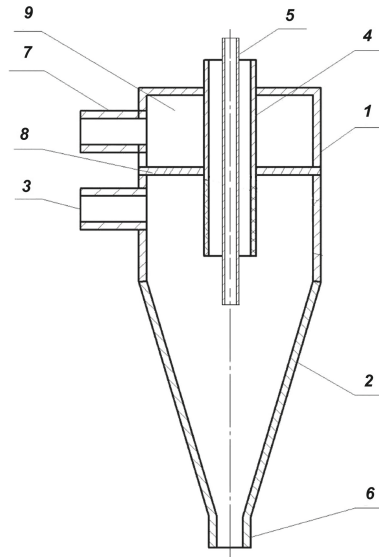
Based on the results of a systematic analysis of data from domestic and foreign literature sources [3–13] obtained from the experience of using several innovative solutions, mathematical modeling of the processes of inertial separation of mixtures [14, 15], a description of the process of purification of oily waters obtained in oil fields is given. In the study, the possibility of calculating the velocities of the phases in the hydrocyclone, the hydraulic resistance, and the efficiency of operation in terms of the size of the fixed particles was substantiated. The possibility of applying the theory of turbulent migration in the calculations of hydrocyclone installations without involving an extensive array of experimental data is shown.

### 4 Results

To improve the efficiency and reliability of the OFW purification units and oil mixture separation systems, a hydrocyclone was developed (Fig. 1), which contains cylindrical 1 and conical 2 shells, tangential inlet 3 for feeding the initial product, drain 4, and sand pipes 6 for removing purified water and sludge, respectively. A pipe 5 is installed inside the drainpipe, which provides the gas phase discharge contained in the wastewater. The separating permeable partition 8 forms a chamber 9 in the upper part of the apparatus for collecting purified water with an additional drainpipe 7.

Water containing coarse and fine mechanical particles and impurities of petroleum products and gases enters the tangential inlet 3 into the inner space. Here the flow swirls, while coarse particles with a density more significant than the density of water are thrown against the wall, lose speed, fall down along the conical part of the apparatus 2, and are discharged through the sand pipe 6. The central part of the clarified water is discharged through the drain pipe 7.

Light fractions, when moving in a centrifugal field, are directed to the axis of the apparatus, are concentrated at the nozzle 4, and, due to the pushing force, are directed to



**Fig. 1.** Hydrocyclone for complex purification of oily water: 1 – cylindrical shell, 2 – conical shell, 3 – tangential inlet, 4 – drain, 5 – drain pipe, 6 – sand pipe, 7 – additional drain pipe, 8 – permeable partition, 9 – chamber

the upper part of the apparatus and removed. The purified water passes into the chamber 9 then is discharged through an additional nozzle 7. Through nozzle 5, the gas phase is removed from the hydrocyclone. Thus, the combination of centrifugal separation processes in a hydrocyclone makes it possible to remove dispersed and floating organic impurities and gas from the wastewater. This reduces the multi-stage water treatment process, allowing to achieve the set goals.

Based on the mechanism of destruction of oil emulsions and the analysis of studies [3–5] of two-product cylindrical-conical hydrocyclones for the separation of OFW, an installation has been developed in which not only the destruction of the armor shells on oil droplets and partial separation of oil/water type emulsions is carried out, but also coalescence (enlargement) of oil droplets and an increase in the monodispersity of oil emulsions, which significantly intensifies the subsequent process of purification of oily wastewater by sedimentation. The efficiency of the OFW purification process due to the influence of gravitational forces in the separator-settling tanks is increased by the use of filter coalescing nozzles in which oil-containing effluents are treated before they enter the settling tanks of various designs.

The technological scheme of the installation is designed for oilfield wastewater treatment and consists of pressure cylindrical-conical multihydrocyclones, pressure separator tanks, pipelines, shut-off, and control valves.

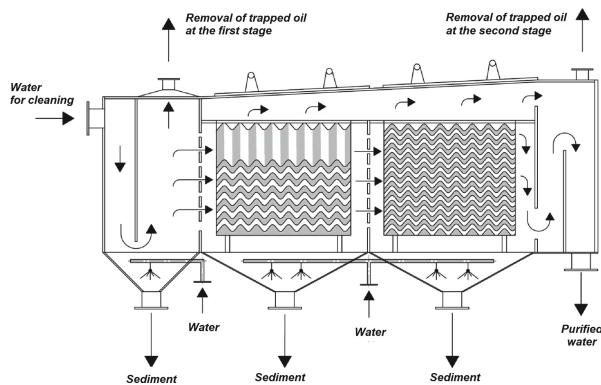
Wastewater is supplied to the hydrocyclone for cleaning under an excess pressure of at least 0,4 MPa. Hydrocyclones work as hydrodynamic droplet generators and preliminary flow separators. Purified water, trapped petroleum products, sediment, and dissolved gases are discharged from the hydrocyclone – separator tank installation. The separator

tank is divided into a preliminary compartment and an additional settling compartment. The coalescing nozzle through which the OFW passes when moving from compartment to compartment is used for pretreatment of OFW before settling. Their use significantly intensifies the process of oily water cleaning. Structurally, coalescing nozzles are placed in the separator and contribute to the coalescence of fine oil droplets remaining in the wastewater after pretreatment of wastewater in hydrocyclones and pre-settling, which increases the efficiency of installations of the hydrocyclone- separator tank block.

Block hydrocyclone installations complete with separator tanks with coalescing nozzles increase the efficiency of purification of oil-containing wastewater from oil fields, car washes, drainage water from fuel oil tanks, wastewater from cooling systems of technological equipment.

In multi-product hydrocyclones, heavy suspensions are separated through the lower slurry nozzle and petroleum products through a special nozzle located along the axis of the hydrocyclone in the upper part of the drain nozzle. At the second stage of water purification from residual contaminants, we suggest using [16] a coalescer separator with plates of various profiles.

Compact modular packages of corrugated plates made of various materials are used in such devices. The distance between the plates is usually from 6 to 20 mm. The plate supports included in their design guarantee the exact step of their placement.



**Fig. 2.** Separator-coalescer for separation of water, petroleum, and solid suspensions.

The separator-coalescer for the second stage of water purification from petroleum products and solid suspensions is shown in Fig. 2. The plates in the first block are installed with an inclination to the horizon to facilitate the removal of suspended particles. The gaps between the plates in the first (in the direction of water movement) block are more significant than in the second to avoid contamination by contamination.

Water containing petroleum products flows through the channel between the plates, following the shape of the gap and turning alternately down and up. Drops of petroleum products having a lower density than water float up, touch the plates' lower surface and are held by them due to the action of adhesion forces. As more and more oil droplets are captured, they coalesce into large droplets and finally form a film. Under the influence



of the high-speed pressure of the liquid flow, the film migrates along the surface of the plates to the oil outlet holes, passes into the overlying channel, and subsequently collects on the water surface. The design creates conditions for effective capture of petroleum products and their rapid transportation to the surface.

The separator-coalescer makes it possible to purify water to residual concentrations of suspensions and petroleum products, which is sufficient for organizing a local water supply cycle or using water in formation pressure maintenance systems.

Hydrocyclones used for the OFW treatment are characterized by high performance, absence of moving parts, compactness, simplicity and ease of maintenance, low cost, and broad scope of application. In addition, more acceptable separation can be achieved in hydrocyclones with a higher discharge density and without enlargement (flocculation) of small particles.

The main parameters characterizing the operation of cyclones are the degree of purification and the amount of pressure loss of the medium on the hydraulic resistance. The primary size of the cyclone is the diameter of the cylindrical part. The remaining dimensions are usually determined depending on the diameter  $D$  [17].

Empirical formulas for the rate of turbulent deposition of particles are quite diverse [18, 19] and include such quantities as:  $u_t^+ = u_t/u^*$  - dimensionless velocity of turbulent migration;  $l_t^+ = l_t u^*/\nu_L$  - the average dimensionless length of the free inertial path of the particles;  $\nu_L$  - the kinematic velocity of the medium,  $\text{m}^2/\text{s}$ ;  $\tau^+$  - dimensionless relaxation time,  $\tau^+ = \tau_p(u^*)^2/\nu_L$ .

The dependences obtained during the turbulent movement of aerosols and dusty gases in pipes cannot be used for calculation  $u_t$  in hydrocyclones.

The migration rate  $u_t$  characterizes the intensity of particle deposition from the turbulent flow to the channel wall  $u_t = j/c$  or  $j = u_t c$ , where  $j$  - is the specific particle flow to the wall,  $\text{kg}/(\text{m}^2\text{s})$ ;  $c$  - average cross-sectional particle concentration,  $\text{kg}/\text{m}^3$ .

The expression  $j = u_t c$  is an analogue of the well-known mass transfer equation  $j = \beta \Delta c$ , where  $\beta$  - is the mass transfer coefficient,  $\text{m}/\text{s}$ ;  $\Delta c$  - is the driving force of mass transfer (the difference in concentrations in the core of the flow and on the surface).

It follows that  $u_t = \beta_d$  for the deposition process of fine disperse particles. The theoretical methods for determining the transfer coefficient of the dispersed phase  $\beta_d$  allow us to calculate the efficiency of separators with minimal involvement of experimental data. To do this, we can use the method in which the turbulent deposition of a finely particulate phase is considered a kind of dispersion process using the usual equations from the mass transfer theory.

For very small particles ( $\omega_E \tau_p \ll 1$ ) ( $\omega_E \tau_p$  - inertia index [18]), their motion practically does not differ from the motion of the carrier turbulent vortices of the medium and then  $D_d = D_T$ , where  $D_d, D_T$  are the coefficients of turbulent diffusion of particles and the medium,  $\text{m}^2/\text{s}$ .

Let's write down the specific particle flux using an analogue of Fick's first law:

$$j = -(D_d + D_{br}) \frac{dc}{dy}, \quad (1)$$

where  $D_{br}$  - is the Brownian diffusion coefficient,  $\text{m}^2/\text{s}$ .

The resistance to the transfer of particles in the wall layer, taking into account Brownian and turbulent diffusion [20], is written as

$$\frac{1}{\beta_d} = \int_0^\delta \frac{j^* dy}{D_d + D_{br}} \quad (2)$$

where  $j^*$  - is the dimensionless particle flux density.

If the particles have some inertia and are not sufficiently carried away by turbulent pulsations, then the coefficient of turbulent diffusion of particles can be determined by the equation:

$$D_d = \frac{D_T}{1 + \omega_E \tau_p} \quad (3)$$

Usually, with a small error use the assumption  $D_T \approx \nu_T$ , where  $\nu_T$  - is the coefficient of turbulent viscosity,  $\text{m}^2/\text{s}$ .

In the Eq. (3).

$$\omega_E = \frac{u^*}{0,1R}, \quad \tau_p = \frac{\rho_{part} d_{part}^2}{18\mu_L}$$

In cyclones and hydrocyclones, the rotational motion of the medium is transferred by changing the rectilinear motion of the flow into a rotational-axial one as a result of tangential insertion or using a static twisting element with rigid guide walls. In this case, the separation efficiency increases with increasing speed and decreasing the radius of the apparatus.

The formula [21] is used for the coefficient of turbulent diffusion in a hydrocyclone

$$D_T = 0,0112V_t r, \quad (4)$$

where  $V_t$  - is the tangential component of the flow velocity,  $\text{m/s}$ ;  $r$  - the calculated radius of the hydrocyclone,  $\text{m}$ .

The particle transfer coefficient based on (2), (3) and (4) can be determined by integrating the expression

$$\frac{1}{\beta_d} = \int_0^\delta \frac{dr}{D_{br} + 0,0112V_t r}, \quad (5)$$

With a known function  $V_t(r)$ , the equation for the calculation  $\beta_d$  can be obtained in an analytical form.

The dynamic velocity on the hydraulic flow on the wall can be determined using the average coefficient of friction  $C_f$  or the average volumetric energy dissipation  $\bar{\varepsilon}$ .

Using the approach for  $u^*$  determination, through the rate of energy dissipation, we can write [20]

$$u^* = 2 \left( \frac{\bar{\varepsilon} \nu_L}{\rho_L} \right)^{0,25}, \quad (6)$$

where the average energy dissipation is expressed in terms of the pressure drop  $\Delta P$ :

$$\bar{\varepsilon} = \frac{\Delta P S u_{in}}{V_L}$$

and  $v_L$  - the kinematic velocity of the medium,  $m^2/s$ ;  $\rho_L$  - density of liquid suspension,  $kg/m^3$ ;  $S$  - the square area of the inlet pipe,  $m^2$ ;  $u_{in}$  - the velocity of the medium in the inlet pipe,  $m/s$ ;  $V_L$  - the volume of liquid in the hydrocyclone,  $m^3$ .

For example, in a hydrocyclone with a diameter of 150 mm, a liquid suspension with a density  $\rho_L = 1100 \text{ kg/m}^3$ , a viscosity  $\mu = 1,5 \cdot 10^{-3} \text{ Pa} \cdot \text{s}$  with a particle density  $\rho_{part} = 3000 \text{ kg/m}^3$  is cleaned at a capacity  $Q = 1000 \text{ l/min}$ . It is necessary to determine the minimum diameter of the captured particles and the diameter of the particles entrained by turbulent pulsations.

Let the walls of the hydrocyclone be smooth. The working length of the hydrocyclone according to known recommendations is  $L = 5 \cdot 150 = 750 \text{ mm}$  (0,75 m).

Diameter of the inlet pipe  $b = 0,28 \cdot 150 = 42 \text{ mm}$ . We accept  $b = 50 \text{ mm}$  (0,05 m).

The speed in the inlet pipe of the hydrocyclone is found by the formula:

$$u_{in} = \frac{4Q}{\pi b^2}, u_{in} = 8,49 \text{ m/s}.$$

Given the ratio  $Q_1/Q = 0,9$ , the Euler criterion is calculated by the formula [20]:

$$Eu = 1 + 3,5A \left( \frac{Q_1}{Q} \right)^{0,8}; Eu = 1 + (3,5 \cdot 3 \cdot 0,9^{0,8}) = 10,56$$

where the value of A is determined according to chart (5)–(6) [22],  $A = 3,0$ .

The hydraulic resistance of the hydrocyclone is found by the formula

$$\Delta P = Eu \rho u_{in}^2, \Delta P = 10,56 \cdot 1100 \cdot 8,49 = 98650 \text{ H/m}^2$$

The minimum diameter of the captured particles is determined by the formula:

$$d_{part} = \sqrt{\frac{K\mu}{L \left( \frac{\rho_{part} - \rho_L}{\rho_L} \right) \frac{\Delta P}{Q}}} = \sqrt{\frac{3,5 \cdot 1,5 \cdot 10^{-3}}{0,75 \left( \frac{3000 - 1100}{1100} \right) \cdot \frac{98650}{0,01666}}} = 2,616 \cdot 10^{-5} \text{ m}$$

where  $k = 3,5$ ,  $Q = 1/60 = 0,01666 \text{ m}^3/\text{s}$

Energy dissipation

$$\bar{\varepsilon} = \frac{\Delta P S u_{in}}{V_L}, \bar{\varepsilon} = \frac{98650 \cdot 0,00785 \cdot 8,49}{0,05} = 131493 \text{ Wt/m}^3.$$

Dynamic speed  $u^* = 0,278 \text{ m/s}$ .

$$u^* = 2 \left( \frac{\bar{\varepsilon} v_L}{\rho_L} \right)^{0,25}, u^* = 2 \left( \frac{131493 \cdot 50 \cdot 10^{-6}}{1100} \right)^{0,25} = 0,278 \text{ m/s}$$

Let 's make an estimate of the particle sizes by the equation

$$d_{part} < 0,134 \sqrt{\frac{R\mu}{\rho_{part} \cdot u^*}}; d_{part} < 0,134 \sqrt{\frac{0,075 \cdot 1,5 \cdot 10^{-3}}{3000 \cdot 0,278}}; d_{part} < 36,78 \cdot 10^{-5} \text{ m}$$

Thus, particles in a hydrocyclone with a diameter of 0.15 m with dimensions of  $d_{part} < 36,78 \cdot 10^{-5} \text{ m}$  will be wholly carried away by turbulent pulsations of the medium and the considered approach can be used to calculate the efficiency of turbulent separation.

## 5 Conclusions

Based on the analysis of wastewater from oil fields and methods of their purification, the following can be stated.

The composition of contaminants in the studied wastewater is very diverse, which determines the type of cleaning method [23, 24] and the choice of equipment for this purpose [25, 26].

In systems with similar types of pollution, it is advisable to use multi-product multi-hydrocyclones and separators-coalescer with plates having holes and curves both for the removal of petroleum products and for the removal of suspended solids with a density higher than the density of water.

Local treatment equipment, consisting of an average, of four product hydrocyclones and separators with coalescent plates, will allow organizing water purification systems at wells and using purified wastewater for formation pressure maintenance systems.

The article also provides a method for calculating the particle deposition process using the theory of turbulent migration of particles and the boundary layer theory. This approach helps to determine the effectiveness of hydrocyclones with minimal involvement of experimental data.







## References

1. Shtepa, V.N., Chernysh, Y.Y., Danilov, D.V.: Preventive improvement of wastewater treatment efficiency. *J. Eng. Sci.* **8**(1), H8–H15 (2021). [https://doi.org/10.21272/jes.2021.8\(1\).h2](https://doi.org/10.21272/jes.2021.8(1).h2)
2. Alekseevsky, D.G., Chernysh, Y.Y., Shtepa, V.N.: Formalization of the task of creating a mathematical model of combined wastewater treatment processes. *J. Eng. Sci.* **8**(2), H1–H7 (2021). [https://doi.org/10.21272/jes.2021.8\(2\).h1](https://doi.org/10.21272/jes.2021.8(2).h1)
3. Tronov, V.P., Tronov, A.V.: Purification of various types of water for use in the PPD system. Kazan. Feng (2001)
4. Verin, D., Valeev, S.I., Bulkin, V.A.: Hydrodynamics of cylindrical-conical hydrocyclone for separation of emulsions. *Bull. Kazan Technol. Univ.* **15**, 117–118 (2012)
5. Barkhatov, V.I.: Improving the Efficiency of Oil Refining and the Use of the Resulting Products: Monograph. Chelyabinsk State Publishing House, Chelyabinsk (2013)
6. Skydanenko, M., Sklabinskyi, V., Saleh, S., Barghi, S.: Reduction of dust emission by monodisperse system technology for ammonium nitrate manufacturing. *Processes* **5**(3), 37 (2017). <https://doi.org/10.3390/pr5030037>
7. Pavlenko, I., et al.: Effect of superimposed vibrations on droplet oscillation modes in prilling process. *Processes* **8**(5), 566 (2020). <https://doi.org/10.3390/pr8050566>
8. Nazarov, V.D., Rusakovich, A.A.: Preparation of water for flooding of oil reservoirs. *Oil Gas* **5**, 34–36 (2003)
9. Adelshin, A.B.: Intensification of hydrodynamic purification of oily wastewater. St. Petersburg (1998)
10. Laptev, A.G., Basharov, M.M., Farrakhova, A.I.: Efficiency of turbulent separation of the shallow phase in thin-layer settling tanks. *Energy Saving Water Treat.* **73**(5), 43–46 (2011)
11. Liaposhchenko, O., Moiseev, V., Starynskiy, O., Manoilo, E., Seif, H.: Equipment for oilfield wastewater treatment using swirling flows. In: Ivanov, V., Pavlenko, I., Liaposhchenko, O., Machado, J., Edl, M. (eds.) *DSMIE 2021. LNME*, pp. 237–246. Springer, Cham (2021). [https://doi.org/10.1007/978-3-030-77823-1\\_24](https://doi.org/10.1007/978-3-030-77823-1_24)

12. Adelshin, A.A.: Modeling of processes and development of oil-containing wastewater treatment plants based on the use of swirling streams. Penza (2009)
13. Adelshin, A.A., Adelshin, A.B., Urmitova, N.S.: Hydrodynamic purification of oilfield wastewater on the basis of swirling flows usage. KSUAE, Kazan (2011)
14. Liaposhchenko, O., et al.: Improvement of parameters for the multi-functional oil-gas separator of 'heater-treater' type. In: 2019 IEEE 6th International Conference on Industrial Engineering and Applications (ICIEA), pp. 66–71. Tokyo, Japan (2019). <https://doi.org/10.1109/IEA.2019.8715203>
15. Pavlenko, I., Ivanov, V., Gusak, O., Liaposhchenko, O., Sklabinskyi, V.: Parameter identification of technological equipment for ensuring the reliability of the vibration separation process. In: Knapcikova, L., Balog, M., Perakovic, D., Perisa, M. (eds.) 4th EAI International Conference on Management of Manufacturing Systems. EICC, pp. 261–272. Springer, Cham (2020). [https://doi.org/10.1007/978-3-030-34272-2\\_24](https://doi.org/10.1007/978-3-030-34272-2_24)
16. Ivanenko, A., Yablokova, M.A., Petrov, S.I.: Modeling of the process of separation of emulsified petroleum products from water in an apparatus with oleophilic plates of sinusoidal profile. *Theor. Found. Chem. Technol.* **44**(5), 588–600 (2010)
17. Laptev, A.G., Farakhov, M.I.: Hydro-mechanical processes in petrochemistry and power engineering. Kazan (2008)
18. Mednikov, E.P.: Turbulent transfer and deposition of aerosols. Moscow (1980)
19. Sklabinskyi, V., Liaposhchenko, O., Pavlenko, I., Lytvynenko, O., Demianenko, M.: Modelling of liquid's distribution and migration in the fibrous filter layer in the process of inertial-filtering separation. In: Ivanov, V., et al. (eds.) DSMIE 2018. LNME, pp. 489–497. Springer, Cham (2019). [https://doi.org/10.1007/978-3-319-93587-4\\_51](https://doi.org/10.1007/978-3-319-93587-4_51)
20. Laptev A.G.: Boundary layer models and calculation of heat and mass transfer processes. Kazan (2007)
21. Adelshin, A.B.: Flow energy in the processes of intensification of oil-containing wastewater treatment. Part 1. Hydrocyclones. Kazan (1996)
22. Bushmelev, V.A., Volman, N.S.: Processes and apparatuses of pulp and paper production. Moscow (1969)
23. Bourgeois, F., Majumder, A.K.: Is the fish-hook effect in hydrocyclones a real phenomenon. *Powder Technol.* **237**, 367–375 (2013). <https://doi.org/10.1016/j.powtec.2012.12.017>
24. Dueck, J., Farghaly, M., Neesse, T.: The theoretical partition curve of the hydrocyclone. *Miner. Eng.* **62**, 25–30 (2014). <https://doi.org/10.1016/j.mineng.2013.10.004>
25. Nageswararao, K.: Comment on: 'experimental study of particle separation and the fish Hook effect in a mini-hydrocyclone' by G. Zhu and J.L. Liow. *Chem. Eng. Sci.* **122**, 182–184 (2014). <https://doi.org/10.1016/j.ces.2014.08.062>
26. Guofeng, Z., Jong-Leng, L.: Experimental study of particle separation and the fish-hook effect in a mini-hydrocyclone. *Chem. Eng. Sci.* **111**, 94–105 (2014). <https://doi.org/10.1016/j.ces.2014.02.017>



# Comparative Evaluation of the Contact Elements Efficiency for Barium Sulfide Solution Carbonization

Yurij Masikevych<sup>1</sup> , Musii Tseitlin<sup>2</sup>  , Valentyna Raiko<sup>2</sup> ,  
Oleksii Shestopalov<sup>2</sup> , and Vladimir Panasenko<sup>3</sup> 

<sup>1</sup> Bukovinian State Medical University, 2, Teatralna Sq., Chernivtsi 58002, Ukraine

<sup>2</sup> National Technical University “Kharkiv Polytechnic Institute”, 2, Kyrpychova Street, Kharkiv 61002, Ukraine

michelzeitlin@gmail.com

<sup>3</sup> State Institution “State Research and Design Institute of Basic Chemistry”, 25, Myronositska Street, Kharkiv 61002, Ukraine

**Abstract.** The article presents the results of an experimental study aimed at obtaining scientifically valid data on the kinetics of absorption of carbon dioxide by a barium sulfide solution and the effect of the design of contact elements (trays) on the mass transfer coefficient in this process. The work was carried out using a laboratory model of the absorber, in which it was possible to install trays of various types. Analysis of literature sources showed that the process of a BaS solution carbonization takes place in two stages, sharply differing in pH. An experimental study of CO<sub>2</sub> absorption kinetics under the conditions of the first stage of the process made it possible to identify the most significant factors influencing its rate. It was also found that the limiting stage of mass transfer is the resistance in the gas phase. The carbonization rate at the second stage is significantly lower than at the first stage and is controlled by the kinetics of the chemical reaction of CO<sub>2</sub> hydration. Mathematical processing of the results of testing models of the cap, sieve, and double-flow trays made it possible to obtain formulas for calculating the mass transfer coefficients for each of them. In the studied range of gas velocities, the mass transfer coefficient on a dual-flow tray was 1.5–2 times lower than on a sieve tray and 2–2.5 times lower than on a cap tray. The data obtained were used in the design of the absorption apparatus.

**Keywords:** Process innovation · Absorption · Carbon dioxide · Barium Sulfide solution · Mass transfer kinetics · Mass transfer ratio · Cap tray · Sieve tray · Dual flow tray

## 1 Introduction

One of the leading products in the range of barium compounds is barium carbonate. This substance is used primarily in the glass industry and as raw material for producing many other barium salts.

At present, barium carbonate is obtained from barite concentrate using rather complex technology, including roasting, leaching of barium sulfide, processing it with hydrochloric acid, and precipitation of  $\text{BaCO}_3$  with sodium carbonate. The advantage of this technology is the high purity of the product obtained. The disadvantages are the use of expensive chemicals, cumbersome equipment, and the high cost of the product.

The search for cheaper methods for obtaining barium carbonate led to the idea of direct carbonization of a barium sulfide solution [1]. Particular difficulties in implementing this technology appear due to insufficient knowledge of the kinetics of the process, which complicates the choice of an appropriate method for organizing mass transfer and the design of the main apparatus, i.e., the absorber.

Barium sulfide carbonation, as it will be shown below, is a complex, multi-stage process. Therefore, it is practical and scientific interest to determine the limiting stages and factors affecting its kinetics. Thus, from the viewpoint of the possibility of creating equipment for implementing the direct carbonization method of barium sulfide solution, it is essential to study this process to obtain scientifically proved data for the design of the absorber.

## 2 Literature Review

Barium sulfide solution, a strong base salt, and a weak acid are alkaline. The absorption of carbon dioxide by alkaline solutions is widespread in technology [2] and used in numerous food and chemical industries branches.

$\text{CO}_2$  absorption takes place in several stages. The main ones, in terms of the film theory [3, 4], are a diffusion of carbon dioxide from the bulk of the gas to the interface;  $\text{CO}_2$  dissolution; diffusion from the interface deep into the liquid; chemical interaction of carbon dioxide with the active component of the liquid. The two last stages mentioned run simultaneously.

In the case of carbon dioxide absorption by barium sulfide solution, the process is complicated due to simultaneous desorption of hydrogen sulfide, which should affect the mass transfer coefficient in the gas phase and pH of the absorbent [5]. Considering the latter factor, the desorption of hydrogen sulfide should also affect the rate of carbon dioxide reaction in the liquid. In addition, the crystallization of barium carbonate is a diffusion process related to crystallization supersaturation [6, 7], and it can affect the kinetics of  $\text{CO}_2$  absorption.

The interaction of carbon dioxide with alkaline solutions has been studied in detail. In works [3, 5, 6], it was shown that carbon dioxide in alkaline solutions could enter into the following reactions:

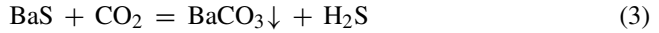


The kinetics of carbon dioxide hydration reactions was studied in [3] and [8–10]. The authors obtained equations for calculating the kinetic coefficients of reactions (1), (2). In particular, it was found out that at pH from 8 to 11.5, reaction (2) generally proceeds,

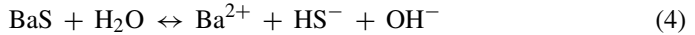
and at  $\text{pH} > 10$ , the rate of carbon dioxide hydration is mainly determined by reaction (1).

When carbonizing barium sulfide solution, the products of reactions (1) and (2) in an aqueous solution enter into a range of reactions proceeding in the ionic form that is relatively fast, thus, they do not control the process rate.

Barium sulfide carbonation can be described in the following gross equation [11]:



However, the mechanism of this process, in our opinion, should be more complicated since the reactions in solution proceed in the ionic form [5]. Barium sulfide hydrolyses in an aqueous solution:



As a result of a reaction (4), an excess of  $\text{OH}^-$  ions appear in the solution, which determines the alkaline reaction of barium sulfide solution.

The barium ion formed in the process (4) reacts with the carbonate ion as follows:



The reaction (5) proceeds in the ionic form, and its rate should be sufficiently high, at least higher than reactions (1), (2); nevertheless, the crystallization of the barium carbonate formed over is a heterogeneous process, so there should be some saturation providing crystallization.

Barium sulfide, a salt with a strong base, is almost completely dissociated from the solution. Therefore, at the initial stages of the carbonization process at a molar ratio of  $\text{Ba/S}^- > 0.5$ , the solution has a high pH value [5, 11] due to reaction (4). At subsequent stages, at  $\text{Ba/S} < 0.5$ , i.e., after barium sulfide is wholly converted into hydrosulfide, the pH of the solution reduces rapidly. The hydrosulfide ion formed by reaction (4) adds a proton to the reaction.



The rate of this reaction increases with decreasing pH. The formed hydrogen sulfide is desorbed from the solution.

Considering the above analysis of the literature, it can be outlined that the kinetics of the reactions of carbon dioxide hydration and the formation of barium carbonate is related to pH, which was experimentally confirmed in [11]. This relation can become a criterion for whether the chemical reaction is the limiting stage of the absorption process. It should be noted that, among the relatively limited data available in the literature on the kinetics of carbonization of barium sulfide, it was not possible to find information that would make it possible to determine the limiting stages of the process. For example, in [12], the study of kinetics was carried out only at high pH, and in [13], pH control was not carried out, and the decrease in the absorption rate at the end of the experiment was not commented on.

Also, no recommendations were found on choosing a suitable design of a contact element for the industrial implementation of the process under study.



### 3 Research Methodology

#### 3.1 Laboratory Set

The process study of barium sulfide carbonization was carried out in three stages. In the first preliminary experiments, the dependence of the absorption rate of carbon dioxide to the conversion of barium sulfide into carbonate (carbonization level) was studied. In this part of the work, a bubbling apparatus was used as the main element of the laboratory setup, which was a cylindrical container with a jacket 800 mm high. The inner diameter of the cylinder was 43 mm. The apparatus was equipped with nipples for inlet and outlet of gas, heating water, and sampling.

The second stage aimed to identify factors that significantly affect the process's kinetics and compare the mass transfer characteristics of the cap, sieve, and dual flow trays that were supposed to be used in the designed absorber. The laboratory apparatus used in this part of the study differed from the one described above in its inner diameter, which was 60 mm, and in the presence of a connector in the lower part, into which the models of the studied trays were set up. An externally adjustable overflow was built into the connector.

The trays under study had the following characteristics. The dual-flow tray was a 1 mm thick stainless steel disc with holes 10 mm in diameter. The free section of the tray was 19.4%. The sieve tray had a similar design, but the hole diameter was 6 mm, and the free section was 17%. The cap tray had one cap. The outer diameter of its cylindrical part was 30 mm. 9 slots 5 mm wide and 10 mm high were cut evenly along its perimeter.

At the preliminary stage of the study, the laboratory setup consisted of a gas mixture preparation unit, an absorber, and an equipment set for measuring and regulating gas flow rates, measuring temperatures, and taking liquid samples for analysis. The setup was supplemented with supply and liquid drainage systems at the second and third stages.

#### 3.2 Experiment Method

At the preliminary stage, barium sulfide carbonization was researched in batch mode. At the beginning of the experiment, the flow rates of carbon dioxide and nitrogen were set by the program of experiments. The gas mixture obtained was fed through a mixer into a laboratory absorber, and then the prepared and previously analyzed absorbent was added to it. During the experiment, liquid and gas samples were periodically taken for analysis.

In the experiments carried out according to the described method, it was found out that after reaching the conversion of sulfide into barium carbonate (further referred to as carbonization level) value of 50%, the rate of carbonation was significantly reduced. Within each of these intervals, the carbonation rate practically did not change. This phenomenon can only be explained by a fundamental change in the mechanism of the process. Therefore, further research was carried out separately for solutions with carbonization levels less than and more than 50%.

The experiments of the second stage were carried out in a flow-through mode. The liquid, heated to a predetermined temperature, was continuously pumped into the absorber and drained into the collector. After the experimental model was established, the values

of the contacting media flow rates were recorded, and gas and liquid samples were taken for analysis before and after the absorber. In addition, the temperature and pressure in the apparatus were recorded.

The primary processing of the experimental results included calculations: gas velocity, the density of irrigation with liquid, absorption rate, its driving force. The mass transfer coefficient was calculated using the well-known formula.

$$K_g = r_{\text{CO}_2} / (S \cdot \Delta p_{\text{CO}_2}) \quad (7)$$

where  $r_{\text{CO}_2}$  is the absorption rate of carbon dioxide, mol/m<sup>2</sup>s;  $S$  is the cross-sectional area of the laboratory absorber, m<sup>2</sup>;  $\Delta p_{\text{CO}_2}$  is a mean logarithmic value of CO<sub>2</sub> partial pressures before and after the absorber, Pa.

## 4 Results

### 4.1 Study of the Carbonation of Barium Sulfide Solution at a Carbonation Level of Less Than 50%

Noted in the literature review high absorption rate at a carbonation degree of less than 50% may indicate that the limiting stage is the diffusion of CO<sub>2</sub> from the gas to the interface. Confirmation of this fact would allow rejecting the further study of the carbonization process in this concentration range and using the relations known from the literature to calculate the corresponding equipment. Thus, the task of the studies on this phase was to find the limiting stage of the process. For this purpose, the effect of the carbon dioxide concentration in the gas, barium sulfide in the initial liquid, the gas velocity, the liquid irrigation density, and the temperature on the kinetics of carbon dioxide absorption was researched. The study was carried out in a laboratory apparatus with a dual flow tray set in it.

Mathematical processing of the experimental results by the method of regression analysis showed that a significant effect (the p-level coefficient estimated the significance) on the rate of CO<sub>2</sub> absorption is exerted by: the average partial pressure of carbon dioxide in the gas (the driving force of absorption), gas velocity and temperature. So, the following equation was obtained:

$$\ln r_{\text{CO}_2} = 17,8 - 2100T^{-1} + 0.94 \ln v + 1.03 \ln \Delta p_{\text{CO}_2} \quad (8)$$

where  $v$  is the gas velocity, m/s;

The accuracy of the obtained equation is characterized by the following values: determination coefficient  $R^2 = 0.986$ , standard error of equation  $\ln r_{\text{CO}_2} - 0.073$ .

As follows from the above experimental results, the barium sulfide concentration within the limits of the accuracy of the experiments does not affect the absorption rate. It can be explained by the fact that in the considered range of carbonization level, BaS concentration has little effect on the concentration of the hydrogen ion, which determines the rate of CO<sub>2</sub> absorption at high pH values.

The effect of temperature on the absorption rate was also insignificant. In total, this indicates that the resistance to the absorption process is due to diffusion, i.e., mass transfer, and a chemical reaction is not the limiting stage of the process.

From Eq. (8), in particular, it follows that the rate of CO<sub>2</sub> absorption is proportional to the driving force of the process, which makes it possible to calculate the kinetics of absorption using the classical two-film model.

Thus, the data obtained allow us to assert that when a barium sulfide solution absorbs carbon dioxide with a carbonization degree of less than 50%, mass transfer in the gas phase is the limiting stage.

#### 4.2 Study of Barium Sulfide Carbonization at Carbonization Level More Than 50%

Barium sulfide solution with a carbonization level of more than 50% does not contain barium sulfide since the latter is wholly converted into barium hydrosulfide. Therefore, we will consider the carbonization of the Ba(HS)<sub>2</sub> solution further.

At this stage of the work, the effect of CO<sub>2</sub> concentration in the gas, barium concentration in the initial liquid (in terms of sulphide), the gas velocity, the density of liquid irrigation and temperature, on the kinetics of carbon dioxide absorption was studied.

In experiments with a dual flow tray, the direct proportionality between the absorption rate and the mean logarithmic concentration of carbon dioxide in the gas was experimentally confirmed. This made it possible to further characterize the absorption kinetics in terms of the mass transfer coefficient.

In the same experiments, it was found that the rate of carbon dioxide absorption is lower than this indicator has at carbonation level less than 50%, and significantly. Since the conditions of all diffusion stages of the process did not change, such a significant decrease in the absorption rate can only be explained by changes in the mechanism of chemical reactions caused by the pH decrease of an absorbent. For example, the control over the rate of CO<sub>2</sub> binding is transferred from reaction (1) to reaction (2).

In experiments with the same contact element, the effect of barium concentration in the solution on the absorption rate was evaluated. Under the following conditions, the experiments were carried out: volume fraction of CO<sub>2</sub> in gas is 40%; gas velocity is 0.7 m/s; irrigation density is 0.015 m<sup>3</sup>/m<sup>2</sup>s; temperature is 50 °C. The mass fraction of barium in the absorbent in terms of BaS varied from 5 to 9%.

The analysis of the experimental results did not show significant differences in the value of the mass transfer coefficient about barium concentration in the solution. Based on it, with an accuracy admissible in engineering calculations, it can be assumed that the effect of Ba(HS)<sub>2</sub> concentration on the absorption rate can be neglected. This means that the process chemistry at the consideration stage of carbonization is determined by reaction (2), i.e., by CO<sub>2</sub> hydration. Since the water concentration in the solution varies insignificantly with a change in barium hydrosulfide concentration, the latter does not affect the carbonization rate.

The study of the effect of the other factors (gas velocity, irrigation density, and temperature) was combined with the data obtained to select an appropriate contact element for carbonization. The experiments were carried out under the following conditions: CO<sub>2</sub> volume fraction in gas is 40%; mass fraction of barium in terms of sulfide in solution is 7%. The parameters studied varied in the following ranges: gas velocity is from 0.2 to 1.2 m/s; irrigation density is from 0.004 to 0.04 m<sup>3</sup>/m<sup>2</sup>s; temperature is from 20 to 80 °C; overflow height is from 0 to 20 cm.

To facilitate the calculation of the absorber, the experimental data obtained have been summarized in the form of the following empirical equation for calculating the mass transfer coefficient

$$\frac{K_g}{K_{g,0}} = 10^{a_1 \frac{t}{t_0}} \left( a_2 + a_3 \frac{h}{h_0} \right) \left( \frac{v}{v_0} \right)^{a_4} \left( \frac{l}{l_0} \right)^{a_5} \quad (9)$$

where  $a_1 \dots a_5$  are the coefficients of the equation;  $h$  is overflow height, cm;  $h_0 = 10$  cm,  $t$  is temperature, °C;  $t_0 = 50$  °C,  $v$  is gas velocity, m/s;  $v_0 = 0.7$  m/s,  $l$  is irrigation density,  $\text{m}^3/\text{m}^2\text{s}$ ;  $l_0 = 0.015$   $\text{m}^3/\text{m}^2\text{s}$ ;  $K_{g,0}$  is the mass transfer coefficient of the corresponding tray at  $h = h_0$ ,  $t = t_0$ ,  $v = v_0$  and  $l = l_0$ ,  $\text{mol}/\text{m}^2\text{s Pa}$ .

The coefficients of Eq. (9), the characteristics of its accuracy, and the values of  $K_{g,0}$  for each of the studied trays, calculated using the nonlinear evaluation program, are given in Table 1.

**Table 1.** Coefficients and the accuracy characteristics of Eq. (9).

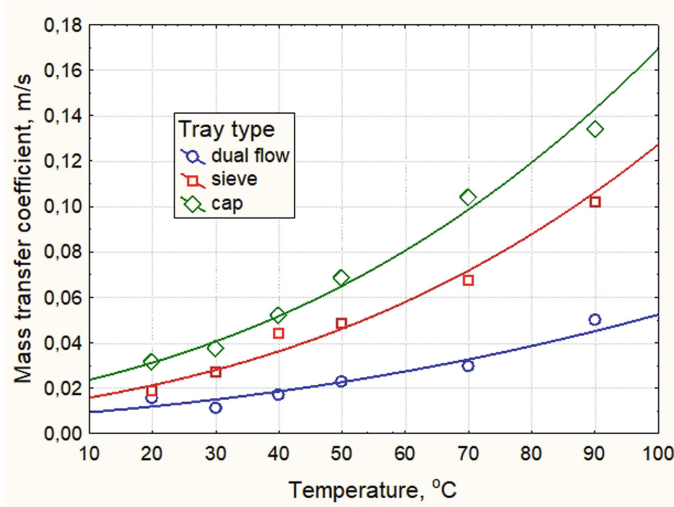
Type of tray	Coefficients					$K_{g,0}$	Residual RMS	Coefficient of determinization
	$a_1$	$a_2$	$a_3$	$a_4$	$a_5$			
Dual flow	-0.042	1.12	0	0.72	0.58	4.8	0.178	0.935
Sieve	0.074	0.33	0.51	0.33	0.17	9.5	0.085	0.955
Cap	0.068	0.57	0.27	0.47	0.21	14.8	0.063	0.964

The value of coefficient  $a_4$  can estimate the effect of gas velocity on absorption kinetics. Thus, its highest value for a dual-flow tray indicates that with an increase in the gas velocity, the absorption rate increases to a greater extent than other tested contact devices. On cap and sieve trays, the increase in the mass transfer coefficient with an increase in the gas velocity is approximately the same. These features are explained by the fact that the height of the foam layer and, consequently, the interface on the dual-flow tray is related to the gas velocity to a much greater extent than in the overflow trays. In the latter, the height of the foam is mainly determined by the height of the overflow.

According to the value of coefficient  $a_5$ , the irrigation density's effect on the mass transfer coefficient is less than the gas velocity. The most significant change in the mass transfer coefficient with an increase in the irrigation density is observed on the dual flow tray. As in the previous case, the relation of the height of the foam layer on the tray to the irrigation density.

Since the carbon dioxide absorption at carbonization level of the absorbent more than 50% is presumably controlled by the chemical reaction in the liquid, the estimation of the dependence of the rate of carbonization on temperature was based on the consideration of its influence on the coefficient of mass transfer in a liquid. According to the theory of absorption, in the case under consideration the mass transfer coefficient related to liquid ( $K_l$ ) can be calculated using the experimentally found values of the mass transfer coefficient related to gas, using the ratio  $K_l = H_{\text{CO}_2} K_g$  where  $H_{\text{CO}_2}$  is Henry's coefficient.

In Fig. 1, the graphs of the relations of  $K_l$  calculated by the method described above to the temperature at the gas velocity 0.7 m/s; irrigation density 0.015 m<sup>3</sup>/m<sup>2</sup>s, and overflow height 10 cm are shown.



**Fig. 1.** The mass transfer coefficient refers to the liquid, to the temperature for the dual flow tray - 1, sieve tray - 2, and cap tray - 3.

Figure 1 demonstrates that the temperature dependence of the mass transfer coefficient related to the liquid has an exponential character. This form of dependence is more typical for the rate of a chemical reaction than for the diffusion coefficient.

The relation of the absorption kinetics to the overflow height is the most significant factor affecting the determination of the stage that limits the absorption rate. In the experiments, the overflow height varied from 0 to 20 cm with a step of 2 cm. We used an external overflow. Its height was not equal to the height of the foam. It characterizes the height of the layer of light liquid on the tray. The absorbent temperature was 50 °C, and the gas velocity and irrigation density were the same as the experiments evaluating the temperature effect.

As Eq. (9) shows, the mass transfer coefficient increases linearly with the overflow height. The kinetics of a chemical reaction is proportional to the volume of the liquid in which it flows. Therefore, the presence of a linear relation of the mass transfer coefficient on the overflow height and the effect of temperature on it proves the assumption that the process chemistry limits the absorption rate.

## 5 Conclusions

The article presents the results of an experimental study to obtain data on the kinetics of carbon dioxide absorption by a barium sulfide solution and the choice of contact elements type (trays) for the absorber design.

The literature review has shown that two stages are significantly different in pH in barium sulfide carbonization. The first occurs when less than 50% of BaS is converted to BaCO<sub>3</sub> and pH is more than 11, and the second – is when more than 50% of BaS is converted, and pH is from 7.5 to 9. It was also found that the kinetics of CO<sub>2</sub> hydration under the conditions of the first and second stages is controlled by different reactions. This made it possible to assume that the absorption rate of carbon dioxide at various stages will also differ.

Our study of carbonation kinetics confirmed this assumption. It was shown that only the partial pressure of CO<sub>2</sub> in the gas, gas velocity, and temperature, has a significant effect on the absorption rate at the first stage. Any considerable effect of BaS concentration in the absorbent and the irrigation density was not found. The results obtained indicate that the absorption process is limited by resistance in the gas.

The carbonization rate at the second stage of the process, as experiments showed, is controlled by the kinetics of the chemical reaction of CO<sub>2</sub> hydration and is substantially lower than at the first stage of the process. The concentration of barium hydrosulfide (the reaction product at the first stage) in the absorbent has no significant effect on the kinetics of the process.

A further study of the BaS solution's carbonization was carried out to select an appropriate contact element for the equipment used in the process. Cap, sieve, and dual flow trays were tested, and the absorption rate of carbon dioxide was evaluated, characterized by the mass transfer coefficient.

As a result of an experimental study, equations were obtained for calculating the mass transfer coefficient about the temperature, gas velocity, and irrigation density for all types of trays mentioned.

Comparison of the obtained experimental data showed that the highest absorption intensity is achieved on the cap tray. The sieve plate turned out to be somewhat worse. On the dual flow tray, the absorption rate was the lowest. It was approximately two times lower than on a sieve tray and 2.5 times lower than on a cap tray. However, this does not characterize the dual flow tray as inappropriate for use in this process. The technical capabilities of conducting laboratory experiments did not allow us to achieve gas velocity in a laboratory absorber exceeding 1.2 m/s. At the same time, dual-flow trays in soda ash production operate at gas velocities of 2.5 m/s and higher. Extrapolating the relation of the mass transfer coefficient to the gas velocity, it can be shown that at high gas velocities, the indices of all the considered trays approach each other.

Thus, it can be concluded that all the trays studied are appropriate for carrying out the carbonization process of barium hydrosulfide solution. The selection of a specific type from considered contact elements for designing an absorption tower can be based primarily on design approaches that consider the designer's experience, the experience of operating particular devices, and the possibility of modifying the existing equipment for carrying out this process.

The work results were transferred to a specialized organization to design a pilot plant for BaS solution carbonization.

## References

1. Mulopo, J., Zvimba, J.N., Swanepoel, H., et al.: Regeneration of barium carbonate from barium sulphide in a pilot-scale bubbling column reactor and utilization for acid mine drainage. *Water Sci. Technol* **65**(2), 324–331 (2012). <https://doi.org/10.2166/WST.2012.857>
2. Peng, Y., Zhao, B., Li, L.: Advance in post-combustion CO<sub>2</sub> capture with alkaline solution. A brief review. *Energy Procedia* **14**, 1515–1522 (2012). <https://doi.org/10.1016/j.egypro.2011.12.1126>
3. Astarita, G.: Carbon dioxide absorption in aqueous monoethanolamine solutions. *Chem. Eng. Sci.* **16**(3–4), 202–207 (1961)
4. Mustafa, N.F.A., Mohd-Shariff, A., Tay, W.H., et al.: Mass transfer performance study for CO<sub>2</sub> absorption into non-precipitated potassium carbonate promoted with glycine using packed absorption column. *Sustainability* **12**(9), 3873 (2020). <https://doi.org/10.3390/su12093873>
5. Tseitlin, M.A., Raiko, V.F.: Mathematical modeling of pH dependence on barium sulfide to hydrosulfide ratio in a solution. In: *A Collection of Scientific Articles CMChT-2014*, pp. 29–35. NTUU “KPI”, Kyiv (2014)
6. Zhang, W., Zhang, F., Ma, L., et al.: Prediction of the crystal size distribution for reactive crystallization of barium carbonate under growth and nucleation mechanisms. *Cryst. Growth Des.* **19**(7), 3616–3625 (2019). <https://doi.org/10.1021/acs.cgd.8b01067>
7. Whittaker, M.L, Smeets, P.J.M., Asayesh-Ardakani, H., et al.: Multi-step crystallization of barium carbonate: rapid interconversion of amorphous and crystalline precursors. *Angewandte Chemie* **56**(50), 16028–16031 (2017). <https://doi.org/10.1002/anie.201709526>
8. Benamor, A., Mahmud, N., Nasser, M., et al.: Reaction kinetics of carbon dioxide with 2-Amino-1-butanol in aqueous solutions using a stopped-flow technique. *Ind. Eng. Chem. Res.* **57**(8), 2797–2804 (2018). <https://doi.org/10.1021/acs.iecr.7b04654>
9. Maragheh, M., Shahhosseini, S.: Kinetics and absorption rate of CO<sub>2</sub> into partially carbonated ammonia. *Chem. Eng. Commun.* **198**(10), 1169–1181 (2011). <https://doi.org/10.1080/00986445.2010.525204>
10. Skydanenko, M., Sklabinskyi, V., Saleh, S., Barghi, S.: Reduction of dust emission by monodisperse system technology for ammonium nitrate manufacturing. *Processes* **5**(3), 37 (2017). <https://doi.org/10.3390/pr5030037>
11. Masukume, M., Maree, J. P., Ruto1 S., Joubert H.: Processing of barium sulphide to barium carbonate and sulphur. *J. Chem. Eng. Process Technol* **4**(4), 1–4 (2013). DOI: <https://doi.org/10.4172/2157-7048.1000157>
12. Gaikwad, A.A., Challapalli, N., Bhaskarwar, A.N.: Carbonation of barium sulfide in a foamed reactor. *Chem. Eng. Commun.* **197**(6), 804–829 (2010). <https://doi.org/10.1080/00986440903359103>
13. Rukhadze, V.V., Kamushadze, I.D., Kinetic regularity study of barium sulfide solutions interaction with carbonic acid. *Proceedings of universities. Appl. Chem. Biotechnol.* **2**(5), 11–14 (2013)



# Hydraulic Resistance and Spray Transfer in a Stabilized Three-Phase Foam Layer

Viktor Moiseev<sup>(✉)</sup> , Eugenia Manoilo , Kalif Repko , Natalia Ponomarova ,  
and Denis Davydov 

National Technical University «Kharkiv Polytechnic Institute»,  
2, Kyrpychova Street, Kharkiv 61002, Ukraine  
bublikova1@gmail.com

**Abstract.** One of the promising areas for intensifying the mass transfer process is the improvement of separation columns using a stabilized foam mode of interaction of gas-liquid flows, including movable nozzle bodies. A new design of the stabilizer with a sizeable free volume and a spherical movable nozzle was developed. The advantage of the proposed design is the transition to a structured foam mode of operation at relatively low gas speeds and a developed phase contact surface. After experimental studies of the hydrodynamic characteristics of the combined contact element, empirical data on hydrodynamic resistance and experimental indicators of spray attribution for a contact stage with combined contact elements were obtained. As a result of research, it was found that when using foam layer stabilizers, the spraying ratio at the contact stage is reduced, which leads to a more stable operation of the device. An empirical equation for determining the value of the spray attribution is given.

**Keywords:** Hydrodynamics · Stabilization · Foam layer · Hole plate · Turbulization · Movable nozzle · Spray removal reducing · Energy efficiency

## 1 Introduction

Discover the most efficient and cost-effective technology of cleaning industrial emissions in the present situation of sizeable anthropogenic impact on the environment. Cleaning technology and developed equipment should consider the possibility of functioning in a wide variety of operating conditions.

To decrease energy spending in systems for capturing toxic and harmful substances, it is required to lessen hydraulic resistance while maintaining high effectiveness in cleaning gas flows.

Specific to the contradictory requirements for technique and regardless of the large quantity of offered devices for mass transfer processes, new intensified and capable equipment is of significant attention to ecological technologies in various industries.

A standard methodology of cleaning gas flows is absorption methods for absorbing dangerous components from exhaust manufacturing gases. In this case, either the absorbent enters into chemical interaction with the absorbed component, or the process of physical absorption occurs. And the way to intensify these processes is to carry them out in a stabilized three-phase foam layer [1].



## 2 Literature Review

Foam devices and foam mode of the classical kind are presented in research works [2, 3]. Because of its high effectiveness [4], high unit ability, the excellent operational behavior of their application, they can get better the stages of gas cleansing for sanitary and technological purposes, enlarge effectiveness, and boost the degree of reliability gas-cleaning techniques [5]. One of the promising areas of amplification of the mass transfer process is the improvement of column techniques using a stabilized foam mode of interaction of gas-liquid flows, including with the presence of movable nozzle bodies [6].

Previously studied devices with a foam layer [7] were used mainly in technological cycles with significant specific loads on gas and liquid, which led to high energy consumption [8].

At the same time, in systems for cleaning industrial gases from harmful components [9, 10], which are usually present in low concentrations [11], it is necessary to ensure a high degree of gas purification with minimal liquid consumption and a low spray ratio [12, 13].

## 3 Research Methodology

For these purposes, a new design of a stabilizer with a sizeable free volume and a movable spherical nozzle was developed. The advantage of the proposed design is the transition to a structured foam mode of operation at relatively low gas speeds and a developed inner phase contact surface. The cellular structure of the stabilizer and movable nozzle makes it possible to achieve increased values of mass transfer coefficients due to the effect of film formation in small cells. The structure has high porosity and relatively low hydraulic resistance. The structure may have different wet abilities depending on the selection of material.

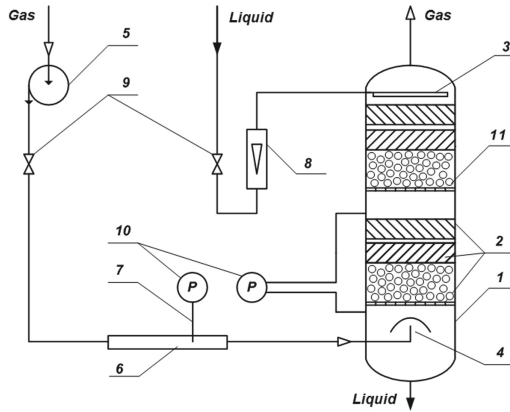
The new designs are simple and have a relatively low cost, which allows them to be effectively used in gas cleaning processes in various industries.

The combined contact block consists of a hole plate and one or two contact elements acting as stabilizers, and a movable ball-shaped nozzle located inside the block. The bubbling layer is formed on hole plates on which a movable nozzle is located.

The hydraulic resistance of the proposed design and spray transfer indicators were studied in this work.

A schematic picture of an experimental equipment setup for studying hydrodynamic is shown in Fig. 1. The laboratory unit is combined apparatus that has an internal diameter of 240 mm, made of stainless steel, with viewing windows made of organic glass. The experimental unit has the following main elements: a vertical column with contact combined blocks, a fan with a flue, water supply, water distribution, and catchment systems.

A combined contact unit with a movable ball-shaped nozzle is installed in the center working section of the column, a water distribution system and a separator are placed in the higher segment of the column, and the lower segment is designed to enter the gas flow through the windows located in it for gas supply and water gathering.



**Fig. 1.** Experimental equipment setup for studying the hydraulic resistance of a combined contact element: 1 – column; 2 – block of a combined contact element with a stabilized three-phase foam layer and movable nozzle inside; 3 – liquid distributor; 4 – gas distributor; 5 – gas blower; 6 – measuring pipe; 7 – Pitot tube; 8 – rotameter; 9 - valves; 10 – diffmanometers, 11 – movable nozzle.

In the column is organized countercurrent phase movement. Gas (air) from the blower is fed through the outlet to the lower section of the unit. Then it passes through the mesh distributor, as a result of which a uniform speed profile is achieved at the access to the contact unit. The liquid phase from the pressure reservoir is fed into the experimental column for irrigation.

A distributor is installed on top of the column, designed for the uniform initial distribution of the liquid phase over the cross-section of the contact device. Passing through the contact device, the liquid is distributed over the surface of the contact elements. Simultaneously, the gas phase occupies the entire free volume of the device. After that, the liquid phase is sent to the storage tank, and the air is discharged into the atmosphere. Three combined contact blocks were installed in the column. The middle block is a working one. Selectors were used to measuring pressure drops. They were placed inside the experimental column and connected to the differential micromanometer using rubber hoses through special fittings provided for this purpose.

Air was used as an experimental working medium. The research was carried out for several variants of contact combined blocks, which differed from each other by the existence of one or two stabilizers installed at a distance from the hole plate and the distance between the stabilizers and the movable nozzle.

To measure the hydraulic resistance of the irrigated unit, water was supplied to the column by a pump, the flow rate of which was synchronized by a tap and set according to the rotameter indications; with the help of a sprinkler, water was evenly distributed over the cross-section of the column [14]. After that, the air supply was turned on, and the hydraulic resistance of the irrigated contact device was measured, like the hydraulic resistance of the dry contact device.

Spray transfer from contact elements is one of the essential hydrodynamic characteristics of mass transfer columns designed to process gas and liquid flows. It largely

determines the upper limit loads, the distribution of interfacial mass and heat transfer forces in the column, and its hydraulic resistance. Two methods are used to measure splash removal, a catcher was used that separates the removed drops of liquid from the stream [15, 16].

The study of inter-plate spray transfer was carried out on the experimental stand, which was upgraded after hydrodynamic studies. One combined contact unit with a movable nozzle was left for research.

Spray transfer is measured by weight method using a fiber separator made of felt, which blocks the flue at the device's exit. After starting the gas and forming a bubbling layer in the device (3–10 s after starting the gas), the dried and suspended felt separator was installed in the flue in the upper part of the device, and the start time of the experiment was cut off. Thus, the entire gas flow passed through the separator, and the splashes contained in the gas were captured.

The experiment duration ranged from 60–120 s, depending on the gas load. After the experiments, the fiber separator was removed from the flue, re-weighed, and the gas phase's liquid flow rate was calculated based on the change in its mass during the experiment. The wet separator was weighed on an electronic scale. Experiments on measuring spray transfer were carried out in the same range of changes in loads on gas and liquid as experiments on determining other hydrodynamic characteristics of the combined device.

## 4 Results

The gas velocity influences the combined contact element's hydrodynamic characteristics in the entire cross-section of the contact element, the irrigation density, and the free cross-section of the contact stage, which depends mainly on the free cross-section of the hole plate.

Therefore, we can write a general relationship for the air-water phases:

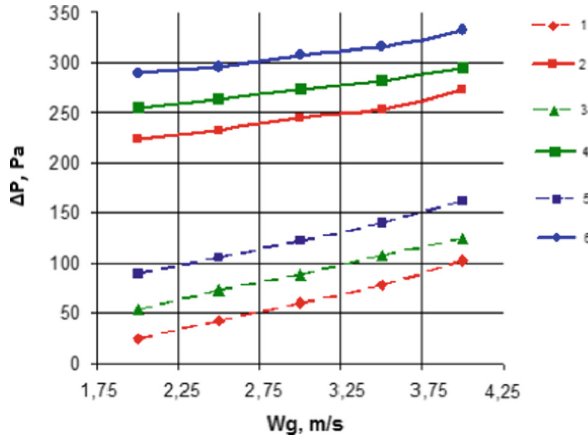
$$\Delta P = f(W_g, L_0, S_0, d_0) \quad (1)$$

The hydraulic resistance of the contact element and the gas-liquid layer created in the inner space of contact elements depends on the operating parameters, the diameter of the hole plates, the free cross-section, and the mass flow rates of gas and liquid. A general form of the equation for determining the hydraulic resistance of a contact stage with a foam layer is given in the paper [9]:

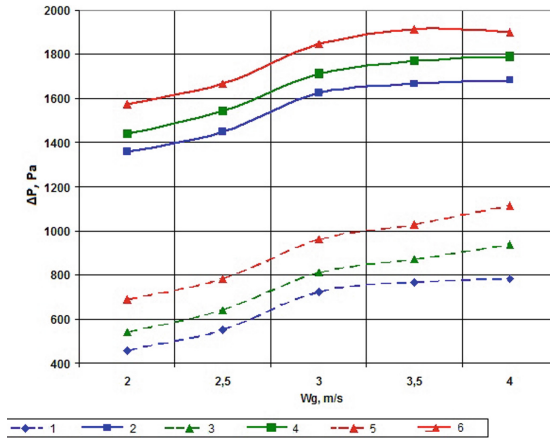
$$\Delta P = P_1 + P_2 + P_3 \quad (2)$$

where,  $P_1$  – dry contact element hydraulic resistance;  $P_2$  – hydraulic resistance of foam layer in the contact element;  $P_3$  – resistance resulting from the action of surface tension forces.

Figure 2 shows the dependence of the hydraulic resistance of a dry contact element on the gas velocity in the free cross-section of the column when using hole plates of different free cross-sections in the presence of a movable nozzle and without it. From Fig. 2, it can be seen that as the gas velocity increases, the hydraulic resistance increases.



**Fig. 2.** Dependence of the hydraulic resistance of a dry contact element on the gas velocity: 1, 2 –  $S_0 = 0,38 \text{ m}^2/\text{m}^2$ ,  $d_o = 0,02 \text{ m}$ ; 3, 5 –  $S_0 = 0,217 \text{ m}^2/\text{m}^2$ ,  $d_o = 0,015 \text{ m}$ ; 5, 6 –  $S_0 = 0,095 \text{ m}^2/\text{m}^2$ ,  $d_o = 0,01 \text{ m}$ . 1, 3, 5 – without movable ball nozzle, 2, 4, 6 – with movable ball nozzle layer thickness is 0,1 m.



**Fig. 3.** Dependence of the hydraulic resistance of the contact element on the gas velocity and the diameter of the holes of the hole plate at  $L_0 = 5 \text{ m}^3/\text{m}^2 \cdot \text{h}$ ; 1, 2 –  $d_o = 0,02 \text{ m}$ ; 3, 4 –  $d_o = 0,015 \text{ m}$ ; 5, 6 –  $d_o = 0,01 \text{ m}$ ; 1, 3, 5 – without movable ball nozzle, 2, 4, 6 – with movable ball nozzle layer thickness is 0,1 m.

The smaller the free cross of hole plates and the diameter of the holes in the plate leads to greater hydraulic resistance.

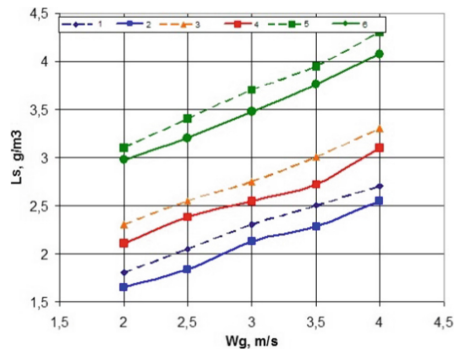
The hydraulic resistance of the foam layer mode is used to judge the energy spent on the process and the intensity of the process as a whole since the height of the foam and its hydrodynamic resistance are interrelated.

Analyzing the obtained results, we can say that  $\Delta P$  is most affected by the gas velocity in the entire device cross-section and the free cross-section, confirmed in Fig. 3.

So the increase of gas velocity causes the hydraulic resistance of the contact element to increase. This fact is associated with an increase in the gas velocity, which increases the height of the gas-liquid layer and, with a sufficient level of irrigation, leads to a proportional increase in hydraulic resistance. The hydraulic resistance and free cross-section of the contact element has an inverse relationship – with an enlarge in the free cross-section, the hydrodynamic resistance decreases since the foam height and holding capacity of the contact stage decrease, and at low gas speeds, the liquid failure on the lower contact stages increases [17]. These results are confirmed by studies [18, 19].

#### 4.1 Spray Transfer in the Combined Contact Element with Movable Nozzle

One of the most essential characteristics of column apparatuses is splash transfer. During studies at gas velocities from 2–4 m/s, modes of a highly tubulated gas-liquid system were observed, and the phenomenon of splash transfer was present.



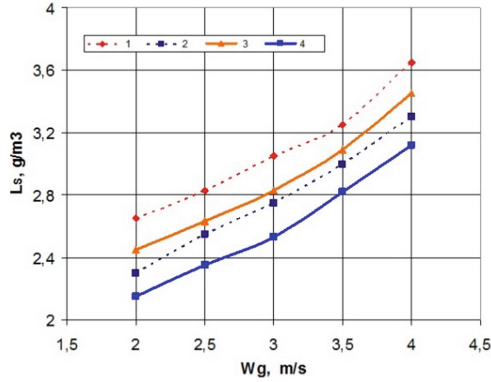
**Fig. 4.** Dependence of specific spray transfer on the free cross-sectional area of the plates and the gas velocity:  $L_0 = 5 \text{ m}^3/\text{m}^2 \cdot \text{h}$ , contact element with two stabilizers without a gap: 1, 2 –  $S_0 = 0,095 \text{ m}^2/\text{m}^2$ ; 3, 4 –  $S_0 = 0,217 \text{ m}^2/\text{m}^2$ ; 5, 6 –  $S_0 = 0,383 \text{ m}^2/\text{m}^2$ . 1, 3, 5 – without movable ball nozzle; 2, 4, 6 – with movable ball nozzle.

Experiments on Splash removal were carried out depending on several parameters affecting the gas-liquid foam layer mode in the three-phase phase. These include the gas velocity, the liquid load, the free cross-section of the contact stage, and the holes diameter of the hole plate.

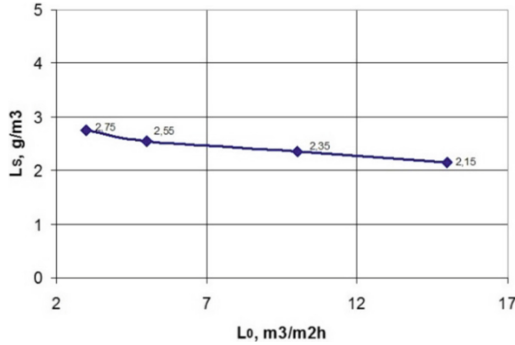
From Fig. 4, we can see that the larger holes in the plate, the greater the splash transfer value. This fact is explained by increasing the diameter of the holes, the kinetic force increases, which forms larger gas vortices.

As a result, the kinetic energy of the foam layer increases, and droplets and spray transfer, which is not entirely restrained even by dual stabilization of the foam layer. However, this significantly reduces splash removal compared to the operation of a hole plate without stabilizing the foam layer.

The gas velocity in the free cross-section has a noticeable effect on spray transfer (Fig. 5).



**Fig. 5.** Dependence of specific spray transfer on gas velocity:  $L_0 = 5 \text{ m}^3/\text{m}^2 \cdot \text{h}$ ,  $S_0 = 0,217 \text{ m}^2/\text{m}^2$ ,  $d_o = 0,015 \text{ m}$ ; without movable ball nozzle: 1 – with the use of 1 stabilizer; 2 – with the help of 2 stabilizers; in the presence of a movable ball nozzle: 3 - with the use of 1 stabilizer; 4 – with the use of 2 stabilizers.



**Fig. 6.** Dependence of spray transfer on the fusion density when using two stabilizers and a movable ball nozzle:  $W_g = 3 \text{ m/s}$ ;  $S_0 = 0,217 \text{ m}^2/\text{m}^2$ ,  $d_o = 0,015 \text{ m}$ .

The quantitative value of spray transfer on small hole plates is described by the following empirical equation,  $\text{g/m}^3$ :

$$L_{s(1)} = 1,2W_g^{2,4}L_0^{-0,2}S_0^{0,5} \tag{3}$$

The quantitative value of spray transfer on large hole plates using two stabilizers is described by the equation of the form,  $\text{g/m}^3$ ,

$$L_{s(2)} = 0,9W_g^{2,2}L_0^{-0,2}S_0^{0,5} \tag{4}$$

After installing the second stabilizer (Fig. 5) in the upper part of the foam layer, a significant reduction in splashes was observed. The gas-liquid flow has additional twisting and the direction of gas and liquid at an angle to the device’s wall.

When the irrigation density increases (Fig. 6), there is a slight decrease in the amount of spray transfer.

After analyzing Eqs. (3) and (4), we can conclude that the gas velocity in the free cross-section has the more significant splash effect, even when using dual stabilization of the foam layer. The calculation error based on Eqs. (3) and (4) is  $\pm 10\%$ .

After experimental studies of the hydrodynamic characteristics of the combined contact element with movable nozzle, experimental data on hydrodynamic resistance and experimental indicators of spray transfer attribution for the contact stage with combined contact elements with movable nozzle were obtained.

The primary purpose of the first stabilizer located in the bubbling zone is to prevent the appearance of longitudinal pulsation of the gas-liquid layer at high linear values of the gas velocity in the entire cross-section of the device. Due to the placement of the contact element in the pulsation zone of the gas-liquid layer, the device creates a full-fledged, highly developed foam contact surface of the gas and liquid phases on every stage of the apparatus. The use of such a design of the stabilizer does not significantly increase the hydraulic resistance of the device due to the large free volume.

The installation of the second stabilizer above the first helps reducing splash transfer from the contact zone and subsequent longitudinal mixing of phases, which generally improves the mass transfer processes in the device. The slope of the corrugation at an angle to the horizon ensures effective rebound of liquid droplets falling from the hole plate onto the device's wall with their return to the phase contact zone under their weight. Placement in the space between the hole plate and the ball's first movable nozzle's first stabilizer contributes to the constant updating of the phase contact surface in the specified zone. The design of the movable nozzle has a permeable structure, which additionally turbulize the foam layer. Even at small values of the gas velocity in the column, nozzles pass into a suspended state and actively turbulize the system of interacting phases.

As a result of research, it was found that when using foam layer stabilizers, the spray transfer ratio at the contact stage is reduced, which leads to a more stable and uniform operation of the device. Empirical dependences for determining the value of the spray transfer attribution are given.

Thus, for further intensification of absorption apparatuses, it is possible to use the proposed design using a three-phase foam layer with a movable nozzle. Previously, it was suggested that the use of mesh materials for the manufacture of nozzle bodies is promising. Then it is necessary to emphasize the peculiarity of the operation of devices with such nozzles type.

In apparatuses with movable ball nozzles, gas passes between the channels formed by the nozzle bodies, and liquid in the form of films and drops flows down the surface of the balls. In the case of a mesh nozzle, the interaction of gas with liquid occurs not only on the surface of the nozzle but also inside its volume. Therefore, the nozzle's transition mechanism to the advanced fluidization mode differs significantly from conventional ball nozzles [20].

These equations are empirical, which determines the possibility of their application only for the conditions of experiments on the example of which they are derived. Therefore, the calculation and design of devices with a foam layer and a fluidized bed nozzle [21] is carried out so far only based on experimental data [22] obtained on a limited number of interacting systems [23].

## 5 Conclusions

A promising direction for intensifying absorption/desorption processes is the development of devices with a three-phase stabilized pseudo-liquefied layer of an irrigated movable nozzle made of mesh materials. For gas purification systems from gaseous components, it is necessary to ensure low loads on the liquid while maintaining a high degree of purification. This can be achieved using a hole plate with a small or medium free cross-section and a new ball-shaped movable nozzle and stabilizers when the device operates in a developed foam mode with stabilization.

The industrial implementation of the stabilization method of a gas-liquid three-phase layer makes it possible to enlarge the range of application of foam apparatuses considerably. It opens a new possibility for going up technical processes with a slight reconstruction of the existing equipment of technological installations. All at once, it is possible to create low-waste technologies simultaneously.

## References




1. Liaposhchenko, O., Khukhryanskiy, O., Moiseev, V., Ochowiak, M., Manoilo, E.: Intensification of layered foam apparatus by foam stabilization. *J. Eng. Sci.* **5**(2), F13–F18 (2018). [https://doi.org/10.21272/jes.2018.5\(2\).f3](https://doi.org/10.21272/jes.2018.5(2).f3)
2. Pavlenko, A.N., et al.: Overview of methods to control the liquid distribution in distillation columns with structured packing: improving separation efficiency. *Renew. Sustain. Energy Rev.* **132**(6), 110092 (2020). <https://doi.org/10.1016/j.rser.2020.110092>
3. Moiseev, V., Manoilo, E., Hrubnik, A., Vasyliiev, M., Davydov, D.: Cleaning and disposal of gas emissions from the production of calcinated soda ash. *J. Eng. Sci.* **4**(2), B1–B6 (2017). [https://doi.org/10.21272/jes.2017.4\(2\).b1](https://doi.org/10.21272/jes.2017.4(2).b1)
4. Zbytovsky, J., Sommer, T., Zapletal, M., Trejbal, J.: Comparison of various column packing materials efficiency for hydrocarbons and aqueous mixtures. *Chem. Biochem. Eng. Q.* **33**(2), 183–190 (2019)
5. Perry, D.C.: Gas absorption and reaction in a wet pneumatic foam. *Chem. Eng. Sci.* **126**, 177–185 (2015). <https://doi.org/10.1016/j.ces.2014.11.037>
6. Wang, S., Wang, S., Wu, B., Lu, Y., Zhang, K., Chen, H.: Effect of packing structure on anisotropic effective thermal conductivity of thin ceramic pebble bed. *Nucl. Eng. Technol.* **53**(7), 2174–2183 (2021). <https://doi.org/10.1016/j.net.2021.01.013>
7. Clavier, R., Chikhi, N., Fichot, F., Quintard, M.: Modeling of inertial multi-phase flows through high permeability porous media: friction closure laws. *Int. J. Multiphas. Flow.* **91**, 243–261 (2017). <https://doi.org/10.1016/j.ijmultiphaseflow.2017.02.003>
8. Fourati, M., Roig, V., Raynal, L.: Experimental study of liquid spreading in structured packings. *Chem. Eng. Sci.* **80**, 1–15 (2012). <https://doi.org/10.1016/j.ces.2012.05.031>
9. Skydanenko, M., Sklabinskyi, V., Saleh, S., Barghi, S.: Reduction of dust emission by monodisperse system technology for ammonium nitrate manufacturing. *Processes* **5**(3), 37 (2017). <https://doi.org/10.3390/pr5030037>
10. Kuznetsov, P.V.: Structural parameters of the foam layer on fine-grained countercurrent lattices with a stabilizer. *East Euro. J. Adv. Technol.* **4**(10), 84–88 (2004)
11. Rahmonov, O.K.: Study of the process of deposition of fine particles in the apparatus with a movable nozzle. *Austrian J. Tech. Nat. Sci.* **2**, 78–81 (2017). <https://doi.org/10.20534/AJT-17-11.12-78-81>



12. Pavlenko, I., et al.: Effect of superimposed vibrations on droplet oscillation modes in prilling process. *Processes* **8**(5), 566 (2020). <https://doi.org/10.3390/pr8050566>
13. Moiseev, V., Manoilo, E., Ponomaryova, N., Repko, K., Davydov, D.: Methodology of calculation of construction and hydrodynamic parameters of a foam layer apparatus for mass-transfer processes. *Bull. NTU “KhPI”. Ser. New Solu. Mod. Technol.* **16**(1292), 165–176 (2018). <https://doi.org/10.20998/2413-4295.2018.16.25>
14. Sklabinskyi, V., Liaposhchenko, O., Pavlenko, I., Lytvynenko, O., Demianenko, M.: Modelling of liquid’s distribution and migration in the fibrous filter layer in the process of inertial-filtering separation. In: Ivanov, V., et al. (eds.) *DSMIE 2018. LNME*, pp. 489–497. Springer, Cham (2019). [https://doi.org/10.1007/978-3-319-93587-4\\_51](https://doi.org/10.1007/978-3-319-93587-4_51)
15. Pavlenko, I., Ivanov, V., Gusak, O., Liaposhchenko, O., Sklabinskyi, V.: Parameter identification of technological equipment for ensuring the reliability of the vibration separation process. In: Knapcikova, L., Balog, M., Perakovic, D., Perisa, M. (eds.) *4th EAI International Conference on Management of Manufacturing Systems. EICC*, pp. 261–272. Springer, Cham (2020). [https://doi.org/10.1007/978-3-030-34272-2\\_24](https://doi.org/10.1007/978-3-030-34272-2_24)
16. Pavlenko, I., Liaposhchenko, A., Ochowiak, M., Demyanenko, M.: Solving the stationary hydroaeroelasticity problem for dynamic deflection elements of separation devices. *Vibrat. Phys. Syst.* **29**, 2018026 (2018)
17. Arakelyan, V.B., Danko, V.P., Grigoryan, R.P.: Influence of the external noise intensity on the kinetics of ligands binding to receptors. Influence of the external noise intensity on the kinetics of ligands binding to receptors. *J. Contemp. Phys.* **52**(1), 70–75 (2017). <https://doi.org/10.3103/S106833721701011X>
18. Shestova, T.D., Markvart, A.S., Lozovsky, T.L., Zhelezny, V.P.: Cubical equations of state for predicting the phase equilibria of poorly studied substances. *Russ. J. Phys. Chem.* **87**(6), 883 (2013). <https://doi.org/10.1134/S0036024413060253>
19. Valueva, E.P., Purdin, M.S.: Hydrodynamics and heat exchange of the pulsing laminar stream in channels. *Teploenergetika* **9**, 24 (2015). <https://doi.org/10.1134/S0040601515090116>
20. Vitcovskaya, R.F., Zibina, N.F.: Polymeric contact equipment made of volumeric textile structures for heatmass-transfer apparatus. *Bull. Saint Petersburg State Univ. Technol. Des.* **2**, 120–127 (1998)
21. Kunii, M., Kuroda, K., Yamagiwa, K., Ohkawa, A.: Performance characteristics of nozzle foam-breakers fitted to tower aerator. *J. Chem. Eng. Jpn.* **27**(1), 129–132 (1994). <https://doi.org/10.1252/jcej.27.129>
22. Song, J., Hyndman, C., Jakher, R.K., Hamilton, K.: Fundamentals of hydrodynamics and mass transfer in a three-phase fluidized bed system. *Chem. Eng. Sci.* **54**(21), 4967–4973 (1999). [https://doi.org/10.1016/S0009-2509\(99\)00219-5](https://doi.org/10.1016/S0009-2509(99)00219-5)
23. Song, J., Hyndman, C., Kantzas, A.: Effect of particle tethering and scale-up on solid-liquid mass transfer in three-phase fluidized beds of light particles. *Can. J. Chem. Eng.* **79**(4), 557–563 (2001). <https://doi.org/10.1002/cjce.5450790413>



# Design of Reactors with Mechanical Mixers in Biodiesel Production

Mikhailo Mushtruk<sup>1</sup> , Larysa Bal-Prylypko<sup>1</sup> , Natalia Slobodyanyuk<sup>1</sup> ,  
Yuriy Boyko<sup>2</sup> , and Mykola Nikolaienko<sup>1</sup>

<sup>1</sup> National University of Life and Environmental Sciences of Ukraine,  
15, Heroes of Defense Street, Kyiv 03041, Ukraine  
mixej.1984@ukr.net

<sup>2</sup> National University of Food Technology, 68, Volodymyrska Street, Kyiv 01601, Ukraine

**Abstract.** Theoretically substantiated prerequisites for improving the production process of liquid biofuels from technical animal fats (TAF) and fat-containing wastes from food and livestock products, which makes it possible to design reactors for the production of liquid biofuels. A mathematical model for converting coolant and fat-containing waste into diesel biofuel has been developed. The feasibility of its use in the design of batch reactors with mechanical mixers has been proved. Turbulence models and their parameters are determined, which adequately characterize the velocity fields in reactors with turbine stirrers and provide an adequate description of the kinetic energy dissipation rates in different technological zones of reactors for the production of biofuels from TAF and fatty waste. It was found that the change in the distance between the stirrers and their diameters leads to a significant change in the rate of kinetic energy dissipation, which allows to unambiguously determine the place of introduction of alcohol-catalytic solvent and affect the degree of dispersion of reagents. The proposed ratio for determining the power criterion for reactors with two-stage six-bladed turbine stirrers and four baffles. Rational relations between the diameters of stirrers and the distance between them ensure the maximum yield of biofuels from the TAF and fatty waste from the food and processing industries. The technique of designing reactors with mechanical mixers for the production of diesel biofuel has been developed and substantiated.

**Keywords:** Industrial growth · Reactor · Model · Mixer · Biofuel · Technique · R&D investment

## 1 Introduction

The energy crisis has affected almost all countries of the world. It has not bypassed Ukraine. Therefore, they began to introduce alternative energy sources actively. Production of diesel biofuel by esterification and transesterification is promising and affordable [1]. The purpose of alcohol analysis of lipid raw materials is to obtain diesel biofuel, reduce the viscosity to a level close to mineral diesel fuel, and ensure compliance with applicable standards [2]. The main factors influencing the reaction rate and the degree

of conversion of lipid raw materials into fuel are the molar ratio of alcohol and fat, the type of catalyst and its concentration, temperature and reaction time, the level of FFA, and water in the feedstock [3, 4]. Diesel biofuel production uses refined vegetable oils, mainly triglycerides, and little FFA [5]. Such refined oils (soybean and rapeseed) have a high cost, which is about 60–80% of the total fuel cost. In this regard, biofuels produced from such oils are not commercially competitive in the market compared to mineral diesel. About 200 thousand tons of animal fats are accumulated annually at the meat processing enterprises of Ukraine alone, and if we consider the plants for the production of meat and bone meal, it is about 100 thousand tons [6, 7]. In the world economy, commercial production of diesel biofuel from technical animal fats (TAF) was widespread. To date, scientists are intensively researching the processing of lipid raw materials, which has the lowest possible cost to reduce the cost of biofuel production and increase its competitiveness in the energy market. Such raw materials, as a rule, have a high acid number containing water and protein impurities, which requires in-depth research, design, and development of new technologies and equipment for the production of diesel biofuels [8, 9]. Therefore, technological processes and their rational hardware implementation for processing fats, such as into diesel biofuels, can be created only based on a detailed study of the physicochemical mechanics of basic and auxiliary materials involved in the processes [10]. Only on this basis, it is possible to create essential, high-performance equipment that provides high fuel yield and compliance with current domestic and foreign standards.

## 2 Literature Review

After conducting an extensive analysis of the literature, it was found that the production of diesel biofuels by esterification and transesterification of technical fats (TF) is promising and affordable [11]. Fundamentals of theory and results of experimental research of technological processes, machines, and equipment for production and use of diesel biofuel in the agro-industrial complex of Ukraine are presented in detail in the scientific works of M. Virevka, V. Voitov, J. Gukov, V. Dubrovin, S. Kovalishin, V. Kravchuk, V. Myronenko, S. Pastushenko, G. Ratushnyak, V. Semenov, Y. Sukhenko and others. [12, 13].

Reactor designs for diesel biofuel production are diverse and must meet specific requirements to ensure maximum yield and high fuel quality. They must ensure a minimum cost of raw materials, energy and labor costs [14].

It is necessary to use many initial data to select a rational design of the reactor:

- kinetics of the chemical reaction (information about the basis of the reaction leading to the target product) [15];
- data on side processes that lead to irrational consumption of raw materials and the formation of unnecessary and sometimes harmful substances [16];
- the level of heat released or absorbed during the reaction [17];
- mixing efficiency, which will depend on the viscosity of the components, the mutual solubility of the starting materials, costs, geometric parameters of the reactor, and various devices for the introduction of reagents [18];

- chemical reaction time, which has a significant impact on the mixing process [19];
- conducting the process under appropriate temperature conditions, following the requirements of the kinetic process to optimize the reaction rate and ensure high yield and separation of by-products [20];
- data from sources of information on the possible degree of conversion of crude fat into biofuels [21].

All these problems are solved by chemical thermodynamics to carry out the reaction of the molecule of starting reagents (fat, alcohol, catalyst), which must react, and therefore the reaction mixture must be mixed well to provide the necessary phase contact [22].

In general, designing reactors for the production of liquid biofuels is complicated. However, little attention is paid to the study of this problem in the production of diesel biofuels, which leads to increased costs and can lead to reduced yields and deteriorate the quality of the final product (biodiesel), although the amount of raw materials is quite large, this problem can be minimized by using some boundary models. Therefore, the relevance of the chosen area of research is beyond doubt.

### 3 Research Methodology

Modern theoretical concepts of physical and mathematical modeling of viscous and liquid media, similarity theory, fundamental laws of hydrodynamics, numerical method, which includes: mathematical model, sampling method, numerical grid, final approximation, and solution method, were used in theoretical research [23].

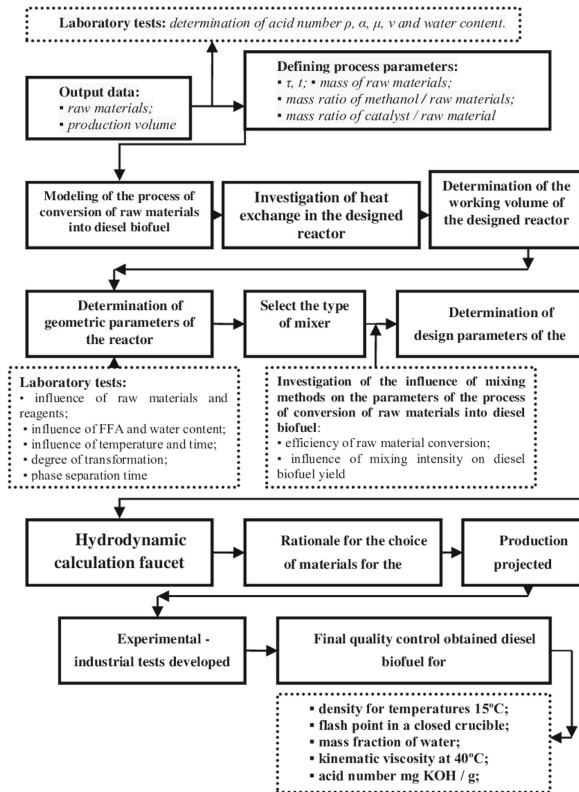
The standard, RNG, and realizable  $k$ - $\epsilon$  turbulence models were investigated. These are two-parameter models of turbulence, in which two equations are solved that determine the kinetic energy of turbulence  $k$  and the rate of its dissipation  $\epsilon$ . The software was used to investigate a complex mixing process with many statistical parameters. Power criterion determines the amount of energy for mixing and introducing it directly into the reaction zone. Simplexes of geometric similarity were used in the laboratory to assess the yield of biofuels. The results of modeling and experimental studies were used to design an industrial reactor.

Based on the developed methodology using Flow Vision 2.5 software, seven reactors with different diameters and heights with four baffles and two open turbine stirrers on one shaft were investigated. The diameters of the stirrers were changed within (0.15–0.35) of the diameter of the reactor ( $D$ ) and the distance between the stirrers within (1.0–2.5) of the diameter of the stirrer blades ( $d_m$ ) to analyze the change in the criterion of power and kinetic energy dissipation. During the research, the change of geometric simplexes  $d_m/D$ ,  $C_{1-2}/d_m$ ,  $C_{D-2}/D$ ,  $C_{N-k}/d_m$  was used, allowing the velocity fields on which such essential characteristics as the kinetic energy dissipation rate and the power criterion depend. The assumption is that with increasing power criterion, the degree of conversion into biodiesel increases, and therefore the output of biodiesel directly depends on the amount of energy input.

After conducting mathematical modeling, in the laboratory were conducted studies to determine the impact of design parameters of the simulated mixer, which made it possible to assess:

- the yield of diesel biofuel;
- change in the kinematic viscosity of the reaction mixture during the reaction;
- the phase separation period.

Based on the conducted research and the recommendations following from scientific works of predecessors and considering features of the technological process of production of diesel biofuel, the scheme of designing of reactors of periodic action for biofuel production is developed (Fig. 1).



**Fig. 1.** Block diagram of the method of design of reactive reactors for the production of diesel biofuel: AN - acid number,  $\rho$  - density,  $\alpha$  - kinematic viscosity,  $\mu$  - kinematic viscosity,  $\nu$  - dynamic viscosity,  $\tau$  - reaction time,  $t$  - reaction temperature, FFA - free fatty acids.

As a result of the research, the methods of a multiple reference system (MRS) and computational snapshot were used in which an imaginary cylindrical zone with a radius greater than the radius of the mixer and less than the inner radius of the edges of the baffle plates and a sufficient height, including the entire mixer, divides the apparatus into two regions. These methods require the detailing of the mixing device. Attempts have also been made to model using large-eddy models (LES). However, the computational requirements for this model are large, and therefore the application of this method is

limited to relatively simple forms of mixing devices. Also, this model has not been sufficiently tested to assert the adequacy of the results obtained.

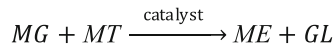
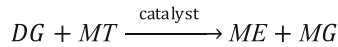
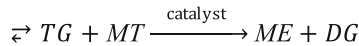
The experimental research uses equipment from the manufacturer Robotron, modern systems to assess the kinematic and energy characteristics of the production process and the physical and mechanical properties of the final product of biodiesel.

## 4 Results

Mathematically modeled technological process of conversion of TAF in the production of diesel biofuel in a batch reactor considering the physicochemical mechanics of raw materials, reagents and determined rational design and technological parameters of a batch reactor with a two-stage turbine mixer.

A computer model of the technological process of conversion of TAF into diesel biofuel has been developed, which consists of several interconnected subprograms: the first defines the variables that regulate the process of conversion of TAF into diesel biofuel; the second analyzes the factors that depend on the conditions of the process of conversion of TAF into diesel biofuel, primarily temperature; the third calculates the kinetics of the formation of fatty acid esters (biodiesel); the fourth describes the heat transfer in the designed reactor, selects the boundary conditions of the process and the productivity of fat conversion depending on the conditions of the process; the fifth determines the mechanical parameters of the designed reactor.

The stages of conversion of TAF into methyl ether (biodiesel) are as follows:



where: TG - triglycerides, DG - diglycerides, MG - monoglycerides, the catalyst - sulfuric acid ( $H_2SO_4$ ), MT - methanol, GL - glycerin; ME - methyl ether.

A method for calculating the field of mixing rates of reagents in reactors with mechanical turbine stirrers, which consists in the numerical solution of the system of differential equations of conservation of mass and momentum with partial derivatives in cylindrical coordinates in the three-dimensional formulation:

$$\frac{\rho}{r} \frac{\partial}{\partial r}(rU\varphi) + \frac{\rho}{r} \frac{\partial}{\partial \theta}(V\varphi) + \rho \frac{\partial}{\partial z}(W\varphi) = \frac{1}{r} \frac{\partial}{\partial r} \left( \Gamma_{\varphi} r \frac{\partial \varphi}{\partial r} \right) + \frac{\rho}{r} \frac{\partial}{\partial \theta} \left( \frac{\Gamma_{\varphi}}{r} \frac{\partial \varphi}{\partial \theta} \right) + \frac{\partial}{\partial z} \left( \Gamma_{\varphi} \frac{\partial \varphi}{\partial z} \right) + S_{\varphi} \quad (1)$$

In reactors with high-speed turbine stirrers, two characteristic regions can be distinguished: the first region adjacent to the stirrer is characterized by a large velocity gradient, and the region extends to the walls of the apparatus. The requirements for the calculation grids for modeling the velocity fields and cell sizes are investigated: for the convergence of the solution, it is necessary that the grid pitch in the area adjacent to the mixer was  $\leq 3$  mm, and outside is  $\leq 8$  mm.

The adequacy of the description of the velocity field was tested for devices with two types of mixing devices: 1 - with a six-bladed standard open turbine stirrer, 2 - with two-tier open turbine stirrers. Quantitative experimental data in the form of profiles of velocity components (axial, radial, and tangential) and power criteria are known for them (Table 1).

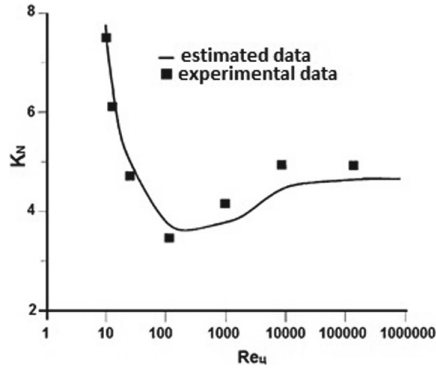
**Table 1.** Dependencies.

Equation	$\varphi$	$\Gamma_\varphi$	$S_\varphi$
Continuity	1	0	0
U	$\mu_M + \mu_t$		$-\frac{\partial p}{\partial r} + \frac{1}{r} \frac{\partial}{\partial r} \left( \Gamma_\varphi r \frac{\partial U}{\partial r} \right) + \frac{1}{r} \frac{\partial}{\partial \theta} \left( \Gamma_\varphi r \frac{\partial (V/r)}{\partial \theta} \right) + \frac{\partial}{\partial z} \left( \Gamma_\varphi \frac{\partial W}{\partial r} \right) -$ $-\frac{2\Gamma_\varphi}{r^2} \frac{\partial V}{\partial \theta} - \frac{2\Gamma_\varphi U}{r^2} + \frac{\rho V^2}{r}$
Movement			
V	$\mu_M + \mu_t$		$-\frac{1}{r} \frac{\partial p}{\partial \theta} + \frac{1}{r} \frac{\partial}{\partial r} \left( \Gamma_\varphi \frac{\partial U}{\partial \theta} \right) + \frac{1}{r} \frac{\partial}{\partial \theta} \left( \Gamma_\varphi \frac{\partial V}{\partial \theta} \right) + \frac{\partial}{\partial z} \left( \Gamma_\varphi \frac{\partial W}{\partial \theta} \right) +$ $+\Gamma_\varphi \frac{\partial (V/r)}{\partial r} - \frac{1}{r} \frac{\partial}{\partial r} \left( \Gamma_\varphi V \right) - \frac{\rho UV}{r} + \frac{\Gamma_\varphi}{r^2} \frac{\partial U}{\partial \theta} + \frac{1}{r} \frac{\partial}{\partial \theta} \left( \frac{2\Gamma_\varphi U}{r} \right)$
W	$\mu_M + \mu_t$		$-\frac{\partial p}{\partial z} + \frac{1}{r} \frac{\partial}{\partial r} \left( \Gamma_\varphi r \frac{\partial U}{\partial z} \right) + \frac{1}{r} \frac{\partial}{\partial \theta} \left( \Gamma_\varphi r \frac{\partial V}{\partial z} \right) + \frac{\partial}{\partial z} \left( \Gamma_\varphi \frac{\partial W}{\partial z} \right)$

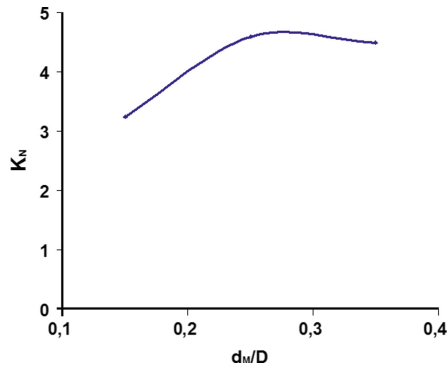
where:  $r, \Theta, z$  – coordinates;  $p$  – pressure;  $\rho$  – is the density of the reaction mixture in the reactor,  $\text{kg/m}^3$ ;  $W$  – axial component of velocity,  $\text{m/s}$ ;  $V$  – tangential component of velocity,  $\text{m/s}$ ;  $U$  – is the radial component of velocity,  $\text{m/s}$ ;  $\mu_M$  – dynamic molecular viscosity coefficient,  $\text{Pa}\cdot\text{s}$ ;  $\mu_t$  – is the dynamic coefficient of turbulent viscosity,  $\phi$  – is the value (velocity, scalar);  $\Gamma_\phi$  – is the transfer coefficient (laminar/turbulent viscosity, diffusion coefficient);  $S_\phi$  - forces are not included in the convective and diffusion parts, as well as additional forces.

Figure 2 shows the experimental and calculated values of the power criterion depending on the centrifugal Reynolds number  $Ret$  for a reactor with an open turbine stirrer and four baffles with a width  $b = (D \text{ is the reactor diameter})/12$ , which shows that the difference between them does not exceed 8%. For the same reactor, the power criterion was determined for different diameters of the stirrer. As a result, it turned out that with an increase in the diameter of the stirrer 2 times, the power criterion increases by 1.5 times (Fig. 3).

The choice of mixing method and type of stirrer is determined by the process’s intended purpose and specific conditions. Therefore, when choosing a stirrer, the approximate characteristics of the appropriate use of different types of stirrers [24]. After analyzing the results of theoretical and experimental studies, an open turbine mixer was



**Fig. 2.** Dependence of the KN power criterion for a reactor with an open turbine stirrer and four baffles on the centrifugal Reynolds number.



**Fig. 3.** Dependence of the power criterion KN on the simplex  $d_m/D$  for the reactor with one open turbine stirrer on the shaft ( $D$  is the inner diameter of the reactor,  $d_m$  is the diameter of the stirrer).

chosen. Because when using it: the yield of biofuel was 92–95%, the kinematic viscosity of the reaction mixture during the reaction was the lowest complete phase separation completed in 20–25 min.

Figure 4 shows the distribution of flow velocities in three of the seven considered devices with stirrers with a diameter of  $d_m = 0.264D$  and the distances between them (1.0–2.5)  $d_m$ .

At a distance between the stirrers  $C_{1-2} = d_m$ , the combined flow structure is realized, and at  $C_{1-2} = 2.5 d_m$ , the parallel structure of the reagent flow is realized. When the distance between the stirrers is greater than the diameter of the stirrers, the interaction between the flows of the upper and lower stirrers weakens and leads to the division of the reactor volume into two equal symmetrical parts in height. It can also be noted that more circulating circuits are formed with increasing distances between the stirrers.

The maximum value of the rate of dissipation of kinetic energy determines the intensity of mixing the components of the reaction mixture at the micro-level, which ensures



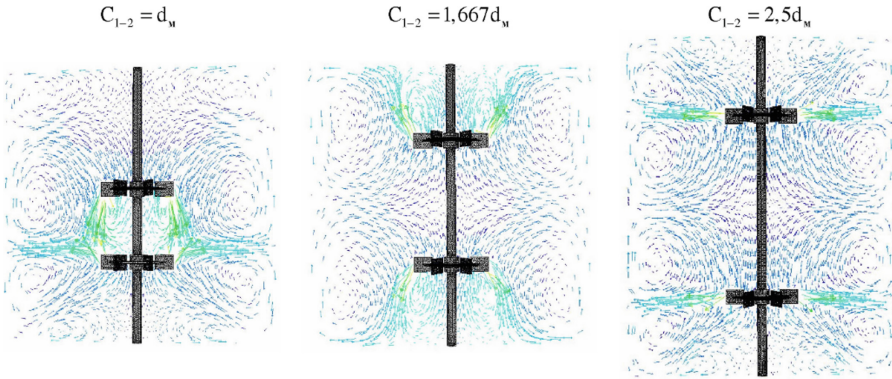


Fig. 4. Flow distribution in devices with two-tier turbine stirrers.

the occurrence of their small-scale shear deformations and, consequently, obtaining finely dispersed emulsions and suspensions.

The analysis of the distribution of the kinetic energy dissipation rate in the seven considered devices allowed us to conclude that increasing the distance between the stirrers leads to an increase in the kinetic energy dissipation rate  $\epsilon$  (Fig. 5) and, at  $C_{1-2} = 1.7d_m$ , its limit value is reached. It is also necessary to consider the fact that an increase in the rate of energy dissipation can be achieved with small diameters of stirrers, as can be seen from Fig. 6. However, it should be remembered that the increase in  $C_{1-2}$  leads to the formation of weakly interacting flows, which leads to the appearance of stagnant zones, and, thus, these effects should be considered in the complex.

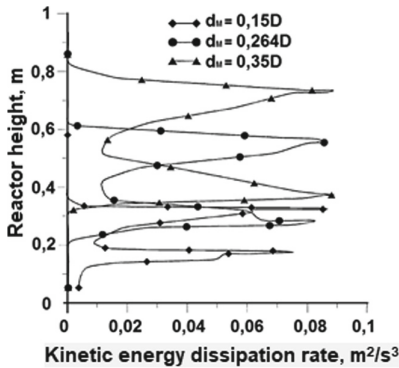
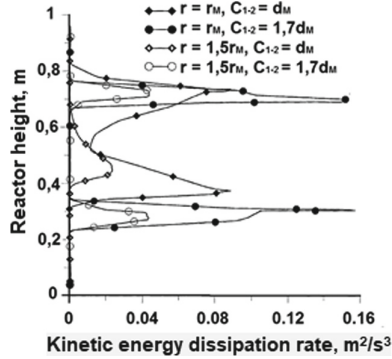


Fig. 5. The rate of dissipation of kinetic energy  $\epsilon$ , along with the height of the reactor at a distance equal to  $r_m$  from the Central axis of the shaft for three reactors with two-stage stirrers:  $d_m = (0.15-0.35) D$  and the distance between them  $C_{1-2} = d_m$ .

Rational design and technological parameters of a batch reactor with a turbine mixer for the production of diesel biofuel are substantiated. In determining the design features of the reactor, the need for mixing reagents without stagnant zones, ensuring unimpeded



**Fig. 6.** The rate of dissipation of kinetic energy  $\epsilon$ , along with the height of the reactor at a distance of  $r_m$  and 1.5  $r_m$  from the central axis of the shaft of two reactors with two-stage stirrers:  $d_m = 0.35D$  and the distances between them  $C_{1-2} = d_m$  and 1.7 $d_m$ .

deposition of the glycerol phase, and periodic draining of intermediate and final products is considered.

Other parameters of the reactor depend on some specific design solutions. The given algorithm and the scheme of a design technique allow calculating the basic design parameters of reactors of any productivity with mechanical mixers of any type.

## 5 Conclusions

It is established that the change of geometric simplexes  $d_m/D$ ,  $C_{1-2}/d_m$ ,  $CD - 2/D$ ,  $CN - k/d_m$  leads to entirely different velocity fields in reactors with stirring devices, on which such essential characteristics as the power criterion depend, and the rate of dissipation of kinetic energy.

It is established that the power criteria (Euler) for reactors with two-stage turbine stirrers depend on the simplex  $C_{1-2}/d_m$  and have the form of symmetric function with S-like shape (sigmoid).

An analysis of the distribution of the kinetic energy dissipation rate in seven simulated reactors was performed to identify areas with maximum values of this value for the correct selection of the zone of introducing the alcohol-catalytic fluid solution into the reactor.

The analysis of the distribution of the kinetic energy dissipation rate in the seven considered devices allowed us to conclude that increasing the distance between the stirrers leads to an increase in the kinetic energy dissipation rate, and at  $C_{1-2} = 1.7d_m$ , its limit value is reached, which allows determining the catalytic fluid solution.

The multiple reference frame method looks promising as a tool for simulating agitators, as it can be extended to mixers of various shapes, to units with multi-tiered agitators, when simulating multiphase flows without excessive demands on computational resources, and, most importantly, it is available in many CFD complexes.




## References

- Ardebili, S., Khademalrasoul, A.: An analysis of liquid-biofuel production potential from agricultural residues and animal fat (case study: Khuzestan Province). *J. Clean. Prod.* **204**, 819–831 (2018)
- Srinivasan, G.R., Jambulingam, R.: Comprehensive study on biodiesel produced from waste animal fats—a review. *J. Environ. Sci. Technol.* **11**(3), 157–166 (2018)
- Petchsoongsakul, N., Ngaosuwan, K., Kiatkittipong, W., et al.: Different water removal methods for facilitating biodiesel production from low-cost waste cooking oil containing high water content in hybridized reactive distillation. *Renew. Energy* **162**, 1906–1918 (2020)
- Nisar, J.: Enhanced biodiesel production from *Jatropha* oil using calcined waste animal bones as the catalyst. *Renew. Energy* **101**, 111–119 (2017)
- Sander, A., Koščak, M., Kosir, D., Milosavljević, N.: The influence of animal fat type and purification conditions on biodiesel quality. *Renew. Energy* **118**, 752–760 (2018)
- Kirubakaran, M., Selvan, V.: A comprehensive review of low-cost biodiesel production from waste chicken fat. *Renew. Sustain. Energy Rev.* **82**, 390–401 (2018)
- Xiong, H., Guo, X., Xie, W.: Biodiesel remote monitoring system design based on IOT. In: Zu, Q., Hu, B., Gu, N., Seng, S. (eds.) *Human Centered Computing, HCC 2014, LNISA*, vol. 8944, pp. 750–756 (2018). [https://doi.org/10.1007/978-3-319-15554-8\\_65](https://doi.org/10.1007/978-3-319-15554-8_65)
- Brännström, H., Kumar, H., Alén, R.: Current and potential biofuel production from plant oils. *BioEnergy Res.* **11**(3), 592–613 (2018)
- Vasquez, M.C., Silva, E.E., Castillo, E.F.: Hydrotreatment of vegetable oils: a review of the technologies and its developments for jet biofuel production. *Biomass Bioenerg.* **105**, 197–206 (2017)
- Sani, S., Kaisan, M.U., Kulla, D.M., et al.: Determination of physicochemical properties –of biodiesel from *Citrullus lanatus* seeds oil and diesel blends. *Ind. Crops Prod.* **122**, 702–708 (2018)
- Nielsen, P., Rancke-Madsen, A., Holm, H.: Production of biodiesel using liquid lipase formulations. *J. Am. Oil Chem. Soc.* **93**(7), 905–910 (2016)
- Mushtruk, M., Vasylyv, V., Slobodaniuk, N., Mukoid, R., Deviatko, O.: Improvement of the production technology of liquid biofuel from technical fats and oils. In: Ivanov, V., Pavlenko, I., Liaposhchenko, O., Machado, J., Edl, M. (eds.) *DSMIE 2020, LNME*, pp. 377–386. Springer, Cham (2020). [https://doi.org/10.1007/978-3-030-50491-5\\_36](https://doi.org/10.1007/978-3-030-50491-5_36)
- Surendra, K., Olivier, R., Tomberlin, J., et al.: Bioconversion of organic wastes into biodiesel and animal feed via insect farming. *Renew. Energy* **98**, 197–202 (2016)
- Mohadesi, M., Anghel, B., Maleki, M., Ansari, A.: Production of biodiesel from waste cooking oil using a homogeneous catalyst: study of the semi-industrial pilot of the microreactor. *Renew. Energy* **136**, 677–682 (2019)
- Bentivoglio, D., Rasetti, M.: Biofuel sustainability: a review of implications for land use and food price. *Rivista di Economia Agraria Anno LXX*, 7–31 (2015)
- Mushtruk, M., Deviatko, O., Ulianko, S., Kanivets, N., Mushtruk, N.: An agro-industrial complex fat-containing wastes synthesis technology in ecological biofuel. In: Ivanov, V., Pavlenko, I., Liaposhchenko, O., Machado, J., Edl, M. (eds.) *DSMIE 2021, LNME*, pp. 361–370. Springer, Cham (2021). [https://doi.org/10.1007/978-3-030-77823-1\\_36](https://doi.org/10.1007/978-3-030-77823-1_36)
- Ferrero, G., Rojas, H., Argaraña, C., Eimer, G.: Towards sustainable biofuel production: design of a new biocatalyst to biodiesel synthesis from waste oil and commercial ethanol. *J. Clean. Prod.* **139**, 495–503 (2016)
- Wang, C., Xie, S., Zhong, M.: Effect of hydrothermal pretreatment on kitchen waste for biodiesel production using the alkaline catalyst. *Waste Biomass Valorization* **8**(2), 369–377 (2017)

19. Balajii, M., Niju, S.: A novel biobased heterogeneous catalyst derived from *Musa acuminata* peduncle for biodiesel production—process optimization using central composite design. *Energy Convers. Manage.* **189**, 118–131 (2019)
20. Elango, R., Sathiasivan, K., Muthukumaran, C., et al.: Transesterification of castor oil for biodiesel production: process optimization and characterization. *Microchem. J.* **145**, 1162–1168 (2019)
21. Aguiéiras, E.C., de Barros, D.S., Sousa, H., et al.: Influence of the raw material on the final properties of biodiesel produced using lipase from *Rhizomucor miehei* grown on babassu cake as biocatalyst of esterification reactions. *Renew. Energy* **113**, 112–118 (2017)
22. Sakdasri, W., Ngamprasertsith, S., Daengsanun, S., Sawangkeaw, R.: Lipid-based biofuel synthesized from palm-olein oil by supercritical ethyl acetate in a fixed-bed reactor. *Energy Convers. Manage.* **182**, 215–223 (2019)
23. Dehghani, S., Haghghi, M.: Influence of various irradiation time on sono-functionalization of zirconia-doped mesoporous-silica by sulfuric acid for biofuel production from waste cooking oil. *Waste Biomass Valorization* **11**(8), 4167–4180 (2019). <https://doi.org/10.1007/s12649-019-00715-9>
24. Dhinesh, B., Raj, Y., Kalaiselvan, C., Krishna Moorthy, R.: A numerical and experimental assessment of a coated diesel engine powered by high-performance nano biofuel. *Energy Convers. Manage.* **171**, 815–824 (2018)



# Justification of Vibroventrentic External Load During Mechanical Pressing of Glycerin-Containing Products

Igor Palamarchuk<sup>1</sup> (✉) , Mikhailo Mushtruk<sup>1</sup>, Igor Lypovy<sup>2</sup>,  
Ievgenii Petrychenko<sup>3</sup> , and Ivan Vlasenko<sup>4</sup> 

<sup>1</sup> National University of Life and Environmental Sciences of Ukraine,  
15, Heroes of Defense Street, Kyiv 03041, Ukraine

[mixej.1984@ukr.net](mailto:mixej.1984@ukr.net)

<sup>2</sup> Podolsk Scientific and Technical Lyceum, 9, Warriors-Internationalists Street,  
Vinnytsia 21012, Ukraine

<sup>3</sup> Uman National University of Horticulture, 1, Institutska Street, Uman 20300, Ukraine

<sup>4</sup> Vinnytsia Institute of Trade and Economics of KNUTE, 25, Khmelnytske highway Street,  
Vinnytsia 21012, Ukraine

**Abstract.** The research results established possible ways of using pharmacopeial or distilled glycerin in confectionery, microbiological, pharmaceutical, enzymatic, and other processing industries. The analysis of research in dehydration of dispersed materials shows that the technological process of glycerol purification is quite complex. It was established that all physical and mechanical properties of the final product and technical and economic characteristics of the equipment can significantly impact the quality of glycerol dehydration. The mechanical dehydration method of glycerin by giving the working drums planetary motion and additional oscillations in the horizontal plane was substantiated. The value of the pressure arising in the drum of the vibrating-planetary installation was determined. A comparative analysis of the vibrating component's influence on the pressure was studied depending on the angular velocities of water and drum and the loading degree. Existing schemes of moisture transportation and methods of dehydration of viscous and liquid materials were investigated. The analysis of diffusion, mechanical and thermal mechanisms, and their influence on moisture-binding properties of raw materials and the comparative analysis of driving force and speed of processes were carried out. A brief description of the diffusion mechanism and process of moisture transfer in products was given.

**Keywords:** Glycerin · Dehydration · Vibration-planetary motion · Driving force · Pressure · Process innovation

## 1 Introduction

Traditionally, in the food and processing industry, convective drying technologies are widely used, implemented in a variety of design dryers: shaft, belt, drum, in which the

heat transfer to the raw material is carried out using a drying agent through the outer shell of the product to the inner layers. A detailed analysis of the most common technologies of convective drying [1] shows that drying equipment in terms of energy intensity, environmental regulations, product safety do not meet modern requirements. Traditional approaches to drying technology are faced with an insurmountable contradiction. On the one hand, to intensify the heat and mass transfer processes, it is required to increase the drying agent's speed (i.e., consumption). Therefore, with increasing coolant consumption, the amount of heat lost by the installation increases and vice versa. The way out for the solution of the indicated contradiction is connected with the change of the principles of energy supply to the product [2].

A new technical idea protected in this work is based on 2 provisions [3]. First, it is necessary to remove from the air the tasks of the coolant and leave only the tasks of the diffusion medium, the medium that ensures the effective "reception" of moisture from the product. Secondly, to organize a volumetric supply of energy to the product. Implementing the first position will significantly reduce heat loss from the exhaust air, and the second will significantly reduce the processing time.

Mechanisms of moisture transfer from capillary-porous bodies. According to the generally accepted classification of P.A. Rabinder, there are 3 forms of physical connection of moisture with the material. It seems that different types of communication in physical nature require different mechanisms for their breaking. Moreover, it does not necessarily have to be only diffusion processes [4]. All determine the driving forces that may have a diverse nature. Currently, new, promising types of equipment have been created, the effectiveness of which is difficult to explain from the standpoint of the modern theory of drying. Therefore:

1. The dehydration technique develops faster than the theoretical substantiation of the new principles of moisture removal;
2. The driving forces of these processes do not correspond to the diffusion principles;
3. Often, dehydration is a complex of combined processes involving processes that require proper consideration of the actual mechanisms of moisture transfer.

The problems arising from the description of the drying process are explained by the fact that the authors, supporters of the phenomenological approach, consider drying as a kind of one process with constant transfer coefficients and form models from these assumptions. This paper hypothesizes that drying is the result of the action, on the principle of superposition, of at least three processes: moisture transfer from the surface of a solid, moisture transfer in constrained capillary conditions, and moisture desorption. Each of these processes is characterized by the driving force and the kinetic coefficient of the process.

## 2 Literature Review

Analysis of research in dehydration of wet dispersed materials shows that this is a rather complicated technological process. Its course is primarily influenced by the physico-mechanical properties of the product, such as initial moisture, elasticity, viscosity, plasticity,

internal friction between particles of the solid phase, adhesion, cohesion, and other properties, as well as the characteristics and modes of operation of the process equipment [5]. In removing moisture, structural, mechanical, and technological properties of the product may vary within wide limits. This determines the complexity of the study of filtration rheological properties of technological raw materials and the process itself as a whole [6, 7].

Glycerin was discovered in 1783 by the Swedish chemist Carl Wilhelm Scheele, who showed that fragments of this compound formed the basis of all-natural fats and called it (sugar from fat) because the product had a sweet taste [8]. Scheele boiled olive oil with lead oxide (lead glitt). Wilhelm Scheele could not determine these fragments' exact composition and structure - organic chemistry was just beginning to develop [9, 10]. Pharmacopoeial or distilled glycerin is in increasing demand in confectionery, microbiological, pharmaceutical, enzyme, and other processing industries. In pharmaceutical practice, glycerin is used to manufacture a wide range of dosage forms, namely: solutions, syrups, elixirs, potions, suspensions, emulsions, ointments, pastes, candles, and others. It is also used as a drug with various pharmacological actions [11, 12].

Glycerin can be a solvent for various chemicals, has antiseptic properties and is used to prepare various medicinal solutions [13]. The antiseptic and preservative properties of glycerin are related to its hygroscopicity, due to which bacterial dehydration occurs. It is part of many cosmetics. When purifying crude glycerin in the first stage (long-term settling), many problems significantly affect the productivity of food (pharmacopoeial) glycerin [11].

Crude glycerin contains a non-volatile organic residue, fats, acids, salts, and ash, significantly complicating the separation process without prior long-term settling. From the whole complex chain of the technological process of obtaining glycerol, we distinguish the stage of separation of free (and non-free) moisture from intermediate raw materials. This is usually done by centrifugation, separation, rarely simple filtration [12].

The use of conventional centrifuges with a single rotating drum, where the product is exposed only to centrifugal force, is quite expensive in modern conditions since the working capacities of these machines must be quite large and dispersed to significant angular speeds [16]. The use of centrifuges with a planetary and at the same time vibrating movement of the working drums can significantly intensify and qualitatively improve the dehydration process, significantly increasing the driving force of mechanical squeezing, which determines the relevance and future of these studies [17].

It should also be noted that it is relatively easy to remove free and capillary-bound moisture when using mechanical squeezing, and considerable effort is necessary to extract the absorption-bonded and osmotic fluid.

The raw materials can be processed with heat or structured additionally [18, 19] to reduce the resistance during the fluid movement through the micropores of the product.

The results of scientific work are based on the research of A. Babicheva, P. Bernika, I. Blechmana, P. Zaiki, I. Palamarchuka, M. Pushanka, V. Sokolova, V. Stabnikov, L. Tishchenko, and others [20].

The use of vibrating equipment to separate inhomogeneous liquid systems is one of the effective ways to implement the process. Therefore, developing a vibrocentric

machine for the primary purification of crude glycerin is an urgent scientific and applied task.

This research aims to evaluate the effectiveness and justification of the method for determining the driving force of mechanical dehydration of insulin-containing raw materials due to the comparative analysis and determination of the driving force of centrifugal centrifugal-planetary, vibration, and vibrational-planetary actions.

The following tasks were set to achieve the aim:

- conduct a comparative analysis of centrifugal, vibrational, planetary, and combined vibration-planetary technological actions in terms of the intensity of the created force field;
- choose a schematic diagram and an experimental model of the installation for the combined vibration-planetary dehydration of insulin-containing raw materials;
- evaluate the patterns of pressure created in the working zone from the kinetic characteristics of the investigated technical systems.

In the process of analysis of the studied oscillatory system as evaluation criteria, changes in external force load were accepted from the action of vibration, planetary and combined vibroplanetary influence on the mass of the technological environment, and the results of such action in the studied processes.

### 3 Research Methodology

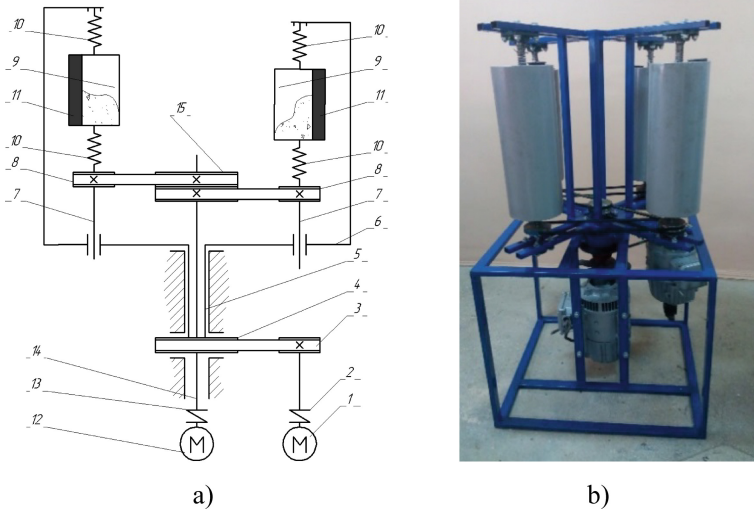
Among the main parameters used in this study, we used the change in pressure inside the working tank; angular velocities of rotation of the carrier of the planetary mechanism and angular movement of the container; centrifugal forces, which arise respectively by vibrational, planetary, and vibroplanetary action; the value of the mass of the liquid phase, which is pressed under the corresponding external load.

The National University Life and Environmental Sciences laboratory of Ukraine has developed a set of equipment for the mechanical dehydration of food and processing industries, characterized by either vibratory, centrifugal, or planetary technological effects or their combination. Under centrifugal effects, the growth of the driving force is determined by the design parameters of the working bodies and the angular velocity of their rotation. Vibration action allows, due to alternating accelerations in the contact zone, to significantly increase the intensity of the force field. The planetary model of the movement of the working bodies due to the peculiarities of the mechanism kinematics makes it possible to significantly increase the potential of the mechanical effect on the processed products.

For evaluating the presented characteristics, an experimental model of a vibroplanetary machine for pressing the mass of the load in oppositely located containers was designed and manufactured (Fig. 1).

It is assumed that the combination of actions of the above factors creates the most favorable conditions for effective mechanical dehydration of elastic-plastic products in terms of both the intensification of the powerful effect and the reduction of the damage degree to the feedstock.





**Fig. 1.** Vibration-planetary machine: a) schematic diagram; b) appearance; 1, 12 – drive motors; 2, 13 – elastic couplings; 3, 8 – V-belt transmission; 4 – driven drive pulley; 5 – hollow shaft; 6 – carrier; 7 – container drive shaft; 9 – container; 10 – springs; 11 – drum weight assemblies; 14 – central shaft; 15 – central pulley.

Features of this machine are the ability to change the above types of external load by appropriately replacing individual components of the drive mechanism, mainly removing or installing unbalanced masses 11, switching off or on engines 1 and 12.

One of the results of these works is a vibration-planetary machine. The schematic diagram and its appearance are shown in Fig. 1.

Performing such permutations on one installation indicates the purity of the experiment. The obtained dependencies were processed for the specified parameters of the studied processes using graph-analytical analysis in the mathematical environment Math CAD.

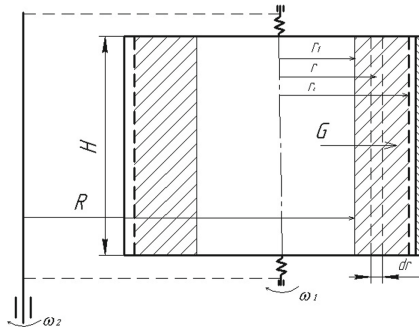
## 4 Results

A distinctive feature of this machine is the ability of the working drum to rotate simultaneously around its axis, the central axis, and perform vibrations in the horizontal plane. In addition, in the installation, there is the possibility of independent regulation of the angular velocities of rotation of the container and carrier, which allows choosing its operation modes within wide limits.

To determine the dynamic characteristics of the dehydrated products in a vibration-planetary machine, let's consider the scheme shown in Fig. 2.

Let's select inside the product layer inside the drum an elementary layer of thickness  $dr$  at a distance  $r$  from its axis of rotation and determine for comparison the pressure

that will be created on this layer with only the rotational motion of the drum (normal centrifugation), with only planetary motion and with vibration its planetary movement.



**Fig. 2.** Calculation scheme for determining the driving force of vibration-planetary dehydration.

The mass of the selected ring layer is equal to:

$$dm = 2\pi r dr \cdot H \cdot \rho \quad (1)$$

where:  $\rho$  – product density  $H$  – the height of the product layer.

It is known that in a conventional centrifuge, the pressure created on this layer of production can be determined by the formula:

$$p = \frac{1}{2} \rho \omega_1^2 (r_2^2 - r_1^2), \quad (2)$$

where:  $\omega_1$  – the angular velocity of rotation of the centrifuge drum.

During the planetary movement of the working capacity, the working pressure on the specified product layer will be determined by the centrifugal force due to its rotation around its axis  $F_{b1}$  and the centrifugal force  $F_{b2}$  from the rotation of the carrier with containers. Simultaneously, considering (1):

$$dF_{b1} = 2\pi H \rho \omega_1^2 r^2 dr \quad \text{and} \quad dF_{b2} = 2\pi H \rho \omega_2^2 (R + r) r dr, \quad (3)$$

where:  $\omega_2$  – the angular velocity of carrier rotation.

Then the total pressure force will be equal to:

$$dG = dF_{b1} + dF_{b2} = 2\pi H \rho \omega_1^2 r^2 dr + 2\pi H \rho \omega_2^2 (R + r) r dr, \quad (4)$$

The pressure created on the product (highlighted annular layer) is:

$$dp = dG/S \quad (5)$$

where:  $S = 2\pi rH$  – the lateral surface of the annular cylinder.

Then

$$dp = \rho \omega_1^2 r^2 dr + \rho \omega_2^2 (R + r) dr \quad (6)$$

Integrating this equality, let's obtain the expression for the average pressure during centrifugal planetary dehydration:

$$p_1 = \frac{1}{2}\rho(\omega_1^2 + \omega_2^2) \cdot (r_2^2 - r_1^2) + \rho\omega_2^2 R(r_2 - r_1) \tag{7}$$

If simultaneously with the planetary motion, the drum of the installation oscillates in a horizontal plane. Then an additional force will act on the selected loading layer:

$$dF_{e\omega\delta} = m_\delta\omega_1^2 e \frac{dr}{r} \tag{8}$$

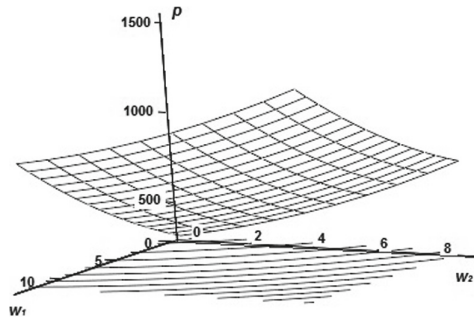
and extra pressure

$$p_2 = m_\delta\omega_1^2 e / 2\pi H \cdot (1/r_1 - 1/r_2) \tag{9}$$

where:  $m_d$  – drum weight assembly mass;  $e$  – eccentricity.

The total pressure inside the drums of the vibration-planetary machine will be

$$p = p_1 + p_2 = \frac{1}{2}\rho(\omega_1^2 + \omega_2^2)(r_2^2 - r_1^2) + \rho\omega_2^2 R(r_2 - r_1) + \frac{m_\delta\omega_1^2 e}{2\pi H} \cdot \left(\frac{1}{r_1} - \frac{1}{r_2}\right) \tag{10}$$



**Fig. 3.** The dependence of the pressure inside the drum on the ratio of the angular velocity of the working capacity and carrier.

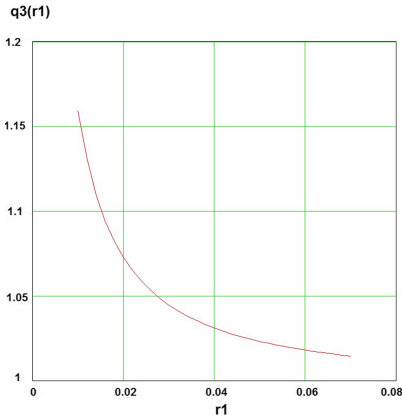
Figure 3 shows the resulting pressure as a function of the ratio of the angular velocities for the working capacity and the carrier. The graph shows the increase in pressure from increasing specified angular velocities.

The influence of the vibration movement of working tanks on the pressure generated on the processing load is also investigated (11):

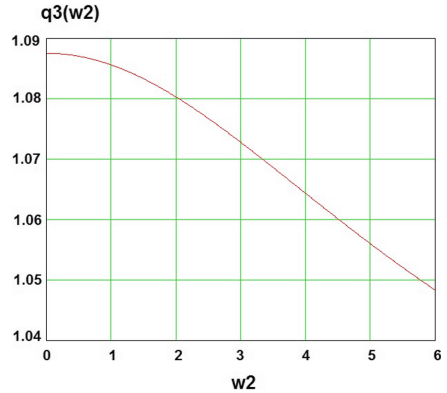
$$q = \frac{p}{p_1} = \frac{\frac{1}{2}\rho(\omega_1^2 + \omega_2^2)(r_2^2 - r_1^2) + \rho\omega_2^2 R(r_2 - r_1) + \frac{m_\delta\omega_1^2 e}{2\pi H} \left(\frac{1}{r_1} - \frac{1}{r_2}\right)}{\frac{1}{2}\rho(\omega_1^2 + \omega_2^2)(r_2^2 - r_1^2) + \rho\omega_2^2 R(r_2 - r_1)} \tag{11}$$

The increase in pressure depending on the degree of drum loading is shown in Fig. 4, from changes in the angular velocity of carrier rotation – in Fig. 5, and from the change in the angular velocity of container rotation – in Fig. 6

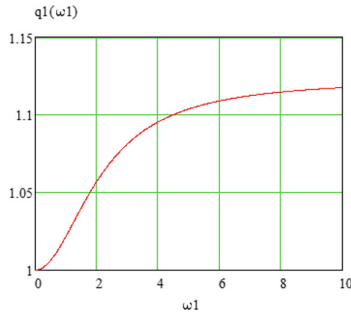
As can be seen from the graphs, as obtained from the research, vibration has a significant effect on many indicators: the pressure decreases with increasing load, increasing angular velocity of the carrier, and increasing angular velocity of the container.



**Fig. 4.** The effect of the degree of container loading on the change in pressure due to its vibratory motion



**Fig. 5.** The effect of the angular velocity of carrier rotation on the change in pressure due to its vibratory motion



**Fig. 6.** The effect of the angular velocity of the container on the change in pressure due to its vibratory motion

## 5 Conclusions

Effective technological schemes for the implementation of dehydration of elastic-plastic products are presented, or such evaluation criteria as performance, energy, and material costs, damage to the feedstock.

A schematic diagram and an experimental model of a vibration-planetary machine for dehydration of glycerin-containing products, in which a combination of the above power factors of influence are implemented.

The pressure occurring inside the drum, which makes a vibration-planetary motion, is determined.

Graphic dependences of the influence of the kinematic characteristics of the investigated technical systems on the driving force of these processes are obtained, which display:

- increase in pressure on the processing load with an increase in the angular velocities of the carrier and the working drum;
- influence of the vibration component on the pressure inside the drum, which decreases when the angular velocity increases;
- alignment of the influence of the vibration component at the level of 10–11% with an increase in the angular velocity of the container.

## References

1. Liu, J., Chen, X., Başar, T., Belabbas, M.A.: Exponential convergence of the discrete-and continuous-time Altafini models. *IEEE Trans. Autom. Control* **62**(12), 6168–6182 (2017)
2. Nicolás-Carlock, J., Carrillo-Estrada, J., Dossetti, V.: Fractality à la carte: a general particle aggregation model. *Sci. Rep.* **6**(1), 1–8 (2016)
3. Rousseau, J., Szabo, B.: Asymptotic behavior of the empirical Bayes posteriors associated to maximum marginal likelihood estimator. *Ann. Stat.* **45**(2), 833–865 (2017)
4. Guzik, G.: On the construction of asymptotically stable iterated function system with probabilities. *Stoch. Anal. Appl.* **34**(1), 24–37 (2016)
5. Chuang, Y. L., Huang, Y. R., D’Orsogna, M. R., Bertozzi, A. L.: Multi-vehicle flocking: scalability of cooperative control algorithms using pairwise potentials. In: *IEEE International Conference Robotics Automation*, pp. 2292–2299 (2017)
6. Ma, Y., Yuen, R., Lee, E.: Effective leadership for crowd evacuation. *Physica A* **450**, 333–341 (2016)
7. Czako, P., Zajác, P., Čapla, J., et al.: The effect of UV-C irradiation on grape juice turbidity, sensory properties, and microbial count. *Potravinárstvo Slovak J. Food Sci.* **12**(1), 1–10 (2018)
8. Ha, S.-Y., Liu, J.-G.: A simple proof of the Cucker-Smale flocking dynamics and mean-field limit. *Comm. Math. Sci.* **7**, 297–325 (2019)
9. Zhao, C., He, B., Liu, J., Han, Y., Wen, B.: Design method of dynamic parameters of a self-synchronization vibrating system with dual mass. *J. Multi-body Dyn.* **232**(1), 3–20 (2018)
10. Sukhenko, Y., Mushtuk, M., Vasylyv, V., Sukhenko, V., Dudchenko, V.: Production of pumpkin pectin paste. In: Ivanov, V., et al. (eds.) *DSMIE 2019. LNME*, pp. 805–812. Springer, Cham (2020). [https://doi.org/10.1007/978-3-030-22365-6\\_80](https://doi.org/10.1007/978-3-030-22365-6_80)
11. Casali, B., Brenna, E., Parmeggiani, F., Tessaro, D., Tentori, F.: Enzymatic methods for the manipulation and valorization of soapstock from vegetable oil refining processes. *Sustain. Chem.* **2**(1), 74–91 (2021)
12. de Haro, J., Izarra, I., Rodríguez, J., et al.: Modelling the epoxidation reaction of grape seed oil by peracetic acid. *J. Clean. Prod.* **138**, 70–76 (2016)
13. Karapuzha, A.S., Fraser, D., Zhu, Y., Wu, X., Huang, A.: Effect of solution heat treatment and hot isostatic pressing on the microstructure and mechanical properties of Hastelloy X manufactured by electron beam powder bed fusion. *J. Mater. Sci. Technol.* **98**, 99–117 (2022)
14. Navi, P., Heger, F.: Combined densification and thermo-hydro-mechanical processing of wood. *MRS Bull.* **29**(5), 332–336 (2004)
15. Gómez-Estaca, J., Pintado, T., Jiménez-Colmenero, F., Cofrades, S.: Assessment of a healthy oil combination structured in ethyl cellulose and beeswax oleogels as animal fat replacers in low-fat, PUFA-enriched pork burgers. *Food Bioprocess Technol.* **12**(6), 1068–1081 (2019). <https://doi.org/10.1007/s11947-019-02281-3>
16. Singh, R., Kaushik, R., Gosewade, S.: Bananas as underutilized fruit having huge potential as raw materials for food and non-food processing industries: A brief review. *Pharma Innov. J.* **7**(6), 574–580 (2018)

17. Thiel, E., Ziegler, M., Studemund, T.: Localization of subsurface defects in uncoated aluminum with structured heating using high-power VCSEL laser arrays. *Int. J. Thermophys.* **40**(2), 17 (2019)
18. Mushtruk, M., Vasylyv, V., Slobodaniuk, N., Mukoid, R., Deviatko, O.: Improvement of the production technology of liquid biofuel from technical fats and oils. In: Ivanov, V., Pavlenko, I., Liaposhchenko, O., Machado, J., Edl, M. (eds.) *DSMIE 2020. LNME*, pp. 377–386. Springer, Cham (2020). [https://doi.org/10.1007/978-3-030-50491-5\\_36](https://doi.org/10.1007/978-3-030-50491-5_36)
19. Dehghani, S., Haghighi, M.: Influence of various irradiation time on sono-functionalization of zirconia-doped mesoporous-silica by sulfuric acid for biofuel production from waste cooking oil. *Waste Biomass Valorization* **11**(8), 4167–4180 (2019). <https://doi.org/10.1007/s12649-019-00715-9>
20. Dhinesh, B., Raj, Y., Kalaiselvan, C., Krishna Moorthy, R.: A numerical and experimental assessment of a coated diesel engine powered by high-performance nano biofuel. *Energy Convers. Manage.* **171**, 815–824 (2018)



# Reduction of Granular Material Losses in a Vortex Chamber Supercharger Drainage Channel

Andrii Rogovyi<sup>1</sup> (✉) , Volodymyr Korohodskyi<sup>2</sup> , Artem Neskorozhenyi<sup>2</sup> ,  
Iryna Hrechka<sup>1</sup> , and Serhii Khovanskyi<sup>3</sup> 

<sup>1</sup> National Technical University Kharkiv Polytechnic Institute,  
2, Kyrpychova Street, Kharkiv 61000, Ukraine  
asrogovoy@ukr.net

<sup>2</sup> Kharkiv National Automobile and Highway University, 25, Yaroslava Mudrogo Street,  
Kharkiv 61002, Ukraine

<sup>3</sup> Sumy State University, 2, Rymyskogo-Korsakova Street, Sumy 40007, Ukraine

**Abstract.** Increasing the reliability and durability of superchargers in pneumatic and hydraulic transport is possible due to vortex chamber jet superchargers. Their efficiency significantly exceeds pumping bulk mediums in pneumatic transport using direct-flow jet ejectors. However, the pumped medium losses in the vortex chamber supercharger drainage channel do not allow it to be widely used in such systems. Based on experimental and numerical studies, the influence of the density of the granular material on the losses in the drainage channel has been determined. Mathematical modeling was done by solving the Reynolds-averaged Navier-Stokes (RANS) equations with the Shear Stress Transport (SST) turbulence model. Rational densities of the medium can be varied by changing the vortex chamber height or swirling the inlet flow using a swirler. The design changes are explained by the kinematic features of the solid particle motion. If the vortex chamber height is small, then the particle does not have time to start rotating near the chamber axis and enters the supercharger drainage channel. The absence of the drainage channel in the design will lead to the outlet pressure decrease. As a result of the research, the granular material losses in the supercharger drainage channel have been reduced by 50%, with a twofold increase in the swirl number.

**Keywords:** Vortex chamber supercharger · Experiment · Numerical simulation · Drainage channel · Granular material losses · Energy efficiency · Process innovation

## 1 Introduction

Bulk cargoes pumping in hydraulic and pneumatic transport is accompanied by high wear of the blowers and pumps with the low reliability and durability of hydropneumatic transport systems [1, 2]. Ways to increase the durability of such systems are practically exhausted due to the limited choice of wear-resistant materials [3] and improvements of

the pumps vane systems [4]. Increasing the reliability and durability of systems must be done with a simultaneous solution to the problem of growing energy-saving indicators and reliability [5].

The solution to the problems of the blower's reliability can be the use of jet superchargers [6]. Still, low-efficiency indicators prevent the widespread use of direct-flow water and two-phase ejectors. Using centrifugal force has made it possible to create more efficient devices for pumping granular materials - vortex chamber supercharger [1, 7]. Its efficiency when it pumps a bulk medium with air is more than twice as high as the efficiency of classical jet pumps. However, the working process of such a blower is implemented with the release of a part of the pumped medium through the drainage channel, which creates significant inconveniences in its use. Thus, improving the design of a vortex-chamber supercharger, studying the features of its working process, and minimizing losses of the pumped medium is an urgent scientific problem.

## 2 Literature Review

Ejectors with a vortex mixing chamber have been used for a long time [8, 9], but their main application is the vacuuming of closed volumes [10]. The use of an additional tangential outlet channel in the vortex chamber allows collecting the pumped bulk medium into it and realizing the pumping and operation of such blowers in pneumatic and hydraulic transport [11]. The use of positive displacement pumps for pumping granular materials is usually impractical due to rapid wear and performance deterioration [12, 13]. Hydrodynamic pumps are subject to intense wear, leading to performance and reliability deterioration [14]. In the papers [1, 7], the operation of vortex chamber superchargers is considered. However, the features of pumping bulk cargoes are not considered. Also, no attention was paid to the occurrence of granular materials losses. Experimental studies of the dynamics of the solid particles are complicated due to the rapidity of dynamic processes inside the vortex chamber [15, 16]. Therefore, experimental studies are usually limited to comparing integral indicators [17, 18].

One of the main disadvantages of vortex chamber superchargers is the presence of the pumped medium in the axial drainage channel [1, 7], which reduces the operational efficiency and the supercharger use in hydropneumatic systems. Thus, this paper aims to reduce granular material losses in the vortex chamber supercharger drainage channel. Minimization of losses directly affects the adaptation of resource-saving technologies [19, 20] by increasing the efficiency of pumping bulk cargoes.

Numerical modeling of processes in various devices has been actively developed recently [21, 22], including vortex chamber pumps. CFD (computational fluid dynamics) could track each solid particle pumped by the pump and determine the efficiency of its operation [23]. Modeling the behavior of solid particles in a blower can be carried out based on the approaches of Euler [24] and Lagrange [25]. Since the concentration of solid particles in the supercharger is low, it would be appropriate to use the Lagrange approach. According to this approach, the trajectories of each particle are calculated considering their influence on the primary liquid or gas flow. For these purposes, a three-dimensional model is built [26, 27], a mesh, and a calculation is performed based on numerical methods.



### 3 Research Methodology

The study was carried out in three stages. First, mathematical modeling of the fluid flow in the supercharger was carried out with the interaction between solid particles based on the calculation of the Reynolds averaged Navier-Stokes (RANS) system of equations [1, 28]. Since the flow simulation led to a vacuum error near the axis, a rotation-curvature correction was included [28]. OpenFoam free open source CFD software was used. The results were compared on three grids: 1 million elements, 2 million, and 7 million. Since the simulation results on grids 2 and 7 million elements differed by no more than 1%, further calculations were made on grids in 2 million items.

In the second stage, an experimental study of the shifting of bulk cargoes was carried out, and the flow rate of material losses in the supercharger drainage channel was measured. In the third stage, the experimental and calculated data were compared with further modeling based on the CFD approach and the development of optimal pumping conditions with the goal function to minimize losses in the drain channel of the supercharger.

The Venturi flow meters and liquid manometers were used for measurements. They made it possible to determine pressures and flow rates with sufficient accuracy. The error in measuring the pressure and flow rate did not exceed 1%. Mass flow rates of bulk medium were measured by weighing the mass accumulated in the corresponding hopper per unit of time, measured by a stopwatch. The error in determining the mass flow rate did not exceed 1%.

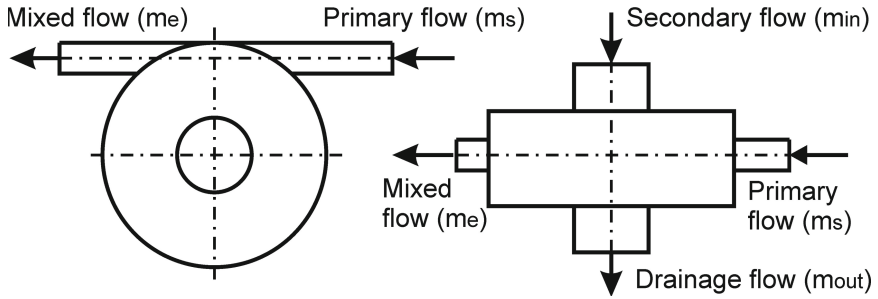
## 4 Results

### 4.1 Vortex Chamber Supercharger

Figure 1 presents the construction of the vortex device considered in the present study. The vortex chamber supercharger is a mixing chamber with four channels (two axial channels and two tangential ones). The primary flow (water or air) is supplied through the tangential inlet channel and creates a swirling flow inside the chamber with characteristic hydrodynamic flow features: gauge pressure at the periphery of the vortex chamber and vacuum near the axis. The near-axis vacuum creates a differential pressure that facilitates the pumping process. The granular material enters through the inlet axial channel to the vortex chamber, acquires kinetic energy, and also moves to the vortex chamber periphery under the centrifugal force influence. The gauge pressure magnitude at the periphery of the vortex chamber depends on how the second axial channel is used.

It is possible to implement two different work processes depending on the geometric ratio of the tangential and axial channels of the vortex chamber supercharger. The first working process is characterized by relatively high pressure at the periphery and a relatively lower outlet mass flow rate. The second, on the contrary, is a higher flow rate at relatively low pressure at the vortex chamber outlet.

The flow direction in the second (usually lower) axial channel is distinctive of the two pumping work processes. In the first working process, the primary flow is thrown away through the axial channel and forms the loss flow rate. In the second working process, the shifted granular material is sucked through the axial inlet, due to which the



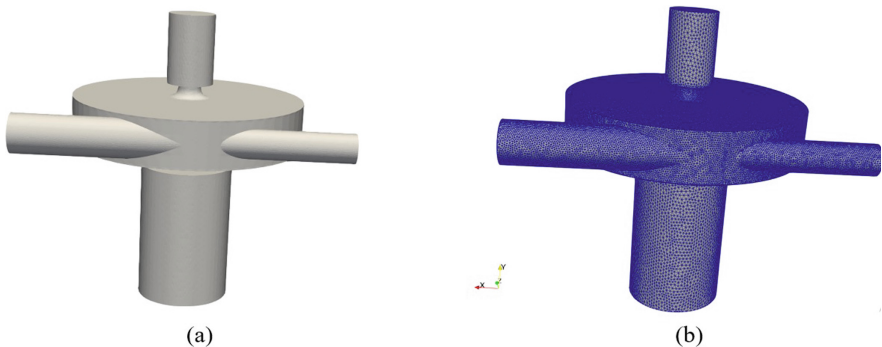
**Fig. 1.** Vortex chamber supercharger layout.

mass flow rate of the bulk at the pump outlet increases. Thus, the main disadvantage of the first working process implementation is solid particles in the axial (drainage) channel. This paper is devoted to modeling the movement of solid particles in the vortex chamber supercharger and studying the loss flow rate in the drainage channel during the implementation of a working process with the drainage channel.

The second working process without the drainage channel makes it possible to ultimately reduce the losses of the pumped granular materials to zero and change the drainage channel function to the suction channel. But, in this case, the pressure at the blower periphery is significantly reduced, which leads to a noticeable decrease in the energy efficiency of pumping bulk cargoes. Therefore, optimizing the flow rate of the drainage losses while maintaining the working process features allows counting on the higher energy efficiency of the supercharger operation at zero losses of the pumped medium.

## 4.2 Numerical Simulations

The computational domain and grid model of the vortex chamber supercharger are shown in Fig. 2.



**Fig. 2.** Schematic of the computational domain for the supercharger: (a) solid model, (b) unstructured mesh used in the present simulation.

The simulation of the trajectories of the solid particles was carried out by the Lagrange method by numerically solving Newton's second law equation, considering particle collisions and wall interaction and the effect of particles affection the gas flow [29–31]. The basic equation used to determine the trajectories of solid particles [32, 33]:

$$x_f = x_i + u_p \delta t$$

where,  $x_i$ ,  $x_f$  are the initial and final position of the solid particle, respectively;  $u_p$  is the velocity of the particle;  $\delta t$  is the time step. After completing the calculations at each time step, the new velocity was determined according to the equation:

$$m \frac{du_p}{dt} = \sum F, \quad (2)$$

where  $m$  is the mass of the solid particle;  $\sum F$  is the sum of all forces acting on the particle. In this study, only the drag force was considered, for a significant reduction in the calculation time, considering the particles affection the gas flow. In the future, it is planned to evaluate the influence of many other forces available in modern software products for modeling solid particles behavior. Information about possible forces acting on the solid particle in gas flows can be found in articles [32].

The flow patterns of the gas and solid phases are shown in Fig. 3. Comparison of the gas flow into the blower with and without solid particles shows that the particle concentration is insufficient for a severe effect of particles on the flow characteristics. The main parameters of the supercharger remain independent of solid particles' presence [1, 7].

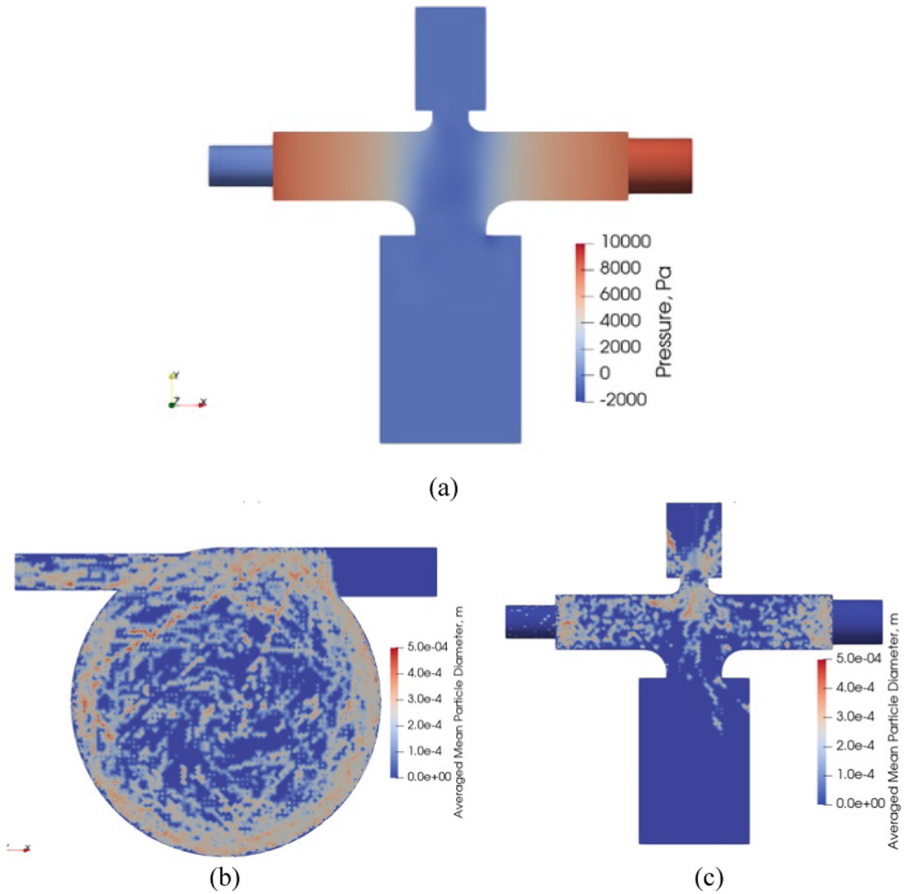
The distribution of solid particles by diameter (Fig. 3b and 3c) shows the instantaneous arrangement of particles in the meridional and horizontal planes. The distribution of particles qualitatively confirms the adequacy of the mathematical model and corresponds to the instantaneous flow patterns observed in the experiment. As a result of the calculation, the mass flow rates of solid particles passing through the boundary conditions were determined, making it possible to compare the mass flow rates with the experiment.

Using particle trajectories mathematical modeling in the supercharger, it was possible to determine the pumped medium's mass flow rate of losses. The flow rate was determined by calculating the number of particles entering the drainage channel about the total amount of solid particles. The simulation results were verified by experimental studies. Reducing losses allows for improved industrial design and efficiency of supercharger applications.

### 4.3 Experimental Results

An experimental plant was created for studies of the bulk cargoes pumping, which made it possible to measure the mass flow rates of the granular material, as well as the main parameters of the blower by measuring the pressure and flow rate of the gas in each channel.

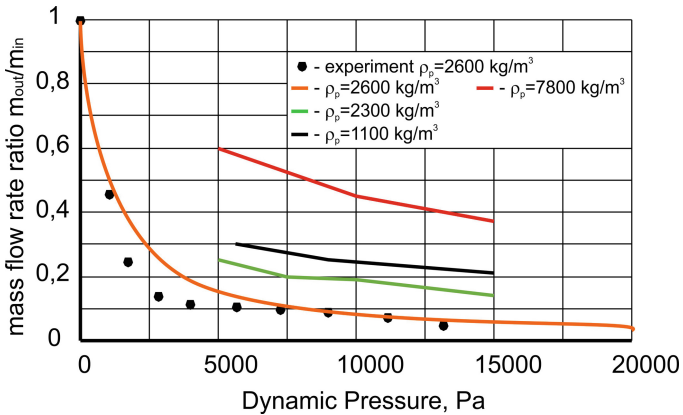
Experimental studies have made it possible to confirm the adequacy of mathematical modeling based on a comparison of the loss of solid particles in the drainage channel.



**Fig. 3.** Simulation results: (a) pressure contours of the pump flow field; (b) solid particles in the horizontal plane; (c) solid particles in the meridian plane.

Increasing the primary flow dynamic pressure leads to a decrease in the losses in the drainage channel (Fig. 4). At dynamic pressure of more than 5 kPa, the simulation results were in excellent agreement with the experiment. However, such a mode of operation of the blower with low dynamic pressures and, accordingly, with small swirl numbers is not rational and is usually not used. There are minimal losses of the secondary flow if the solid particle density is 2000–3000 kg/m<sup>3</sup>. Density values with a minimal mass flow rate ratio of losses are explained by the peculiarities of energy transfer to the pumped particle. With an increase in density, the particle does not have time to gain speed and begin to rotate near the vortex chamber axis, which leads to the particle falling into the drainage channel. The decrease in losses can be the increase in the vortex chamber height or the setting of a rotary motion to a particle in the inlet hopper.

The increase in the vortex chamber height can worsen the energy characteristics of the blower operation and its efficiency; therefore, it is more promising to create rotational flow at the chamber inlet, for example, using a vane swirler.



**Fig. 4.** Effect of the dynamic pressure and solid particle density on drainage mass flow rate ratio ( $m_{out}$  is the drainage mass flow rate and  $m_{in}$  is the inlet mass flow rate).

The future is being planned to create an autonomous installation for the transportation of bulk cargoes based on solar batteries [34, 35]. This opens the possibility of widespread use of such systems in many industries. This installation will have a minimum drainage flow rate.

## 5 Conclusions

Numerical simulations of the gas-particle two-phase flow in the vortex chamber supercharger were conducted. The mass flow rates of the solid phase in each channel were determined.

Experimental studies confirmed the adequacy of the CFD results. The value compared the flow rate in the supercharger drainage channel. At dynamic pressures of more than 5 kPa, the simulation results agreed with the experiment. The maximum calculation error is observed at low values of the dynamic pressure at the supercharger inlet.

The solid particle density with a minimal mass flow rate ratio of losses should be in the range of 2000–3000 kg/m<sup>3</sup> for the investigated vortex chamber supercharger.

An increase in the primary flow dynamic pressure makes it possible to reduce the losses of the pumped medium in the drainage channel by 50% with a twofold increase in the dynamic pressure.

## References



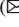
1. Rogovyi, A., Korohodskiy, V., Khovanskyi, S., Hrechka, I., Medvediev, Y.: Optimal design of vortex chamber pump. *J. Phys. Conf. Ser.* **1741**(1), 012018 (2021)
2. Noon, A.A., Kim, M.H.: Erosion wear on centrifugal pump casing due to slurry flow. *Wear* **364**, 103e11 (2016)
3. Voloshina, A., Panchenko, A., Titova, O., Panchenko, I.: Changes in the dynamics of the output characteristics of mechatronic systems with planetary hydraulic motors. *J. Phys. Conf. Ser.* **1741**, 012045 (2021)

4. Kondus, V.Y., Gusak, O.G., Yevtushenko, J.V.: Investigation of the operating process of a high-pressure centrifugal pump with taking into account of improving the process of fluid flowing in its flowing part. *J. Phys. Conf. Ser.* **1741**(1), 012012 (2021)
5. Arhun, S., Migal, V., Hnatov, A., Hnatova, H., Ulyanets, O.: System approach to evaluating the traction electric motor quality. *EAI Endorsed Trans. Energy Web* **7**(27), 1–9 (2020)
6. Evdokimov, O.A., Piralishvili, S.A., Veretennikov, S.V., Elkes, A.A.: Experimental study of cleaning aircraft GTE fuel injectors using a vortex ejector. *J. Phys. Conf. Ser.* **925**(1), 012027 (2017)
7. Rogovyi, A., Korohodskiy, V., Medvediev, Y.: Influence of Bingham fluid viscosity on energy performances of a vortex chamber pump. *Energy* **218**, 119432 (2021)
8. Merzliakov, I., Pavlenko, I., Chekh, O., Sharapov, S., Ivanov, V.: Mathematical modeling of operating process and technological features for designing the vortex type liquid-vapor jet apparatus. In: Ivanov, V., et al. (eds.) *DSMIE 2019. LNME*, pp. 613–622. Springer, Cham (2020). [https://doi.org/10.1007/978-3-030-22365-6\\_61](https://doi.org/10.1007/978-3-030-22365-6_61)
9. Kozii, I.S., Plyatsuk, L.D., Hurets, L.L., Volnenko, A.A.: Capturing aerosol particles in a device with a regular pulsating nozzle. *J. Eng. Sci.* **8**(2), F1–F5 (2021). [https://doi.org/10.21272/jes.2021.8\(2\).f1](https://doi.org/10.21272/jes.2021.8(2).f1)
10. Evdokimov, O.A., Piralishvili, S.A., Veretennikov, S.V., Guryanov, A.I.: CFD simulation of a vortex ejector for use in vacuum applications. *J. Phys. Conf. Ser.* **1128**(1), 012127 (2018)
11. Chernetskaya-Beletskaya, N., Rogovyi, A., Shvornikova, A., Baranov, I., Mirosnikova, M., Bragin, N.: Study on the coal-water fuel pipeline transportation taking into account the granulometric composition parameters. *Int. J. Eng. Technol.* **7**(4.3), 240–245 (2018)
12. Panchenko, A., Voloshina, A., Titova, O., Panchenko, I.: The influence of the design parameters of the rotors of the planetary hydraulic motor on the change in the output characteristics of the mechatronic system. *J. Phys. Conf. Ser.* **1741**, 012027 (2021)
13. Voloshina, A., Panchenko, A., Titova, O., Milaeva, I., Pastushenko, A.: Prediction of changes in the output characteristics of the planetary hydraulic motor. In: Tonkonogyi, V., et al. (eds.) *InterPartner 2020. LNME*, pp. 744–754. Springer, Cham (2021). [https://doi.org/10.1007/978-3-030-68014-5\\_72](https://doi.org/10.1007/978-3-030-68014-5_72)
14. Pavlenko, I., Ivanov, V., Kuric, I., Gusak, O., Liaposhchenko, O.: Ensuring vibration reliability of turbopump units using artificial neural networks. In: Trojanowska, J., Ciszak, O., Machado, J.M., Pavlenko, I. (eds.) *MANUFACTURING 2019. LNME*, pp. 165–175. Springer, Cham (2019). [https://doi.org/10.1007/978-3-030-18715-6\\_14](https://doi.org/10.1007/978-3-030-18715-6_14)
15. Sokolov, V., Porkuian, O., Krol, O., Baturin, Y.: Design calculation of electrohydraulic servo drive for technological equipment. In: Ivanov, V., Trojanowska, J., Pavlenko, I., Zajac, J., Peraković, D. (eds.) *DSMIE 2020. LNME*, pp. 75–84. Springer, Cham (2020). [https://doi.org/10.1007/978-3-030-50794-7\\_8](https://doi.org/10.1007/978-3-030-50794-7_8)
16. Sokolov, V., Porkuian, O., Krol, O., Stepanova, O.: Design calculation of automatic rotary motion electrohydraulic drive for technological equipment. In: Ivanov, V., Trojanowska, J., Pavlenko, I., Zajac, J., Peraković, D. (eds.) *DSMIE 2021. LNME*, pp. 133–142. Springer, Cham (2021). [https://doi.org/10.1007/978-3-030-77719-7\\_14](https://doi.org/10.1007/978-3-030-77719-7_14)
17. Voloshina, A., Panchenko, A., Titova, O., Pashchenko, V., Zasiadko, A.: Experimental studies of a throughput of the distribution systems of planetary hydraulic motors. *IOP Conf. Ser. Mater. Sci. Eng.* **1021**(1), 012054 (2021)
18. Marchenko, A., Tkachuk, M.A., Kravchenko, S., Tkachuk, M.M., Parsadanov, I.: Experimental tests of discrete strengthened elements of machine-building structures. In: Tonkonogyi, V., et al. (eds.) *InterPartner 2019. LNME*, pp. 559–569. Springer, Cham (2020). [https://doi.org/10.1007/978-3-030-40724-7\\_57](https://doi.org/10.1007/978-3-030-40724-7_57)

19. Kirichenko, M.V., Drozdov, A.N., Zaitsev, R.V., Khrypunov, G.S., Drozdova, A.A., Zaitseva, L.V.: Design of electronic devices stress testing system with charging line based impulse generator. In: 2020 IEEE KhPI Week on Advanced Technology (KhPIWeek), pp. 38–42. IEEE (2020)
20. Patlins, A., Hnatov, A., Arhun, S. C., Bogdan, D., Dzyubenko, O.: Development of an energy generating platform for converting kinetic energy into electrical energy using the kinematic synthesis of a three-stage multiplier. In: Transport Means-Proceedings of the International Conference, pp. 403–408 (2019)
21. Krol, O., Sokolov, V.: Research of toothed belt transmission with arched teeth. *Diagnostyka* **21**(4), 15–22 (2020)
22. Tkachuk, M.A.: Numerical method for axisymmetric adhesive contact based on Kalker's variational principle. *Eastern-Euro. J. Enterp. Technol.* **3**(7), 34–41 (2018)
23. Hasečić, A., Imamović, J., Bikić, S., Džaferović, E.: Investigation of the contamination influence on the parameters of gas flow through multihole orifice flowmeter. *IEEE Trans. Instrum. Measure.* **70**, 1–8 (2021)
24. Berberović, E., Bikić, S.: Computational study of flow and heat transfer characteristics of eg-si3n4 nanofluid in laminar flow in a pipe in forced convection regime. *Energies* **13**(1), 74 (2020)
25. Brazhenko, V., Mochalin, I.: Numerical simulation and experimental tests of the filter with a rotating cylindrical perforated filter element. *Proc. Inst. Mech. Eng. C J. Mech. Eng. Sci.* **235**(12), 2180–2191 (2021)
26. Krol, O., Porkuian, O., Sokolov, V., Tsankov, P.: Vibration stability of spindle nodes in the zone of tool equipment optimal parameters. *Comptes rendus de l'Acadé'mie bulgare des Sci.* **72**(11), 1546–1556 (2019)
27. Voloshina, A., Panchenko, A., Boltyansky, O., Titova, O.: Improvement of manufacture workability for distribution systems of planetary hydraulic machines. In: Ivanov, V., et al. (eds.) DSMIE 2019. LNME, pp. 732–741. Springer, Cham (2020). [https://doi.org/10.1007/978-3-030-22365-6\\_73](https://doi.org/10.1007/978-3-030-22365-6_73)
28. Smirnov, P.E., Menter, F.R.: Sensitization of the SST turbulence model to rotation and curvature by applying the Spalart-Shur correction term. *J. Turbomach.* **131**(4), 041010 (2009)
29. Pavlenko, I., Liaposhchenko, A., Ochowiak, M., Demianenko, M.: Solving the stationary hydroaeroelasticity problem for dynamic deflection elements of separation devices. *Vib. Phys. Syst.* **29**, 2018026 (2018)
30. Sommerfeld, M., Sgrott, O.L., Jr., Taborda, M.A., Koullapis, P., Bauer, K., Kassinos, S.: Analysis of flow field and turbulence predictions in a lung model applying RANS and implications for particle deposition. *Eur. J. Pharm. Sci.* **166**, 105959 (2021)
31. Chelabi, M.A., Basova, Y., Hamidou, M.K., Dobrotvorskiy, S.: Analysis of the three-dimensional accelerating flow in a mixed turbine rotor. *J. Eng. Sci.* **8**(2), D1–D7 (2021). [https://doi.org/10.21272/jes.2021.8\(2\).d2](https://doi.org/10.21272/jes.2021.8(2).d2)
32. Appadurai, A., Raghavan, V.: Numerical investigations on particle separation in dynamic separators. *Int. J. Numeric. Methods Heat Fluid Flow* **30**(4), 1677–1688 (2019)
33. Liaposhchenko, O., Pavlenko, I., Monkova, K., Demianenko, M., Starynskiy, O.: Numerical simulation of aeroelastic interaction between gas-liquid flow and deformable elements in modular separation devices. In: Ivanov, V., et al. (eds.) DSMIE 2019. LNME, pp. 765–774. Springer, Cham (2020). [https://doi.org/10.1007/978-3-030-22365-6\\_76](https://doi.org/10.1007/978-3-030-22365-6_76)
34. Zaitsev, R.V., Khrypunov, G.S., Veselova, N.V., Kirichenko, M.V., Kharchenko, M.M., Zaitseva, L.V.: The cadmium telluride thin films for flexible solar cell received by magnetron dispersion method. *J. Nano Electron. Phys.* **9**(3), 03015 (2017)
35. Minakova, K.A., Zaitsev, R.V.: Improving the solar collector base model for PVT system. *J. Nano Electron. Phys.* **12**(4), 04028 (2020)



# Application of Low-Frequency Mechanical Vibrations for Development of Highly Efficient Continuous Extraction Equipment

Volodymyr Zavalov , Taras Mysiura  , Nataliia Popova ,  
Yuliia Zaporozhets , and Valentyn Chorny 

National University of Food Technologies of Ukraine, 68, Volodymyrska Street, Kyiv 01601,  
Ukraine

{zavalov, taras\_as}@nuft.edu.ua

**Abstract.** Research results of the regularities of pulsating turbulent flows distribution generated with the transport elements of a vibrating extractor for solid-liquid systems with a small difference in phase densities in a non-flowing liquid medium are presented. The experimental results in the entire investigated range of hydrodynamic operating modes of the apparatus are summarized by the dependences by which it becomes possible to determine the distance between vibro-mixing devices, the dimensions of the apparatus, the height of the unloading device for removing the meal, to choose the design of the transporting open element of the plate, to optimize and scale the process. The proposed operating parameters of the apparatus make it possible to effectively use the energy of mechanical vibrations to intensify mass transfer and countercurrent phase separation of the working mixture. Mathematical models have been developed that can be used for the scaling and design of vibration extraction equipment. For the industry, a new design of the vibroextractor with a conveying system has been proposed, which ensures effective phase separation under conditions of countercurrent vibroextraction of target components from plant materials.

**Keywords:** Industrial innovation · Vibroextraction · Mathematical model · Scaling · Hydrodynamics · Pulsating flow · Phase separation

## 1 Introduction

The effectiveness of traditional technologies for extracting from raw materials with a high degree of grinding is due to the low permeability for an extractant in a continuous countercurrent process [1–4]. In this respect, vibration extractors are the most promising due to the use of low-frequency mechanical oscillation to intensify the process with a complex morphological structure of the solid phase at the macro and micro levels, including countercurrent phase separation with minimal longitudinal mixing [2, 5, 6]. In this case, the characteristics of the pulsating spectrum depend on the design of the vibrating partitions and the mode of their oscillation [5, 7]. Regularities of spreading



pulsating jets in the longitudinal (transporting) and transverse direction can be determined by fundamental spatio-temporal dependencies that allow calculating the intensity of oscillations at different distances from their source [8, 9].

## 2 Literature Review

The main direction of improving the extraction process is to create a large surface of interphase interaction and its active renewal over time. Analysis of traditional extraction methods indicated the direction of solving this problem, the essence of which is to create a mode of intensive alternating turbulence of the workflow [5, 6]. General trends in mass transfer in devices of this type have identified a number of important factors influencing the process: the share of a free cross-section of sectional partitions, as well as the size, shape, configuration of holes through which the interacting phases pass, the distance between plates [2, 10]. However, to take into account, all these factors is almost impossible. Several monographs on the theory and practice of extraction have been published [11, 12]. It is possible to observe that the interests of the authors and the scientific basis of their research do not exceed the foundations of the extraction processes theory set out by G. A. Axelrud, V. M. Lysiansky, P. G. Romankov, S. M. Karpachova, and other scientists who have worked effectively in this field. At the same time, there is no separate literature devoted to the theoretical foundations of vibroextraction of target components from plant raw materials and issues of practice and methods of engineering calculation to date.

The information of the last decade and the practice of research and creation of vibroextraction equipment highlights the need to study the following issues: features of hydrodynamic conditions of the process (speed characteristics, flow structure), mass transfer and time characteristics at all scale levels, energy consumption for vibration mixing, scaling. Here it is necessary to name a number of works that reflect the distribution of the residence time of individual liquid particles in the apparatus [4, 13–18]. Also, sources that provide an analytical description of fluid movement in the apparatus's working volume with mixing devices [5, 19], provisions of the turbulent jets theory, and flow velocities modeling are presented [15, 20].

Purposefully designing and optimizing this type of extractor's operating parameters are impossible without deepening the fundamental ideas about the hydrodynamics of turbulent pulsating jets created by vibratory mixing devices. Modern theories of turbulent jets consider only a stationary issue. However, pulsating flows are non-stationary unstable in time [14–21].

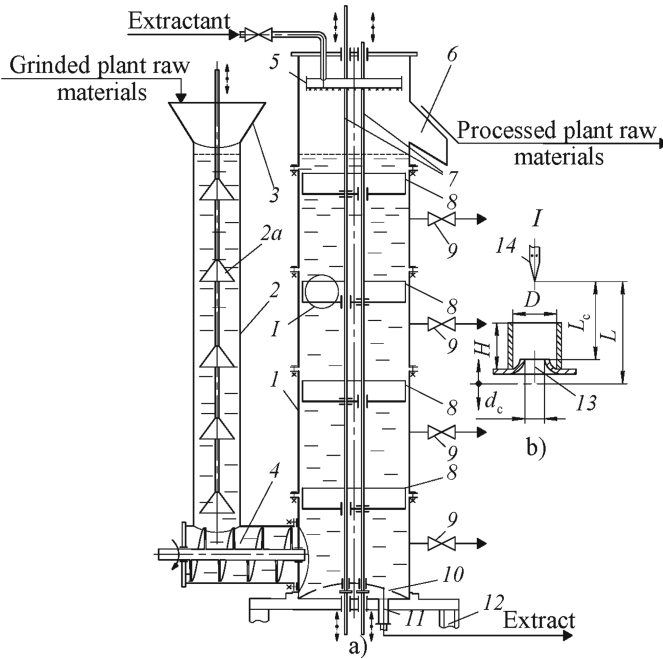
New approaches to assessing hydrodynamics and mass transfer of the process of vibromixing and countercurrent phase separation should be based on the fundamental laws of motion of pulsating jets generated by vibromixing devices of unique designs, as well as the basics of systemic and evolutionary approaches [22, 23].

## 3 Research Methodology

The effect of vibrating mixing devices on the experimental setup was studied according to the scheme shown in Fig. 1 with oscillation parameters: amplitude 0.005–0.015 m,

frequency varied from 1 to 10 Hz. The length of the working part was 1.5 m with a diameter of 0.3 m. Simulation of the solid phase was carried out with a nylon crumb.

The process of continuous vibroextraction was investigated on the model of the vibroextractor of continuous action developed and made in the conditions of the Department of Processes and Apparatus of NUFT according to the scheme shown in Fig. 1.



**Fig. 1.** a) Laboratory extractor with vibrating mixing devices: 1 – body; 2 – loading device; 2a – pusher; 3 – funnel; 4 – screw; 5 – extractant dispenser; 6 – unloading tray; 7 – rod system; 8 – system of transport plates; 9 – sampler; 10 – extract filter; 11 – branch pipe; 12 – support; b) scheme of measuring the spreading of pulsating flows: 13 – nozzle; 14 – Pito Prandtl tube.

The installation consists of a side-bar 1 with an internal diameter of 0.3 m and a height of 0.4 m. To supply the grinded plant materials to the apparatus, the lower side-bar at the level of 0.2 m from the bottom is connected via a screw 4 with a loading device 2 made in the form of a u-shaped glass tube with a diameter of 0.15 m with a funnel 3. To supply the extractant in the last upper side-bar fixed shower distributor 5 and unloading tray 6. Inside the column, there is a balanced vibrotransporting device, consisting of a system of vertical rods 7 with fixed horizontally conveying plates 8. Plates with a diameter of 0.295 m are fixed on rods alternately and installed in the body of the apparatus with a minimum gap on the periphery, with the ability to adjust their number and distance between them through a set of remote bushings.

Low-frequency mechanical oscillations are transmitted to the vibrotransport system through rods 7 from the vibrating drive located under frame 12. The frequency of oscillations of the vibrotransporting system within 10 Hz was carried out by an autotransformer. The amplitude was fixed  $(5; 10; 15) \cdot 10^{-3}$  m by changing the length of the shoulder of the crank mechanism. Multi-directional installation of filter and open conveyor elements ensures phase separation. The time intervals between successive single jets generated by these elements are half the period of oscillations. The phase separation mechanism and extraction process are described in the study [2].

Modern integrated systems MathCAD, OriginPro 8.6, and others were used to process and calculate experimental data.

## 4 Results

### 4.1 Determination of Velocities of Pulsating Turbulent Flows

To determine the velocities of pulsating jets' velocities, a Pitot-Prandtl tube with a hole diameter of 2 mm with appropriate calibration, as shown in Fig. 1a.

During the research, the ratio of the diameters of the branch pipes and nozzles and their height and diameter varied within, respectively  $D/d = 1 \dots 3$ ;  $H/d = 1 \dots 4$ . Nozzles with a diameter of 15, 20, 25 mm were installed in branch pipe with 35 and 55 mm diameters, height 45 and 60 mm. The designs of plates with a living cross-section of 5.5...14.2% were studied.

At a given distance from the source of oscillations using a differential pressure gauge, the average integral velocity of pulsating jets was determined:

$$w_L = 2/\pi k \sqrt{2gh} \quad (1)$$

where  $k = w/\bar{w}_{\max}$ —relative velocity ( $k = 0,5$  for laminar flow; for turbulent— $k = 0,75 \dots 0,87$  [15, 20];  $h$ —Pito-Prandtl tube readings;  $g$ —acceleration of gravity. The determined value of  $w_L$  was attributed to the initial average integral for the period of oscillation of the pulsating flow velocities:

$$w_0 = 2Af(1 - \varepsilon)/\varepsilon, \quad (2)$$

where  $A$ —oscillation amplitude,  $f$ —oscillation frequency,  $\varepsilon$ —a total living cross-section of the plate at the place of its installation in the apparatus.

The distance  $L$  was determined by analogy with stationary turbulent jets

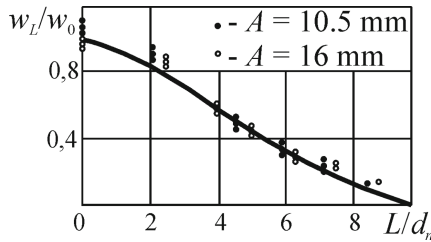
$$L = L_n + 4,5r_n \quad (3)$$

where  $L_n$ —distance from the measuring point to the cut of the nozzle;  $r_n$ —nozzle radius.

When analyzing the results of experimental data, it was found that the relative velocity  $w_L/w_0$  at  $Re_p > 5000$ , where

$$Re_p = 4A^2f(1 - \varepsilon)/\varepsilon\nu \quad (4)$$

Reynolds pulsation criterion,  $\nu$ —kinematic viscosity of water.



**Fig. 2.** Attenuation of the relative velocity of pulsating flows.

Figure 2 presents experimental data for a nozzle with a diameter of  $d_n = 15 \cdot 10^{-3}$  m, installed in a branch pipe with a diameter  $(35 \times 45) \cdot 10^{-3}$  m.

The dashed line shows the universal profile of the relative velocity in the cross-section of a stationary turbulent jet [15, 20], calculated by the Schlichting equation:

$$w_L/w_0 = \left[ 1 - (L/L_t)^{1.5} \right]^2, \tag{5}$$

where  $L_t = 2,44 L_{0,5}$ —theoretical range of jet spreading;  $L_{0,5}$ —distance from the plate at which  $w_L/w_0 = 0.5$ .

The range of jet spreading depends on the accepted limiting degree of attenuation

$$\beta = 1 - w_L/w_0 \tag{6}$$

The value of  $L_t$  is determined at  $\beta = 0.983$ . Due to the complexity of measuring the pulsating flows velocities, the range of action in these experiments was determined when  $\beta = 0.85$ .

It is established that the experimental data mainly correspond to the universal profile of relative velocity in the cross-section of turbulent jets, calculated by the Schlichting equation. Therefore, to describe the patterns of attenuation of pulsating flows at  $\beta > 0.5$ , the dependence is proposed:

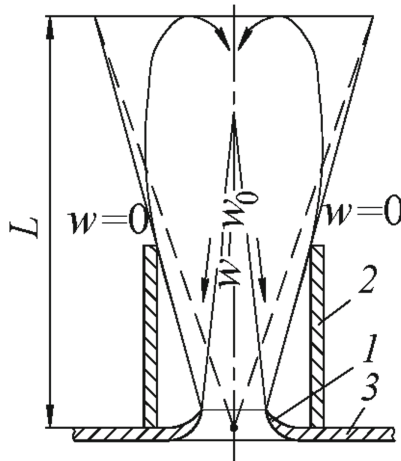
$$w_L/w_0 = 0,5(1 + L_{0,5}/d_n)^2 / (1 + L/d_n)^2 \tag{7}$$

The identity of universal functions to describe the profile of gas velocities in the flooded jet flowing out in a stationary or fluidized bed, as well as pulsating flooded jets of liquid, is not accidental and indicates the qualitative similarity of processes and turbulent mixing (in mixing zones) in all cases.

#### 4.2 Fundamental Description of Regularities of Hydrodynamics of Turbulent Pulsating Jets in a Liquid Medium During Vibroextraction

The simplest and most studied jet motion case is the liquid’s leakage with a uniform initial velocity field ( $w_0 = \text{const}$ ) into a medium moving at a constant velocity ( $w_L = \text{const}$ ) or flooded in a stationary medium. The development of the jet is accompanied by the capture of liquid particles surrounding the jet, the gradual inhibition of the jet,

and the increase of its cross-section. With a uniform velocity field in the initial section, the boundaries of the boundary layer have conical surfaces that intersect at the edges of the nozzle. The outer side of this edge touches the surrounding fluid. Using a simplified scheme of the flooded jet (Fig. 3), take the length of the transition section and the velocity at the boundary of the boundary layer equal to zero [20].



**Fig. 3.** The structure of the pulsating flow in the transport element: 1—transport element (nozzle); 2—branch pipe; 3—vibrotransport device.

If a section is selected away from the nozzle edge, then the jet profile is “lower” and “wider”. The structure of pulsating turbulent jets was visualized by tracing the flow of air bubbles through the compressor in the open transport element, shown in Fig. 4. A single non-stationary jet is a certain volume of fluid that has passed through a nozzle in half the period of oscillation at average integral velocity  $w_0$  with a certain scale of turbulent pulsations. During the next half-period, the amount of liquid is returned back through all the holes in the vibrotransport device.

Assuming the affinity of the regularities of spreading of stationary flooded and pulsating jets, the physically substantiated confirmation of this will be the establishment of the relations of determining spatiotemporal characteristics in relative quantities in the form of a velocity profile at the intersection of a flat turbulent trace according to Prandtl-Schlichting theory [15, 20]. That is, if the distribution of the relative velocity at the intersection of a stationary jet at relative distances from the source is universal, then it becomes possible to hope for a corresponding coincidence of similar characteristics for the pulsating jet, at least in some part of this characteristic.

Being the result of averaging the velocity of single jets that have reached a distance  $L$  and moving in time one after the other with the oscillation frequency of the vibrating partition  $f$ , the velocity  $w_L$  can be represented as.

$$w_L = 2A_L f, \quad w_0 = 2A_0 f, \tag{8}$$

where  $A_L$ —the oscillations amplitude of the pulsating jet at the distance  $L$ ;  $A_0 = A(1 - \varepsilon)/\varepsilon$ —initial amplitude of oscillations. The relative velocity of the pulsating jet at a distance  $L$  from its pole will be equal to.

$$w_L/w_0 = A_L f / A_0 f = A_L / A_0, \tag{9}$$

it is converted into the ratio of amplitudes observed when visualizing the hydrodynamic situation in the vibroextractor.

On the other hand, considering the sequential movement of individual single jets, which are in fact vortex rings moving in the direction of spreading of the pulsating jet, the velocity  $w_L$  can be written as follows:

$$w_L = \omega_L R, \tag{10}$$

where  $R$  and  $\omega_L$ —the radius of the cross-section of the vortex ring and the angular velocity of its rotation around the vortex thread.

The specificity of the generation of vortex rings by a vibrating nozzle moving opposite to the formed jet in the vacuum zone formed by the vibrating partition contributes to the final formation of the ring with radius  $R$  in the initial section of the jet.

Given that  $R$  is constant in the process of jet development, its relative velocity can be converted into a form:

$$w_L/w_0 = \omega_L R / \omega_0 R = \omega_L / \omega_0 \tag{11}$$

The results of studies in the turbulent regime of pulsating flows were generalized in the form of the dependence of the relative velocity  $w_L/w_0$  on the functional spatial characteristic  $\eta_f = \ell/\ell_f$ , where  $\ell = L/r_n$ —the relative distance, and  $\ell_f$ —its value, at which  $w_L/w_0 = e^{-1}$ , where  $e$ —the basis of natural logarithms. In these functional spatio-temporal coordinates (Fig. 4), the entire data array was generalized at  $\eta_f$ , less than the critical value

$$(\eta_f)_k = 0, 1 e \ln 10 / (1 - e^{-0.5})^{2/3} = 1,1656538, \tag{12}$$

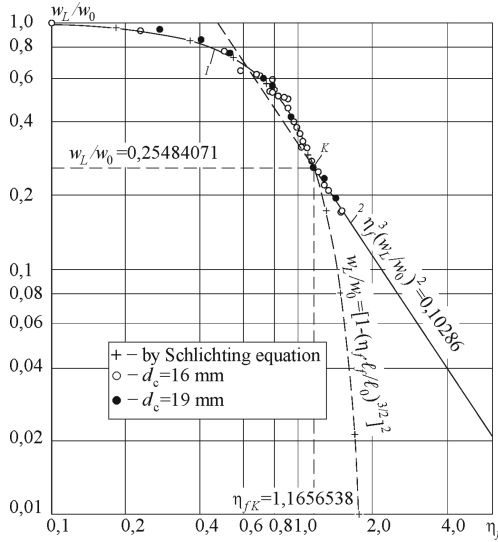
by the known Schlichting formula [20] for the universal velocity profile in distant turbulent traces:

$$w_L/w_0 = [1 - (\eta_f \ell_f / \ell_0)^{3/2}]^2, \tag{13}$$

$$\text{and at } \eta_f > (\eta_f)_k \text{ dependence } (\eta_f)^3 (w_L/w_0)^2 = C_T, \tag{14}$$

$$\text{where } C_T = (\eta_f)_k^3 [1 - (\eta_f)_k^{3/2} (1 - e^{-0.5})]^4 = 0,10286 \tag{15}$$

is a fundamental constant;  $\ell_0 = L_0/r_n$ —the relative limiting range of the turbulent pulsating jet spreading, and  $L_0$ —its absolute value.



**Fig. 4.** Generalization of experimental data on the hydrodynamics of turbulent pulsating jets by a dimensionless profile of the relative velocity of pulsating jets: 1—according to the Schlichting equation; 2—by Eq. (13).

The solid line on the graph shows the universal hydrodynamic profile of the relative velocity of a stationary flat flooded jet, built according to the Schlichting equation [20]. As can be seen from the graphical dependence shown in Fig. 4, the experimental data in the new coordinate system obtained for the pulsating jet generated by the transport element of the vibromixing device are grouped around the curve of the universal hydrodynamic profile of a turbulent stationary flooded jet. The point “K” is the limit to which there is an almost complete coincidence with the universal profile. There is a deviation at significant distances from the pulsating jet’s source.

The proposed dependences summarize the experimental data with a standard deviation of  $8 \cdot 5 \cdot 10^{-3}$  in the confidence interval of 98%. The theoretical value  $(\ell_f/\ell_0)_T$  is equal to  $(1 - e^{-0.5})^{2/3} = 0.53695838$ .

Having determined based on dependence  $w_L/w_0$  on  $\ell$  experimental value  $\ell_f$ , it is possible to calculate  $L_K$  and  $w_L$ , necessary for designing vibroextractors.

The constant  $C_T$  allows to specify the constant  $C$  in one of the basic equations of the semi-empirical theory of turbulent jets  $\delta = C \cdot x$ , where  $\delta$ —the half-width of the jet,  $x$ —the distance to its pole. Equation (15) describes the hydrodynamic profile of the main section of a flat turbulent jet at a theoretical value

$$(\ell_f)_T = 10(1 - e^{-0.5})^{2/3}, \tag{16}$$

replacing the relative velocity of the pulsating jet  $w_L/w_0$  with the relative angular velocity  $\omega_L/\omega_0$  and the specified value of  $C = 0.22170$  (empirical constant  $C = 0.22$ ).

Thus, the possibility of using fundamental regularities to calculate the hydrodynamics of turbulent jets that ensure the efficient operation of vibroextractors is established.

## 5 Conclusions

The basic scaling criteria of vibroextractors are defined, affinity with regularities of the hydrodynamics of a stationary flooded jet and jets generated by usual mixing devices of the paddle mixer creating mainly circular motion in the smooth-walled device without internal devices is established.

According to the research results of features of pulsating jets hydrodynamics generated by vibrating working devices in a vibroextractor of continuous action, using new representations based on the introduction of functional spatio-temporal relations, the fundamental description of regularities of change of their velocity is received in functional spatio-temporal coordinates. New data necessary for the design and calculation of vibroextraction apparatus are obtained. The obtained scaling results were used to design an industrial vibroextractor of continuous action for processing plant raw materials and its waste by the company “TMA” in Kyiv.

## References






1. Dyachok, V., Dyachok, R., Gaiduchok, O.: Mathematical model of mass transfer from Lamina of the leaf into extractant. *Chem. Chem. Technol.* **9**(1), 107–110 (2015)
2. Pouria, A., Safdari, J., Hossein, A., Mallah, M.H., Davari, A.: Two-phase pressure drop and flooding characteristics in a horizontal-vertical pulsed sieve-plate column. *Int. J. Heat Fluid Flow* **65**, 266–327 (2017). <https://doi.org/10.1016/j.ijheatfluidflow.2017.01.003>
3. Zavialov, V., Mysiura, T., Popova, N., Zaporozhets, Y., Chorny, V.: Justification of local expenditure characteristics of vibrotransporting devices in design modeling of continuous vibroextractors. In: Ivanov, V., Pavlenko, I., Liaposhchenko, O., Machado, J., Edl, M. (eds.) *DSMIE 2021. LNME*, pp. 296–305. Springer, Cham (2021). [https://doi.org/10.1007/978-3-030-77823-1\\_30](https://doi.org/10.1007/978-3-030-77823-1_30)
4. Rafiei, V., Safdari, J., Moradi, S., Amani, P., Mallah, M.H.: Investigation of mass transfer performance in an L-shaped pulsed sieve plate extraction column using axial dispersion model. *Chem. Eng. Res. Des.* **128**, 130–145 (2017). <https://doi.org/10.1016/j.cherd.2017.10.006>
5. Khajenoori, M., Haghghi-Asl, A., Safdari, J., Mallah, M.: Prediction of drop size distribution in a horizontal pulsed plate extraction column. *Chem. Eng. Process.* **92**, 25–32 (2015)
6. Zavialov, V., Mysiura, T., Popova, N., Sukmanov, V., Chorny, V.: Regularities of solid-phase continuous vibration extraction and prospects for its industrial use. In: Ivanov, V., et al. (eds.) *DSMIE 2019. LNME*, pp. 920–930. Springer, Cham (2020). [https://doi.org/10.1007/978-3-030-22365-6\\_92](https://doi.org/10.1007/978-3-030-22365-6_92)
7. Khajenoori, M., Safdari, J., Asl, A.H., Mallah, M.H.: Slip and characteristic velocities in a horizontal pulsed-plate extraction column. *Chem. Eng. Technol.* **38**(10), 1783–1792 (2015). <https://doi.org/10.1002/ceat.201400797>
8. Castillo-Santosa, K., Ruiz-López, I., Rodríguez-Jimenes, G., Carrillo-Ahumadac, J., García-Alvarado, M.: Analysis of mass transfer equations during solid-liquid extraction and its application for vanilla extraction kinetics modeling. *J. Food Eng.* **192**, 36–44 (2017)



9. Jurinjak, A., et al.: Kinetics and thermodynamics of the solid-liquid extraction process of total polyphenols, antioxidants and extraction yield from Asteraceae plants. *Ind. Crops Prod.* **91**, 205–214 (2016)
10. Olayiwola, B., Schaldach, G., Walzel, P.: Residence time distribution of steady and pulsed flow in a parallel-plate channel with staggered fins. *Chem. Eng. Technol.* (2011). <https://doi.org/10.1002/ceat.201000524>
11. Beloborodov, V.: The problem of extraction in the food industry. *Izvestiya vuzov. Food technology* (1986)
12. Zaki, M., Abdel-Aziz, M.H., Nirdosh, I., Sedahmed, G.H.: Intensification of the rate of heat and mass transfer in a batch and continuous parallel plate contactor by pulsed flow. *Chem. Eng. J.* **398**, 125–140 (2020)
13. Song, J., Law, A.-K.: Longitudinal dispersion of turbulent oscillatory pipe flows. *Environ. Fluid Mech.* **15**(3), 563–593 (2014). <https://doi.org/10.1007/s10652-014-9374-z>
14. Slavnić, D.S., Živković, L.V., Bjelić, A.V., Bugarski, B.M., Nikačević, N.M.: Residence time distribution and Peclet number correlation for continuous oscillatory flow reactors. *J. Chem. Technol. Biotechnol.* **92**, 2178–2188 (2017)
15. Abramovych, H.: *Theory of Turbulent Jets*, 2nd edn. Nauka, Moscow (1984)
16. Skydanenko, M., Sklabinskyi, V., Saleh, S., Barghi, S.: Reduction of dust emission by monodisperse system technology for ammonium nitrate manufacturing. *Processes* **5**(3), 37 (2017). <https://doi.org/10.3390/pr5030037>
17. Pavlenko, I., et al.: Effect of superimposed vibrations on droplet oscillation modes in prilling process. *Processes* **8**(5), 566 (2020). <https://doi.org/10.3390/pr8050566>
18. Pylypaka, S., Nesvidomin, V., Zaharova, T., Pavlenko, O., Klendiy, M.: The investigation of particle movement on a helical surface. In: Ivanov, V., et al. (eds.) *DSMIE 2019. LNME*, pp. 671–681. Springer, Cham (2020). [https://doi.org/10.1007/978-3-030-22365-6\\_67](https://doi.org/10.1007/978-3-030-22365-6_67)
19. Reis, M.N.E., Hanriot, S.: Incompressible pulsating flow for low Reynolds numbers in orifice plates. *Flow Meas. Instrum.* **54**, 146–157 (2017)
20. Loboda, P.: Prospects for the application of universal spatio-temporal relations in the intensification and scale of technological processes. *Sci. Works UDUHT* **1**, 60–64 (1993). [in Ukrainian]
21. Panahinia, F., Safdari, J., Ghannadi-Maragheh, M., Amani, P., Mallah, M.H.: Modeling and simulation of a horizontal pulsed sieve-plate extraction column using axial dispersion model. *Sep. Sci. Technol.* **52**(9), 1537–1552 (2017). <https://doi.org/10.1080/01496395.2017.1293097>
22. Nagarajan, K., Renganathan, T., Krishnaiaha, K.: Hydrodynamics of a continuous counter-current liquid–solid system: experiments and modeling. *RSC Adv.* **6**, 35486–35497 (2016). <https://doi.org/10.1039/C6RA05595H>
23. Walzel, P.: Effects and new applications of pulsed flow. *Chem. Eng. Technol.* **36**(1), 15–21 (2012). <https://doi.org/10.1002/ceat.201200566>



# Research of Wheat Fiber with Pumpkin Pectin Plant Additive

Marija Zheplinska<sup>1</sup> (✉) , Volodymyr Vasyliv<sup>1</sup> , Olena Deviatko<sup>1</sup> ,  
Sergii Ulianko<sup>2</sup> , and Nataliia Kanivets<sup>2</sup> 

<sup>1</sup> National University of Life and Environmental Sciences of Ukraine,  
15, Heroes of Defense Street, Kyiv 03041, Ukraine  
jeplinska@ukr.net

<sup>2</sup> Poltava State Agrarian Academy, 1/3, Skovorody Street, Poltava 36003, Ukraine

**Abstract.** The scientific work presents the results of improving the technology of making cooked sausages with the addition of wheat fiber with pumpkin pectin. The advantage of improving the technology of sausages was determined, particularly increasing their quality for the consumer and the prospects of using plant additives to improve their nutritional value. This paper explores the possibility of adding the combined plant additive of wheat fiber and pumpkin pectin to minced meat. A rational grinding mode is 3–4 min to fractions of 500–600  $\mu\text{m}$  was established, which ensured the homogeneity of the plant additive and would contribute to its uniform distribution in minced meat in the cooked sausages production. The influence of the plant additive grinding level on the functional properties was presented, which showed that the best results for water-holding, water-binding, and fat-holding capacity are provided by particles of a size of 600  $\mu\text{m}$ . Rational parameters for preliminary preparation of the plant additive for mixing with the minced meat associated with hydration at hydromodule were determined. This stage of the technological process provides the highest water-holding capacity, and the 1:3 ratio of the plant additive to refined oil provides a high fat-holding capacity. The solution to this problem improves the biological value and therapeutic and preventive properties of cooked sausages.

**Keywords:** Fat-holding capacity · Grinding · Hydromodule · Plant additive · Water-binding capacity · Water-holding capacity · Water resource

## 1 Introduction

Nowadays, a promising direction in providing the population with high-quality food products of increased nutritional and biological value is the combination of raw materials of plant and animal origin, considering adequate human needs according to the modern nutritional requirements [1]. Innovative approaches to solving the nutrition problem consist of creating products with an increased nutritional value which is one of the priority areas for solving problems highlighted in the concept of the state policy in product quality management [2].

The socio-economic problem of the shortage, high cost, and low quality of food, including meat products in Ukraine, is particularly critical. Recently, there have been specific changes in people's lives: a significant decrease in physical activity, a change in healthy eating habits, and consumers' needs. Considering this, some of the previously declared features of sausages do not correspond to the current demand, for example, high-calorie content, which does not attract but requires adjustment instead.

## 2 Literature Review

The analysis of scientific literature has determined the main directions of modern technologies for the production of cooked sausages. First of all, these technologies replace meat raw materials with food additives and ingredients. Thus, a technology for the production of cooked sausages has been developed, which differs from the traditional one that at the stage of preparation of minced meat, 1–2% of a multifunctional additive is added to the cutter based on animal protein, alginate, carrageenan, and guar gum [3].

Scientists pay special attention to balancing the amino acid composition of the proteins. There is a specific deficiency of three amino acids - tryptophan, methionine, and lysine in the diet of a significant number of people in the world. This deficiency limits the absorption of proteins from food and is explained, mainly, by the predominant consumption of plant-based food [4].

In Ukraine, there are meat and vegetable raw materials for manufacturing combined products. Sausages are essential products in the population's diet. Their production is the most common meat and other animal products processing in the meat industry [5]. Development of the new generation products by combining plant and animal raw materials with a therapeutic and preventive effect is of particular importance. Plant-based ingredients can protect the human body from the harmful effects of the environment, prevent the formation of diseased cells, and prevent diabetes as they reduce blood sugar levels [6]. Such products are cooked sausage products, combining plant and animal raw materials. By the way, such a combination makes it possible to reduce the cost of final products and produce a high-quality and nutritious product that will be tasty and healthy in terms of overall nutrients and energy value [7].

However, many issues remain unresolved. In Ukraine, the market for cooked sausages with high biological value is minimal. At the same time, the industry produces wheat fiber with pumpkin pectin, which can be used in cooked sausages to produce more balanced products in terms of essential nutrients [8].

Dietary fiber's positive role in cereals and vegetables' cell walls, which significantly affects digestion and excretion of harmful toxic substances, salts of heavy metals, and radionuclides, is well-known [9, 10]. The low-calorie content of the cereals and vegetables is also an additional argument for their use in high-calorie meat products [11]. There are raw materials for the production of wheat fiber with pumpkin pectin in Ukraine. Therefore, the purpose of the work was to study this complex additive for inclusion in the recipe of cooked sausages [12, 13].

### 3 Research Methodology

The experimental part of the work was performed in the laboratory of the technology departments of meat, fish and seafood, processes and equipment for processing agricultural products and microbiology, virology and biotechnology of the National University of Life and Environmental Sciences Ukraine, the Institute of Biochemistry. OV Paladin, in the Ukrainian laboratory of quality and safety of agricultural products, in the production conditions of PE “Zlagoda-Lutsk”, Rivne region, Boromel village.

The raw materials and materials used in the research complied with the current regulations in Ukraine in terms of quality and safety, approved for use by the Ministry of Health of Ukraine. The following raw materials were used for research:

- lean beef I grade - muscle tissue with a mass fraction of connective and adipose tissue, not more than 6% – DSTU 6030: 2008. State standard of Ukraine. Meat. Beef and veal in carcasses, carcasses and quarters;
- lean pork semi-fat - muscle tissue with a mass fraction of adipose tissue from 50% to 85% - DSTU 7158: 2010. State standard of Ukraine. Meat. Pork in carcasses and half-carcasses;
- wheat fiber with pumpkin pectin TU U 15.8-2783308472-005: 2010. Technical conditions of Ukraine. Biologically active additive “Wheat fiber with pumpkin pectin” in the composition: 20.0% - pumpkin pectin, 80.0% – a crushed shell of wheat grain;
- multi-component minced meat, which includes lean semi-fat pork, beef, and grade, plant additive PKZPG in different ratios (3%, 5%, 7%, respectively);
- ready cooked sausage with vegetable additive.

The experimental studies included three stages. At the first stage, a study of physicochemical parameters of PFWPP (pectin fiber with pumpkin pectin) supplement, the amino acid composition of its proteins, mineral and vitamin composition. Based on the obtained indicators, the energy value and coefficients were calculated: protein, protein-water, fat-water, food saturation, potential biological value, the difference of amino acid SKORu [14, 15], utilitarianism of amino acid composition of protein; an indicator of excess content and index of essential amino acids.

The safety of raw materials was assessed by microbiological parameters, the content of heavy metals, pesticides (insecticides, pesticides, herbicides), the content of mycotoxin “patulin” and radionuclides.

At the second stage, the development and substantiation of the technology of cooked sausages were carried out, which included:

- determining the features of the preliminary preparation of vegetable additives for the introduction of cooked sausages into the minced meat system, and the time of grinding to a homogeneous state;
- study of the hydraulic module and the ratio of crushed vegetable additives before the formation of cooked sausages;
- substantiation of the prescription composition of cooked sausages with the addition of PFWPP and the method of its introduction into the minced meat;

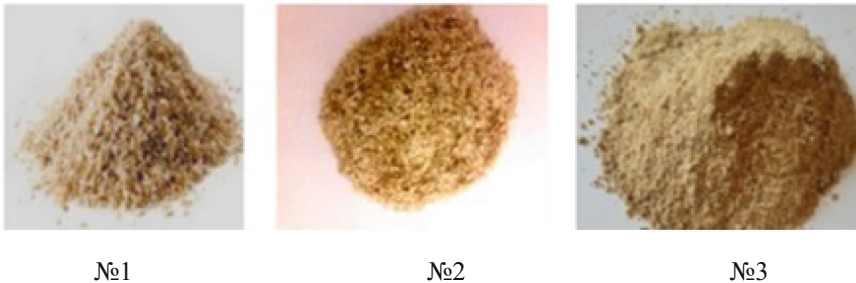
- assessment of structural-mechanical and organoleptic indicators of cooked sausages using vegetable additive PFWPP and changes in these indicators during storage.

The third stage of research included the characterization of ready-cooked sausages by organoleptic, physicochemical, biochemical, microbiological, and rheological parameters. The kinetics of changes in organoleptic and microbiological parameters of cooked sausages during storage at a temperature from 0 °C to + 6 °C for up to 10 days of storage in a polyamide shell were studied. The shelf life of sausages was set based on the research. The work aimed to study the plant supplement of wheat fiber with pumpkin pectin and replace it with a certain amount of meat to enrich the nutrients in ready-made sausages.

## 4 Results

The study of combining a dry plant additive into the model minced meat showed the inexpediency of its use in this form because the proper structure of the cooked sausage did not occur.

Dry wheat fiber's shape and particle size with pumpkin pectin have a heterogeneous composition. By shape, the particles are divided into three groups: arrow-shaped, rod-shaped, and spherical. By size, we found particles with sizes of 1000–700  $\mu\text{m}$ , 600–500  $\mu\text{m}$ , and 400–100  $\mu\text{m}$  (Fig. 1).



**Fig. 1.** Shapes of wheat fiber with pumpkin pectin.

The fractional composition of wheat fiber with pumpkin pectin is presented in Table 1.

The analysis of these data shows that the particles of 600–500  $\mu\text{m}$  have the largest mass fraction of wheat fiber with pumpkin pectin (45%), particles of 400–100  $\mu\text{m}$  have the smallest mass fraction (15%), and particles of 1000–700  $\mu\text{m}$  have the mass fraction of 40%.

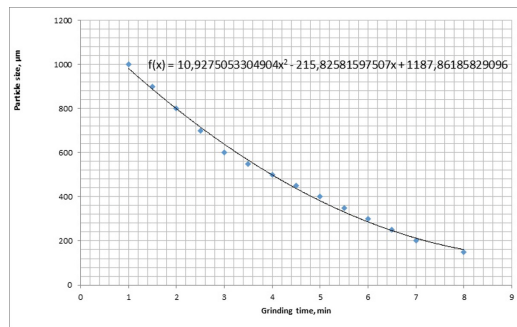
The technological process of preparing a plant additive is associated with the influence of various factors on the components of wheat fiber with pumpkin pectin (mechanical grinding, classification by particle size, temperature, solvent, and hydromodule). Adding the dry plant additive to the meat grinding system did not produce a positive

**Table 1.** Research results of wheat fiber’s particles fractional composition characteristics with pumpkin pectin.

Nº grist	Size, μm	Mass fraction, % of the total mass
1	1000–700	35 ± 1.5
2	600–500	45 ± 3.8
3	400–100	15 ± 2.4

result. The heterogeneity of the size and shape of the plant additive did not provide a satisfactory consistency of the cooked sausage. Thus, it was necessary to determine the degree of grinding of wheat fiber with pumpkin pectin to a uniform state and particle size.

A meat shop universal drive PM-1.1 with a replaceable grinding mechanism was used to fine grind wheat fiber with pumpkin pectin. The degree of grinding (grist size) of the wheat fiber with pumpkin pectin depends on the plant additive’s strength, hardness, ultrastructure, and the time of grinding (Fig. 2).



**Fig. 2.** Dependence of the grinding degree of the wheat fiber with pumpkin pectin on time.

Studies have shown that after 3–4 min of grinding wheat fiber with pumpkin pectin has a homogeneous structure with a grain size of 500–600 μm. The longer grinding time of wheat fiber with pumpkin pectin leads to its transformation into a sticky flour state. High homogenization of the additive results in the adhesive interaction of its particles, and a technological problem of the separation of individual fractions arises. The resulting crushed mixture of plant additive was sieved on a sieve with a magnetic metal contamination trap. As a result, the obtained plant additive looked like a uniform color powder of free-flowing consistency with pleasant taste and smell.

During the manufacture of cooked sausages, there are properties that, to a greater extent, provide organoleptic and structural properties of these products. Such properties include indicators of water-binding, water-holding, and fat-holding. Previous research has shown that one factor affecting these functional properties is the grinding degree of

plant additives. The results of studies on the dependence of the functional parameters of wheat fiber with pumpkin pectin on the degree of its grinding are presented in Table 2.

**Table 2.** The influence of the grinding degree of wheat fiber with pumpkin pectin on functional properties.

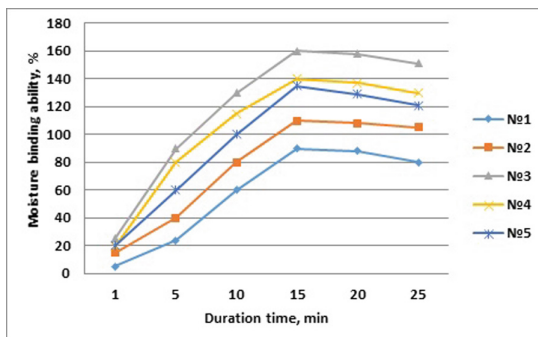
Additive particle size, $\mu\text{m}$	Functional parameters		
	Water-holding, %	Water-binding, %	Fat-holding, g
1000	$30.62 \pm 2,1$	$16.10 \pm 1,8$	$2.01 \pm 0.5$
800	$40.41 \pm 1,9$	$18.23 \pm 1,5$	$2.12 \pm 0.1$
600	$45.24 \pm 2,5$	$20.44 \pm 1,7$	$2.51 \pm 0.3$
400	$39.32 \pm 1,7$	$17.21 \pm 0,9$	$2.03 \pm 0.2$
200	$35.14 \pm 1,3$	$16.32 \pm 2,4$	$1.95 \pm 0.4$
100	$28.51 \pm 2,1$	$14.35 \pm 1,3$	$1.72 \pm 0.2$

The results of studies indicate that particles with a size of  $600 \mu\text{m}$  have the largest water-holding, water-binding, and fat-holding capacities.

According to the literature, many dry plant additives are added into the meat-grinding system as water suspensions because plant additives have a high-water absorption capacity [16]. However, this characteristic for each additive is unique and depends on many factors. Adding dry, ground to  $600 \mu\text{m}$  wheat fiber with pumpkin pectin to the minced meat did not result in homogeneous consistency; the signs of plant additives were visible on the cut of the sausage and were even more noticeable after the heat treatment.

Since the plant additive increases the water-binding capacity of minced meat, the kinetics of this process has been studied.

The water-binding capacity of the plant additive depends on the time of water absorption at different ratios of the additive and water (1 - 1:1; 2 - 1:2, 3 - 1:3, 4 - 1:4, 5 - 1:5) is shown in Fig. 3.

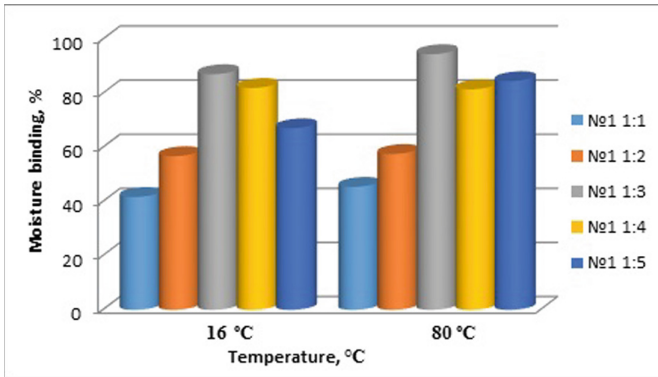


**Fig. 3.** Wheat fiber with pumpkin pectin water-binding capacity versus the hydromodule and time of keeping in water.

While analyzing the data from Fig. 3, we can see that for all hydromodules the water-binding capacity of the plant supplement grows gradually as time increases up to 15 min. The best water-binding capacity of wheat fiber with pumpkin pectin was reached at hydromodule 3. After keeping the plant additive in water for 15 min, the water-binding capacity decreases at all the hydromodules used in the experiment. An increase in the hydromodule index to 4 and 5 leads to a decrease in the water-binding capacity. Therefore, the best results were obtained at hydromodule 3 and keeping the plant additive in water for 15 min.

The cooked sausages technology uses the cooking temperature up to +80 °C; therefore, it is advisable to determine the influence of this temperature on the water-binding capacity depending on the hydromodule.

The results of the study of the wheat fiber with pumpkin pectin plant additive water-binding capacity at a temperature of +80 °C for different hydromodules are presented in Fig. 4, which shows the most remarkable water-absorbing capacity occurs at hydromodule 3 at a temperature of +16°C. An increase in temperature to 80°C results in an increase of the water-binding capacity for all hydromodules.



**Fig. 4.** Dependence of the water-binding capacity of a complex plant additive on temperature.

Therefore, the best water-binding capacity of the plant additive at temperatures from +16 to +80 °C is for hydromodule 3.

It is known that when the various plant additives are used in the technology of cooked sausages, vegetable oils are used to improve the products’ functional and technological properties [17].

We have studied the effects of fat-holding capacity at different ratios of plant additive to oils to achieve quality indicators of plant additives to water absorption. When the oil ratio was increased to 4 and 5, the mixture became thin. An increase in temperature to +80 °C leads to an increase in fat-holding capacity for all ratios between plant additive and oil. Therefore, a further increase in the content of refined oil is useless as it leads to a significant deterioration in the functional properties of the plant additive.

We suggest using the 1:2 ratio of plant additive to oil. The 1:2 ratio of additive to oil at +16 °C provides more oil absorption. The binding property of oil is higher at +80 °C due to the binding energy of oil molecules in the plant additive.



The increase in water-binding and fat-holding capacities of plant additives is due to the dry matter content in wheat fiber with pumpkin pectin, which expands in a liquid medium (water, oil) and has better viscosity. Therefore, the highest expansion degree of wheat fiber with pumpkin pectin was observed at +80 °C and above. The high temperature significantly increases the water-binding capacity and fat-holding capacity of the combined plant additive, which should be considered when creating a new recipe and developing the technology for sausages with a plant additive. However, raising the temperature above +80 °C is ineffective because it will contribute to the denaturation of protein substances in the plant additive.

It is essential to consider the rheological properties of the ingredients - effective viscosity and shear stress when creating new recipes for cooked sausages.

Studying these properties enables the technological process of making cooked sausages with specified organoleptic properties. It is known that these properties depend on the chemical composition of hydromodules.

Table 3 presents the data on the chemical composition of wheat fiber with pumpkin pectin at different plant additive to water ratios.

**Table 3.** The chemical composition of wheat fiber with pumpkin pectin at different plant additive to water ratios.

Plant additive to water ratio	Mass fraction, %				
	Water	Protein	Fat	Ash	Carbohydrates
Control	9.10 ± 1.23	15.01 ± 2.1	3.43 ± 0.41	4.31 ± 0.02	65.80 ± 2.46
1:1	18.21 ± 1.33	13.29 ± 1.75	3.03 ± 0.09	3.9 ± 0.25	58.26 ± 2.33
1:2	27.31 ± 0.58	11.92 ± 1.21	2.72 ± 0.82	3.42 ± 0.84	52.27 ± 3.45
1:3	36.41 ± 1.55	10.55 ± 0.92	2.41 ± 0.43	3.03 ± 0.09	46.29 ± 2.85
1:4	45.51 ± 1.78	9.19 ± 0.87	2.40 ± 0.51	2.64 ± 0.89	40.30 ± 3.35
1:5	54.61 ± 1.85	7.82 ± 1.31	1.78 ± 0.43	2.25 ± 0.85	34.31 ± 2.36

It is found that the increase in moisture leads to a corresponding decrease in dry matter content (i.e., protein from 15.01 to 7.82%, fat - from 3.0 to 1.78%, ash - from 4.31 to 2.25%, and carbohydrates - from 65.80 to 34.31%) while changing the hydromodule from 1 to 5. The change in the chemical composition will result in a change in functional and technological properties. Therefore, a study of the dependence of the effective viscosity shear force on the ratio of plant additives to water was conducted.

It was established that the hydration of the combined plant additive was insufficient, and the additive was dry at hydromodule 1 and 2; the additive had a dense consistency which was suitable for combining with minced meat for the cooked sausages at hydromodule 3; with an increase of the hydromodule to more than 4, a liquid consistency of the additive was formed, resulting in a decrease in the effective viscosity value. Under these conditions, hydration occurs due to the action of water dipoles on the molecules of the peptide groups of the main chains (between which there are hydrogen bonds [18]).

Therefore, the optimal result was obtained at the hydromodule 3, which helped improve the plant additive's viscosity and consistency.

It has been determined that a compact coagulation system's structural and mechanical properties are changed depending on the proportion of the dispersion medium in the system and the presence or absence of a stabilizing component [19]. At low shear stresses, they act like elastic bodies. At high stresses, they get the ability to flow. When the shear stress is higher than the conditional yield point, the conditionally plastic body can undergo irreversible deformations and a relatively slow flow with a high constant viscosity. When the shear stress is above the conditional yield point, the destruction of the body structure in the flow begins, accompanied by a significant drop in viscosity [20].

It can be concluded from Fig. 3 that the complex plant additive has a high effective viscosity due to the high water-binding capacity at specific parameters of the hydromodule. The structural and mechanical properties of the plant additive can be attributed to compact solid coagulation structures.

## 5 Conclusions

The fractional composition of the additive wheat fiber with pumpkin pectin was studied, the largest mass fraction of which was the particles with sizes 600–500  $\mu\text{m}$  (45%), the smallest – particles with sizes 400–100  $\mu\text{m}$  (15%), and the rest – particles with sizes 1000–700  $\mu\text{m}$ .

The influence of the plant additive grinding degree on the functional indicators is presented, which shows that the particles with a size of 600  $\mu\text{m}$  have the best indicators of water-holding, water-binding, and fat-holding capacities.

The rational mode of preliminary preparation of plant additive for combining with minced meat, which is the hydration at hydromodule 3, is determined. This stage of the technological process provides the highest water-holding capacity, and the 1:3 ratio of plant additive to refined oil provides a high rate of fat-holding.

The benefit of improving the technology of sausages has been determined, particularly increasing their consumer qualities and the prospects of using plant additives to improve their nutritional value.

It is proved that wheat fiber with pumpkin pectin has all the necessary properties to be recommended as the plant additive in the technology of cooked sausages to improve the functional, technological, and organoleptic properties.

## References






1. Podkovko, O., Rashevskaya, T.: Butter paste with the high minerals content. *Sci. Messenger LNU Vet. Med. Biotechnol.* **17**(4), 100–104 (2015)
2. Agudelo, A., Varela, P., Sanz, T., Fiszman, S.: Freezing and baking stability of a tapioca starch–pectin mixture model. *Food Hydrocolloids* **40**, 203–213 (2014)
3. Palamarchuk, I., Mushtuk, M., Sukhenko, V., Dudchenko, V., et al.: Modelling of the process of vibromechanical activation of plant raw material hydrolysis for pectin extraction. *Potravinarstvo Slovak J. Food Sci.* **14**, 239–246 (2020)

4. Sukhenko, Y., Sukhenko, V., Mushtruk, M., Litvinenko, A.: Mathematical model of corrosive-mechanic wear materials in technological medium of food industry. In: Ivanov, V., et al. (eds.) DSMIE 2018. LNME, pp. 507–514. Springer, Cham (2019). [https://doi.org/10.1007/978-3-319-93587-4\\_53](https://doi.org/10.1007/978-3-319-93587-4_53)
5. Zheplinska, M., Mushtruk, M., Vasylyv, V., Sarana, V., et al.: The influence of cavitation effects on the purification processes of beet sugar production juices. *Potravinárstvo Slovak J. Food Sci.* **15**, 18–25 (2021)
6. Shanina, O., Galyasnyj, I., Gavrysh, T., Dugina, K., et al.: Development of gluten-free non-yeasted dough structure as factor of bread quality formation. *Potravinárstvo Slovak J. Food Sci.* **13**, 971–983 (2019)
7. Bober, A., Liashenko, M., Protsenko, L., Slobodyanyuk, N., et al.: Biochemical composition of the hops and quality of the finished beer. *Potravinárstvo Slovak J. Food Sci.* **14**, 307–317 (2020)
8. Correa, M., Ferrero, C.: Thermal behaviour of wheat starch and flour at different water levels: Effect of pectins, modified celluloses and NaCl. *Starch Stärke* **67**(3–4), 338–347 (2015)
9. Zheplinska, M., Mushtruk, M., Vasylyv, Kuts, A., et al.: The micronutrient profile of medicinal plant extracts. *Potravinárstvo Slovak J. Food Sci.* **15**, 528–535 (2021)
10. Kolyanovska, L.M., Palamarchuk, I.P., Sukhenko, Y., Mussabekova, A., et al.: Mathematical modeling of the extraction process of oil-containing raw materials with pulsed intensification of heat of mass transfer. In: Proceedings of SPIE - The International Society for Optical Engineering, vol. 25 (2019)
11. Rogovskii, I.L., Palamarchuk, I.P., Voinash, S.A., Butenko, A.F., et al.: Engineering of constructive parameters of vibroaspiration separator of oil-containing grain seeds. *J. Phys: Conf. Ser.* **1679**(4), 042034 (2020)
12. Ruhee, R.T., Sams, S., Begum, A., Alam, M.K., et al.: Dietary fibre content in ethnic and unconventional vegetables and fruits growing in Bangladesh. *Potravinárstvo Slovak J. Food Sci.* **14**, 33–41 (2020)
13. Cherednichenko, O., Bal-Prylypko, L.: Rationale and economic feasibility of improving the technology of long-term storage of meat products. *IOP Conf. Ser. Earth Environ. Sci.* **548**(2), 022053 (2020)
14. Bal'-Prylypko, L., Derevyanko, L., Slobodyanyuk, N., Starkova, E., Androshchiuk, O.: Using of the *Ampullaria glauca* snails' caviar for correction of the effects of the ionizing radiation exposure in small dose. *Nucl. Phys. Atom. Energy* **19**(2), 159–165 (2018)
15. Lebskaya, T.K., Bal-Prylypko, L.V., Menchinskaya, A.A., Lebsky, S.O.: Lipid profile of the black sea shrimp *Palaemon adspersus* Rathke, 1837. *Vopr. Pitan.* **89**(1), 96–100 (2020)
16. Smetanska, I., Tonkha, O., Patyka, T., Hunaefi, D., et al.: The influence of yeast extract and jasmonic acid on phenolic acids content of in vitro hairy root cultures of *Orthosiphon aristatus*. *Potravinárstvo Slovak J. Food Sci.* **15**, 1–8 (2021)
17. Rogoskii, I., Mushtruk, M., Titova, L., Snezhko, O., et al.: Engineering management of starter cultures in study of temperature of fermentation of sour-milk drink with apiproducs. *Potravinárstvo Slovak J. Food Sci.* **14**, 1047–1054 (2020)
18. De Escalada Pla, M., Ponce, N., Stortz, C., Gerschenson, L., Rojas, A.: Composition and functional properties of enriched fiber products obtained from pumpkin (*Cucurbita Moschata* Duchesne ex Poiret). *LWT-Food Sci. Technol.* **40**(7), 1176–1185 (2007)
19. Awad, S., Shokry, A.: Evaluation of physical and sensory characteristics of jam and cake processed using pumpkin (*Cucurbita Moschata*). *Middle East J. Appl. Sci.* **8**, 295–306 (2018)
20. Pogorelova, N., Moliboga, E.: Defining qualitative indicators of the pumpkin semi-finished product included in the confectionary technology in terms of competitiveness. *J. Pharm. Sci. Res.* **9**(10), 1705–1710 (2017)

# **Energy Efficient Technologies**



# Development of the Gas-Dynamic Cooling System for Gas Turbine Over-Expansion Circuit

Dmytro Konovalov<sup>(✉)</sup> , Halina Kobalava , Mykola Radchenko ,  
Viktor Gorbov , and Ivan Kalinichenko 

Admiral Makarov National University of Shipbuilding, 9, Heroes of Ukraine Avenue,  
Mykolayiv 54025, Ukraine  
dimitriyko79@gmail.com

**Abstract.** One of the ways to increase the efficiency of a gas turbine is an additional expansion of combustion products below atmospheric pressure in an auxiliary turbine installed after the main (power) turbine, that is, the use of an over-expansion turbine. The power received in the overexpansion turbine is spent on pressing the exhaust gases to atmospheric pressure by the compressor. Excess power can be transferred to mechanical or electrical energy. To cool the gas in the overexpansion circuit, it is promising to use a thermopressor, in which an increase in the total gas pressure occurs due to heat removal from gas. The removal of heat from the gas flow is carried out in the process of dispersed water evaporation, injected into the airflow, which is moving at near sound speed (gas-dynamic cooling). The thermopressor is a compact device. Therefore, using it in the gas turbine overexpansion circuit as a compressor and a cooler is advisable. Gas-dynamic cooling in the overexpansion circuits of a low-power marine gas turbine provides a pressure reduction in the overexpansion turbine by  $0.725\text{--}0.765 \cdot 10^5$  Pa with a corresponding increase in the main (power) turbine power by 60 to 100 kW.

**Keywords:** Energy efficiency · Thermopressor · Overexpansion turbine · Gas cooler

## 1 Introduction

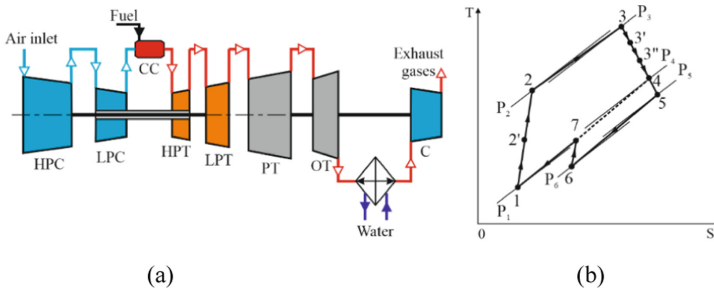
A topical direction for increasing the efficiency of gas turbine plants (GTP) is using of energy-saving technologies that will ensure the low-grade heat utilization from secondary energy resources (SER) and compensate for the negative impact of ambient temperature on the fuel and energy efficiency of gas turbine plants [1, 2].

The main advantage of gas turbines compared to piston internal combustion engines is the possibility of polytropic expansion of the working fluid (combustion products) to atmospheric pressure [3, 4]. One of the ways to increase the efficiency of a gas turbine is an additional expansion of combustion products below atmospheric pressure in an auxiliary turbine installed after the main (power) turbine, that is, the use of an overexpansion turbine [5, 6]. The power received in the overexpansion turbine is spent on pressing the exhaust gases to atmospheric pressure by the compressor [7, 8]. Excess power can be transferred to mechanical or electrical energy [9, 10].

## 2 Literature Review

Gas turbine engines are widely used in stationary transport power engineering, particularly ship power engineering [11, 12]. Low-power turbines (up to 1 MW) are used in autonomous power supply units and small-tonnage ships [13, 14], in particular on hovercraft as a ship power plant [15, 16]. As an example, low-power turbines GTG-100K (power 100 kW) are used on the Zubr and Murena ships. The Zubr power plant consists of drive units with a total capacity of 40 MW to maintain the ship's progress and an autonomous power plant with a capacity of 400 kW, based on the GTG-100K. Gas turbines are sensitive to inlet conditions [17]: a specific fuel consumption rises by 0.4 to 1.0 g/(kWh) per 1 °C increases air temperature. The cyclic air cooling methods are directed to increase engine output due to operating at stabilized temperature by applying jet and absorption chiller technologies [18, 19]. One of the ways to increase the efficiency of a gas turbine is an additional expansion of combustion products below atmospheric pressure in an auxiliary turbine installed after the main (power) turbine, that is, the use of an overexpansion turbine [20, 21].

A scheme and a cycle of the GTP additional circuit with an overexpansion turbine are shown in Fig. 1. The principle of the GTP operation is following: pressure gas  $P_4$  equal to atmospheric, and a high temperature (400–600 °C) after the main (power) turbine enters the auxiliary turbine, where the polytropic one expands to a pressure of  $P_5 = 0.35 \cdot 10^5$  Pa (process 4–5 in Fig. 1b). The gas is cooled in the heat exchanger (process 5–6) to reduce the compressor's compression work. As a result of the aerodynamic resistance presence  $\Delta P$  in the heat exchanger, the pressure is  $P_6 < P_5$ . For example, cold gas with a temperature of  $t_3 = 50$  °C is compressed by a turbocharger to atmospheric pressure (polytropic process 6–7).



**Fig. 1.** Scheme (a) and cycle (b) of the GTP with an overexpansion turbine: HPC, LPC – high- and low-pressure compressor; CC – combustion chamber; HPT, LPT, PT – high- and low-pressure and power turbine; OT – overexpansion turbine; C – compressor.

In the operation process behind the GTP power turbine, an under pressure is created up to 0.09 MPa. This increases the specific power and efficiency by 14 to 18% [22, 23]. The disadvantage of such a solution is a gas turbine complex and dimensional design [24], which requires an overexpansion turbine and a compressor, which leads to a decrease in overall efficiency [25].

### 3 Research Methodology

In modern ship power engineering, processes are widely used in which the movement of gas through channels occurs under various influences: a change in the flow area of a channel, an energy exchange with the environment by heat transfer [26, 27], friction against the channel walls, a change in gas flow due to the supply of liquid into the flow, a complex mechanical process and thermal interaction of liquid droplets with a gas stream [28]. With intensive heat removal and organization of the working process, it becomes possible to increase the total pressure of the gas flow. In this case, its compression occurs due to the overall thermal effect (heat removal) compared to the pressure loss due to friction. The device in which the increase in the total gas pressure occurs due to heat removal is called a thermopressor [29]. Heat removal from the gas flow can be carried out by heat transfer through the channel walls (non-contact method) [30] or in the process of evaporation of the injected liquid into the gas flow (contact or evaporative cooling) moving at a speed of sound [31, 32]. The thermopressor is a reasonably compact device that combines the functions of gas compression and deep cooling; therefore, it is obvious to use it in the overexpansion loop of a gas turbine unit as a compressor and a cooler at the same time [33, 34]. The thermopressor is a compact device placed in a limited space [35, 36].

The main objectives of the study are as follows:

- to develop methods for cooling the gas turbine exhaust gases in overexpansion circuits with a simultaneous increase in pressure using thermogasdynamic compression;
- to determine the rational parameters of the process of gas-dynamic cooling of GTP exhaust gases in the overexpansion circuit using a thermopressor, which ensures the maximum increase in the capacity of the overexpansion turbine accordingly, the maximum increase in the GTP power as a whole.

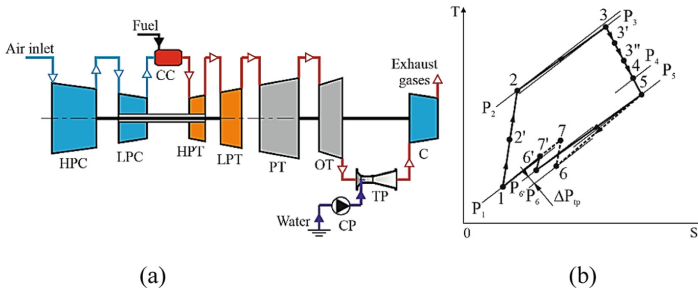
As a result, a reduction in specific fuel consumption; to develop diagrams of gas-dynamic cooling systems for GTP off-gases in an overexpansion circuit using a thermopressor.

Research methods: parameters of GTP exhaust gases and the processes of gas-dynamic cooling in the thermopressor were calculated according to the developed method and program using the equations of thermodynamics and gas dynamics of the flow [37, 38]. The gas turbine cycle and parameters were calculated according to the classical methods [39, 40] and the developed software package based on them.

### 4 Results

A diagram of the gas turbine additional circuit with an overexpansion turbine and the GTP cycle is shown in Fig. 2. The gas cooler in the circuit can be replaced with a compact thermopressor. In the thermopressor plant with an overexpansion turbine, the gas after the gas turbine enters, as in the previous case, into the auxiliary turbine, where the pressure  $P_5$  expands polytropically (process 4–5 in Fig. 2b).

In the nozzle of the thermopressor, the gas expands adiabatically to an even lower pressure and is polytropically compressed in the diffuser of the apparatus to a pressure



**Fig. 2.** Scheme (a) and cycle (b) of the GPT with an overexpansion turbine with a thermopressor: TP – thermopressor; CP - circulation pump.

$P_{6'} > P_6$ . Line 5–6' is essentially a conditional process of gas flow compression in the thermopressor. In this case, the total gas consumption increases by an amount equal to the amount of water injected into the thermopressor. Providing the same cooling depth in the thermopressor as in the gas cooler, the outlet temperatures will be equal ( $T_{6'} = T_6$ ). It can be seen that the compressor operation (process 6'–7') decreases due to a decrease in the compression ratio  $\pi_c = P_7/P_{6'}$  (Fig. 2b), and therefore leads to an increase in the thermal efficiency of the GTP cycle  $\eta_t$ . Then the gas is polytropically compressed in the compressor to a pressure equal to atmospheric pressure, the initial pressure at the inlet to the auxiliary turbine.

The operation of the thermopressor gas turbine circuit as part of the UGT-2500 gas turbine produced by “Zarya-Mashproekt” (Ukraine) was analyzed. Initial data for calculations: the gas temperature at the main gas turbine (at the inlet to the overexpansion turbine)  $t_4 = 460$  and  $550$  °C; gas consumption  $G = 16.5$  kg/s; gas pressure according to GTP  $P_4 = 10^5$  Pa; gas temperature after the thermopressor  $t_5 = 50$  °C; the average diameter of droplets at the thermopressor outlet is 15 microns. Calculations show that the hydraulic resistance tube-plate heat exchangers with the in-line arrangement of tubes do not exceed 600 Pa. The efficiency of the turbine and compressor was assumed to be 0.86.

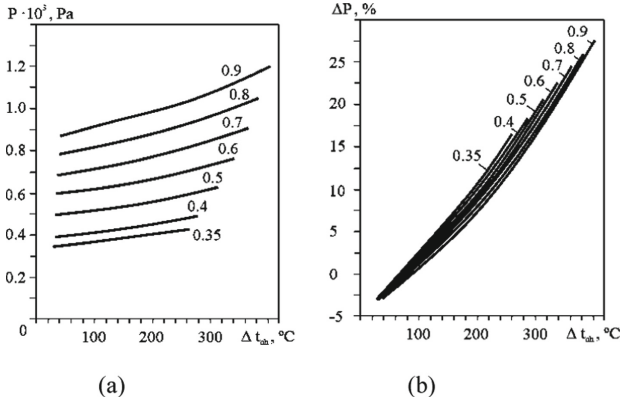
The results of calculating the thermopressor as part of the gas turbine overexpansion circuit (Fig. 2a) show that the gas temperature through the overexpansion turbine (at the inlet to the thermopressor) is 300 to 400 °C. When a significant temperature difference in the gas is triggered in the thermopressor, that is, overheating  $\Delta t_{oh}$  from a temperature of 300–400 °C at the inlet to 50 °C at the outlet, it is possible to obtain a significant increase in pressure (Fig. 3a). So, at a gas temperature at the turbine inlet, overexpansion  $t_4 = 450$  °C, the relative increase in gas pressure is 10–35%, depending on the pressure  $P_5$  in the turbine (Fig. 3a).

As can be seen from Fig. 3a, and at a pressure downstream of the turbine  $P_5 = 0.8 \cdot 10^5$  Pa and a temperature difference over the gas in the thermopressor of more than 300 °C, the GTP can operate without a compressor at all, since the thermopressor can increase the gas pressure above atmospheric. In this case, the relative increase in pressure  $\Delta P$  in the thermopressor will be 24%.

At a gas temperature at the inlet to the overexpansion turbine  $t_4 = 550$  °C, the GTP operation without a compressor is possible with a slightly more significant relative



increase in gas pressure up to 26% in the thermopressor (Fig. 3b). As can be seen from Fig. 3a and Fig. 3b, the relative pressure increase  $\Delta P$  is the more the higher the temperature difference  $\Delta t_{oh}$  and the initial pressure in the thermopressor  $P_5$  (after the overexpansion turbine). The calculation results show the possibility of increasing the useful power of the GTP due to the use of an overexpansion turbine with a compressor and a thermopressor by  $\Delta N = 23\%$  in comparison with the primary UGT-2500 gas turbine at a gas temperature at the overexpansion turbine inlet  $t_4 = 450^\circ\text{C}$ , and at  $t_4 = 550^\circ\text{C} - \Delta N = 33\%$ .



**Fig. 3.** Dependence of the pressure at the thermopressor outlet  $P$  (a) on overheating  $\Delta t_{oh}$  at different pressures  $P_5$  after the overexpansion turbine (at the inlet of the thermopressor) and the gas temperature in front of the overexpansion turbine: a)  $t_4 = 450^\circ\text{C}$ ;  $t_4 = 550^\circ\text{C}$ .

In this case, the gas pressure at the outlet of the overexpansion turbine, at which the GTP can operate without a compressor, in the first case is  $P_5 = 0.76 \cdot 10^5 \text{ Pa}$ , and in the second case is  $P_5 = 0.66 \cdot 10^5 \text{ Pa}$ , the gas flow temperature difference in the thermopressor must be at least  $300^\circ\text{C}$ .

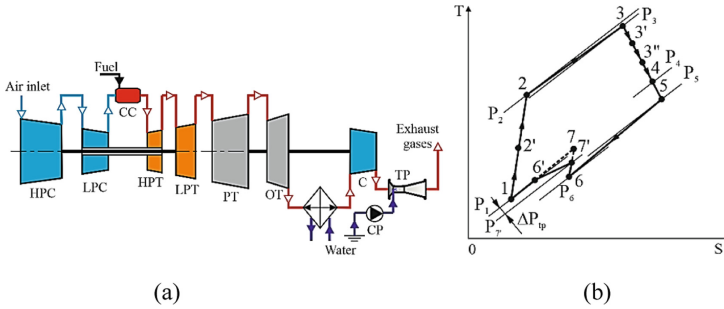
Distilled water is used for the thermopressor, and since it is necessary to spend an additional amount of energy in the desalination plant for its production on the ship, hence the not so significant increase in efficiency  $\eta_{GTP} = 11\%$  at  $t_1 = 450^\circ\text{C}$  and  $\eta_{GTP} = 16\%$  at  $t_1 = 550^\circ\text{C}$ . For the UGT-2500, the additional steam consumption for the desalination plant is 16–17 kg/s (60–62 t/h). Therefore, it is advisable to use such a scheme in the presence of freshwater sources that do not require additional costs for its production.

Alternatively, a combined plant's scheme can be offered with a thermopressor installed after the compressor (Fig. 4a,b). The gas after the overexpansion turbine is cooled in a cooler and compressed in a compressor to a pressure of no higher than  $0.9 \cdot 10^5 \text{ Pa}$ , after which it enters a thermopressor, where it is compressed to equal atmospheric pressure. This scheme allows to reduce the flow rate of water injected into the thermopressor to  $g = 0.05$  (5%). This scheme makes it possible to increase the helpful power of the gas turbine by 14%.

The operation of the thermopressor circuit as part of the following low-power gas turbine plants was analyzed for GTG100K (“Zarya-Mashproekt”, Ukraine), Capstone

C200 (“Capstone Turbine Corporation”, USA), Toyota 300A (“Toyota turbine system”, Japan).

Initial data for the calculation: the temperature and gas flow rate for the gas turbine unit were taken under the characteristics of the gas turbine plant (Fig. 4a), given depending on the air temperature at the inlet to the compressor. The gas temperature over the thermopressor was taken equal to  $t_{g'} = 50\text{ }^{\circ}\text{C}$ .

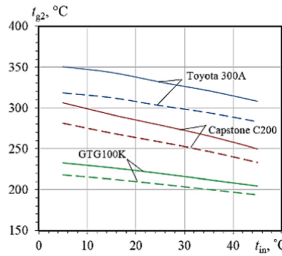


**Fig. 4.** Scheme (a) and cycle (b) of the GTP with an overexpansion turbine after the thermopressor

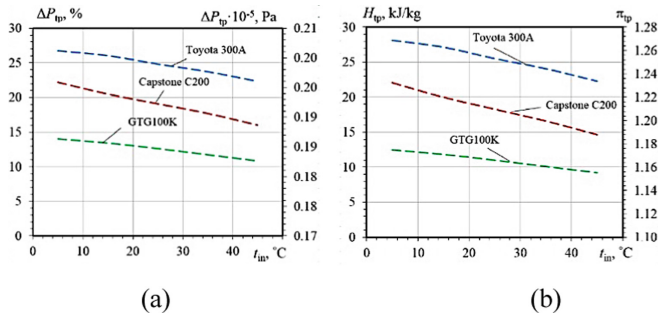
The use of an overexpansion turbine reduces the gas temperature  $t_{g2}$  at the GTP outlet by 50–60 °C (Fig. 5). However, the thermal potential of waste gases for use in a thermopressor is quite significant: GTG100K -  $t_{g2} = 440\text{--}480\text{ }^{\circ}\text{C}$ , Capstone C200 -  $t_{g2} = 470\text{ }^{\circ}\text{C}$ , Toyota 300A -  $t_{g2} = 400\text{--}440\text{ }^{\circ}\text{C}$ . When the temperature difference in the gas is triggered in the thermopressor (removable overheating  $\Delta t_{tp}$ ), from the temperature  $t_{g2}$  at the inlet to 50 °C at the thermopressor outlet, it is possible to obtain a significant increase in pressure (Fig. 6).

The pressure increase in the thermopressor for GTG100K is  $P_{tp} = 36\text{--}40\%$ , Capstone C200 -  $P_{tp} = 35\text{--}38\%$ , Toyota 300A -  $P_{tp} = 32\text{--}36\%$ . The rather large pressure drop is explained by the large temperature drop in the thermopressor, which is  $t_{tp} = 350\text{--}430\text{ }^{\circ}\text{C}$ . This makes it possible to increase the expansion ratio of the turbine  $\pi_{tp}$  with a corresponding increase in the work on the rotor blades and the turbine power (Fig. 7a): GTG100K -  $N_t = 60\text{--}70\text{ kW}$ , Capstone C200 -  $N_t = 75\text{--}90\text{ kW}$ , Toyota 300A -  $N_t = 95\text{--}105\text{ kW}$ . At the temperature  $t_{in} = 15\text{--}20\text{ }^{\circ}\text{C}$ , it can be seen that the power value is maximum, which is explained by the opposite behavior of the values on which the turbine power depends: the flow rate of waste gases  $G_g$  decreases with increasing  $t_{in}$ , and the temperature  $t_{g2}$  increases with a corresponding increase in pressure  $\Delta P_{tp}$  in the thermopressor.

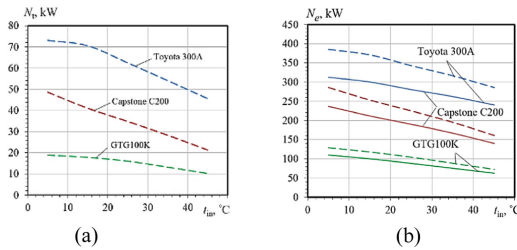
Additional power of the overexpansion turbine increases the GTP total power in comparison with the base one (Fig. 7b): GTG100K -  $N_e = 10\text{--}20\text{ kW}$  (9–18%), Capstone C200 -  $N_e = 25\text{--}50\text{ kW}$  (11–20%), Toyota 300A -  $N_e = 50\text{--}75\text{ kW}$  (16–24%). The mass fraction of injected water in the thermopressor is  $g_w = 0.03\text{--}0.10$  (3–10%). It can be concluded that using a thermopressor in conjunction with an overexpansion turbine is more effective at low GTP capacities since turbines of this type correspond to higher gas outlet temperatures  $t_{g2}$ , and hence, to higher values of increase in pressure  $\Delta P_{tp}$ .



**Fig. 5.** Dependences of the exhaust gas temperature  $t_{g2}$  for the gas turbine on the inlet air temperature  $t_{in}$  for different gas turbines: \_\_\_\_\_ – without the overexpansion turbine; \_\_\_\_\_ – with overexpansion turbine.



**Fig. 6.** Dependences of the pressure increase in the thermopressor  $\Delta P_{tp}$  (a), the operation of the overexpansion turbine  $H_{tp}$  and the degree of expansion in the turbine  $\pi_{tp}$  (b) on the inlet air temperature  $t_{in}$  for different types of gas turbines.



**Fig. 7.** Dependences of the overexpansion turbine power  $N_t$  and the GTP power  $N_e$  on the inlet air temperature  $t_{in}$  for different gas turbines.

It should be added that the results of the theoretical study are in good agreement with the experimental data obtained in [29, 33], which shows an increase in the pressure of the gas turbine exhaust gases by thermopressor type devices by 10–25%.

## 5 Conclusions

The use of combustion products energy in the GTP by overexpansion below atmospheric pressure in an additional overexpansion turbine, installed after the main turbine with a subsequent increase in pressure in the thermopressor, provides an increase in the GTP capacity by 2 to 3%. Due to the use of the thermopressor, it is possible to operate the GTP without an additional compressor, but the temperature of the exhaust gases must be at least 300 °C.

The use of thermopressor compression makes it possible to combine several functions in one apparatus (thermopressor) at once: compression (compressor) and cooling (gas cooler), which, in turn, makes it possible to apply gas overexpansion in gas turbines on specialized hovercraft, where the installation of additional equipment is problematic due to the limited space of the engine room.

## References







1. Radchenko, M., Mikielewicz, D., Andreev, A., Vanyeyev, S., Savenkov, O.: Efficient ship engine cyclic air cooling by turboexpander chiller for tropical climatic conditions. In: Nechyporuk, M., et al. (eds.) ICTME-2020. ICTM 2020. LNNS, vol. 188, 498–507 (2021)
2. Radchenko, A., Stachel, A., Forduy, S., Portnoi, B., Rizun, O.: Analysis of the efficiency of engine inlet air chilling unit with cooling towers. In: Ivanov, V., Pavlenko, I., Liaposhchenko, O., Machado, J., Edl, M. (eds.) DSMIE 2020. LNME, pp. 322–331. Springer, Cham (2020). [https://doi.org/10.1007/978-3-030-50491-5\\_31](https://doi.org/10.1007/978-3-030-50491-5_31)
3. Kowalski, M., Badyda, K.: Performance analysis of a gas turbine air heat recovery unit using GateCycle software. *J. Power Technol.* **92**(1), 48–54 (2012)
4. Radchenko, R., Pyrysunko, M., Kornienko, V., Scurtu, I.-C., Patyk, R.: Improving the ecological and energy efficiency of internal combustion engines by ejector chiller using recirculation gas heat. In: Nechyporuk, M., Pavlikov, V., Kritskiy, D. (eds.) ICTM 2020. LNNS, vol. 188, pp. 531–541. Springer, Cham (2021). [https://doi.org/10.1007/978-3-030-66717-7\\_45](https://doi.org/10.1007/978-3-030-66717-7_45)
5. Khalatov, A., Karp, I., Isakov, B.: Prospects of the Maisotsenko thermodynamic cycle application in Ukraine. *Int. J. Energy Clean Environ.* **12**(2–4), 141–157 (2011)
6. Kornienko, V., Radchenko, R., Bohdal, Ł., Kukielka, L., Legutko, S.: Investigation of condensing heating surfaces with reduced corrosion of boilers with water-fuel emulsion combustion. In: Nechyporuk, M., Pavlikov, V., Kritskiy, D. (eds.) ICTM 2020. LNNS, vol. 188, pp. 300–309. Springer, Cham (2021). [https://doi.org/10.1007/978-3-030-66717-7\\_25](https://doi.org/10.1007/978-3-030-66717-7_25)
7. De Biasi, V.: LM6000 sprint design enhanced to increase power and efficiency. *Gas Turbine World* **30**(4), 16–19 (2000)
8. The Brown Boveri Review. *The House Journal of Brown, Boveri & Company* 9/10(XXIX), 220–315 (1942)
9. Kornienko, V., Radchenko, R., Stachel, A., Andreev, A., Pyrysunko, M.: Correlations for pollution on condensing surfaces of exhaust gas boilers with water-fuel emulsion combustion. In: Tonkonogyi, V., et al. (eds.) GICAMP. InterPartner-2019. LNME, pp. 530–539. Springer, Cham (2020). [https://doi.org/10.1007/978-3-030-40724-7\\_54](https://doi.org/10.1007/978-3-030-40724-7_54)
10. Radchenko, M., Mikielewicz, D., Tkachenko, V., Klugmann, M., Andreev, A.: Enhancement of the operation efficiency of the transport air conditioning system. In: Ivanov, V., Pavlenko, I., Liaposhchenko, O., Machado, J., Edl, M. (eds.) DSMIE 2020. LNME, pp. 332–342. Springer, Cham (2020). [https://doi.org/10.1007/978-3-030-50491-5\\_32](https://doi.org/10.1007/978-3-030-50491-5_32)

11. Nourin, F.N., Amano, R.S.: Review of gas turbine internal cooling improvement technology. *J. Energy Resour. Technol.* **143**(8), 8 (2021)
12. Payrhuber, K., Walker, T.: LMS100® program update on the world's first intercooled gas turbine (2008)
13. Kozak, D., Mazuro, P.: Review of small gas turbine engines and their adaptation for automotive waste heat recovery systems. *Int. J. Turbomach. Propul. Power* **5**(2), 8 (2020)
14. Yeranee, K., Rao, Y.: A review of recent studies on rotating internal cooling for gas turbine blades. *Chin. J. Aeronaut.* **34**(7), 85–113 (2021)
15. Jonsson, M., Yan, J.: Humidified gas turbines – a review of proposed and implemented cycles. *Energy* **30**, 1013–1078 (2005)
16. Bhargava, R.K., Bianchi, M., De Pascale, A., Negri di Montenegro, G., Peretto, A.: Gas turbine based power cycles - a state-of-the-art review. In: Cen, K., Chi, Y., Wang, F. (eds.) *Challenges of Power Engineering and Environment*. Springer, Heidelberg (2007). [https://doi.org/10.1007/978-3-540-76694-0\\_56](https://doi.org/10.1007/978-3-540-76694-0_56)
17. Radchenko, R., Pyrysunko, M., Radchenko, A., Andreev, A., Kornienko, V.: Ship engine intake air cooling by ejector chiller using recirculation gas heat. In: Tonkonogyi, V., et al. (eds.) *InterPartner. LNME*, pp. 734–743. Springer, Cham (2021). [https://doi.org/10.1007/978-3-030-68014-5\\_71](https://doi.org/10.1007/978-3-030-68014-5_71)
18. Radchenko, A., Trushliakov, E., Tkachenko, V., Portnoi, B., Prjadko, A.: Improvement of the refrigeration capacity utilizing for the ambient air conditioning system. In: Tonkonogyi, V., et al. (eds.) *InterPartner. LNME*, pp. 714–723. Springer, Cham (2021). [https://doi.org/10.1007/978-3-030-68014-5\\_69](https://doi.org/10.1007/978-3-030-68014-5_69)
19. Kornienko, V., Radchenko, R., Mikielewicz, D., Pyrysunko, M., Andreev, A.: Improvement of characteristics of water-fuel rotary cup atomizer in a boiler. In: Tonkonogyi, V., et al. (eds.) *InterPartner. LNME*, pp. 664–674. Springer, Cham (2021). [https://doi.org/10.1007/978-3-030-68014-5\\_64](https://doi.org/10.1007/978-3-030-68014-5_64)
20. Nourin, F.N., Amano, R.S.: Review of gas turbine internal cooling improvement technology. *J. Energy Resour. Technol.* **143**(8), 080801 (2021)
21. Najjar, Y.S.H.: The over-expansion gas turbine cycle using hydrogen. *Int. J. Hydrogen Energy* **16**(9), 625–629 (1991)
22. Boyce, M.P.: *Gas Turbine Engineering Handbook*. Gulf Publishing Company, Houston (2002)
23. Farouk, N., Sheng, L., Hayat, Q.: Effect of ambient temperature on the performance of gas turbines power plant. *Int. J. Comput. Sci.* **10**(3), 439–442 (2013)
24. Yin, F., Rao, A.G.: A review of gas turbine engine with inter-stage turbine burner. *Progress in Aerospace Sciences*, 121 (2020)
25. Bhargava, R.K., Meher-Homji, C.B., Chaker, M.A., et al.: Gas turbine fogging technology: a state-of-the-art review – part I: Inlet evaporative fogging – analytical and experimental aspects. *J. Eng. Gas Turbines Power* **129**(2), 443–453 (2007)
26. Bohdal, L., Kukielka, L., Świłło, S., Radchenko, A.M., Kułakowska, A.: Modelling and experimental analysis of shear-slitting process of light metal alloys using FEM, SPH and vision-based methods. In: *AIP Conference Proceedings*, vol. 2078, p. 020060 (2019), 04 March 2019. <https://doi.org/10.1063/1.5092063>
27. Bohdal, L., Kukielka, L., Radchenko, A.M., Patyk, R., Kułakowski, M., Chodór, J.: Modelling of guillotining process of grain oriented silicon steel using FEM. In: *AIP Conference Proceedings*, vol. 2078, p. 020080 (2019)
28. Paepe, W., Delattin, F., Bram, S.: Water injection in a micro gas turbine – Assessment of the performance using. *Appl. Energy* **112**, 1291–1302 (2013)
29. Konovalov, D., Kobalava, H., Radchenko, M., Sviridov, V., Scurtu, I.C.: Optimal sizing of the evaporation chamber in the low-flow aerothermopressor for a combustion engine. In: Tonkonogyi, V., et al. (eds.) *InterPartner. LNME*, pp. 654–663. Springer, Cham (2021). [https://doi.org/10.1007/978-3-030-68014-5\\_63](https://doi.org/10.1007/978-3-030-68014-5_63)

30. Sexton, W.R., Sexton, M.R.: The effects of wet compression on gas turbine engine operating performance. In: Proceedings of GT2003 ASME Turbo Expo: Power for Land, Sea and Air, pp. 1–7, Atlanta, Georgia, USA (2009)
31. Sun, J., Hou, H., Zuo, Z.: Numerical study on wet compression in a supercritical air centrifugal compressor. Proc. IMechE, Part A J. Power Energy **234**(3), 384–397 (2020)
32. Shapiro, H., Wadleigh, K.R., Gavril, B.: The aerothermopressor – a device for improving the performance of a gas-turbine power plant. Trans. ASME **78**(7), 617–653 (1956)
33. Radchenko, M., Radchenko, A., Radchenko, R., Kantor, S., Konovalov, D., Kornienko, V.: Rational loads of turbine inlet air absorption-ejector cooling systems. Proc. Inst. Mech. Eng. A: J. Power Energy **236**(3), 450–462 (2022)
34. Fowle, A.: An Experimental Investigation of an Aerothermopressor Having a Gas Flow Capacity of 25 Pounds per Second. Massachusetts Institute of Technology, Cambridge (1972)
35. Erickson, J.: A Theoretical and Experimental Investigation of the Aerothermopressor Process. Massachusetts Institute of Technology, Cambridge (1958)
36. Mackay, R.T.: Experimental Investigation of an Aerothermopressor with Supersonic Inlet. Massachusetts Institute of Technology, Cambridge (1955)
37. Bohdal, Ł, Kukiełka, L., Legutko, S., Patyk, R., Radchenko, A.M.: Modeling and experimental research of shear-slitting of AA6111-T4 aluminum alloy sheet. Materials **13**(14), 3175 (2020)
38. Sirignano, W.A.: Fluid Dynamics and Transport of Droplets and Sprays, 2nd edn. Cambridge University Press, New York (2010)
39. Bhargava, R., Bianchi, M., Peretto, A., Spina, P.R.: A feasibility study of existing gas turbines for recuperated, intercooled, and reheat cycle. J. Eng. Gas Turbines Power **126**(3), 531–544 (2004)
40. Bergman, T.L., et al.: Fundamentals of Heat and Mass Transfer, 7th edn. Wiley, Hoboken (2011)



# Marine Diesel Engine Inlet Air Cooling by Ejector Chiller on the Vessel Route Line

Maxim Pyrysunko , Andrii Radchenko  , Veniamin Tkachenko ,  
Anatoliy Zubarev , and Artem Andreev 

Admiral Makarov National University of Shipbuilding, 9, Heroes of Ukraine Avenue,  
Mykolaiv 54025, Ukraine  
nirad50@gmail.com

**Abstract.** The fuel efficiency of marine slow-speed diesel engines with cooling the air at the turbocharger suction by ejector chiller that recovers the waste heat of exhaust gas and scavenge air was analyzed. The application of ejector chiller is caused due to its the simplest design that enables easy it's assembling in free space of engine room and reliable operation in a marine application. An assessment was made of air temperature drops in the air cooler at the inlet to the turbocharger of a marine diesel engine and a reduction in fuel consumption under variable climatic parameters along the Odesa-Yokohama-Odesa route. The application of an ejector chiller provides reducing the engine intake air temperature by about 10 °C with a corresponding decrease of specific fuel consumption by 1.0...1.2 g/(kWh) when using only the heat of exhaust gas. The fuel reduction of the marine diesel engine is increased practically twice when additional heat of scavenging air is used by an ejector chiller (ECh). The corresponding schemes of the systems for cooling the air at the turbocharger suction by ejector chiller are proposed.

**Keywords:** Internal combustion engine · Ejector chiller · Energy efficiency · Fuel consumption · Exhaust gas · Scavenge air

## 1 Introduction

The fuel efficiency of combustion engines: gas turbines [1, 2] and gas engines [3, 4], internal combustion engines including diesel engines [5, 6] considerably depends on the temperature of sucked air, falling with its raising. Low-speed diesel engines gained the widest applications as the main ship engines [7, 8]. The specific fuel consumption of the main marine engine increases by 0.11 to 0.12 g/(kWh) for a 1 °C increase in the air temperature at the inlet to the turbocompressor unit.

To improve the engine's fuel economy, the sucked air at the turbocharger intake could be used. Heat losses accompanied by exhaust gases and scavenge air consist of a main part of the total waste heat in combustion engines [9, 10]. Therefore, the waste heat recovery chillers can be applied for engine air cooling [11, 12].

## 2 Literature Review

The most used for air cooling down to 15 °C are The absorption lithium-bromide chillers (ACh). They have a high coefficient of performance (COP) of 0.7 to 0.8 [13]. But it should be noted that their placement in the engine room is problematic due to their large dimensions. At the same time, the ECh consists of heat exchangers [14], which are rationally installed in free space. The use of the ECh allows for deep air cooling but at the same time has a low COP of 0.2 to 0.35 [15, 16] and is suitable for transport applications [17, 18].

The heat of water vapor condensation with subsequent condensation of sulfuric acid vapor is used in low-temperature economizers [19]. This method makes it possible to increase thermal and hydraulic resistance [20, 21]. This is achieved because the condensed acid vapors emit ash in the exhaust gases [22], and subsequently, they settle on the heating surface [23].

The purpose of the study is to evaluate the efficiency of cooling the sucked air of marine low-speed diesel engine [24, 25] by waste heat recovery [26] in ejector chiller with account the changeable climatic conditions [27] during the voyage line.

## 3 Research Methodology

A low-speed MAN diesel engine 6S60MC6.1-TI (rated power 12.24 MW and continuous operating power 10 MW) [28] is chosen as an example of the main drive engine of the transport ship. The engine turbocharger sucked air cooling efficiency is estimated by specific fuel consumption reduction  $\Delta b_e$  gained due to the sucked air temperature drop  $\Delta t_a$ .

For air cooling in ECh, the following parameters were chosen in the research: refrigerant – R142b; refrigerant condensing temperature in the condenser to = 25–45 °C; refrigerant evaporation temperature in the evaporator-air cooler  $t_0 = 5$  °C.

According to the calculations using the “mandieselturbo” software package [29], cooling turbocharger inlet air for every 1 °C of temperature drop results in a reduction of specific fuel consumption within 0.11 to 0.12 g/(kWh) for low-speed diesel engine 6S60MC6.1-TI.

The sucked air temperature drop  $\Delta t_a$  depends on the waste heat  $Q_h$  extracted from the engine (heat of exhaust gas, scavenge air) and the efficiency of its converting to refrigeration capacity  $Q_0$  by the chiller, characterized by a coefficient of performance. The coefficient of performance  $\zeta = Q_0/Q_h$  is the ratio of the refrigeration capacity  $Q_0$  received to the heat  $Q_h$  consumed through its extracted from the engine exhaust gas, scavenge air, and other heat sources.

The available refrigeration capacity is calculated as

$$Q_0 = Q_h \zeta, \quad (1)$$

where  $Q_h$  – the heat extracted from the engine exhaust gases and scavenge air.

The available sucked air temperature drop in the air cooler  $\Delta t_a$  due to using available refrigeration capacities  $Q_0$  is calculated following the heat balance

$$Q_0 = G_a \xi_a c_a \Delta t_a, \quad (2)$$



where  $G_a$  – air mass flow rate, kg/s;  $c_a$  – air specific heat capacity, kW/(kg·K);  $\xi_a$  – specific heat ratio.

The temperature of cooled air at the air cooler outlet:

$$t_{a2} = t_{a1} - \Delta t_a. \tag{3}$$

The current values of specific fuel consumption reduction per 1 h:

$$\Delta b_e = \Delta t_a \cdot \Delta b_{e1^\circ\text{C}}, \text{ g/kWh}; \tag{4}$$

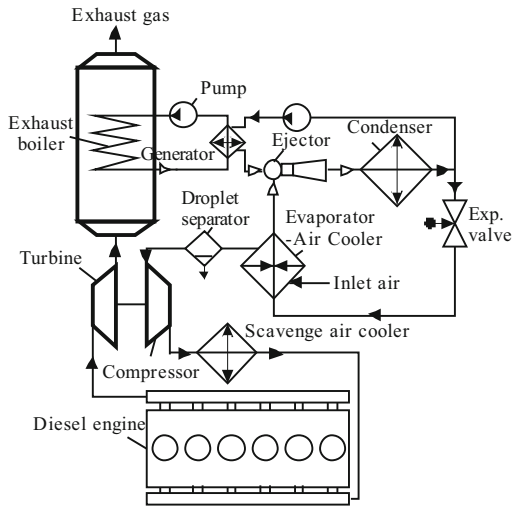
the total fuel reduction per 1 h:

$$\Delta B_e = N_s \Delta b_e, \text{ g/h}. \tag{5}$$

where  $\Delta b_{e1^\circ\text{C}}$  – specific fuel consumption reduction referred to engine sucked air temperature drop in 1 °C,  $\Delta b_{e1^\circ\text{C}} = \Delta b_e / \Delta t_a = 0.12 \text{ g/(kWh}\cdot\text{K)}$ ;  $N_s$ , kW – diesel engine power.

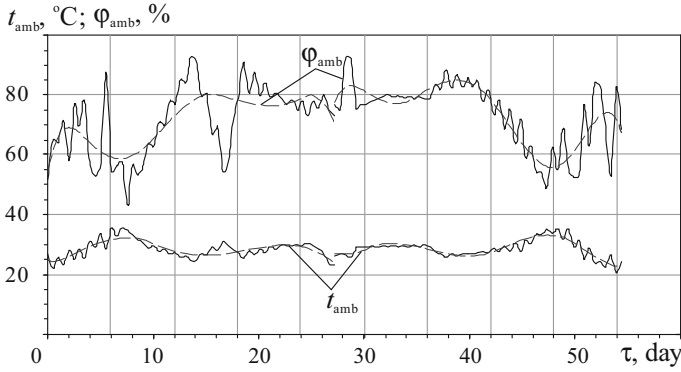
### 4 Results

A circuit of the ship diesel sucking air cooling system by ECh recovering exhaust gas heat was developed (Fig. 1).



**Fig. 1.** A circuit of diesel engine sucking air cooling system by ECh recovering exhaust gas heat.

The generator of ECh consumes the heat of engine exhaust gas to generate the refrigerant vapor of a high pressure as a induce fluid for the ejector to compress the refrigerant vapor of low pressure, sucked from the evaporator-air cooler at the ship engine turbocharger, up to the condensing pressure of refrigerant in the condenser.



**Fig. 2.** Ambient relative humidity  $\varphi_{amb}$  and air temperature  $t_{amb}$  changes along Odesa-Yokohama and Yokohama-Odesa’s voyage routes.

The changes in climatic conditions along the voyage route Odesa-Yokohama and Yokohama-Odesa (June–July) 2019 are considered (Fig. 2).

The values of ambient relative humidity  $\varphi_{amb}$  and air temperature  $t_{amb}$  were taken each 3 h along the voyage routes Odesa-Yokohama and Yokohama-Odesa by applying for the program “meteomanz.com” [30].

As mentioned above, the efficiency of application of engine turbocharger sucked air cooling by ECh is estimated by specific fuel consumption reduction  $\Delta b_e$  due to sucked air temperature drop  $\Delta t_a$ .

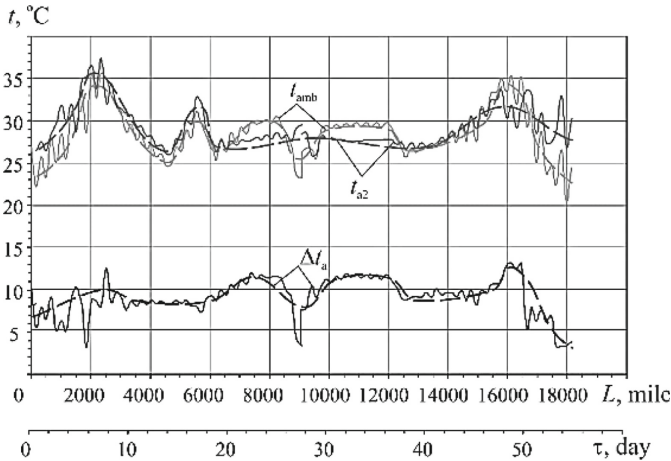
A reduction in the temperature  $\Delta t_a$  of air at the engine turbocharger suction and, accordingly, the effect of its cooling depends on the available heat of exhaust gas boiler (ExhB), according to Fig. 1, and the efficiency of its converting to refrigeration capacity by ECh, id est. on the coefficient of performance (COP) of ECh.

In addition, a reduction in temperature  $\Delta t_a$  of air in the air cooler at the ship diesel engine turbocharger suction  $\Delta t_a = t_{a1} - t_{a2}$  depends on the temperature  $t_{a1}$  of the air at the inlet of the air cooler that, which in turn, depends on the way of the air suction by engine turbocharger. If the engine turbocharger sucks the air from the engine room, the temperature  $t_{a1}$  at the inlet of air cooler, id est. in the engine room the air temperature  $t_{ER}$ , surpass environing temperature by 10 °C:  $t_{a1} = t_{amb} + 10$  °C. But when the engine turbocharger sucks the ambient air passing through the suction duct, the temperature  $t_{a1}$  at the inlet of an air cooler is higher than ambient temperature by 5 °C due to heat influx from engine room surroundings to suction duct:  $t_{a1} = t_{amb} + 5$  °C.

A target temperature  $t_{a2}$ , which limits the depth of engine turbocharger sucked air cooling, relies on the temperature of refrigerant boiling in the evaporator-air cooler at the intake. Issuing from a desirable value of refrigerant boiling temperature about  $t_0 = 7$  °C to keep a coefficient of performance (COP) of ECh about 0.3 and temperature distinction among boiling refrigerant and cooled air of about 8 °C the minimum temperature of refrigerated sucked air is accepted as  $t_{a2} = 15$  °C.

The cooling of the air that enters the turbocharger from the engine room was calculated. Changes in the air temperature drop  $\Delta t_a = t_{a1} - t_{a2}$  and the temperatures of cooled air  $t_{a2}$  available due to recovering exhaust gas heat by ECh for each time interval of 3

h on the voyage routes Odesa-Yokohama and Yokohama-Odesa (June–July, 2019) are presented in Fig. 3. With this, the temperature of the air sucked from the engine room was calculated as  $t_{a1} = t_{amb} + 10\text{ }^{\circ}\text{C}$ .



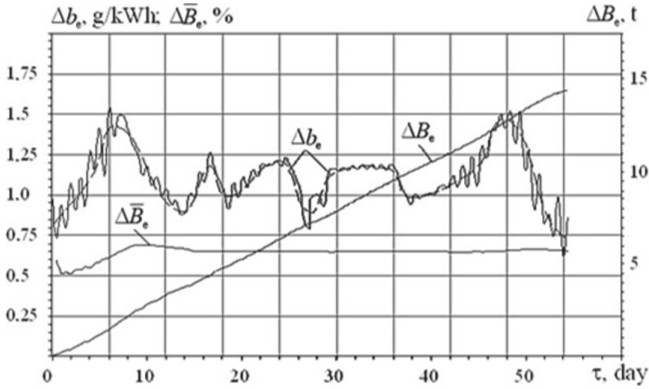
**Fig. 3.** Changes in air temperature drop  $\Delta t_a$  and temperatures of cooled air  $t_{a2}$  available due to recovering exhaust gas heat by ECh on the routes Odesa-Yokohama and Yokohama-Odesa (June–July, 2019).

As Fig. 3 shows, temperature reduction of turbocharger sucked air in the air cooler  $\Delta t_a$  is about  $10\text{ }^{\circ}\text{C}$ , id est. just enough to compensate the temperature increment of about  $10\text{ }^{\circ}\text{C}$  for ambient air incoming the engine room caused by heat influx from the engine room environment. The values approve of cooled air temperature  $t_{a2}$  at the air cooler outlet closed to  $t_{amb}$  (Fig. 3). Thus, when using in ECh only the heat of exhaust gas, the temperature reduction of sucked air  $\Delta t_a$  in the air cooler is not enough for its reducing to the minimum value of about  $15\text{ }^{\circ}\text{C}$ , which might be achieved at boiling refrigerant temperature  $t_0 = 7\text{ }^{\circ}\text{C}$ .

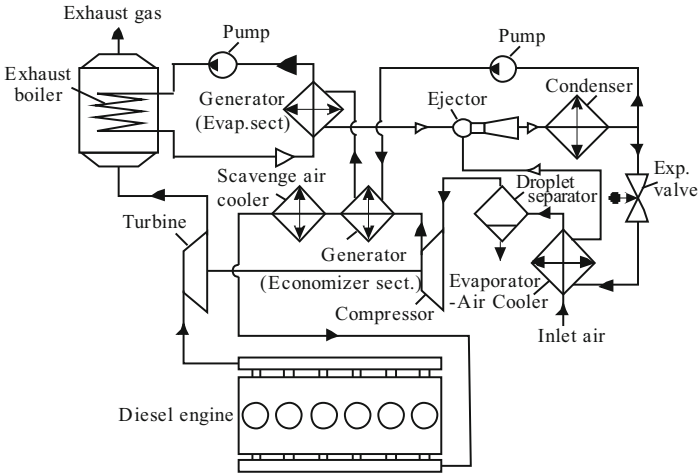
The results of calculation of fuel efficiency enhancement for marine diesel engine 6S60MC6.1-TI due to its turbocharger sucked air cooling by ECh, recovering the heat of exhaust gas, on the routes Odesa-Yokohama and Yokohama-Odesa are presented in Fig. 4. A reduction of diesel engine specific fuel consumption  $\Delta b_e$  due to turbocharger sucked air cooling was calculated by applying the program “mandieselsturbo” [29].

As Fig. 4 shows, due to the cooling of the intake air by ECh while using the heat of the exhaust gases, the reduction in specific consumption will be  $\Delta b_e = 1.0 \dots 1.2\text{ g}/(\text{kW} \cdot \text{h})$ , and absolute fuel-saving  $\Delta B_e$  during the voyage routes Odesa-Yokohama and Yokohama-Odesa, June–July 2019, is about 15 t and relative fuel saving  $\Delta \bar{B}_e$  is about 0.7%, id est. comparatively small. To enhance further fuel efficiency due to deeper engine sucked air cooling down to the temperature  $t_{a2}$  of about  $15\text{ }^{\circ}\text{C}$ , the additional heat, for instance of scavenging air, is to be used.

A developed scheme for cooling the charge air of a marine engine in the ECh with heat recovery from the charge air and exhaust gases is shown in Fig. 5.



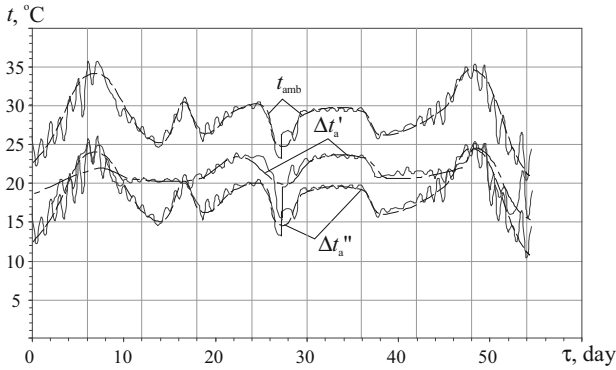
**Fig. 4.** Current values of specific fuel consumption reduction  $\Delta b_e$  and summarized fuel-saving  $\Delta B_e$ , t, for two routs Odesa-Yokohama and Yokohama-Odesa and its relative value  $\Delta \bar{B}_e$ , %, as related to the total engine fuel consumption due to cooling air sucked by turbocharger from the engine room and recovering the heat of exhaust gas.



**Fig. 5.** A circuit of engine turbocharger sucked air cooling system with ECh recovering the exhaust gas and scavenging air heat.

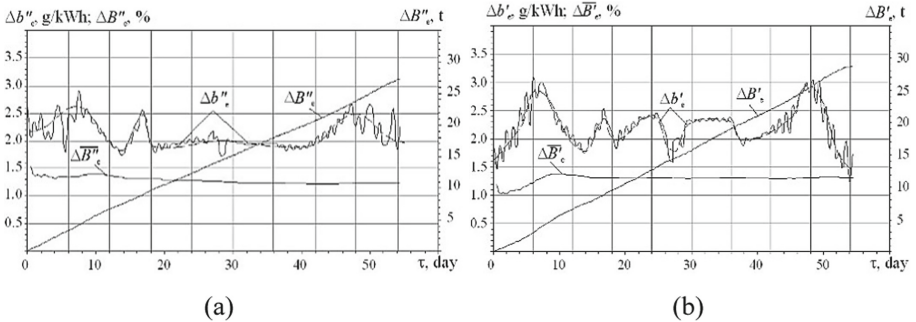
With this, a scavenge air heat is used in the economizer section of the refrigerant generator to increase the temperature of liquid refrigerant from condenser to the temperature of its boiling in the evaporative section of the generator by using the heat of exhaust gas.

Values of temperature reduction  $\Delta t_a'$  and  $\Delta t_a''$  in the air cooler for the air sucked from the engine room when the temperature  $t_{a1}$  at the inlet of air cooler  $t_{a1} = t_{amb} + 10$  °C and for the ambient air passing through a suction duct with the temperature  $t_{a1} = t_{amb} + 5$  are presented in Fig. 6.



**Fig. 6.** Air temperature reduction  $\Delta t_a$  in the engine sucked air cooler due to recovering the heat of exhaust gas and scavenge air on the routes Odesa-Yokohama and Yokohama-Odesa (June–July, 2019):  $\Delta t_a = t_{a1} - \Delta t_a$ ;  $\Delta t_a$ –for  $t_{a1} = t_{amb} + 10$  °C;  $\Delta t_a''$ –for  $t_{a1} = t_{amb} + 5$  °C.

The results of calculations of fuel efficiency enhancement of marine diesel engine 6S60MC6.1-TI due to its turbocharger sucked air cooling by ejector chiller, recovering the heat of exhaust gas and scavenge air, on the routes Odesa-Yokohama and Yokohama-Odesa are presented in Fig. 7.



**Fig. 7.** Current values of specific fuel consumption reduction  $\Delta b_e$  and summarized fuel-saving  $\Delta B_e$ , t, for two routs Odesa-Yokohama and Yokohama-Odesa and its relative value  $\Delta \overline{B}_e$ , %, as related to the total engine fuel consumption: a –  $\Delta b_e''$ ,  $\Delta B_e''$ ,  $\Delta \overline{B}_e''$ ;  $t_{a1} = t_{amb} + 5$  °C; b –  $\Delta b_e'$ ,  $\Delta B_e'$ ,  $\Delta \overline{B}_e'$ ;  $t_{a1} = t_{amb} + 10$  °C; diesel engine power  $N_s = 10$  MW.

As one can see, heat recovery of charge air and exhaust gases in the ejector chiller by cooling the intake air of the turbocharger makes it possible to reduce the specific fuel consumption on the routes Odesa-Yokohama and Yokohama-Odesa is  $\Delta b_e = 2.0 \dots 2.5$  g/(kW · h). With this summarized, total fuel saving is  $\Delta B_e = 26 \dots 28$  t, and its relative value  $\Delta \overline{B}_e$  is about 1.3% for marine diesel engine 6S60MC6.1-TI.

To gain engine more fuel-saving through deeper turbocharger sucked air cooling to the temperature 10 °C and lower the two-stage cooling in water-refrigerant air cooler by applying absorption-ejector chillers with higher COP might be realized.

## 5 Conclusions

The efficiency of the waste heat recovery ejector chiller application for cooling the intake air of marine diesel engine has been analyzed for actual changeable climatic conditions on the trip line Odesa-Yokohama-Odesa.

The efficiency of cooling the sucked air of marine diesel engine by waste heat recovery in ejector chiller with account the changeable climatic conditions during the voyage line Odesa-Yokohama-Odesa was analyzed.

The ejector chiller was chosen due to the simplest design that enables its accessible location aboard the ship. But its coefficient of performance COP is not high: of 0.2 to 0.3, which requires enlarged heat consumption.

The application of an ejector chiller provides reducing the engine intake air temperature by about 10 °C with a corresponding decrease of specific fuel consumption by 1.0...1.2 g/(kWh) when using only the heat of exhaust gas. The fuel reduction of the marine diesel engine is increased practically twice when the ejector chiller uses additional heat of scavenging air. The corresponding schemes of the systems for cooling the air at the turbocharger suction by ejector chiller are proposed.

The application of an ejector chiller provides reducing the engine intake air temperature by 20...23 °C with a corresponding decrease of specific fuel consumption by 2.0...2.5 g/(kWh).

To provide a more profound engine intake air cooling to the temperature  $t_{a2}$  of about 10 °C and lower, it is necessary to apply two-stage cooling air in a hybrid water-refrigerant air cooler by combined absorption-ejector chillers with a higher COP.

## References

1. Chaker, M., Meher-Homji, C.B., Mee, T.R.: Inlet fogging of gas turbine engines-part a: fog droplet thermodynamics, heat transfer and practical considerations. In: Proceedings of ASME Turbo Expo 2002, GT 2002-30562 (2002)
2. Konovalov, D., Kobalava, H., Radchenko, M., Scurtu, I.C., Radchenko, R.: Determination of hydraulic resistance of the aerothermopressor for gas turbine cyclic air cooling. In: TE-RE-RD 2020, E3S Web of Conferences, vol. 180, p. 0101231 (2020). <https://doi.org/10.1051/e3s/conf/202018001012>
3. Wärtsilä Environmental Product Guide. <https://cdn.wartsila.com/docs/default-source/product-files/egc/product-guide-o-env-environmental-solutions.pdf>. Accessed 7 Apr 2017
4. Influence of Ambient Temperature Conditions: Main Engine Operation of MAN B&W Two-Stroke Engines: MAN Diesel & Turbo. Copenhagen (2010)
5. Wojs, M.K., Orliński, P., Kamela, W., Kruczyński, P.: Research on the influence of ozone dissolved in the fuel-water emulsion on the parameters of the CI engine. In: IOP Conference Series: Materials Science and Engineering, vol. 148, pp. 1–8 (2016)
6. Konovalov, D., Kobalava, H., Radchenko, M., Sviridov, V., Scurtu, I.C.: Optimal sizing of the evaporation chamber in the low-flow aerothermopressor for a combustion engine. In: Tonkonogyi, V. (ed.) InterPartner 2020. LNME, pp. 654–663. Springer, Cham (2021). [https://doi.org/10.1007/978-3-030-68014-5\\_63](https://doi.org/10.1007/978-3-030-68014-5_63)
7. Radchenko, R., Pyrysunko, M., Radchenko, A., Andreev, A., Kornienko, V.: Ship engine intake air cooling by ejector chiller using recirculation gas heat. In: Ivanov, V., Trojanowska, J., Oborskyi, G., Grabchenko, A., Pavlenko, I., Edl, M. (eds.) InterPartner 2020. LNME, pp. 734–743. Springer, Cham (2021). [https://doi.org/10.1007/978-3-030-68014-5\\_71](https://doi.org/10.1007/978-3-030-68014-5_71)







8. Nag, S., Sharma, P., Gupta, A., Dhar, A.: Experimental study of engine performance and emissions for hydrogen diesel dual fuel engine with exhaust gas recirculation. *Int. J. Hydrogen Energy* **44**(23), 12163–12175 (2019)
9. Fan, C., Pei, D., Wei, H.: A novel cascade energy utilization to improve efficiency of double reheat cycle. *Energy Convers. Manag.* **171**, 1388–1396 (2018)
10. MARPOL Consolidated edition 2020/International Maritime Organization. [www.idgca.org/doc/app5\\_290115.%20pdf](http://www.idgca.org/doc/app5_290115.%20pdf). Accessed 22 June 2019
11. Mito, M.T., Teamah, M.A., El-Maghlany, W.M., Shehata, A.I.: Utilizing the scavenge air cooling in improving the performance of marine diesel engine waste heat recovery systems. *Energy* **142**, 264–276 (2018). [www.idgca.org/doc/app5\\_290115.%20pdf](http://www.idgca.org/doc/app5_290115.%20pdf)
12. Krucker, S., Wuelser, J.-P., Vourlidis, A.: 12th European Solar Physics Meeting. Freiburg, Germany (2008)
13. Toghiani, S., Afshari, E., Baniasadi, E.: Performance evaluation of an integrated proton exchange membrane fuel cell system with ejector absorption refrigeration cycle. *Energy Convers. Manage.* **185**, 666–677 (2019)
14. Huang, S., Li, C., Tan, T., Fu, P., Xu, G., Yang, Y.: An improved system for utilizing low-temperature waste heat of flue gas from coal-fired power plants. *Entropy* **19**(423), 1–17 (2017)
15. Butrymowicz, D., et al.: Investigations of prototype ejection refrigeration system driven by low grade heat. In: HTRSE-2018, E3S Web of Conferences, vol. 70 (2018)
16. Trushliakov, E., Radchenko, M., Bohdal, T., Radchenko, R., Kantor, S.: An innovative air conditioning system for changeable heat loads. In: Tonkonogyi, V., et al. (eds.) *InterPartner 2019*. LNME, pp. 616–625. Springer, Cham (2020). [https://doi.org/10.1007/978-3-030-40724-7\\_63](https://doi.org/10.1007/978-3-030-40724-7_63)
17. Radchenko, M., Mikielewicz, D., Tkachenko, V., Klugmann, M., Andreev, A.: Enhancement of the operation efficiency of the transport air conditioning system. In: Ivanov, V. et al. (eds.) *Advances in Design, Simulation and Manufacturing III. DSMIE 2020. Lecture Notes in Mechanical Engineering*, pp. 332–342. Springer, Cham (2020)
18. Sugiarta, N., Tassou, S.A., Chaer, I.: Trigeneration in food retail: an energetic, economic and environmental evaluation for a supermarket application. *Appl. Thermal Eng.* **29**(13), 2624–2632 (2009)
19. Kornienko, V., Radchenko, R., Bohdal, T., Radchenko, M., Andreev, A.: Thermal characteristics of the wet pollution layer on condensing heating surfaces of exhaust gas boilers. In: Ivanov, V., Pavlenko, I., Liaposhchenko, O., Machado, J., Edl, M. (eds.) *DSMIE 2021. LNME*, pp. 339–348. Springer, Cham (2021). [https://doi.org/10.1007/978-3-030-77823-1\\_34](https://doi.org/10.1007/978-3-030-77823-1_34)
20. Sugeng, D.A., Ithnin, A.M., Amri, N.S.M.S., Ahmad, M.A., Yahya, W.J.: Water content determination of steam generated water-in-diesel emulsion. *J. Adv. Res. Fluid Mech. Thermal Sci.* **49**(1), 62–68 (2020)
21. Baskar, P., Senthil Kumar, A.: Experimental investigation on performance characteristics of a diesel engine using diesel-water emulsion with oxygen enriched air. *Alex. Eng. J.* **56**(1), 137–146 (2017)
22. Kornienko, V., Radchenko, R., Bohdal, L., Kukielka, L., Legutko, S.: Investigation of condensing heating surfaces with reduced corrosion of boilers with water-fuel emulsion combustion. In: Nechyporuk, M., Pavlikov, V., Kritskiy, D. (eds.) *ICTM 2020. LNNS*, vol. 188, pp. 300–309. Springer, Cham (2021). [https://doi.org/10.1007/978-3-030-66717-7\\_25](https://doi.org/10.1007/978-3-030-66717-7_25)
23. Luo, C., Luo, K., Wang, Y., Ma, Z., Gong, Y.: The effect analysis of thermal efficiency and optimal design for boiler system. *Energy Procedia* **105**, 3045–3050 (2017)

24. Konovalov, D., Kobalava, H., Maksymov, V., Radchenko, R., Avdeev, M.: Experimental research of the excessive water injection effect on resistances in the flow part of a low-flow aerothermopressor. In: Ivanov, V., Pavlenko, I., Liaposhchenko, O., Machado, J., Edl, M. (eds.) DSMIE 2020. LNME, pp. 292–301. Springer, Cham (2020). [https://doi.org/10.1007/978-3-030-50491-5\\_28](https://doi.org/10.1007/978-3-030-50491-5_28)
25. Gupta, R.K., Sankeerth, K.A., Sharma, T.K., Rao, G., Murthy, K.M.: Effects of water-diesel emulsion on the emission characteristics of single cylinder direct injection diesel engine - a review. *Appl. Mech. Mater.* **592**, 1526–1533 (2014)
26. Shu, G., Liang, Y., Wei, H., Tian, H., Zhao, J., Liu, L.: A review of waste heat recovery on two-stroke IC engine aboard ships. *Renew. Sustain. Energy Rev.* **19**, 385–401 (2013)
27. Radchenko, M., Radchenko, R., Tkachenko, V., Kantor, S., Smolyanoy, E.: Increasing the operation efficiency of railway air conditioning system on the base of its simulation along the route line. In: Nechyporuk, M., Pavlikov, V., Kritskiy, D. (eds.) *Integrated Computer Technologies in Mechanical Engineering*. AISC, vol. 1113, pp. 461–467. Springer, Cham (2020). [https://doi.org/10.1007/978-3-030-37618-5\\_39](https://doi.org/10.1007/978-3-030-37618-5_39)
28. MAN Diesel & Turbo. MAN B&W Two-stroke Marine Engines. Emission Project Guide. [https://marine.man-es.com/applications/projectguides/2stroke/content/special\\_pg/7020-0145-09\\_uk.pdf](https://marine.man-es.com/applications/projectguides/2stroke/content/special_pg/7020-0145-09_uk.pdf). Accessed 22 June 2022
29. MAN Diesel Turbo. CEAS Engine Calculations. <https://marine.man-es.com/two-stroke/ceas>. Accessed 22 June 2022
30. METEOMANZ. <http://meteomanz.com>. Accessed 21 Dec 2021





# Exhaust Heat Recovery in Integrated Energy Plant

Andrii Radchenko<sup>1</sup>  , Serhiy Forduy<sup>2</sup> , Viktor Khaldobin<sup>1</sup> ,  
Oleksii Zielikov<sup>1</sup> , and Oleksandr Rizun<sup>1</sup> 

<sup>1</sup> Admiral Makarov National University of Shipbuilding, 9, Heroes of Ukraine Avenue,  
Mykolaiv 54025, Ukraine

nirad50@gmail.com

<sup>2</sup> PepsiCo, Inc., Kyiv, Ukraine

**Abstract.** The combined refrigeration, heat, and power generation (trigeneration) gained widespread application. The reciprocating combustion gas engines are used as drive engines. They are the most adapted to match the actual refrigeration, heat, and electricity needs and manufactured as cogenerative engine modules equipped with heat exchangers to release the heat of exhaust gas, scavenge gas-air mixture, engine jacket, and lubricant oil cooling water to produce hot water converted to refrigeration for technological, space conditioning and heating duties. The efficiency of recovering the heat released from gas engines in a typical integrated energy plant with an absorption lithium-bromide chiller has been analyzed. Issuing from monitoring data on the parameters of heat utilization circuit, the reserves for utilizing the heat usually not recovered by absorption chiller and removed to the atmosphere by radiator are revealed. The advanced heat recovery system that transforms the heat, typically extracted to the atmosphere, by ejector chiller to generate supplementary refrigeration for gas engine intake air cooling was developed as the simplest and expedient solution for implementation at a typical integrated power plant.

**Keywords:** Energy efficiency · Gas engine · Waste heat · Utilization · Absorption chiller · Ejector chiller · Industrial innovation

## 1 Introduction

The combined refrigeration, heat, and power generation (trigeneration) achieved wide application [1, 2]. The reciprocating combustion gas engines are used as drive engines [3, 4]. The gas engines are the most adapted to matching the actual refrigeration, heat, and electricity needs [5, 6]. They are manufactured as cogenerative engines equipped with heat exchangers to release exhaust gas heat, scavenge gas-air mixture, engine jacket, and lubricant oil cooling water to produce hot water converted to refrigeration for technological space conditioning and heating duties [7, 8].

Rising gas engines' air temperature reduces their thermodynamic efficiency: electrical power decreases, and fuel efficiency falls [9]. Issuing from this, the heat released from the engines is reasonable to be used for cooling engine intake air through its converting to refrigeration [10, 11].

## 2 Literature Review

The advanced technologies for the utilization of combustion engine exhaust are used to increase the heat released [12, 13].

The absorption lithium-bromide chillers (ACh) are mainly applied for converting waste heat to refrigeration [14, 15]. They can produce chilled with the temperature of about 7 °C and cool the air to the temperature of about 15 °C accordingly with an increased coefficient of performance (COP) of 0.7 to 0.8.

The jet devices using water [16, 17] or refrigerant [18, 19] as coolants such as thermopressors [20, 21] and ejector chillers (ECh) are the most simple in design and cheap. The ECh has less COP of about 0.3 but can cool the air to 10 °C and lower [18, 19]. They include heat exchangers with a two-phase flow of refrigerant [22, 23]. Their efficiency can be enhanced by heat transfer intensification in evaporators [24] and improving refrigerant distribution [25, 26] in minichannels with advanced circuits of refrigerant circulation [27, 28]. Applying modern simulation methods as ANSYS [29, 30] provides their rational design to match actual operation conditions [31, 32]. Deep utilization of engine exhaust heat is achieved by applying, for instance, low-temperature condensing surfaces [33, 34]. Various techniques increase the heat released [35, 36] and convert it to refrigeration [37, 38]. All of them are accompanied by considerable ecological effects [39, 40].

The enlarged waste heat and heat losses caused by conflicting temperature conditions for the effective operation of ACh and gas engines were revealed in the typically integrated energy plants (IEP). Thus, to provide the condition of safe engine operation at the required thermal level, the temperature of a return hot water from ACh at the exit of engine heat removing contour is limited to 70 °C. In the opposite case, the excessive heat of return hot water is removed to the atmosphere through the so-called emergency radiator.

The general approach of the present research is to convert the heat of return hot water not used by ACh and removed to the atmosphere in typical IEP to refrigeration by ECh for engine intake air cooling.

The work focuses on enhancing the utilization of gas engine released heat through converting the waste heat not used by ACh to refrigeration in ECh to provide the effective operation of the engine.

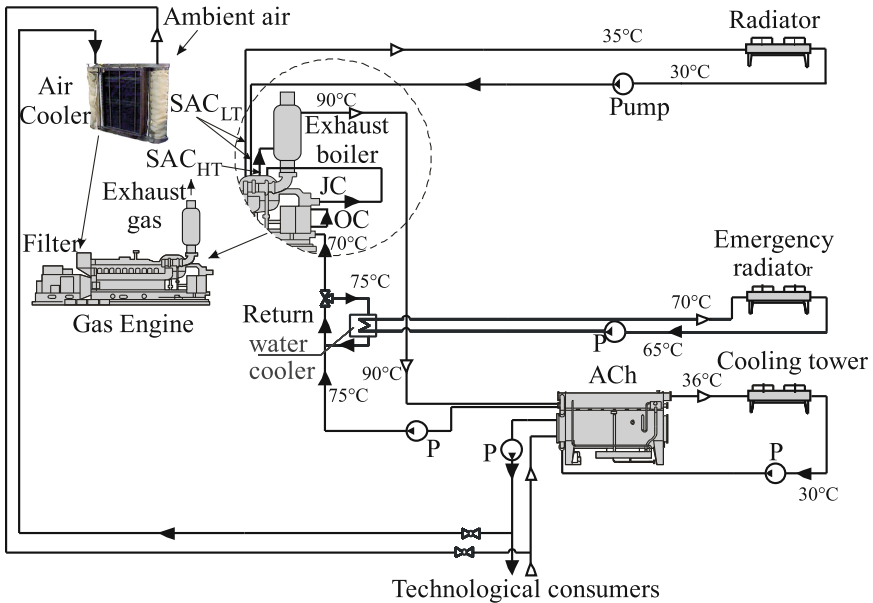
## 3 Research Methodology

The efficiency integrated energy plants of the factory “Sandora”–“PepsiCo Ukraine” (Mykolayiv, Ukraine) was investigated. The IEP consists of two GE JMS 420 GS (electric power output  $P_e = 1400$  kW, heat power output  $Q_h = 1500$  kW) and ACh.

The ACh recovers the heat of exhaust gas, scavenging gas-air mixture, and the water cooling engine jacket and lubricant oil to receive hot water and convert the latter to refrigeration for technological and space conditioning and heating duties.

The circuit of the typical system for converting gas engine released heat to refrigeration by ACh is presented in Fig. 1.

In the typical IEP (Fig. 1), the temperature of return hot water after ACh  $t_{wA2}$  is 75 to 80 °C, that is more higher than 70 °C at the inlet to cogenerative engine module to



**Fig. 1.** The circuit of the typical system for converting gas engine released heat to refrigeration by ACh: OC – oil cooler; JC – engine jacket cooler; SAC<sub>LT</sub> and SAC<sub>HT</sub> – low- and high-temperature stages of scavenging air cooler

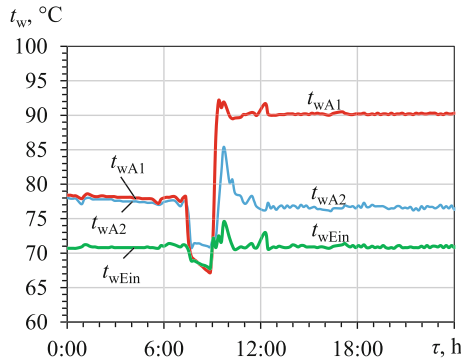
provide its safe thermal rate. Therefore, the excessive heat of return water after ACh is removed through the return water cooler and emergency radiator to the atmosphere.

So as the temperature of return water after ACh  $t_{wA2} = 75 \dots 80 \text{ }^\circ\text{C}$  is much less than its values 90 to 95  $^\circ\text{C}$  that might provide the efficient operation of a single-stage ACh with a high COP of about 0.7, it is impossible to use its heat again in ACh. The use of supply hot water with such lowered temperature would cause falling the COP of ACh from its rated value of about 0.7 to 0.5 and lower.

The analyses of monitoring data on the temperatures of hot water from the gas engine during converting its heat were done to estimate the value of the rest of the heat removed to the atmosphere and convert it to additional refrigeration.

The temperatures of hot water from the engine at the inlet of ACh  $t_{wA1}$  and outlet of ACh  $t_{wA2}$  and return water  $t_{wEin}$  at the inlet of engine previously cold in the emergency radiator through removing excessive heat to the atmosphere are shown in Fig. 2.

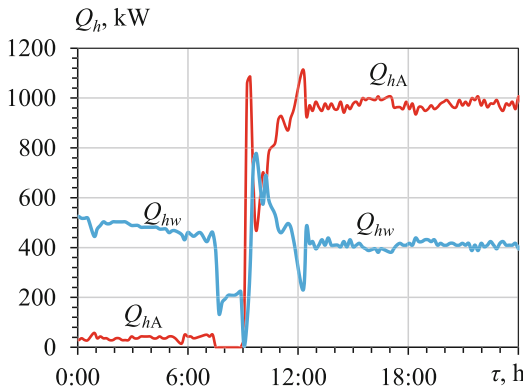
As Fig. 2 shows, the temperature depression  $t_{wA1} - t_{wA2}$  of hot water in ACh due to converting its heat to refrigeration is a bit less than 15  $^\circ\text{C}$ . Accordingly, a temperature decrease of return water after ACh  $t_{wA2} - t_{wEin}$  is more than 5  $^\circ\text{C}$ , and the heat losses to the atmosphere caused by removing the excessive heat not converted to refrigeration by ACh are quite considerable.



**Fig. 2.** Temperatures of hot water at the inlet of ACh  $t_{wA1}$  and outlet of ACh  $t_{wA2}$  and return water  $t_{wEin}$  at the inlet of engine cold in the emergency radiator

### 4 Results

The values of the waste heat  $Q_{hw}$  not converted to refrigeration by ACh and the heat  $Q_{hA}$  used by ACh calculated according to monitoring data on the temperatures of hot water (Fig. 2) are presented in Fig. 3.



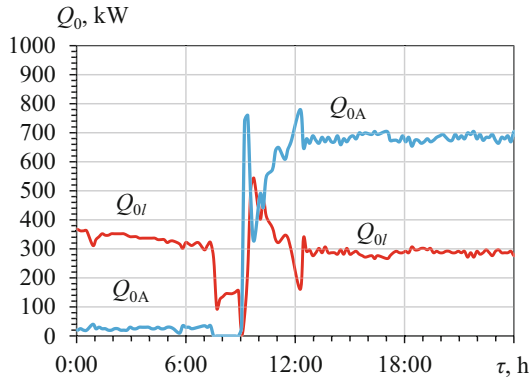
**Fig. 3.** Values of heat converted to refrigeration by ACh  $Q_{hA}$  and the waste heat  $Q_{hw}$

As Fig. 3 shows, the waste heat  $Q_{hw}$  as a lost heat removed to the atmosphere by the emergency radiator to keep the temperature of return hot water at the inlet of the gas engine not higher than 70 °C, is about 40% of the heat converted by ACh to refrigeration or 30% of the engine heat capacity (1400 kW).

Therefore, the waste heat recovery system was developed to utilize the heat of return hot water after ACh (usually removed to the atmosphere) to generate additional refrigeration for gas engine intake air cooling. Its efficiency was estimated proceeding from monitoring data.

To increase the temperature of return hot water from 75 °C to 90 °C providing the operation of ACh with a high COP of 0.7 to 0.8, a booster gas boiler available at any

factory can be applied. In this case, the additional refrigeration capacities  $Q_{0l}$  might be generated due to the use of the lost waste heat besides the basic refrigeration capacities of ACh  $Q_{0A}$  converting the originally available heat  $Q_{hA}$  (Fig. 3) as it is shown in Fig. 4.



**Fig. 4.** Refrigeration capacities of ACh  $Q_{0A}$  due to converting the available heat of high rate  $Q_{hA}$  (Fig. 3) and additional refrigeration  $Q_{0l}$  received by recovering the lost heat  $Q_w$

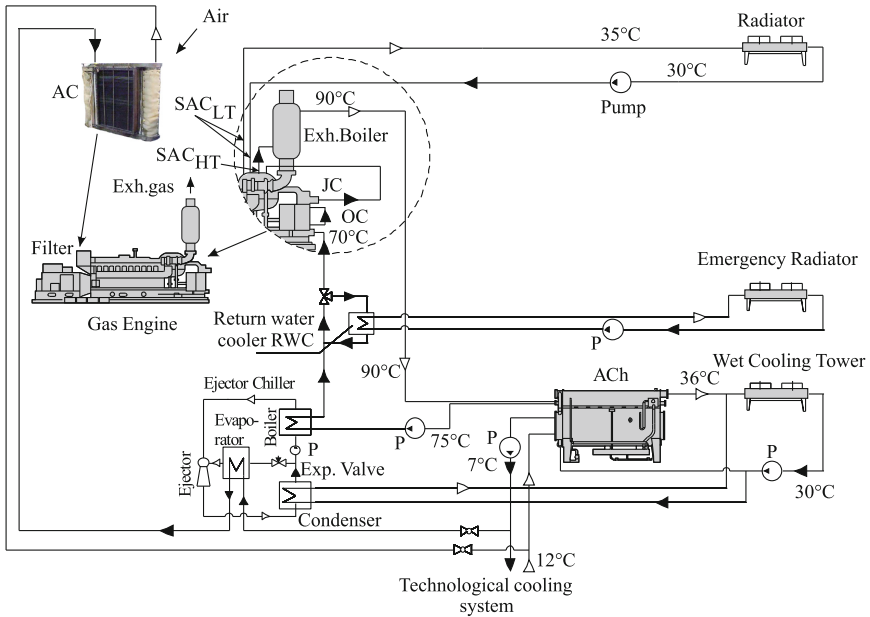
As Fig. 4 shows, due to recovering waste heat  $Q_{hw}$ , conventionally lost through removing to the atmosphere, it is possible to increase the basic refrigeration capacity by about 300 kW for trigeneration plant based on gas engine JMS 420 GS-N.LC.

It should be mentioned that the application of a boost gas boiler to raise heat potential of waste heat of return hot water left from the ACh can be efficient for multi engines trigeneration plant with two and more ACh. The additional boosted heat is used to feed the other ACh, thereby improving the operational flexibility of the overall trigeneration plant.

To recover the waste heat of return hot water after ACh, the simplest in design ECh is applied. It operates as a boost low-temperature stage of combined absorption-ejector chiller (AECh).

The refrigeration capacity, received by recovering the waste heat of return hot water, can be used for engine intake air cooling by chilled water from ACh preliminary subcooled by boiling refrigerant of ECh (Fig. 5).

The use of increased refrigeration capacity for gas engine intake air cooling enables to enlarge the engine electricity production with reduced specific fuel consumption. Thus, such deep utilization of the heat released from gas engines enhances engine fuel efficiency and prolongs the duration of trigeneration plant efficient operation even within periodic cooling and heating demands.



**Fig. 5.** The circuit of deep utilization of the heat released from gas engine in AECh

## 5 Conclusions

The analysis of converting the heat released from gas engine to refrigeration by ACh in typical IEP, proceeding from monitoring data on the temperatures of hot water during utilization of its heat, revealed the heat losses of about 40% of the heat converted in ACh. This is caused by conflicting requirements to temperature conditions for the effective operation of ACh and gas engine. To provide the condition of safe engine operation at the required thermal level, the temperature of return hot water after ACh at the entry of engine heat removing circuit is limited to 70 °C. Therefore in the typical IEP the return hot water excessive heat is removed to the atmosphere through an emergency radiator.

The innovative waste heat recovery system for IEP through converting the rest of heat (not used by ACh and usually removed to the atmosphere) in ECh to generate addition refrigeration for gas engine intake air cooling is developed as the simplest solution to be implemented at the typical IEP.

The absorption-ejector chiller (AECh) with a low-temperature ECh stage and a high-temperature absorption stage for the deep waste heat recovery system of IEP is proposed.

Such a deep waste heat recovery system makes it possible to enhance engine fuel efficiency due to intake air cooling and prolong the time of IEP performance even within periodical technological cooling needs.

## References

1. Canova, A., Cavallero, C., Freschi, F., Giaccone, L., Repetto, M., Tartaglia, M.: Optimal energy management. *IEEE Ind. Appl. Mag.* **15**, 62–65 (2009)

2. Radchenko, A., Stachel, A., Forduy, S., Portnoi, B., Rizun, O.: Analysis of the efficiency of engine inlet air chilling unit with cooling towers. In: Ivanov, V., Pavlenko, I., Liaposhchenko, O., Machado, J., Edl, M. (eds.) DSMIE 2020. LNME, pp. 322–331. Springer, Cham (2020). [https://doi.org/10.1007/978-3-030-50491-5\\_31](https://doi.org/10.1007/978-3-030-50491-5_31)
3. Cogeneration & Trigeneration – How to produce energy efficiently. A practical guide for experts in emerging and developing economies. Zellner, S., Burgtorf, J., Kraft-Schäfer, D. (eds.) Deutsche Gesellschaft für Internationale Zusammenarbeit (GIZ) GmbH, 144 p. (2016)
4. Gluesenkamp, K., Hwang, Y., Radermacher, R.: High efficiency micro trigeneration systems. *Appl. Therm. Eng.* **50**, 6 (2013)
5. CIMAC WG17 Position Paper - Gas Engine Aftertreatment Systems. <https://www.cimac.com/news-press/news/cimac-wg17-position-paper-gas-engine-aftertreatment-systems.html>. Accessed 21 Nov 2021
6. Jenbacher. <https://www.innio.com/en/jenbacher/gas-engines>. Accessed 21 Nov 2021
7. Rouse, G., Czachorski, M., Bishop, P., Patel, J.: GTI Integrated Energy System for Buildings. Modular System Prototype, GTI Project report 15357/65118: Gas Technology Institute (GTI), 495 p, January 2006
8. Elsenbruch, T.: Jenbacher gas engines a variety of efficient applications. București October **28**, 73 (2010)
9. Radchenko, A., Radchenko, M., Trushliakov, E., Kantor, S., Tkachenko, V.: Statistical method to define rational heat loads on railway air conditioning system for changeable climatic conditions. In: 5th International Conference on Systems and Informatics, ICSAI 2018, Jiangsu, Nanjing, China, pp. 1294–1298 (2019). <https://doi.org/10.1109/ICSAI.2018.8599355>
10. Radchenko, M., Radchenko, A., Radchenko, R., Kantor, S., Konovalov, D., Kornienko, V.: Rational loads of turbine inlet air absorption-ejector cooling systems. In: Proceedings of the Institution of Mechanical Engineers, Part A: Journal of Power and Energy (2021). <https://doi.org/10.1177/09576509211045455>
11. Radchenko, A., Trushliakov, E., Tkachenko, V., Portnoi, B., Prjadko, A.: Improvement of the refrigeration capacity utilizing for the ambient air conditioning system. In: Tonkonogyi, V., et al. (eds.) InterPartner 2020. LNME, pp. 714–723. Springer, Cham (2021). [https://doi.org/10.1007/978-3-030-68014-5\\_69](https://doi.org/10.1007/978-3-030-68014-5_69)
12. Kornienko, V., Radchenko, R., Stachel, A., Andreev, A., Pyrysunko, M.: Correlations for pollution on condensing surfaces of exhaust gas boilers with water-fuel emulsion combustion. In: Tonkonogyi, V., et al. (eds.) InterPartner 2019. LNME, pp. 530–539. Springer, Cham (2020). [https://doi.org/10.1007/978-3-030-40724-7\\_54](https://doi.org/10.1007/978-3-030-40724-7_54)
13. Radchenko, M., Radchenko, R., Kornienko, V., Pyrysunko, M.: Semi-empirical correlations of pollution processes on the condensation surfaces of exhaust gas boilers with water-fuel emulsion combustion. In: Ivanov, V., Pavlenko, I., Liaposhchenko, O., Machado, J., Edl, M. (eds.) DSMIE 2019. LNME, pp.853–862. Springer, Cham (2020). [https://doi.org/10.1007/978-3-030-22365-6\\_85](https://doi.org/10.1007/978-3-030-22365-6_85)
14. Ortiga, J., Bruno, J.C., Coronas, A.: Operational optimization of a complex trigeneration system connected to a district heating and cooling network. *Appl. Therm. Eng.* **50**, 1536–1542 (2013)
15. Radchenko, M., Mikielewicz, D., Tkachenko, V., Klugmann, M., Andreev, A.: Enhancement of the operation efficiency of the transport air conditioning system. In: Ivanov, V., Pavlenko, I., Liaposhchenko, O., Machado, J., Edl, M. (eds.) DSMIE 2020. LNME, pp. 332–342. Springer, Cham (2020). [https://doi.org/10.1007/978-3-030-50491-5\\_32](https://doi.org/10.1007/978-3-030-50491-5_32)
16. Konovalov, D., Kobalava, H., Maksymov, V., Radchenko, R., Avdeev, M.: Experimental research of the excessive water injection effect on resistances in the flow part of a low-flow aerothermopressor. In: Ivanov, V., Pavlenko, I., Liaposhchenko, O., Machado, J., Edl, M. (eds.) DSMIE 2020. LNME, pp. 292–301. Springer, Cham (2020). [https://doi.org/10.1007/978-3-030-50491-5\\_28](https://doi.org/10.1007/978-3-030-50491-5_28)

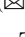




17. Yang, Z., Radchenko, M., Radchenko, A., Mikielwicz, D., Radchenko, R.: Gas turbine intake air hybrid cooling systems and a new approach to their rational designing. *Energies* **15**(4), 1474 (2022). <https://doi.org/10.3390/en15041474>
18. Butrymowicz, D., et al.: Investigations of prototype ejection refrigeration system driven by low grade heat. In: HTRSE-2018, E3S Web of Conferences, vol. 70, 7 p. (2018)
19. Smierciew, K., Gagan, J., Butrymowicz, D., Karwacki, J.: Experimental investigations of solar driven ejector air-conditioning system. *Energy Build.* **80**, 260–267 (2014)
20. Konovalov, D., Kobalava, H., Radchenko, M., Sviridov, V., Scurtu, I.C.: Optimal sizing of the evaporation chamber in the low-flow aerothermopressor for a combustion engine. In: Tonkonogyi, V., et al. (eds.) *InterPartner 2020. LNME*, pp. 654–663. Springer, Cham (2021). [https://doi.org/10.1007/978-3-030-68014-5\\_63](https://doi.org/10.1007/978-3-030-68014-5_63)
21. Kornienko, V., Radchenko, R., Mikielwicz, D., Pyrysunko, M., Andreev, A.: Improvement of characteristics of water-fuel rotary cup atomizer in a boiler. In: Tonkonogyi, V., et al. (eds.) *InterPartner 2020. LNME*, pp. 664–674. Springer, Cham (2021). [https://doi.org/10.1007/978-3-030-68014-5\\_64](https://doi.org/10.1007/978-3-030-68014-5_64)
22. Dąbrowski, P., Klugmann, M., Mikielwicz, D.: Selected studies of flow maldistribution in a minichannel plate heat exchanger. *Arch. Thermodyn.* **38**, 135–148 (2017)
23. Radchenko, M., Mikielwicz, D., Andreev, A., Vanyeyev, S., Savenkov, O.: Efficient ship engine cyclic air cooling by turboexpander chiller for tropical climatic conditions. In: Nechyporuk, M., Pavlikov, V., Kritskiy, D. (eds.) *Integrated Computer Technologies in Mechanical Engineering - 2020. ICTM 2020. LNNS*, vol. 188, pp. 498–507. Springer, Cham (2021). [https://doi.org/10.1007/978-3-030-66717-7\\_42](https://doi.org/10.1007/978-3-030-66717-7_42)
24. Bohdal, T., Kuczynski, W.: Boiling of R404A refrigeration medium under the conditions of periodically generated disturbances. *Heat Transf. Eng.* **32**, 359–368 (2011). <https://doi.org/10.1080/01457632.2010.483851>
25. Kumar, R., Singh, G., Mikielwicz, D.: A new approach for the mitigating of flow maldistribution in parallel microchannel heat sink. *J. Heat Transfer* **140**, 72401–72410 (2018)
26. Dąbrowski, P., Klugmann, M., Mikielwicz, D.: Channel blockage and flow maldistribution during unsteady flow in a model microchannel plate heat exchanger. *J. Appl. Fluid Mech.* **12**, 1023–1035 (2019)
27. Mikielwicz, D., Klugmann, M., Wajs, J.: Flow boiling intensification in minichannels by means of mechanical flow turbulising inserts. *Int. J. Therm. Sci.* **65**, 79–91 (2013)
28. Radchenko, R., Kornienko, V., Pyrysunko, M., Bogdanov, M., Andreev, A.: Enhancing the efficiency of marine diesel engine by deep waste heat recovery on the base of its simulation along the route line. In: Nechyporuk, M., Pavlikov, V., Kritskiy, D. (eds.) *Integrated Computer Technologies in Mechanical Engineering (ICTM 2019). Advances in Intelligent Systems and Computing*, vol. 1113, pp. 337–350. Springer, Cham (2020)
29. Radchenko, R., Radchenko, N., Tsoy, A., Zybarev, A., Kalinichenko, I.: Utilizing the heat of gas module by an absorption lithium-bromide chiller with an ejector booster stage. In: *AIP Conference Proceedings*, vol. 2285, p. 030084 (2020). <https://doi.org/10.1063/5.0026788>
30. Kumar, R., Singh, G., Mikielwicz, D.: Numerical study on mitigation of flow maldistribution in parallel microchannel heat sink: channels variable width versus variable height approach. *J. Electron. Packag.* **141**, 21009–21011 (2019)
31. Dawoud, B., Zurigat, Y.H., Bortmany, J.: Thermodynamic assessment of power requirements and impact of different gas-turbine inlet air cooling techniques at two different locations in Oman. *Appl. Therm. Eng.* **25**, 1579–1598 (2005)
32. Trushliakov, E., Radchenko, M., Bohdal, T., Radchenko, R., Kantor, S.: An innovative air conditioning system for changeable heat loads. In: Tonkonogyi, V., et al. (eds.) *InterPartner 2019. LNME*, pp. 616–625. Springer, Cham (2020). [https://doi.org/10.1007/978-3-030-40724-7\\_63](https://doi.org/10.1007/978-3-030-40724-7_63)



33. Khaliq, A., Dincer, I., Sharma, P.B.: Development and analysis of industrial waste heat based trigeneration for combined production of power heat and cold. *J. Energy Inst.* **83**(2), 79–85 (2010)
34. Kornienko, V., Radchenko, R., Bohdal, Ł, Kukielka, L., Legutko, S.: Investigation of condensing heating surfaces with reduced corrosion of boilers with water-fuel emulsion combustion. In: Nechyporuk, M., Pavlikov, V., Kritskiy, D. (eds.) *ICTM 2020. LNNS*, vol. 188, pp. 300–309. Springer, Cham (2021). [https://doi.org/10.1007/978-3-030-66717-7\\_25](https://doi.org/10.1007/978-3-030-66717-7_25)
35. Rodriguez-Aumente, P.A., Rodriguez-Hidalgo, M.C., Nogueira, J.I., Lecuona, A., Venegas, M.C.: District heating and cooling for business buildings in Madrid. *Appl. Therm. Eng.* **50**, 1496–1503 (2013)
36. Radchenko, R., Pyrysunko, M., Kornienko, V., Konovalov, D., Girzheva, O.: Enhancing energy efficiency of ship diesel engine with gas ecological recirculation. In: Ivanov, V., Pavlenko, I., Liaposhchenko, O., Machado, J., Edl, M. (eds.) *DSMIE 2021. LNME*, pp. 391–400. Springer, Cham (2021). [https://doi.org/10.1007/978-3-030-77823-1\\_39](https://doi.org/10.1007/978-3-030-77823-1_39)
37. Oktay, Z., Coskun, C., Dincer, I.: A new approach for predicting cooling degree-hours and energy requirements in buildings. *Energy* **36**(8), 4855–4863 (2011)
38. Forsyth, J.L.: Gas turbine inlet air chilling for LNG. In: *Proceedings of the IGT International Liquefied Natural Gas Conference*, vol. 3, pp. 1763–1778 (2013)
39. Radchenko, R., Pyrysunko, M., Kornienko, V., Scurtu, I.-C., Patyk, R.: Improving the ecological and energy efficiency of internal combustion engines by ejector chiller using recirculation gas heat. In: Nechyporuk, M., Pavlikov, V., Kritskiy, D. (eds.) *ICTM 2020. LNNS*, vol. 188, pp. 531–541. Springer, Cham (2021). [https://doi.org/10.1007/978-3-030-66717-7\\_45](https://doi.org/10.1007/978-3-030-66717-7_45)
40. Kalhori, S.B., Rabiei, H., Mansoori, Z.: Mashad trigeneration potential – an opportunity for CO<sub>2</sub> abatement in Iran. *Energy Convers. Manag.* **60**, 106–114 (2012)



# Turbine Intake Air Combined Cooling Systems

Mykola Radchenko <sup>(✉)</sup>, Volodymyr Korobko , Serhiy Kantor ,  
Anatoliy Zubarev , and Olena Girzheva 

Admiral Makarov National University of Shipbuilding, 9, Heroes of Ukraine Avenue, Mykolaiv  
54025, Ukraine  
nirad50@gmail.com

**Abstract.** The application of absorption lithium-bromide chillers (ACh) for turbine inlet air cooling (TIC) is very effective in hot climatic conditions due to enlarged ambient air temperature drops and fuel reduction. But in temperate climatic conditions, the efficiency of TIC by ACh of a simple cycle is considerably reduced decreased ambient air temperature drops cause that. The last is limited by a comparatively raised temperature of chilled water of about 7 °C that makes it unable to cool ambient air lower than 15 °C. The application of low boiling refrigerants as a coolant enables deeper turbine inlet air cooling to 10 °C and lower. Therefore, the low boiling refrigerants can be used for subsequent cooling air after its pre-cooling in ACh. A refrigerant ejector chiller (ECh) is the most simple in design and cheap and can be applied for subcooling air from 15 °C to 10 °C. Such deep cooling air to 10 °C in combined absorption-ejector chiller (AECh) provides about twice the annual fuel reduction in temperate climate compared with conventional TIC to 15 °C by ACh. The method to determine rational refrigeration capacity of AECh and distribute it between ACh and ECh that provides practically maximum annual fuel reduction at reduced design refrigeration capacity by about 20% is developed. With this current excessive refrigeration, capacities are used to cover peaked loads.

**Keywords:** Energy efficiency · Gas turbine · Fuel efficiency · Inlet air · Chilled water · Refrigerant

## 1 Introduction

The fuel efficiency of combustion engines and especially gas turbines (GT), is strictly influenced by ambient air temperature at their inlet [1, 2]. The application of absorption lithium-bromide chillers (ACh) [3, 4] for turbine inlet air cooling (TIC) is very effective in hot climatic conditions due to high ambient air temperatures and enlarged their drops and fuel reduction as a result [5, 6]. But in temperate climatic conditions, the efficiency of TIC by ACh of a simple cycle is much lower than is caused by decreased ambient air temperature drops [7, 8]. The last is limited by a comparatively raised temperature of chilled water of about 7 °C that makes it unable to cool ambient air lower than 15 °C. The application of low boiling refrigerants as a coolant enables deeper turbine inlet air cooling to 10 °C and lower [9, 10]. Therefore the low boiling refrigerants can be used for

subsequent cooling air after its pre-cooling in ACh. A refrigerant ejector chiller (ECh) is the most simple in design and cheap and can be applied for cooling air from 15 °C to 10 °C [11, 12]. Such deep cooling air to 10 °C in combined absorption-ejector chiller (AECh) provides about twice the annual fuel reduction in temperate climate compared with conventional TIC to 15 °C by ACh. The efficiency of ECh is very sensitive to thermal load changes. Ambient air pre-cooling to 15 °C in ACh practically covers thermal load fluctuations and provides operation of ECh at about stable loading.

The operation of ACh at variable current loads is accompanied by the formation of excess refrigeration capacity that can cover peaked thermal loads. A rational refrigeration capacity distribution within the range of fluctuated thermal loads enables to reduce a design refrigeration capacity of ACh and the overall AECh. A corresponding method to determine a rational refrigeration capacity of AECh in the whole and its distribution between ACh and ECh is to consider the actual current thermal loads and yearly effect gained due to TIC, for instance, as annual fuel saving.

## 2 Literature Review

A lot of research is focused on enhancing the efficiency of combustion engine inlet air cooling by waste heat recovery [13, 14]. The exhaust heat utilization can be improved by the application of fuel afterburning and exhaust gas boilers with low-temperature heating surfaces [15, 16] that enlarges the available heat to be converted to refrigeration for TIC to lowered temperature of 10 °C and less as compared with conventional TIC to 15 °C in ACh. The advanced system to utilize the exhaust heat by jet technics [17, 18] for cooling cyclic engine air was developed [19]. Some modern simulation methods such as ANSYS [20–22] can be applied for rational designing heat exchangers to match actual operation conditions.

A lot of publications were devoted to combined cooling, heating, and power (CCHP) generation [23, 24] or trigeneration [25, 26].

Practically all the analyses focus on enhancing engine fuel efficiency due to inlet air cooling through rational loading [27, 28]. Many of those methods are based on cooling degree-hour (CDH) numbers and modified methods of their calculation [29, 30] to match current cooling demands in respect to actual climatic conditions [31, 32] and thermal management [33, 34] proceeding from various criteria [35, 36]. The research to determine the input ambient air data for estimating TIC [37].

Most of the TIC system designing methods are based on the approach to cover the maximum yearly thermal loads [38, 39]. Such assumption inevitable leads to overestimating the design refrigeration capacity of TIC system and its oversizing.

The research focuses on developing the advanced TIC system with combined AECh to provide deep TIC and the method to define a rational refrigeration capacity that enables practically maximum annual fuel reduction and distributes it between ACh and ECh matching current loading.

### 3 Research Methodology

A developed method of designing the TIC system focuses on determining the refrigeration capacity of AECh to achieve practically maximum annual fuel reduction and rational distribute it between ACh and ECh according to actual thermal loads to reduce design refrigeration capacities of the chillers.

The annual GT fuel reduction  $\Sigma B_e$  due to (TIC) is considered a primary criterion when defining a rational refrigeration capacity  $Q_0$  of the TIC system. The current fuel savings  $B_e$  is yearly summarized to calculate the annual value:

$$\Sigma B_e = \sum (\Delta t_a \cdot \tau) \cdot b_{et} \cdot N_e \cdot 10^{-3}, \text{ t}, \quad (1)$$

where:  $\Delta t_a = t_{amb} - t_{a2}$  – current air temperature drop at GT inlet, °C;  $t_{amb}$  and  $t_{a2}$  – temperatures of ambient air at the entrance and cooled air at the exit of the cooler at the GT intake, °C;  $N_e$  – GT power, kW;  $\tau$  – time interval, h;  $b_{et}$  – specific fuel reduction for 1 °C turbine intake air temperature drop, accepted as 0.7 g/(kWh·K) for turbine UGT10000 (power 10000 kW) [40].

A refrigeration capacity  $Q_0$  for air mass flow  $G_a$ , kg/s:

$$Q_0 = G_a \Delta t_a \xi \cdot c_{ma}, \text{ kW}, \quad (2)$$

where:  $\xi$  – specific heat ratio;  $c_{ma}$  – specific moist air heat, kJ/(kg·K);  $G_a = 40$  kg/s – total air mass flow for UGT10000.

Specific refrigeration capacity  $q_0$  referred to unit air mass flow rate 1 kg/s:

$$q_0 = Q_0 / G_a, \text{ kW}/(\text{kg}/\text{s}) \text{ or } \text{kJ}/\text{kg}. \quad (3)$$

The variations in the current turbine fuel reduction  $B_e$  are taken into account by the rate of their annual increment in relative value  $\Sigma B_e / Q_0$  related to required refrigeration capacity  $Q_0$ .

So the relative annual fuel reduction increment  $\Sigma B_e / Q_0$  is applied as an indicator to determine a maximum rate of yearly fuel-saving increment, and its maximum corresponds to optimum refrigeration capacity  $Q_{0,\text{opt}}$ .

The optimum refrigeration capacity  $Q_{0,\text{opt}}$  corresponds to the minimum sizes of the chillers and TIC system accordingly.

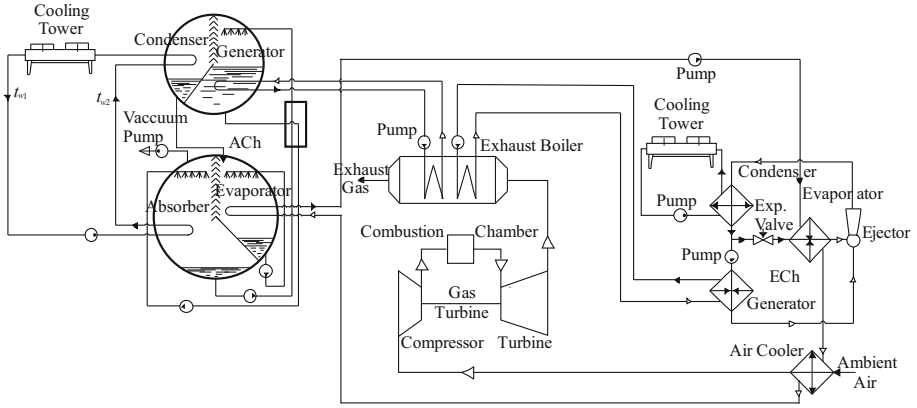
### 4 Results

A circuit of the developed TIC system with AECh is presented in Fig. 1.

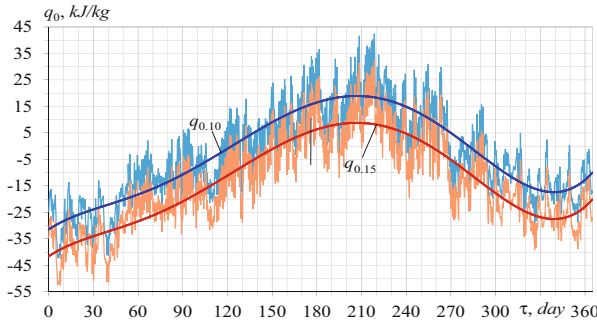
Current specific thermal loads  $q_{0,10}$  and  $q_{0,15}$  for cooling air to 10 and 15 °C during 2017 in Mykolayiv, southern Ukraine, are presented in Fig. 2.

As seen, large variations in current specific thermal loads  $q_0$  for cooling ambient air make it problematic to determine a design refrigeration capacity of TIC system providing maximum annual fuel reduction  $\Sigma B$  without overestimating.

According to the advanced proposed method, the variations of the current required refrigeration capacity  $q_0$  (for 1 kg/s) and  $Q_0$  (for  $G_a = 40$  kg/s, UGT10000) and corresponding fuel-saving  $B_e$  are considered the relative annual fuel reduction increment  $\Sigma B_e / Q_0$  related to the required refrigeration capacity  $Q_0$ .



**Fig. 1.** A circuit of developed TIC system with AECh



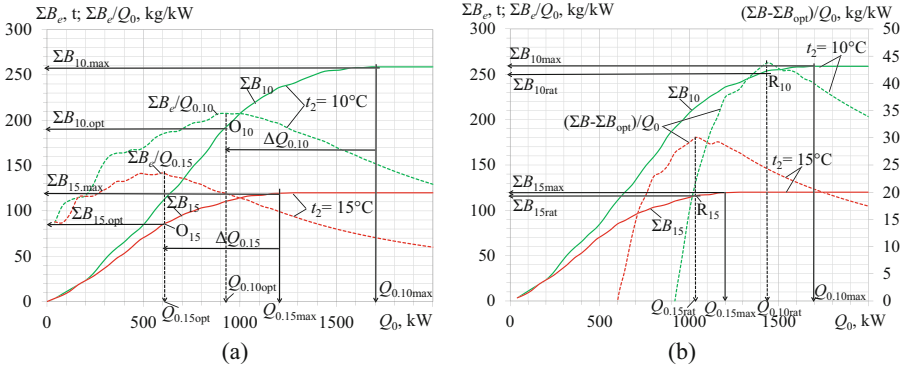
**Fig. 2.** Current values of ambient air temperature  $t_{amb}$ , specific thermal loads  $q_{0.10}$  and  $q_{0.15}$  for cooling ambient air to  $t_{a2} = 10$  and  $15$  °C during 2017

The results of the calculation of optimum design refrigeration capacity  $Q_{0,opt}$  that enables a maximum rate of annual fuel saving  $\sum B_e/Q_0$  for gas turbine UGT 10000 are presented in Fig. 3a.

As seen, a maximum rate of annual fuel saving increment  $\sum B_e/Q_0$  for  $t_{a2} = 10$  °C occurs at the optimum refrigeration capacity  $Q_{0.10,opt}$  of about 1050 kW and corresponding  $\sum B_{10,opt}$  of about 140 t (Fig. 3a).

To determine a reasonable value of design refrigeration capacity  $Q_{0,rat}$ , enabling practically maximum annual fuel saving  $\sum B_e$  it is necessary to define the next maximum value of annual fuel saving rate  $\sum B_e$  above the first one:  $Q_0 > Q_{0,opt}$  and  $\sum B_e > \sum B_{e-opt}$  (Fig. 3b).

A maximum value of annual fuel saving rate  $\sum (B_e - B_{e-opt})/Q_0$  above the  $\sum B_{f-opt} = 140$  t corresponds to  $Q_{0,opt} = 900$  kW and occurs at the rational value  $Q_{0,rat}$  about 1400 kW and enables annual fuel saving  $\sum B_{e-rat} = 150$  t about the maximum value 160 t but at a reduced design refrigeration capacity  $Q_{0,rat} = 1400$  kW less than  $Q_{0,max} = 1800$  kW by about 15%.

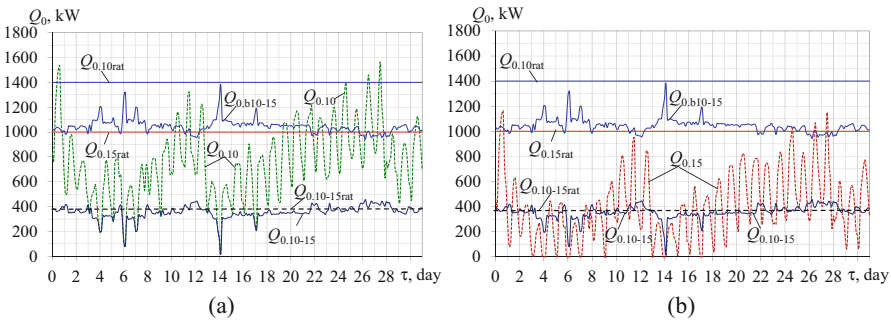


**Fig. 3.** Annual fuel-saving  $\Sigma B_e$ , and its relative increment  $\Sigma B_e/Q_0$  (a), annual fuel saving  $\Sigma B_e$  and relative values  $(\Sigma B_e - \Sigma B_{e,\text{opt}})/Q_0$  above the optimum ones  $\Sigma B_{e,\text{opt}}$  and  $Q_{0,\text{opt}}$  (b) versus refrigeration capacities  $Q_0$  required for cooling ambient air to 10 and 15 °C

The optimum designing of TIC systems enables reduction of the chillers refrigeration capacities by  $\Delta Q_{0.10,15}$ , i.e., 15 to 20% compared with their maximum values  $Q_{0.10,15\text{max}}$ , received in typical designing (Fig. 3b).

Deeper turbine intake air cooling to 10 °C in AECh compared with typical cooling air to 15 °C in ACh provides practically twice the increase in annual fuel saving  $\Sigma B_{10\text{max}}$  compared with  $\Sigma B_{15\text{max}}$  for ACh in temperate climatic conditions (Fig. 3b).

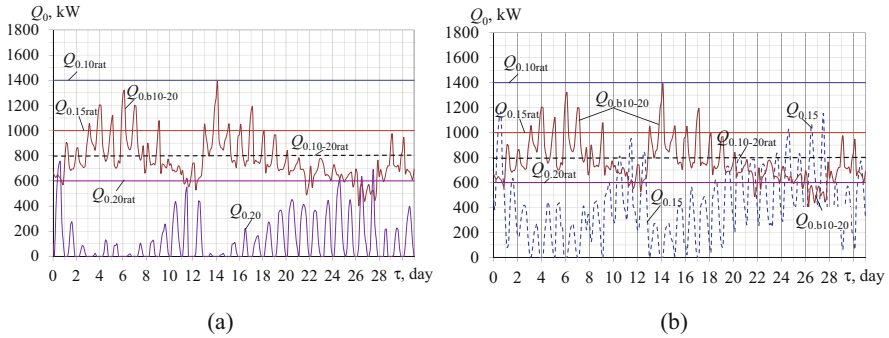
The refrigeration capacities  $Q_{0.15}$  required for cooling air to 15 °C, values of rational cooling capacities  $Q_{0.10\text{rat}}$  and  $Q_{0.15\text{rat}}$  for cooling air to 10 and 15 °C, the basic refrigeration capacity as difference  $Q_{0.10-15} = Q_{0.10} - Q_{0.15}$ , required for cooling air from 15 °C to 10 °C and the rest boost refrigeration capacities  $Q_{0,\text{b}10-15}$  were calculated for temperate climatic conditions in Mykolayiv region, southern Ukraine, July 2017 (Fig. 4).



**Fig. 4.** The refrigeration capacities  $Q_{0,10}$  (a) and  $Q_{0,15}$  (b) for cooling air to 10 and 15 °C, rational refrigeration capacities  $Q_{0,10\text{rat}}$  and  $Q_{0,15\text{rat}}$  for 10 and 15 °C, capacities differences  $Q_{0,10-15}$  for subcooling air from 15 °C to 10 °C, boost refrigeration capacity  $Q_{0,\text{b}10-15}$  for 15 °C:  $Q_{0,\text{b}10-15} = Q_{0,10\text{rat}} - Q_{0,10-15}$ , where  $Q_{0,10-15} = Q_{0,10} - Q_{0,15}$

Such significant variations in the current thermal loads  $Q_{0.15}$  when cooling the ambient air to 15 °C indicates to considerable excess of refrigeration capacities. But when subcooling air from 15 °C to 10 °C, the thermal load variations  $\Delta Q_{0.10-15} = Q_{0.10} - Q_{0.15}$  is small. The boost part of  $Q_{0.10rat}$  is used for pre-cooling ambient air to 15 °C and calculated as  $Q_{0.b10-15} = Q_{0.10} - \Delta Q_{0.10-15}$ . The boost cooling capacity  $Q_{0.b10-15}$  completely covers current loads  $q_{0.15}$  for cooling air to  $t_{a2} = 15$  °C (Fig. 4b).

Further enhancing the efficiency of TIC due to advanced design method is possible through shearing the unstable boost range of refrigeration capacity  $Q_{0.b10-15}$  in two parts:  $Q_{0.b10-20}$  and  $\Delta Q_{0.15-20}$  (Fig. 5).



**Fig. 5.** The refrigeration capacities  $Q_{0.20}$  (a) and  $Q_{0.15}$  (b) for cooling air to 20 and 15 °C, rational values of refrigeration capacities  $Q_{0.10rat}$ ,  $Q_{0.15rat}$  and  $Q_{0.20rat}$  for 10, 15 and 20 °C, rational design refrigeration capacity  $Q_{0.10-20rat}$  for cooling air from 20 °C to 10 °C and capacities  $Q_{0.10-20}$  for cooling air from  $t_{a2} = 20$  °C to  $t_{a2} = 10$  °C, boost capacity  $Q_{0.b10-20}$  for cooling air to 20 °C:  $Q_{0.b10-20} = Q_{0.10rat} - Q_{0.10-20}$ , where  $Q_{0.10-20} = Q_{0.10} - Q_{0.20}$ ;  $Q_{0.10-20rat} = Q_{0.10rat} - Q_{0.20rat}$

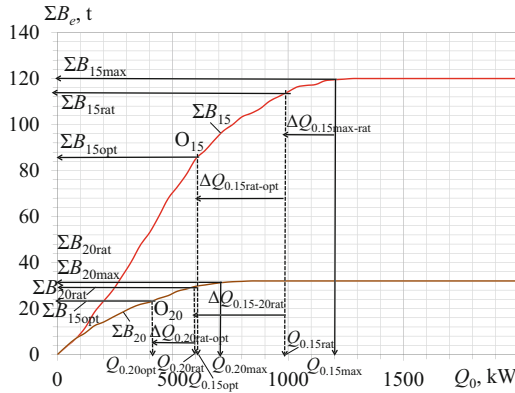
Comparing the boost refrigeration capacity  $Q_{0.b10-20}$  with current thermal loads  $Q_{0.15}$  indicates that the boost refrigeration capacity  $Q_{0.b10-20}$  generally covers even the current loads  $Q_{0.15}$  (Fig. 5b).

Issuing from this, the hypothesis of reducing a design boost refrigeration capacity  $Q_{0.b10-15}$  or  $Q_{0.15rat}$  practically twice due to using  $Q_{0.20rat}$  to cover current thermal loads  $Q_{0.15}$  has been approved (Fig. 5b).

The installed refrigeration capacity of ACh rational distribution makes it possible to reduce a design boost one by  $\Delta Q_{0.15-20rat} = Q_{0.15rat} - Q_{0.20rat}$  (Fig. 5b and Fig. 6), which is practically twice less as compared with  $Q_{0.15rat}$ .

As Fig. 6 shows, rational designing of TIC systems provides a decrease of installed refrigeration capacities of the chillers by  $\Delta Q_{0.15,20max-rat}$ , i.e., by 15 to 20% compared with their maximum values  $Q_{0.15,20max}$  received in conventional designing.

In a temperate climate, applying the proposed TIC system with combined AECh enables achieving nearly twice higher annual fuel reduction  $\sum B_{10}$  than  $\sum B_{15}$  for ACh. It can be supposed as a prosperous trend in TIAC.



**Fig. 6.** The annual fuel reduction  $\Sigma B_e$  and refrigeration capacities  $Q_0$  for cooling air at GT inlet to 15 and 20 °C:  $\Delta Q_{0,max-rat} = Q_{0,max} - Q_{0,rat}$ ;  $\Delta Q_{0,rat-opt} = Q_{0,rat} - Q_{0,opt}$ ;  $\Delta Q_{0,15-20rat} = Q_{0,15rat} - Q_{0,20rat}$ .

### 5 Conclusions

A new trend in enhancing TIC efficiency by applying combined AECh is proposed for temperate climatic conditions that provide practically twice higher annual fuel reduction than ACh.

An advanced TIC systems rational designing method is developed to achieve practically maximum annual fuel reduction; moreover, the installed refrigeration capacities are reduced by 15 to 20% compared with conventional designing practice.

The method is based on the rational distribution of design refrigeration capacity of AECh between ACh for ambient air pre-cooling within unstable thermal load range and ECh for further air cooling within a comparatively stable load range.

With this, the annual fuel reduction of GT is assumed as a primary criterion, and the variations of the current values of  $B_e$  due to TIC are taken into account by the rate of the annual increment as its value  $\Sigma B_e/Q_0$  related to required refrigeration capacity  $Q_0$ .

The maximum rate of annual fuel saving  $\Sigma B_e/Q_0$  and minimum sizes of the chillers is achieved at the optimum value of design refrigeration capacity  $Q_{0,opt}$ .

The hypothesis of reducing a design boost refrigeration capacity  $Q_{0,b10-15}$  or  $Q_{0,15rat}$  of ACh to  $Q_{0,b10-20}$  or  $Q_{0,20rat}$ , id est. practically twice has been approved.

### References

1. Tahaineh, H.: Cooling of compressor Air inlet of a gas turbine power plant using ammonia-water vapor absorption system. *Int. J. Energy Eng.* **3**(5), 267–271 (2013)
2. Barreto, D., Fajardo, J., Carrillo Caballero, G., Cardenas Escorcía, Y.: Advanced exergy and exergoeconomic analysis of a gas power system with steam injection and air cooling with a compression refrigeration machine. *Energy Technol.* **9**(5), 2000993 <https://doi.org/10.1002/ente.202000993>
3. Zhu, G., Chow, T.-T., Lee, C.-K. Performance analysis of biogas-fueled Maisotsenko combustion turbine cycle. *Appl. Thermal Eng.* **195**, 117247 <https://doi.org/10.1016/j.applthermaleng.2021.117247>





4. Elberry, M., Elsayed, A., Teamah, M., Abdel-Rahman, A., Elsafty, A.: Performance improvement of power plants using absorption cooling system. *Alex. Eng. J.* **57**, 2679–2686 (2018)
5. Ehyaei, M.A., Hakimzadeh, S., Enadi, N., Ahmadi, P.: Exergy, economic and environment (3E) analysis of absorption chiller inlet air cooler used in gas turbine power plants. *Int. J. Energy Res.* **36**, 486–498 (2011)
6. Andi, B., Venkatesan, J., Suresh, S., Mariappan, V.: Experimental analysis of triple fluid vapour absorption refrigeration system driven by electrical energy and engine waste heat. *Therm. Sci.* **23**, 2995–3001 (2019)
7. Radchenko, A., Stachel, A., Forduy, S., Portnoi, B., Rizun, O.: Analysis of the efficiency of engine inlet air chilling unit with cooling towers. In: Ivanov, V., Pavlenko, I., Liaposhchenko, O., Machado, J., Edl, M. (eds.) *DSMIE 2020*. LNME, pp. 322–331. Springer, Cham (2020). [https://doi.org/10.1007/978-3-030-50491-5\\_31](https://doi.org/10.1007/978-3-030-50491-5_31)
8. Radchenko, A., Trushliakov, E., Tkachenko, V., Portnoi, B., Prjadko, A.: Improvement of the refrigeration capacity utilizing for the ambient air conditioning system. In: Tonkonogyi, V., et al. (eds.) *InterPartner 2020*. LNME, pp. 714–723. Springer, Cham (2021). [https://doi.org/10.1007/978-3-030-68014-5\\_69](https://doi.org/10.1007/978-3-030-68014-5_69)
9. Bohdal, T., Kuczynski, W.: Boiling of R404A refrigeration medium under the conditions of periodically generated disturbances. *Heat Transf. Eng.* **32**, 359–368 (2011)
10. Mikielewicz, D., Klugmann, M., Wajs, J.: Flow boiling intensification in minichannels by means of mechanical flow turbulising inserts. *Int. J. Therm. Sci.* **65**, 79–91 (2013)
11. Kornienko, V., Radchenko, R., Stachel, A., Andreev, A., Pyrysunko, M.: Correlations for pollution on condensing surfaces of exhaust gas boilers with water-fuel emulsion combustion. In: Tonkonogyi, V., et al. (eds.) *Advanced Manufacturing Processes*. InterPartner-2019. LNME, pp. 530–539. Springer, Cham (2020). [https://doi.org/10.1007/978-3-030-40724-7\\_54](https://doi.org/10.1007/978-3-030-40724-7_54)
12. Radchenko, R., Pyrysunko, M., Kornienko, V., Scurtu, Ionut-C., Patyk, R.: Improving the ecological and energy efficiency of internal combustion engines by ejector chiller using recirculation gas heat. In: Nechyporuk, M., Pavlikov, V., Kritskiy, D. (eds.) *ICTM 2020*. LNNS, vol. 188, pp. 531–541. Springer, Cham (2021). [https://doi.org/10.1007/978-3-030-66717-7\\_45](https://doi.org/10.1007/978-3-030-66717-7_45)
13. Rodriguez-Aumente, P.A., Rodriguez-Hidalgo, M.C., Nogueira, J.I., Lecuona, A., Venegas, M.C.: District heating and cooling for business buildings in Madrid. *Appl. Therm. Eng.* **50**, 1496–1503 (2013)
14. Butrymowicz, D., et al.: Investigations of prototype ejection refrigeration system driven by low grade heat. In: *HTRSE-2018, E3S Web of Conferences*, vol. 70, 7 p. (2018)
15. Kornienko, V., Radchenko, R., Mikielewicz, D., Pyrysunko, M., Andreev, A.: Improvement of characteristics of water-fuel rotary cup atomizer in a boiler. In: Tonkonogyi, V., et al. (eds.) *InterPartner 2020*. LNME, pp. 664–674. Springer, Cham (2021). [https://doi.org/10.1007/978-3-030-68014-5\\_64](https://doi.org/10.1007/978-3-030-68014-5_64)
16. Radchenko, M., Radchenko, A., Radchenko, R., Kantor, S., Konovalov, D., Kornienko, V.: Rational loads of turbine inlet air absorption-ejector cooling systems. In: *Proceedings of the Institution of Mechanical Engineers, Part A: Journal of Power and Energy* (2021). <https://doi.org/10.1177/09576509211045455>
17. Konovalov, D., Kobalava, H., Radchenko, M., Sviridov, V., Scurtu, I.C.: Optimal sizing of the evaporation chamber in the low-flow aerothermopressor for a combustion engine. In: Tonkonogyi, V., et al. (eds.) *InterPartner 2020*. LNME, pp. 654–663. Springer, Cham (2021). [https://doi.org/10.1007/978-3-030-68014-5\\_63](https://doi.org/10.1007/978-3-030-68014-5_63)

18. Radchenko, M., Mikielewicz, D., Andreev, A., Vanyeyev, S., Savenkov, O.: Efficient ship engine cyclic air cooling by turboexpander chiller for tropical climatic conditions. In: Nechyporuk, M., Pavlikov, V., Kritskiy, D. (eds.) *Integrated Computer Technologies in Mechanical Engineering - 2020. ICTM 2020. LNNS*, vol. 188, pp. 498–507. Springer, Cham (2021). [https://doi.org/10.1007/978-3-030-66717-7\\_42](https://doi.org/10.1007/978-3-030-66717-7_42)
19. Konovalov, D., Kobalava, H., Maksymov, V., Radchenko, R., Avdeev, M.: Experimental research of the excessive water Injection effect on resistances in the flow part of a low-flow aerothermopressor. In: Ivanov, V., Pavlenko, I., Liaposhchenko, Oleksandr, Machado, J., Edl, M. (eds.) *DSMIE 2020. LNME*, pp. 292–301. Springer, Cham (2020). [https://doi.org/10.1007/978-3-030-50491-5\\_28](https://doi.org/10.1007/978-3-030-50491-5_28)
20. Bohdal, Ł., Kukielka, L., Radchenko, A.M., Patyk, R., Kułakowski, M., Chodór, J.: Modelling of guillotining process of grain oriented silicon steel using FEM. In: *AIP Conference Proceeding*, vol. 2078, p. 020080 (2019)
21. Bohdal, Ł., Kukielka, L., Legutko, S., Patyk, R., Radchenko, A.M.: Modeling and experimental research of shear-slitting of AA6111-T4 aluminum alloy sheet. *Materials* **13**(14), 3175 (2020)
22. Bohdal, Ł., Kukielka, L., Świłło, S., Radchenko, A.M., Kułakowska, A.: Modelling and experimental analysis of shear-slitting process of light metal alloys using FEM, SPH and vision-based methods. In: *AIP Conference Proceedings*, vol. 2078, p. 020060 (2019)
23. Cardona, E., Piacentino, A.: A methodology for sizing a trigeneration plant in mediterranean areas. *Appl. Therm. Eng.* **23**, 15 (2003)
24. Lozano, M.A., Ramos, J.C., Serra, L.M.: Cost optimization of the design of CHCP (combined heat, cooling and power) systems under legal constraints. *Energy* **35**, 794–805 (2010)
25. Radchenko, M., Mikielewicz, D., Tkachenko, V., Klugmann, M., Andreev, A.: Enhancement of the operation efficiency of the transport air conditioning system. In: Ivanov, V., Pavlenko, I., Liaposhchenko, O., Machado, J., Edl, M. (eds.) *Advances in Design, Simulation and Manufacturing III. DSMIE 2020. LNME*, pp. 332–342. Springer, Cham (2020). [https://doi.org/10.1007/978-3-030-50491-5\\_32](https://doi.org/10.1007/978-3-030-50491-5_32)
26. Kalhori, S.B., Rabiei, H., Mansoori, Z.: Mashad trigeneration potential—an opportunity for CO<sub>2</sub> abatement in Iran. *Energy Conv. Manag.* **60**, 106–114 (2012)
27. Oktay, Z., Coskun, C., Dincer, I.: A new approach for predicting cooling degree-hours and energy requirements in buildings. *Energy* **36**(8), 4855–4863 (2011)
28. Radchenko, A., Andreev, A., Konovalov, D., Qiang, Z., Zewei, L.: Analysis of ship main engine intake air cooling by ejector turbocompressor chillers on equatorial voyages. In: Nechyporuk, M., Pavlikov, V., Kritskiy, D. (eds.) *ICTM 2020. LNNS*, vol. 188, pp. 487–497. Springer, Cham (2021). [https://doi.org/10.1007/978-3-030-66717-7\\_41](https://doi.org/10.1007/978-3-030-66717-7_41)
29. Forsyth, J.L.: Gas turbine inlet air chilling for LNG. *IGT Int. Liquefied Nat. Gas Conf. Proc.* **3**, 1763–1778 (2013)
30. Kornienko, V., Radchenko, R., Konovalov, D., Andreev, A., Pyrynsunco, M.: Characteristics of the rotary cup atomizer used as afterburning installation in exhaust gas boiler flue. In: Ivanov, V., Pavlenko, I., Liaposhchenko, O., Machado, J., Edl, M. (eds.) *DSMIE 2020. LNME*, pp. 302–311. Springer, Cham (2020). [https://doi.org/10.1007/978-3-030-50491-5\\_29](https://doi.org/10.1007/978-3-030-50491-5_29)
31. Wajs, J., Mikielewicz, D., Jakubowska, B.: Performance of the domestic micro ORC equipped with the shell-and-tube condenser with minichannels. *Energy* **157**, 853–861 (2018)
32. Radchenko, R., Pyrynsunco, M., Kornienko, V., Andreev, A., Hrych, A.: Improvement of environmental and energy efficiency of marine engines by utilizing the ecological recirculation of gas heat in an absorption chiller. In: Tonkonogyi, V., Ivanov, V., Trojanowska, J., Oborskiy, G., Pavlenko, I. (eds.) *InterPartner 2021. LNME*, pp. 644–654. Springer, Cham (2022). [https://doi.org/10.1007/978-3-030-91327-4\\_62](https://doi.org/10.1007/978-3-030-91327-4_62)
33. Zhang, T., Liu, Z., Hao, H., Chang, L.J.: Application research of intake-air cooling technologies in gas-steam combined cycle power plants in China. *Power Energy Eng.* **2**, 304–311 (2014)

34. Kornienko, V., Radchenko, R., Bohdal, Ł, Kukielka, L., Legutko, S.: Investigation of condensing heating surfaces with reduced corrosion of boilers with water-fuel emulsion combustion. In: Nechyporuk, M., Pavlikov, V., Kritskiy, D. (eds.) ICTM 2020. LNNS, vol. 188, pp. 300–309. Springer, Cham (2021). [https://doi.org/10.1007/978-3-030-66717-7\\_25](https://doi.org/10.1007/978-3-030-66717-7_25)
35. Suamir, I.N., Tassou, S.A.: Performance evaluation of integrated trigeneration and CO<sub>2</sub> cooling systems. *Appl. Therm. Eng.* **50**(2), 1487–1495 (2013)
36. Shukla, A.K., Singh, O.: Thermodynamic investigation of parameters affecting the execution of steam injected cooled gas turbine based combined cycle power plant with vapor absorption inlet air cooling. *Appl. Therm. Eng.* **122**, 380–388 (2017)
37. Shukla, A.K., Sharma, A., Sharma, M., Mishra, S.: Performance improvement of simple gas turbine cycle with vapor compression inlet air cooling. *Mater. Today Proc.* **5**(9) Part 3, 19172–19180 (2018) <https://doi.org/10.1016/j.matpr.2018.06.272>
38. Kornienko, V., Radchenko, R., Bohdal, T., Radchenko, M., Andreev, A.: Thermal characteristics of the wet pollution layer on condensing heating surfaces of exhaust gas boilers. In: Ivanov, V., Pavlenko, I., Liaposhchenko, O., Machado, J., Edl, M. (eds.) DSMIE 2021. LNME, pp. 339–348. Springer, Cham (2021). [https://doi.org/10.1007/978-3-030-77823-1\\_34](https://doi.org/10.1007/978-3-030-77823-1_34)
39. Rocha, M.S., Andreos, R., Simões-Moreira, J.R.: Performance tests of two small trigeneration pilot plants. *Appl. Therm. Eng.* **41**, 84–91 (2012)
40. Gas turbine electrical stations. Nikolaev: Zorya-Mashproject, 16 p. (2007)



# Jet-Reactive Turbine Circular Efficiency

Tetiana Rodymchenko<sup>1</sup> (✉) , Serhii Vanieiev<sup>1</sup> , Stanislav Meleychuk<sup>1</sup> ,  
Michal Hatala<sup>2</sup> , and Olha Miroshnychenko<sup>1</sup> 

<sup>1</sup> Sumy State University, 2, Rymskogo-Korsakova Street, Sumy 40007, Ukraine  
t.rodymchenko@kttf.sumdu.edu.ua

<sup>2</sup> Technical University of Kosice, 1, Bayerova Street, Presov 08001, Slovak Republic

**Abstract.** The Ukrainian power generation industry is a fundamental branch for developing the state economy and keeping its sovereignty. A significant problem is the reasonable use of Earth's power resources today. Ukraine has been trying to resolve this issue, which is proved by the implemented program "Safety, Energy Performance, Competitiveness (the Ukrainian Power Strategy till 2035)". It provides a shift from the old energy industry model to the new one with a larger competitive space and opportunities to increase energy performance via renewable and alternative power sources. A sensible way to complete this task is waste energy recycling. Turbine-generator sets can decrease pressure and utilize potential energy of gas or steam pressure to produce electricity. It is another economic and technological challenge for Ukraine and the whole world. Simultaneously, that opens new prospects for introducing innovative projects. The article is devoted to studying gas-dynamic processes in jet-reactive turbine (JRT) flow ducts. The research assesses the off-design traction nozzle influence on the JRT circular efficiency. There are detected dependencies between circular efficiency and dimensionless velocity  $\lambda_{Wout,t}$  by certain feed-in nozzle inlet pressure during design ( $S = 1$ ) and off-design conditions ( $S > 1$ ). Diagrams of circular efficiency against blade wheel velocity ( $\bar{U} = 0 \dots 1$ ) are drawn. The research established that the feed-in nozzle inlet pressure rise causes the circular efficiency to fall. The efficiency optimum is defined by the blade wheel velocity for design and non-design circumstances. The highest efficiency is found by design traction nozzle operation ( $S = 1$ ).

**Keywords:** Energy efficiency · Jet-reactive turbine · Circular efficiency · Relative velocity · Absolute velocity · Moving moment · Gas mass flow · Characteristics · Sustainable development · Industrial growth

## 1 Introduction

Increasing power generation and consumption requires new science and technology changes for people's welfare. Industrial energy performance comprises a more reasonable use of all resources with significant environmental damage fall. Therefore, the proper application of energy performance and Earth power potential have always been top-priority questions. In particular, developed countries pay massive attention to financing projects of energy performance and correct compressed gas or steam use.

Many compressed gas and steam exergy are irreversibly lost in gas distribution stations' reduction gears and pressure regulators. An urgent way to settle this problem is waste energy recycling. Among promising solutions in energy performance, there is a creation of low-capacity turbo-expanders (up to 500 kW) based on jet-reactive turbines (JRT) to utilize compressed gas and steam energy. As usual, such sets are repaid for less than two years. These units allow producing environmentally friendly energy (mechanical energy on the turbine shaft or electricity from an electric generator) in contrast to classic gas turbine and steam turbine plants, which need to burn fuel to produce this energy, the combustion products of which pollute the environment. That is, we have energy-saving, environmentally friendly technology that meets sustainable development goals [1].

## 2 Literature Review

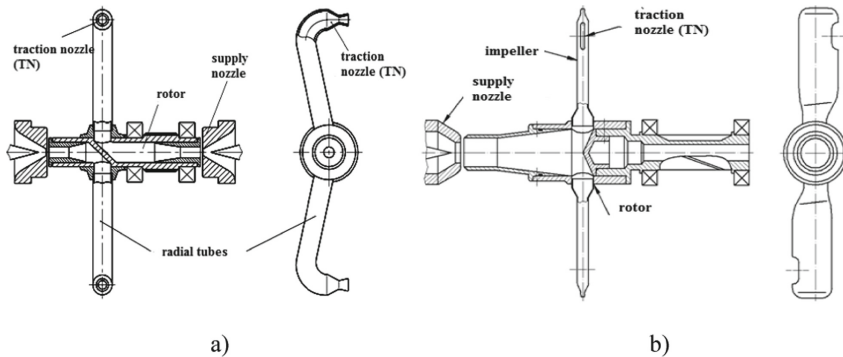
In our previous publications, we stated that the essential task of the modern gas transit branch is constructing a reliable and serviceable pneumatic drive for safe gas pipeline operations. More information on the safe [2] and effective run of gas turbines and their engines may be read in materials [3].

Those studies stress the current research topicality [4, 5].

The research object is JRT operation processes.

The research subject is the description of JRT features and characteristics.

JRTs are principally not popular in use because their design and internal flow are not sufficiently learned [6]. In our previous papers, the internal turbine flow was explained in detail. There is a foreign experience on this topic [7, 8]. Gas flow models of such machines significantly differ from our JRT operations (Fig. 1).



**Fig. 1.** JRT structure: reversible (a) and irreversible (b).

Also, there are several research works in ensuring the energy efficiency of rotary machines. Particularly, analytical and practical approaches for condition monitoring and vibro-diagnostics of turbines are presented in [9].

Ways for increasing the load capacity of bearings and impulse end seals are proposed in [10] and [11], respectively. Also, different algorithms for ensuring real power loss

reduction have been developed in [12, 13]. Moreover, numerical methods for ensuring vibration reliability of turbopump units using artificial neural networks are proposed in [14, 15].

Overall, according to the thorough analysis of recent studies in the design and calculation of rotary machines, their reliability, and energy efficiency, the paper aims to assess the influence of different factors on the circular turbine.

### 3 Research Methodology

The JRT circular efficiency ( $\eta_U$ ) is calculated as:

$$\eta_U = \frac{h_U}{h_s} = \frac{N_U}{G_t h_s} = \frac{M_U \omega_T}{G_t h_s} = \frac{2U_{out,t} M_U}{LC_s^2 G_t} = \frac{2\bar{U} M_U}{LC_s G_t} \quad (1)$$

$h_U$  - 1 kg of gas work in the traction nozzle (Euler work).  $h_s$  - 1 kg of gas work by isentropic expansion from inlet parameters to environment pressure.  $M_U$  - moving moment.  $N_U$  - capacity for  $M_U$ .  $\omega_T$  - turbine shaft revolution velocity.  $G_t$  - gas mass flow through the traction nozzle.  $C_s$  - velocity for isentropic work  $h_s'$  ( $C_s = \sqrt{2h_s}$ ).  $L$  - distance from the JRT axis to the traction nozzle section center.  $U_{out,t}$  - blade wheel circular velocity in the traction nozzle section center.  $\bar{U}$  - indicated blade wheel circular velocity ( $\bar{U} = U/C_s$ ).

Within this JRT design (Fig. 1), gas mass flow through the traction nozzle  $G_t$ , in case of no leak, is equal to gas mass flow through the feed-in nozzle  $G_{in}$ .

Moving moment is measured as [16].

$$M_U = [G_t C_{out,t} + f_{out,t}(p_{out,t} - p_{a,p})]L = [G_{in} C_{out,t} + f_{out,t} p_{a,p}(S - 1)]L \quad (2)$$

$C_{out,t}$ ,  $p_{out,t}$ ,  $f_{out,t}$  - absolute velocity, static pressure, and gas flow square in the traction nozzle section.  $p_{a,p}$  - environment pressure (when gas leaves the traction nozzle).  $S$  - off-design traction nozzle degree (ratio between traction nozzle section pressure and environment pressure ( $S = p_{out,t}/p_{a,p}$ )).

Subsequently, we have:

$$\eta_U = \frac{2\bar{U}[G_{in} C_{out,t} + f_{out,t} p_{a,p}(S - 1)]}{C_s G_{in}} \quad (3)$$

For the JRT design run ( $S = 1$ ), the equation is:

$$\eta_U = \frac{2\bar{U}[G_{in} C_{out,t} + f_{out,t} p_{a,p}(S - 1)]}{C_s G_{in}} = 2\bar{U} \frac{C_{out,t}}{C_s} \quad (4)$$

Gas flow velocity in the traction nozzle section (absolute and relative) is interpreted via the equation:

$$C_{out,t} = W_{out,t} - U_{out,t} \quad (5)$$

$W_{out,t}$  - gas flow velocity in the traction nozzle section (relative).

The dependence  $W_{out,t} = f(U_{out,t})$  is revealed as.

$$W_{out,t} = \lambda_{Wout,t} \sqrt{a_{kr}^2 + \frac{k-1}{k+1} U_{out,t}^2} \quad (6)$$

$a_{kr}$  – gas flow critical velocity in the feed-in nozzle.;  $\lambda_{Wout,t}$  – dimensionless gas flow velocity in the traction nozzle section (relative). It depends on the traction nozzle off-design and JRT power loss:

$$\lambda_{Wout,t} = \sqrt{\frac{k+1}{k-1} \left[ 1 - \left( \frac{p_{out,t}}{p_{Wout,t}^*} \right)^{\frac{k-1}{k}} \right]} = \sqrt{\frac{k+1}{k-1} \left[ 1 - \left( \frac{P_a p S}{\sigma p_{in}^*} \right)^{\frac{k-1}{k}} \right]} \quad (7)$$

$k$  – gas isentrope coefficient.  $\sigma$  – JRT total pressure recovery coefficient (from the feed-in nozzle inlet to the traction nozzle outlet).  $p_{Wout,t}^*$  – inhibited flow pressure in the traction nozzle section.  $p_{in}^*$  – inhibited flow pressure in the JRT inlet.

Accordingly, we have:

$$\begin{aligned} \eta_U &= \frac{2\bar{U} [G_{in}(W_{out,t} - U_{out,t}) + f_{out,t} P_a p (S - 1)]}{C_s G_{in}} \\ &= 2\bar{U} \left[ \lambda_{Wout,t} \sqrt{\frac{a_{kr}^2}{C_s^2} + \frac{k-1}{k+1} \bar{U}^2} - \bar{U} + \frac{f_{out,t} P_a p (S - 1)}{C_s G_{in}} \right] \end{aligned} \quad (8)$$

From the mass loss equation in the traction nozzle (TN)

$$G_t = \frac{p_{out,t} f_{out,t} \gamma (\lambda_{Wout,t})^k \beta_{kr}}{\alpha_{Wkr}} \quad (9)$$

the equation to measure the traction nozzle section square is obtained

$$f_{out,t} = \frac{G_t \alpha_{Wkr}}{p_{out,t} \gamma (\lambda_{Wout,t})^k \beta_{kr}} \quad (10)$$

$\beta_{kr}$  – critical pressure ratio:  $\beta_{kr} = \left( \frac{2}{k+1} \right)^{\frac{k}{k-1}}$ .  $\alpha_{Wkr}$  – gas flow critical velocity in the traction nozzle (relative):

$$\begin{aligned} \alpha_{Wkr} &= \sqrt{\frac{2k}{k+1} R T_{Wout,t}^*} \\ &= \sqrt{\frac{2k}{k+1} R \left[ T_{in}^* + \frac{U_{out,t}^2 (k-1)}{2kR} \right]} = \sqrt{a_{kr}^2 + \frac{k-1}{k+1} U_{out,t}^2} \end{aligned} \quad (11)$$

$T_{Wout,t}^*$  – inhibited gas flow temperature in the TN.;  $T_{in}^*$  – inhibited gas flow temperature in the JRT inlet.

Then, the circular efficiency equation is regarded as:

$$\begin{aligned} \eta_U &= 2\bar{U} \left[ \lambda_{W_{out,t}} \sqrt{\frac{a_{kr}^2}{C_s^2} + \frac{k-1}{k+1} \bar{U}^2} - \bar{U} + \frac{(S-1)}{Sy(\lambda_{out,t})k\beta_{kr}} \sqrt{\frac{a_{kr}^2}{C_s^2} + \frac{k-1}{k+1} \bar{U}^2} \right] \\ &= 2\bar{U} \left[ \sqrt{\frac{a_{kr}^2}{C_s^2} + \frac{k-1}{k+1} \bar{U}^2} \left( \lambda_{W_{out,t}} + \frac{S-1}{Sy(\lambda_{out,t})k\beta_{kr}} \right) - \bar{U} \right] \end{aligned} \tag{12}$$

The JRT circular efficiency includes energy losses during gas duct friction, wave losses (sealing leaps), and losses with the outlet velocity.

As a research result, the preliminary JRT shaft efficiency calculation may be done via a simpler velocity value:  $C_{d.t.s=0}$  instead of  $W_{out,t}$  ( $C_{d.t.s=0}$  – gas flow velocity of the traction nozzle section in the starting mode). The formula that shows the relation between relative gas flow velocity of the traction nozzle section and gas flow velocity of the traction nozzle section in the starting mode:

$$W_{out,t} = \lambda_{W_{out,t}} \sqrt{a_{kr}^2 + \frac{k-1}{k+1} U_{out,t}^2} = C_{d.t.s=0} \sqrt{1 + \frac{k-1}{2kRT_n^*} U_{out,t}^2} \tag{13}$$

Formula (13) states that the higher the circular velocity  $U$  is, the more significant difference is between gas flow relative velocity of the traction section and gas flow velocity of the traction nozzle section in the starting mode.

In previous studies, one of the JRT dimensionless coefficients has been discussed. It is a gas-dynamic traction nozzle off-design  $S$ . That measures static pressure of the traction nozzle concerning environment pressure, which is taken from rocket engine theory.

### 4 Results

In case the difference between  $W_{out,t}$  and  $C_{d.t.s=0}$  is neglected, the JRT circular efficiency formula for design traction nozzle operation  $S = 1$  can be written as:

$$\eta_U = 2\bar{U} \left[ \lambda_{W_{out,t}} \frac{a_{kr}}{C_s} - \bar{U} \right] \tag{14}$$

Within Eq. (14),  $\lambda_{W_{out,t}}$  is calculated by Eq. (7) when  $S = 1$ .

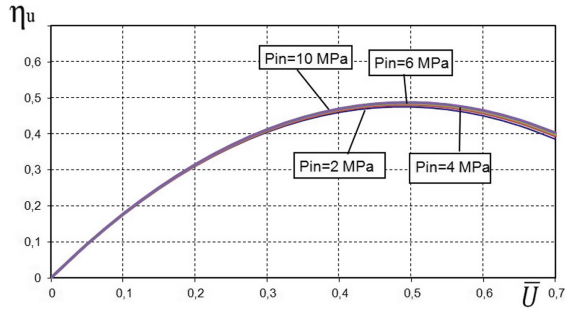
Dependence “operating space – air” according to formula (14) is indicated by Fig. 2.

Analysis of the Fig. 1 diagram concludes that the same circular velocity increases efficiency within JRT inlet pressure change. The highest efficiency value (by the inlet pressure 2 MPa and 10 MPa) is 47% and 49%, respectively.

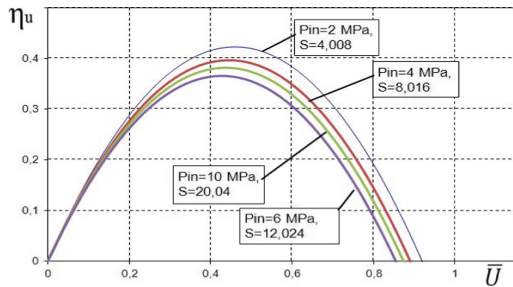
The JRT circular efficiency formula for the off-design mode when the traction nozzle off-design degree is  $S > 1$  with no including the difference between  $W_{out,t}$  and  $C_{d.t.s=0}$  ( $W_{out,t} = C_{d.t.s=0}$ ):

$$\eta_U = 2\bar{U} \left[ \frac{a_{kr}}{C_s} \left( \lambda_{W_{out,t}} + \frac{S-1}{Sy(\lambda_{out,t})k\beta_{kr}} \right) - \bar{U} \right] \tag{15}$$





**Fig. 2.** Dependence of design circular efficiency change on circular velocity ( $W_{out,t} = C_{d,t,s=0}$ ); inlet pressure  $P_{in} = 2; 4; 6; 10$  MPa.



**Fig. 3.** Dependence of off-design circular efficiency change on circular velocity  $W_{out,t} = C_{d,t,s=0}$ ; inlet pressure  $P_{in} = 2; 4; 6; 10$  MPa.

Figure 3 reveals dependences as to formula (9) at  $\lambda_{W_{out,t}} = 1, 4$ .

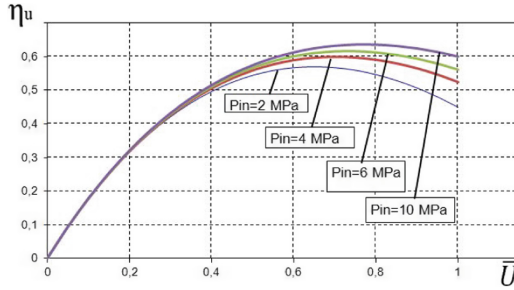
Comparison of Figs. 2 and 3 clarifies the exact influence of the traction nozzle off-design degree on the JRT efficiency by  $W_{out,t} = C_{d,t,s=0}$ : higher feed-in nozzle inlet pressure decreases the off-design efficiency ( $S > 1$ ) (Fig. 3). For Fig. 2, the design pressure change influence is minimal while the optimum efficiency shifts to the circular velocity rise. The most significant design efficiency value is about 50%. According to Fig. 3, the efficiency optimum with an inlet pressure of 2–10 MPa shifts within the circular velocity of 0,4–0,43. The maximal efficiency is 42% at 2 MPa.

The JRT off-design efficiency ( $S = 1$ ) with the difference between  $W_{out,t}$  and  $C_{d,t,s=0}$  concerning Eq. (12):

$$\eta_U = 2\bar{U} \left[ \lambda_{W_{out,t}} \sqrt{\frac{a_{kr}^2}{C_s^2} + \frac{k-1}{k+1} \bar{U}^2} - \bar{U} \right] \tag{16}$$

Figure 4 illustrates dependence as to formula (16) where  $\lambda_{W_{out,t}}$  is defined via formula (7).

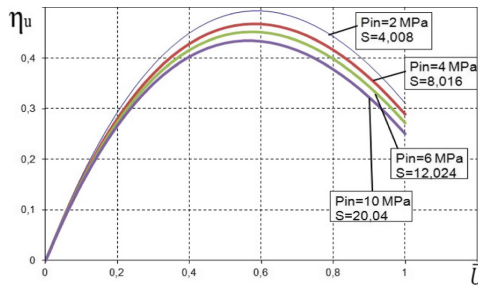
Figures 2 and 4 reveal that the higher relative velocity of the traction nozzle section affects circular efficiency (thanks to the compressor effect during JRT blade wheel revolutions) compared to starting mode leak velocity according to the formula (13). Within



**Fig. 4.** Dependence of design circular efficiency change on circular velocity ( $W_{out.t} > C_{d.t.s=0}$ ); inlet pressure  $P_{in} = 2; 4; 6; 10$  MPa.

the given JRT inlet pressure variations, the maximal circular efficiency is 11–16% higher than the Fig. 2 dependence. Such a value is reached with blade wheel velocity of 0,65–0,8 while the efficiency top shifts to a more significant circular velocity. Therefore, the compressor effect influence on the circular efficiency is significant (in contrast to JRT shaft efficiency, whose maximum with the same pressure changes by 1–5% and is kept when blade wheel velocity is 0,25–0,40 [17]).

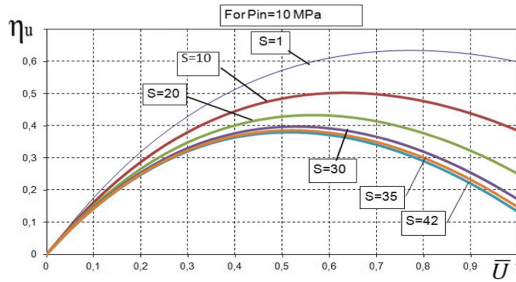
Figure 5 shows dependence as to formula (12) with  $\lambda_{Wout.t} = 1, 4$ . Review of Figs. 3 and 5 detects that higher relative velocity of the traction nozzle section affects circular efficiency in contrast to the starting mode for the off-design JRT run at  $\lambda_{Wout.t} = 1, 4$ : efficiency rises by about 8%. In contrast to the design JRT mode, circular efficiency fell by about 12% (Fig. 4). Efficiency tops are indicated in Figs. 3 and 5 with a circular velocity of 0,47 ... 0,5. Analyzing these diagrams provides an opportunity to assess off-design degrees on the JRT efficiency.



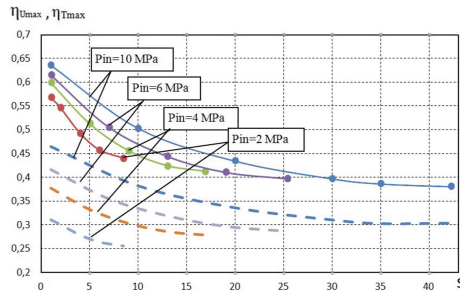
**Fig. 5.** Dependence of off-design circular efficiency change on circular velocity ( $W_{out.t} > C_{d.t.s=0}$ ); inlet pressure  $P_{in} = 2; 4; 6; 10$  MPa.

In Fig. 6, there is the dependence of circular efficiency change on circular velocity during the design and off-design JRT modes (inlet pressure  $P_{in} = 2; 4; 6; 10$  MPa). According to the diagram, when  $S = 1$ , efficiency is the highest. The most significant value for 10 MPa is traced with  $S = 42$  (respectively,  $\lambda_{Wout.t} = 1$ ). Through similar calculations, we drew diagrams for  $P_{in} = 2; 4; 6$  MPa.

The obtained Fig. 6 dependence reproduced a Fig. 7 diagram. It shows the change of design and off-design circular efficiency top values concerning the traction nozzle off-design degree (with corresponding inlet pressure). Also, a diagram of turbine shaft efficiency maximum is represented [17]. It clarifies that the highest efficiency is at  $S = 1$ . Solid lines stand for circular efficiency dependences. Dash lines imply shaft efficiency.

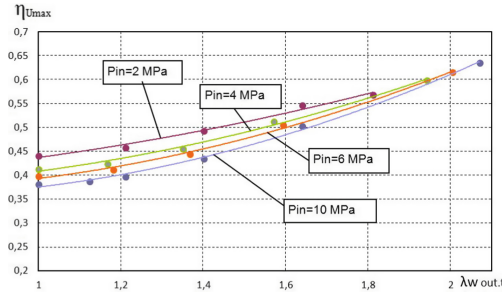


**Fig. 6.** Dependence of circular efficiency change on circular velocity during the design and off-design JRT modes ( $\lambda W_{out,t} > C_{d,t,s=0}$ ); inlet pressure  $P_{in} = 10$  MPa; different values of traction nozzle off-design degrees.



**Fig. 7.** Dependence of top design and off-design circular efficiency change on the traction nozzle off-design degree; inlet pressure  $P_{in} = 2; 4; 6; 10$  MPa (solid lines – circular efficiency; dash lines – JRT shaft efficiency).

Figure 8 indicates the dependence of top design (the right extreme points) and off-design circular efficiency change on the dimensionless gas flow velocity in the traction nozzle section. That is calculated via formula 7 for each specific value of the traction nozzle off-design degree. Efficiency rises when  $\lambda W_{out,t} = 1$  is kept for each pressure value (the off-design degree is the highest), and if  $\lambda W_{out,t}$  increases. Thus, the most significant efficiency is traced at  $S = 1$ .



**Fig. 8.** Dependence of top off-design circular efficiency change on the dimensionless gas flow velocity in the traction nozzle section; inlet pressure  $P_{in} = 2; 4; 6; 10$  MPa.

### 5 Conclusions

We derived JRT circular efficiency formulas for:

- more general case, for the off-design mode of operation of the JRT in the course of rotation of unexpanded sound and supersonic jet from the traction nozzle (static pressure in the outlet section of the traction nozzle more than ambient pressure, the degree off-design mode  $S > 1$ ) and taking into account the difference between flow velocities at the exit from the traction nozzle in relative motion and in start-up mode ( $W_{out,t} > C_{d.ts} = 0$ );
- the off-design mode (the degree off-design mode  $S > 1$ ) and without taking into account the difference between flow velocities at the exit from the traction nozzle in relative motion and in start-up mode  $W_{out,t} = C_{d.t.s=0}$ ;
- the design mode of operation of the traction nozzle (static pressure in the outlet section of the traction nozzle is equal to the ambient pressure, the degree off-design mode  $S = 1$ ) and taking into account the difference between flow velocities at the exit from the traction nozzle in relative motion and in start-up mode ( $W_{out,t} > C_{d.ts} = 0$ );
- the design mode ( $S = 1$ ) and without considering the difference between flow velocities at the exit from the traction nozzle in relative motion and in start-up mode  $W_{out,t} = C_{d.t.s=0}$ .

According to the obtained formulas, the graphical dependences of top JRT circular efficiencies on the given circular velocities of the impeller at different values of the inlet pressure in the JRT in the range from 2 to 10 MPa and their analysis. It is established that:

- maximum values of circular efficiency (56–63% depending on the gas pressure at the inlet to the leading nozzle) are achieved at much higher values of the reduced circular velocities of the impeller ( $\bar{U} = 0,65-0,8$ ) than the value of the efficiency on the turbine shaft (30–46% at  $\bar{U} = 0,25-0,45$  [17]) therefore, when calculating the circular efficiency, it is necessary to take into account the difference between the flow velocities at the outlet of the traction nozzle in relative motion and on the starting mode;

- the efficiency optimum proved to shift to higher blade wheel circular velocity (for the design and off-design modes).

There are drawn and interpreted diagrams of the top JRT circular and shaft efficiencies the degree off-design mode  $S$  and from the dimensionless gas flow rate at the section of the traction nozzle  $\lambda_{out,t}$  at different values of the inlet pressure in the JRT in the range from 2 to 10 MPa. It was found that for each set value of the pressure at the inlet to the turbine at  $\lambda_{out,t} = 1$ , when the degree of miscalculation of the traction nozzle becomes the largest value, the maximum efficiency has the lowest values and increases with increasing  $\lambda_{out,t}$  and acquire the most significant values in the design mode of operation of the traction nozzle at  $S = 1$ .

**Acknowledgment.** The results have been obtained within the project “Fulfillment of tasks of the perspective plan of development of a scientific direction “Technical sciences” Sumy State University” funded by the Ministry of Education and Science of Ukraine (State reg. no. 0121U112684). The research was partially supported by the Research and Educational Center for Industrial Engineering (Sumy State University) and International Association for Technological Development and Innovations.







## References

1. Varela, M.L.R., Putnik, G.D., Manupati, V.K., Rajyalakshmi, G., Trojanowska, J., Machado, J.: Integrated process planning and scheduling in networked manufacturing systems for I4.0: a review and framework proposal. *Wirel. Netw.* **27**(3), 1587–1599 (2019). <https://doi.org/10.1007/s11276-019-02082-8>
2. Garner, S., Ibrahim, Z.: Gas turbine common issues, failure investigations, root cause analyses, and preventative actions. In: Proceedings of the ASME 2016 Power Conference collocated with the ASME 2016. 10th International Conference on Energy Sustainability and the ASME 2016. 14th International Conference on Fuel Cell Science, Engineering and Technology. ASME 2016 Power Conference, pp. V001T02A007. ASME, Charlotte (2016). <https://doi.org/10.1115/POWER2016-59352>
3. Oyegoke, T., Akanji, I.I., Ajayi, O.O., Obajulu, E.A., Abemi, A.O.: Thermodynamic and economic evaluation of gas turbine power plants. *J. Eng. Sci.* **7**(1), G1–G8 (2020). [https://doi.org/10.21272/jes.2020.7\(g1\)](https://doi.org/10.21272/jes.2020.7(g1))
4. Utschick, M., Eiringhaus, D., Köhler, C., Sattelmayer, T.: Predicting flashback limits of a gas turbine model combustor based on velocity and fuel concentration for H<sub>2</sub>-air mixtures. *J. Eng. Gas Turbines Power* **139**(4), 0415021 (2017). <https://doi.org/10.1115/1.4034646>
5. Anderson, W.S., Polanka, M.D., Zelina, J., Evans, D.S., Stouffer, S.D., Justinger, G.R.: Effects of a reacting cross-stream on turbine film cooling. *J. Eng. Gas Turbines Power* **132**(5), 051501 (2010). <https://doi.org/10.1115/1.3204616>
6. Badami, M.: Theoretical model with experimental validation of a regenerative blower for hydrogen recirculation in a PEM fuel cell system. *Energy Convers. Manage.* **51**, 553–560 (2010). <https://doi.org/10.1016/j.enconman.2009.10.022>
7. Zuo, W., Kang, S., Qiu, Y.-X., Chen, X.-M., Yu, C.-R.: Numerical simulation of the aerodynamic performance of H type wind turbine. *Kung Cheng Je Wu Li Hsueh Pao. J. Eng. Thermophys.* **34**(8), 1462–1465 (2013)
8. Chen, X.-M., Kang, S., Zuo, W.: Research of yaw aerodynamic characteristic of horizontal-axis wind turbine based FlowVision. *J. Eng. Thermophys.* **35**, 1758–1761 (2014)

9. Monkova, K., et al.: Condition monitoring of Kaplan turbine bearings using vibro-diagnostics. *Int. J. Mech. Eng. Robot. Res.* **9**(8), 1182–1188. <https://doi.org/10.18178/ijmerr.9.8.1182-1188>
10. Martsinkovsky, V., Yurko, V., Tarel'nik, V., Filonenko, Y.: Designing thrust sliding bearings of high bearing capacity. *Procedia Eng.* **39**, 148–156 (2012). <https://doi.org/10.1016/j.proeng.2012.07.019>
11. Tarel'nik, V.B., Martsinkovskii, V.S., Zhukov, A.N.: Increase in the reliability and durability of metal impulse end seals Part 1. *Chem. Pet. Eng.* **53**(1–2), 114–120 (2017). <https://doi.org/10.1007/s10556-017-0305-y>
12. Kanagasabai, L.: Heat transfer and simulated coronary circulation system optimization algorithms for real power loss reduction. *J. Eng. Sci.* **8**(1), E1–E8 (2021). [https://doi.org/10.21272/jes.2021.8\(1\).e1](https://doi.org/10.21272/jes.2021.8(1).e1)
13. Kanagasabai, L.: Real power loss reduction by enhanced RBS algorithm. *J. Eng. Sci.* **8**(2), E1–E9. [https://doi.org/10.21272/jes.2021.8\(2\).e1](https://doi.org/10.21272/jes.2021.8(2).e1)
14. Pavlenko, I., Ivanov, V., Kuric, I., Gusak, O., Liaposhchenko, O.: Ensuring vibration reliability of turbopump units using artificial neural networks. In: Trojanowska, J., Ciszak, O., Machado, J.M., Pavlenko, I. (eds.) *MANUFACTURING 2019. LNME*, pp. 165–175. Springer, Cham (2019). [https://doi.org/10.1007/978-3-030-18715-6\\_14](https://doi.org/10.1007/978-3-030-18715-6_14)
15. Pavlenko, I., Trojanowska, J., Ivanov, V., Liaposhchenko, O.: Scientific and methodological approach for the identification of mathematical models of mechanical systems by using artificial neural networks. In: Machado, J., Soares, F., Veiga, G. (eds.) *HELIX 2018. LNEE*, vol. 505, pp. 299–306. Springer, Cham (2019). [https://doi.org/10.1007/978-3-319-91334-6\\_41](https://doi.org/10.1007/978-3-319-91334-6_41)
16. Vanyeyev, S.M., Meleychuk, S.S., Baga, V.N., Rodymchenko, T.S.: Investigation of the influence of gas pressure at the inlet in jet-reactive turbine on its performance indicators. *Probl. Reg. Energ.* **3**(38), 71–82 (2018). <https://doi.org/10.5281/zenodo.2222341>
17. Vaneev, S., Rodymchenko, T., Meleychuk, S., Baga, V., Bolotnikova, O.: Influence of the degree of off-design of the traction nozzle of a jet reaction turbine on its efficiency. *J. Phys. Conf. Ser.* **1741**(1) (2021). <https://doi.org/10.1088/1742-6596/1741/1/012004>



# Innovative Hybrid Power Plant Design

Lyudmila Rozhkova<sup>1</sup> , Marina Savchenko-Pererva<sup>1</sup> , Oleg Radchuk<sup>1</sup> ,  
Sergey Sabadash<sup>1</sup> , and Eduard Kuznetsov<sup>2</sup>  

<sup>1</sup> Sumy National Agrarian University, 160, Herasyima Kondratieva Street, Sumy 40021, Ukraine

<sup>2</sup> Sumy State University, 2, Rymaskogo-Korsakova Street, Sumy 40007, Ukraine

kuznetsov@opm.sumdu.edu.ua

**Abstract.** Currently, humanity is beginning to experience difficulties with unlimited energy consumption since there are fewer and fewer opportunities to increase capacity generation. The use of renewable energy sources is an effective method of solving the problem of shortage of energy sources. One way to do this is to develop a wind-solar power plant, called a “hybrid”, which simultaneously uses both wind and solar energy. For such a hybrid power plant, it is suggested to use a new type of medium-speed vertical axial wind power station, with a high utilization coefficient of wind energy and improved strength characteristics. Wind turbine models proposed for vertical axial wind power stations were tested in a wind tunnel. A comparison of the capacity of the specific vertical axial wind power station and the proposed wind turbine confirms the value of the wind utilization coefficient at the level of world samples with an average speed coefficient. The simultaneous working wind power station analysis and solar cells and energy utilization are performed. It is indicated that the feasibility and cost-effectiveness of solar cells should be analyzed in each specific case. Formulas for determining the amount of energy produced by a hybrid power station over a certain period are proposed.

**Keywords:** Energy efficiency · Industrial growth · Wind-solar power plant · Wind turbine · Solar cells

## 1 Introduction

Only sustainable development of humanity can ensure the further progress of life on Earth with the satisfaction of the needs of society while not threatening the ability to meet the needs of future generations [1]. Currently, humanity is limited in energy consumption because available generation capacity is insufficient. New energy technologies are not used globally, and their development leaves much to be desired. It should be noted that the existing energy transfer methods inhibit its uniform distribution. In addition to the high cost of equipment, the processes of long-range energy transmission lead to significant energy losses – according to some data, up to 20% of the amount of power generated [2]. Traditional energy (which uses fossil fuel and energy resources) threatens a stable climate and planet ecology. The main hazard is an increase in the atmosphere temperature and its pollution. Developed countries are elaborating new doctrines on fuel

and energy complexes, which provide for the global introduction of alternative energy sources, such as wind and solar [3].

The purpose of this study is to study the prospects of using vertical-axial wind turbines of medium speed with a new type of blades in a wind-solar power plant based on the results of studies of wind turbines models of proposed wind power plants and analysis of the features of the joint operation of the proposed wind power plant and solar cells with further use of energy.

## 2 Literature Review

It is known that now, one-third of the world's electricity is already generated by renewable energy sources, but the growing population of the planet and the need for energy until 2050 may cause an increase in the share of renewable energy sources to maintain climate stability [3]. Thus, researchers believe that we should completely abandon fossil fuels. Therefore, the priority direction for the electric power industry globally is renewable energy. Now the global market offers enough options for designing wind and solar power plants. However, both of them are obviously justified in certain climatic conditions. Both wind and solar energy have a significant drawback, namely time instability caused by both the time of the day and the time of the year. The peaks of electric power generation at solar and wind power plants occur at different times of the year and the day. In addition, factors such as the location latitude of solar radiation receivers, the time of year, and the daily irradiation play a determining role for the amount of solar energy produced [4]. The feasibility of solar cells should be analyzed in each specific case, depending on the location latitude, the range of changes in the angle of incidence of the directed radiation flow, the presence or absence of atmospheric pollution, and other climatic conditions. Currently, the maximum efficiency of solar energy conversion does not exceed 25% [5].

As for the wind as a renewable energy, many countries of the world are currently successfully developing this source of alternative energy. It is known that wind power station capacity is determined by the formula:

$$P = C_p \frac{\rho_a}{2} U_\infty^3 S. \quad (1)$$

where  $C_p$  is the wind energy utilization coefficient;  $U_\infty$  is the air density;  $U_\infty$  is the wind speed;  $S$  is the area of the axial section of the figure swept by the wind power station blades.

The wind speed  $U_\infty$  is unstable, its magnitude and direction change stochastically over time, which complicates the direct utilization of wind energy. Therefore, the problem of instability in time of both solar and wind energy needs to be solved in terms of reducing the ripples of the received energy at the output.

One of the ways to do so is to develop a wind-solar power plant, called "hybrid", which simultaneously uses both wind and solar energy. Hybrid wind-solar power plants may be preferable to independent solar and wind power plants, especially as the autonomous power supply for cottages, small farms, mini-enterprises of food industries, etc. The uninterrupted power supply from a centralized source is not fully guaranteed for various reasons. To ensure an uninterrupted power supply and a centralized



power system, it is advisable to use local low-powered autonomous power plants close to energy consumers. There are various methods and ways to choose a suitable location for installing wind turbines. One of the most common, using a Multifactorial method of analyzing the possibilities of wind power in the municipality of Knyazhevac (Eastern Serbia), is the unification of the process of analytical structuring and geo-information systems [6]. Geodata acquisition and processing included meteorological data from available sources, an electronic terrain model for analyzing terrain orography, and Landsat 8 satellite data for analyzing land cover. Finding optimal locations for wind turbines (wind farms) through multifactorial analysis using decision theory methods helped figure out how to choose the best places to invest and minimize the impact on the environment. The document [7] shows that such a source will be sufficient to meet the global needs for electricity and energy in its other forms. Special attention is paid to China and the United States of America – the world’s largest producers of greenhouse gases. Possible volumes of energy extraction from wind are discussed. Information on hybrid power plants offered on the market is sufficient. The report on the developed hybrid (wind-solar) electric system ECOSPECTR (ECOSPECTR Co. USA-Ukraine) is worth noticing. This system is designed to convert wind and solar energy into high-quality electricity for residential and small industrial facilities and sell surplus electricity to the central electrical grid at a “green tariff”. Analysis of information sources shows that in the combination of “wind turbine + solar cell”, traditional schemes of wind power stations with wind turbines having a horizontal axis position prevail. However, vertical axial wind power stations are also used, which is due to certain advantages in comparison with horizontal ones: vertical axial wind turbines do not require a change in positioning when the wind direction changes, energy conversion, and storage devices can be located on the ground, it is possible to connect the shaft of a wind power station directly to the shaft of any mechanical power device. In work [8], designs of modern small wind power stations offered on the global market are analyzed. The wind energy utilization coefficient  $C_p$  of most wind power stations does not exceed 0.3, along with their high cost.  $C_p$  of most wind power stations does not exceed 0.3, along with their high cost. Traditional blade systems are used for vertical axial wind turbines: Savona’s, with wing blades. The density of flows of both solar and wind energy is low. The energy supply is unstable, so ensuring a large and stable energy potential over time is associated with certain difficulties [9]. In the study [10], K. Eureka et al. offers the methodologies and assumptions used in developing robust estimates of global terrestrial and offshore wind technical potential. The global trends in the use of wind energy discussed in this document show that renewable energy technologies in common assessment models contribute to demonstrating growth and improvement. These studies help to more accurately determine the impact of renewable energy technologies on the global electricity sector. The methods of stimulating and attracting investors, the procedure for obtaining permits, social and scientific issues, the provision of data on green energy sources and regional production capacities, and support policies are discussed [11]. Possible obstacles to the placement of wind farms and possible ways to increase the received power are considered. The analysis and forecasting of economic development are evaluated, considering the prospects for the introduction of wind power facilities. In favorable developments, the amount of power received from wind could reach 10 GW by 2030. The hybrid wind-solar power plants,

to a certain extent, solve the problem of achieving the maximum possible stability. An analysis of simultaneous working wind power stations, solar cells, storage devices, and conversion devices shows that existing power generators often cannot provide the quality of output energy required by the consumer. Therefore, to increase the efficiency of wind and solar energy and meet the requirements of consumers regarding energy quality, it is necessary to improve existing power generators and create fundamentally new ones [12, 13]. Also, in [14], offshore wind turbines are described, which have a special type of structures that have not been tested by long-term tests or industrial operation. In this part, issues related to the development and adaptation of such turbines for use in the maritime territories of China are considered. The natural loads on the turbine typical for this region in conditions of the predominance of typhoons and earthquakes are considered. Attention is paid to loose and layered marine soil from the point of view of the successful installation of the turbine. The problems associated with the combined impact of the above factors are also indicated [15].

There are many designs of vertical-axial wind turbines in the world [16, 17]. A new type of vertical-axial wind turbines with original blades having an open aerofoil has been developed [12]. Power characteristic of wind turbines with such blades have shown that their speed ratio coefficient  $\theta$  is in the range from 1 to 3 (the so-called average speed ratio). Studies shows the presence of self-starting wind turbines, a fairly high utilization coefficient of wind energy and operation at both high and low wind speeds [18].

### 3 Research Methodology

#### 3.1 Key Research Results of the Wind Wheel Model with Original Blades of Medium Speed

The research was carried out at the aerodynamic stand of Sumy state university and the wind tunnel of National Aerospace University “Kharkiv Aviation Institute”. In the experiments the following parameters were measured: wind velocity, the torque on the propeller axis, the number of revolutions of the axis of the model propeller. Using obtained parameters, the wind energy utilization coefficient  $C_p$  and the power-speed coefficient  $\theta$  were determined using these formulas:

$$C_p = \frac{P}{P_f}. \quad (2)$$

where  $P$  is the shaft power of the wind wheel,  $P_f$  is the energy of the flow:

$$P_f = \frac{\rho_a}{2} U_\infty^3 S. \quad (3)$$

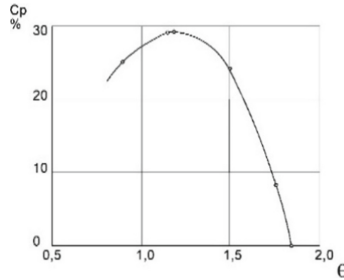
where  $\rho_a$  is the air density;  $U_\infty$  is the flow speed;  $S$  is the axial section area, swept by the blades of the wind power installation.

The average speed coefficient is according to the formula:

$$\theta = \frac{U_r}{U_\infty}. \quad (4)$$

where  $U_r$  is the blade speed,  $U_\infty$  is the flow speed.

As a result of the physical experiments carried out in the wind tunnel, the power characteristic of the wind turbine model with KN-M (KN-6) blades in the coordinates  $\theta - C_p$  is obtained, shown in Fig. 1. It should be noted that full-scale wind turbines may have a higher wind energy utilization coefficient  $C_p$ , compared to the model due to the scale effect [18].



**Fig. 1.** Characteristics of  $C_p = f(\theta)$  wind wheel with KN-M (KN-6) blades,  $i = 3$ .

Analysis of the power characteristic of vertical axial wind power installations shows that in general, the dependence curves  $C_p = f(\theta)$  maybe approximated by cubic (left branch) and quadratic (right branch of the characteristic) parabolas that have a common vertex at the point with the ordinate  $C_{p_{max}}$  (for  $\theta_{opt}$ ). As a result of this approximation, equations were obtained for calculating the left and right branches of the power characteristics of vertical axial wind power plants [14]:

- the left part of the power characteristic (power-speed coefficient area  $\theta < \theta_{opt}$ ):

$$C_p = C_{p_{max}} \left( \frac{\theta}{\theta_{opt}} \right)^2 \left[ 3 - 2 \left( \frac{\theta}{\theta_{opt}} \right) \right] \quad ; \quad (5)$$

- the right part of the power characteristic (power-speed coefficient area  $\theta_{opt} < \theta$ ):

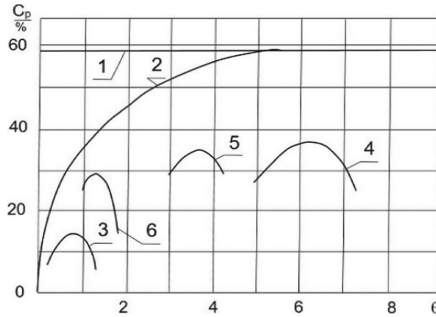
$$C_p = C_{p_{max}} - \frac{C_{p_{max}}}{(\theta_{max} - \theta_{opt})^2} (\theta - \theta_{opt})^2 = C_{p_{max}} \left[ 1 - \frac{(\theta - \theta_{opt})^2}{(\theta_{max} - \theta_{opt})^2} \right] \quad (6)$$

The results obtained in physical experiments on models of specific vertical axial wind turbines of average speed with KN-M (KN-6) blades showed that these equations are also valid for vertical axial wind power plants with original KN-M (KN-6) blades. Thus, based on the research of the wind wheel with KN-M blades ( $i = 3$ ),  $C_{p_{max}} = 29\%$ ;  $\theta_{opt} = 1.2$ ;  $\theta_{max} = 1.85$  [14], we obtain the following approximation formulas [6]:

- left part of power characteristic  $C_p = 20,14\theta^2(3 - 1,66\theta)$ ;
- right part of power characteristic  $C_p = 29 \left[ 1 - \frac{(\theta - 1,2)^2}{0,4225} \right]$ .

Obtained  $C_p$  values correspond to experimental findings. Tests of the wind turbine with the original KN-M blades showed the presence of self-starting.

The obtained experimental power characteristics of a vertical-axial wind turbine with original KN-M (KN-6) blades are compared with the Betz, Glauert criteria and the characteristics of known vertical-axial wind turbines [5], Fig. 2.



**Fig. 2.** Comparison of the power characteristics of vertical-axial wind power plants in accordance with the Betz (1) and Glauert's (2) criteria [19]; 3 – Savona's rotor [19]; 4 – Darrius wind power installation [19]; 5 – rotor with straight wing blades NACA0018 [16]; 6 – rotor with KN-M (KN-6) blades [18].

The comparison of characteristics shows that the  $C_p$  of a new type of wind turbine is high at average  $\theta$ . Since the value of the power speed coefficient  $\theta$  of a specific wind unit with KN-M blades is within 1...1.85, the circumferential speed of the blade and the number of revolutions of the shaft of the wind unit are small.

Thus, the operation of a medium-speed wind turbine is accompanied by a significant decrease in the centrifugal force on the blades compared to high-speed ones. The magnitude of the decrease depends on the ratio of the circumferential speeds of the blade with the same mass of the blades and the radius of rotation. This is certainly a positive effect since the requirements for structural strength are reduced. In addition, the low value of the circumferential speed of the blades causes low noise characteristics. Thus, a new type of vertical-axial wind turbines with a sufficiently high wind energy utilization coefficient has improved strength, reliability, environmental friendliness, and maintenance characteristics.

Thus, considering the above, the use of a vertical-axial wind power plant with KN-M blades in a wind-solar power plant is highly advisable.

### 3.2 Analysis of Simultaneous Working Wind Power Stations and Solar Cells with Energy Utilization

As for solar energy, factors such as the location latitude of solar radiation receivers, the time of the year, and the daily irradiation play a determining role. Daily irradiation is generally determined by the formula [19]:

$$H = \int G dt. \tag{7}$$

where  $H$  is the daily irradiation,  $G$  is the intensity of solar radiation per unit of time, and  $dt$  is the time period under consideration.

The intensity of solar radiation  $G$  includes the components of directed and scattered radiation:

$$G = G_b + G_d. \quad (8)$$

where  $G$  is the total irradiance of a random site,  $G_b$  is the intensity of directed radiation flow,  $G_d$  is the intensity of scattered radiation.

Thus, the feasibility of solar cells should be analyzed in each specific case, depending on the location latitude, the range of changes in the incidence angle of the directed radiation flow, the presence or absence of atmospheric pollution, and other climatic conditions. Electric energy from solar cells can be obtained in two ways [19]: using a heat engine and photovoltaic generation.

At a hybrid power plant, of course, as a source of electromotive force, solar cells are functioning in the presence of a radiation flux. Thus, the amount of energy that can be obtained from a solar cell can be determined by the formula:

$$P_c = C_{pc} \int G dt. \quad (9)$$

where  $G$  is the intensity of solar radiation at a given period,  $t$  is the period under consideration,  $C_{pc}$  is the efficiency coefficient of a solar cell. The amount of solar insolation in a specific area can be found in the relevant sources.

The efficiency coefficient of a solar cell ( $C_{pc}$ ) is the ratio of the battery energy to the energy of the solar flow at a specific area on the receiving surface of a solar cell.

The capacity characteristic of a wind-solar power plant is the sum of two energy sources capacities, which ensures greater stability of its supply to the consumer. In general, the amount of energy received over a certain period can be determined by the formula:

$$P = C_{pc} \int_{t_1}^{t_2} G dt + C_p \eta S \frac{\rho}{2} \int_{t_1}^{t_2} U_{\infty}^3 dt. \quad (10)$$

where  $C_{pc}$  is the efficiency coefficient of a solar cell,  $G$  is the intensity of solar radiation per unit of time (the  $t$  function);  $C_p$  is the utilization coefficient of wind power,  $\eta$  is the coefficient of efficiency of mechanical components of wind power installations,  $U_{\infty}$  is the wind velocity (the  $\tau$  function),  $\rho$  is the air density,  $S$  is the wind wheel area,  $t$  is the time.

The annual amount of energy can be determined using the formula:

$$R_{year} = C_{pc} \sum C_{tcp} R_{year} = C_{pc} \sum C_{tcp} \tau_Y + \frac{\rho}{2} S \sum U_{\infty}^3 \tau_n C_p \eta. \quad (11)$$

where  $G_{tcp}$  is the average insolation value per hour,  $\tau^Y$  is the annual working time, hour;  $\tau_n$  is the sum of the time (number of hours) when each type of wind speed repeats,  $\eta$  is the efficiency of the mechanical components of the wind power installation.

## 4 Results

The results of the study of the prospects for using a vertical-axial wind turbine of medium speed with a new type of blades as part of a wind-solar power plant and the analysis of the features of the joint operation of the proposed wind power plant and solar cells with further use of energy are as follows.

The expediency of using a vertical-axial wind power plant is justified, since:

1. The wind energy utilization factor of the proposed wind unit has a high value for the speed coefficient range ( $1 \leq \theta \leq 3$ ) and is at the world level of wind energy utilization values for both low- and high-speed wind turbines [20, 21].
2. The circumferential speed of the blades in the proposed wind turbine is low. This causes a small amount of centrifugal force, which is important from the point of view of the strength and reliability of operation requirements. In addition, the low circumferential speed of the wind turbine blades ensures a low noise level, which allows you to place a power plant near housing.
3. The presence of self-starting of the wind wheel and the absence of wind orientation requirements greatly simplifies the maintenance of the power plant.

The performed analysis showed that changes in solar insolation to one degree or another have a certain pattern and can be predicted. Speed changes and, consequently, wind energy, are unpredictable. In the second case, the amount of energy received changes and the circumferential speed of the blades, and the number of revolutions of the axis (shaft) of the wind turbine.

Formulas are proposed for determining the amount of energy that a wind-solar power plant will generate over a certain period of time (see above).

Since the speed of the shaft (axis) of the wind turbine of the proposed wind unit ( $1 < \theta < 3$ ) is small, it requires the use of multipliers to increase the number of revolutions, which reduces the overall efficiency and increases the cost of the wind unit. Thus, it is logical to use low-speed generators with soft characteristics for a wind plant [21].

It is concluded that since the amount of energy generated at the wind and solar power plants is unstable, it is necessary to use energy storage and storage systems to organize an uninterrupted supply of high-quality energy to the consumer. They allow storing excess generated electricity and using it in windless and cloudy weather [22]. The choice of accumulating and converting devices, as a rule, is determined by the required amount of energy given over a certain period, the requirements for its quality and consumption schedule, on the one hand, and on the other hand, the time required for energy storage [23]. For an autonomous power plant, an uninterrupted power supply to the consumer is obviously possible due to a storage device accumulating the necessary amount of energy, which can be distributed over time according to the consumer's schedule [24].

## 5 Conclusions

Analysis of information sources has shown the feasibility of wind-solar power plants, especially autonomous ones.

The prospects of using vertical-axial wind turbines of medium speed with a new type of blades in a wind-solar power plant have been studied.

A new type of medium-speed ( $1 < \theta < 3$ ) vertical-axial wind power plants is promising for use in wind and solar power plants ( $1 < \theta < 3$ ) since it has such qualities of a wind wheel as a sufficiently high wind energy utilization factor, self-starting of the wind turbine, no need for wind orientation, low centrifugal force on the blades, low noise, i.e., it shows improved characteristics in strength, reliability, ecology, and maintenance.

The features of the joint operation of the proposed wind power plant and solar cells with the further use of energy are analyzed. Recommendations are given for determining the capacity of a wind-solar power plant in terms of climatic conditions and its compliance with energy consumption requirements.

Recommendations on the choice of an electric generator and converting devices are offered, taking into account the peculiarities of the proposed wind power station.

## References






1. Plachkova, S., Plachkov, I., Dunaevskaya, N., Podgurenko, V., et al.: Energy: History, Present and Future. Vol. I: From Fire and Water to Electricity: in 4 vol. Kyiv (2020). [in Russian]
2. Global energy storage outlook 2019: 2018 year-in-review and outlook to 2024. <https://gisprofi.com/gd/documents/globalnyj-rynok-sistem-hraneniya-energii-do-2024-goda-vyrastet-v-13-raz.html>. Accessed 9 June 2021
3. Dai, H., Fujimori, S., Herran, D., Shiraki, H., Masui, T., Matsuoka, Y.: The impacts on climate mitigation costs of considering curtailment and storage of variable renewable energy in a general equilibrium model. *Energy Econ.* **64**, 627–637 (2017)
4. Kannan, N., Vakeesan, D.: Solar energy for future world: - a review. *Renew. Sustain. Energy Rev.* **62**, 1092–1105 (2016). <https://doi.org/10.1016/j.rser.2016.05.022>
5. Xu, X., Wei, Z., Ji, Q., Wang, C., Gao, G.: Global renewable energy development: influencing factors, trend predictions and countermeasures. *Resour. Policy* **63**, 101470 (2019). <https://doi.org/10.1016/j.resourpol.2019.101470>
6. Potić, I., Joksimović, T., Milinčić, U., Kićović, D., Milinčić, M.: Wind energy potential for the electricity production - Knjaževac Municipality case study (Serbia). *Energ. Strat. Rev.* **33**, 100589 (2021). <https://doi.org/10.1016/j.esr.2020.100589>
7. Lu, X.B., McElroy, M.: Chapter 4 - Global Potential for Wind-Generated Electricity. *Wind Energy Engineering*, Academic Press (2017). <https://doi.org/10.1016/B978-0-12-809451-8.00004-7>
8. Peimani, H.: Appropriate Technologies for Removing Barriers to the Expansion of Renewable Energy in Asia: Vertical Axis Wind Turbines (2021). <https://www.adb.org/publications/appropriate-technologies-removing-barriers-expansion-renewable-energy-asia>. Accessed 12 Sept 2021
9. Agresti, A., Pazniak, A., Pescetelli, S., et al.: Titanium-carbide MXenes for work function and interface engineering in perovskite solar cells. *Nat. Mater.* **18**, 1228–1234 (2019). <https://doi.org/10.1038/s41563-019-0478-1>
10. Eurek, K., Sullivan, P., Gleason, M., Hettinger, D., et al.: An improved global wind resource estimate for integrated assessment models. *Energy Econ.* **64**, 552–567 (2017). <https://doi.org/10.1016/j.eneco.2016.11.015>
11. Kudelin, A., Kutcherov, V.: Wind energy in Russia: the current state and development trends. *Energ. Strat. Rev.* **34**, 100627 (2021). <https://doi.org/10.1016/j.esr.2021.100627>

12. Ermolenko, B., Ermolenko, G., Fetisova, Y., Proskuryakova, L.: Wind and solar PV technical potentials: measurement methodology and assessments for Russia. *Energy* **137**, 1001–1012 (2017). <https://doi.org/10.1016/j.energy.2017.02.050>
13. Lu, X., McElroy, M.B.: Global potential for wind-generated electricity. *Wind Energy Engineering a Handbook for Onshore Offshore Wind Turbines*, pp. 51–73. Academic Press, San Diego (2017). <https://doi.org/10.1016/B978-0-12-809451-8.00004-7>
14. Bhattacharya, S., Wang, L., Liu, J., Hong, Yi: Chapter 13 - Civil Engineering Challenges Associated with Design of Offshore Wind Turbines with Special Reference to China. *Wind Energy Engineering*, Academic Press, San Diego (2017). <https://doi.org/10.1016/B978-0-12-809451-8.00013-8>
15. Whittlesey, R.: Vertical Axis Wind Turbines: Farm and Turbine Design. *Wind Energy Engineering: A Handbook for Onshore and Offshore Wind Turbines*. Academic Press, San Diego (2020)
16. International Energy Agency (IEA): Data and Statistics - Electricity Generation by Source, World 1990–2017. <https://www.iea.org/data-and-statistics/charts/world-electricity-generation-by-fuel-1971-2017>. Accessed 20 Feb 2021
17. Fried, L., Shukla, Sh., Sawye, S.: Growth Trends and the Future of Wind Energy. In: Chapter 26 - Global Wind Energy Council. *Wind Energy Engineering*, pp. 559–586 (2017)
18. Rozhkova, L.G.: Decentralization of power supply and operational characteristics of autonomous wind turbines. *Compr. Power Eng.* **3**(57), 25–27 (2019). [in Ukrainian]
19. Twidell, J., Anthony, D., Weir, T.: *Renewable Energy. Resources*. 2nd edn. Taylor & Francis, Abingdon (2006)
20. Nazarova, J., Gavrusev, S.: Prospects for renewable energy industry In Russia to solve unemployment problems. *Natl. Interes. Priorities Secur.* **14**, 1649–1664 (2018)
21. Vasiliev, I.: Alternative energy - harnessed wind. <https://neftegaz.ru/science/ecology/332200-alternativnaya-energiya-obuzdannyy-veter/>. Accessed 10 May 2020
22. Msuya, R.A., Kainkwa, R., Mgwatu, M.: Design of a small scale wind generator for low wind speed areas. *Tanzan. J. Sci.* **43**(1), 136–150 (2017). <https://doi.org/10.4314/TJS.V43I1>
23. Public Opinion on Climate Change and Energy Security in Europe and Russia (2018). [http://www.europeansocialsurvey.org/docs/findings/ESS8\\_pawcer\\_climate\\_RU.pdf](http://www.europeansocialsurvey.org/docs/findings/ESS8_pawcer_climate_RU.pdf). Accessed 10 May 2020
24. Sabadash, S., Savchenko-Pererva, M.Y., Radchuk, O.V., et al.: Improvement of equipment in order to intensify the process of drying dispersed food products. *East. Euro. J. Enterpr. Technol.* **1/11**(103), 15–21 (2020). <https://doi.org/10.15587/1729-4061.2020.192363>





# Correction to: Mathematical Model of Lifting Particles of Technological Material by Vertical Auger

Serhii Pylypaka , Tatiana Volina , Iryna Hryshchenko ,  
Serhii Dieniezhnikov , and Iryna Rybenko 

**Correction to:**  
**Chapter “Mathematical Model of Lifting Particles of Technological Material by Vertical Auger” in:**  
**V. Ivanov et al. (Eds.): *Advances in Design, Simulation and Manufacturing V*, LNME,**  
[https://doi.org/10.1007/978-3-031-06044-1\\_11](https://doi.org/10.1007/978-3-031-06044-1_11)

The book has been inadvertently published with misattributed affiliations in chapter 11. The affiliations of Serhii Dieniezhnikov and Iryna Rybenko were revised and updated with the correct information.

---

The updated original version of this chapter can be found at  
[https://doi.org/10.1007/978-3-031-06044-1\\_11](https://doi.org/10.1007/978-3-031-06044-1_11)

© The Author(s), under exclusive license to Springer Nature Switzerland AG 2022  
V. Ivanov et al. (Eds.): DSMIE 2022, LNME, p. C1, 2022.  
[https://doi.org/10.1007/978-3-031-06044-1\\_30](https://doi.org/10.1007/978-3-031-06044-1_30)

# Author Index

## A

Abdullo, Mamadamon A., 133  
Andreev, Artem, 259  
Avdieieva, Olena, 66  
Avershyn, Andrii, 3

## B

Babak, Tatiana, 147  
Bal-Prylypko, Larysa, 197  
Boltianska, Nataliia, 133  
Boltyansky, Oleg, 101  
Bondar, Oleksandr, 47  
Boyko, Yuriy, 197

## C

Cherkashenko, Mikhaylo, 81  
Chorni, Valentyn, 227

## D

Davydov, Denis, 187  
Demirskyy, Alexey, 147  
Deviatko, Olena, 237  
Dieniezhnikov, Serhii, 112

## F

Fatieieva, Nadezhda, 81  
Fatyeyev, Aleksandr, 81  
Fomin, Oleksandr, 47  
Forduy, Serhiy, 269

## G

Gasiyk, Alexander, 81  
Girzheva, Olena, 278

Gorbov, Viktor, 157, 249  
Gursky, Volodymyr, 91  
Gusak, Oleksandr, 81

## H

Hatala, Michal, 288  
Hrechka, Iryna, 218  
Hryshchenko, Iryna, 112

## I

Ilchuk, Nataliia, 13  
Ivanov, Vitalii, 33  
Ivchenko, Oleksandr, 33

## K

Kachur, Oleksandr, 91  
Kalinichenko, Ivan, 157, 249  
Kaniivets, Nataliia, 237  
Kantor, Serhiy, 278  
Khaldobin, Viktor, 269  
Khavin, Gennadii, 147  
Khovanskyi, Serhii, 218  
Kobalava, Halina, 249  
Konovalov, Dmytro, 157, 249  
Korendiy, Vitaliy, 91  
Kornienko, Victoria, 157  
Korobko, Volodymyr, 278  
Korohodskyi, Volodymyr, 218  
Kozlova, Olena, 55  
Krasnikov, Sergey, 3  
Kremets, Yaroslav, 55  
Kuzio, Igor, 91  
Kuznetsov, Eduard, 299

**L**

Liaposhchenko, Oleksandr, 167  
 Lingur, Valeriy, 23  
 Lypovy, Igor, 208

**M**

Machado, José, 13  
 Manoilo, Eugenia, 167, 187  
 Masikevych, Yuriy, 177  
 Meleychuk, Stanislav, 288  
 Mikhalchenko, Stepan, 133  
 Miroschnychenko, Olha, 288  
 Mishchenko, Igor, 3  
 Moiseev, Viktor, 167, 187  
 Mushtruk, Mikhailo, 197, 208  
 Mysiura, Taras, 227

**N**

Naidenko, Elena, 47  
 Neskorozhenyi, Artem, 218  
 Nikolaïenko, Mykola, 197

**P**

Palamarchuk, Igor, 208  
 Panasenko, Vladimir, 177  
 Panchenko, Anatolii, 101  
 Panina, Valeriia, 101  
 Pasternak, Viktoriya, 13  
 Pavlenko, Ivan, 33  
 Petrychenko, Ievgenii, 208  
 Ponomarova, Natalia, 187  
 Popova, Nataliia, 227  
 Pylypaka, Serhii, 55, 112  
 Pyrysunko, Maxim, 259

**R**

Radchenko, Andrii, 259, 269  
 Radchenko, Mykola, 249, 278  
 Radchenko, Roman, 157  
 Radchuk, Oleg, 299  
 Raiko, Valentyna, 177  
 Rebrii, Alla, 55  
 Repko, Kalif, 187  
 Riabova, Irina, 147  
 Rizun, Oleksandr, 269  
 Rodymchenko, Tetiana, 288  
 Rogovyi, Andrii, 3, 218  
 Rozhkova, Lyudmila, 299  
 Rybenko, Iryna, 112

**S**

Sabadash, Sergey, 299  
 Sadullozoda, Shahriyor S., 101  
 Savchenko, Ievgen, 123  
 Savchenko-Pererva, Marina, 299  
 Seif, Houssein, 167  
 Semenyuk, Vladimir, 23  
 Shestopalov, Oleksii, 177  
 Simonovskiy, Vitalii, 33  
 Slobodyanyuk, Natalia, 197  
 Solodov, Valerii, 3  
 Svirzhevskiy, Kostiantyn, 13  
 Sydorenko, Ihor, 23

**T**

Tarasevych, Yuliia, 123  
 Tkachenko, Veniamin, 259  
 Tkachev, Aleksey, 47  
 Tkachev, Anatolii, 47  
 Tonkonogyi, Vladimir, 23  
 Torba, Yuri, 66  
 Tseitlin, Musii, 177

**U**

Ulianko, Sergii, 237  
 Usatyi, Oleksandr, 66

**V**

Vanieiev, Serhii, 288  
 Vasyliv, Volodymyr, 237  
 Verbovyi, Anton, 33  
 Verkholantseva, Valentyna, 133  
 Vlasenko, Ivan, 208  
 Volina, Tatiana, 55, 112  
 Voloshina, Angela, 101

**Y**

Yeremenko, Oksana, 133

**Z**

Zabolotnyi, Oleg, 13  
 Zaporozhets, Yuliia, 227  
 Zavialov, Volodymyr, 227  
 Zhang, Yunxuan, 23  
 Zheplinska, Marija, 237  
 Zhyrkov, Oleksandr, 66  
 Zielikov, Oleksii, 269  
 Zubarev, Anatolii, 259, 278